Dissolution of Lignocellulosic Biomass in Ionic Liquids: Insights from Molecular Modeling and Experimental Studies

A Thesis

Submitted in Partial Fulfilment of the Requirement for the Degree of

DOCTOR OF PHILOSOPHY

By

Mood Mohan

Department of Chemical Engineering
Indian Institute of Technology Guwahati
Guwahati-781039, Assam, India
May, 2018

Dissolution of Lignocellulosic Biomass in Ionic Liquids: Insights from Molecular Modeling and Experimental Studies

A Thesis

Submitted in Partial Fulfilment of the Requirement for the Degree of

Doctor of Philosophy

in

Chemical Engineering

By

Mood Mohan

Department of Chemical Engineering
Indian Institute of Technology Guwahati
Guwahati-781039, Assam, India
May, 2018

Dedicated To
My Parents, Teachers, and Friends

Indian Institute of Technology Guwahati

Department of Chemical Engineering

Statement

I, hereby declare that the content embodied in this thesis entitled "**Dissolution of Lignocellulosic Biomass in Ionic Liquids: Insights from Molecular Modeling and Experimental Studies**" is the result of investigations carried out by me at the Department of Chemical Engineering, Indian Institute of Technology Guwahati, Guwahati, India, under the supervision of **Prof. Tamal Banerjee and Dr. Vaibhav V Goud**.

In keeping with the general practice of reporting scientific observations, due acknowledgements have been made wherever the work described is based on the findings of other investigators.

Guwahati,
May, 2018

Mood Mohan

Indian Institute of Technology Guwahati

Department of Chemical Engineering

Certificate

It is certified that the work described in this thesis entitled "**Dissolution of Lignocellulosic Biomass in Ionic Liquids: Insights from Molecular Modeling and Experimental Studies**" by Mr. Mood Mohan for the award of degree of Doctor of Philosophy is an authentic record of the results obtained from the research work carried out under our supervision at the Department of Chemical Engineering, Indian Institute of Technology Guwahati, Guwahati, India, and this work has not been submitted elsewhere for a degree.

Dr. Tamal Banerjee
Professor
Department of Chemical Engineering
IIT Guwahati, Guwahati – 781039
Assam, India

Dr. Vaibhav V Goud
Associate Professor
Department of Chemical Engineering
IIT Guwahati, Guwahati – 781039
Assam, India

ACKNOWLEDGEMENTS

My doctoral dissertation would not have come to a successful completion without the help of several people. I take this opportunity to express my sincere gratitude to all of them.

First of all, I am extremely grateful to my thesis supervisors **Prof. Tamal Banerjee** Sir and **Dr. Vaibhav V Goud** Sir, Department of Chemical Engineering, who motivated and made me more confident and for their valuable suggestions, incisive thinking, and cogent advice throughout whole research period. Their consistent encouragement, criticisms and painstaking planning have aided a long way for the preparation of present thesis. Their true scientific spirit, independence and self-reliance have helped me an immense to develop the quality of my research work. This feat was possible only because of the unconditional support provided by them. Whenever I went to their office, they have always made themselves available to clarify my doubts despite their busy schedules. I always strongly believe that I am blessed by God to do my doctoral programme under their guidance. To be honest, whatever knowledge I have gained during my research period that is just because of them. It was really honoured to work under them. Thank you very much sir, for your unforgettable help and support.

I would like to thank my doctoral committee members **Dr. R. Anandalakshmi**, **Dr. Nageswara Rao Peela**, **Dr. Senthilkumar Sivaprakasam**, and **Dr. Manas Das** for their valuable suggestions and comments during all assessments of the Ph. D. program. I would like to also thank my comprehensive committee members **Prof. G. Pugazhenthi**, **Dr. Chandan Das**, and **Dr. Pankaj Tiwari**.

I am thankful to **Prof. Ramgopal Uppaluri**, Department of Chemical Engineering, IIT Guwahati and **Prof. Sandip Paul**, Department of Chemistry, IIT Guwahati for given me useful suggestions and moral support during my research work. I also thank **Prof. Bishnupada Mandal**, Head, Department of Chemical Engineering, for his administrative support.

Furthermore, I would like to thank other faculty members, research scholars, supporting staff of the Department of Chemical Engineering, IIT Guwahati for their kind cooperation in all aspects.

I take this time to express my sincere gratitude to my teachers Prof. Basava Rao, Prof. Prabhakar Reddy (B.Tech project guide), Mr. Venkanna, Late Mr. Narayana, Mr. Venkateshwarlu, Mr. Yadav Reddy, and Mr. Srinivas Reddy, for their encouragement and motivation.

I owe my sincere thanks to Mr. Viswanath Pasumarthi (Ph.D., University at Buffalo, USA), Mr. Debashis Kundu (Ph.D., IITG), Mr. Kishant Kumar (Ph.D., IITG), and Mr. Narendra Naik (Ph.D., IITG). Mr. Viswanath Pasumarthi, Mr. Debashis Kundu, and Mr. Kishant Kumar helped me to learn molecular dynamics simulations while Mr. Narendra Naik helped me in enzymatic saccharification experiments.

I would also like to thank Central Instruments Facility (CIF), IIT Guwahati for providing NMR Analysis. Computational time from *PARAM-ISHAN* supercomputer (162 nodes and 3024 cores in each node), Karplus (3 nodes, 12 cores in each node), and K-80 GPU (4 nodes, 2048 cores in each node), facility of Institute, Department of Chemical Engineering, and Centre for Environment, IIT Guwahati is highly acknowledged.

Special thanks to academic people, Library facilities and staff and Core I-IV people for their necessary support in every aspect. We would like to thank each and every website from where we have acquired beneficial information. I would also like to acknowledge all the staff members of Security, Plumbing, Hospital, working AC and bus services for their friendly support throughout the stay in the campus.

I acknowledge Ministry of Human Resource Development (MHRD) and our institute for providing fellowship throughout the PhD program. I would also like thanks to Department

of Science and Technology (DST), India for financially supporting to attending an International Conference “Thermodynamics2017” which was held in Edinburgh, UK.

I deeply acknowledge my research group members Ms. Basudhriti Banerjee, Ms. Garima Srivastava, Mr. Chitta Ranjan Barik, Mr. Atanu Kumar Paul, Mr. Robinson Timung, Mr. Abhishek Shukla, Mr. Roopesh Verma, Ms. Rima Biswas, Mr. Debashis Kundu, Mr. Papu Kumar Naik, Mr. Pyari Mohan, Ms. Upasana, Ms. Sutapa Das, Ms. Debeni Devi, Mr. Sukumar Purohit, Mr. Pravin Suryawanshi, Mr. Abebe, Mr. Dhirendra Mishra, Ms. Pushpita Das, Mr. Rupjyoti Bhuyan, Mr. Nabendu Paul, Mr. Nikhil Kumar, Mr. Gaurab Sarkar, Ms. Tooba Fatma, Mr. Sarvesh Namdeo, Mr. Akash, Mr. Ankit, Mr. Vikas Kumar, Mr. Rahul Tiwari, Mr. Ravi, Mr. Janardan, Mr. Tapan Sarma for providing a co-operative research environment.

I would like to express my profound gratitude to my seniors Dr. Venu Babu, Mr. Chilakoti Balaji, Dr. Santhi Raju Pilli, Dr. Swaroopa Rani Dasari, Dr. Dharamashibhai V. Rabary, Dr. Anand Bharti, Dr. Sanjukta Boi, Dr. Ali S. Reshad, Dr. Soumya Sasmal, Dr. Ananth Praveen Kumar, Dr. Devendra Kumar, and Dr. Amrita Difusa for their immense support, encouragement and help.

My sincere thanks to IIT Guwahati friends Dr. Kelothu Suresh, Dr. Sanjib Barma, Dr. Vikranth Volli, Dr. Gopi Kiran (Gurujee), Dr. Shyam Yadav, Dr. Chinna Kaniganti, Dr. Bandi Chandrashekar, Dr. Yadav, Dr. Anil Kumar, Dr. Kanchapogu Suresh, Dr. Madhusmita Dash, Dr. Prashanth Roy, Dr. T. Bheem Raju, Dr. Shilpi Verma, Dr. P. Gopikrishna, Dr. Karuna Mahato, Dr. Ramanjaneyulu Unnava, Dr. Devulapalli Mahesh, Dr. Nitesh Kumar Mund, Mr. Radhakrishna Gattu, Mr. Raj Kumar Das, Mr. Ramavath Sunil, Mr. Ramesh Naik Bhukya, Mr. Kiran Naik Bhukya, Mr. Sohanbhir Singh, Mr. Shailesh Varade, Mr. Katila Dilleswar Rao, Mr. Manjunath Reddy, Mr. Srinu Nagireddi, Mr. Vanaparthi Satheesh, Mr. Rahul Narasimhan, Mr. Upendar Reddy, Mr. Endalu Lemma, Mr. Mayur Mitra, Ms. Ayushi Tripati, Ms. Srijita Paul, Ms. Sri Devi, Ms. Athira V.B., Mr. Vamsi Krishna Sagar, Ms. Nibedita

Behera, Ms. Kemeli Gogai, Ms. Preethi Arul Murugan, Mr. Pankaj Jha, Mr. Vidyapu Sandeep, Mr. Ogene Fortunate, Mr. Nasaba John Ceasar, Mr. D.V. Ganesh, and many more for making my stay at IIT Guwahati memorable.

I would like to thank my B.Tech friends (seniors, classmates and juniors) Mr. Balaji Guguloth, Mr. Ajith Kumar, Mr. Banoth Laxman, Mr. Hari Kishan, Mr. Nandipati Ravi, Mr. Kishan Banoth, Mr. Bhattu Naresh, Mr. Koteswar Rao Dharavath, Mr. Raju Amarlapudi, Mr. Amarender Yennamalla, Mr. Ashok Kodama, Mr. Anurag, Mr. Rajamahender, Mr. Manohar, Mr. Tekula Srinu, Mr. Madhusudhan, Mr. Santhosh, Mr. Chaitanya, Mrs. Meghana, Mr. Nadeem, Mr. Nafeez, Mr. Vinay, Mr. Vishnu Boddupally, Mr. Hanumanth Naik, Mr. Hanumanth Kethavath, Mr. Manoj Kumar, Ms. Uma Chaitanya, Ms. Rajitha Reddy, Ms. Rohita Divva, Ms. Leena Christina, Ms. Prashanthi, Mr. Panga Mahesh, and Mr. Vinod Kumar, for their help during my B.Tech life.

I express my sincere blessings and sweet thanks to my little friends Indu Priya, Vishnu Priya, Dharmateja, Rohith Chandra, Shanvi, Viharika, Tanmai, Nikshitha, Lokeshwar, Surya Prakash, Surendar, Harshith (Bunna), Dinesh Karthik, Lokesh, Laxmi Prasanna, Muskaan, Bhavana, and Lourishka, for given me lots of memorable fun and joy. My dear little friends, May God bless you with everything you desire, May you get to new heights of success, and I hope you always see higher.

Words of motivation and encouragement from some of my friends and relatives were only a call away. They always appreciated my efforts and outcomes of my research work. My sincere gratitude to Mr. Chandru Garu, late Mrs. Poolamma Garu, Mr. Biksham Garu, Mrs. Sattemma Garu, Mr. Bhikku Garu, Mrs. Kamili Garu, Mrs. Jakkamma Garu, Mr. Venkanna annaya, Mrs. Vijaya, Mr. Ramesh annaya, Mrs. Devi, Mr. Ravinder annaya, Mrs. Srilatha, Mrs. Bhagya Laxmi akka, Mrs. Jyothi akka, Mr. Veeranna annaya, Mrs. Padma, Mr. Hanma Garu, Mrs. Mangamma Garu, Mr. Ramesh Bava, Mrs. Punnamma, Mr. Madhu, Mr. Amru

Naik, Mr. Kishan, Mr. Srinu annaya, Mrs. Nagamma, Mr. Yadagiri, Mrs. Laxmi, Mrs. Vanaja, Mr. Suresh Banoth, Mr. Laxman Banoth, Mrs. Soniya Banoth, Ms. Rani Banoth, Mr. Vinod Guguloth, Mr. Jaffer Baba, Mrs. Shahina, Mrs. Shameena, Mrs. Srilatha, Mrs. Shailaja, Mrs. Parvathi, Mrs. Santhoshi, Mrs. Navya (Nagamani), and many more.

Last but not least, I want to convey my sincere gratitude to my parents and family members for their sustained help and encouragement in all my personal and academic ventures. I feel proud and blessed to have such parents my mother **Mrs. Kanthamma** Garu and my father **Mr. Golia** Garu, my uncles **Mr. Krishna** Garu and, late **Mr. Dharma** Garu and my aunties **Mrs. Bujamma** Garu, **Mrs. Manikyamma** Garu, and **Mrs. Neelamma** Garu. Special thanks to my one and only loving brother **Krishna** and his wife **Shravani** who always strengthened my morale by standing by me in all situations. I sincerely express my wholehearted gratitude to "QUEEN MLA". I will be thankful to them and I promise I shall never forget their uncountable help and encouragement. Today, I am in this position that is just because of my parents. I do not find words to express my gratitude to them and they are always in my heart. I feel deeply indebted to them for whatever I have achieved so far.

I wish to thank many other people whose names are not mentioned here but this does not mean that I have forgotten their help. Above all, I am thankful to GOD for giving me a wonderful and healthy life.

We have no right to ask when a sorrow comes, "why did this happen to me?" unless we ask the same question for every joy that comes our way.

- **Lord Rama to Laxman**

MOOD MOHAN

ABSTRACT

Lignocellulosic biomass has been identified as a suitable feedstock for the production of fuels and chemicals. This is required due to the high utilization of fossil fuels which has increased the production of carbon dioxide and had a direct impact on the economic, environmental, political, and life quality of population. Therefore, the current thesis work aims at to dissolve the lignocellulosic biomass and its derived components namely cellulose, hemicellulose, disaccharides and monosaccharides in suitable ionic liquids (ILs). Precise experimental data and reliable theoretical models are basic requirements for the better understanding the dissolution process. In order to evaluate the potential ILs, COSMO-RS model has been used to screen the vast number of ILs for the solvation of cellulose, hemicellulose and simple sugars. Based on the infinite dilution activity coefficients (IDAC) of the components in IL, the selected anions and cations were then visualized by observing their interactions with cellulose, hemicellulose and simple sugars using interaction energies, natural bonding orbital (NBO) analysis and molecular dynamics (MD) simulations. The experimentally obtained solid-liquid equilibria (SLE) values of monosaccharide and disaccharides were then compared with COSMO-RS predicted values. The solubility of monosaccharides and disaccharides in ILs were found to increase with increasing temperature. In addition, the NRTL and UNIQUAC models were successfully correlated with experimental data with a maximum deviation of 5%.

The dissolution order of cellulose and hemicellulose in ILs was primarily determined by the evaluation of hydrogen bonds between the oxygen atom of anion and hydroxyl proton of cellulose/hemicellulose. From this discernible fact, the anion of the IL was observed to play a leading role in the dissolution process as compared to the cation in the solvation process. Eventually, acetate $[OAc]^-$ anion and 1-ethyl-3-methylimidazolium $[Emim]^+$ cation were found

to be good candidates for the dissolution of cellulose and hemicellulose. Furthermore, two categories of cosolvents namely protic and aprotic solvents have been selected in order enhance the cellulose dissolution IL. From MD simulations results, aprotic solvents were found to be a best cosolvent for the enhancement of cellulose dissolution in IL. This was further confirmed by the measurement of solid-liquid equilibria with cellulose. The regenerated cellulose powder was then characterized by Fourier transform spectroscopy (FTIR), X-ray diffraction (XRD) and thermal gravimetric analysis (TGA).

Pretreatment of lignocellulosic biomass is an essential step in a commercial biorefinery. Therefore, the current thesis also investigates the efficiency of two pretreatment pathways of biomass, namely ionic liquid and dilute acid (H_2SO_4) hydrolysis. Both the processes are compared in terms of their composition and enzymatic saccharification efficacy. For the IL process, bamboo was dissolved in [Emim][OAc] at different temperatures (90 °C, 110 °C, 130 °C, and 150 °C) for 3 h. The crystallinity index, thermal decomposition temperature, hemicellulose and lignin content of bamboo found to decrease during [Emim][OAc] pretreatment. The enzymatic hydrolysis rate for IL pretreated biomass was 4.7 times higher than that of the dilute acid. This was primarily attributed to the difference in the crystallinity and delignification in IL process. To improve the enzymatic hydrolysis efficiency of bamboo, combined pretreatment (dilute acid + ionic liquid) process was also employed and compared with IL pretreated cellulose and bamboo samples. The results of the study revealed that IL pretreatment may offer unique advantages compared to dilute acid pretreatment process for bamboo which can produce high sugar yields with IL pretreatment.

Table of Contents

List of Figures

List of Tables

List of Abbreviations and Symbols

Abbreviations	
AMBER	Assisted Model Building with Energy Refinement
AARD	Average Absolute Relative Deviation
ABS	Aqueous biphasic system
AcM	Acetamide
B3LYP	Becke three-parameter, Lee-Yang-Parr
BSSE	Basis Set Superposition Error
CHARMM	Chemistry at Harvard Macromolecular Mechanics
CHELPG	CHarges from Electrostatic Potentials using a Grid based method
CN	Coordination Number
COSMO-RS	COnductor like Screening MOdel for Real Solvents
DFT	Density Functional Theory
DGA1	Density Gradient Approximation
DMAc	N,N-dimethylacetamide
DMF	N,N-dimethylformamide
DMSO	Dimethyl sulfoxide
EA	Electron Affinity
FRM	Formamide
FTIR	Fourier transform spectroscopy
GA	Genetic Algorithm
GAFF	Generalized AMBER Force Field
GEPOL	GEometry of POLyhedron
HF	Hartree–Fock
HOMO	Higher Occupied Molecular Orbital
HPLC	High Pressure Liquid Chromatography
IDAC	Infinite Dilution Activity Coefficient
IL	Ionic Liquid

IE	Interaction Energy
IP	Ionization Potential
LUMO	Lower Unoccupied Molecular Orbitals
MCC	Microcrystalline Cellulose
MD	Molecular Dynamics
MOLDEN	Molecular Density from the ab Initio packages
M Wt	Molecular Weight
NAMD	Nanoscale Molecular Dynamics
NBO	Natural Bonding Orbitals
NMR	Nuclear Magnetic Resonance
NPA	Natural Population Analysis
NRTL	Non-Random Two-Liquid model
PCM	Polarizable Continuum Model
QC	Quantum Chemical
R_{DMSO}	IL to DMSO molar ratio
$R_{cosolvent}$	IL to Cosolvent molar ratio
$R_{Antisolvent}$	IL to Antisolvent molar ratio
RDF	Radial Distribution Functions
RESP	Restrained Electrostatic Potential
RMSE	Root Mean Square Error
SCRF	Self-Consistent Reaction Field
SLE	Solid-Liquid Equilibrium
TGA	Thermo-Gravimetric Analysis
TZVP	Triple Zeta Valence Potential
UNIQUAC	UNIversal QUAsi-Chemical
VMD	Visual Molecular Dynamics
XRD	X-ray Diffraction

Ionic Liquids	
[EMIM][SCN]	1-ethyl-3-methylimidazolium thiocyanate
[AMIM]Cl	1-allyl-3-methylimidazolium chloride
[TMA][$MeSO_4$]	Tris(2-hydroxyethyl)methylammonium methylsulfate
[EMIM][Br]	1-ethyl-3-methylimidazolium bromide
[HMIM][HSO_4]	1-hexyl-3-methylimidazolium hydrogensulfate
[BMIM][OAc]	1-butyl-3-methylimidazolium acetate
[BMIM][HSO_4]	1-butyl-3-methylimidazolium hydrogensulfate
[EMIM][OAc]	1-ethyl-3-methylimidazolium acetate
[EMIM][$EtSO_4$]	1-ethyl-3-methylimidazolium ethylsulfate
Aliquat®336 or [MTOA][Cl]	Methyltrioctylammonium chloride
[BMPyr][DCA]	1-butyl-1-methylpyrrolidinium dicyanamide
[BMP][DCA]	1-butyl-1-methylpiperidinium dicyanamide
[BMPyr][Cl]	1-butyl-1-methylpyrrolidinium chloride
[BMIM][Cl]	1-butyl-3-methylimidazolium chloride
[EtOHMIM][Cl]	1-ethanol-3-methylimidazolium chloride
[DMIM][MPh]	1,3-dimethyl-imidazolium methylphosphonate
[TTDP][DCA]	Trihexyltetradecylphosphonium dicyanamide
[EMIM][DCA]	1-ethyl-3-methylimidazolium dicyanamide
[BMIM][DCA]	1-butyl-3-methylimidazolium dicyanamide
[BMIM][Me_2PO_4]	1-butyl-3-methylimidazolium dimethylphosphate
[EMIM][$MeSO_3$]	1-ethyl-3-methylimidazolium methanesulfonate
[EMIM][Tos]	1-ethyl-3-methylimidazolium Tosylate
[BMIM][HCOO]	1-butyl-3-methylimidazolium formate
[OMIM][OAc]	1-octyl-3-methylimidazolium acetate
[EMIM][F]	1-ethyl-3-methylimidazolium fluoride
[BMIM][BF_4]	1-butyl-3-methylimidazolium tetrafluoroborate
[BMIM][PF_6]	1-butyl-3-methylimidazolium hexafluorophosphate

List of symbols	
a_{eff}	Effective contact surface area of a segment in Å^2
C_{hb}	Hydrogen-bonding coefficient
E_{misfit}	Misfit interaction energy
E_{vdW}	Van der Waals (vdW) interaction energy
$p_s(\sigma)$	Probabilistic surface charge distribution for mixture (S)
$p^{X_i}(\sigma)$	Sigma profile of the pure component *i*
r_{n}	Radius of the nth segment
r_{eff}	Radius of the standard surface segment (a_{eff}) in Å
r	Pure component volume
q	Pure component area
r_{avg}	Average radius in Å
R	Universal gas constant in (kcal mol^{-1} K^{-1})
T	Temperature in K
SG	Staverman-Guggenheim term
Q	Normalized area parameter
x_i	Mole fraction of species '*i*'
d_{mn}	Distance between the m^{th} and n^{th} segment
A^{PCM}	Molecular surface area in Polarizable Continuum Model, in^2
A_{ws}	Standard segment area, cm^2 mol^{-1}
V^{PCM}	Molecular surface volume in Polarizable Continuum Model, in^3
V_{ws}	Standard segment volume, cm^3 mol^{-1}
g_{ij}	Energy parameter characterizing the interaction of species i and j (NRTL binary interaction parameter)
u_{ij}	Energy parameter characterizing the interaction of species i and j (UNIQUAC binary interaction parameter)
x_{solute}^{exp}	Experimental mole fraction of solute
x_{solute}^{pred}	Predicted mole fraction of solute

Greek Symbols	
$\Gamma_s(\sigma)$	Segment activity coefficient for mixture (S)
$\Gamma_i(\sigma)$	Segment activity coefficient for pure component (i)
$\gamma_{i/s}$	Component activity coefficient in the mixture (S)
Φ_i	Fugacity coefficient of the component in mixture
α	Non-randomness parameter
α'	Misfit constant in kJ mol^{-1} Å^{-2}
σ, σ'	Screening charge density in e Å^{-2}
σ_{don}	Screening charge density for hydrogen-bond donor in e Å^{-2}
σ_{acc}	Screening charge density for hydrogen-bond acceptor in e Å^{-2}
σ_{hb}	Screening charge density for hydrogen-bond in e Å^{-2}
τ_{vdW}	Dispersion coefficient in kJ mol^{-1} Å^{-2}
$\mu_s(\sigma)$	Sigma potential in kJ mol^{-1} Å^{-2} for a surface segment in solution S

Chapter – 1

Introduction and Literature Review for the Dissolution of Lignocellulosic Biomass and its Derived Compounds in Ionic Liquids

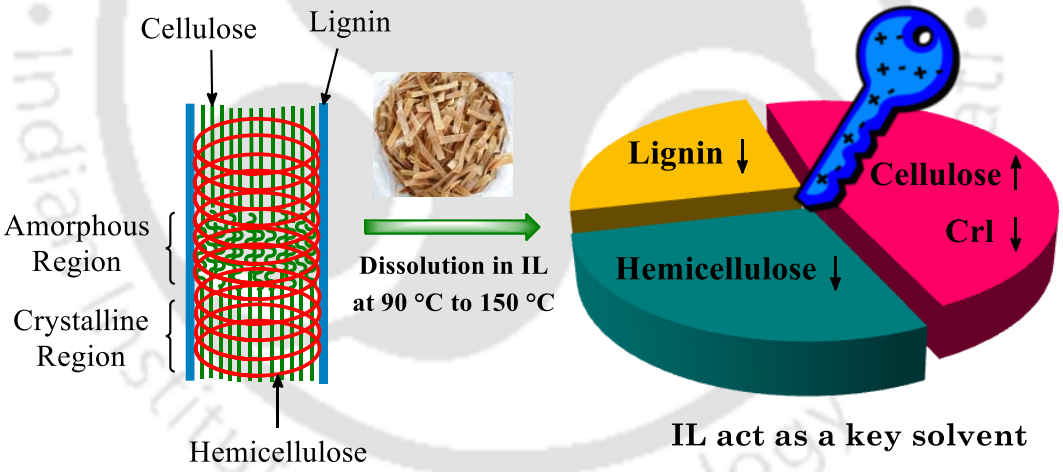

1 Introduction to Lignocellulosic Biomass Dissolution

1.1. Liquid Fuels and Chemicals from Lignocellulosic Biomass

Since the last few decades, a continuous increase in the worldwide energy demand and population growth have pushed the utilization of fossil fuels for the production of energy and chemicals, especially in emerging market economies [1]. The high utilization rates of fossil resources have henceforth provided a direct impact on the economic, environmental, political spectrum, and life quality of the population. Further with increasing emission of greenhouse gases have also aggravated the global warming. This has led to the search for an alternative energy solution so as to decrease the consumption of fossil resources. A potential alternative solution to this problem could be the utilization of lignocellulosic biomass as an alternative renewable energy source for the future. It can be also used to produce value-added chemical and additionally these resources do not compete with the food production [2,3]. Currently, an extensive research is being undertaken to transform lignocellulosic biomass to environmentally friendly power energy and value-added chemicals [4,5]. The use of biomass for energy also inhibits an increase of CO_2 in the atmosphere [6]. As per the facts, the aggregate energy prepared from photosynthesis is ten times higher than that of fossil fuel asset utilized within the world [7]. For the management and maintenance of natural resources, 170 states have signed on the action program for the 21st century (Agenda 21) in the year 1992 in Brazil. The aim is to decrease the fossil resources and non-renewable resources (petroleum, natural gas, coal, and minerals) [8].

Lignocellulosic biomass is mainly dominated by three naturally occurring polymers, cellulose (30-50%), hemicellulose (25-35%) and lignin (5-30%) [3]. The sources of lignocellulosic biomass are waste agriculture residue, wood, grass, forestry and municipal solid wastes and these are acknowledged as tempting feedstock for the production of fuel alcohol, due to their accessibility in huge amounts at a lower price [9]. Among the three major

components of lignocellulosic biomass, cellulose is the primary constituent in any biomass which produces oligosaccharides (cellotetraose, cellotriose, and cellobiose), and monomeric sugars (glucose and fructose) [10]. It is cheap and most abundant organic matter on the earth [11]. Cellulose has three hydroxyl groups in each glucose molecule combines at β(1→4) position (Figure 1.1a). Cellulose has more affinity to water due to which it dissolves in water at high temperature [10]. Cellulose molecule has strong inter and intramolecular hydrogen linkages through the hydroxyl groups and forms crystal structure at typical conditions (Figure 1.1b) [12].

Hemicellulose is the second most abundant polymer (20-50%) of lignocellulose biomass and differs from cellulose in that it is not chemically homogeneous [13]. Hemicelluloses are branched, heterogeneous polymers of pentose (xylose, arabinose), hexose (mannose, glucose, and galactose), and acetylated sugars (Figure 1.2). Hemicellulose sugars have a lower molecular weight compared to cellulose and limbs with short horizontal chains that are effortlessly hydrolyzed [13]. Hemicelluloses in agricultural biomass like straw and grasses are composed mainly of xylan while softwood hemicelluloses contain mainly glucomannan [8]. In many plants, xylans are heteropolysaccharides with backbone chains of (1,4)-linked β-D-xylopyranose units. Among the key components of lignocellulosic biomass, hemicelluloses are the most thermo-chemically sensitive [14].

Lignin is one of the most abundant polymer and renewable bio-resource in nature with unique functionalities. It is asymmetrical, cross-linked and a polyphenolic polymer which binds the wood compounds together. It is relatively aromatic while at the same time hydrophobic in nature. Lignin comprises of three phenylpropanoid monomers that are coniferyl alcohol, sinapyl alcohol, and p–coumaryl alcohols (Figure 1.3) [14].

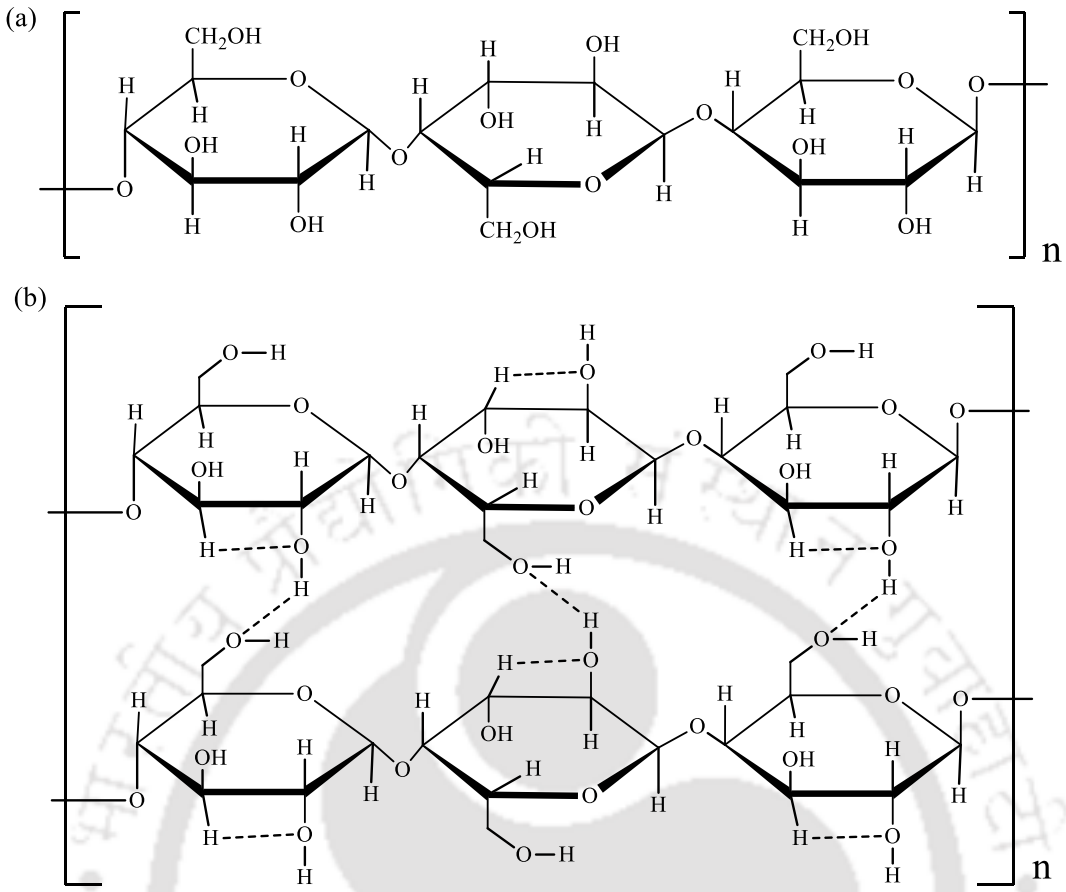

Figure 1.1: The network of (a) cellulose chain and (b) inter and intra-molecular hydrogen bonds present in cellulose

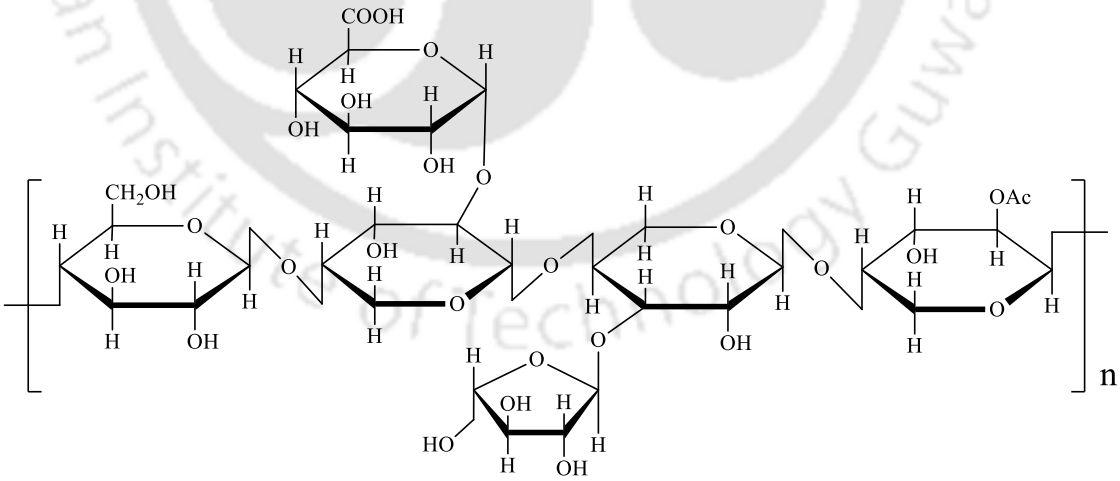

Figure 1.2: The chemical structure of hemicellulose

Lignin is by and large acknowledged as “glue” that binds the dissimilar compound of lignocellulosic biomass together, making it insoluble in water [13]. Softwood lignin is made

out of coniferyl moieties, whereas hardwood lignin comprises of both coniferyl and sinapyl alcohols. Lignin is used in dispersants, froths, surfactants, phenolic and thermosetting resins [15,16]. Coniferyl alcohol is an intermediate in the biosynthesis of eugenol, stilbenoids, and coumarin. As opposed to utilizing lignin within the aforementioned provisions, it is can fundamentally be also used as fuels.

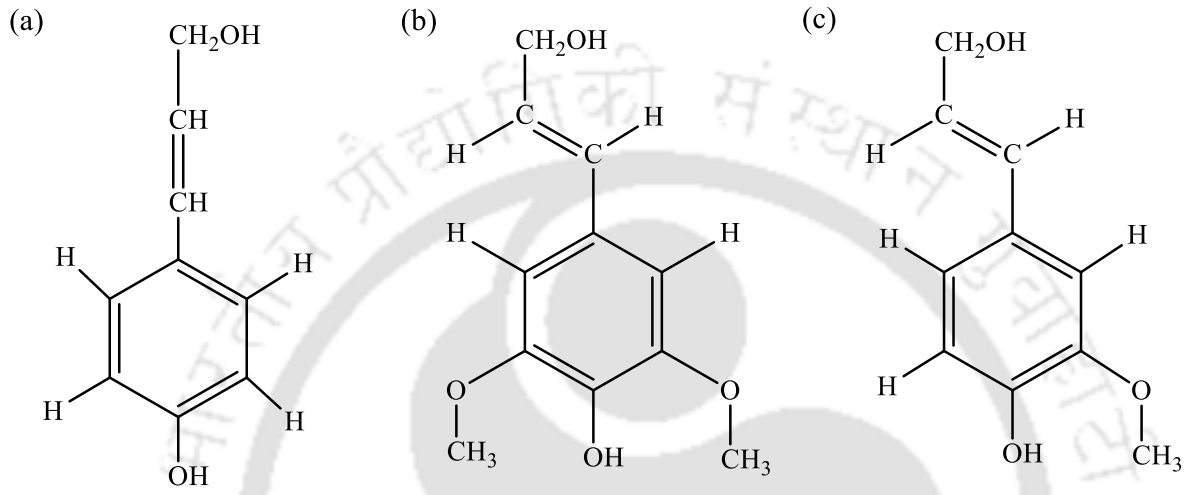

Figure 1.3: Chemical structure of lignin components: (a) p–coumaryl alcohol, (b) sinapyl alcohol and (c) coniferyl alcohol

From the aforementioned discussions, it is clear that different lignocellulosic materials have different physio-chemical characteristics, so it is necessary to take up suitable pretreatment technologies based on the lignocellulosic biomass properties of each raw material. Biomass pretreatment is needed for several reasons. The primary point of lignocellulosic biomass pretreatment is to alter the cellulose structure and make the cellulose structure more accessible to enzymatic hydrolysis and/or chemicals production [3]. The lignin seal of the cellulose must be broken which enables the disruption of the crystalline structure of cellulose (Figure 1.4). One of the primary routes of fuels under consideration involves the isolation of the cellulose and hemicellulose components of biomass, and then its hydrolysis to produce glucose and xylose, and further subsequent fermentation of these sugars to produce ethanol or butanol [3,13].

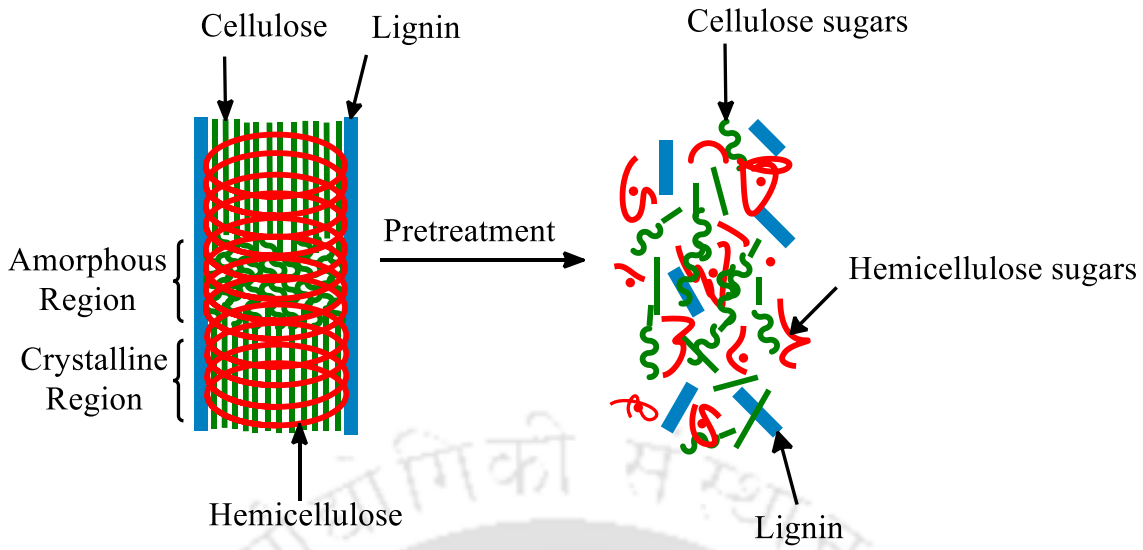

Figure 1.4: Aim of lignocellulosic biomass pretreatment

1.2. Assessment of Pretreatment Technology

The pretreatment process produces a disrupted, hydrated substrate that is easily hydrolyzed. However, it does not aid in the formation of sugar degradation products and fermentation inhibitors. Assessment of biomass pretreatment processes depends on a parameter called the "severity factor", which is defined as the combined effect of temperature, acidity or solvent to solute ratio, and duration of pretreatment. Studies on biomass pretreatment have used the severity factor for comparing pretreatment results even though it does not provide an accurate measure of the severity. In other words, it is used for rough estimate [17]. Pretreatment assessment is conducted by following steps

i) Analyzing the sugars (both monomers and oligomers) released in the liquid and the carbohydrate content of the water-insoluble solids (WIS) after pretreatment. This gives the total amount of recoverable carbohydrates

ii) Enzymatic hydrolysis of either the washed or unwashed WIS

iii) Fermentation of the pretreated liquid to assess its fermentability directly or diluted to target concentration and inhibition of fermenting microorganisms with respect to growth

iv) Fermentation of either the slurry or washed WIS for biofuel production, and

v) Assessment of additional biotechnological potential of the pretreated fractions such as value-added products. For example, Ammonia Fibre/Freeze Explosion pretreated (AFEX) WIS can be used as a nutritional supplement in cattle feed.

1.3. Pretreatment Methods for Lignocellulosic Biomass

Many pretreatment processes have been proposed for lignocellulosic biomass conversion. They includes physical pretreatment (mechanical comminution), biological pretreatment, chemical pretreatment (acid, alkaline, ionic liquid, sub and supercritical water treatments), and physio-chemical pretreatment (steam explosion, liquid hot water, Ammonia fiber explosion, Wet oxidation, Carbon dioxide (CO_2) explosion, organosolv, and Ozonolysis) [7,8,13,17-19]. Altogether, these processes require suitable solvents for the dissolution of biomass based components [20]. Biomass is hard to dissolve in common organic solvents due to their complex structure and strong intra- and inter-molecular hydrogen bonding [7]. It is also well known that cellulose is insoluble in water and hard to dissolve in common organic solvents [21]. Even though certain organic solvents, water, and inorganic salt mixtures have been used to break the highly ordered crystalline structure of cellulose. However, most reported solvents have drawbacks of one kind or another, such as volatility, toxicity, high cost, and difficulty in solvent recovery, high processing temperature, and process instability [22,23]. Table 1.1 represents the summary of various pretreatment methods with their advantages and disadvantages. It is difficult to evaluate and compare pretreatment technologies because they involve upstream and downstream processing, capital cost, chemical recycling and waste treatment systems [19]. Further, the pretreatment process should be environmentally friendly and possess low capital and operational cost. Therefore, it is imperative to develop greener solvents for biomass or cellulose dissolution under mild conditions. If a special solvent is available that is able to dissolve any of the three components, it would then weaken the

biomass structure and make the biomass more accessible for enzyme hydrolysis [18]. Among all the pretreatment methods, ionic liquids (ILs), sub and super-critical water treatments are considered as green treatment methods because ILs and water are green solvents [9,13].

Table 1.1: Summary of various processes used for the pretreatment of lignocellulosic biomass

Method	Pretreatment process	Mode of action	Advantages	Disadvantages
Physical	Mechanical Comminution	Room temperature Energy input < 30 kW per ton biomass	Reduces cellulose crystallinity	Power consumption usually higher than inherent biomass energy
Physio-chemical	Steam explosion	High pressure (0.69-4.83 MPa) and temperature (160-260 °C) for 5-15 min	Causes hemicellulose degradation and lignin transformation; cost-effective for hardwoods and agricultural residues	Destruction of a portion of the xylan in hemicellulose; incomplete disruption of the lignin-carbohydrate matrix; generation of inhibitory compounds
	AFEX (Ammonia fiber explosion method)	Anhydrous liquid ammonia loading of 1:1 to 1:2 (1- 2 kg ammonia /kg dry biomass) for 10-60 min at 60-90 °C and 3 MPa.	Increases accessible surface area removes lignin and hemicellulose to an extent; does not produce inhibitors for downstream processes	Not efficient for biomass with high lignin content i.e., 18-30 %. environmental concerns with the stench of ammonia has a negative impact on the pilot as well as industrial scale applications
	Lime or caustic pretreatment (LP)	The pretreatment utilizes aqueous $Ca(OH)_2$ at low temperatures (25-130 °C) and pressures as a pretreatment agent to solubilize hemicellulose and lignin.	Performed at lower temperature and pressure which avoids the huge energy demands required to maintain high thermal steady state conditions during pretreatment	Higher reaction time (2 h). Remove the acetyl and uronic acid substitutions on hemicellulose making biomass less accessible to enzymes. LP is not very effective for removing lignin

Table 1.1: Continued…

Method	Pretreatment process	Mode of action	Advantages	Disadvantages
	Wet oxidation	148-200 °C for 30 min	Efficient removal of lignin; low formation of inhibitors; low energy demand	High cost of oxygen and alkaline catalyst
	Organosolv (OP)	OP is conducted at high temperatures (100–250 °C) using low and high boiling point solvents	Hydrolyzes lignin and hemicelluloses	Solvents need to be drained from the reactor, evaporated, condensed, and recycled; High costs due to the solvents recovery
	Carbon dioxide (CO_2) explosion (CDE)	4 kg CO_2/kg fiber at 5.62 MPa 160 bar for 90 min at 50 °C under supercritical carbon dioxide	Increases accessible surface area; cost-effective; does not cause formation of inhibitory compounds	It is not suitable for biomass with high lignin content (such as woods and nut shells) Does not modify lignin either hydrolyze hemicellulose
	Liquid hot water (LHW)	Operated at lower temperatures (160–190 °C)	LHW is that lower temperatures are used, minimizing the formation of degradation products.	The amount of solubilized product is higher, while the concentration of these products is lower; Down-stream processing is also more energy demanding because of the large volumes of water involved.
	Ozonolysis	Room temperature	Reduces lignin content; does not produce toxic residues	Large amount of ozone required; expensive
Chemical	Dilute acid hydrolysis	DA pretreatment using preheated sulfuric acid at the desired temperature from 140 to 215 °C for 1-3 h.	Hydrolyzes hemicellulose to xylose and other sugars; alters lignin structure	High cost; equipment corrosion; formation of toxic substances.

	Alkaline hydrolysis	Low temperature and high time; Concentration of the base; For soybean straw: ammonia liquor (10 %) for 24 h at room temperature	Removes hemicelluloses and lignin; increases accessible surface area	Long residence times required; irrecoverable salts formed and incorporated into biomass
Biological	Biological	Several fungi (brown-, white- and soft-rot fungi	Degrades lignin and hemicelluloses; low energy requirements	Rate of hydrolysis is very low; Large amount of space is required; 10-14 days requirement of careful growth conditions

1.4. Ionic Liquids for Biomass Dissolution

Till date, researchers have employed a variety of experimental techniques to study the dissolution mechanism of the lignocellulosic biomass or cellulose [13,19]. But in recent years, ILs has gained more attention towards the dissolution of lignocellulosic biomass [24]. ILs are a special group of organic salts (*i.e.*, organic cations and organic/inorganic anions) that can exist in liquid form at relatively low temperatures (less than 100 °C) and some can even exist as liquids at room temperature [25]. ILs are suitable solvents in the biorefining processes because ILs exhibits several attractive properties such as negligible vapor pressure, high thermal and chemical stability, non-flammability, non-toxic and high ionic conductivity [26,27]. It was also reported that the decomposition temperature of numerous imidazolium based ILs ranges from 253 °C to 455 °C. They are described as “tunable solvents” due to the convenience of making modifications in their anion or cation types according to specific targets. Therefore, ILs could be used as a solvent, extracting agent and catalyst for some special kind of reactions [28,29]. ILs are considered to be environmentally friendly, because of its non-volatility and other properties**.** ILs are applied in many applications such as separation, nanotechnology, bio-refineries and electrolytic materials (see Figure 1.5) [30]. ILs

have proven to be better solvents for the dissolution of carbohydrates. The IL such as ethylammonium nitrate ($[EtNH_3][NO_3]$) was first synthesized in 1914. In 1980, there were few ILs which increased to 100 in the year of 2004 and 800 by the end of 2008 [31]. A small change in cationic or anionic structure results in a large variation in the physical and chemical properties such as density, viscosity and chemical affinity [29,31]. For a better solubility, ILs should satisfy the following conditions: 1) the anion should be a good hydrogen bond acceptor, 2) the cation should be a moderate hydrogen bond donor as the cation possess a moderate activated hydrogen for forming hydrogen bonding with oxygen atoms [3]. Figure 1.6 and 1.7 shows the structures of cations and anions, which are generally used in biomass dissolution process.

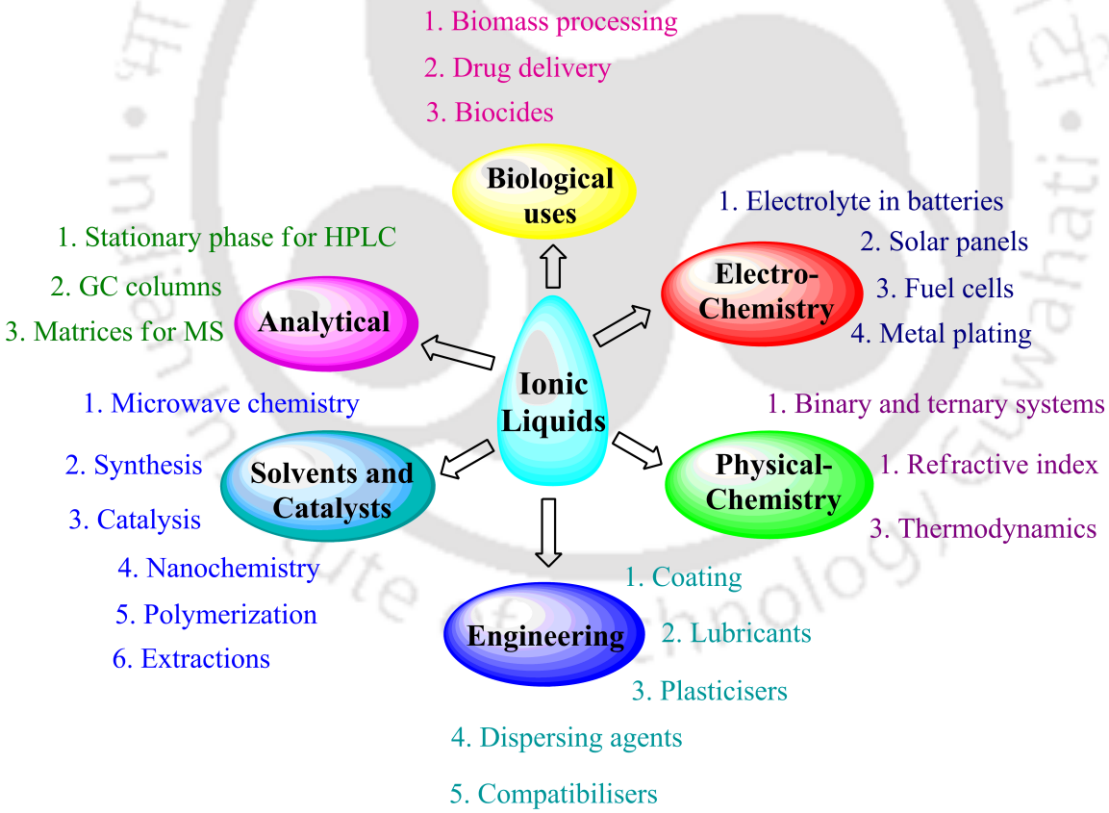

Figure 1.5: Various applications of ionic liquids

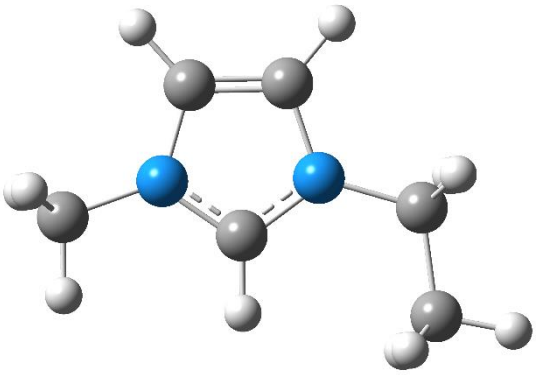

1-ethyl-3-methylimidazolium $[Emim]^+$

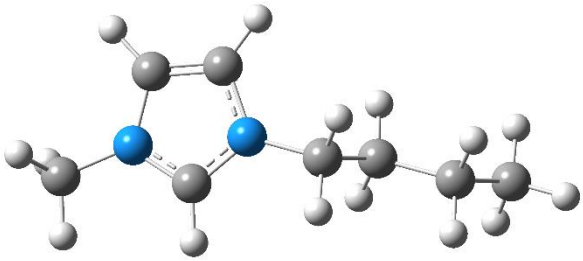

1-butyl-3-methylimidazolium $[Bmim]^+$

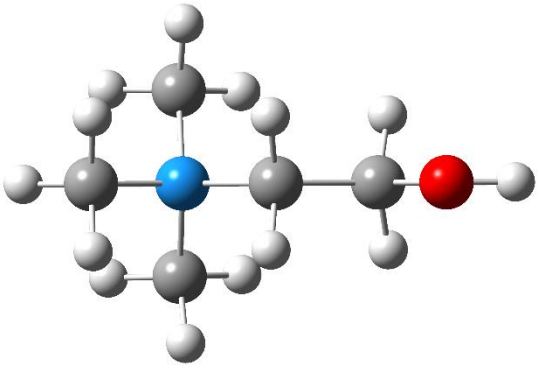

Choline

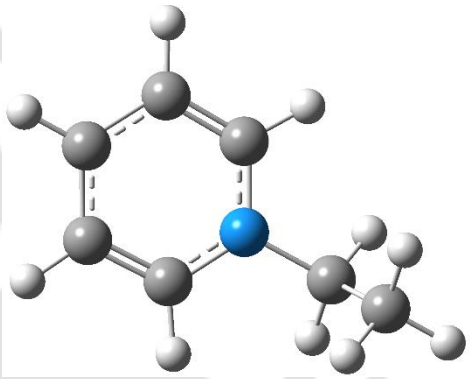

1-ethylpyridinium $[EPy]^+$

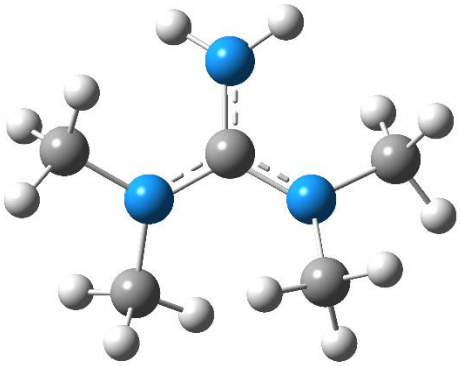

1,1,3,3-tetranethylguanidine

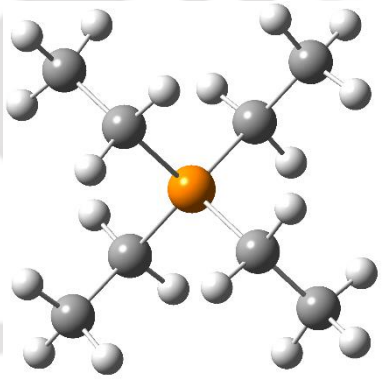

Tetraethylphosphonium $[TEPh]^+$

Figure 1.6: Examples of ionic liquid cations with their corresponding geometry optimized structures. Color scheme used for different atoms are blue: N, grey: C, red: O, orange: P, and white: H atoms, respectively.

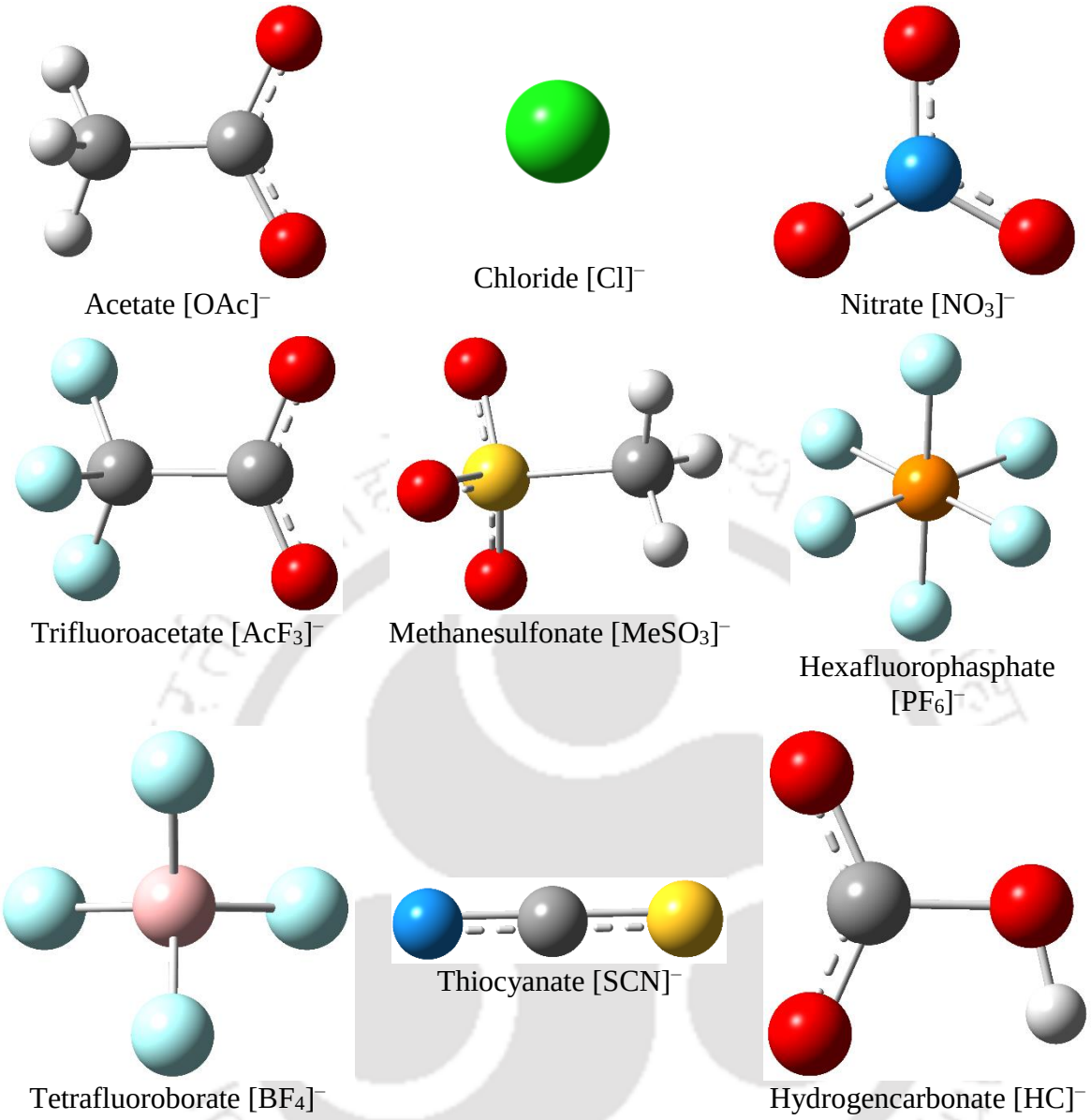

Figure 1.7: Examples of ionic liquid anions with their corresponding geometry optimized structures. Color scheme used for different atoms are blue: N, grey: C, red: O, orange: P, yellow: S, green: Cl, light pink: B, cyan: F, and white: H atoms, respectively.

The advantage of ILs in these processes is that it can dissolve whole biomass or selectively polysaccharides (cellulose, hemicellulose, and lignin) without any pretreatment [7,20]. Further hydrolysis of polysaccharides produces reducing sugars. In order to study the solvation property, the solubility data of biomass components in ILs are a prerequisite for the design of separation and reaction units [32,33]. It is a known fact that the anions of the ILs plays a major role in the dissolution process. Overall ILs helps in reducing the biomass

recalcitrance by the following methods (1) amorphization of cellulose, (2) delignification, and (3) deacetylation of hemicellulose [18,34].

One of the disadvantages of ILs are its high viscosity which brings the processing of dissolution quite difficult [35,36]. To overcome this issue, cosolvent can be added to IL which helps to reduce the viscosity of ILs enabling faster mass transfer rate and dissolution of solute [37-39]. The addition of highly polar cosolvent to ILs has proven to significantly increase the cellulose dissolution at lower conditions [40]. Nevertheless, ILs with acetate, thiocyanate, ethyl sulfate and phosphate anions have lower viscosities enabling them in their utilization in various applications [41,42]. It has been confirmed that anions such as $[OAc]^-$, $[AcF_3]^-$, $[Me_2PO_4]^-$ and $[Cl]^-$ being hydrogen bond acceptors are known to be effective in dissolving both cellulose and hemicellulose [28,43,44]. The low basicity anions namely dicyanamide and thiocyanate are not efficient in dissolving cellulose even though they are known to dissolve monosaccharides [1,45]. ILs containing non-coordinating anions such as $[BF_4]$ or $[PF_6]$ are also unable to dissolve cellulose [21]. Further, when ILs are used as a solvent, there is also a possibility for regeneration and reutilization which will overall reduce the process cost [46]. ILs can also provide a new platform for the dissolution of biomass at lower operating conditions without any pretreatment.

Dipolarity/polarizability ratio (π), hydrogen bond acidity (α) and basicity (β) are other tunable parameters that have an influence on the interaction of ILs with biomass. Hydrogen bond acidity (α) and basicity (β) are the indicators of the solvent to donate and accept hydrogen bonds, respectively. In fact, these three parameters are closely associated with each other and correlated *via* series of equations derived by Kamlet and Taft (1976) [47]. The magnitudes of each parameter gives an idea about how effective the IL deconstructs the hydrogen bond network of cellulose present in a biomass [28]. The magnitude of these solvation parameters is strongly associated with the type of the cation and anion that the IL composes. While

hydrogen basicity of an IL depends on the anion type, hydrogen bond acidity is related to the cation type [47]. Dipolarity/polarizability (π) is generally high for all ILs [48]. For biomass processing, ILs that possess high hydrogen bond basicity (β) are preferred since they are more effective in disrupting the hydrogen bond network of cellulose [49].

In 1934, Graenacher was the first to file a patent on the dissolution of cellulose in ILs. He claimed to have used molten N-ethylpyridinium chloride IL in the presence of nitrogen containing bases to dissolve cellulose without derivation [50]. Not enough attention was paid to this kind of application because there were no priority for cellulosic ethanol and green chemistry at that time. Although, some of the claims in the patent were found to be inaccurate by Sun *et al.* [32], however, Graenacher was still considered the first person who brought up the use of ILs for the dissolution of cellulose. It was Swatloski *et al.* [21] who explored this research area by publishing a widely cited study in 2002 on the use of ILs for dissolution of pulp cellulose. On heating to 100–110 °C, cellulose slowly dissolved in the $[Cl]^-$, $[Br]^-$ and $[SCN]^-$ containing ILs to yield higher viscous solutions (Table 1.2). They also reported that dissolved cellulose could be precipitated using water as antisolvent. Luo *et al.* reported that there has been an explosion in the number of publications dealing with IL pretreatment in the past few years [18]. Dozens of ILs are found to dissolve cellulose [28,34]. The dissolved cellulose can be recovered and hydrolyzed using enzymes with much higher glucose yields. Research in this area was also expanded to raw biomass containing lignin and hemicellulose in addition to cellulose that was used as a model biomass for early investigations in its essentially pure form (*e.g.*, Avicel, microcrystalline cellulose, and pulp cellulose). Many ILs are found to dissolve lignin and hemicellulose as well [43,51]. By removing lignin and hemicellulose, enzyme hydrolysis of cellulose can also be improved greatly.

Table 1.2: Solubility of dissolving pulp cellulose in ionic liquids (Swatloski *et al.* (2002) [21])

Ionic Liquid	Method	Solubility (%)
[Bmim][Cl]	Heat 100 °C	10%
[Bmim][Cl]	Heat 70 °C	3%
[Bmim][Cl]	Heat 80 °C + sonication	5%
[Bmim][Cl]	Microwave heating 3-5 s pulses	25%
[Bmim][Br]	Microwave	5-7%
[Bmim][SCN]	Microwave	5-7%
[Bmim][BF_4]	Microwave	Insoluble
[Bmim][PF_6]	Microwave	Insoluble
[Hmim][Cl]	Heat 100 °C	5%
[Omim][Cl]	Heat 100 °C	Slightly Soluble

Kilpelainen *et al.* (2007) investigated the structural properties and enzymatic hydrolysis of IL-treated wood samples. The spruce sawdust samples were regenerated after dissolution in 1-ally-3-methylimidazolium chloride [Amim]Cl and 1-butyl-3-methylimidazolium chloride [Bmim]Cl. This resulted in lower crystallinity and enhanced glucose yields as compared to biomass in its native structure. It was also reported that increased water content of ILs and biomass with bigger particle sizes exhibited adverse effects on the dissolution of biomass in ILs [52]. Zavrel *et al.* (2009) screened a variety of ILs with respect to their effect on the dissolution of softwoods and hardwoods. Among the ILs [Amim]Cl was found to dissolve all softwood and hardwood samples namely silver fir, spruce, common beach, chestnut completely [43]. Furthermore, Lee *et al.* (2009) have also performed a comprehensive dissolution experiments with biomass. They investigated the effect of pretreatment time and temperature on structural changes (crystallinity and amount of lignin extracted) and enzymatic hydrolysis of the maple wood flour subjected to 1-ethyl-3-methylimidazolium [Emim][OAc] pretreatment. According to the findings, the amount of

lignin extracted (%) was found to increase from 16% to 86% with an increase in pretreatment time from 30 min to 70 h. Cellulose digestibility was achieved at 91% for the biomass subjected to [Emim][OAc] pretreatment at 90 °C for 5 h. The increase of pretreatment time from 5 to70 h resulted in an increase of cellulose digestibility from 91 to 96% only [53].

Xie *et al.* (2005) studied the dissolution and blending of wool keratin fibers in several ILs. The maximum dissolution of wool keratin fibers was 11 wt% in [Bmim][Cl] IL at the temperature of 130 °C and 10 h of reaction time [54]. The solubility of wool keratin in ILs is given in Table 1.3.

Table 1.3: Solubility of wool keratin fibers in ionic liquids (data taken from Xie *et al.* (2005) [54])

Ionic Liquid	Condition/°C	Time/h	Solubility (wt %)
[Bmim][Cl]	100	10	4
[Bmim][Cl]	130	10	11
[Bmim][Br]	130	10	2
[Amim][Cl]	130	10	8
[Bmim][BF_4]	130	24	Insoluble
[Bmim][PF_6]	130	24	Insoluble

Zhao *et al.* (2010) investigated the dissolution of Switchgrass in different ILs at the temperature of 110 °C (Table 1.4). The IL containing different types of imidazolium based cations with chloride and acetate anions were used. They found that the acetate anion based ILs gave good dissolution capacity when compared to chloride based ILs [55]. Li *et al.* (2010 and 2011) reported two extensive studies which compared the IL pretreatment with the dilute acid and AFEX pretreatments with respect to their effects on the lignocellulosic feedstock namely switchgrass and corn stover. IL pretreatment gave an outstanding impact on both biomass and was seen to hydrolyze much faster than the dilute acid and AFEX pretreated

samples. Enzymatic hydrolysis rates for [Emim][OAc] pretreated switchgrass and corn stover were 16.7 and 15.2 fold higher than those observed for untreated switchgrass and corn stover [56,57]. The literature studies which were discussed up to this point composed of IL pretreatments which have been conducted at a biomass loading of 3 to 5% (w/w). Lower biomass loadings were found to result with biomass dissolution rather than biomass pretreatment.

Table 1.4: Solubility (wt %) of cellulose, hemicellulose, and lignin in ILs at 110 °C (data taken from Zhao *et al.* (2010) [55])

Ionic Liquid	Avicel PH-101	Xylan	Lignin
[Bmim][Cl]	10	7	>15
[Emim][OAc]	15	11	>17
[Bmim][OAc]	12	10	>18
$[Me(OEt)_2 – Et_3N][OAc]$	10	6	>13
$[Me(OEt)_3 – Et_3N][OAc]$	10	14	>21
$[Me(OEt)_2$ – Et-Im][OAc]	12	13	>21
$[Me(OEt)_3$ – Et-Im][OAc]	12	15	>22

1.5. Computational Approaches towards Biomass Dissolution

The focus of this section is to introduce computational simulation techniques and their underpinning methodologies which have been able to provide valuable information in understanding the effects of ILs on organic reaction outcomes, particularly when utilized in the context of experimental data. Computational methodologies have been used extensively in recent times to validate the experimental studies in ionic liquids with a great deal of success. There have been a relatively limited number of studies that combine both experimental and computational techniques to understand the effect of ILs on reaction outcome. In addition, some of the studies that have considered basic properties of the ILs themselves, provided important physicochemical information. And also it is not possible to synthesize all kinds of

ILs and investigate their affinity towards biomass and its derived compounds such as cellulose, hemicellulose, glucose, xylose, fructose, cellobiose etc. Hence, molecular modeling approach is a viable method to estimate the solubility of solute with various cation and anion combinations prior to synthesis. Molecular modeling calculation has been widely recognized and proved as a powerful tool for the design of new molecular ligands with specified properties, and for explaining their coordination mechanism with solutes. Furthermore, accurate theoretical calculations can provide pathways to obtain important chemical and physical information that cannot be easily obtained by experimental approaches.

The standard computational techniques for molecular solvents include dispersion, π-stacking interactions, hydrogen-bonding interactions, and other polar interactions. When modeling with ILs, strong Coulombic forces are plays a dominant role [58,59]. The other challenge is that individual components will often have very different electronic distributions, which further adds to the complexity of the interactions present, as well as introducing the possibility of selective aggregation of like components [59]. Overall, it is very difficult to accurately describe the subtle balance of these interactions. This is further complicated by the nature of computational chemistry, for which assumptions need to be made in any molecular description [58]. The extent of the assumptions made is dependent on the theoretical approach taken, as is the 'computational cost' of the method; that is, the amount of time and the computing resources required. As such, when modeling an IL the limitations of the available approaches must be matched with the information required from the simulation to arrive at the optimal technique.

In recent years, a number of researchers have addressed both the technical aspects of computational approaches used in IL modeling and the experimental work relating to chemical reaction mechanisms [23,60,61]. Solubility studies are significant as they highlight some of the reinforcement concepts regarding the use of ILs as solvents, along with helping to shape

our understanding of IL mixtures. Interactions between the IL and species are important in directing the outcome of many solubility studies. Early reports observed that the solubility of sugars compounds such as glucose and fructose are higher in ILs when compared to other conventional organic solvents [1,62]. It has also been demonstrated that the nature of the cation and anion is also important. A number of experimental and computational studies has tend to be function of anion than the cation. Or in other words the anion-sugar interactions decrease the anion-cation interactions within the mixture [63,64].

Xuan *et al.* (2011) investigated the cation-anion interactions of 1-allyl-3-methylimidazolium-based ILs by *ab initio* calculations. The magnitude of the interaction energy follows the order [Amim][OAc] > [Amim][HCOO] > [Amim][Cl] > [Amim][DCN]. The anion and hydrogen atom of the imidazolium ring plays a dominating role in the formation of most stable ionic pairs of ILs [64]. Ding *et al.* (2012a, 2012b) studied the theoretical and experimental investigation on the dissolution of cellulose in IL. Quantum chemical calculations (DFT theory) were performed to investigate the molecular mechanism of cellulose dissolution, where (1,4)-dimethoxy-D-glucose (GLc) was chosen as the model cellulose. From their theoretical results, it was observed that the interaction of [Emim][OAc] with GLc is stronger than that of GLc with GLc. Further, the acetate anion of IL forms strong H-bonds with hydroxyl groups of GLc. This important phenomenon certifies that the cellulose molecule does interact with ILs *via* H-bonds [65]. It is also observed that the H-bonds between [Emim][OAc] and Glc are weakened or even destroyed by the addition of water thereby decreasing the cellulose solubility [63]. Kahlen *et al.* (2010) and Casas *et al.* (2012) employed the activity coefficient model namely COnductor like Screening MOdel for Real Solvents (COSMO-RS) to screen a large number of anions and cations for the solubility of biomass [23,51].

Payal *et al.* (2014) reported the dissolution of cellulose in a room temperature IL [Emim][OAc] by *ab initio* molecular dynamics simulation (AIMD). The considered conformers of cellulose such as *anti-anti* and *anti-syn*-cellobiose. They reported that the presence of low concentration of water in the solution does not significantly alter the nature of the coordination environment of cellulose [26]. Furthermore, Hanbin *et al.* (2011) studied the interaction between binary and ternary systems of the IL [Emim][OAc] with water (different concentrations) and cellulose oligomer. To investigate these interactions, classical molecular dynamics (MD) simulations have been used. It was reported that as the concentration of water increases, more water molecules diffused into the anion-sugar network. As water diffuses inside the first solvation shell of cellulose, the number of hydrogen bonds among water molecules and the number of hydrogen bonds between the anion and the sugar decreases, resulting in the formation of an anion-water-cellulose hydrogen bonding network. The formation of this network displaces the cation out of the first solvation shell and leads to cellulose precipitation. This work provides a fundamental understanding of water as an antisolvent in regeneration processes [66].

From QC and classical MD simulations, it was reported that the cations interacts more closely with the non-polar regions of cellulose, whereas the anions interact with the polar region. The solvation of cellulose is driven by the strong interaction between the anion and the polar regions of cellulose. This idea is supported by other computational and experimental studies where it has been concluded that the anion disrupts the intermolecular forces between the cellulose polymers. Therefore, this section gives the theoretical information on the dissolution of cellulose in ILs through QC calculation and MD study for understanding the dissolution mechanism as well as the interaction between them.

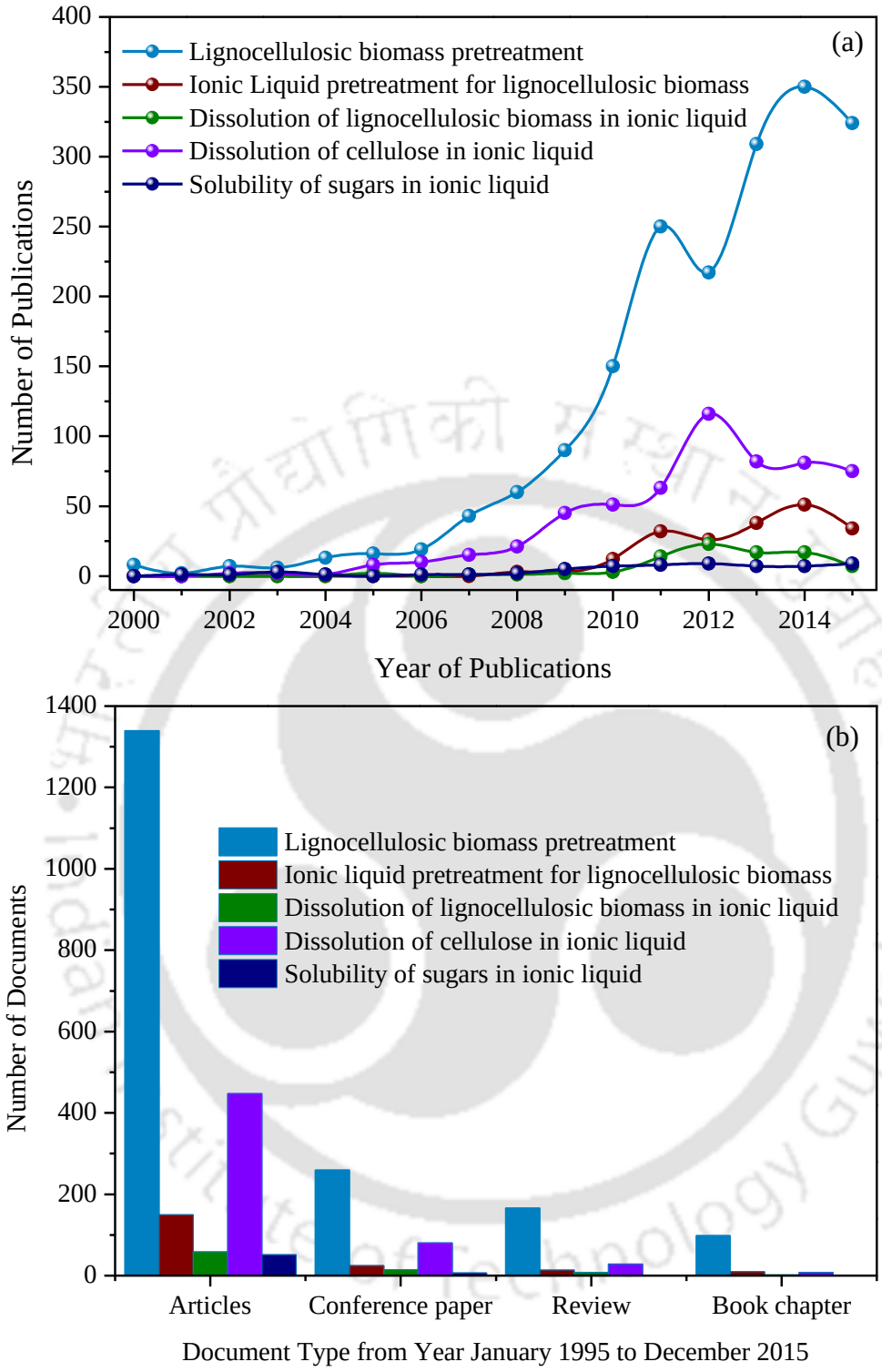

Figure 1.8: Current status of biomass related research survey from Scopus with respects to annual publication and type of document (a) Number of publications *vs* year of publications, for given queries indicated in legend and (b) Number of document *vs* document type from year January 1995 to December 2015, for given queries indicated in legend.

Limited data are available discussing the dissolution of lignocellulosic biomass and its derived components in ILs (Figure 1.8). Hence, the present thesis is undertaken to explore the dissolution of sugars, cellulose/hemicellulose and entire biomass in selected IL by employing both computational and experimental approaches. This study also includes the comparison of acid pretreatment with ILs for the dissolution of lignocellulosic biomass. We have also assessed various difficulties, opportunities/challenges linked with biomass processing in IL such as economic viability, scale-up, and sustainability.

1.6. Objectives of the Thesis

The current thesis aims at to dissolve the lignocellulosic biomass and its derived components namely cellulose, hemicellulose, disaccharides and monosaccharides in suitable ionic liquids. Precise experimental data and reliable theoretical models are basic requirements for the better understanding of the dissolution process and also to optimize the process design. Therefore, in this thesis, both experimental and theoretical aspects are addressed. The following objectives have been framed for the thesis work:

(a) *Initiate*, COSMO-RS based screening of ionic liquids for the solubility of monosaccharides and disaccharides in ionic liquids

(b) *Select* Potential ionic liquids for the dissolution of cellulose and hemicellulose by COSMO-RS model as per objective (a). This shall further involve insights with selected ionic liquids using quantum chemical (QC) and molecular dynamics (MD) simulations

(c) *Measure* and validate the experimental dissolution and subsequently propose a mechanism for the cellulose solvation in IL with protic and aprotic cosolvents

(d) *Formulate* the separation of sugars from ionic liquids by using antisolvents.

(e) *Undertake* dissolution of lignocellulosic biomass (bamboo) in ionic liquids and subsequent its enzymatic hydrolysis for the production of reducing sugars

1.7. Outline of Thesis

The current thesis is organized into following chapters. Schematic outlines of the current thesis are presented in Figure 1.9.

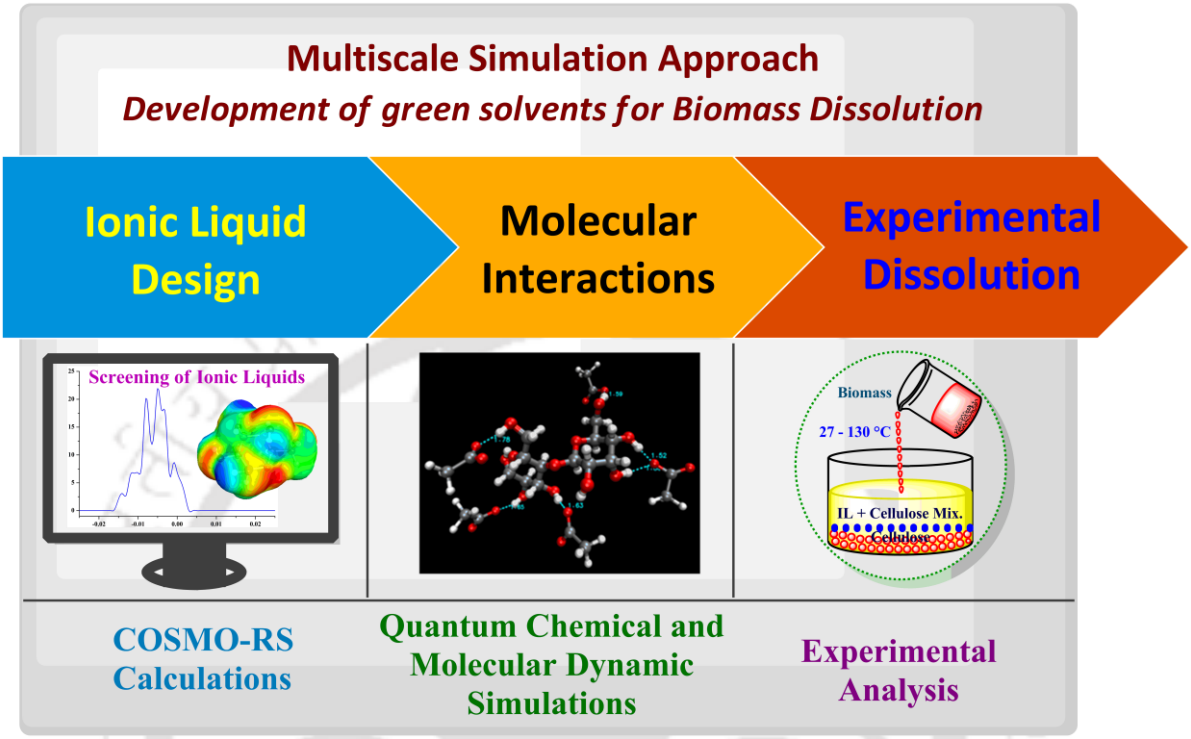

Figure 1.9: Schematic outline of the current thesis

Chapter 2 presents the solubility of simple sugars like monosaccharides in ionic liquids by employing both experimental and theoretical approaches. Here, COSMO-RS model was used to screen the ionic liquids for the solubility of monosaccharide. After the screening study, the selected IL was considered for experimental solubility measurements and a comparison is then made between experimental and predicted solubility. Further, the solubility data was correlated with local thermodynamic models namely NRTL and UNIQUAC.

Chapter 3 deals the solubility of disaccharides in ionic liquids. Disaccharides are formed when two monosaccharides are joined by glycosidic linkages. The idea behind this chapter is to elucidate the carbohydrate mechanism in ionic liquids and also measure the solubility data for disaccharides. The disaccharides are dissolved in two ionic liquids which

were selected from chapter 2. In addition, quantum chemical calculations are also employed to understand the intermolecular interactions by computing their interaction energies with ILs. Finally, the measured solubility data is correlated with the predicted COSMO-RS solubility.

After the dissolution of monomeric sugars and disaccharides in ILs, further, we have focused on the dissolution behavior of polysaccharides in ILs by observing their structural changes. To design a better combination of cation and anion for the dissolution of cellulose, hemicellulose and biomass, multiscale molecular simulations have been carried out. **Chapter 4** reveals the dissolution behavior of cellulose and hemicellulose in potential ionic liquids using both Quantum Chemical (QC) and experimental studies. For converging upon the recommended IL, 1428 ILs were screened with the COSMO-RS model. After extensive screening study, the selection of potential anions and cations were then visualized by observing their interactions with cellulose and hemicellulose by two approaches namely interaction energy and natural bonding orbital (NBO) analysis by QC calculations. The second approach is to use of MD simulations to understand their microscopic structural properties. In order to confirm the findings of both QC and MD simulations, experimental studies have been performed for the selected ILs.

One of the disadvantages of ILs are its high viscosities which brings the processing of dissolution cumbersome. To overcome this issue, protic or aprotic solvents can be added as a cosolvent which helps in reducing the viscosity of ILs without precipitation of cellulose. Therefore, **Chapter 5** addresses the role of cosolvent on the dissolution of cellulose in IL/cosolvent mixtures. Furthermore, the better cosolvent and their molar ratio's with IL has been optimized by molecular dynamic (MD) simulations. We have also proposed a dissolution mechanism for the cellulose in IL/cosolvents system.

Chapter 6 addresses the separation of dissolved carbohydrates from ILs using antisolvent method. Here again, COSMO-RS model is used to screen the suitable antisolvent for IL-sugars separations. After the antisolvents are screened, experiments are conducted for the separation of sugars at different experimental conditions. Apart from experiments, MD simulations are also adopted to understand the structural properties of carbohydrates with ILs and antisolvents *via* interaction energies (IE), hydrogen bonding (H-bonds) and coordination numbers (CN).

Chapter 7 describes the dissolution of lignocellulosic biomass in the selected IL from chapters 4 and 5. We have also investigated the efficiency of two biomass pretreatment processes (a) dissolution in an ionic liquid and (b) dilute acid hydrolysis, and then compared them in terms of composition and enzymatic saccharification efficiency of biomass. The regenerated bamboo samples are characterized by X-ray diffraction (XRD) and thermogravimetric analysis (TGA) to measure biomass crystallinity and thermal decomposition temperature. Moreover, a combined pretreatment method is developed to enhance the reducing sugars yield by enzymatic hydrolysis. Finally, **chapter 8** summarises the key findings of these thesis work and also presents a discussion on future directions.

References

[1] Carneiro AP, Rodríguez O, Macedo EA. Fructose and Glucose Dissolution in Ionic Liquids: Solubility and Thermodynamic Modeling. Ind Eng Chem Res 2013;52:3424-35.

[2] Carneiro AP, Rodríguez O, Macedo EA. Solubility of xylitol and sorbitol in ionic liquids – Experimental data and modeling. J Chem Thermodyn 2012;55:184-92.

[3] Holm J, Lassi U. Ionic Liquids in the Pretreatment of Lignocellulosic Biomass. In: Kokorin PA, editor. Ionic Liquids: Applications and Perspectives: InTech; 2011. p. 545-60.

[4] Hassan ESRE, Mutelet F, Pontvianne S, Moise JC. Studies on the dissolution of glucose in ionic liquids and extraction using the antisolvent method. Environ Sci Tech 2013;47:2809-16.

[5] Balaji C, Banerjee T, Goud VV. COSMO-RS Based Predictions for the Extraction of Lignin from Lignocellulosic Biomass Using Ionic Liquids: Effect of Cation and Anion Combination. J Solution Chem 2012;41:1610-30.

[6] Asghari FS, Yoshida H. Conversion of Japanese red pine wood (Pinus densiflora) into valuable chemicals under subcritical water conditions. Carbohydr Res 2010;345:124-31.

[7] Wang J, Zheng Y, Zhang S. The application of ionic liquids in dissolution and separation of lignocellulose. In: Eguchi K, editor. Clean Energy Systems and Experiences: InTech; 2010. p. 71-84.

[8] Kamm B, Kamm M. Principles of biorefineries. Appl Microbial Biotechnol 2004;64:137-45.

[9] Roque RMN, Baig MN, Leeke GA, Bowra S, Santos RCD. Study on sub-critical water mediated hydrolysis of Miscanthus a lignocellulosic biomass. Resour Conserv Recy 2012;59:43-6.

[10] Sasaki M, Kabyemela b, Malaluan R, Hirose S, Takeda N, Adschiri t, et al. Cellulose hydrolysis in subcritical and supercritical water. J Supercrit Fluids 1998;13:261-8.

[11] Kumar S, Gupta R, Lee YY, Gupta RB. Cellulose pretreatment in subcritical water: effect of temperature on molecular structure and enzymatic reactivity. Bioresour Technol 2010;101:1337-47.

[12] Kabyemela BM, Takigawa M, Adschiri T, Malaluan RM, Arai K. Mechanism and Kinetics of Cellobiose Decomposition in Sub- and Supercritical Water. Ind Eng Chem Res 1998;37:357-61.

[13] Agbor VB, Cicek N, Sparling R, Berlin A, Levin DB. Biomass pretreatment: fundamentals toward application. Biotechnol Adv 2011;29:675-85.

[14] Hendriks AT, Zeeman G. Pretreatments to enhance the digestibility of lignocellulosic biomass. Bioresour Technol 2009;100:10-8.

[15] Alonso MV, Oliet M, Rodriguez F, Astarloa G, Echeverria JM. Use of a methylolated softwood ammonium lignosulfonate as partial substitute of phenol in resol resins manufacture. J Appl Polym Sci 2004;94:643-50.

[16] Botello JI, Gilarranz MA, Rodriguez F, Oliet M. Preliminary study on products distribution in alcohol pulping of Eucalyptus globulus. J Chem Technol Biotechnol 1999;74:141-8.

[17] Galbe M, Zacchi G. Pretreatment of Lignocellulosic Materials for Efficient Bioethanol Production. In: Olsson L, editor. Biofuels. Berlin Heidelberg: Springer; 2007. p. 41-65.

[18] Luo J, Cai M, Gu T. Pretreatment of Lignocellulosic Biomass Using Green Ionic Liquids. In: Gu T, editor. Green Biomass Pretreatment for Biofuels Production. Netherlands: Springer; 2013. p. 127-53.
[19] Kumar P, Barrett DM, Delwiche MJ, Stroeve P. Methods for Pretreatment of Lignocellulosic Biomass for Efficient Hydrolysis and Biofuel Production. Ind Eng Chem Res 2009;48:3713–29.
[20] Zhao H, Xia S, Ma P. Use of ionic liquids as 'green' solvents for extractions. J Chem Technol Biotechnol 2005;80:1089–96.
[21] Swatloski RP, Spear SK, Holbrey JD, Rogers RD. Dissolution of Cellose with Ionic Liquids. J Am Chem Soc 2002;124:4974-5.
[22] Kosan B, Michels C, Meister F. Dissolution and forming of cellulose with ionic liquids. Cellulose 2008;15:59-66.
[23] Kahlen J, Masuch K, Leonhard K. Modelling cellulose solubilities in ionic liquids using COSMO-RS. Green Chem 2010;12:2172-81.
[24] Fukaya Y, Hayashi K, Wada M, Ohno H. Cellulose dissolution with polar ionic liquids under mild conditions: required factors for anions. Green Chem 2008;10:44-6.
[25] Pilli SR, Banerjee T, Mohanty K. Extraction of pentachlorophenol and dichlorodiphenyltrichloroethane from aqueous solutions using ionic liquids. J Ind Eng Chem 2012;18:1983-96.
[26] Payal RS, Balasubramanian S. Dissolution of cellulose in ionic liquids: an ab initio molecular dynamics simulation study. Phys Chem Chem Phys 2014;16:17458-65.
[27] Liu W, Hou Y, Wu W, Ren S, Jing Y, Zhang B. Solubility of Glucose in Ionic Liquid + Antisolvent Mixtures. Ind Eng Chem Res 2011;50:6952-6.
[28] Wang H, Gurau G, Rogers RD. Ionic liquid processing of cellulose. Chem Soc Rev 2012;41:1519-37.
[29] Pinkert A, Marsh KN, Pang A, Staiger MP. Ionic Liquids and Their Interaction with Cellulose. Chem Rev 2009;109:6712–28.
[30] Islas LMC, Medrano RV, Tlacuahuac AF. Optimal Molecular Design of Ionic Liquids for High-Purity Bioethanol Production. Ind Eng Chem Res 2011;50: 5153–68.
[31] Vancov T, Alston A-S, Brown T, McIntosh S. Use of ionic liquids in converting lignocellulosic material to biofuels. Renew Energ 2012;45:1-6.
[32] Sun N, Rodriguez H, Rahman M, Rogers RD. Where are ionic liquid strategies most suited in the pursuit of chemicals and energy from lignocellulosic biomass? Chem Commun 2011;47:1405–21.
[33] Lopes DCAM, Joao KG, Rubik DF, Lukasik EB, Duarte LC, Andreaus J, et al. Pre-treatment of lignocellulosic biomass using ionic liquids: Wheat straw fractionation. Bioresour Technol 2013;142:198-208.
[34] Shill K, Padmanabhan S, Xin Q, Prausnitz JM, Clark DS, Blanch HW. Ionic liquid pretreatment of cellulosic biomass: enzymatic hydrolysis and ionic liquid recycle. Biotechnol Bioeng 2011;108:511-20.
[35] Froschauer C, Hummel M, Iakovlev M, Roselli A, Schottenberger H, Sixta H. Separation of hemicellulose and cellulose from wood pulp by means of ionic liquid/cosolvent systems. Biomacromolecules 2013;14:1741-50.
[36] Brandt A, Hallett JP, Leak DJ, Murphy RJ, Welton T. The effect of the ionic liquid anion in the pretreatment of pine wood chips. Green Chem 2010;12:672-9.
[37] Xu A, Cao L, Wang B, Ma J. Dissolution Behavior of Cellulose in IL + DMSO Solvent: Effect of Alkyl Length in Imidazolium Cation on Cellulose Dissolution. Adv Mater Sci Eng 2015;2015:1-4.

[38] Huo F, Liu Z, Wang W. Cosolvent or antisolvent? A molecular view of the interface between ionic liquids and cellulose upon addition of another molecular solvent. J Phys Chem B 2013;117:11780-92.
[39] Parthasarathi R, Balamurugan K, Shi J, Subramanian V, Simmons BA, Singh S. Theoretical Insights into the Role of Water in the Dissolution of Cellulose Using IL/Water Mixed Solvent Systems. J Phys Chem B 2015;119:14339-49.
[40] Xu A, Zhang Y, Zhao Y, Wang J. Cellulose dissolution at ambient temperature: role of preferential solvation of cations of ionic liquids by a cosolvent. Carbohydr Polym 2013;92:540-4.
[41] Isik M, Sardon H, Mecerreyes D. Ionic liquids and cellulose: dissolution, chemical modification and preparation of new cellulosic materials. Int J Mol Sci 2014;15:11922-40.
[42] Seoud OAE, Koschella A, Fidale LC, Dorn S, Heinze T. Applications of Ionic Liquids in Carbohydrate Chemistry: A Window of Opportunities. Biomacromolecules 2007;8:2629–47.
[43] Zavrel M, Bross D, Funke M, Buchs J, Spiess AC. High-throughput screening for ionic liquids dissolving (ligno-)cellulose. Bioresour Technol 2009;100:2580-7.
[44] Kosan B, Michels C, Meister F. Dissolution and forming of cellulose with ionic liquids. Cellulose 2007;15:59-66.
[45] Carneiro AP, Held C, Rodriguez O, Sadowski G, Macedo EA. Solubility of Sugars and Sugar Alcohols in Ionic Liquids: Measurement and PC-SAFT Modeling. J Phy Chem B 2013;117:9980-95.
[46] Mäki-Arvela P, Anugwom I, Virtanen P, Sjöholm R, Mikkola JP. Dissolution of lignocellulosic materials and its constituents using ionic liquids—A review. Ind crop prod 2010;32:175-201.
[47] Welton T. Ionic liquids in catalysis. Coord Chem Rev 2004;248:2459-77.
[48] Brandt A, Hallett JP, Leak DJ, Murphy RJ, Welton T. The effect of the ionic liquid anion in the pretreatment of pine wood chips. Green Chem 2010;12:672.
[49] Fukaya Y, Sugimoto A, Ohno H. Superior Solubility of Polysaccharides in Low Viscosity, Polar, and Halogen-Free 1,3-Dialkylimidazolium Formates. Biomacromolecules 2006;7:3295–7.
[50] Graenacher C. Cellulose solution. U.S. Patents; 1934. p. 176.
[51] Casas A, Palomar J, Alonso MV, Oliet M, Omar S, Rodriguez F. Comparison of lignin and cellulose solubilities in ionic liquids by COSMO-RS analysis and experimental validation. Ind crop prod 2012;37:155–63.
[52] Kilpeläinen I, Xie H, King A, Granstrom M, Heikkinen S, Argyropoulos DS. Dissolution of wood in ionic liquids. J Agric Food Chem 2007;55:9142-8.
[53] Lee S-H, Teramoto Y, Endo T. Enzymatic saccharification of woody biomass micro/nanofibrillated by continuous extrusion process I – Effect of additives with cellulose affinity. Bioresour Technol 2009;100:275-9.
[54] Xie H, Li S, Zhang S. Ionic liquids as novel solvents for the dissolution and blending of wool keratin fibers. Green Chem 2005;7:606-8.
[55] Zhao H, Baker GA, Cowins JV. Fast enzymatic saccharification of switchgrass after pretreatment with ionic liquids. Biotechnol Prog 2010;26:127-33.
[56] Li Q, He Y-C, Xian M, Jun G, Xu X, Yang J-M, et al. Improving enzymatic hydrolysis of wheat straw using ionic liquid 1-ethyl-3-methyl imidazolium diethyl phosphate pretreatment. Bioresour Technol 2009;100:3570-5.
[57] Li C, Knierim B, Manisseri C, Arora R, Scheller HV, Auer M, et al. Comparison of dilute acid and ionic liquid pretreatment of switchgrass: Biomass recalcitrance, delignification and enzymatic saccharification. Bioresour Technol 2010;101:4900-6.

[58] Matthews RP, Welton T, Hunt PA. Competitive pi interactions and hydrogen bonding within imidazolium ionic liquids. Phys Chem Chem Phys 2014;16:3238.
[59] Fumino K, Ludwig R. Analyzing the interaction energies between cation and anion in ionic liquids: The subtle balance between Coulomb forces and hydrogen bonding. J Mol Liq 2014;192:94-102.
[60] Dommert F, Wendler K, Berger R, Delle Site L, Holm C. Force Fields for Studying the Structure and Dynamics of Ionic Liquids: A Critical Review of Recent Developments. ChemPhysChem 2012;13:1625-37.
[61] Montañés F, Olano A, Ibáñez E, Fornari T. Modeling solubilities of sugars in alcohols based on original experimental data. AIChE J 2007;53:2411-8.
[62] Carneiro AP, Rodríguez O, Macedo EA. Solubility of monosaccharides in ionic liquids – Experimental data and modeling. Fluid Phase Equilib 2012;314:22-8.
[63] Ding ZD, Chi Z, Gu WX, Gu SM, Liu JH, Wang HJ. Theoretical and experimental investigation on dissolution and regeneration of cellulose in ionic liquid. Carbohydr Polym 2012;89:7-16.
[64] Xuan X, Guo M, Pei Y, Zheng Y. Theoretical study on cation-anion interaction and vibrational spectra of 1-allyl-3-methylimidazolium-based ionic liquids. Spectrochim Acta A Mol Biomol Spectrosc 2011;78:1492-9.
[65] Ding Z-D, Chi Z, Gu W-X, Gu S-M, Wang H-J. Theoretical and experimental investigation of the interactions between [emim]Ac and water molecules. J Mol Struct 2012;1015:147-55.
[66] Liu H, Sale KL, Simmons BA, Singh S. Molecular dynamics study of polysaccharides in binary solvent mixtures of an ionic liquid and water. J Phys Chem B 2011;115:10251-8.

Chapter – 2

Solubility of Monosaccharides in Ionic Liquids: Experimental and Theoretical Studies using a Continuum Solvation Model

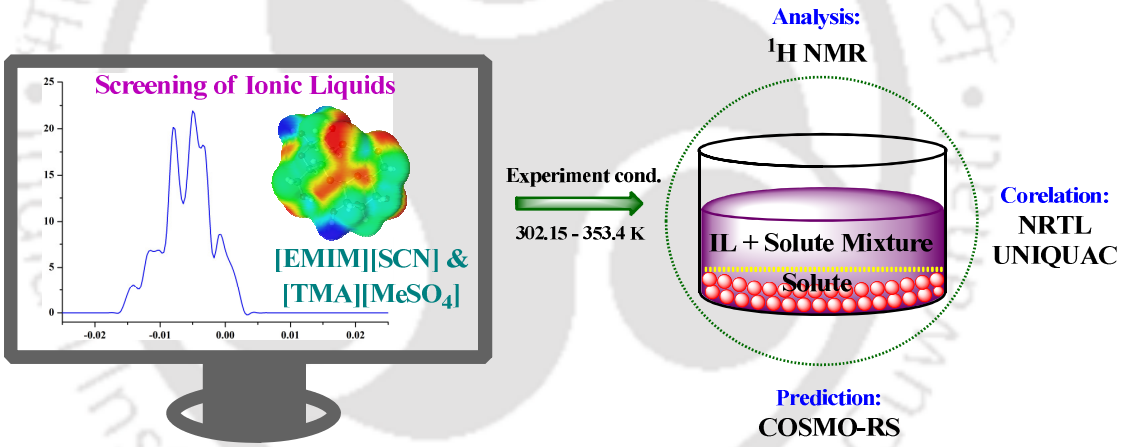

Published Article

Mohan M, Goud VV, Banerjee T. Solubility of glucose, xylose, fructose and galactose in ionic liquids: Experimental and theoretical studies using a continuum solvation model. *Fluid Phase Equilib* 2015; 395: 33-43

2 Solubility of Monosaccharides in Ionic Liquids

The current chapter reports a molecular screening of 64 ILs for the solubility of monosaccharides such as D-(+)-Glucose, D-(+)-Xylose, D-(-)-Fructose and D-(+)-Galactose were performed by COSMO-RS model over the temperature range of 303.15-373.15 K. The IL data set consisted of 31 cations and 23 anions comprising of cations such as imidazolium, ammonium, pyridinium, pyrrolidinium, phosphonium, sulfonium and piperidinium. Based on the screening studies, the following two ILs were chosen: 1-ethyl-3-methylimidazolium thiocyanate ([EMIM][SCN]) and Tris(2-hydroxyethyl)methylammonium methylsulfate [TMA][MeSO$_4$] to study the experimental solubility of monosaccharides in ILs at a temperature range 303.15-373.15 K. Further, the apparent standard thermodynamic function of dissolution such as standard molar Gibbs energy $\Delta^{o}_{dissol}G$, molar enthalpy $\Delta^{o}_{dissol}H$ and standard molar entropy $\Delta^{o}_{dissol}S$ were also calculated from the modified van't Hoff equation.

2.1 Introduction

The simple sugars namely monosaccharides and disaccharides can be dissolved in organic solvents, but on the other side they suffer from serious issues such as volatility, toxicity, difficulty in solvent recovery, and attained lower solubility [1]. In order to enhance the solubility of monosaccharides and disaccharides, ILs have proven as judicious solvents for dissolution [2,3]. In order to study the solvation property, the solubility data of ILs in biomass components are a prerequisite for the design of separation and reaction units [4,5]. Further, when ILs are used as solvents, there is also a possibility for its regeneration and reutilization which ultimately reduces the associated process cost [6]. There has been recent work which reports the solubility of carbohydrates in ILs. Liu *et al.* (2011) determined the solubility of glucose in IL + antisolvent mixtures at 273.15-333.15 K. [EMIM][Br] gave the

highest solubility as compared to [BMIM][Cl], [HMIM][HSO_4], [BMIM][OAc] and [EMIM][OAc]. It was also reported that, ethanol was a better antisolvent to separate glucose and IL, when compared to methanol, acetone and acetonitrile [7]. Carneiro *et al.* (2012) measured the solubility of monosaccharides in two ILs at a temperature range of 288-328 K. [EMIM][$EtSO_4$] have shown a higher dissolution capacity of monosaccharides than Aliquat®336. Among all the monomers, D-(-)-Fructose had the more solubility, whereas D-(+)-Galactose gave the less solubility [3]. In another study of Carneiro *et al.* (2013), the solubility of glucose and fructose in ILs was measured by using HPLC (High-performance liquid chromatography) [8].

Furthermore, Domanska *et al.* (2013) investigated the solubility of sugar alcohols in the dicyanamide based ILs namely [BMIM][DCA], [BMPyr][DCA], and [BMP][DCA] by experimental and PC-SAFT modeling over the temperature range of 293.15 to 363.15 K [9]. The sugar alcohols, xylitol, and sorbitol have been considered for their solubility study. The measured solubility data of xylitol and sorbitol have shown satisfactory results with PC-SAFT predicted data. Hasan et al. (2013) studied the dissolution of glucose in ILs and extraction using the antisolvent method. In this work, they reported the solubility of D-glucose in four ILs with ethanol as antisolvent. This was measured within a temperature range from 283 to 373 K. The solubility order of glucose in IL + ethanol were: [BMPyr][Cl] < [EMIM][SCN] < [BMIM][Cl] < [EtOHMIM][Cl] < [DMIM][MPh] [10].

From the aforementioned literature, it was clear that the ILs are potential solvents for the dissolution of carbohydrates. However, the reported solubility data was mainly drawn from experimental studies with randomly selected ILs. It should be noted that it is not possible to perform the solubility of sugars in ILs at all times due to higher cost and time involved. Hence, molecular modeling calculation is an efficient method to circumvent this problem. Quantum chemical based solvation model such as COSMO-RS is an alternative for

such solvents [11,12]. It requires the universal parameters and component specific parameters fitted with a small experimental dataset [13]. COSMO-RS requires the chemical structure of the component as the only information [14,15]. By COSMO-RS model, we can predict the solubility of any component in the mixtures. This model can be used to calculate the infinite dilution activity coefficient (IDAC) of any solute in a solvent [12,14,15]. Thus, the solid-liquid equilibria (SLE) calculation merely requires the melting point temperature and heat of fusion values of the solute which is monosaccharides in this case. Local thermodynamic models such as NRTL and UNIQUAC can also be used to describe and predict the phase equilibria of the mixtures [16-18]. Nevertheless, both NRTL and UNIQUAC model are dependent on experimental data for generating the binary interaction parameters. Data for new functional groups involving ILs and monosaccharides are not available which leads to the application of such models are defunct. Therefore, the present chapter focuses on the COSMO based screening of ILs and subsequently predicts the monosaccharides solubility data.

2.2 Computational Details

2.2.1 Geometry Optimization

The initial structures of selected monosaccharides and ILs were drawn in the MOLDEN freeware software [19]. Particular attention has been paid for the selection of the cation and anion. ILs having melting point less than the room temperature was chosen in COSMO-RS studies. The structures of all ILs are depicted in appendix-A (Table A.1). The melting properties (melting temperature and heat of fusion) of monosaccharides reported in Table 2.1 are used in the COSMO-RS (SLE) predictions. The initial molecular geometries of monosaccharides and ILs were fully optimized by HF/6-31G* *via* *Gaussian*03 package [15,20]. To detect the presence of any negative or imaginary frequencies, frequency optimization was done using the *freq* keyword in *Gaussian*03 [12,15,19].

Table 2.1: Melting point and heat of fusion of monosaccharides used in this work[a]

Solute	Chemical Formula	M. Wt. (g mol^{-1})	T_{fus} (K)	$\Delta_{fus}H$ (J mol^{-1})
D-(+)-Glucose	$C_6H_{12}O_6$	180.2	431.15	32220
D-(+)-Xylose	$C_5H_{10}O_5$	150.1	416.15	31700
D-(-)-Fructose	$C_6H_{12}O_6$	180.2	378.15	26000
D-(+)-Galactose	$C_6H_{12}O_6$	180.2	443.15	43740

[a] T_{fus} and $\Delta_{fus}H$ values are taken from Carneiro *et al.* [3] and Gray *et al.* [21]

2.2.2 COSMO-RS Theory

Owing to the importance of solvents in biochemical, catalytic, and separation processes, attempts have been made for the last two or three decades to combine the quantum chemical description of molecules with an appropriate continuum description of the surrounding solvent. To describe the electrostatic behavior of solvents, dielectric models have been chosen among which COSMO represent the most significant advancement [22]. In the COSMO approach, a cavity is formed in the midst of a perfect conductor with certain atom-specific dimensions. The molecule's inherent moments then draw charges from the surroundings to the surface of the cavity so as to cancel the resulting electric field within the conductor and tangential to it. The charge induced at the surface is then calculated and is termed as the screening charge. This forms the most important descriptor used in the COSMO-RS approach, also known as local screening charge density 'σ', which in other words would be induced on the molecular surface if the molecule is embedded in a virtual conductor. The detailed description of COSMO-RS model is reported elsewhere [11,23].

After the geometry optimization step, the next step is to generate the COSMO file using the final optimized structure. The first step of COSMO-RS calculation is to estimate the sigma profiles (*i.e.*, the screening charge densities) of each species [24]. The equilibrium geometry of the molecules in the ideal gas phase is first obtained using the density functional

theory of P BV86 [12,19]. The triple zeta valance potential (TZVP) basis set is then used in combination with the density fitting basis set of DGA1 [14]. The combination of TZVP and DGA1 basis sets allows the electron density to adjust spatially to the extent appropriate to the particular molecular environment. The ideal screening charges on the molecular surface are then computed using the same level of theory P BV86 *via* the keyword "scrf=COSMORS". The default radii of the elements as used in *Gaussian*03 for the keyword "scrf=COSMORS" was used to instruct *Gaussian* to do a COSMO solvation calculation [12,25].

The physical parameters such as a_{eff} = 6.32 Å^2 (surface area of a standard segment), α' = 8419 (kcal.Å^4).(mol^{-1}.e^{-2}) (misfit constant for misfit energy interaction), c_{hb} = 75006 (kcal.Å^4).(mol^{-1}.e^{-2}) (constant for hydrogen bonding interaction) and σ_{hb} = 0.0084 e.Å^{-2} (the cut off value for hydrogen bonding interactions) were taken from the work of Balaji *et al.* (2012) [19] and were used as global parameters. The equations used in the COSMO-RS calculations are given in the Table A.2 (appendix-A).

We have assumed a complete dissociation of ILs into cations and anions with equimolar quantities. The sigma profile of the IL is the linear addition of the sigma profiles of the cation and anion (Eqn (2.1)):

$$p_{\text{ionic liquid}}(\sigma) = p_{\text{cation}}(\sigma) + p_{\text{anion}}(\sigma) \tag{2.1}$$

Where, $p_{\text{cation}}(\sigma)$ and $p_{\text{anion}}(\sigma)$ are the sigma profiles for cation and anion, respectively. We have obtained the sigma profile of cation and anion separately and then added them up by simple algebraic addition. After the addition, the sigma profile has been normalized. Thus, the profile will behave as a profile of single molecule [19]. This is equivalent to calculating the sigma profile of a mixture of cation and anion. Along with the sigma profile, the COSMO volume (*i.e.*, the cavity surface volume) and area (cavity surface area) also get added linearly. Thus, an independent ion model has been used in this work.

2.3 Materials and Methods

2.3.1 Materials

Monosaccharides such as D-(+)-Glucose, D-(+)-Xylose, D-(-)-Fructose and D-(+)-Galactose were purchased from Sigma-Aldrich, Germany. All the carbohydrates have purities greater than ≥99% as per the supplier specification. D-(-)-Fructose was dried at 318 K for 24 h, before the experiments. The ILs [EMIM][SCN] (≥ 95%), and [TMA][$MeSO_4$] (≥ 95%) were supplied from Sigma-Aldrich, Germany and were used without further purification. Dimethylsulfoxide-d_6 (DMSO-d_6) was used as NMR solvent with a purity of ≥ 99.8% was purchased from Merck, India. Table 2.2 summarizes the compound details which are used in the experimental study.

Table 2.2: List of compounds (monosaccharides, ionic liquids, and NMR solvent) used in the experimental study

Entry	Compound Name	CAS no.	Purity (%)	Supplier	Product
1.	D-(+)-Glucose	50-99-7	≥99.5	Sigma-Aldrich	France
2.	D-(+)-Xylose	58-86-6	≥99.0	Sigma-Aldrich	Germany
3.	D-(-)-Fructose	57-48-7	≥99.0	Sigma-Aldrich	Germany
4.	D-(+)-Galactose	59-23-4	≥99.5	Sigma-Aldrich	Switzerland
5.	[EMIM][SCN]	331717-63-6	≥99.8	Sigma-Aldrich	Germany
6.	[TMA][$MeSO_4$]	29463-06-7	≥95.0	Sigma-Aldrich	Germany
7.	DMSO-d_6	2206-27-1	≥99.8	Merck	India

2.3.2 Experimental Solubility Measurements

For the experimental studies, 50 mL of conical flasks were used, in which specified amount of IL (10-12 g) was placed and heated up to set temperature (TARSONS SPINOT-magnetic stirrer and hot plate-DIGITAL, MC 02, India), having an uncertainty of ±0.1 K. After the desired temperature was achieved, slightly excess amount of monosaccharide (slight excess

of the estimated solubility) was added. Preliminary experiments were made to estimate the amounts to be added of each compound. Weighing was carried out with an accuracy of ±0.001 (Sartorius, BSA 224S-CW max 220 g d=0.1 mg, India). The internal temperature of the conical flask was measured with the thermometer and maintained at the desired temperature. The solution mixture was magnetically stirred for 48 h and then kept overnight for equilibrium. In order to ensure sharp phase transition, we centrifuged the sample for one hour and then kept it for 5-6 h to attain equilibrium. In order to evaluate whether the system has reached the equilibrium state, samples were drawn using the micropipette at different dissolution times while at the same time also measure the concentration of monosaccharides. The equilibrium was obtained when two successive concentrations did not have any change in the variation in concentration. The measured concentration is then corresponds to the solubility concentration of the particular component *i.e.*, monosaccharide at that desired temperature. The top layer here indicates a clear liquid (see Figure A.1). The equilibrium solubility of monosaccharides is determined by ^{1}H NMR spectrophotometer (600 MHz NMR, Brucker, Germany). The compositional analysis were performed in triplicate and average values were reported here.

2.3.3 Compositional Analysis

For the composition analysis, the SLE compositions were determined by ^{1}H NMR spectroscopy. 0.1µL sample was dissolved in 0.6 mL of DMSO-d_6 and placed in NMR tubes (thrift grade) which were properly sealed with a cap and parafilm. The NMR spectrometer of 11.74T (600 MHz response of ^{1}H) was used to record the ^{1}H NMR spectral analysis. Peak areas proportional to the hydrogen moles associated with the referred component are noted down. The ^{1}H NMR spectrum of D-(+)-Glucose in both ILs [EMIM][SCN] and [TMA][$MeSO_4$] are shown in Figure 2.1.

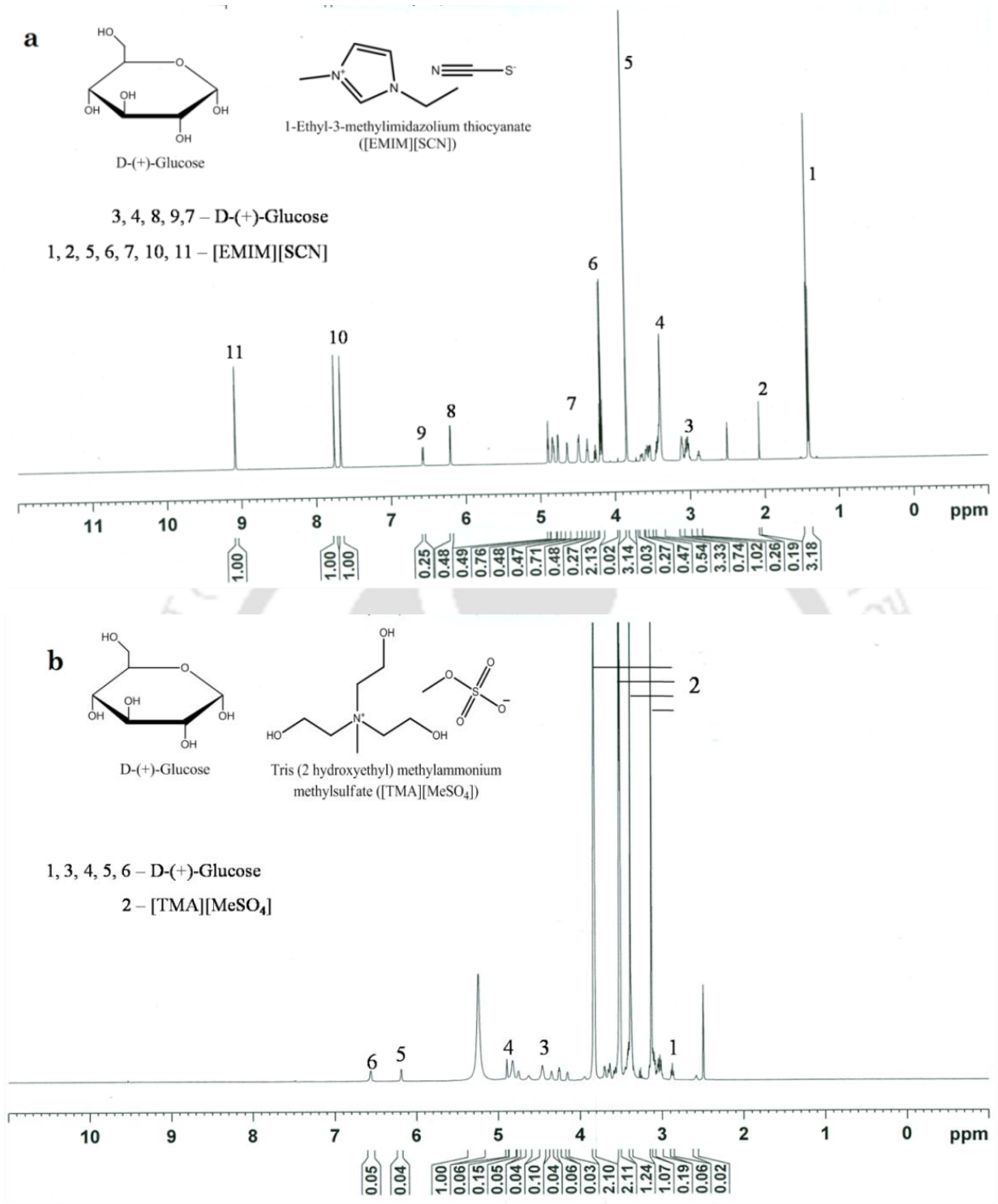

Figure 2.1: ^{1}H NMR spectra of D-(+)-Glucose in (a) [EMIM][SCN], (b) [TMA][$MeSO_4$]

In this work, equations are formed where the areas of a particular species are added up and then equated with the total number of hydrogen atoms for the same species. Thereafter, the contribution of area for each hydrogen atom was individually performed for IL and monosaccharide. The ratio of these gives us the mole fraction of solute and solvent

using ^{1}H NMR spectra with an uncertainty of ±0.01 in mole fraction. Finally the mole fraction was obtained by dividing the area of specified component to the total sum of the area of all components from the NMR peak areas [26,27]. The equation used to determine the mole fraction is given as follows (Eqn (2.2)),

$$x_i = \frac{H_i}{\sum_{i=1}^{n} H_i} \tag{2.2}$$

Where x_i is the mole fraction of species i and H_i is the peak area of the single hydrogen atom in the component *'i'*. The next section discusses the measurement of physiological properties of the pure Ionic Liquids which are used in the experiments.

2.3.4 Solid-Liquid Equilibrium

The solubility of a solid (monosaccharide) in liquid (IL) is given by the following assumptions [3,28] such as (a) disappearance of solvent molecule in solid phase, (b) triple-point of solute to be the same as normal melting point temperature, T_m; and (c) solute's heat capacity difference between the pure liquid and pure solid carbohydrate is considered as temperature independent and is equal at its melting temperature, ΔC_p^{S-L}. The solubility equation for SLE is as follows:

$$\ln(\gamma^{L}_{solute} x^{L}_{solute}) = \frac{-\Delta H_f}{R}\left(\frac{1}{T} - \frac{1}{T_m}\right) - \frac{\Delta c_p}{R}\left(\frac{T_m - T}{T}\right) + \frac{\Delta c_p}{R}\ln\left(\frac{T_m}{T}\right) \tag{2.3}$$

The triple point temperature here has been replaced with the fusion (or melting point) temperature, T_m, since these can be considered equal in most of the cases. Besides, it has been assumed that the specific heat change is constant over the temperature change considered, which does not yield any formidable error in the calculation. Also, the difference between the last two terms on the right hand side of the Eqn (2.3) can be considered to be

very close to each other so that they cancel out. Thus, we get a simplified form of the solubility equation as,

$$\ln(\gamma^{L}_{solute} x^{L}_{solute}) = \frac{-\Delta H_f}{RT_m}\left(\frac{1}{T} - \frac{1}{T_m}\right) \tag{2.4}$$

For the ideal situation, the activity coefficient of the solute in the liquid phase is unity *i.e.*, $\gamma^{L}_{solute} = 1$. Therefore, the ideal solubility equation is given as:

$$\ln x^{L}_{solute} = \frac{-\Delta H_f}{RT_m}\left(\frac{1}{T} - \frac{1}{T_m}\right) \tag{2.5}$$

And in terms of entropy change,

$$\ln x^{L}_{solute} = \frac{-\Delta S_f}{R}\left(\frac{1}{T} - \frac{1}{T_m}\right) \tag{2.6}$$

For the prediction of experimental mole fraction, mole fraction at ideal solvation from Eqn (2.5) is predicted. This value is then used to obtain the activity coefficient of the component in the mixture using COSMO-RS model as given below [29]:

$$\ln \gamma_{i/S} = n_i \sum_{\sigma} p_i(\sigma)[\ln \Gamma_S(\sigma) - \Gamma_i(\sigma)] + \ln \gamma^{SG}_{i/S} \tag{2.7}$$

In Eqn (2.7), $\Gamma_S(\sigma)$ and $\Gamma_i(\sigma)$ are the segment activity coefficients of the component in mixture(s) and itself (*i*). $p_i(\sigma)$ refers to the sigma profile of the individual solute and n_i the total number of segments for component '*i*'. $\ln \gamma^{SG}_{i/S}$ refers to the Staverman-Guggenheim (combinatorial contribution) and is calculated using the Eqn (2.8):

$$\ln \gamma^{SG}_{i/S} = \ln \frac{\phi_i}{x_i} + \frac{z}{2} q_i \ln \frac{\theta_i}{\phi_i} + li - \frac{\phi_i}{x_i} \sum_j x_j l_j \tag{2.8}$$

Where $\theta_i = \dfrac{x_i q_i}{\sum_j x_j q_j}$, $\phi_i = \dfrac{x_i r_i}{\sum_j x_j r_j}$ and $\mathrm{l_i} = \dfrac{z}{2}\left((r_i - q_i) - (r_i - 1)\right)$ (2.9)

Here, r_i and q_i are normalized using the volume (66.69 Å^3) and surface area (79.53 Å^2) of a functional group [25]

$$r_i = \frac{COSMO\ Volume}{66.69},\ q_i = \frac{COSMO\ Area}{79.53} \tag{2.10}$$

Here, the cavity COSMO volume and Cavity COSMO area are the output from COSMO file. The activity coefficient then predicted by COSMO-RS model is then replaced in Eqn (2.4) and we get the actual solubility or x^{L}_{solute}. For experimental and predicted data, the root mean square error (RMSE) is calculated by the following expression:

$$RMSE = \left[\frac{1}{N_p}\sum_{i=1}^{N_p}\left(x^{\exp}_{solute} - x^{pred}_{solute}\right)^2\right]^{1/2} \tag{2.11}$$

Where, x^{exp}_{solute} and x^{pred}_{solute} are the experimental and predicted solubility respectively. 'N_p' is the number of data points.

2.3.5 NRTL and UNIQUAC Correlations

According to NRTL [16] model, the non-ideal liquid phase activity coefficient of any component *'i'* is calculated by the following equation:

$$\ln\gamma_i = \frac{\sum_{j=1}^{n}\tau_{ji}G_{ji}x_j}{\sum_{l=1}^{n}G_{li}x_l} + \sum_{j=1}^{n}\left[\frac{G_{ij}x_j}{\sum_{l=1}^{n}G_{lj}x_l}\left(\tau_{ij} - \frac{\sum_{r=1}^{n}\tau_{rj}G_{rj}x_j}{\sum_{l=1}^{n}G_{lj}x_l}\right)\right] \tag{2.12}$$

$$G_{ij} = \exp\left(-\alpha_{ji}\tau_{ji}\right),\ \tau_{ji} = \left[\left(g_{ji} - g_{ii}\right)/RT\right] \text{ and } \alpha_{ji} = \alpha_{ij} = \alpha$$

Here 'G_{ij}' is an energy parameter characterizing the interaction of species *i* and *j*, x_i is the mole fraction of component *i* and α is the non-randomness parameter. 'α' can be treated as an adjustable parameter and is equal to 0.2 according to the literature [10]. For UNIQUAC model [18], the non-ideal liquid phase activity coefficient of any component '*i'* is calculated by using the following Eqn (2.13):

$$\ln\gamma_i = \ln\left(\frac{\Phi_i}{x_i}\right) + \frac{z}{2} q_i \ln\left(\frac{\theta_i}{\Phi_i}\right) + l_i - \frac{\Phi_i}{x_i}\sum_{j=1}^{n} x_j l_j - q_i\left(1 - \ln\sum_{j=1}^{n}\theta_j\tau_{ji} - \sum_{j=1}^{n}\frac{\theta_j\tau_{ji}}{\sum_{k=1}^{n}\theta_k\tau_{kj}}\right) \quad (2.13)$$

Where $\Phi_i = \frac{r_i x_i}{\sum_{j=1}^{n} r_j x_j}$, $\theta_i = \frac{q_i x_i}{\sum_{j=1}^{n} q_j x_j}$, $l_i = \frac{z}{2}\left(r_j - q_j\right) + \left(1 - r_j\right)$, and $\tau_{ji} = \frac{g_{ji} - g_{ii}}{RT}$.

Here θ, τ and Φ represents the area fraction, interaction parameter and segment fraction, respectively. '*x*' is the mole fraction of component in liquid phase. Here *r* and *q* are the pure component volume and area parameter, respectively. 'z' is the coordination number and is assumed to be equal to 10.

2.3.6 Measurement of Experimental Density and Viscosity of Ionic Liquids

The density and viscosity of both the ILs were measured at atmospheric pressure and the temperature range from 298.15-333.15 K. A digital densitometer (Anton Paar, DMA-4500 M model) with the vibrating tube was used for the measuring the density of two investigated ILs. A U-shaped tube with the sample was excited to vibrate at its characteristic frequency relating to the density of the sample. The densitometer converts this frequency into density. The densitometer deliberates the viscosity correction factor, compensates ambient air pressure, and perceives bubble in sample injection. The temperature of the measuring cell was automatically controlled by densitometer with a resolution of 0.01 K and an accuracy of ±0.03 K. The viscosity measurements were measured on the interfacial rheometer (Anton Paar, Phsica MCR301 model) where the gap between the rheometer geometry plates is about 0.100 mm. The steady shear and dynamic oscillatory shear experiments were carried out in the shear rate range of 5–500 s^{-1}. The details regarding the operational system can be found elsewhere [30,31]. The uncertainty in temperature is ±0.01 K while for density and viscosity it is 0.0002 g cm^{-3} and 0.5 mPa.s, respectively.

2.4 Results and Discussion

2.4.1 Benchmarking Study

Before predicting the solubility data of monosaccharides in ILs using COSMO-RS model, the model was validated with known experimental SLE data as reported in the literature [8,32]. Experimental SLE of sugars (glucose, fructose) and sugar alcohols (xylitol, sorbitol) in ILs were chosen from previous work of Carneiro *et al.* (2013) [8]. Here, the benchmarking studies on solubility were carried out for glucose and fructose in [EMIM][DCA], [BMIM][DCA], and [TTDP][DCA]. The summary of the predicted results are available in Table 2.3 (Glucose in IL) and Table 2.4 (Fructose in IL). The RMSE values for [EMIM][DCA], [BMIM][DCA], and [TTDP][DCA] were 8.86%,6.32% and 0.87%, respectively in glucose. The corresponding RMSE values for fructose were 8.63%, 6.92%, and 6.06%, respectively. The results from the above validation study shows an excellent agreement with the experimental data.

Table 2.3: Predicted (COSMO-RS) solubility data (mole fraction) of glucose in Ionic liquids[a]

T (K)	[EMIM][DCA]		[BMIM][DCA]		[TTDP][DCA]	
	Expt.	Pred.	Expt.	Pred.	Expt.	Pred.
288.25	0.1710	0.0663	0.1330	0.0579	-	-
298.25	0.2070	0.0956	0.1650	0.0841	0.0018	0.0071
308.15	0. 2290	0.1335	0.1920	0.1186	0.0024	0.0100
318.15	0.2548	0.1821	0.2095	0.1634	0.0037	0.0138
328.25	0.2810	0.2424	0.2360	0.2196	0.0048	0.0186
RMSE (%)	8.86		6.32		0.87	

[a] Experimental data were taken from Carneiro *et al.* (2013) [8]

Table 2.4: Predicted (COSMO-RS) solubility data (mole fraction) of fructose in Ionic liquids[a]

T (K)	[EMIM][DCA]		[BMIM][DCA]		[TTDP][DCA]	
	Expt.	Pred.	Expt.	Pred.	Expt.	Pred.
288.25	0.3330	0.1901	0.2810	0.1697	-	-
298.25	0.3600	0.2534	0.3100	0.2286	0.0028	0.0593
308.15	0.3940	0.3266	0.3400	0.2981	0.0070	0.0753
318.15	0.4400	0.4097	0.3780	0.3784	0.0110	0.0940
328.25	0.4950	0.4991	0.4100	0.4668	0.0552	0.1155
RMSE (%)	8.63		6.92		6.06	

[a] Experimental data were taken from Carneiro *et al.* (2013) [8]

In a similar manner, the SLE of sugar alcohols [32] in [EMIM][$EtSO_4$] were also predicted and compared in Table 2.5. The RMSE values of xylitol and sorbitol in [EMIM][$EtSO_4$] was 12.11% and 12.86%, respectively. Further, we have also benchmarked the COSMO-RS model by predicting the experimental solubility data of monosaccharides which were taken from Carneiro *et al.* (2012) [3]. The experimental data for glucose, fructose, galactose, and xylose were predicted successfully in two ILs namely: 1-ethyl-3-methylimidazolium ethylsulphate [EMIM][$EtSO_4$] and methyltrioctylammonium chloride [MTOA][Cl] or [Aliquat®336]. This is shown in Figure 2.2 and 2.3, respectively. The average absolute relative deviation (AARD) in both the systems was 15 and 17%, respectively indicating a reasonable agreement. It can also be inferred that the model is capable to validate the temperature range which varied from 298.15 to 330 K.

Table 2.5: Predicted (COSMO-RS) solubility data (mole fraction) of sugar alcohols (xylitol and sorbitol) in [EMIM][$EtSO_4$][a]

T (K)	Xylitol		Sorbitol	
	Expt.	Pred.	Expt.	Pred.
289.2	0.1130	0.1196	-	-
298.1	0.1460	0.1752	0.2000	0.1965
308.2	0.1870	0.2631	0.2283	0.2780
318.4	0.2470	0.3744	0.2830	0.3913
328.3	0.3100	0.5347	0.3377	0.5995
RMSE (%)	12.11		12.86	

[a] Experimental data were taken from Carneiro *et al.* (2012) [32]

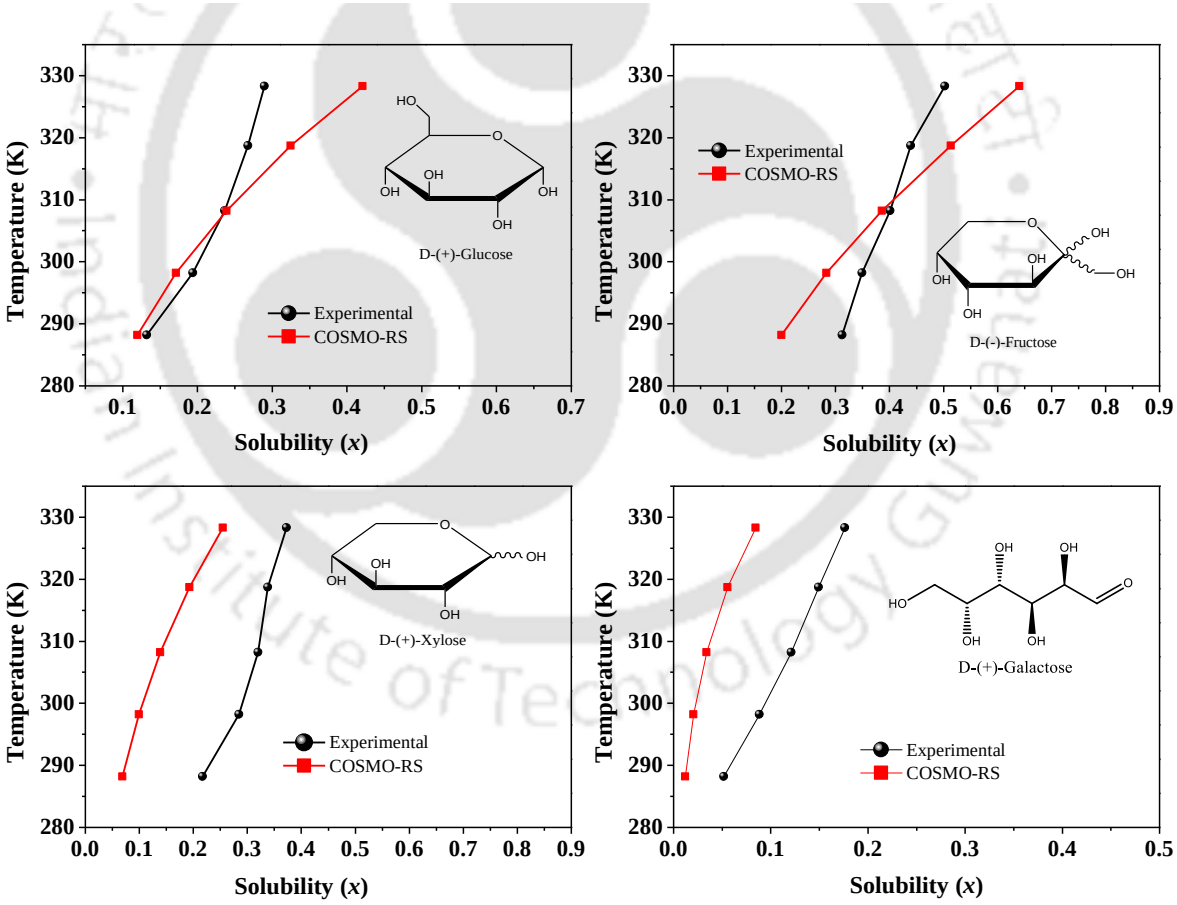

Figure 2.2: Experimental and COSMO-RS predicted solubility (mole fraction) of D-(+)-glucose, D-(-)-fructose, D-(+)-xylose, and D-(+)-galactose in [EMIM][$EtSO_4$]. The experimental data was taken from Carneiro *et al.* (2013) [3].

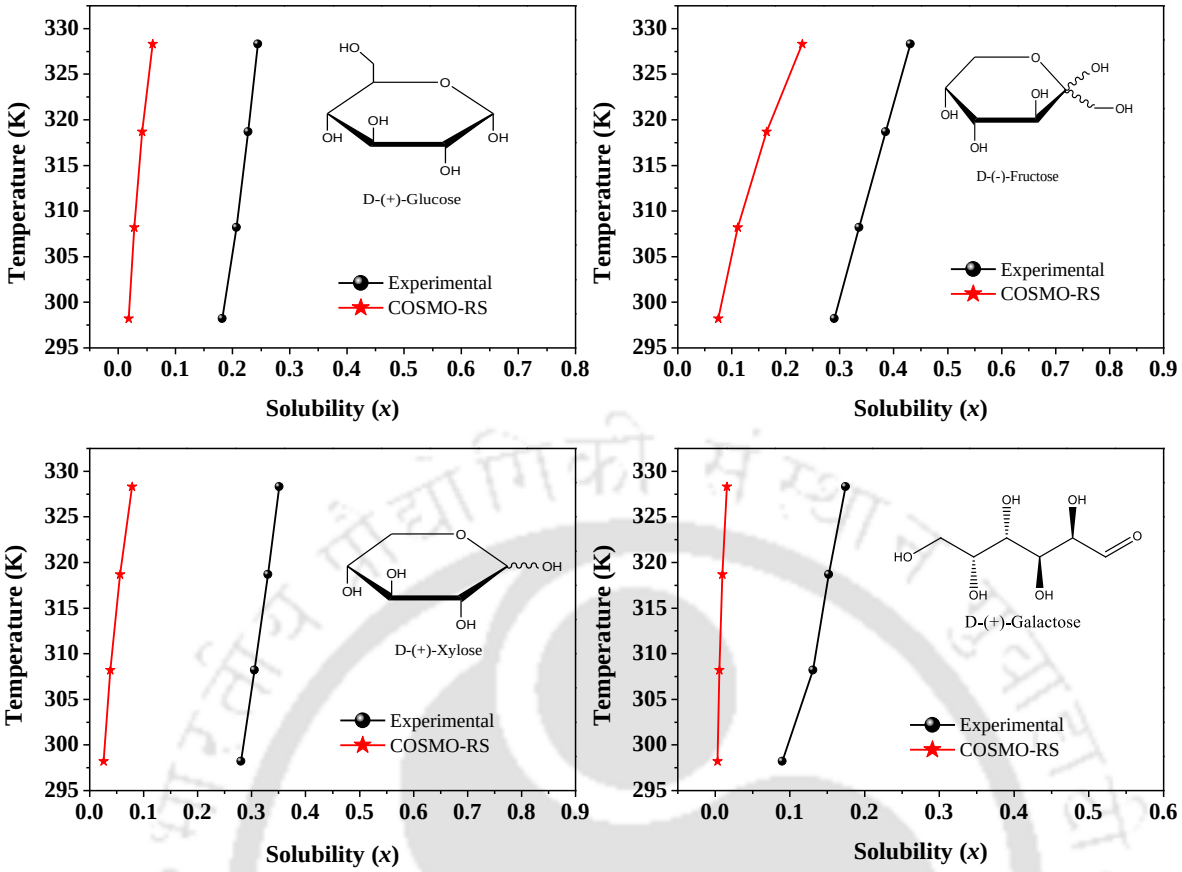

Figure 2.3: Experimental and COSMO predicted solubility (mole fraction) of D-(+)-Glucose, D-(-)-Fructose, D-(+)-Xylose, and D-(+)-Galactose in Aliquat®336. The experimental data was taken from Carneiro *et al.* (2013) [3].

A comparison of COSMO-RS model with UNIQUAC and NRTL model was also made for liquid phase which comprises of only monosaccharides and IL. This has been provided in Table 2.6. It is to be noted that the excess Gibb's free energy model always regress the binary interaction parameters *i.e.*, Δg and Δu by regressing the experimental data through an objective function which is non-linear in nature. The experimental data is available beforehand [3]. However, COSMO-RS performs the same prediction by computing the screening charges densities when a solute is immersed in a conductor. It is fit to very few universal parameters and can predict virtually any mixture barring small exception such as isomers etc. On the other hand, the NRTL and UNIQUAC parameters have limited applicability *i.e.*, the binary interaction parameters cannot be used for other system and are

only specific to the particular system. So in such cases, NRTL and UNIQUAC will always show better agreeability as compared to COSMO-RS. After an extensive benchmarking study, we then attempted the screening of 64 ionic liquids which were formulated from the combination of 31 cations and 23 anions.

2.4.2 Screening of Ionic Liquids by COSMO-RS

Initially, the screening of ILs for the solubility of monosaccharides by COSMO-RS was carried out in the different ionic liquids at 303.15 K. The selected 64 ILs (imidazolium, ammonium, pyridinium, pyrrolidinium, phosphonium, Piperidinium, Sulfonium and other cationic types based ILs) structure and properties are given in the Appendix-A (Table A.1). The optimised geometries and melting properties of monosaccharides are depicted in Figure 2.4 and Table 2.1. It should be noted that without the screening of potential ILs, experimental studies are not possible because of the high cost and time involved. Thus, the actual mole fraction from equation 2.4 is used to rank and choose the potential IL for the dissolution of monosaccharides. Higher the mole fraction values, greater is the tendency for the IL to dissolve the monosaccharides. Hence, separate studies involving the monosaccharides are beyond the scope of this paper.

Table 2.7 shows the solubility of monosaccharides such as D-(+)-Glucose, D-(+)-Xylose, D-(-)-Fructose and D-(+)-Galactose in 64 ILs at 303.15 K. The D-(+)-Glucose solubility was found to be greater than x = 0.05 in 22 ILs (Table 2.7) while D-(+)-Xylose has solubility greater than x = 0.05 in 27 ILs (Table 2.7). D-(-)-Fructose has a solubility greater than x = 0.10 in 38 ILs (Table 2.7) and D-(+)-Galactose solubility having less than x = 0.01 solubility in 37 ILs (Table 2.7). It is clear that D-(-)-Fructose and D-(+)-Galactose shows the highest and lowest solubility, respectively.

Table 2.6: Comparison of NRTL, UNIQUAC and COSMO-RS model with experimental data[a]

Binary system		NRTL			UNIQUAC			COSMO-RS
Solvent	Solute	Δg_{12} (J mol^{-1})	Δg_{21} (J mol^{-1})	AARD (%)	Δu_{12} (J mol^{-1})	Δu_{21} (J mol^{-1})	AARD (%)	AARD (%)
[EMIM][$EtSO_4$]	D-(+)-Glucose	-6337	4454	3.02	-2327	2161	3.21	4.27
	D-(-)-Fructose	-2190	-2057	0.96	-2635	3533	1.14	0.25
	D-(+)-Xylose	-2241	-4730	0.93	-3622	8610	0.91	11.9
	D-(+)-Galactose	-6765	2580	3.52	-1662	572	3.64	15.9
Aliquat®336	D-(+)-Glucose	1490	-4672	2.33	-2803	5333	2.43	20.7
	D-(-)-Fructose	-461	-2840	1.5	-2278	3674	1.42	14.93
	D-(+)-Xylose	-282	-6913	0.96	-3516	-96187	0.85	21.1
	D-(+)-Galactose	-7688	4090	7.08	-2428	2334	7.28	23.4

[a] Experimental data is taken from Carneiro *et al.* (2012) [3]

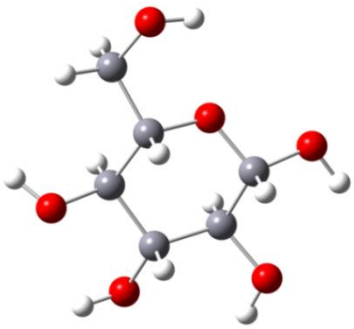

D-(+)-Glucose

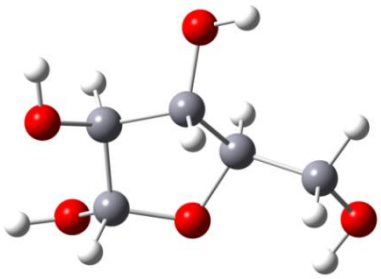

D-(+)-Xylose

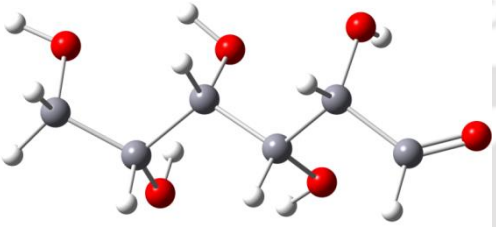

D-(+)-Galactose

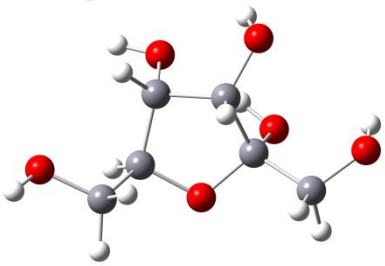

D-(-)-Fructose

Figure 2.4: Structures of monosaccharides used in this work. Color represents the different atoms are C (grey), O (red), and H (white) atoms, respectively.

From the observation of Table 2.7, imidazolium and ammonium based ILs gave the highest solubility for cations possessing less number of carbon side chains. A larger carbon chain length decreases the solubility, which possess a larger van der Waals area and thus allows the entrapment of the all the components in the cation core, thereby reducing selectivity [3,8]. It can be inferred that the imidazolium based ILs are more soluble than ammonium based ILs. For better solubility, the IL thus should obey the following criteria: (a) cation size should not be too large so that hydrogen atoms residing in the core of the cation structure can contribute as hydrogen bond donor and (b) the anion must be a good hydrogen bond acceptor which is possible only when the charge is localized [3]. Therefore, from the COSMO-RS predicted solubility data the following ILs were chosen for experimental studies namely 1-ethyl-3-methylimidazolium thiocyanate ([EMIM][SCN]) and Tris(2-hydroxyethyl)methylammonium methylsulphate ([TMA][$MeSO_4$]). These two ILs

were selected based on their cost, interactions with solutes and lacking of experimental solubility data reported.

Table 2.7: COSMO-RS Predicted solubility (mole fraction) of monosaccharides in 64 ILs at 303.15 K

Ionic Liquid	D-(-)-Fructose	D-(+)-Xylose	D-(+)-Glucose	D-(+)-Galactose
[AMIM][DCA]	0.237	0.052	0.038	0.012
[AMIM][Br]	0.415	0.187	0.127	0.084
[AMIM][TFMS]	0.081	0.019	0.007	0.002
[BeMIM][Cl]	0.397	0.118	0.075	0.026
[BeMIM][BF_4]	0.150	0.045	0.038	0.007
[BMIM][Ac]	0.497	0.247	0.217	0.133
[BMIM][DCA]	0.260	0.056	0.042	0.014
[BMIM][$MeSO_4$]	0.360	0.076	0.064	0.021
[BMIM][PF_6]	0.087	0.018	0.006	0.001
[BMIM][$AlCl_4$]	0.237	0.108	0.076	0.021
[BMIM][TFMS]	0.058	0.013	0.004	0.001
[BMIM][BF_4]	0.162	0.086	0.078	0.032
[BMIM][SCN]	0.358	0.074	0.063	0.022
[BMIM][AcF_3]	0.423	0.186	0.148	0.107
[BMIM][MSF_3]	0.104	0.024	0.013	0.005
[EMIM][Ac]	0.554	0.281	0.243	0.170
[EMIM][AMAc]	0.391	0.116	0.094	0.051
[EMIM][TFMS]	0.071	0.016	0.006	0.001
[EMIM][DCA]	0.264	0.057	0.044	0.014
[EMIM][$DiEtPO_4$]	0.485	0.228	0.164	0.093
[EMIM][$DiMePO_4$]	0.507	0.237	0.174	0.108
[EMIM][$EtSO_4$]	0.362	0.076	0.064	0.021
[EMIM][HSO_4]	0.381	0.082	0.075	0.010
[EMIM][$AlCl_4$]	0.296	0.133	0.103	0.072
[EMIM][BF_4]	0.181	0.095	0.086	0.047
[EMIM][SCN]	0.360	0.074	0.061	0.023
[EMIM][Tos]	0.445	0.287	0.236	0.205
[EMIM][MSF_3]	0.111	0.026	0.014	0.005
[EMIM][AcF_3]	0.473	0.209	0.185	0.140
[HMIM][TFMS]	0.052	0.012	0.003	0.0008
[HMIM][Cl]	0.272	0.138	0.127	0.092

Table 2.7: Continued…

Ionic Liquid	D-(-)-Fructose	D-(+)-Xylose	D-(+)-Glucose	D-(+)-Galactose
[HMIM][MSF_3]	0.095	0.022	0.011	0.004
[HMIM][BF_4]	0.103	0.0221	0.015	0.008
[MOIM][Cl]	0.365	0.128	0.106	0.062
[MOIM][PF_6]	0.068	0.014	0.004	0.0008
[MOIM][MSF_3]	0.086	0.020	0.010	0.004
[PMIM][TFMS]	0.062	0.014	0.005	0.001
[BDMIM][PF_6]	0.033	0.004	0.001	0.0002
[13MIM][DCA]	0.184	0.042	0.031	0.008
[13DMIM][$DiMePO_4$]	0.171	0.067	0.041	0.013
[DMPIM][TFMS]	0.029	0.004	0.001	0.0003
[MTOA][TSC]	0.166	0.051	0.023	0.008
Aliquat336	0.103	0.032	0.023	0.0043
[BTMA][TFMS]	0.035	0.006	0.002	0.0005
[EtA][NO_3]	0.033	0.008	0.006	0.0014
[EDMPA][TFMS]	0.030	0.005	0.001	0.0004
[PrA][NO_3]	0.048	0.012	0.009	0.0024
[TMAM][OH]	0.038	0.003	0.001	0.0009
[TEMA][MC]	0.020	0.002	0.001	0.0008
[TMA][$MeSO_4$]	0.196	0.054	0.037	0.009
[HTMA][Lc]	0.043	0.027	0.018	0.0041
[TTDP][Cl]	0.151	0.010	0.007	0.005
[TTDP][DCA]	0.184	0.042	0.026	0.021
[MTBP][$MeSO_4$]	0.125	0.037	0.030	0.005
[MPPy][TFMS]	0.040	0.007	0.002	0.0006
[BMPy][BF_4]	0.110	0.037	0.021	0.004
[BMPyr][TFMS]	0.0246	0.003	0.0008	0.0003
[BMPyr][DCA]	0.131	0.042	0.010	0.006
[BMPyr][MSF_3]	0.110	0.022	0.010	0.006
[123TCP][TFMS]	0.017	0.003	0.0008	0.0002
[123TCP][DCA]	0.061	0.028	0.0081	0.007
[4EMMP][MC]	0.101	0.033	0.022	0.005
[BMP][TFMS]	0.023	0.003	0.0008	0.0002
[TES][TFMS]	0.035	0.006	0.002	0.0005

From the observation of Table 2.7, imidazolium and ammonium based ILs gave the highest solubility for cations possessing less number of carbon side chains. A larger carbon chain length decreases the solubility, which possess a larger van der Waals area and thus allows the entrapment of the all the components in the cation core, thereby reducing selectivity [3,8]. It can be inferred that the imidazolium based ILs are more soluble than ammonium based ILs. Therefore, from the COSMO-RS predicted solubility data the following ILs were chosen for experimental studies: 1-ethyl-3-methylimidazolium thiocyanate ([EMIM][SCN]) and Tris(2-hydroxyethyl)methylammonium methylsulphate ([TMA][$MeSO_4$]). These two ILs were selected based on their cost, interactions, and lacking of experimental solubility data reported.

2.4.3 Experimental and COSMO-RS Predicted Solubility

After an extensive screening of ILs by COMSO-RS model, two types of ILs have been selected for measuring the experimental solubility of monosaccharides. The melting properties of all the monosaccharides used in this study are presented in Table 2.1. The measured solubility (or SLE) data of monosaccharides in two ILs over the temperature range from 303.15-353.4 K are listed in Table 2.8. As obvious from Table 2.8, the solubility of monosaccharides in [EMIM][SCN] is higher than [TMA][$MeSO_4$]. This can be explained due to the nature of interaction between solutes and IL. It should be noted that the hydrophobicity of Tris(2-hydroxyethyl)methylammonium ($[TMA]^+$) cation causes weak interaction between solutes and IL as compared to the hydrophilic IL *i.e.*, [EMIM][SCN]. On the other hand, the alkyl chain length of 1-ethyl-3-methylimidazolium ($[EMIM]^+$) cation is also small as compared to $[TMA]^+$ cation. The ammonium cation has a large alkyl chain length (hydrophobic), which reduces the affinity with polar substances such as monosaccharides.

Table 2.8: Experimental and COSMO-RS predicted solubility of monosaccharides in ILs at atmospheric pressure (p = 1 Atm) and different temperatures[a]

T (K)	D-(+)-Glucose		D-(+)-Xylose		D-(-)-Fructose		D-(+)-Galactose	
	1-ethyl-3-methylimidazolium thiocyanate [EMIM][SCN]							
	Expt.	Pred.	Expt.	Pred.	Expt.	Pred.	Expt.	Pred.
303.15	0.092	0.061	0.110	0.074	0.365	0.360	0.041	0.023
313.20	0.119	0.092	0.145	0.118	0.415	0.440	0.058	0.037
323.25	0.178	0.126	0.210	0.161	0.480	0.519	0.074	0.057
333.30	0.201	0.168	0.246	0.213	0.564	0.593	0.113	0.086
343.35	0.234	0.218	0.290	0.276	0.659	0.660	0.136	0.126
353.40	0.260	0.275	0.331	0.347	0.713	0.723	0.164	0.178
RMSE	3.11%		3.12%		2.32%		1.83%	
$u(x)$[b]	0.040		0.062		0.094		0.021	
T (K)	D-(+)-Glucose		D-(+)-Xylose		D-(-)-Fructose		D-(+)-Galactose	
	Tris(2-hydroxyethyl)methylammonium methylsulfate [TMA][$MeSO_4$]							
	Expt.	Pred.	Expt.	Pred.	Expt.	Pred.	Expt.	Pred.
303.15	0.036	0.037	0.051	0.054	0.191	0.196	0.013	0.009
313.20	0.049	0.054	0.073	0.078	0.253	0.263	0.021	0.015
323.25	0.076	0.078	0.093	0.110	0.330	0.343	0.031	0.024
333.30	0.102	0.109	0.167	0.152	0.395	0.438	0.033	0.038
343.35	0.127	0.149	0.193	0.205	0.500	0.546	0.057	0.058
353.40	0.226	0.200	0.283	0.271	0.630	0.663	0.073	0.086
RMSE	1.47%		1.20%		2.94%		0.70%	
$u(x)$[b]	0.046		0.080		0.020		0.018	

[a] Standard uncertainty for temperature and pressure are u (T) = 0.1 K and u (p) = 1 kPa;

[b] Standard uncertainty calculated by using following equation, $u(x_i) = \left(\frac{1}{n(n-1)} \sum_{k=1}^{n} (x_{i,k} - X_i)^2 \right)^{\frac{1}{2}}$

Further from Table 2.7, the experimental and predicted solubility data of monosaccharides in ILs at different temperatures are given along with their RMSE. It can be seen that the COSMO-RS model is able to correctly account for the trend and the nature of the deviation in the solubilities with respect to temperature. Table 2.7 shows the solubility values of monosaccharides in [EMIM][SCN] and [TMA][$MeSO_4$]. The RMSE values of monosaccharides *i.e.*, D-(+)-Glucose, D-(+)-Xylose, D-(-)-Fructose and D-(+)-Galactose in [EMIM][SCN] are 3.11%, 3.12%, 2.32%, and 1.83%, respectively while the corresponding figures in [TMA][$MeSO_4$] are 1.47%, 1.20%, 2.94% and 0.70%. Thus, the experimental data shows an excellent agreement with COSMO-RS predictions.

The solubility of monosaccharides in both ILs ([EMIM][SCN] and [TMA][$MeSO_4$]) were found to increase with temperature. D-(-)-Fructose shows the highest solubility while D-(+)-Galactose has the lowest solubility in both ILs. This is partially due to the lower melting point of D-(-)-Fructose as compared to D-(+)-Galactose. Higher the melting temperature and enthalpy of fusion values, lower the solubility and vice versa. An additional hydroxyl group in [TMA][$MeSO_4$] seems to be sufficient to make a substantial difference in solubility for [EMIM][SCN], in which solute-solvent interactions are strong. The overall solubility ranking of monosaccharides in two ILs was: D-(-)-Fructose > D-(+)-Xylose > D-(+)-Glucose > D-(+)-Galactose.

Physical properties such as density and viscosity also leads to the faster dissolution of solute (Table 2.8) [33]. From Table 2.8, the density and viscosity of [TMA][$MeSO_4$] were found to be higher in magnitude than [EMIM][SCN]. In recent studies, it was confirmed that the density and viscosity decreases with a lower molecular weight of anions (SCN = 58.08 g mol^{-1} and $MeSO_4$ = 110.10 g mol^{-1}) [34,35]. Thus higher the density and viscosity values, lower the mass transfer rate of IL in the dissolution process. This is also one of the supporting reason that, why [TMA][$MeSO_4$] had a lower solubility than [EMIM][SCN]. We

also measured the temperature dependence of viscosity for both ILs over a temperature range of 298.15-333.15 K (Table 2.8). The temperature dependent viscosities of ILs were then used to fit an Arrhenius equation so as to derive the activation energy for viscous flow and the viscosity at an infinite temperature (Eqn (2.14)) [36,37].

$$\eta = \eta_{\infty} \exp\left(\frac{-E_{\eta}}{RT}\right) \tag{2.14}$$

Here, E_{η} and η_{∞} are the activation energy for viscous flow and viscosity at infinite temperature respectively.

Table 2.9: The experimental density and viscosity data of pure ILs at atmospheric pressure (p = 1 Atm) and different temperatures[a]

Density, ρ (g cm^{-3})[b,c]			Viscosity, η (mPa.s)[b,d]		
T (K)	[EMIM][SCN]	[TMA][MeSO$_4$]	T (K)	[EMIM][SCN]	[TMA][MeSO$_4$]
300.15	1.1151	1.3415	298.15	24	781
303.29	1.1132	1.3397	303.15	17.6	510
308.29	1.1102	1.3367	308.15	13.8	370
313.29	1.107	1.3336	313.15	11.161	278
318.29	1.104	1.3309	318.15	9.7124	213
323.29	1.1012	1.3280	323.15	8.6164	169
333.15	1.0951	1.3221	333.15	7.0783	111

[a] Standard uncertainty u are u (T) = 0.1 K, u (p) = 1 kPa; [b] The relative expanded uncertainty U are $U_r(\rho)$ = 0.004 and $U_r(\eta)$ = 0.17 (0.95 level of confidence)

[c] Equation fitting for density (T in °C) (1) [Emim][SCN]: ρ = -6.05E-04 T + 1.29676, (2) [TMA][MeSO$_4$]: ρ = -5.87E-04 T + 1.51758;

[d] Equation fitting for Viscosity (T in °C) (1) [Emim][SCN]: η = -6.07E-04 T^3 + 0.094 T^2 - 5.032 T + 100.203, (2) [TMA][MeSO$_4$]: η = -0.0262 T^3 + 4.012 T^2 – 210.16 T + 3928.69

Figure 2.5 shows that the variation between the logarithmic of viscosity against temperature. From Figure 2.5, the activation energy for viscous flow (*i.e.*, slope of Figure 2.5) and infinite temperature viscosities (*i.e.*, Figure 2.5 intercept) of [EMIM][SCN] and

[TMA][$MeSO_4$] were 28.51 kJ mol^{-1}, 2.14×10^{-4} mPa.s and 45.44 kJ mol^{-1}, 7.69×10^{-6} mPa.s, respectively. The higher value of E_η makes it difficult for the ions to move at a faster rate. This is attributed to the large physical size of the IL [36]. A method to reduce the viscosity of IL would be to utilize suitable co-solvents. This will reduce the interaction between cation and anions of IL and improves the solubility of solute [38,39].

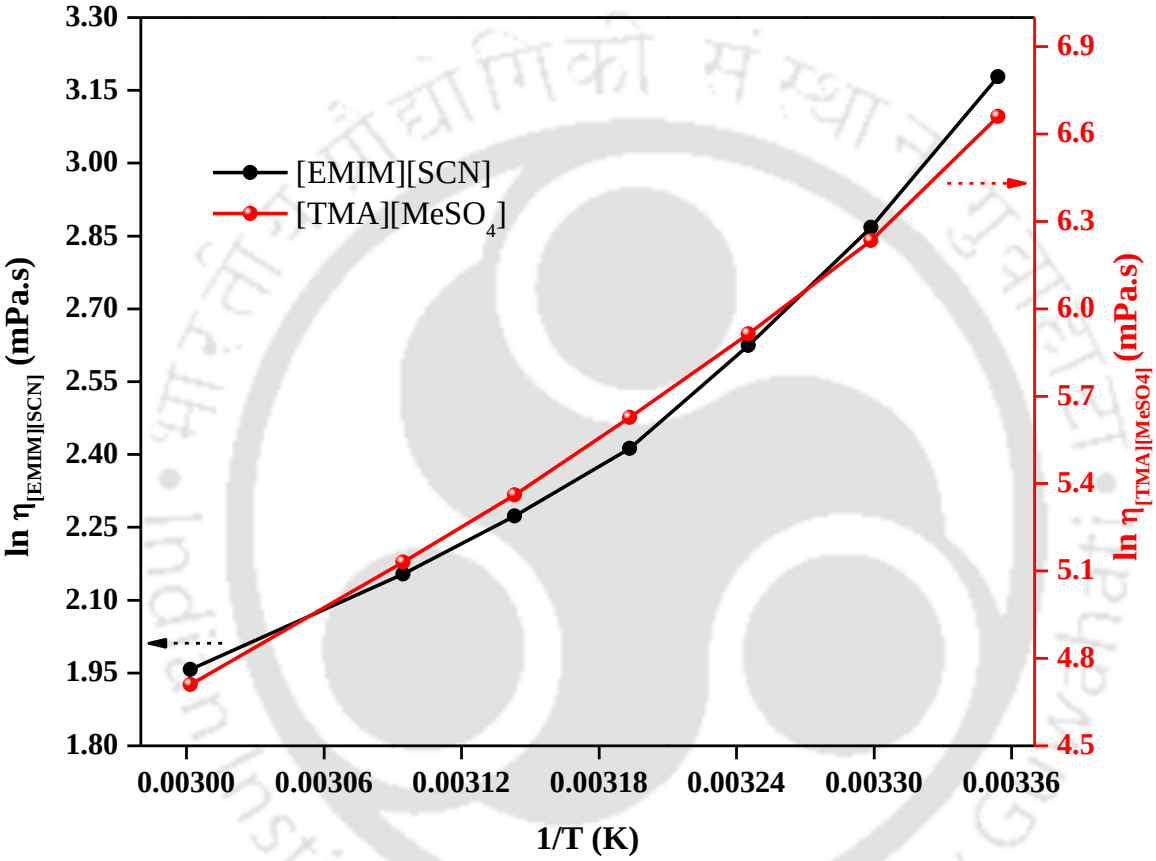

Figure 2.5: Arrhenius plot for ionic liquids as a function of temperature

2.4.4 Thermodynamic Functions of Dissolution

Apparent thermodynamic functions of dissolution, $\Delta^{o}_{dissol.}H$, $\Delta^{o}_{dissol.}G$ and $\Delta^{o}_{dissol.}S$ were obtained from the experimental data. The enthalpy of dissolution $\Delta^{o}_{dissol.}H$ indicates the dissolution process, *i.e.*, the amount of heat absorbed or released. Gibbs free energy, $\Delta^{o}_{dissol.}G$ points indicates the nature of process *i.e.*, spontaneous or non-spontaneous. The entropy of dissolution, $\Delta^{o}_{dissol.}S$ discusses the more favorable state *i.e.*, solution or pure

solvent. These functions are also important since they measure the energetic parameters in equation of state. The approach was proposed by Krug *et al.* (1976) [40] which are based on the modified Van't Hoff equation as given below:

$$\left[\frac{\partial(\ln x_2)}{\partial\left(\frac{1}{T}-\frac{1}{T_{hm}}\right)}\right]_p = -\frac{\Delta^o_{dissol.}H}{R} \tag{2.15}$$

Where x_2 is the mole fraction of solute at saturated condition (solubility), R the universal gas constant J $mol^{-1}K^{-1}$, T the temperature in K, and T_{hm} is the harmonic average of mean of the experimental temperature given by:

$$T_{hm} = \frac{N_p}{\sum_{i=1}^{N_p}\frac{1}{T_i}} \tag{2.16}$$

Where N_p is the number of experimental data points. The enthalpy of dissolution $\Delta^{o}_{dissol.}H$ was obtained from the slope of linear plot of ln x_{exp} *vs* $(1/T\text{-}1/T_{hm})$, as shown in Figure 2.6 (a, b). The apparent standard change of Gibb's free energy during the dissolution can be obtained from the following expression:

$$\Delta^o_{dissol.}G = -RT_{hm}k \tag{2.17}$$

Where the constant k is the intercept for the linear plot of ln x_{exp} *vs* $(1/T\text{-}1/T_{hm})$ as shown in Figure 2.6 (a, b). Finally, the entropy of dissolution $\Delta^{o}_{dissol.}S$ is given in below Eqn (2.17):

$$\Delta^o_{dissol.}S = \frac{\Delta^o_{dissol.}H - \Delta^o_{dissol.}G}{T_{hm}} \tag{2.18}$$

Table 2.9 presents the thermodynamic functions of dissolution for each binary system studied in this work. The experimental enthalpy of dissolution $\Delta^{o}_{dissol.}H$, shows positive values in all cases thereby representing an endothermic behaviour (heat absorbing) in the dissolution processes. Entropy of dissolution also plays an important role as it is an

indicator if the configuration of solvent molecules after dissolution is more or less favorable than the configuration in the pure solvent. The entropy of dissolution $\Delta^{o}_{dissol.}S$, shows a positive value for all systems studied in this work, indicating more degrees of freedom to the ILs when they possess solvating molecules of carbohydrates than pure IL molecules. The positive values of apparent standard change of Gibb's free energy $\Delta^{o}_{dissol.}G$, indicates a dissolution processes which are non-spontaneous and takes place under continuous energy supply.

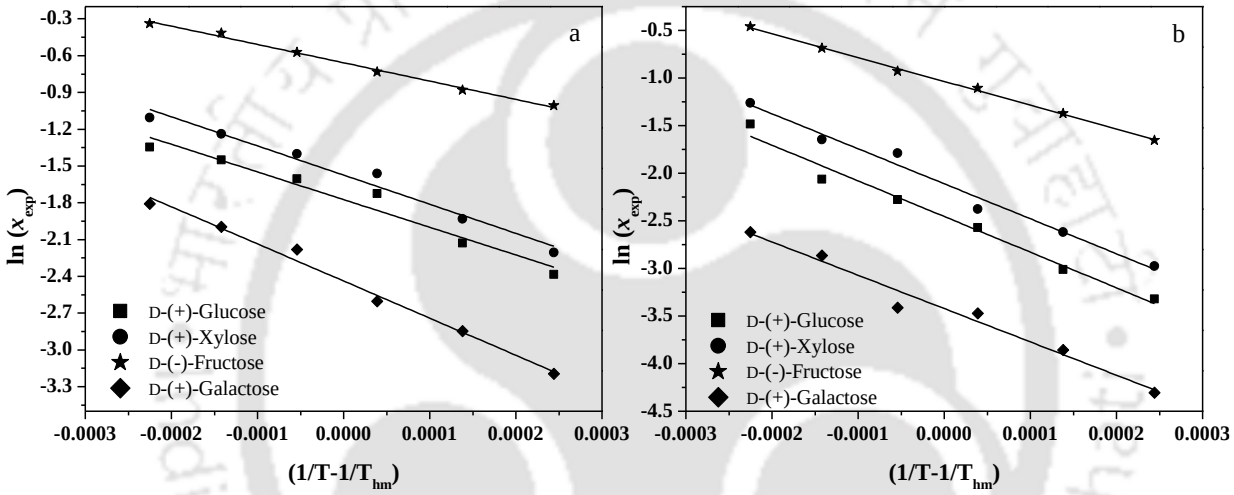

Figure 2.6: Linear representation of ln (x_{exp}) *vs* [(1/T)-(1/T_{hm})] in (a) [EMIM][SCN], (b) [TMA][$MeSO_4$]

Table 2.10: Apparent thermodynamic functions of dissolution at N_p = 6 and T_{hm} = 327.37 K

Solvent	Solute	$\Delta^{o}_{dissol.}H$ (kJ mol^{-1})	$\Delta^{o}_{dissol.}G$ (kJ mol^{-1})	$\Delta^{o}_{dissol.}S$ (J mol^{-1})
[EMIM][SCN]	D-(+)-Glucose	18.76	4.82	42.56
	D-(+)-Xylose	19.75	4.28	47.26
	D-(-)-Fructose	12.41	1.79	32.46
	D-(+)-Galactose	25.18	6.63	56.64
[TMA][$MeSO_4$]	D-(+)-Glucose	31.14	6.68	74.72
	D-(+)-Xylose	30.56	5.74	75.80
	D-(-)-Fructose	20.78	2.81	54.88
	D-(+)-Galactose	29.09	9.31	60.41

2.4.5 Thermodynamic Modeling

The Gibb's free energy models such as NRTL and UNIQUAC were used to correlate the experimental solubility data. The binary interaction parameters of the NRTL and UNIQUAC models were calculated by fitting the experimental data by using Genetic Algorithm (GA) toolbox. Recently, GA toolbox was widely used as an optimization technique and it was first proposed by Holland [41]. It is a method that searches for the global optima of an objective function through the use of simulated evolution, the survival of the fittest strategy [42]. Unlike most of the optimization methods, GA leads to globally optimum values; it does not require any initial guess but only the upper and lower bounds of the interaction parameters. It has also been shown to perform better than Inside Variance Estimation Method and the techniques used in ASPEN and DECHEMA. GA explores all regions of the solution and exploits the promising areas through selection, crossover and mutation operators applied to the interaction parameters constituting the population. It gives us the best population of interaction parameters, based on the upper and lower bound of the interaction parameters. The methodology, application, and the details are presented in our earlier work [42,43]. GA toolbox is only used for maximization, hence for minimizing the error between experimental and calculated mole fractions, a negative *objective function (F)* is written [43]:

$$\text{Maximize}: \quad F_{\left(\begin{array}{l}\text{with respect to } A_{ij}\\ \text{where } i,j=1,2,3\\ \text{and } j\neq i\end{array}\right)} = -\sum_{k=1}^{m}\sum_{l=I}^{II}\sum_{i=1}^{c} w_{ik}^{l}\left(x_{ik}^{l}-\hat{x}_{ik}^{l}\right)^{2}, \quad w_{ik}^{l}=1 \tag{2.19}$$

Here, x_{ik}^{l} and $\hat{x}_{ik}^{l}$ refers to the experimental and predicted mole fractions, respectively. For optimization, we have used the Genetic Algorithm (GA) program toolbox in MATLAB. A population size of 100 and 200 generations has been used in the optimization [42,43]. The modified Rachford-Rice algorithm [44,45] was used to compute the mole fractions.

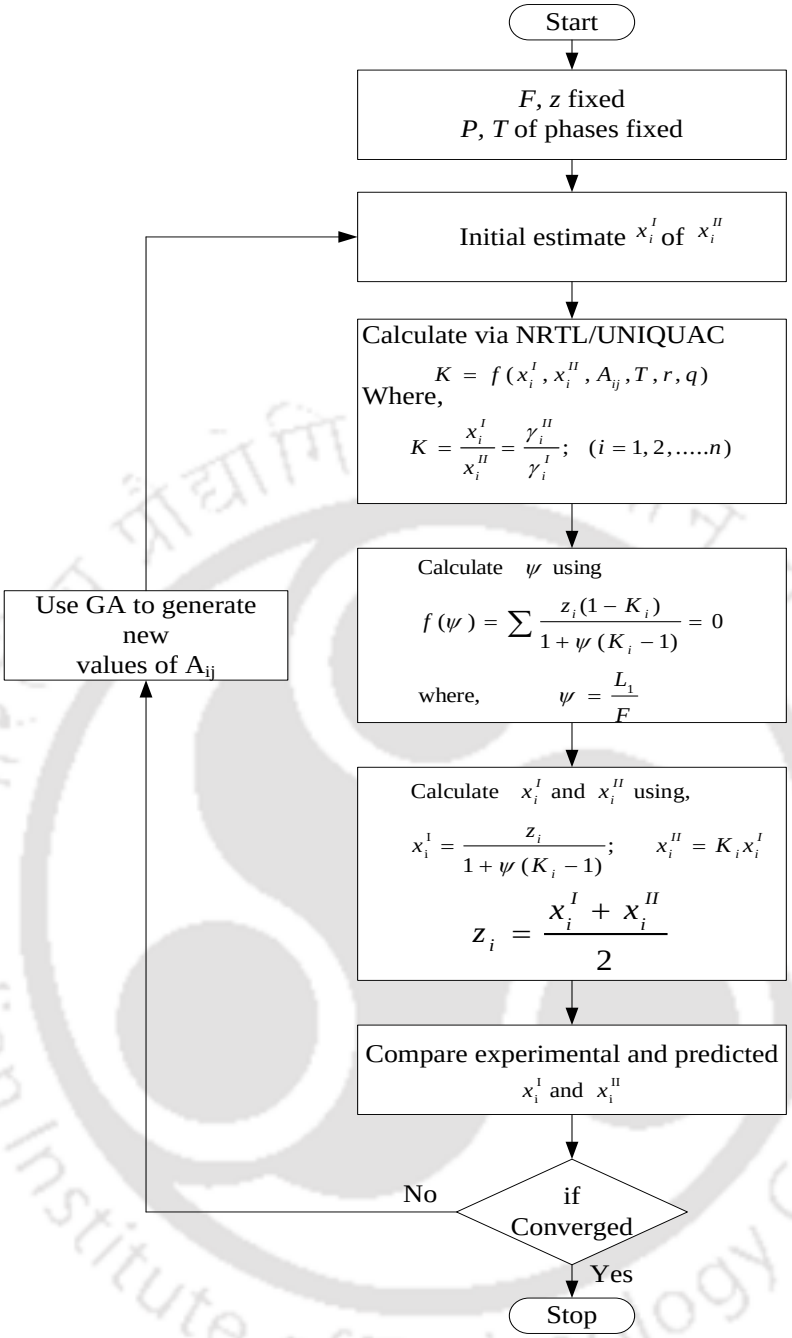

Figure 2.7: Modified Rashford–Rice algorithm for NRTL and UNIQUAC model (adapted from Banerjee and Ramalingam (2015), [45])

The flowchart in Figure 2.7 explains the GA procedure. For the UNIQUAC model, the structure parameters *r* and *q* of the components are predicted from the following equations using the Polarizable Continuum Model (PCM) as outlined in our previous work [46].

$$r = \frac{\left(V^{PCM}\,\text{Å}^3\right)\left(1\times10^{-8}\text{cm}\right)^3 N_{av}}{V_{ws}} \tag{2.20}$$

$$q = \frac{\left(A^{PCM}\,\text{Å}^2\right)\left(1\times10^{-8}\text{cm}\right)^2 N_{av}}{A_{ws}} \tag{2.21}$$

Where, 'N_{av}' is the Avogadro's number. The standard segment volume V_{ws} (15.17 $cm^3\ mol^{-1}$) and area A_{ws} ($2.5\times10^9\ cm^2\ mol^{-1}$) was used the same values as used by bondi. V^{PCM} and A^{PCM} are the molecular volume and surface area computed using PCM calculation [46].

The r and q values of monosaccharides and IL ([TMA][$MeSO_4$]) were available in the literature [3,27]. The PCM calculation was performed only for [EMIM][SCN] as the values were absent and presented in Table 2.10. Table 2.11 gives us the binary interaction parameters for monosaccharides in ILs. Figure 2.8 (a, b) shows the experimental solubility data and their correlation with the NRTL, UNIQUAC models. Both the models had shown a very good agreement with experimental solubility data of monosaccharides. The average root mean square error values are less than 4% for both IL systems. The sigma profile of ILs and monosaccharides has been discussed in the coming section.

Table 2.11: UNIQUAC structural parameters for the different compounds in the SLE systems

Component Name	Volume parameter (r)	Surface Parameter (q)	Reference
D-(+)-Glucose	5.80	4.84	[3]
D-(-)-Fructose	5.80	4.92	[3]
D-(+)-Xylose	4.83	4.03	[3]
D-(+)-Galactose	5.80	4.84	[3]
[EMIM][SCN][a]	5.74	4.24	-
[TMA][$MeSO_4$]	6.15	4.92	[27]

[a] Calculated from Banerjee *et al.* (2005) [46] *via* PCM model

Table 2.12: Correlation of the solid-liquid equilibria data by means of the NRTL and UNIQUAC equations

Binary systems		NRTL Parameters (α = 0.2)			UNIQUAC Parameters		
Solvent	Solute	Δg_{12} (kJ mol^{-1})	Δg_{21} (kJ mol^{-1})	RMSE (%)	Δu_{12} (kJ mol^{-1})	Δu_{21} (kJ mol^{-1})	RMSE (%)
[EMIM][SCN]	D-(+)-Glucose	9.8172	16.424	0.73	365.00	-88.777	2.54
	D-(+)-Xylose	11.172	15.270	1.12	292.73	-48.954	2.94
	D-(-)-Fructose	3.7249	-0.4140	2.33	398.00	-143.64	2.15
	D-(+)-Galactose	5.8324	19.243	0.81	367.86	-62.134	2.17
[TMA][$MeSO_4$]	D-(+)-Glucose	5.0785	19.42	1.20	246.01	-12.626	2.90
	D-(+)-Xylose	4.2648	19.205	1.41	189.11	29.828	3.32
	D-(-)-Fructose	3.1296	17.233	2.70	266.26	-71.182	3.04
	D-(+)-Galactose	5.9219	20.000	1.09	320.97	5.3147	1.21

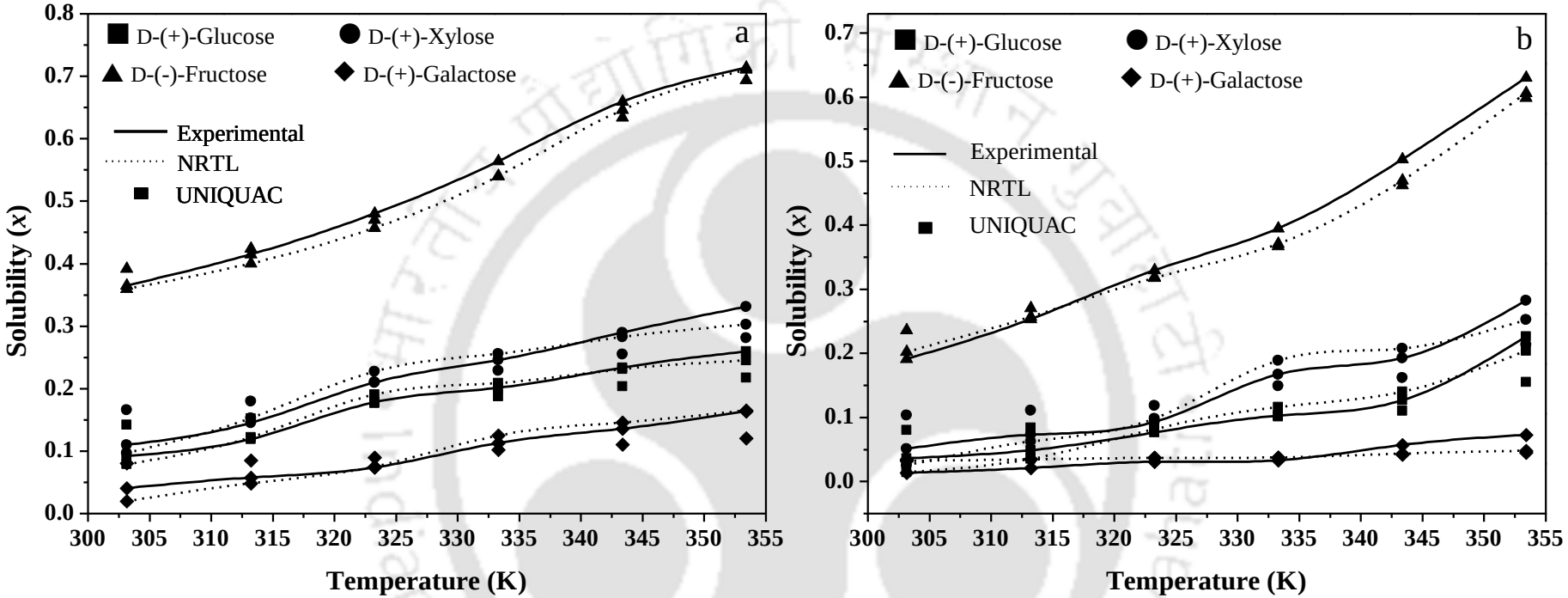

Figure 2.8: Solubility of monosaccharides (%) *vs* temperature (K) in (a) [EMIM][SCN], (b) [TMA][$MeSO_4$]

2.4.6 Sigma Profile of IL-Monosaccharides

The first step of COSMO-RS calculation is to estimate the sigma profile. Sigma profile is the only descriptor which describes the local polarity of molecular surface and finds the interactions between the IL and solute. In the solubility study of monosaccharides in ILs, it is necessary to consider the issue of hydrogen bonding on the solubility process. Figure 2.9 shows the sigma profiles and COSMO cavities of the ILs. The cut-off value for hydrogen bonding interactions in normalised sigma profile lies between -0.0084 e.Å^{-2} > σ > +0.0084 e.Å^{-2}. This signifies that the sigma profile lying on the left side of σ_{hb} = -0.0084 e.Å^{-2} will have high hydrogen bonding donator capacity and the right side of σ_{hb} = +0.0084 e.Å^{-2} will have a hydrogen bonding acceptor capacity. Sigma profile is lying in the negative region because of positive charge of atom/molecule and lying in positive region because of negative charge of atom/molecule. All the neutral charge compounds having both positive and negative charges therefore peak of all compounds lies in between -0.0084 e.Å^{-2} to +0.0084 e.Å^{-2} *i.e.*, neutral region.

From Figure 2.9, a higher fraction of sigma profile in cation lies around the negative side of sigma profile σ_{hb} = -0.0084 e.Å^{-2}, while the prominent peak of the anion lies on the positive side of sigma profile σ_{hb} = +0.0084 e.Å^{-2}. In COSMO cavities, the red colour indicating a positive surface charge screens negative partial charges within the molecule while the blue colour indicating a negative surface charge screens positive partial charges within the molecule. The yellow and green colour symbolised neutral charges. As can be seen from Figure 2.9, the $[EMIM]^+$ cation exhibits less polar in nature than $[TMA]^+$, which results $[EMIM]^+$ has less hydrogen bond donating capacity than $[TMA]^+$. The anions $[SCN]^-$ and $[MeSO_4]^-$ are higher in polar nature (*i.e.*, strong hydrogen bond acceptor capacity). However, [EMIM][SCN] gave higher dissolution capacity of sugars than $[TMA][MeSO_4]$, although $[TMA]^+$ and $[MeSO_4]^-$ has higher fractions of polar segments (Figure 2.9). When

$[MeSO_4]^-$ combines with $[TMA]^+$, the interaction between monosaccharides and $[TMA][MeSO_4]$ gets weakened due to the formation of a strong interaction between $[TMA]^+$ and $[MeSO_4]^-$.

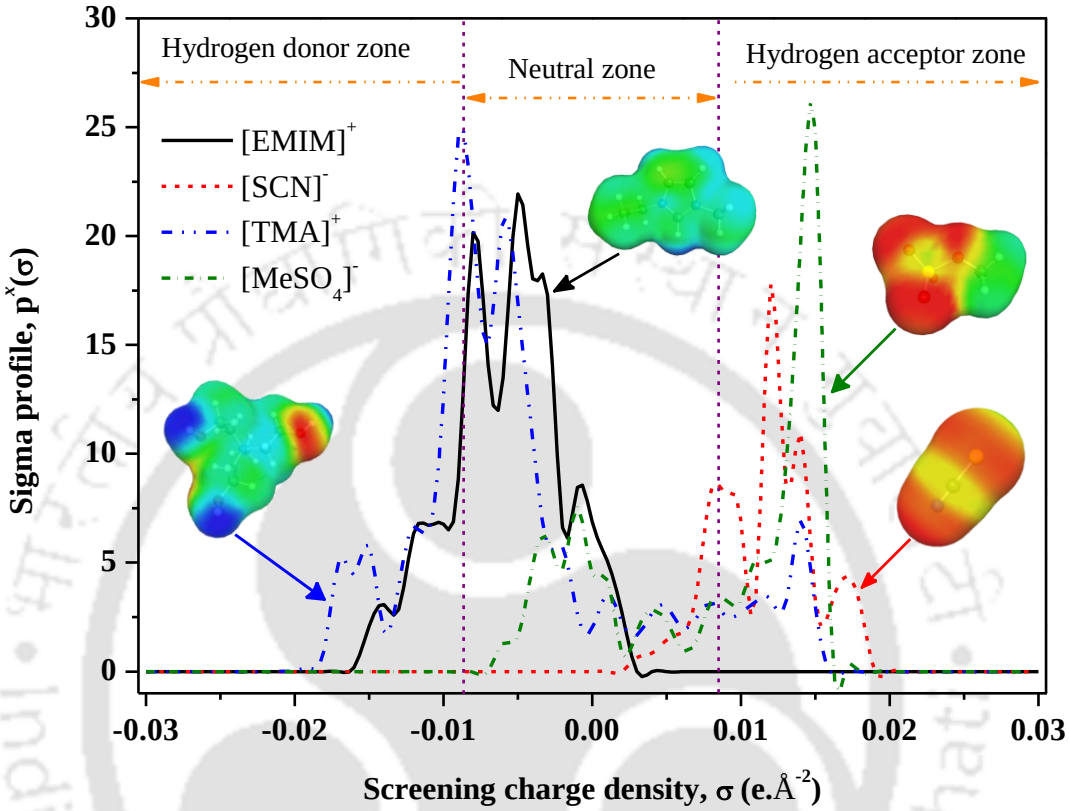

Figure 2.9: Sigma profiles and COSMO cavities of cations and anions

2.5 Summary

COSMO-RS based screening for the solubility of monosaccharides in 64 ionic liquids was predicted over the temperature ranging from 303.15-373.5 K. From the screening studies, imidazolium and ammonium based ILs showed higher solubility than other cations. Hence, the two ILs namely [EMIM][SCN] and [TMA][$MeSO_4$] were chosen for measuring the experimental solubility of monosaccharides. The solubility of monosaccharides in ILs were found to increase with increasing temperature. The results showed that the dissolving capacity for [EMIM][SCN] was higher than [TMA][$MeSO_4$]. The COSMO-RS predictions reproduced the experimental trend with a maximum RMSE deviation of ~5% in both the ILs. The standard thermodynamic functions of dissolution were also determined from the modified van't Hoff equation. The local thermodynamic models namely NRTL and UNIQUAC models were applied to correlate the experimental solubility data. The binary interaction parameters for both models gave an RMSE less than 4% with the experimental data.

References

[1] Kosan B, Michels C, Meister F. Dissolution and forming of cellulose with ionic liquids. Cellulose 2008;15:59-66.

[2] Vancov T, Alston A-S, Brown T, McIntosh S. Use of ionic liquids in converting lignocellulosic material to biofuels. Renew Energ 2012;45:1-6.

[3] Carneiro AP, Rodríguez O, Macedo EA. Solubility of monosaccharides in ionic liquids – Experimental data and modeling. Fluid Phase Equilib 2012;314:22-8.

[4] Sun N, Rodriguez H, Rahman M, Rogers RD. Where are ionic liquid strategies most suited in the pursuit of chemicals and energy from lignocellulosic biomass? Chem Commun 2011;47:1405–21.

[5] Lopes DCAM, Joao KG, Rubik DF, Lukasik EB, Duarte LC, Andreaus J, et al. Pre-treatment of lignocellulosic biomass using ionic liquids: Wheat straw fractionation. Bioresour Technol 2013;142:198-208.

[6] Ferreira AR, Freire MG, Ribeiro JC, Lopes FM, Crespo JG, Coutinho JAP. Overview of the Liquid–Liquid Equilibria of Ternary Systems Composed of Ionic Liquid and Aromatic and Aliphatic Hydrocarbons, and Their Modeling by COSMO-RS. Ind Eng Chem Res 2012;51:3483-507.

[7] Liu W, Hou Y, Wu W, Ren S, Jing Y, Zhang B. Solubility of Glucose in Ionic Liquid + Antisolvent Mixtures. Ind Eng Chem Res 2011;50:6952-6.

[8] Carneiro AP, Rodríguez O, Macedo EA. Fructose and Glucose Dissolution in Ionic Liquids: Solubility and Thermodynamic Modeling. Ind Eng Chem Res 2013;52:3424-35.

[9] Paduszyński K, Okuniewski M, Domańska U. Renewable Feedstocks in Green Solvents: Thermodynamic Study on Phase Diagrams of d-Sorbitol and Xylitol with Dicyanamide Based Ionic Liquids. J Phy Chem B 2013;117:7034–46.

[10] Hassan ESRE, Mutelet F, Pontvianne S, Moise JC. Studies on the dissolution of glucose in ionic liquids and extraction using the antisolvent method. Environ Sci Tech 2013;47:2809-16.

[11] Klamt A, Schuuurmann G. COSMO: a new approach to dielectric screening in solvents with explicit expressions for the screening energy and its gradient. Journal of the Chemical Society, Perkin Transactions 1993;2:799-805.

[12] Banerjee T, Sahoo RK, Rath SS, Kumar R, Khanna A. Multicomponent liquid-liquid equilibria prediction for aromatic extraction systems using COSMO-RS. Ind Eng Chem Res 2007;46:1292–304.

[13] Rosenboom J-G, Afzal W, Prausnitz JM. Solubilities of some organic solutes in 1-ethyl-3-methylimidazolium acetate. Chromatographic measurements and predictions from COSMO-RS. J Chem Thermodyn 2012;47:320-7.

[14] Kahlen J, Masuch K, Leonhard K. Modelling cellulose solubilities in ionic liquids using COSMO-RS. Green Chem 2010;12:2172-81.

[15] Pilli SR, Banerjee T, Mohanty K. Extraction of pentachlorophenol and dichlorodiphenyltrichloroethane from aqueous solutions using ionic liquids. J Ind Eng Chem 2012;18:1983-96.

[16] Xia Q, Chen SN, Chen YS, Zhang MS, Zhang FB, Zhang GL. Solubility of decanedioic acid in binary solvent mixtures. Fluid Phase Equilib 2011;304:105–9.

[17] Domanska U, Pobudkowska A, Gierycz P. Experimental solid-liquid phase equilibria of {cholesterol + binary solvent mixture: 1-Alcohol (C4-C10) + Cyclohexane}. Fluid Phase Equilib 2010;289:20-31.

[18] Domanska U. Solubility of n-Alkanes (C16, C18, C20) in binary solvent mixtures. Fluid Phase Equilib 1989;46:223-48.

[19] Balaji C, Banerjee T, Goud VV. COSMO-RS Based Predictions for the Extraction of Lignin from Lignocellulosic Biomass Using Ionic Liquids: Effect of Cation and Anion Combination. J Solution Chem 2012;41:1610-30.
[20] Frisch MJ, Trucks GW, Schlegel HB, Scuseria GE, Robb MA, Cheeseman JR, et al. Gaussian 03. revision C. 02 ed. Wallingford, CT: Gaussian, Inc.; 2004.
[21] Gray MC, Converse AO, Wyman CE. Sugar Monomer and Oligomer Solubility. Appl Biochem Biotechnol 2003;105-108:179-93.
[22] Barone V, Cossi M. Quantum Calculation of Molecular Energies and Energy Gradients in Solution by a Conductor Solvent Model. Journal of Physical Chemistry A 1998;102:1995–2001.
[23] Bharti A, Kundu D, Rabari D, Banerjee T. Phase Equilibria in Ionic Liquid Facilitated Liquid–Liquid Extractions. 1st ed. Boca Raton, USA: CRC Press; 2017.
[24] Anantharaj R, Banerjee T. Quantum chemical studies on the simultaneous interaction of thiophene and pyridine with ionic liquid. AIChE J 2011;57:749-64.
[25] Varma NR, Ramalingam A, Banerjee T. Experiments, correlations and COSMO-RS predictions for the extraction of benzothiophene from n-hexane using imidazolium-based ionic liquids. Chem Eng J 2011;166:30-9.
[26] Verma NR, Gopal G, Anantharaj R, Banerjee T. (Solid+liquid) equilibria predictions of ionic liquid containing systems using COSMO-RS. J Chem Thermodyn 2012;48:246-53.
[27] Manohar CV, Rabari D, Kumar AAP, Banerjee T, Mohanty K. Liquid–liquid equilibria studies on ammonium and phosphonium based ionic liquid–aromatic–aliphatic component at T=298.15K and p=1bar: Correlations and a-priori predictions. Fluid Phase Equilib 2013;360:392-400.
[28] Prausnitz JM, Lichtenthaler RN, Azevedo EG. Molecular thermodynamics of fluid phase equilibria. 3rd ed. prentice Hall, New Jersey1999.
[29] Anantharaj R, Banerjee T. Evaluation and comparison of global scalar properties for the simultaneous interaction of ionic liquids with thiophene and pyridine. Fluid Phase Equilib 2010;293:22-31.
[30] Rabari D, Patel N, Joshipura M, Banerjee T. Densities of Six Commercial Ionic Liquids: Experiments and Prediction Using a Cohesion Based Cubic Equation of State. J Chem Eng Data 2014;59:571-8.
[31] Carvalho PJ, Regueira T, Santos LMNBF, Fernandez J, Coutinho JoAP. Effect of Water on the Viscosities and Densities of 1-Butyl-3-methylimidazolium Dicyanamide and 1-Butyl-3-methylimidazolium Tricyanomethane at Atmospheric Pressure†. J Chem Eng Data 2010;55:645-52.
[32] Carneiro AP, Rodríguez O, Macedo EA. Solubility of xylitol and sorbitol in ionic liquids – Experimental data and modeling. J Chem Thermodyn 2012;55:184-92.
[33] Fang Z, Smith JRL, Qi X. Production of Biofuels and Chemicals with Ionic Liquids: Springer, Netherlands; 2014.
[34] Freire MG, Teles ARR, Rocha MAA, Schröder B, Neves CMSS, Carvalho PJ, et al. Thermophysical Characterization of Ionic Liquids Able To Dissolve Biomass. J Chem Eng Data 2011;56:4813-22.
[35] Kolbeck C, Cremer T, Lovelock KR, Paape N, Schulz PS, Wasserscheid P, et al. Influence of different anions on the surface composition of ionic liquids studied using ARXPS. J Phys Chem B 2009;113:8682-8.
[36] Okoturo OO, VanderNoot TJ. Temperature dependence of viscosity for room temperature ionic liquids. J Electroanal Chem 2004;568:167-81.

[37] Ghatee MH, Bahrami M, Khanjari N. Measurement and study of density, surface tension, and viscosity of quaternary ammonium-based ionic liquids ([N222(n)]Tf2N). J Chem Thermodyn 2013;65:42-52.

[38] Maki-Arvela P, Anugwom I, Virtanen P, Sjöholm R, Mikkola JP. Dissolution of lignocellulosic materials and its constituents using ionic liquids—A review. Ind Crop Prod 2010;32:175-201.

[39] Mushrif SH, Caratzoulas S, Vlachos DG. Understanding solvent effects in the selective conversion of fructose to 5-hydroxymethyl-furfural: a molecular dynamics investigation. Phys Chem Chem Phys 2012;14:2637-44.

[40] Krug RR, Hunter WG, Grieger RA. Enthalpy-entropy compensation. 2. Separation of the chemical from the statistical effect. J Phy Chem 1976;80:2341-51.

[41] Holland JH. Adaptation in natural and artificial systems : an introductory analysis with applications to biology, control, and artificial intelligence. Ann Arbor: University of Michigan Press; 1975.

[42] Sahoo RK, Banerjee T, Ahmad SA, Khanna A. Improved binary parameters using GA for multi-component aromatic extraction: NRTL model without and with closure equations. Fluid Phase Equilib 2006;239:107-19.

[43] Singh MK, Banerjee T, Khanna A. Genetic algorithm to estimate interaction parameters of multicomponent systems for liquid–liquid equilibria. Comput Chem Eng 2005;29:1712-9.

[44] Seader JD, Henley EJ. Separation Process Principles. 2nd. ed. New York: John Wiley & Sons; 2006.

[45] Banerjee T, Ramalingam A. Desulphurization and Denitrification of Diesel Oil using Ionic Liquids: Experiments and Qunatum chemical Predictions. 1st ed. MA, USA: Elsevier; 2015.

[46] Banerjee T, Singh MK, Sahoo RK, Khanna A. Volume, surface and UNIQUAC interaction parameters for imidazolium based ionic liquids via Polarizable Continuum Model. Fluid Phase Equilib 2005;234:64-76.

Chapter – 3

Solid-Liquid Equilibrium of D-(+)-Cellobiose, Sucrose and Maltose Monohydrate in Ionic Liquids: Experimental and Quantum Chemical Insights

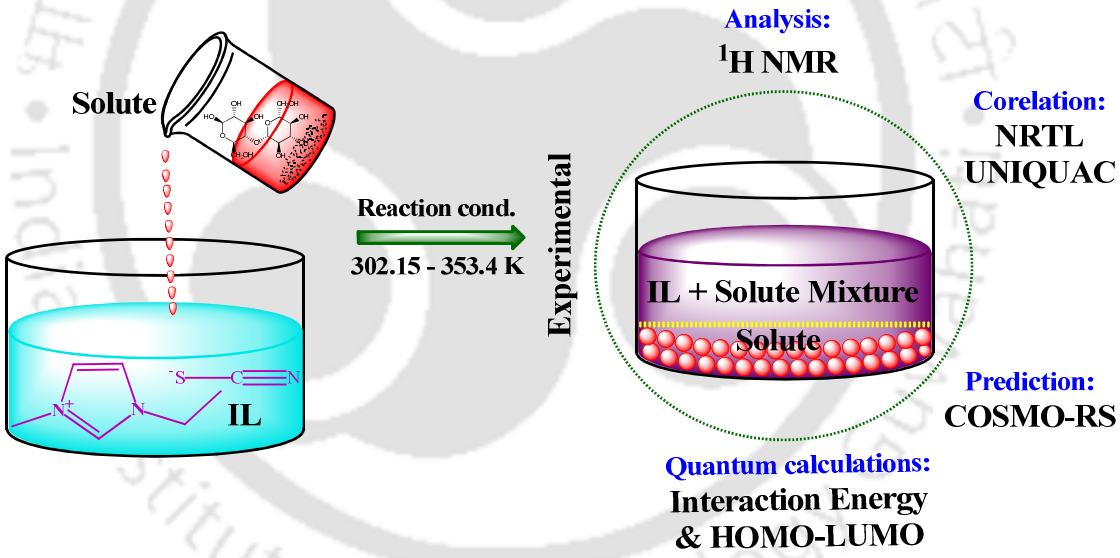

Published Article:

Mohan M., Banerjee T, Goud VV. Solid-Liquid Equilibrium of Cellobiose, Sucrose and Maltose Monohydrate in Ionic Liquids: Experimental and Quantum Chemical Insights. *J Chem Eng Data* (2016); 61(9): 2923–2932

3 Solid-Liquid Equilibrium of D-(+)-Cellobiose, Sucrose and Maltose Monohydrate in Ionic Liquids

In chapter2, we have seen the experimental and COSMO-RS simulations with monosaccharides. We shall now move our attention to disaccharides solubility. Therefore in the present chapter, ILs from two classes of cations namely imidazolium and ammonium have been chosen to examine the solubility of disaccharides namely D-(+)-cellobiose, sucrose, and maltose over a temperature range of 302.15-353.15 K. Further, COSMO-RS model was used to predict the solubility data and quantum chemical calculations were employed to understand their interactions. The apparent standard thermodynamic functions of dissolution such as standard molar Gibbs energy $\Delta^{o}_{dissol}G$*, molar enthalpy* $\Delta^{o}_{dissol}H$ *and entropy of dissolution* $\Delta^{o}_{dissol}S$ *were also calculated from the modified van't Hoff equation. The Gibb's free energy models such as NRTL and UNIQUAC models were then used to correlate with the experimental solubility data.*

3.1 Introduction

With conventional solvent such as water, Gray *et al.* (2003) studied the solubility of monomers and oligomers in water at a temperature range of 293-303 K and reported a 0.91% in weight solubility of cellobiose [1]. This necessitates the exploration of novel solvents for the dissolution of carbohydrates [2] to improve their solubility. Recently, Conceicao *et al.* (2011) measured the solubility of carbohydrates and sugar alcohols using six different ILs. Among the six ILs, 1-butyl-3-methylimidazolium hydrogensulfate [BMIM][HSO_4] gave the highest dissolution capacity for D-(+)-sucrose (35.0% at 388.35 K) [2]. Gong *et al.* (2012) further studied the dissolution of maltose monohydrate and other sugars in water-ethanol mixtures over a temperature range of 278.2- 298.2 K. It was observed that the solubility of maltose monohydrate in pure water was higher than that of ethanol and mixed solvent [3]. In summary,

till date the solubility of monomeric sugars and sugar alcohols have been studied extensively in a series of ILs [1-7]. Contrary to monomeric sugars, solubility data for disaccharides are scarce. Therefore, the current chapter discusses the solubility of disaccharides in the ensuing sections. In line with previous chapter, the COSMO-RS computations are performed followed by experimental validation.

3.2 Computational Details

3.2.1 Geometry Optimization and COSMO-RS Calculations

The structures of disaccharides and ILs were drawn with MOLDEN freeware [8] and are presented in Figure 3.1. In this chapter, we have not carried out a separate COSMO-RS screening study for ILs, as both monosaccharides and disaccharides exhibits relatively similar melting properties. Therefore, the selection of ILs was based on the previous chapter 2 (monosaccharides solubility). The molecular geometries of disaccharides were fully optimized at HF/6-31G* *via Gaussian*03 package [7,9]. After the geometry optimization, the next step is to generate the COSMO file using the final optimized structure. The detailed methodology of COSMO-RS calculations are described in previous chapter 2 (section 2.2.2). For COSMO-RS (SLE) predictions, the melting properties of disaccharides are given in Table 3.1. The computation of SLE was performed with the assumption of completely dissociated anion and cation with equimolar quantities [10].

Table 3.1: Melting temperature (T_m), heat of fusion ($\Delta_{fus}H$) and chemical purity of disaccharides used in this work

Solute	Chemical formula	CAS no.	Purity (%)	M. Wt. (g mol^{-1})	T_m (K)	$\Delta_{fus}H$ (J mol^{-1})
D-(+)-cellobiose	$C_{12}H_{22}O_{11}$	528-50-7	≥98.0	342.30	498.15[a]	31058[a]
Sucrose	$C_{12}H_{22}O_{11}$	57-50-1	≥99.5	342.30	438.15[a]	40356[a]
Maltose monohydrate	$C_{12}H_{24}O_{12}$	6363-53-7	≥99.0	360.31	379.15[b]	45400[b]

[a] values taken from Gray *et al.* (2003) [1]; [b] values taken from Gong *et al.* (2012) [3]

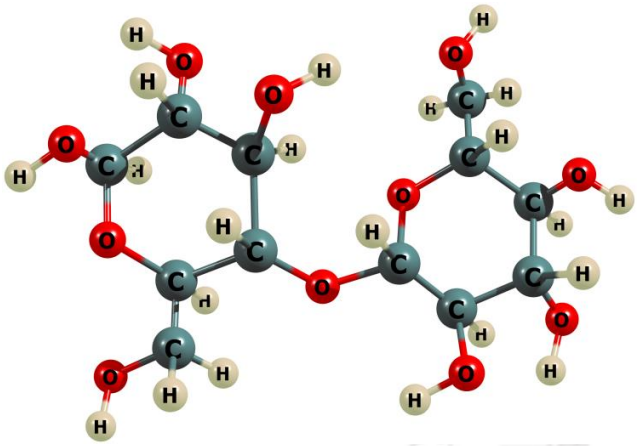

D-(+)-cellobiose

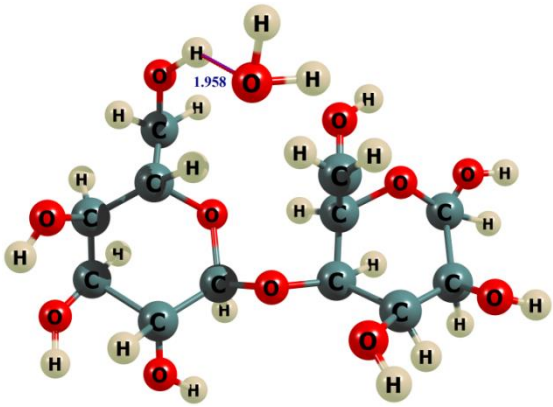

Maltose monohydrate

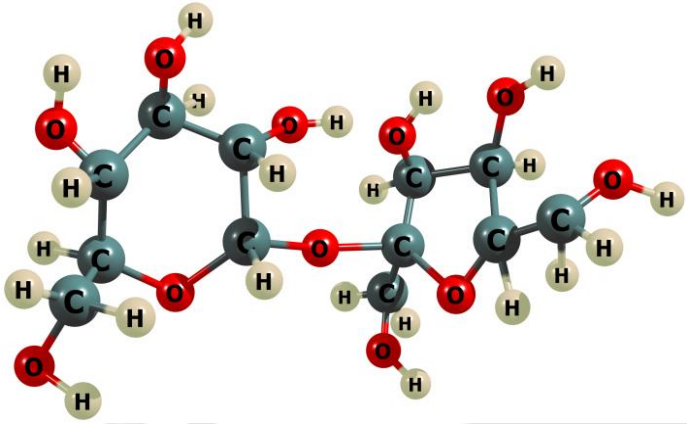

Sucrose

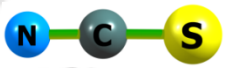

Thiocyanate $[SCN]^-$

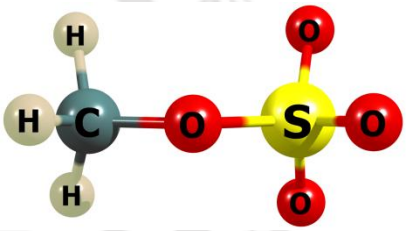

Methylsulfate $[MeSO_4]^-$

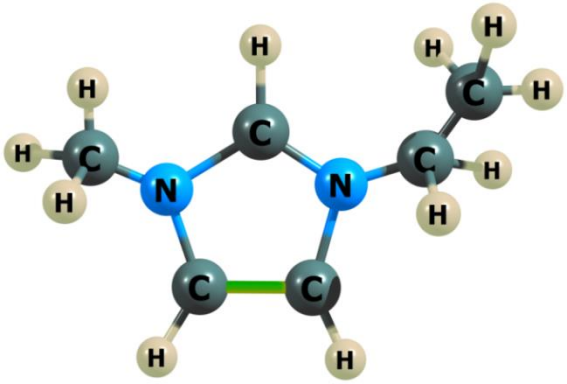

1-Ethyl-3-methylimidazolium $[EMIM]^+$

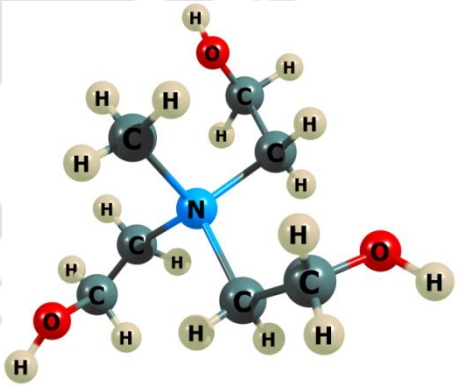

Tris(2-hydroxyethyl)methylammonium $[TMA]^+$

Figure 3.1: Optimized geometries of disaccharides, cations and anions with corresponding atom symbols. Color scheme used for different atoms are: C (cyan), O (red), N (sky blue), S (yellow), and H (white) atoms, respectively.

3.2.2 Interaction Energy Calculations

For the interaction energy calculations, the structures of cellobiose, sucrose, maltose monohydrate, and ILs were drawn in MOLDEN by combining the molecules using a dummy atom. The complex molecular system was optimized using *Gaussian*03 package at Hartree-Fock (HF) theory and 6-31G* basis set. After the geometry optimization, the final structure of optimized complex system appears without a dummy atom [11,12]. As the two molecules interact, a certain amount of energy gets reduced due to the solubility of two components. This decrease corresponds to the interaction energy between molecules [12]. Mathematically, the interaction energy is computed by the difference between the energy of the supramolecular system and sum of energy of individual molecules, as per expression given below [13,14]:

$$I.E\left(kJ\ mol^{-1}\right) = E_{AB} - \left(E_A + E_B\right) \tag{3.1}$$

Here, E_{AB} is total energy for the complex system *AB* (IL-cellobiose or IL-sucrose or IL-maltose monohydrate) in kJ mol^{-1}. The complex system energy was corrected by the basis set superposition error (BSSE) using counterpoise method at the same level of theory [15]. E_A and E_B are the individual energies (kJ mol^{-1}) of *A* (IL) and *B* (cellobiose/sucrose/maltose monohydrate) molecules, respectively. It should be noted that the negative energies are favorable because an extra amount of energy is required for disassembling the complex system [12].

3.2.3 HOMO-LUMO Energy Calculations

For ionic liquids, the dominating interactions are ionic in nature, still they are relatively independent of the higher occupied molecular orbital (HOMO) and lower unoccupied molecular orbitals (LUMO). This is evidenced by the effectiveness of the COSMO method which includes only charge based effects. Covalent effects are secondary for ILs, however they can be an important contributor [16]. This implies that the shape and energy of the HOMO and LUMO orbitals determine the networking within these systems to a certain extent. One of

the important descriptor which is also a function of HOMO and LUMO orbital energy namely chemical potential measures the escaping tendency of an electron cloud and is termed as a global property at the ground state .This can be quantified in terms of electron cloud density which is given by LUMO and HOMO, thus represented in Eqn (3.2) :

$$\mu = \left[\frac{\partial \mathrm{E}}{\partial \mathrm{N}}\right]_{v(r)} = \chi = -\left(\frac{IP + EA}{2}\right) = \left(\frac{\xi_{HOMO} + \xi_{LUMO}}{2}\right) \tag{3.2}$$

$$EA = -\xi_{LUMO;} \qquad IP = -\xi_{HOMO}$$

Here 'E' and 'χ' refers to the total energy and absolute electronegativity, respectively. *IP* and *EA* refer to the Ionization Potential and Electron Affinity, respectively. ξ_{HOMO} and ξ_{LUMO} defines the Kohn–Sham one electron Eigen values which is associated to the frontier molecular orbitals: HOMO and LUMO, respectively. HOMO energies refer to the ionization potential (*IP*) and characterize the susceptibility of the molecules toward attack by electrophiles, while LUMO energies quantify the susceptibility of the molecules when approached by nucleophiles. A large HOMO-LUMO gap implies high stability for the molecules in the sense of its lower charge transfer in complexes. With the QC based descriptors defined we shall now proceed towards the experimental details.

3.3 Materials and Methods

3.3.1 Materials

Disaccharides such as D-(+)-cellobiose, sucrose, and maltose monohydrate were purchased from Sigma-Aldrich, Germany. All the carbohydrates had purities greater than ≥99% as per the supplier specification. The ILs [EMIM][SCN] (≥99%) and [TMA][$MeSO_4$] (≥95%) were purchased from Sigma-Aldrich, Germany. The NMR grade solvent dimethylsulfoxide-d_6 (DMSO-d_6) was purchased from Merck, India with a purity of ≥99.8%. All the chemicals were used without any further purification.

3.3.2 Solubility Measurements

The experimental procedure for the solubility of a solute in ILs is described in the section 2.3.2 (chapter 2). The equilibrium solubility of disaccharides is determined by ^{1}H NMR (600MHz NMR, Brucker, Germany) spectrometer. The compositional analysis procedure for the determination of solubility in ILs is explained in the section 2.3.3 (chapter 2). A sample calculation of disaccharide solubility in [EMIM][SCN] is given in Appendix B (Figure B.1 and Table B.1).

3.4 Results and Discussion

The investigated ILs were selected based on our earlier chapter 2, where we have successfully validated the COSMO-RS model with the available solubility of sugar and sugar alcohols in ILs [7]. With this extensive benchmarking study, it was noticed that the results of COSMO-RS model were showing good agreement with the experimental data. The section outlined below discusses the experiment results and its comparison with excess Gibb's free energy models, COSMO-RS model, and quantum chemical (QC) calculations.

3.4.1 Solubility of Disaccharides

The solubility of disaccharides were measured over the temperature range of 302.15–353.15 K (Table 3.2). The melting temperature and heat of fusion values of the disaccharides used in this study are given in Table 3.1. The results from Table 3.2 indicates that the solubility of disaccharides is higher for [EMIM][SCN] when compared to [TMA][$MeSO_4$]. This is due to the hydrophobic nature of [TMA][$MeSO_4$], which causes weak interaction between solute and IL as compared to the hydrophilic IL [EMIM][SCN]. On the other hand, the alkyl chain length of $[Emim]^+$ cation is smaller as compared to $[TMA]^+$. It is known fact that an increase in the alkyl chain length of the cation results in the decrease in its solubility.

Table 3.2: Experimental and COSMO-RS predicted solubility of disaccharides in ILs at atmospheric pressure (p = 1 Atm) and different temperatures

T (K)	1-ethyl-3-methylimidazolium thiocyanate [EMIM][SCN]					
	D-(+)-cellobiose		Sucrose		Maltose monohydrate [a,b]	
	Expt.	Pred.	Expt.	Pred.	Expt.	Pred.
304.15	0.0480	0.0305	0.0417	0.0313	0.1266	0.1031
314.15	0.0774	0.0415	0.0609	0.0477	0.1649	0.1608
323.50	0.0978	0.0543	0.0712	0.0686	0.1855	0.2350
332.90	0.1111	0.0698	0.1014	0.0960	0.2319	0.3157
344.50	0.1218	0.0929	0.1341	0.1394	0.2755	0.4296
353.15	0.1436	0.1130	0.1635	0.1786	0.4280	0.5173
RMSE (%)[c]	3.25		0.98		8.45	
$u(x)$[d]	0.014		0.020		0.044	
T (K)	Tris(2-hydroxyethyl)methylammonium methylsulfate [TMA][MeSO4]					
	D-(+)-cellobiose		Sucrose		Maltose monohydrate [a,b]	
	Expt.	Pred.	Expt.	Pred.	Expt.	Pred.
302.15	0.0097	0.0180	0.0092	0.0129	0.0240	0.0416
313.15	0.0169	0.0264	0.0141	0.0215	0.0533	0.0745
323.80	0.0235	0.0374	0.0171	0.0341	0.0705	0.1257
334.20	0.0402	0.0512	0.0342	0.0519	0.1304	0.2013
343.15	0.0476	0.0659	0.0625	0.0729	0.1928	0.2925
353.15	0.0788	0.0861	0.1284	0.1044	0.3527	0.4280
RMSE (%)[c]	1.20		1.52		6.38	
$u(x)$[d]	0.010		0.018		0.050	

[a] The mole fractions are calculated based on maltose monohydrate; [b] Equilibrium solid phase is unknown, [c] RMSE values are calculated based on Eqn. 2.8, and [d] Standard uncertainty for temperature and pressure are u (T) = 0.1 K and u (p) = 1 kPa

Furthermore, the ammonium based cation having large alkyl chain length reduces the affinity with polar substances such as disaccharides. A comparison with literature data was made on the solubility of sucrose in common anion $[SCN]^-$ with different alkyl chain lengths

such as ($[EMIM]^+$ and $[BMIM]^+$). It was observed that the dissolution of sucrose was found to be 7.12 wt% in [EMIM][SCN] (Table 3.2) and 5.2 wt% in [BMIM][SCN] at 323.15 K [2]. It was also confirmed that the solubility of glucose and xylose in [EMIM][SCN] and [BMIM][SCN] ILs gave an increase of the solubility of glucose and xylose with decreasing cation alkyl chain length [2,7,17].

The experimental and COSMO-RS predicted data of disaccharides in ILs at different temperatures are given along with their RMSE (see Table 3.2). In terms of absolute values the deviations are on the higher side. However, our aim of this work is to have a predicting tool such as COSMO-RS which can invoke the solubility without necessary experimental regression. We have been successful to some extent which is in line with the average deviation of around 8.4% for all the systems.

This also confirms to a similar trend as available with the solubility of organic chemical compound such as based on the benzopyrone chemical classes, sugars and sugar alcohols in ILs [7,18]. It then explicitly also includes the validation of Hildebrand solubility parameters by COSMO-RS model [10]. The minimum deviation were found to lie between 0.85- 15%. Another study by Diedenhofen *et al.* (2003) [19] predicted the IDAC of alkanes, alkenes, alkylbenzenes, alcohols, polar organics and chloromethanes in different ILs by COSMO-RS model. The predictions were again order of magnitude in deviation within a temperature range of 300 to 350 K. It was observed that the solubility of disaccharides was higher with increase in the temperature. Among all the disaccharides, maltose monohydrate has the highest solubility in both ILs when compared to sucrose and D-(+)-cellobiose. At high temperature (353.15 K), the solubility order of disaccharides in both ILs follows the following trend: Maltose monohydrate > sucrose > D-(+)-cellobiose.

The solubility in terms of SLE is affected by two major contributions *i.e.*, solute melting properties and specific interactions between solute and solvent. Lower the melting

temperature and enthalpy of fusion values, higher the solubility and vice versa [1,3]. By comparing the disaccharides and monosaccharides dissolution in the corresponding ILs, it was concluded that monosaccharides exhibit a noticeably higher solubility than disaccharides [7]. Moreover, the dissolution process also depends on the melting properties of carbohydrates. In order to investigate this phenomenon further, recent studies point out to the fact that the anion plays a major role in the dissolution process since it interacts with the hydroxyl group of the carbohydrate or cellulose molecules [20-22]. In order to prove the fact, we conducted the quantum chemical calculations for IL-disaccharide systems as per the optimized complexes in Figure 3.2.

3.4.2 Quantum Chemical Calculations

Table 3.3 gives the interaction energies along with the HOMO-LUMO energy gap values of IL-disaccharide systems. From the results of Table 3.3, the interaction energy of maltose monohydrate with ILs were higher than sucrose and D-(+)-cellobiose, which implies that the intermolecular hydrogen bonding between the maltose monohydrate and ILs are very strong. It is an evident that the hydroxyl groups of the disaccharides are primarily connected to IL *via* hydrogen bonding (Figure 3.2). This is in agreement with the observation of Kahlen *et al.* (2010) [23], Guo *et al.* (2010) [20] and Araujo *et al.* (2013) [24] for IL based systems.

Table 3.3: Interaction energies and HOMO-LUMO energy gap of disaccharides with ILs

Complex system	Interaction energy (kJ mol^{-1})		HOMO-LUMO energy gap (eV)	
	[EMIM][SCN]	[TMA][$MeSO_4$]	[EMIM][SCN]	[TMA][$MeSO_4$]
D-(+)-cellobiose	-102.31	-6.39	0.4448	0.5516
Sucrose	-430.2	-36.2	0.4231	0.5502
Maltose monohydrate	-441.25	-52.1	0.4133	0.5494

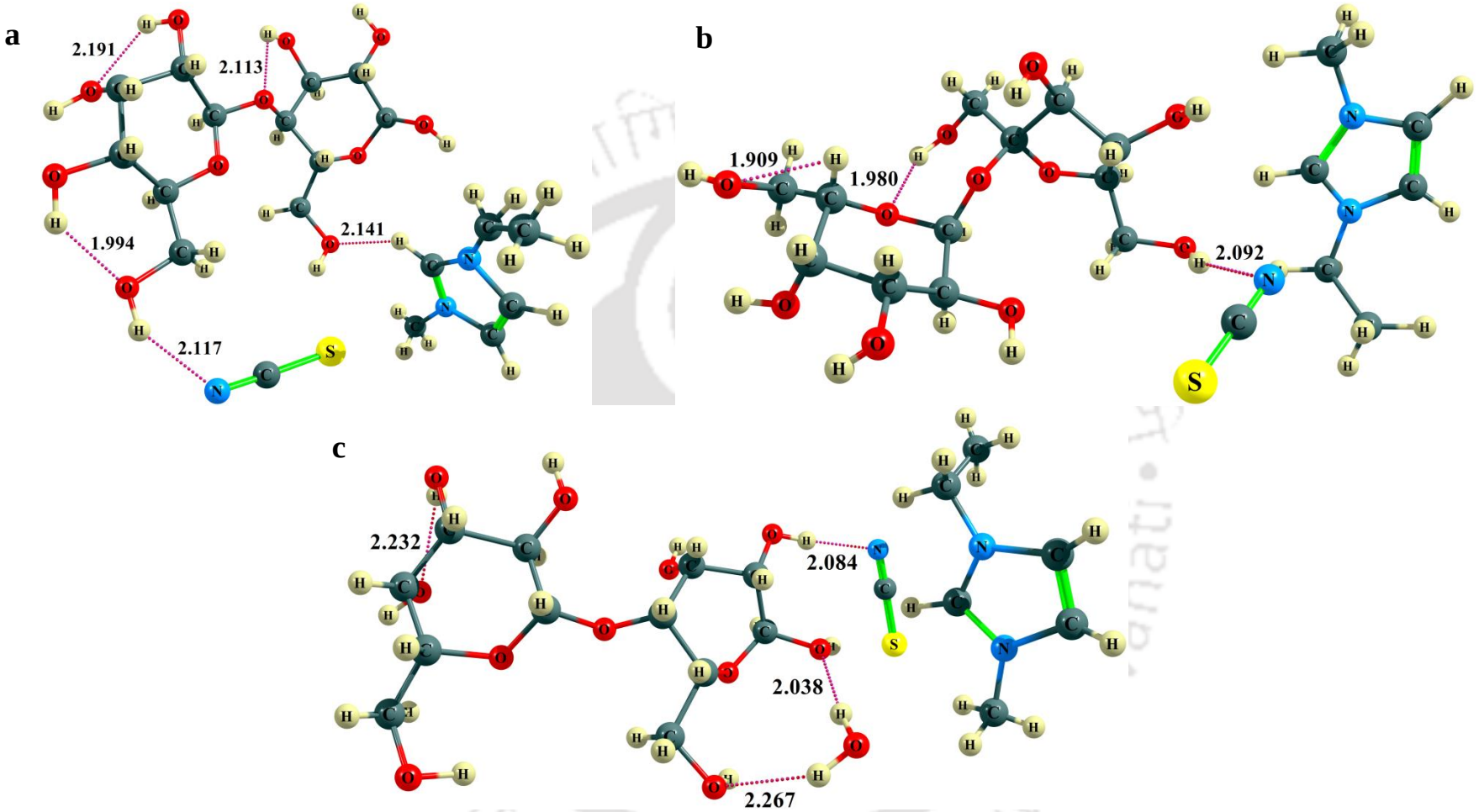

Figure 3.2: Optimized geometries for [EMIM][SCN]-disaccharides (a) D-(+)-cellobiose, (b) Sucrose, and (c) Maltose monohydrate. The H-bonds are indicated by dotted lines (pink color); the bond lengths are in Angstrom (Å). Color scheme used for different atoms are: C (cyan), O (red), N (sky blue), S (yellow), and H (white) atoms, respectively.

A similar trend was also observed in the HOMO-LUMO energy gap (eV) between maltose monohydrate and IL, which was lower in magnitude than the other disaccharides. It should be noted that a higher HOMO-LUMO energy gap results in the stability of the molecule since the charge transfer in the system is smaller in magnitude [16]. Thus, the dissolution of disaccharides in IL was found to increase with interaction energy and decrease with the HOMO-LUMO energy gap between the solute and solvent molecules. The proposed reaction mechanism of disaccharides solubility in ILs is given in Figure 3.3.

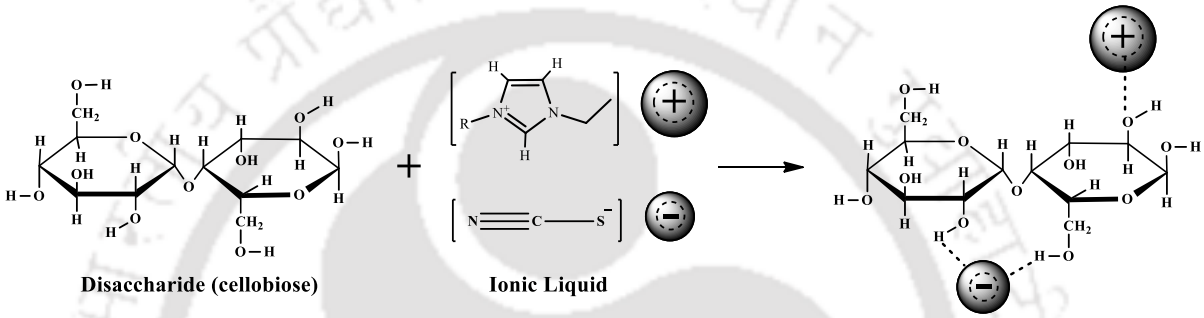

Figure 3.3: Proposed reaction mechanism for the solubility of disaccharides in ionic liquids *via* hydrogen bonds (negative sign indicates anion of IL and positive sign indicates cation)

3.4.3 Effect of Temperature on Disaccharides Solubility

The solubility of disaccharides in both the ILs has been studied as a function of temperature. As per thermodynamic concepts, the temperature has a greater influence on the dissolution of disaccharides in ILs. At higher temperatures, the solubility of disaccharides was found to be more. It is a known fact that the increase of temperature promotes the molecular thermal motion of the entire system which results in an increase in the solubility of disaccharides. D-(+)-cellobiose is more soluble than sucrose in both ILs at lower temperatures (Table 3.2). This tendency is reverse for temperatures at higher than 334.2 K. This attribute may be due to different physiochemical properties of disaccharides. Sucrose exhibits a lower melting temperature, but the heat of fusion value, on the contrary was higher as compared to D-(+)-cellobiose. Indeed, it is generally considered as lower the melting temperature, higher the

solubility. Nevertheless, melting point is not only the key factor to decide the solubility of solute. The heat of fusion of solute may also play a role in the dissolution process.

3.4.4 Thermodynamic Functions for Dissolution

Apparent thermodynamic functions of dissolutions such as enthalpy, Gibb's free energy and entropy were obtained from the experimental data (Table 3.2). The approach for the calculation of thermodynamic function of dissolution was described in chapter 2 (section 2.4.4) and depicted in Figure 3.4. Table 3.4 summarizes the thermodynamic functions of dissolutions. The dissolution of enthalpy $\Delta^{o}_{dissol.}H$, entropy $\Delta^{o}_{dissol.}S$ and Gibb's free energy $\Delta^{o}_{dissol.}G$ shows positive values, which represents an endothermic, entropically favourable and a non–spontaneous process. Apart from this, it was seen that the lowest value of Gibb's free energy of the system ([EMIM][SCN]) reveals highest solubility. Thus this system will require less energy for breaking the intermolecular interactions. This will set up a strong solute–solvent interaction for dissolving large quantities of solute. The positive values of entropy in both the systems indicate the degrees of freedom to the ILs are more when they possess solvating molecules of carbohydrates than pure IL itself.

Table 3.4: Apparent thermodynamic functions of dissolution at N_p = 6 and T_{hm} = 327.86 K[a]

Ionic Liquid	Disaccharide	$\Delta^{o}_{dissol.}H$ (kJ mol^{-1})	$\Delta^{o}_{dissol.}G$ (kJ mol^{-1})	$\Delta^{o}_{dissol.}S$ (J mol^{-1})
[EMIM][SCN]	D-(+)-cellobiose	19.236	6.691	38.265
	Sucrose	24.771	6.498	55.725
	Maltose monohydrate	20.165	4.158	48.821
[TMA][$MeSO_4$]	D-(+)-cellobiose	36.007	9.684	80.287
	Sucrose	44.436	9.635	106.145
	Maltose monohydrate	44.650	6.377	116.737

[a] The standard uncertainty: u (T) = 0.1 K

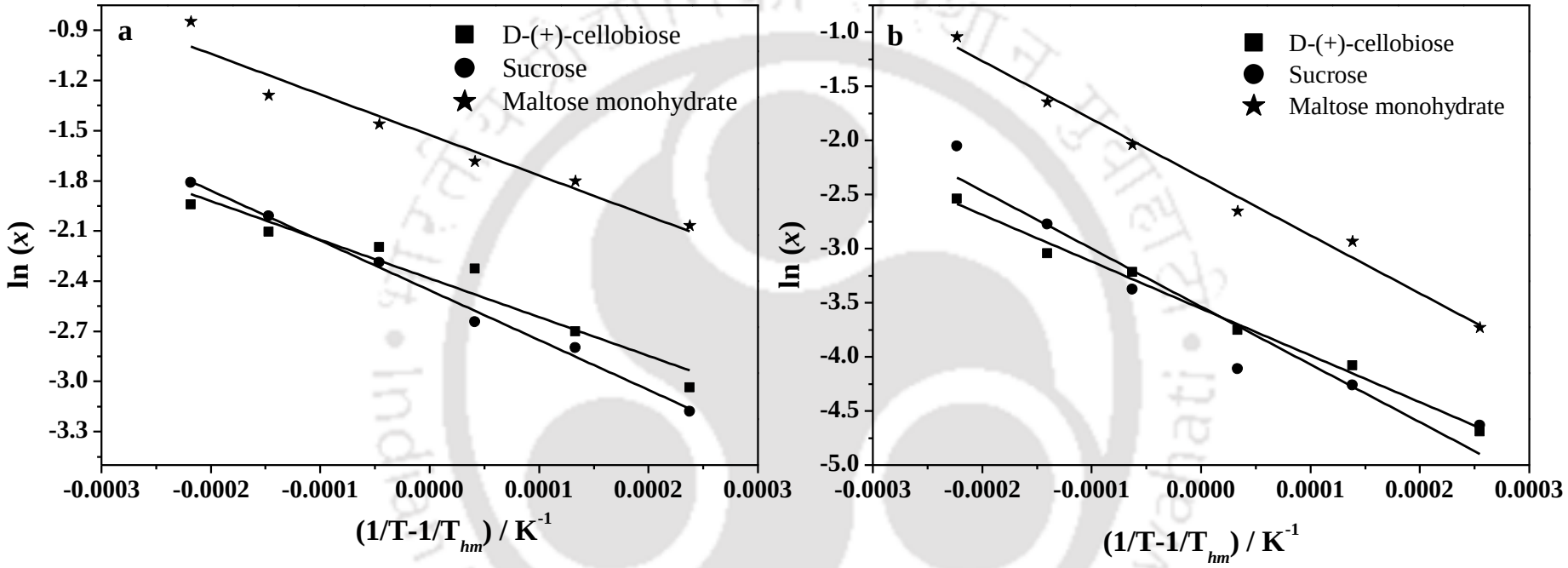

Figure 3.4: Linear representation of ln (x) *vs* [(1/T)-(1/T_{hm})] for disaccharides experimental solubility in (a) [EMIM][SCN], (b) [TMA][$MeSO_4$]

In the concluding section, both the NRTL and UNIQUAC model were used to correlate the experimental SLE data. The expressions for the NRTL and UNIQUAC models are already discussed in the section 2.3.6 (chapter 2). The binary interaction parameters of the NRTL and UNIQUAC models were calculated from experimental data by using Genetic Algorithm (GA) toolbox. The *r* and *q* values for [EMIM][SCN] and [TMA][$MeSO_4$] were taken from chapter 2, Table 2.10 [25].

The PCM calculations were performed to estimate the *r* and *q* values for disaccharides and are presented in Table 3.5. Table 3.6 represents the binary interaction parameters for disaccharides in ILs. Figure 3.5 (a, b) shows the experimental solubility data and their correlation with the NRTL and UNIQUAC models. Both the models here shows an excellent match with experimental solubility data.

Table 3.5: UNIQUAC structural parameters for the different compounds in the SLE systems[a]

Compound name	Volume parameter (*r*)	Surface parameter (*q*)
D-(+)-cellobiose	12.06	8.06
Sucrose	11.81	8.01
Maltose monohydrate	12.40	8.36
[EMIM][SCN]	5.74	4.24
[TMA][$MeSO_4$]	6.15	4.92

Table 3.6: NRTL and UNIQUAC interaction parameters

Binary systems		NRTL Parameters (α = 0.2)			UNIQUAC Parameters		
Solvent	Solute	Δg_{12} (kJ mol^{-1})	Δg_{21} (kJ mol^{-1})	RMSE (%)	Δu_{12} (kJ mol^{-1})	Δu_{21} (kJ mol^{-1})	RMSE (%)
[EMIM][SCN]	D-(+)-cellobiose	5.846	18.926	1.0299	500.25	-135.85	2.3595
	Sucrose	5.834	19.246	1.0773	472.31	-130.75	2.9546
	Maltose monohydrate	3.467	17.57	1.8548	423.02	-143.71	3.5686
[TMA][$MeSO_4$]	D-(+)-cellobiose	5.925	19.999	1.4380	448.11	-112.38	1.8817
	Sucrose	5.866	19.524	1.4162	398.79	-111.57	3.0864
	Maltose monohydrate	3.865	19.017	2.3596	340.21	-120.58	4.7516

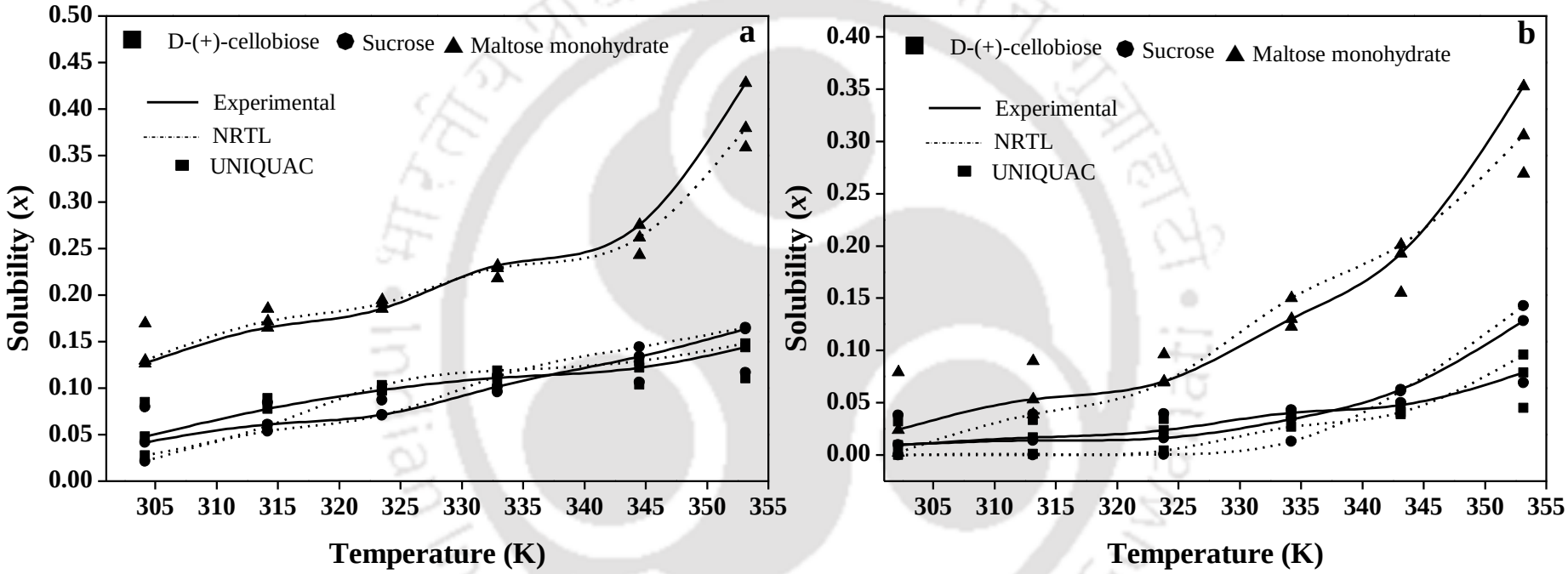

Figure 3.5: Correlation between the experimental and predicted NRTL and UNIQUAC solubilities in (a) [EMIM][SCN], (b) [TMA][$MeSO_4$]

The work reported here in the chapter will help us in narrow the knowledge gap when the extraction or dissolution of biomass components such as D-(+)-cellobiose, sucrose and maltose monohydrate requires to be undertaken. In such a scenario, NRTL and UNIQUAC interaction parameters as derived from Table 3.6 would be very useful because of the scarcity of data involving in ILs especially with respect to UNIFAC model. These binary interaction parameters are usually not available in commercial simulation packages such as ASPEN, HYSIS or CHEMCAD. One way to overcome this issue is to use these parameters directly in the simulation package when NRTL or UNIQUAC is invoked. This particular module is usually present in the process scale up or flow sheeting idea of biorefinery as depicted in Figure 3.6 [26].

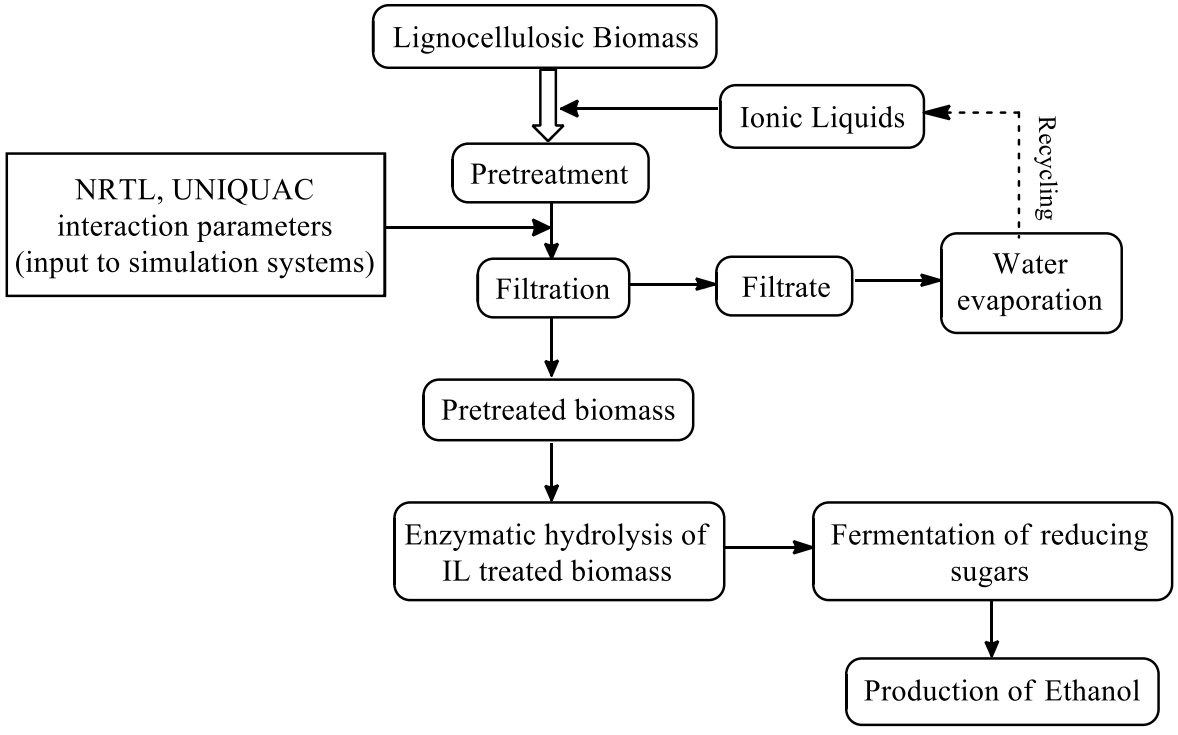

Figure 3.6: Steps involved in the production of ethanol from lignocellulosic biomass based on an IL pretreatment method (adapted from Tang *et al.* (2012) [26])

3.5 Summary

The current work reports the solubility of three disaccharides in two ILs by both experimental and COSMO-RS model over a temperature range of 302.15-353.15 K. The solubility data revealed that maltose monohydrate was more soluble than other sugars in either ILs. Further, the quantum chemical calculations also confirmed the same trend where higher interaction energy was obtained with both ILs. [EMIM][SCN] IL has a higher dissolving capacity of disaccharide than [TMA][$MeSO_4$]. The NRTL and UNIQUAC models were successfully correlated with experimental data with a maximum deviation of 5%. One of the major drawbacks of ILs is its viscosity, which is higher at room temperature. To overcome this issue, adding of suitable co-solvent to the IL may reduce the viscosity and enhance the solubility of the carbohydrates at lower temperatures. In summary both the ILs can be used as potential solvents for the dissolution of lignocellulosic biomass and its derivatives.

References

[1] Gray MC, Converse AO, Wyman CE. Sugar Monomer and Oligomer Solubility. Appl Biochem Biotech 2003;105-108:179-93.

[2] Conceiçao LJA, Bogel-Łukasik E, Bogel-Łukasik R. A new outlook on solubility of carbohydrates and sugar alcohols in ionic liquids. RSC Adv 2012;2:1846-55.

[3] Gong X, Wang C, Zhang L, Qu H. Solubility of Xylose, Mannose, Maltose Monohydrate, and Trehalose Dihydrate in Ethanol–Water Solutions. J Chem Eng Data 2012;57:3264-9.

[4] Carneiro AP, Rodríguez O, Macedo EA. Fructose and Glucose Dissolution in Ionic Liquids: Solubility and Thermodynamic Modeling. Ind Eng Chem Res 2013;52:3424-35.

[5] Carneiro AP, Rodríguez O, Macedo EA. Solubility of monosaccharides in ionic liquids – Experimental data and modeling. Fluid Phase Equilib 2012;314:22-8.

[6] Carneiro AP, Rodríguez O, Macedo EA. Solubility of xylitol and sorbitol in ionic liquids – Experimental data and modeling. J Chem Thermodyn 2012;55:184-92.

[7] Mohan M, Goud VV, Banerjee T. Solubility of glucose, xylose, fructose and galactose in ionic liquids: Experimental and theoretical studies using a continuum solvation model. Fluid Phase Equilib 2015;395:33-43.

[8] Anantharaj R, Banerjee T. COSMO-RS based predictions for the desulphurization of diesel oil using ionic liquids: Effect of cation and anion combination. Fuel Process Technol 2011;92:39-52.

[9] Frisch MJ, Trucks GW, Schlegel HB, Scuseria GE, Robb MA, Cheeseman JR, et al. Gaussian 03. revision C. 02 ed. Wallingford, CT: Gaussian, Inc.; 2004.

[10] Balaji C, Banerjee T, Goud VV. COSMO-RS Based Predictions for the Extraction of Lignin from Lignocellulosic Biomass Using Ionic Liquids: Effect of Cation and Anion Combination. J Solution Chem 2012;41:1610-30.

[11] Mohan M, Balaji C, Goud VV, Banerjee T. Thermodynamic Insights in the Separation of Cellulose/Hemicellulose Components from Lignocellulosic Biomass Using Ionic Liquids. J Solution Chem 2015;44:538-57.

[12] Hizaddin HF, Anantharaj R, Hashim MA. A quantum chemical study on the molecular interaction between pyrrole and ionic liquids. J Mol Liq 2014;194:20-9.

[13] Ding ZD, Chi Z, Gu WX, Gu SM, Liu JH, Wang HJ. Theoretical and experimental investigation on dissolution and regeneration of cellulose in ionic liquid. Carbohydr Polym 2012;89:7-16.

[14] Ding Z-D, Chi Z, Gu W-X, Gu S-M, Wang H-J. Theoretical and experimental investigation of the interactions between [emim]Ac and water molecules. J Mol Struct 2012;1015:147-55.

[15] Boys SF, Bernardi F. The calculation of small molecular interactions by the differences of separate total energies. Some procedures with reduced errors. Mol Phys 1970;19:553-66.

[16] Anantharaj R, Banerjee T. Evaluation and comparison of global scalar properties for the simultaneous interaction of ionic liquids with thiophene and pyridine. Fluid Phase Equilib 2010;293:22-31.

[17] Hassan el SR, Mutelet F, Pontvianne S, Moise JC. Studies on the dissolution of glucose in ionic liquids and extraction using the antisolvent method. Environ Sci Technol 2013;47:2809-16.

[18] Bhoi S, Dey D, Banerjee T, Mohanty K. Solid–liquid equilibria predictions for the dissolution of brown coal in ionic liquids using a continuum solvation model. Fuel Process Technol 2014;126:112-21.

[19] Diedenhofen M, Frank E, Klamt A. Prediction of Infinite Dilution Activity Coefficients of Organic Compounds in Ionic Liquids Using COSMO-RS. J Chem Eng Data 2003;48:475-9.

[20] Guo J, Zhang D, Duan C, Liu C. Probing anion-cellulose interactions in imidazolium-based room temperature ionic liquids: a density functional study. Carbohydr Res 2010;345:2201-5.

[21] Payal RS, Balasubramanian S. Dissolution of cellulose in ionic liquids: an ab initio molecular dynamics simulation study. Phys Chem Chem Phys 2014;16:17458-65.

[22] Janesko BG. Modeling interactions between lignocellulose and ionic liquids using DFT-D. Phys Chem Chem Phys 2011;13:11393-401.

[23] Kahlen J, Masuch K, Leonhard K. Modelling cellulose solubilities in ionic liquids using COSMO-RS. Green Chem 2010;12:2172.

[24] Araujo JM, Pereiro AB, Canongia Lopes JN, Rebelo LP, Marrucho IM. Hydrogen-bonding and the dissolution mechanism of uracil in an acetate ionic liquid: new insights from NMR spectroscopy and quantum chemical calculations. J Phys Chem B 2013;117:4109-20.

[25] Manohar CV, Rabari D, Kumar AAP, Banerjee T, Mohanty K. Liquid–liquid equilibria studies on ammonium and phosphonium based ionic liquid–aromatic–aliphatic component at T=298.15K and p=1bar: Correlations and a-priori predictions. Fluid Phase Equilib 2013;360:392-400.

[26] Tang S, Baker GA, Ravula S, Jones JE, Zhao H. PEG-functionalized ionic liquids for cellulose dissolution and saccharification. Green Chem 2012;14:2922-32.

Chapter – 4

Multiscale Modeling Strategies and Experimental Insights for the Solvation of Cellulose and Hemicellulose in Ionic Liquids

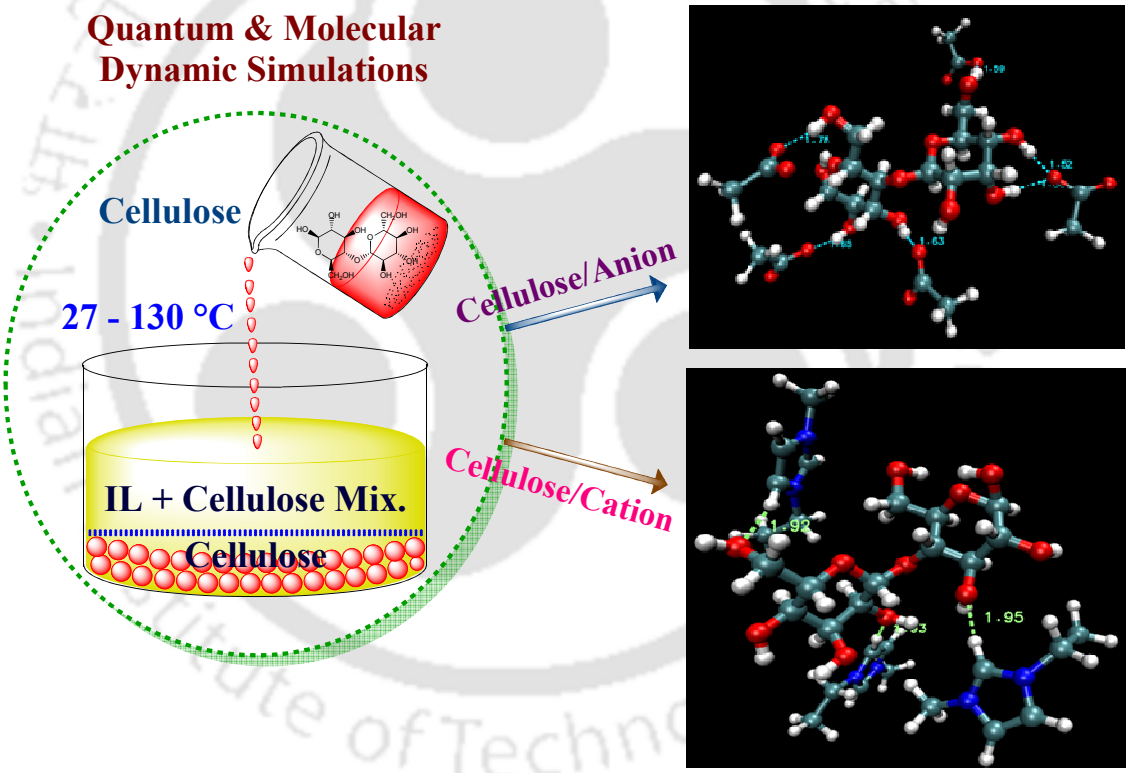

Published Article:

Mohan M., Viswanath P, Banerjee T, Goud VV. Multiscale modeling strategies and experimental insights for the solvation of cellulose and hemicellulose in ionic liquids. *Mol Phys* (2018); 116: 2108-2128

4 Quantum Chemical and Molecular Dynamics simulations of Cellulose/Hemicellulose Dissolutions in Ionic Liquids

In our earlier chapters, we have discussed the dissolution of simple sugars namely monosaccharides (chapter 2) and disaccharides (chapter 3) in ionic liquids by experimental and quantum chemical calculations. The current chapter reports the dissolution mechanism of cellulose and hemicellulose in ILs by quantifying the effect of anions and cations. In this respect a total of 1428 ILs have been screened in this work. An attempt has been made to elucidate the bond strength between the electron donor and acceptor orbitals within cellulose/hemicellulose and IL molecule. In this domain, our objective is to apply both QC and MD simulations for computing the IL-cellulose and IL-hemicellulose interactions. Here, the QC analysis included the COSMO-RS predictions, non-bonded interaction energies, and the NBO analysis. In addition, the effect of ions (cations and anions) on different conformational structures of cellulose and hemicellulose are also explored. Further, in order to confirm the findings of both QC and MD simulations, experimental studies have been performed for the selected ILs over the temperature ranges from 27–130 °C. The characterization techniques such as fourier transform spectroscopy (FTIR), X-ray diffraction (XRD) and thermogravimetric analysis (TGA) were also performed on the regenerated cellulose.

4.1 Introduction

Cellulose is the primary component in any biomass which produces monomeric sugar (glucose). Hemicellulose being the most abundant polymer in biomass produces pentose (xylose, arabinose) and hexose sugars (galactose, glucose, and mannose) [1]. One of the most important drawback remains the direct conversion of cellulose and hemicellulose into

value-added chemicals [2]. Thus, it requires a suitable solvent for the dissolution of cellulose and hemicellulose without necessitating the pretreatment step [3]. The dissolution of cellulose and hemicellulose is known to be a demanding task since water and other organic solvents are not able to dissolve these polymers at relatively milder conditions due to strong inter- and intra-molecular hydrogen bonding present [4]. Hence, extensive research is undertaken to break these complex structures. In 2002, Rogers and co-workers have used ILs for the dissolution of cellulose at mild operating conditions [5]. These solvents provide a new pathway for the dissolution of biomass derivatives at milder conditions without any pretreatment [6,7]. However, the disadvantage of ILs are its high viscosities which brings operating difficulties during the dissolution process. Nevertheless, as compared with bis[trifluoromethylsulfonyl]imide, tetrafluoroborate, and hexafluorophosphate based ILs, the ILs with acetate, thiocyanate, ethyl sulfate and phosphate anions have lower viscosities thereby enabling their utilization in various applications [8,9]. The low basicity anions namely dicyanamide and thiocyanate are not efficient in dissolving cellulose even though they are known to dissolve monosaccharides [10-12]. ILs containing non-coordinating anions such as $[BF_4]^-$ or $[PF_6]^-$ are also unable to dissolve cellulose [5].

It was reported that the dissolution of biomass and its derived components tends to depend on the anion, whereas other researchers inferred it is the combined action of both the ions [13,14]. Kahlen *et al.* (2012), and Casas *et al.* (2012, 2013) employed the activity coefficient model namely COSMO-RS to study the effect of anions and cations on the solubility of cellulose and lignin. In their study, they have considered cellotriose and cellotetraose as model cellulose molecules for COSMO-RS calculations [15,16]. In our previous work by Balaji *et al.* (2012), we have reported the extraction of lignin from lignocellulosic biomass by COSMO-RS. The extraction efficiency of IL for the removal of lignin was determined through Hildebrand solubility parameter (δ_H) which in turn was

predicted as a function of COSMO-RS activity coefficient. It was found that the solubility parameter for both lignin and IL were nearly similar. This led to a higher solubility of lignin in IL [17].

Recently, Cheng *et al.* (2012) studied the impact of 1-ethyl-3-methylimidazolium acetate [EMIM][OAc] IL on the crystalline part of cellulose. 3-20 wt % of cellulose solution was treated with IL and mixture of IL and DMSO at 25 °C and 120 °C for 1 h. It was reported that the crystallinity of cellulose was found to increase with increasing cellulose loading (i.e., 3-20 wt %) [18]. Minnick *et al.* (2016) measured the solubility of cellulose (~61% crystallinity) in 1-ethyl-3-methylimidazolium diethylphosphate [EMIM][DEP] IL at different temperatures ranging from 40 to 120 °C for 48 h. It was found that the solubility of cellulose reached its saturation point at 100 °C (19.8 wt %). Further increase in the temperature to 120 °C gave no increase in the solubility of cellulose [19]. Rabideau *et al.* (2013, 2014) applied molecular dynamics (MD) simulations to study the effect of different imidazolium based cations for the solvation of cellulose with common anions namely: Cl^-, $[OAc]^-$ and $[DMP]^-$. From MD simulations, it was found that the cation interacts favorably with the nonpolar domains of cellulose through dispersion interactions, while the anions bounds at the polar domains of cellulose [20,21]. Lovell *et al.* (2010) reported the influence of cellulose on the ion diffusivity of [EMIM][OAc] through pulsed-field gradient NMR. The self-diffusion coefficients of both $[EMIM]^+$ and $[OAc]^-$ ions were found to reduce with cellulose weight [22]. Further, Uto *et al.* (2017) studied the crystal cellulose dissolution in imidazolium-based ILs by applying MD simulations. From their study, it was revealed that [AMIM]Cl and [EMIM]Cl are more powerful solvents for cellulose dissolution when compared to [BMIM][OAc] and [EMIM][OAc] [23]. Zhao *et al.* (2013) further studied the effect of anionic structures on cellulose dissolution. From their results, it was found that the

interactions of the anions with cellulose decrease in the order: Cl^- > $[OAc]^-$ > $[DEP]^-$ > $[SCN]^-$ > $[PF6]^-$ [24].

Furthermore, Guo *et al.* (2010) and Ding *et al.* (2012) studied the cellulose dissolution in ILs by both experimental and quantum chemical (QC) calculations [25,26]. Here, 1,4-O-dimethyl cellobiose and (1,4)-dimethoxy-β-D-glucose were considered as the cellulosic model. Further, it was observed that the IL tends to form strong H-bonds with hydroxyl groups of cellulose molecule thereby causing the cellulose dissolution. In another work, Payal and Balasubramanian, (2014) reported the cellulose dissolution in [Emim][OAc] IL and IL/water by an *ab initio* MD simulations [27]. They reported their prediction on two different types of cellulose conformers namely cellobiose-anti-anti and cellobiose-anti-syn. Further, Froschauer *et al.* (2012) have reported selective solvent for the xylan dissolution in [BMIM][Me_2PO_4] IL [28]. The phosphate anion was altered by replacing one oxygen atom with sulfur and selenium, respectively. This amendment decreases the hydrogen bond basicity of the IL. As a result, it precludes the dissolution of cellulose fibers, when compared to the less ordered xylan. After an extensive literature survey, the current chapter is another theoretical contribution to elucidate the effect of individual ions on the solvation behavior of cellobiose-anti-anti and cellobiose-anti-syn as model cellulose compounds. To the best of our knowledge, no data on the computational and experimental dissolution of hemicellulose in ILs is available.

4.2 Computational Details

4.2.1 COSMO-RS Model and Quantum Chemical Calculations

The structures of cellulose, hemicellulose, anions, and cations were drawn with the MOLDEN, which is a freeware [29]. For the ease of computation, cellulose has been chosen as cellobiose-anti-syn; and hemicellulose as comprised of an equimolar permutation of both

glucose and xylose. The structures of cellulose and hemicellulose were selected based on our previous works [17,30]. The initial molecular geometries of all molecules were fully optimized by B3LYP/6-31G* *via Gaussian*03 package [31,32]. After geometry optimization, the COSMO file is generated using final optimised geometries. The detailed approach of COSMO-RS calculations is available in our previous chapter 2 (section 2.2.2). The individual cation and anions were modeled with different conformers with respect to relative arrangements of their atoms in the COSMO scheme. Thereafter, the arrangement with the lowest energy was selected for the prediction of infinite dilution activity coefficient (IDAC). A complete dissociation of cations and anions with equimolar quantities resulted in an independent ion model. Obviously, the second approach is much efficient and was successfully implemented in previous chapters 2 and 3. For the interaction energy study, the structures of cellulose, hemicellulose, anions, cations, and ILs were drawn in MOLDEN by combining the molecules using a dummy atom. The details of interaction energy calculations are already discussed in earlier chapter 3 (section 3.2.2) and hence is not discussed here.

Further, Natural Bonding Orbital (NBO) analysis has been carried at the B3LYP level of theory on 6-31G* basis set for a better understanding of the intermolecular H-bonding interactions involved in the molecular systems of this study [33]. The strength of the H-bonding interactions (*i.e.*, electron donor-acceptor orbital) can be quantitatively described in terms of the NBO analysis. The stabilization energy ($E^{(2)*}$) associated with *i* (donor) - *j* (acceptor) delocalization is estimated from the second-order perturbation approach as given below [25,34]:

$$E^{(2)*} = \Delta E_{(i,j)} = q_i \frac{F^2_{(i,j)}}{\varepsilon_j - \varepsilon_i} \quad (4.1)$$

Where q_i is the donor orbital occupancy, ε_i and ε_j are the diagonal elements (orbital energies), and *F(i,j)* is the off-diagonal NBO Fock matrix element.

4.2.2 Molecular Dynamics Simulations

The microscopic interaction between cellulose (*i.e.*, cellobiose-anti-syn) and six different ILs ([EMIM][OAc], [BMIM][OAc], [EMIM][$MeSO_3$], [EMIM][$EtSO_4$], [EMIM][SCN] and [TMA][$MeSO_4$]) were performed by MD simulations using NAMD version 2.10 software [35]. In the entire simulations (COSMO-RS and QC), cellobiose molecule is considered as a cellulose model component. With the aim of avoiding the further confusions on cellulose structure and due to the computational restrictions, we have adopted cellobiose molecule as cellulose model component to carry out the MD simulations. Till date, several literature reports are available for the solvation of cellulose using cellobiose and glucose as a cellulose model molecules [27,36-38]. It should be noted that the ILs were selected based on QC calculations and experimental evidence. For all the molecules, the CHARMM force field parameters were employed and presented in the Appendix C (Table C.1-C.8) along with their structures.

The CHARMM force fields were well defined for carbohydrates and ionic liquids [39-41] and successfully implemented for cellulose-IL systems [41]. The CHARMM force field parameters for cellulose (two order degree of polymerization) and $[BMIM]^+$ were taken from Guvench *et al.* (2008, 2009) [39,40] and Gross *et al.* (2011) [41]. The force field parameters for other cations ($[EMIM]^+$ and $[TMA]^+$) and anions ($[OAc]^-$, $[MeSO_3]^-$, $[EtSO_4]^-$, $[SCN]^-$ and $[MeSO_4]^-$) were developed with the existing CHARMM parameters [42]. The developed force field parameters were further validated by computing the density of ILs at 27 °C (*i.e.*, 300 K) and 1 atm pressure. For measuring the density of ILs, 200 ionic pairs of IL molecule were taken. The deviation between experimental and MD simulated densities gave an excellent agreement and are given in Table 4.1.

Table 4.1: Densities of different ionic liquids obtained from MD simulations and compared with experimental density at 27 °C

Ionic Liquid	ρ_{exp} (g cm^{-3})	ρ_{MD} (g cm^{-3})	Error (%)
[EMIM][OAc]	1.0957	1.0946	0.1031
[BMIM][OAc]	1.0481	1.0252	2.1870
[EMIM][$MeSO_3$]	1.2404	1.2798	-3.1790
[EMIM][$EtSO_4$]	1.2352	1.2775	-3.4237
[EMIM][SCN]	1.1151	1.1787	-5.7035
[TMA][$MeSO_4$]	1.3415	1.3416	-0.0045

All the MD simulations were performed in Langevin thermostat and Nosé-Hoover Langevin barostat at constant temperature (27 °C) and pressure (1 Atm) [43]. A damping coefficient of 1 ps^{-1} was used for temperature control. The Nosé-Hoover barostat with an oscillation period of 100 fs and a damping factor of 50 fs was used for pressure control [44]. As per the NAMD user guidelines [45], it is recommended that the product of full electrostatic frequency and time step does not exceed 4 fs unless rigid bonds (*i.e.*, SHAKE) should be used [35]. In the present study, the full electrostatic frequency of 2.0 is used and the product of full electrostatic frequency and time step (1 fs) is 2 fs. The current work has adopted SHAKE algorithm with a tolerance of 10^{-5} so as to constrain the lengths of covalent bonds which are connected to hydrogen [46]. The Particle Mesh Ewald (PME) method was applied with an accuracy of 10^{-6} (PME Tolerance) for long-range electrostatic interactions at a cut-off distance of 15 Å [47]. The initial configuration of cellulose/ILs pairs was prepared by PACKMOL [48] in a cubic box containing 200 ion pairs of ILs and 10 cellulose molecules [48]. The size of the cubic box was typically larger than the actual box size which makes the packing easier [49]. Three different initial configurations were generated in order to get the starting geometry.

In MD, generally four steps are involved to carry out the simulations: minimization, heating, equilibration and production. The first step *i.e.*, minimization involves a simple energy minization to bring the system to local minimum. Velocities are assigned to each atom selected from a Maxwell distribution to slowely increase the system's kinetic energy untill the target temparature is attained. Equilibration follows, in which velocities corresponding to the target temprature are reassigned constantly, and finaly one enters to a production stage of the simulation. Therefore, *initially* the simulation system energy was minimized for 0.5 ns. After energy minimization, the system was then gradually heated to 27 °C (*i.e.*, 300 K) for 0.5 ns. At target temperature, the simulated systems were equilibrated for 5 ns with isothermal-isobaric (NPT) ensemble in order to converge the system to its experimental condition. This was monitored by measuring the density or the volume of the system. Further, as per literature data, long-time dynamics are necessary for the simulation system containing crystalline cellulose with more than 10 degree of polymerization (i.e., consisting of at least 10 cellulose chains) which is inherently proven from previous work [13,20,50]. The simulations with smaller cellulose model component molecules such as glucose, cellobiose, and cellopentaose requires 5-30 ns of production runs to diffuse significantly [27,37,51,52]. Therefore, the production run has been attempted for 60 ns with canonical (NVT) ensemble which does not show any appreciable variation with respect to non-bonded energies (see Figure 4.1).

At every 5 ps, the trajectory data was saved for structural analysis such as radial distribution functions (RDF) and the non-bonded interaction energy calculations. All the MD computational trajectories were then visualized with the Visual Molecular Dynamics (VMD) software [53]. The interaction energy between the cellulose and ILs were calculated per mole of cellulose. Further, to characterize the stability of the cellulose molecule in ILs, we have calculated the root mean square deviation (RMSD) values in molecular positions of the

cellulose as shown in Figure C.1. The RMSD curve in both ILs [EMIM][OAc] and [BMIM][OAc] is fluctuating in nature indicating that the molecular positions changed sharply during the initial part of simulation (<15 ns) after which steady state diffusion of cellulose molecule occurs.

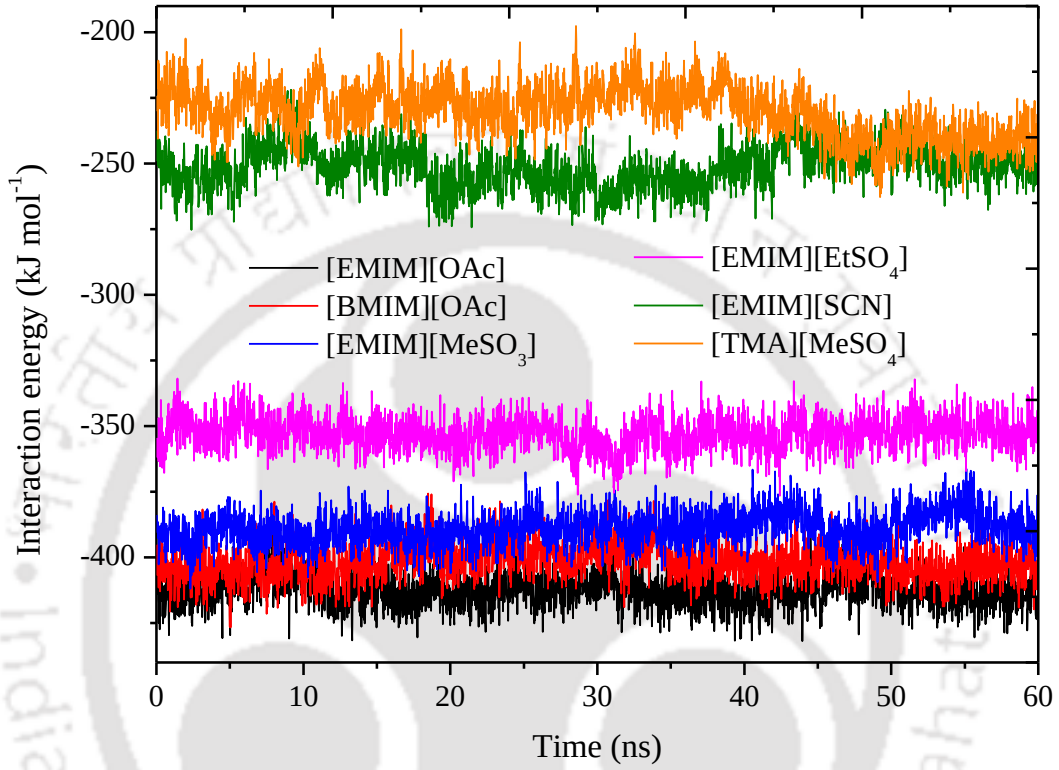

Figure 4.1: MD simulated interaction energies between the cellulose-anion in different ILs

4.3 Materials and Methods

4.3.1 Materials

Microcrystalline cellulose (MCC) powder was purchased from Merck, India. The degree of polymerization (DP) of MCC powder was ≤400. Xylan (hemicellulose) from beech wood was purchased from Sigma–Aldrich, Germany. The ILs, [EMIM][OAc], [BMIM][OAc], [EMIM][$MeSO_3$], [EMIM][$EtSO_4$], [EMIM][SCN] and [TMA][$MeSO_4$] were purchased from Sigma-Aldrich, Germany. All the chemicals were used without any further purification. Table 4.2 summarizes the sample description of cellulose, hemicellulose, and ILs along with their moisture content. The moisture content of ILs were determined by a Karl Fischer

titrator (Metrohm, 787 KF Titrino, Switzerland). Cellulose and xylan were dried at 50 °C for 24 h before the experiments.

Table 4.2: List of chemicals used in the dissolution experiments

Sl. No.	Compound Name	CAS No	Purity (%)	Water content (ppm)
1.	Microcrystalline cellulose	9004-34-6	≥97	NM
2.	Xylan from beech wood	9014-63-5	≥90	NM
3.	[EMIM][OAc]	143314-17-4	≥95	11800
4.	[BMIM][OAc]	284049-75-8	≥95	9650
5.	[EMIM][$MeSO_3$]	145022-45-3	≥95	3600
6.	[EMIM][$EtSO_4$]	342573-75-5	≥95	3000
7.	[EMIM][SCN]	331717-63-6	≥95	7400
8.	[TMA][$MeSO_4$]	29463-06-7	≥95	13100

4.3.2 Experimental Procedure

The experimental procedure for the dissolution of cellulose and hemicellulose in ILs is carried out by following the procedure described in the chapter 2 (section 2.3.2). In a typical dissolution experiment, the ILs [EMIM][OAc], [BMIM][OAc], [EMIM][$MeSO_3$], [EMIM][$EtSO_4$], [EMIM][SCN], [TMA][$MeSO_4$] were added into a 25 mL conical flask containing 6 g of IL. The temperature of the system was maintained from 27 - 130 °C with a precision of ± 0.1 °C (TARSONS SPINOT-magnetic stirrer and hot plate-DIGITAL, MC 02, India). After the desired temperature was achieved, 0.3 g of cellulose and 0.5 g hemicellulose was added. The inside temperature of the flask was measured with thermometer and maintained at the desired temperature. The heated mixture was magnetically stirred for different individual time intervals *i.e.*, 0.5 h, 1 h, and 2 h to know the

effect of time on the solubility study. After completion of system time, cellulose and hemicellulose solution was cooled to room temperature and then regenerated by adding distilled water into the solution with vigorous stirring for 30 min. The cellulose and hemicellulose flocs were then collected by a vacuum filtration and dried at 50 °C for 48 h. Further, the dried cellulose samples were characterized by FTIR, XRD, and TGA. The percent of solubility was calculated according to the following equation:

$$\text{Cellulose or Hemicellulose solubility } (\%) = \frac{m_o - m_f}{m_o} \times 100 \quad (4.2)$$

Where m_o is the initial mass of the cellulose or hemicellulose added and m_f is the final mass of the recovered cellulose and hemicellulose, respectively.

4.3.3 Characterization of Regenerated Cellulose

4.3.3.1 Fourier Transforms Infrared (FTIR) Spectroscopy

FTIR spectroscopy (PerkinElmer, Spectrum Two, Singapore) was used to study the changes of functional groups which are present in treated and untreated cellulose materials. 20 mg of the cellulose sample was mixed with 30 mg of the spectroscopic grade dried KBr. FTIR Analysis was conducted at the wave number range of 4000-400 cm^{-1}, with a resolution of 2 cm^{-1} and 30 scans per sample [54]. The background spectrum of pure dried KBr was deducted from the sample spectrum. Baseline and other necessary corrections for the penetration depth and frequency variations were applied using Spectrum Quant software.

4.3.3.2 X-ray Diffraction (XRD) Analysis

X-ray diffractometer (Brucker D8 Advanced XRD measurement system, Japan) was used to analyze the crystallinity of cellulose before and after treatment. The Rigaku miniflex powder XRD was equipped with Cu Kα (λ=1.541 Å) radiation settled at 40 KW voltages and 40 mA current. The diffraction angle (2θ) was 10 to 30° at a scan speed of 1 °min^{-1} and step size

0.05°. The crystallinity index (CrI) was calculated based on the diffraction intensities of crystalline and amorphous regions as given by the following equation [54-56]:

$$\text{CrI} = \frac{I_{002} - I_{amr}}{I_{002}} \times 100 \quad (4.3)$$

Where, I_{002} = peak intensity corresponding to the 002 lattice plane of a cellulose molecule at 2θ = 22.4°, and I_{amr} = peak intensity of amorphous region at 2θ = 18.5°. I_{002} symbolizes both crystalline and amorphous material while I_{amr} represents amorphous material [57].

4.3.3.3 ThermoGravimetric Analysis (TGA)

TGA analysis was carried out on a NETZSCH instrument (TG 209 *F1 Libra*®, Germany) under inert atmosphere (N_2). TGA chamber was continuously purged with N_2 gas at a flow rate of 40 ml min^{-1}. 8-10 mg of sample was loaded into a platinum pan and subjected to a heating rate of 10 °C min^{-1} over the temperature range from 30-600 °C.

4.4 Results and Discussion

4.4.1 Screening of Ionic Liquids by COSMO-RS Model

ILs are known to be promising solvents for the dissolution of biomass and its constituents at lower reaction conditions. As per standard definition, ILs can be freely combined from organic cations and organic/inorganic anions, thereby forming numerous candidates for the dissolution of biomass. COSMO-RS is a valuable tool for a predefined screening using IDAC predictions at ambient temperature (25 °C). In our study, 42 cations and 34 anions comprising of 1428 combinations were ranked based on their IDAC values. The IDAC value refers to the value of solute (cellulose/hemicelluloses) in IL (solvent). The structures and properties of 42 cations and 34 anions were presented in the Appendix C (Table C.9 and C.10). At this point, it should be noted that all the investigated cation-anion combinations were not liquids at room temperature and hence, a further selection based on the liquid state

were carried out comprehensively. Such combination with a predictive model with IL melting temperatures has been proposed by Krossing *et al.* (2006) [58], for sorting out the solid cation-anion combinations. It should be noted that without a screening of potential ILs, experimental studies become expensive and time consuming.

The IDAC values are often used as a quantitative descriptor for the dissolution power of a solvent. According to the solid-liquid equilibria (SLE) assumptions [10,59], the reciprocal of the activity coefficient characterizes the solubility of cellulose in the respective IL. Figure 4.2 and Figure 4.3 represents the predicted IDAC of 1428 ILs, which arises from the available combination of 42 cations and 34 anions. The predicted IDAC plots correspond to the cellulose (Figure 4.2) and hemicellulose (Figure 4.3), respectively. Cations and anions were sorted according to their dissolving capacity and arranged in such way that ILs with high dissolving power (*i.e.*, $\ln \gamma^{\infty}_{cellulose/hemicellulose} << 0$) are situated in the midline to bottom portion of Figures 4.2 and 4.3, and the weaker ones (positive values of $\ln \gamma^{\infty}_{cellulose/hemicellulose} > 0$) are situated at the top portion of Figures (4.2 and 4.3). Lower the activity coefficient values, greater is the tendency for the IL to dissolve cellulose and hemicellulose. As can be seen from Figures 4.2 and 4.3, anions such as acetate, chloride, nitrate, bromide, iodide, dimethylphosphate, hydrogen carbonate and methyl carbonate are predicted to dissolve the cellulose and hemicellulose molecules more efficiently with most cations. However, in combination with anions such as $[PF_6]^-$, $[BF_4]^-$, tetracyanoborate and bis(trifluoromethylsulfonyl)imide has very high values of IDAC. In the case of cations, they have shown a moderate effect in the dissolution process. In particular, imidazolium based ILs and other cation like ammonium and pyrrolidinium remarkably favorable for the solubility predictions (Figures 4.2 and 4.3). This is due to the fact that the solvent molecules forms strong hydrogen bonds with cellulose and hemicellulose, which alters the extensive hydrogen bond network present within the solute molecules [60]. This phenomenon was

elucidated by Kahlen *et al.* (2010) that the energy of the H-bonds of cellulose is up to 25 kJ mol^{-1} [61], thus the interactions between cellulose and solvent need to go beyond this energy in order to result in cellulose dissolution. Therefore, the ions of IL should obey the following successive criteria: (a) either of the ions should be highly polar or in other words act as a good hydrogen bond acceptor or donor, and (b) the remaining ion to be slightly polar [15].

According to the above assumptions, the ions such as 1-ethyl-3-methylimidazolium ($[EMIM]^+$) cation (less polar) and acetate ($[OAc]^-$) (highly polar; Figure 4.4) are known to be the recommended IL. The interaction between a polar anion and the hydroxyl groups of cellulose or hemicellulose molecules are energetically much stronger than the interaction between anion and cation of an IL, resulting in a high solvation of cellulose and hemicellulose [60]. Kahlen *et al.* (2010) performed a comprehensive COSMO-RS screening study for cellulose dissolution in 2272 ILs resulting from the combinations of 32 anions and 71 cations [15]. Further, Li *et al.* (2016) also screened 357 IL pairs for cellulose solubility [62]. Kahlen *et al.* (2010) and Liu *et al.* (2016) used cellotriose and cellotetraose as cellulose model compounds, whereas in our case cellobiose is used as a cellulose model component. However, the results of COSMO-RS screening study in the current work is in line with the reported findings of both Kahlen *et al.* (2010) and Li *et al.* (2016). Overall with increase in the cation chain length the infinite dilution activity coefficient was found to decrease. On the other hand, the sigma profiles of glucose, cellobiose, cellotriose, and cellopentaose are presented in Figure C.2. From Figure C.2, it is seen that the peak intensity of sigma profiles increases with cellulose chain length irrespective of the magnitude of screening charge densities. The sigma profiles of glucose, cellobiose, cellotriose and cellopentaose shows an increasing trend in both H-bond donor and acceptor zone with increasing glucan rings implying the fact that the polarity of cellulose increases with the number of glucan rings.

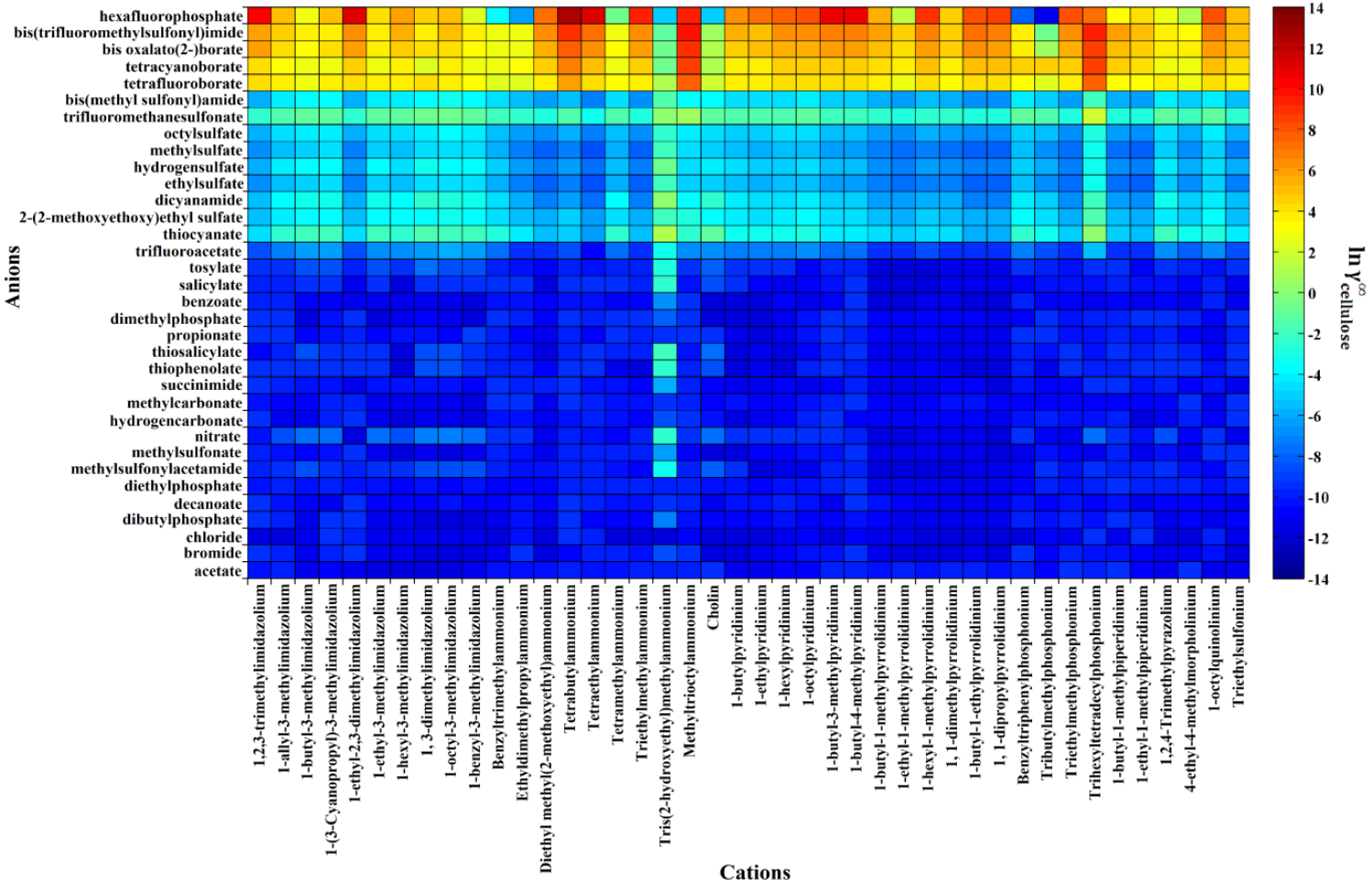

Figure 4.2: Graphical representation of the infinite dilution activity coefficients of cellulose in 1428 different ILs at room temperature by COSMO-RS model

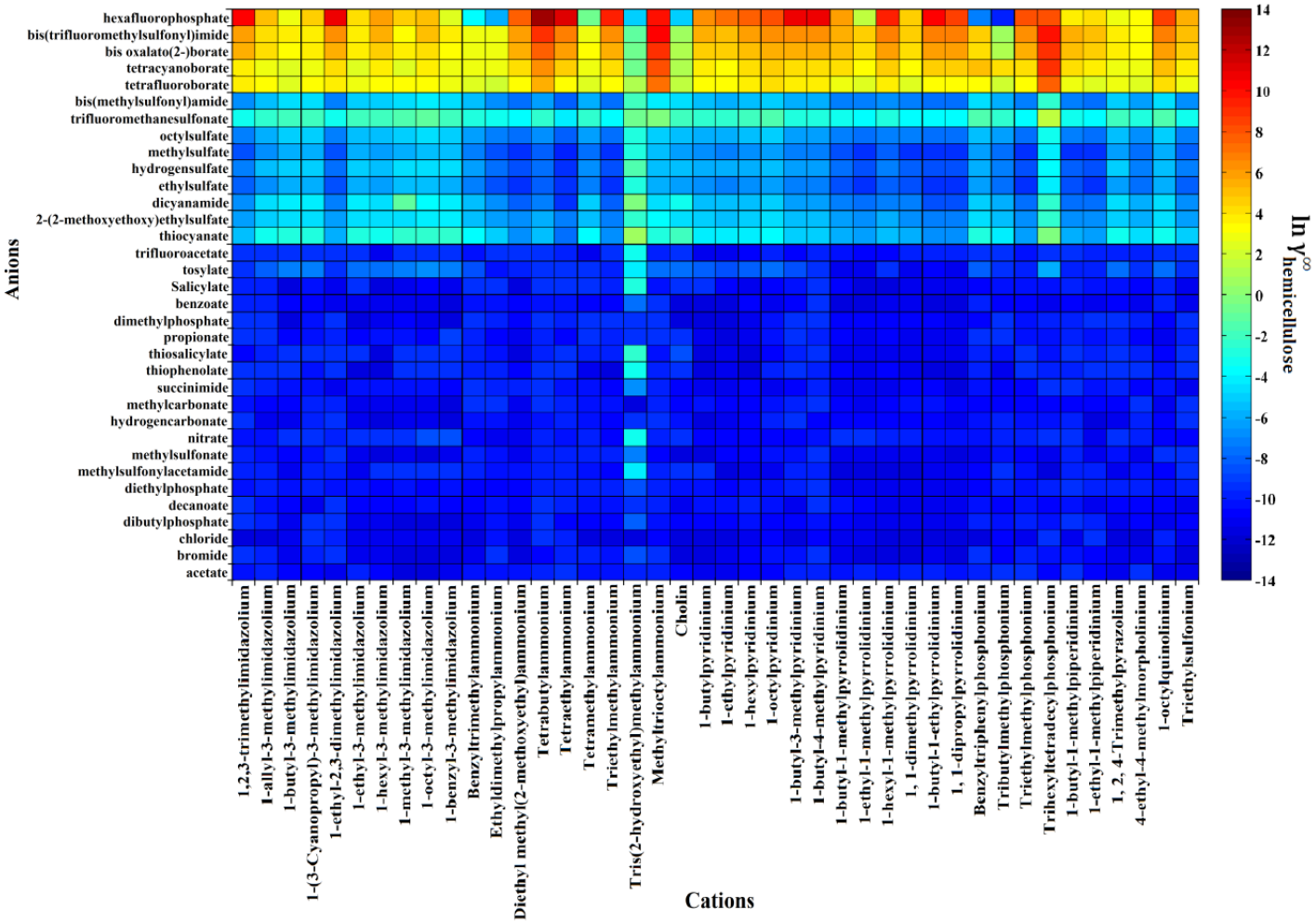

Figure 4.3: Graphical representation of the infinite dilution activity coefficients of hemicellulose in 1428 different ILs at room temperature by COSMO-RS model

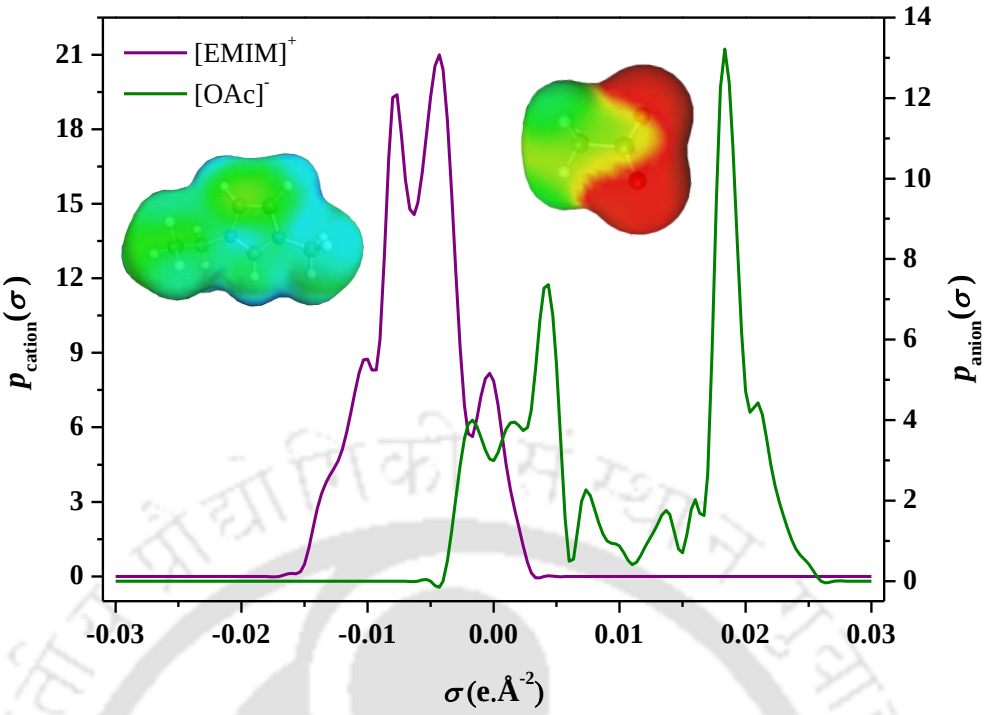

Figure 4.4: Sigma profiles and COSMO-cavities of cation $[EMIM]^+$ and of the anion $[OAc]^-$. Here the extent of screening charge varies from -0.03 e $Å^{-2}$ (red) to +0.03 e $Å^{-2}$ (blue) within the molecule, while the intermediate region is represented by green and yellow color.

4.4.2 Interaction Energies and NBO Analysis

4.4.2.1 Effect of Anions on Cellulose and Hemicellulose Dissolutions

The objective for performing such a study is locating the favorable site within the anion for the incoming cellulose/hemicellulose molecule. For these molecules, a trial quantum chemical calculations were performed for different sites of cellobiose with acetate anion (Figure 4.5). From Figure 4.5, it is clear that the most stable system for acetate anion to attach with the cellobiose molecule is around O3 and O4 atoms (Figure 4.6). This is particularly evident from Figure 4.5 ((a)-(b)) where the interaction energies are the highest among all the conformers. Similar calculations were also performed for hemicellulose and found that the favorable sites for acetate anion to attach hemicellulose molecule was around O3, O4, and O8 atoms, respectively (Figure 4.6). Thereafter, the anions were placed around

these sites. The interaction energy is broken down into anion-cellulose/hemicellulose and cation-cellulose/hemicellulose pairs to understand the effect of individual ions on the solvation of cellulose and hemicellulose [25,26]. This has been primarily performed to screen the potential anions and cations. This is required since the overall interaction energy for IL-cellulose/hemicellulose system is significant. However it is rather cumbersome to understand the effect of each ion on the cellulose/hemicellulose molecules due to the nature of its binding which is short range in QC. Therefore, the interaction energy is broken down into ion-cellulose/hemicellulose pairs.

Table 4.3: Interaction energies of cellulose (cellobiose-anti-syn) and hemicellulose (xylose+glucose) with anions

Sl. No.	Name of the Anion	Interaction Energy (kJ mol^{-1})	
		Cellulose	Hemicellulose
1.	Acetate $[OAc]^-$	-227.02	-222.28
2.	Methylcarbonate $[MC]^-$	-212.80	-205.48
3.	Trifluoroacetate $[AcF_3]^-$	-192.22	-182.30
4.	Chloride $[Cl]^-$	-187.52	-178.03
5.	Hydrogencarbonate $[HC]^-$	-201.57	-207.58
6.	Dimethylphosphate $[Me_2PO_4]^-$	-185.52	-198.61
7.	Nitrate $[NO_3]^-$	-182.77	-166.81
8.	Methanesulfonate $[MeSO_3]^-$	-171.63	-
9.	Methylsulfate $[MeSO_4]^-$	-169.55	-161.31
10.	Ethyl sulfate $[EtSO_4]^-$	-161.29	-
11.	Tetrafluoroborate $[BF_4]^-$	-157.61	-144.01
12.	Trifluoromethanesulfonate $[MSF_3]^-$	-147.03	-135.25
13.	Thiocyanate $[SCN]^-$	-137.25	-137.55
14.	Hexafluorophosphate $[PF_6]^-$	-130.98	-115.24

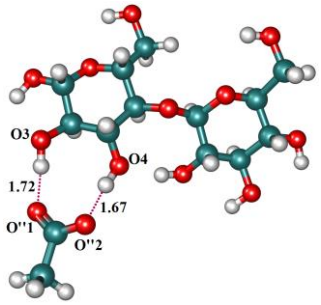

(a) -227.02 kJ mol^{-1}

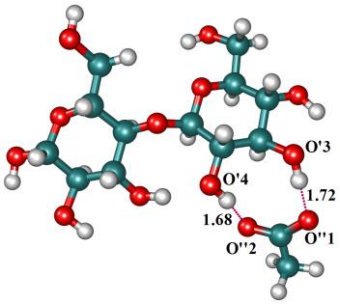

(b) -226.06 kJ mol^{-1}

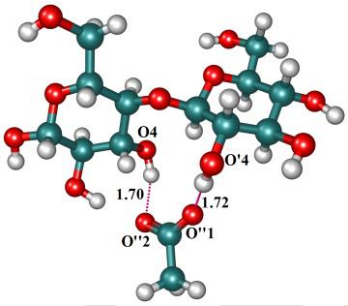

(c) -220.08 kJ mol^{-1}

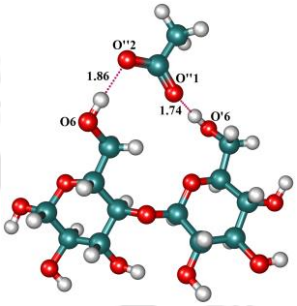

(d) -143.93 kJ mol^{-1}

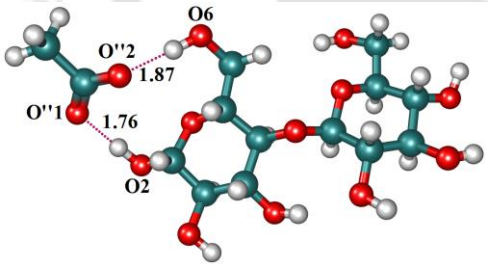

(e) -125.69 kJ mol^{-1}

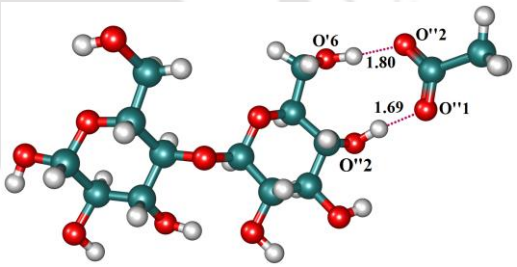

(f) -198.53 kJ mol^{-1}

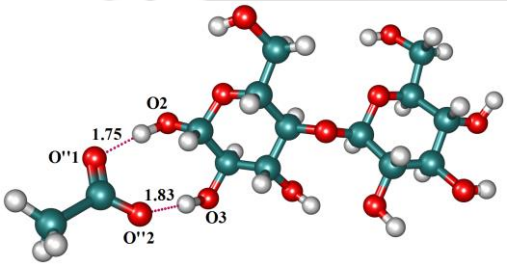

(g) -169.12 kJ mol^{-1}

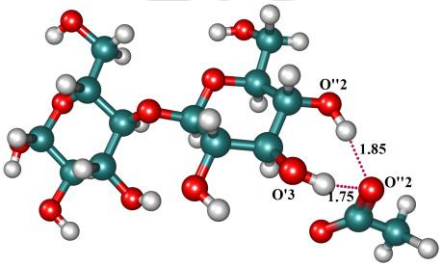

(h) -206.35 kJ mol^{-1}

Figure 4.5: Optimized geometries for different sites of cellulose interacting with acetate anion along with their interaction energies. Color represents the different atoms such as C (cyan), O (red), and H (white) atoms, respectively.

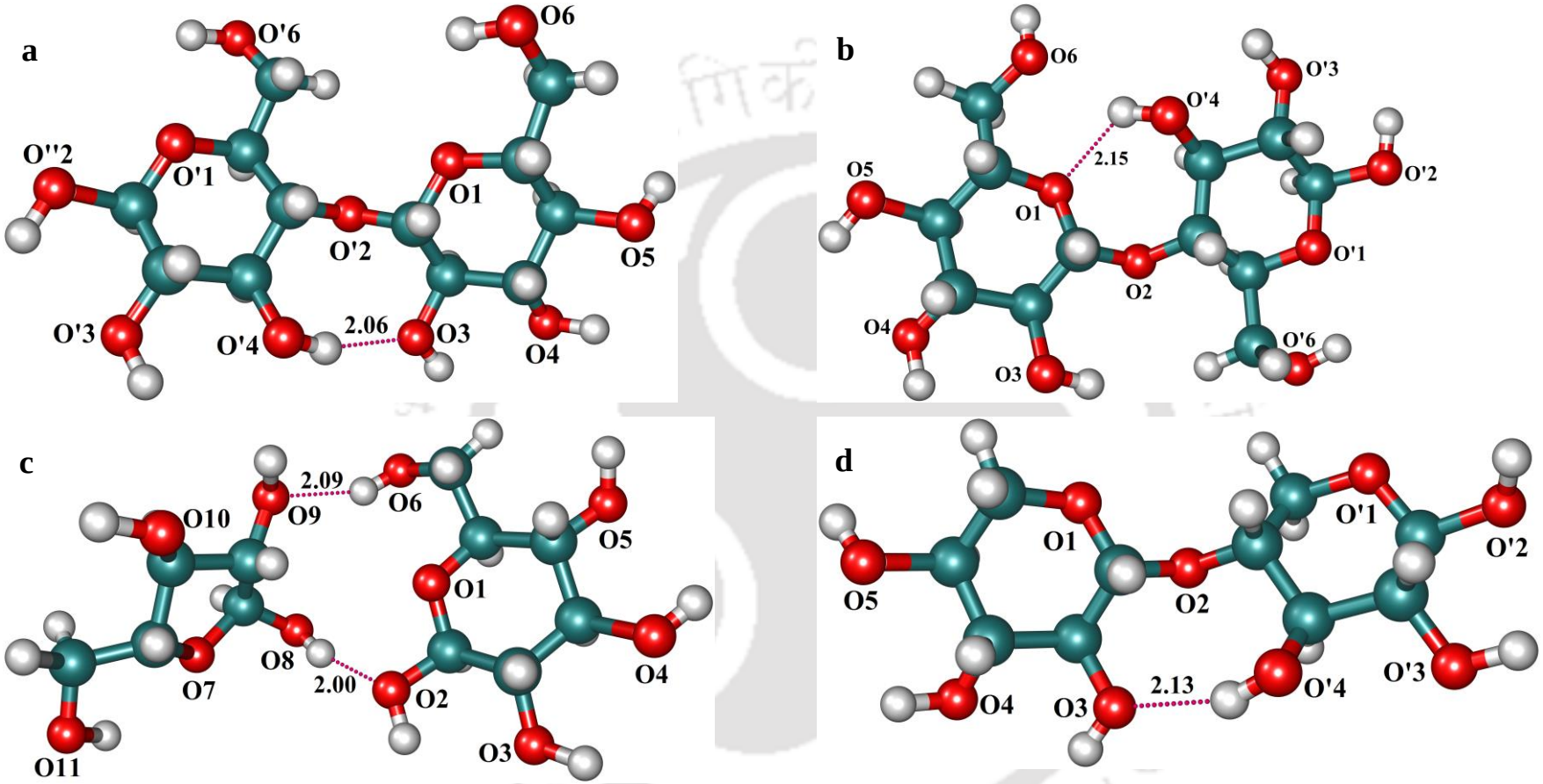

Figure 4.6: Optimized geometries of cellulose and hemicellulose conformers (a) cellobiose-anti-syn, (b) cellobiose-anti-anti are cellulose conformers, and (c) xylose+glucose, (d) xylobiose are hemicellulose conformers with corresponding atom numbers. The bond lengths are in Angstrom (Å). Color represents the different atoms such as C (cyan), O (red), and H (white) atoms, respectively.

The following anions were chosen: $[OAc]^-$, $[MC]^-$, $[AcF_3]^-$, $[Cl]^-$, $[HC]^-$, $[Me_2PO_4]^-$, $[NO_3]^-$, $[MeSO_3]^-$, $[EtSO_4]^-$, $[MeSO_4]^-$, $[MSF_3]^-$, $[BF_4]^-$ $[PF_6]^-$ and $[SCN]^-$ to investigate the interaction energy and NBO analysis. The interaction energies of cellulose and hemicellulose with the 14 anions are presented in Table 4.3. From Table 4.3, it can be seen that the $[OAc]^-$ gave the highest interaction energy with cellulose (-227.02 kJ mol^{-1}) and hemicellulose (-222.28 kJ mol^{-1}). Based on their interaction energies from Table 4.3, the ILs with $[OAc]^-$, $[HC]^-$, $[MC]^-$, $[Cl]^-$, and $[AcF_3]^-$ anions are probable candidates for the dissolution of cellulose and hemicellulose. In contrast, the anions $[BF_4]^-$, $[MSF_3]^-$, $[SCN]^-$, $[PF_6]^-$ exhibits lower interaction energies, which results in their inability to disturb the intramolecular hydrogen bonds.

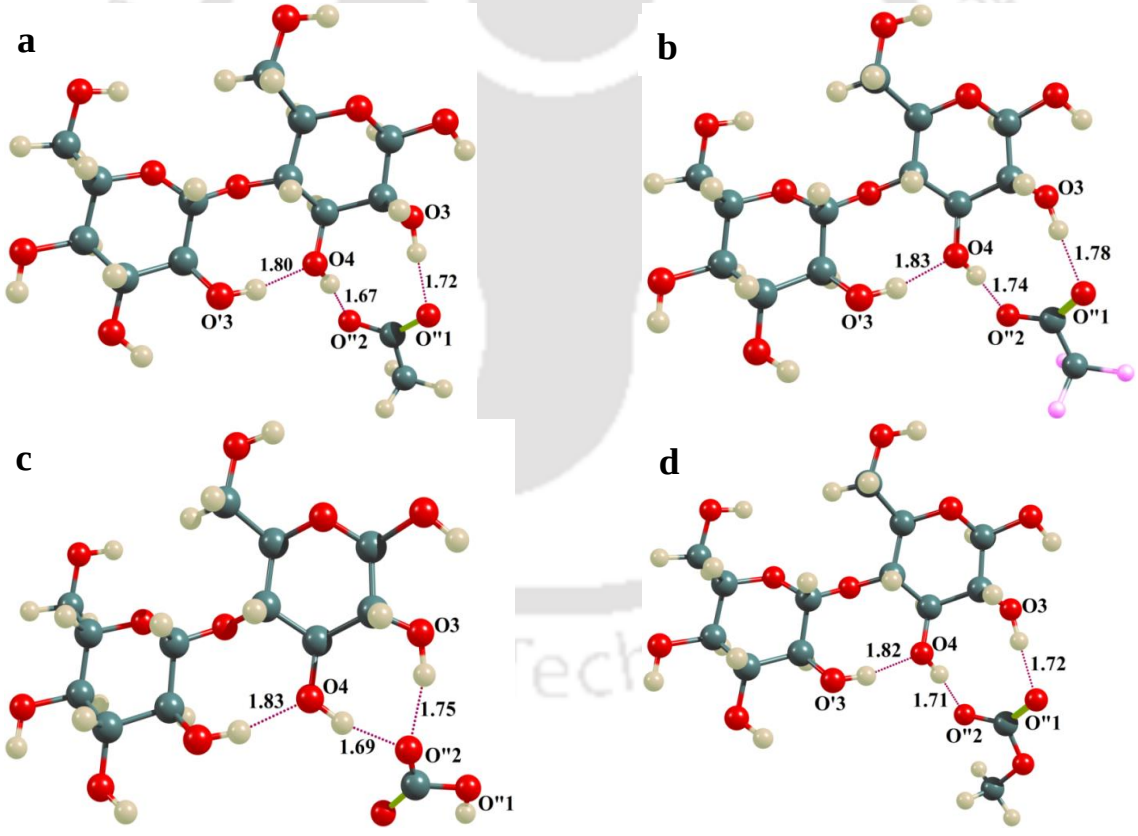

Figure 4.7: Optimized geometries for cellulose-anions (a) $[OAc]^-$, (b) $[AcF_3]^-$, (c) $[HC]^-$, and (d) $[MC]^-$. The H-bonds are indicated by dotted lines, the bond lengths are in Angstrom (Å) and given with corresponding cellulose atom numbers (Figure 4.6a). Color scheme used for different atoms are: C (cyan), O (red), H (white), and F (light pink), respectively.

The optimized geometry with the selected anions namely $[OAc]^-$, $[HC]^-$, $[MC]^-$, and $[AcF_3]^-$ with cellulose and hemicellulose are given in Figures 4.7 and 4.8. From the observation of Figures 4.7a and 4.8a, the complexes namely cellulose-$[OAc]^-$ and hemicellulose-$[OAc]^-$ are energetically more stable than others complexes. The intermolecular distances (O-H…O) of cellulose and hemicellulose molecules with $[OAc]^-$ anion were less than 1.8 Å indicating strong hydrogen bonding. The oxygen atoms of $[OAc]^-$ anion had higher negative partial charge, which gave itself more strength to interact with the other molecule. A similar trend was observed for cellulose/hemicellulose with $[MC]^-$ (Figure 4.7d and 4.8d), where the intermolecular distances were less than 1.9 Å. The interaction energy between cellulose-$[HC]^-$ and hemicellulose-$[HC]^-$ was found to be lower than the $[OAc]^-$ and $[MC]^-$ anion interaction energies. The strength of the H-bonds between the anion ($[AcF_3]^-$ and $[HC]^-$) and hydroxyl hydrogen atoms of cellulose/hemicellulose was relatively weaker than $[OAc]^-$ and $[MC]^-$ anions strengths (Figures 4.7(b-c), and 4.8(b-c)). Similarly, the anions such as $[Me_2PO_4]^-$, $[Cl]^-$, $[NO_3]^-$ $[MeSO_3]^-$, $[EtSO_4]^-$, and $[MeSO_4]^-$ also interacted with cellulose and hemicellulose *via* H-bonds. The bond distances and partial charges of these anions with cellulose and hemicellulose are reported in the Table C.11 and Table C.12 (Appendix C).

Further, the strength of the bond between electron donor-acceptor interactions was explained by NBO analysis, which corresponds to the second-order perturbation approach. The bond energies $E^{(2)*}$ of electron donor-acceptor are reported in Table 4.4. The NBO analysis has been carried for the selected anions namely $[OAc]^-$, $[MC]^-$, $[HC]^-$, and $[AcF_3]^-$ as they posses favorable interaction energies with cellulose and hemicellulose. In the complex system (Figures 4.7 and 4.8), the anion moieties are the electron donors and cellulose/hemicellulose moieties are the electron acceptors. In all the four complexes (Table 4.4), the lone pair (LP) electrons of the anions (oxygen atoms) interact with the antibonding

orbitals (BD*) of cellulose and hemicellulose (hydroxyl proton). These electron donor-acceptor orbitals are responsible for the formation of strong H-bonds between them which is indicated in the bond lengths as discussed earlier.

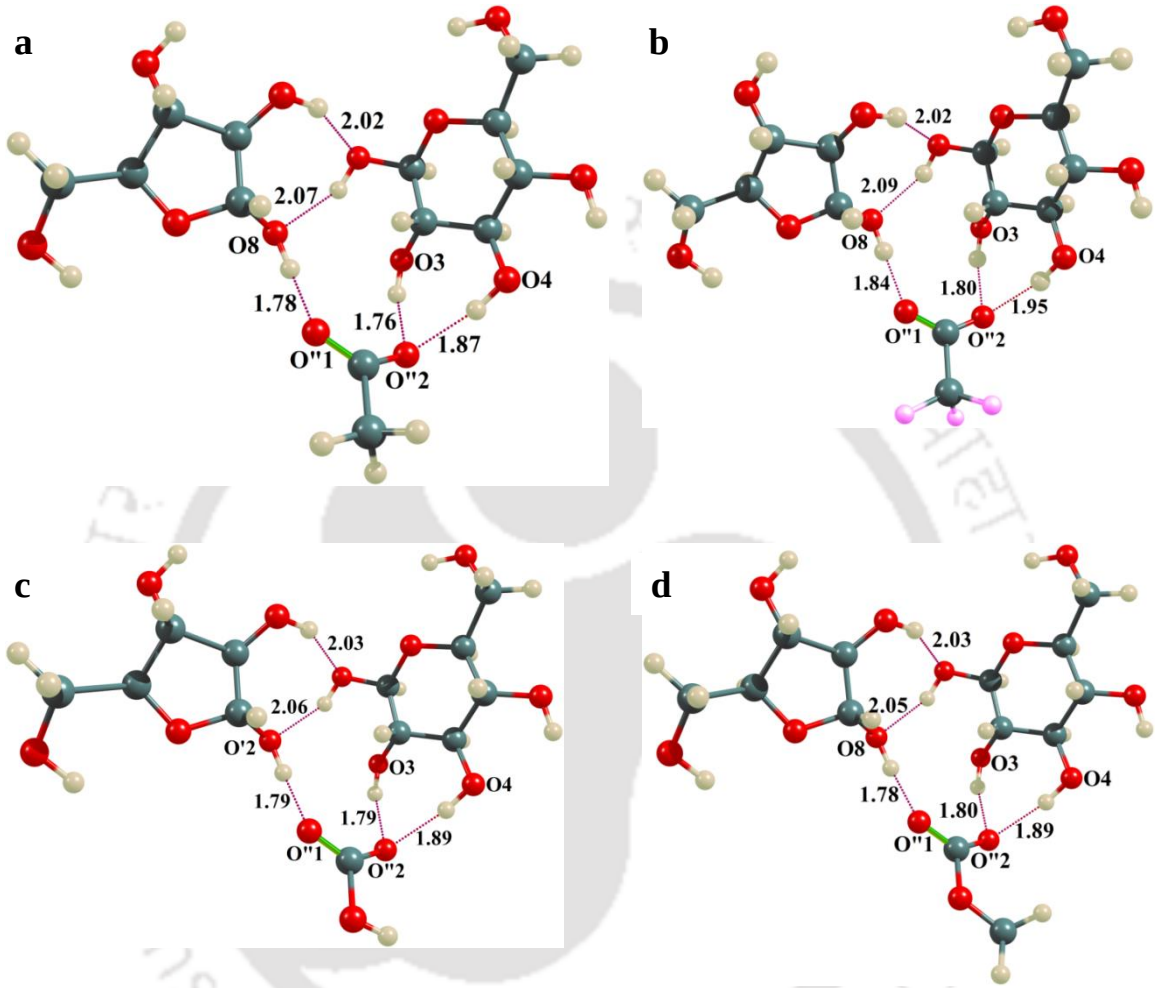

Figure 4.8: Optimized geometries for hemicellulose-anions (a) $[OAc]^{-}$, (b) $[AcF_3]^{-}$, (c) $[HC]^{-}$, and (d) $[MC]^{-}$. The H-bonds are indicated by dotted lines, the bond lengths are in Angstrom (Å) and given with corresponding hemicellulose atom numbers (Figure 4.6c). Color scheme used for different atoms are: C (cyan), O (red), H (white), and F (light pink), respectively.

Table 4.4: The electron donor and acceptor orbitals with their corresponding second order interaction energies $E^{(2)*}$ (NBO analysis)

Donor	Acceptor	$E(2)^*$ (kJ mol^{-1})			
		$[OAc]^-$	$[AcF_3]^-$	$[MC]^-$	$[HC]^-$
Cellulose (cellobiose-anti-syn)					
LP (1) O″1	BD*(1) O3 — H	31.76	32.51	40.96	-
LP (2) O″1	BD*(1) O3 — H	113.80	80.04	101.09	-
LP (1) O″2	BD*(1) O4 — H	35.19	37.61	38.83	49.62
LP (2) O″2	BD*(1) O4 — H	140.46	95.27	108.49	105.31
LP (3) O″2	BD*(1) O4 — H	11.67	7.53	-	6.07
LP (1) O″2	BD*(1) O3 — H	-	-	-	84.18
LP (2) O″2	BD*(1) O3 — H	-	-	-	4.06
LP (3) O″2	BD*(1) O3 — H	-	-	-	25.90
Hemicellulose (xylose+glucose)					
LP (1) O″2	BD*(1) O3 — H	20.63	25.61	24.18	23.56
LP (2) O″2	BD*(1) O3 — H	103.55	77.40	81.84	84.85
LP (3) O″2	BD*(1) O3 — H	—	0.38	0.38	0.46
LP (1) O″2	BD*(1) O4 — H	39.33	31.46	35.27	35.31
LP (2) O″2	BD*(1) O4 — H	4.81	2.05	4.27	5.06
LP (3) O″2	BD*(1) O4 — H	37.66	26.11	36.11	37.07
LP (1) O″1	BD*(1) O8 — H	43.60	41.88	52.55	51.42
LP (2) O″1	BD*(1) O8 — H	78.78	50.75	61.63	60.08

Among all the complexes, the $E^{(2)*}$ values of electron donor-acceptor orbitals which involves the acceptor orbital BD*(1)O4–H for cellulose; and BD*(1)O3–H for hemicellulose are relatively stronger than that of other donor-acceptor orbitals. It is a known fact that a lone

pair donor → antibonding acceptor orbital interaction will weaken the bond associated with the antibonding orbital [34]. Among all the configurations of cellulose and hemicellulose with anions, $[OAc]^-$ anion has displayed a higher H-bond energy than that of other donors (see Table 4.4). Because of the phenomena, $[OAc]^-$ had more interaction energy with cellulose and hemicellulose. Therefore, it can be concluded that the $[OAc]^-$ anion based ILs has excellent dissolution capacity for the biomass and its derivatives as well.

4.4.2.2 Effect of Cations on Cellulose and Hemicellulose Dissolution

In a similarly manner, QC calculations were performed for cellulose and hemicellulose with $[EMIM]^+$ cation. It was noticed that the encouraging sites in the cellulose and hemicellulose molecules for the $[EMIM]^+$ cation results around the O2 and O10 atoms, respectively (see Figure 4.6), and all the cations were placed at the selected sites of solutes. Other cations such as $[EMIM]^+$, $[BMIM]^+$, $[AMIM]^+$, $[TMeA]^+$, $[TEMA]^+$, $[TMA]^+$ $[EPy]^+$, $[B3MPy]^+$, $[BMPyr]^+$ and $[TES]^+$ were also explored. The interaction energies of cellulose and hemicellulose with these ten cations are presented in the Table 4.5. Among all the cations, $[EMIM]^+$ has the strongest interaction with cellulose (-116.26 kJ mol^{-1}) and hemicellulose (-113.24 kJ mol^{-1}). On the other hand, imidazolium based cations exhibit high interaction energies. The interaction strengths of cation for cellulose were found to follow: $[EMIM]^+ > [BMIM]^+ > [AMIM]^+ > [TMeA]^+ > [EPy]^+ > [B3MPy]^+ > [TEMA]^+ > [TES]^+ > [BMPyr]^+ > [TMA]^+$ and for hemicellulose: $[EMIM]^+ > [BMIM]^+ > [AMIM]^+ > [B3MPy]^+ > [EPy]^+ > [TEMA]^+ > [TES]^+ > [BMPyr]^+ > [TMeA]^+$.

Table 4.5: Interaction energies of cellulose (cellobiose-anti-syn) and hemicellulose (xylose+glucose) with cations

Sl. No.	Name of the Cation	Interaction Energy (kJ mol^{-1})	
		Cellulose	Hemicellulose
1.	1-ethyl-3-methylimidazolium $[EMIM]^+$	-116.26	-113.24
2.	1-butyl-3-methylimidazolium $[BMIM]^+$	-111.34	-103.68
3.	1-allyl-3-methylimidazolium $[AMIM]^+$	-109.35	-81.70
4.	Tetramethylammonium $[TMeA]^+$	-107.31	-38.81
5.	Triethylmethylammonium $[TEMA]^+$	-94.50	-73.99
6.	Tris(2-hydroxymethyl)methylammonium $[TMA]^+$	-66.04	-
7.	1-ethylpyridinium $[EPy]^+$	-106.22	-74.60
8.	1-butyl-3-methylpyridinium $[B3MPy]^+$	-106.45	-78.98
9.	1-butyl-1-methylpyrrolidinium $[BMPyr]^+$	-87.25	-39.67
10.	Triethylsulfonium $[TES]^+$	-93.61	-68.92

Apart from interaction energy, the NBO analysis for $[EMIM]^+$ and $[BMIM]^+$ cations with cellulose and hemicellulose are presented in Table 4.6. The optimized geometry configurations and hydrogen bonding distance between the hydroxyl groups of cellulose and hemicellulose with cations are presented in Figure 4.9. From Figure 4.9, the cation moieties act as electron acceptors while the cellulose/hemicellulose moieties as electron donors. In both complexes, the lone pair electrons of hydroxyl oxygen atoms of the cellulose (O2) and hemicellulose (O10) interacts with the antibonding orbitals of cations (C″1–H). The bond length (C–H…O) of cellulose and hemicellulose with cations varies from 2.12-2.33 Å,

which is more than anion bond lengths. These results confirm the reason as why the anions have high interactions with cellulose and hemicellulose than cations. Further, the bond energies of $[EMIM]^+$ cation is relatively higher than that of $[BMIM]^+$ (see Table 4.6). As a result, $[EMIM]^+$ cation based ILs are the better solvents for the dissolution of biomass. On comparing the anion interaction with cations, it was found that the O–H…O bond is stronger than that of C–H…O bond. Therefore, the anionic part of the IL plays a predominating role in the dissolution process. Keeping the advantages in mind the IL: [EMIM][OAc] was chosen to dissolve cellulose/hemicellulose experimentally so as to validate our predictions and comparison was made with respect to cellulose dissolution in others ILs. Hemicellulose was dissolved only in [EMIM][OAc] IL as our main target was on cellulose molecule owing to its highly crystalline structure.

Table 4.6: The electron donor and acceptor orbitals with their corresponding second order interaction energies $E^{(2)*}$ (NBO analysis)

Donor	Acceptor	$E(2)^*$ (kJ mol^{-1})	
		$[EMIM]^+$	$[BMIM]^+$
Cellulose (cellobiose-anti-syn)			
LP (1) O2	BD*(1) C″1 — H	3.81	3.60
LP (2) O2	BD*(1) C″1 — H	13.18	12.55
Hemicellulose (xylose+glucose)			
LP (1) O10	BD*(1) C″1 — H	34.14	32.10

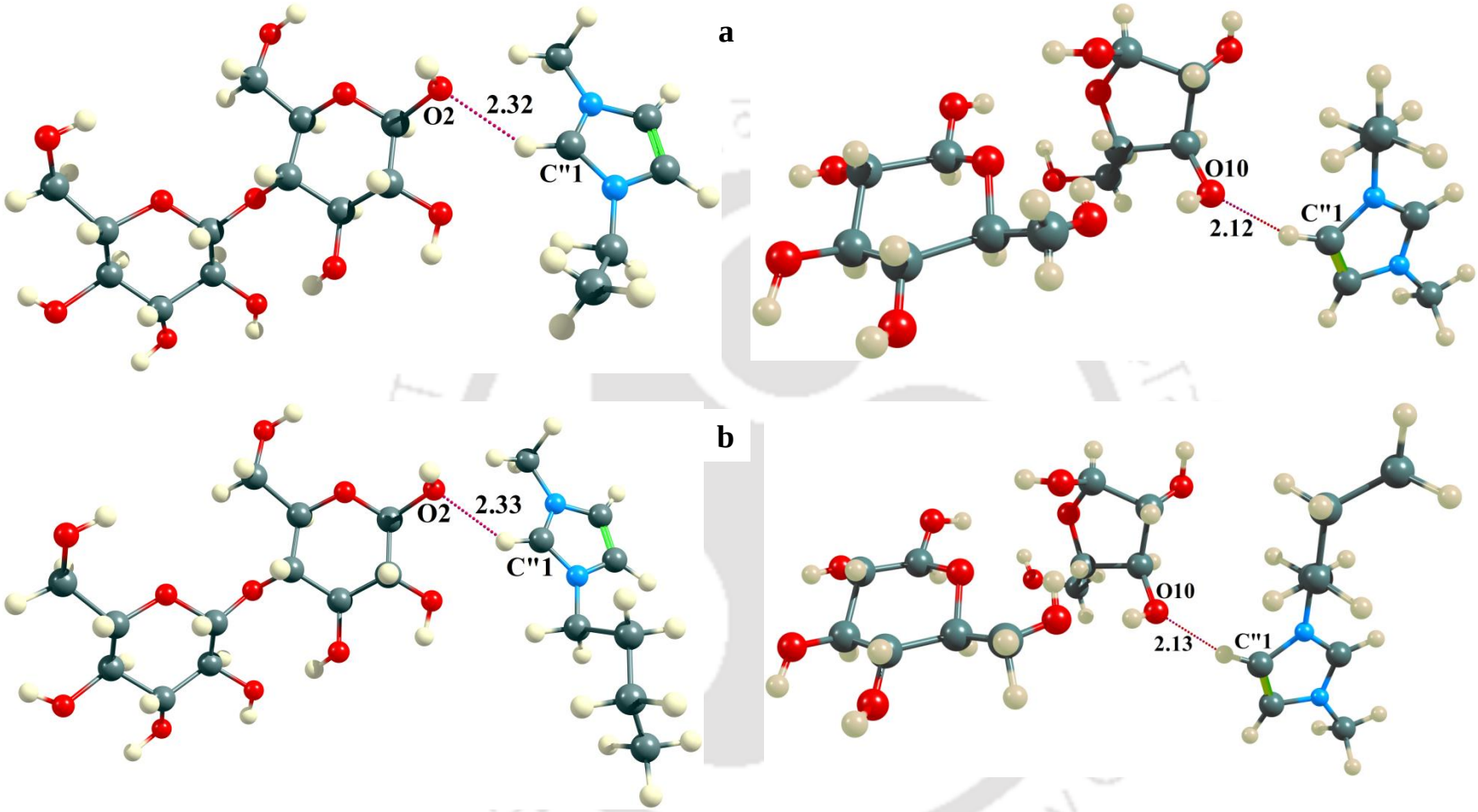

Figure 4.9: Optimized geometries for cellulose and hemicellulose with cations (a) $[EMIM]^+$, and (b) $[BMIM]^+$. The H-bonds are indicated by dotted lines, the bond lengths are in Angstrom (Å), given with corresponding atom numbers (Figure 4.6). Color scheme used for different atoms are: C (cyan), O (red), H (white), and N (sky blue) atoms, respectively.

4.4.3 Effect of Anions and Cations on Different Conformational Structures of Cellulose and Hemicellulose

Furthermore, we have studied the effect of different anions ($[OAc]^-$, $[AcF_3]^-$, $[MC]^-$) and cations ($[EMIM]^+$ $[BMIM]^+$) on the conformational structures of cellulose and hemicellulose. The considered conformational structures for cellulose are cellobiose-anti-syn and cellobiose-anti-anti. The counterpart for hemicellulose are xylose+glucose and xylobiose, respectively (Figure 4.6). Table 4.7 reports the interaction energies of cellulose and hemicellulose with anions and cations for different conformers. From Table 4.7, it is seen that the interaction energy between cellobiose-(anti-syn)-anions/cations is higher than the other conformers of cellulose *i.e.,* cellobiose-(anti-anti)-anions/cations. The interatomic distance between the cellulose-anions (O–H…O) bond representing the cellobiose-(anti-syn)-anions is found to be ranging from 1.67-1.78 Å. On a similar line, the distance for cellobiose-(anti-anti)-anions are in the range 1.71-1.89 Å (Figure C.3). The lower interatomic distance of cellobiose-(anti-syn)-anions was due to the higher partial charge on both oxygen atom of anion and hydrogen atom of the hydroxyl group. This eventually implies a higher strength of the H-bonds between the anions and hydroxyl hydrogen atoms of cellulose-anti-syn. Further, the strength of the bond between the electron donor–acceptor interactions were elucidated by NBO analysis. From Table C.13 and Table C.15, it was also found that the bond energies $E^{(2)*}$ of electron donor–acceptor was greater for 'cellobiose-anti-syn' system when compared with 'cellobiose-anti-anti' systems.

Table 4.7 also reports the interaction energies of hemicellulose-anions/cations with different conformers of hemicellulose. The conformer xylose+glucose exhibited higher interaction energy than xylobiose. The interaction energy deviation between the conformers were relatively higher when compared to cellulose conformers. This higher interaction energy deviation was obtained due to the difference in number of hydroxyl groups present in

conformers. It is to be noted that the Xylose+glucose conformer has a higher number of hydroxyl groups than xylobiose conformer. The intra-molecular H-bonds of xylose+glucose also gets weakened by the formation of strong inter-molecular H-bonds with the anion of the ILs. On the contrary xylobiose retains its strong intra-molecular H-bond (Figure C.4). Thus the interaction energy was higher for xylose+glucose conformer. Further, these results were confirmed by establishing the NBO analysis between hemicellulose conformers and ions of IL (Table C.15 and Table C.16). In addition to interaction energy results, COSMO-RS calculations (sigma profiles) also suggests that cellobiose-anti-syn has a qualitatively higher number of polar segments than cellobiose-anti-anti conformer (Figure C.5a). This is usually obtained from the cut-off distance for hydrogen bonding [15]. A similar trend was observed for xylose-glucose conformer (Figure C.5b).

Table 4.7: Interaction energies for the conformers of cellulose and hemicellulose with anions and cations

Entry	Name of the Anion/Cation	Cellulose I.E. (kJ mol^{-1})		Hemicellulose I.E. (kJ mol^{-1})	
		Cellobiose-anti-syn	Cellobiose-anti-anti	Xylose+Glucose	Xylobiose
1.	$[OAc]^-$	-227.02	-218.23	-222.28	-190.62
2.	$[MC]^-$	-212.80	-208.57	-205.48	-178.07
3.	$[AcF_3]^-$	-192.22	-179.70	-182.30	-153.68
4.	$[EMIM]^+$	-116.26	-77.32	-113.24	-79.49
5.	$[BMIM]^+$	-111.34	-75.35	-103.68	-77.86

In addition, present study interaction energy results were compared with the available literature data of Guo *et al.* (2010) [25]. The interactions between different anions (OAc, Me_2PO_4, BF_4, and PF_6) and 1,4-O-dimethyl cellobiose (structurally similar to cellobiose-anti-anti structure) as a cellulose model were reported. The interaction energy between 1,4-

O-dimethyl cellobiose and $[OAc]^-$ anion was 178.82 kJ mol^{-1}, which was lower than the cellobiose-(anti-anti)-$[OAc]^-$ interaction energy (-218.23 kJ mol^{-1}). In a similar manner, the results of Guo *et al.* (2010) were also compared with cellobiose-anti-syn conformer. The dissimilarity in the interaction energy was mainly due to the number of hydroxyl groups in cellulose moiety. While the 1,4-O-dimethyl cellobiose has seven number of hydroxyl groups, the cellobiose-anti-syn and cellobiose-anti-anti had eight hydroxyl groups. The interaction energy between the cellobiose-(anti-syn)-anions were much higher than the 1,4-O-dimethyl cellobiose-anions (Table 4.8). A comparison with Guo *et al.* (2010) gives the interaction energies with the anions (Table 4.8). The decreasing trend in both the scenarios is seen to follow: $[OAc]^-$ > $[Me_2PO_4]^-$ > $[BF_4]^-$ > $[PF_6]^-$. This eventually confirms our QC approach. For theoretical calculations, the consideration of any conformers of cellulose and hemicellulose molecules provides the similar outcome but has variation in interaction energy values.

Table 4.8: Comparison of interaction energies between conformers of cellulose and anions

Anion Type	Cellulose Conformer I.E. (kJ mol^{-1})	
	Cellobiose-anti-syn	1,4-O-dimethyl cellobiose[a]
$[OAc]^-$	-227.02	-178.82
$[Me_2PO_4]^-$	-185.52	-147.52
$[BF_4]^-$	-157.61	-95.30
$[PF_6]^-$	-130.98	-78.51

[a] Guo *et al.* (2010) [25]

Table 4.9: Experimental solubility of cellulose and hemicellulose in different ILs at different temperatures and time[a]

Entry	Ionic Liquid Type	Condition	Solubility (wt. %)
Microcrystalline Cellulose			
1.	[EMIM][OAc]	27 °C, 1 h	2.10
		50 °C, 1 h	6.90
		70 °C, 1 h	9.46
		90 °C, 0.5 h	11.38
		90 °C, 1 h	14.63
		90 °C, 2 h	18.93
		110 °C, 1 h	19.10
		130 °C, 1 h	27.69
2.	[BMIM][OAc]	90 °C, 1 h	10.28
		110 °C, 1 h	15.78
3.	[EMIM][$EtSO_4$]	90 °C, 1 h	3.73
		110 °C, 1 h	5.27
4.	[EMIM][$MeSO_3$]	90 °C, 1 h	5.17
		110 °C, 1 h	7.49
5.	[EMIM][SCN]	90 °C, 1 h	2.94
		110 °C, 1 h	4.17
6.	[TMA][$MeSO_4$]	90 °C, 1 h	1.40
		110 °C, 1 h	2.84
Xylan (Hemicellulose)			
7.	[EMIM][OAc]	27 °C, 1 h	5.52
		50 °C, 1 h	13.90
		70 °C, 1 h	25.01

[a] The standard uncertainty: $u(T)$ = 0.1 °C and $u(sol)$ = 1.21 wt % at 95% confidence level

4.4.4 Experimental Solubility of Cellulose and Hemicellulose

The experimental solubility of cellulose and hemicellulose was carried out in six different ILs namely [EMIM][OAc], [BMIM][OAc], [EMIM][$MeSO_3$], [EMIM][$EtSO_4$], [EMIM][SCN] and [TMA][$MeSO_4$] at 27-130 °C for 1 h of reaction time. Even though it is a slow process, it still serves our aim to alter the structure of cellulose so as to make it more accessible for enzymatic hydrolysis. A similar dissolution time was undertaken by Balensiefer *et al.* (2008) [7] and Vitz *et al.* (2009) [63]. The solubility of cellulose and hemicellulose in ILs are reported in Table 4.9. The solubility of cellulose and hemicellulose in [EMIM][OAc] was found to increase with both time and temperature. [EMIM][OAc] gave a higher solubility of cellulose when compared to [BMIM][OAc]. This follows the results obtained from the interaction energies of cellulose with [EMIM][OAc] and [BMIM][OAc] which were -462.57 kJ mol^{-1} and -453.76 kJ mol^{-1}, respectively (Figure 4.10). Whereas in the case of hemicellulose, the interaction energies for [EMIM][OAc] and [BMIM][OAc] were -509.17 kJ mol^{-1} and -503.65 kJ mol^{-1}, respectively. On the other hand, the solvents with higher hydrogen bond basicity (β) value, results in a high dissolution capacity for a solute [64]. The hydrogen bond basicity of [EMIM][OAc] (1.107) is also more compared to that of [BMIM][OAc] (1.04) [28,65,66]. It was also confirmed that, for a common anion, the smaller size of the cation has a greater influence on the dissolution of cellulose and hemicelluloses. The similar behaviour was also observed in previous chapters 2 and 3.

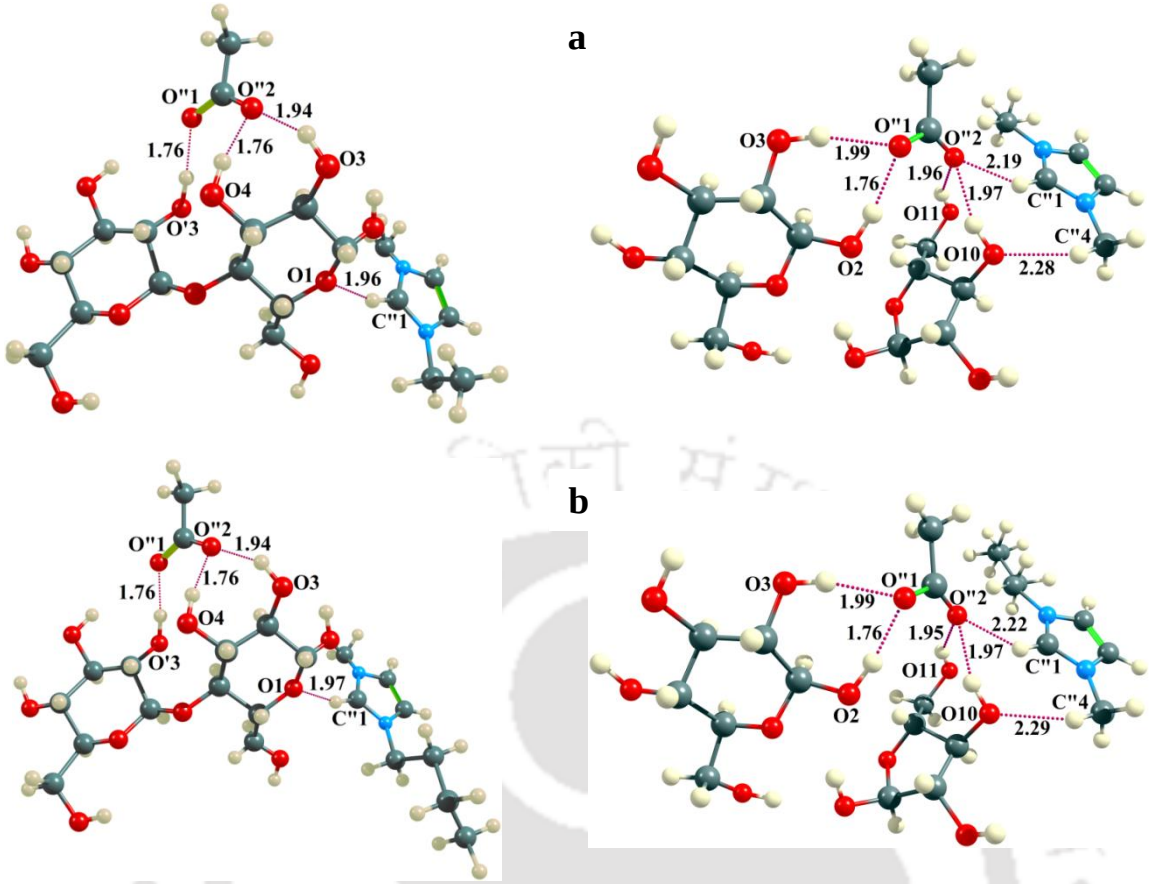

Figure 4.10: Optimized geometries for cellulose and hemicellulose with IL (a) [EMIM][OAc], and (b) [BMIM][OAc]. The H-bonds are indicated by dotted lines, the bond lengths are in Angstrom (Å), given with corresponding atom numbers (Figure 4.6). Color scheme used for different atoms are: C (cyan), O (red), H (white), and N (sky blue), respectively.

In addition, the computed interaction energies from QC (cellulose-IL) and MD (cellulose-anions) simulations are further correlated with the experimental solubility of cellulose (Figure 4.11). From Figure 4.11, it can be observed that higher the interaction energy between IL and cellulose, higher the solubility of cellulose. The IL [EMIM][OAc] gave the highest dissolution capacity of cellulose than other ILs due to its stronger interaction energies with cellulose. The dissolution order of anions for the solubility of cellulose in a common cation (*i.e.*, $[EMIM]^+$) was found to be: $[OAc]^-$ > $[MeSO_3]^-$ > $[EtSO_4]^-$ > $[SCN]^-$. The $[OAc]^-$ anion forms strong H-bonds with cellulose which arises due to the presence of higher fraction of polar segments (Figure C.6). The $[SCN]^-$ anion exhibits

less polarity than oxygen based anions (Figure C.6) thereby resulting in lower interaction energies with cellulose (Table 4.3). On the other hand, [EMIM][SCN] gave higher dissolution capacity than [TMA][$MeSO_4$], even though $[MeSO_4]^-$ anion had stronger interactions with cellulose (Table 2). On the contrary, when $[MeSO_4]^-$ combines with $[TMA]^+$ cation, the interaction between cellulose/$[MeSO_4]^-$ gets weakened due to the formation of a strong interaction between $[TMA]^+/[MeSO_4]^-$ (-413.38 kJ/mol). The difference between QC and MD simulated interaction energies were found to be significantly higher. This is due to the reason that the QC based interaction energies were calculated for favorable sites due to the presence of a single ion. The MD simulated interaction energies included the total molecular system where the interaction of all the ions are accounted. Overall, the interaction energies of IL-cellulose followed a similar pattern in both QC and MD simulations.

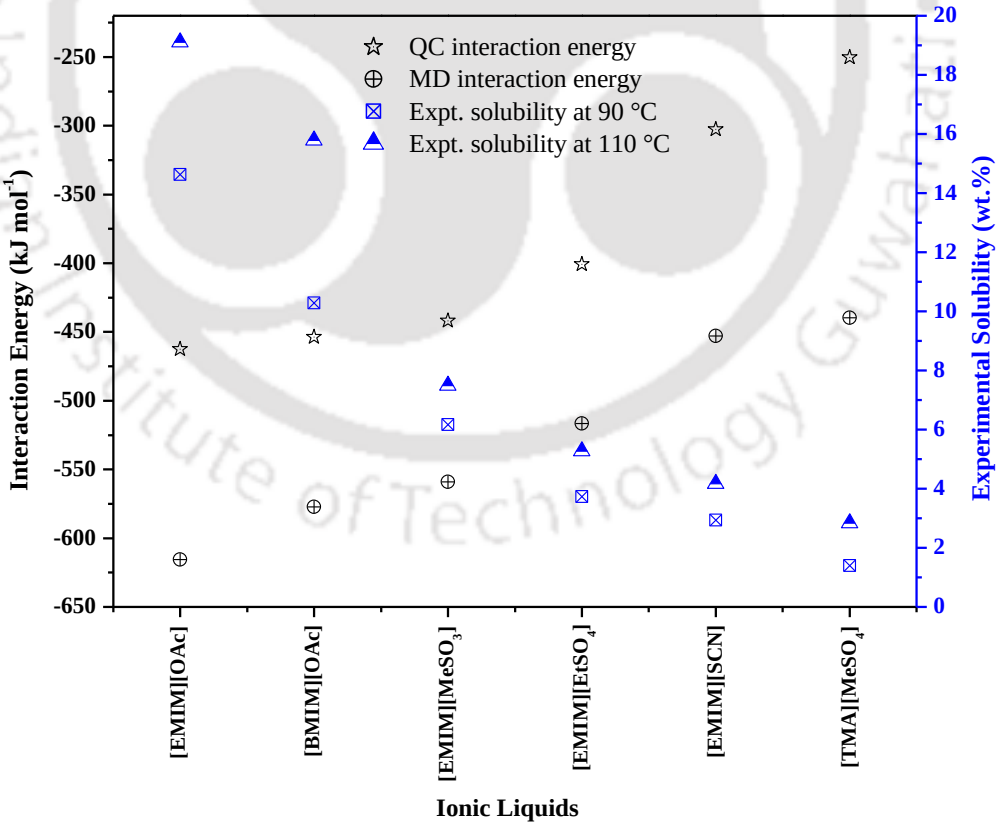

Figure 4.11: Experimental solubility of cellulose (90 °C and 110 °C) is correlated with MD and QC interaction energies in different ILs

Table 4.10: Literature experimental solubility of cellulose and hemicellulose in ionic liquids at different temperatures and time

Ionic Liquid	Cellulose type	Condition	Solubility (Wt. %)	Reference
[EMIM][OAc]	Avicel	110 °C	15	[67]
	Avicel	100 °C, 35 min	10	[7]
	Cellulose	85 °C	13.5	[68]
	Avicel	100 °C	8	[63]
	Avicel (~DP = 225)	110 °C	28	[67]
	D-glucose	60 °C	60	[67]
	MCC (~DP = 400)	90 °C, 1 h	14.6	Present work
	MCC (~DP = 400)	110 °C, 1 h	19.1	Present work
[EMIM][DEP]	MCC (~DP = 950)	100 °C, 48 h	19.8	[19]
	MCC (~DP = 950)	120 °C, 48 h	19.9	[19]
[EMIM][Cl]	Avicel	90 °C	5	[69]
	Avicel (286)	90 °C	12	[9]; [70]
[EMIM][Tos]	Avicel	100 °C, 1 h	1	[63]
[EMIM][Br]	Avicel	100 °C, 1 h	1 to 2	[63]
[EMIM][F]	Avicel	100 °C, 1 h	2	[63]
[BMIM][OAc]	Avicel	100 °C, 1 h	12	[63]
[BMIM][SCN]	Pulp cellulose	Microwave	5–7	[5]
[BMIM][Cl]	Avicel	90 °C	5	[69]
[BMIM][HCOO]	Avicel (225)	110 °C	8	[67]
[OMIM][OAc]	Avicel	110 °C	9	[67]

Further, the current study was also compared with reported experimental solubility of cellulose in different ILs at different conditions Table 4.10. As can be seen from Table 4.10, it was observed that there is no major influence of cation on the dissolution of cellulose. As the alkyl chain length in the cation is increased, the solvent power of ILs for cellulose tends to decrease, *i.e.*, [EMIM][OAc] > [BMIM][OAc] > [OMIM][OAc] (Table 4.10, Avicel, 110 °C). The lower solubility of cellulose in longer chain ILs are primarily due to the reduced strength of acetate anion. This is due to the reduction of hydrophobic interactions of longer chain cations which lowers the ability to screen anion/cellulose complexes [71].

4.4.5 Influence of Viscosity and Density of ILs

The density and viscosity of the ILs also plays a key role in the dissolution process, where it is generally considered that ILs with low viscosity are more efficient in dissolution. The density and viscosity of ILs were measured by a digital densitometer (Anton Paar, DMA-4500 M model) and interfacial rheometer **(**Anton Paar, Phsica MCR301 model**)** at a temperature range from 288.15 K to 383.15 K. The details regarding the operational system are described in chapter 2 (section 2.3.4). The uncertainty in temperature is 0.01 K and the absolute uncertainty in density and viscosity are 0.0001 g cm^{-3} and 0.5 mPa.s, respectively. Figure 4.12 depicts the viscosity and density of six ILs as a function of temperature. As the temperature of the dissolution process increases, the viscosity of the ILs will be decreased, this leads to faster mass transfer rate and higher dissolution of solute. The conflicting data in Figure 4.12 suggest that, perhaps the density and viscosity is not a key factor for the dissolution of cellulose in a given IL [71]. It is true, however, the ILs with lower density and viscosity are easier to handle, but it still seems that the basicity and polarity of the anions is a better indicator of their ability to dissolve cellulose [64]. This led us to adopt MD simulation for better insight.

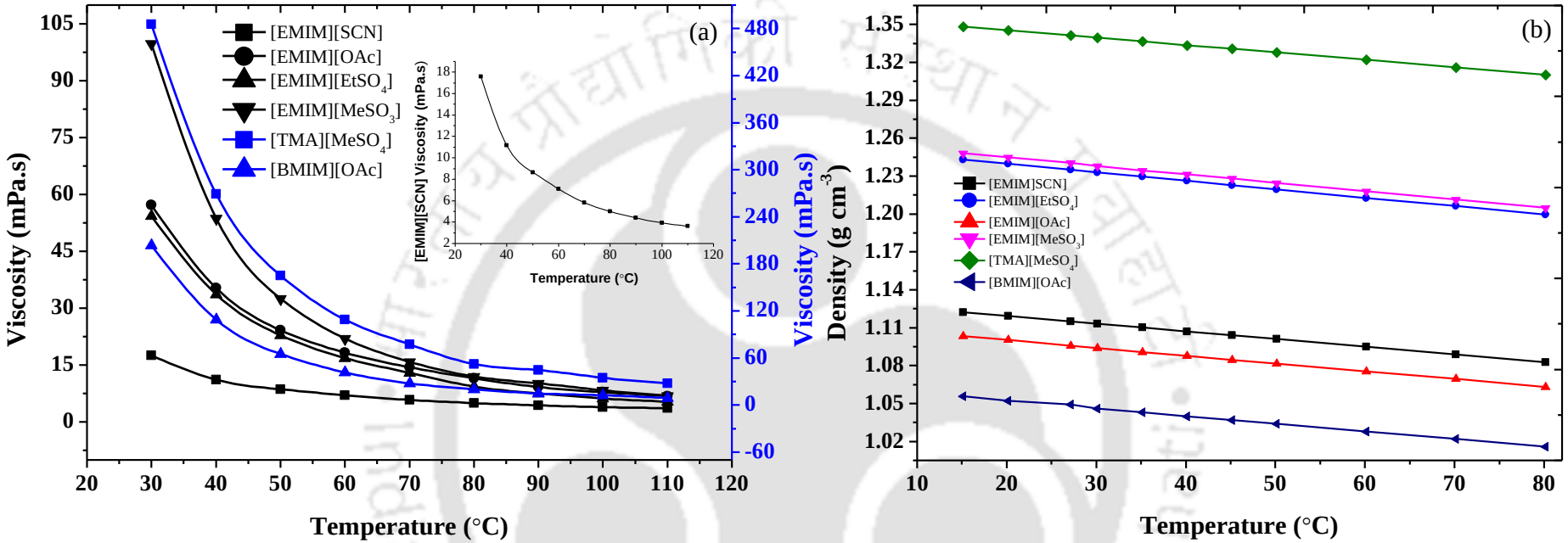

Figure 4.12: Experimental density and viscosity of pure ionic liquids as a function of temperature (a) viscosity, and (b) density of ILs

4.4.6 Molecular Dynamics Simulations

Apart from the QC calculations and experimental confirmations, the MD simulations were also carried to understand the structural properties of cellulose with ILs by radial distribution functions (RDF) and non-bonded interaction energy. Figure 4.13a shows the RDF between the HS atom of cellulose and OA atom of anions (NA for $[SCN]^-$; see Figure C.7 for atom notations). The first solvation shell of RDF plot was located at around 1.65-1.75 Å which indicates a formation of strong hydrogen bond between the cellulose and anions. It should be noted that the corresponding peak for $[SCN]^-$ was obtained at 1.85 Å. In the case of cellulose-cation RDF plot (Figure 4.13b), the peak was obtained at around 2.15 Å and 1.85 Å for $[EMIM]^+$ and $[TMA]^+$, respectively. It is interesting to note that the ring hydrogen of the cation approaches the cellulose moiety within 2 Å indicating a likely formation of a weak cation-cellulose hydrogen bond. This is further confirmed by the coordination number and interaction energies as given in Table 4.11, where cellulose is surrounded by six to eight $[OAc]^-$ anions and are present in the first solvation shell (2.35 Å; Figure C.8). On the contrary, $[MeSO_3]^-$, $[EtSO_4]^-$, $[SCN]^-$ and $[MeSO_4]^-$ anions had a lower coordination number of 4.91, 4.37, 6.96 and 2.85, respectively. In the case of cellulose-cation interaction, the first solvation shell extends up to 3.35 Å with a coordination number ranging from two to five (Figure C.9). Thus, within the first solvation shell, three to eight anions and two to five cations are bounded to cellulose. This fact is supported with the NMR results of Zhang *et al.* (2010) [72], where they suggested that the seven ion pairs of ILs are present in the first solvation shell of cellobiose. In addition, it was worthwhile to note that acetate anion formed multiple hydrogen bonds with cellulose molecule (Figure C.8 and C.10). Similar observations were also reported by Rabideau *et al.* (2015) during their study on the influence of water content on the dissolution of cellulose in acetate based ILs [20]. It was reported that each anion can form up to three to four hydrogen bonds with cellulose.

Table 4.11: Interaction energies (I.E.) and coordination number (C.N.) of the first solvation shell for the different systems obtained from MD simulations[a]

Cellulose-IL System	Cellulose - Anion		Cellulose - Cation		Cation-Anion I. E. (kJ mol^{-1})
	I. E. (kJ mol^{-1})	C. N.	I. E. (kJ mol^{-1})	C. N.	
[EMIM][OAc]	-412.76	7.82	-202.68	5.18	-331.64
[BMIM][OAc]	-401.77	6.47	-175.33	3.16	-376.61
EMIM][$MeSO_3$]	-370.84	4.91	-188.20	3.96	-365.53
[EMIM][$EtSO_4$]	-333.03	4.37	-183.61	3.81	-360.28
[EMIM][SCN]	-254.66	6.96	-198.39	4.27	-303.70
[TMA][$MeSO_4$]	-230.15	2.85	-209.43	2.50	-413.38

[a] Cellobiose-anti-syn as cellulose model

Table 4.11 also reports the MD simulated interaction energies for cellulose-anion and cellulose-cation pairs. From Table 4.11, it is interesting to note that the strength of the non-bonded interaction energies between anion and cellulose is directly proportional to the experimental solubility (Figure 4.11). This is a similar trend as observed with QC energies. The simulated energies were in good agreement with the experimental solubility (Figure 4.11). Apart from cellulose-IL interactions, the cation may diminish the solubility of cellulose by forming hydrogen bonds with anion in the solvation system (Figure C.10). Moreover, the obtained MD simulated interaction energies of cellulose were further compared with literature data [51,73] and shown in Table 4.12. Table 4.12 reports the interaction energies for different degree of polymerizations of cellulose molecule with [EMIM][OAc]. From the observation of Table 4.12, the interaction energies were found to be higher for longer cellulose chains due to the presence of large number of hydroxyl groups. The anion of IL inherits a higher interaction energy with cellulose when compared to cation. The $[OAc]^-$ anion was found to provide a higher interaction energy with cellulose when compared to Cl^- anion [13,50,74]. The reported MD simulations were carried by

applying different force field parameters at different production runs. However, the interaction energy results are in line with the variation of the degree of polymerizations which implies that the energy contribution of each monomer is relatively similar. Further, the obtained interaction energy results of ion-cellulose pairs are in agreement with the reported interaction energies (Table 4.12).

Table 4.12: Interaction energies (kJ mol^{-1}) between cellulose and [EMIM][OAc] obtained from MD simulations and compared with literature data[a]

Cellulose Type	Cellulose			Production run (ns)	Reference
	$[EMIM]^+$	$[OAc]^-$	[EMIM][OAc]		
Cellulose (DP = 10)[b]	-975.82	-2190.15	-3165.97	4.5	[51]
Glucose[b]	-97.58	-219.05	-316.60	4.5	[51]
Cellulose (DP = 10)[c]	-564.30	-702.24	-1266.54	250	[73]
Cellulose (DP = 2)[d]	-202.68	-412.76	-615.44	60	Present study
Cellulose (DP = 6; polar method)[e]	-379.13[f]	-911.24[g]	-1290.37[h]	10	[74]
Cellulose (DP = 6; non-polar method)[e]	-377.87[f]	-1100.60[g]	-1478.47[h]	10	[74]
Cellulose (DP = 8)[i]	-855.26	-1582.50	-2437.76	500 [j]	[13]
Cellulose (DP = 8)[i]	-867.73	-1373.67[g]	-2241.40[k]	500 [j]	[13]
Cellulose (DP = 6)[a]	-500.00	-1111.12	-1611.12	100	[50]

[a] Interaction energies are reported per mole of cellulose; [b] GLYCAM force field parameters are used; [c] GLYCAM06 force field parameters are used and carried at 127 °C; [d] CHARMM force field parameters are used and carried at 27 °C; [e] GAFF force field parameters are used and carried at 127 °C; [f] 1,3-dimethylimidazolium [C_1mim] cation; [g] Chloride anion; [h] [C_1mim]Cl Ionic Liquid; [i] GLYCAM force field parameters are used and carried at 100 °C; [j] for single cellulose chain, production run was 10 ns; [k] [EMIM]Cl Ionic Liquid

In summary, the proposed reaction mechanism for the dissolution of cellulose and hemicellulose in imidazolium based IL ([EMIM][OAc]) is presented in Figure 4.14. Cellulose molecule has strong inter- and intra-molecular hydrogen linkages through its hydroxyl groups and forms a crystal structure. Upon dissolution of cellulose in [EMIM][OAc], the ionic pairs of IL are partially dissociated into cation and anion, which in

turn interacts with the hydroxyl groups of cellulose chain and forms new hydrogen bonds between solute and [EMIM][OAc]. Therefore, the high crystalline order of cellulose gets weakened by disturbing their strong inter- and intra-molecular hydrogen linkages and results in its amorphous structure. From the aforementioned discussions, it is confirmed that the anion of the IL plays a primary role in the dissolution mechanism. As the evidence from RDF plots and coordination numbers, the cation is seen to approach cellulose by forming weak hydrogen bonds.

As a consequence, the dissolution process is seen to follow two opposite pathways. While on one side the cation effects the cellulose solubility due to its strong binding with anion, on the other side anion helps in providing hydrogen bonds with incoming hydroxyl groups of cellulose. A similar mechanism is also applicable for hemicellulose dissolution in IL. However, the proposed reaction mechanism has certain limitations and it is applicable for ILs with highly polar (or strong interacting) anions i.e., $[OAc]^-$, $[Me_2PO_4]^-$, and $[Cl]^-$ along with slightly polar cations. Therefore, the IL could form new strong H-bonds with cellulose by disturbing their inter- and intra-molecular bonds. If the IL contains both polar ions (example: $[TMA]^+$ and $[MeSO_4]^-$), then the dissociation of ionic pairs of ILs would be a challenging task due to the presence strong interactions among the ions which results in lower interactions with cellulose. On the other hand, the IL containing both less polar ions ($[EMIM]^+$ and $[SCN]^-$), the interaction between the cellulose and ions were obviously lower (Table 4.11). Therefore, the proposed mechanism suggests that combination of highly polar and slightly non-polar ions results in a favorable dissolution and also helps in altering the cellulose structure.

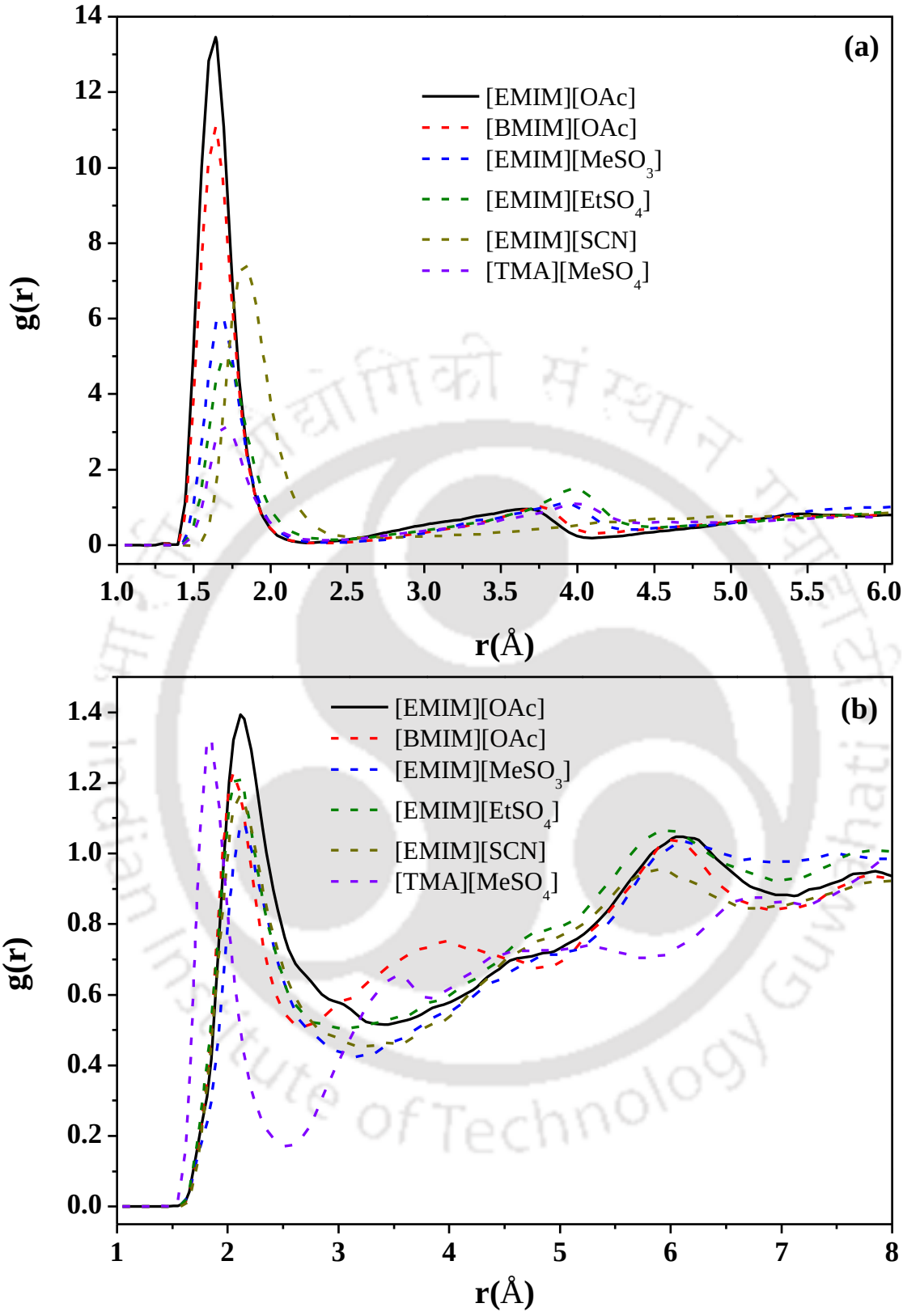

Figure 4.13: Radial distribution function (RDF) of (a) HS of cellulose and OA of the anion (NA for $[SCN]^-$), (b) OS of cellulose and HC of cation (see Figure C.7 for atom notations) the cellulose/IL system

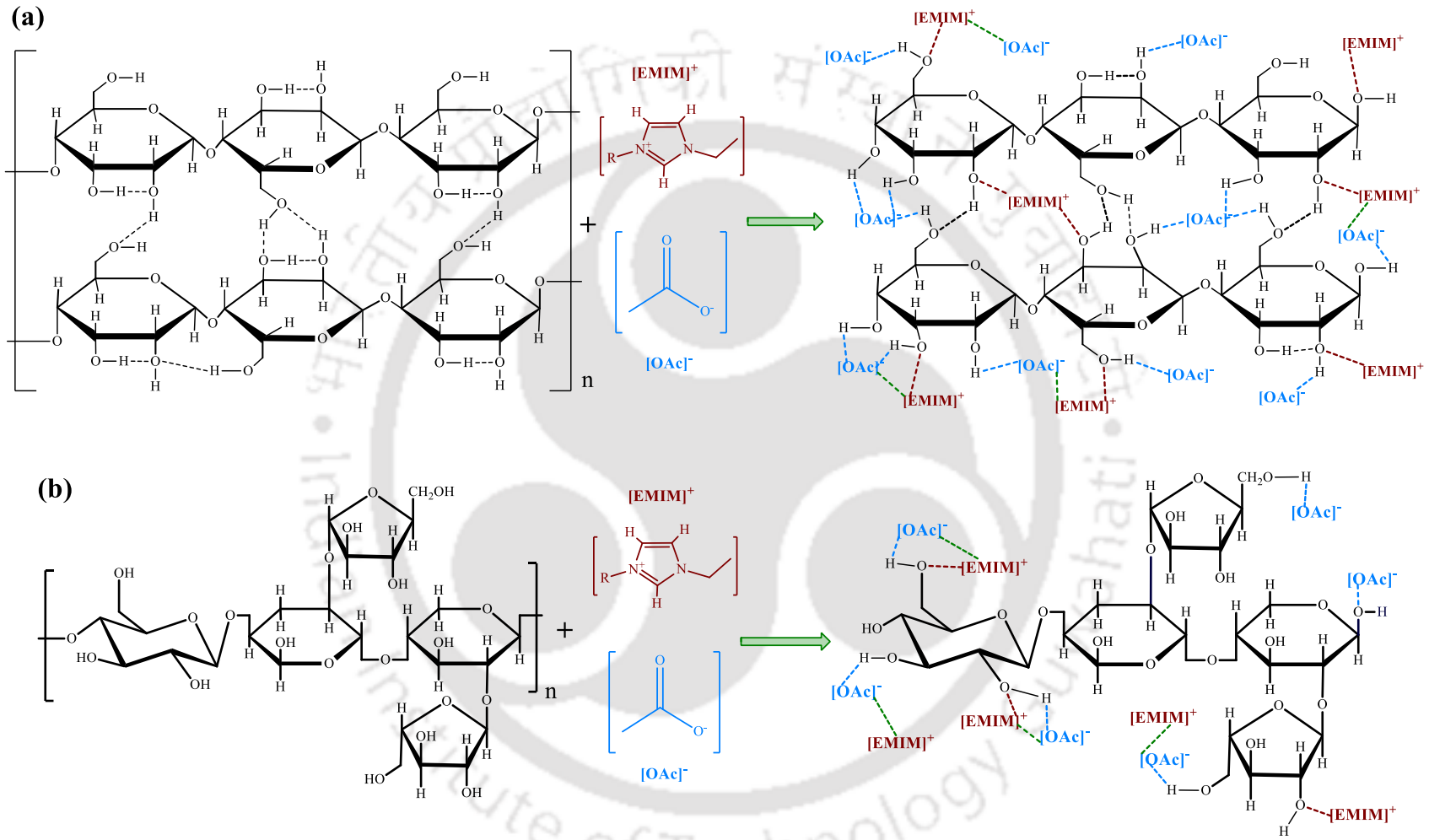

Figure 4.14: Proposed reaction mechanism for (a) cellulose and (b) hemicellulose dissolution in [EMIM][OAc]. $[OAc]^-$ is seen here to form more H-bonds than $[EMIM]^+$ cation

4.4.7 Structure of Regenerated Cellulose

The cellulose was further regenerated by adding distilled water into the solution with vigorous stirring for 30 min. The cellulose flocs were collected by a vacuum filtration and dried at 50 °C for 48 h. Further, the regenerated cellulose was characterized by FTIR, XRD, and TGA to analyze the crystallinity and thermal decomposition behavior of the regenerated material. A comparison with native cellulose was also performed.

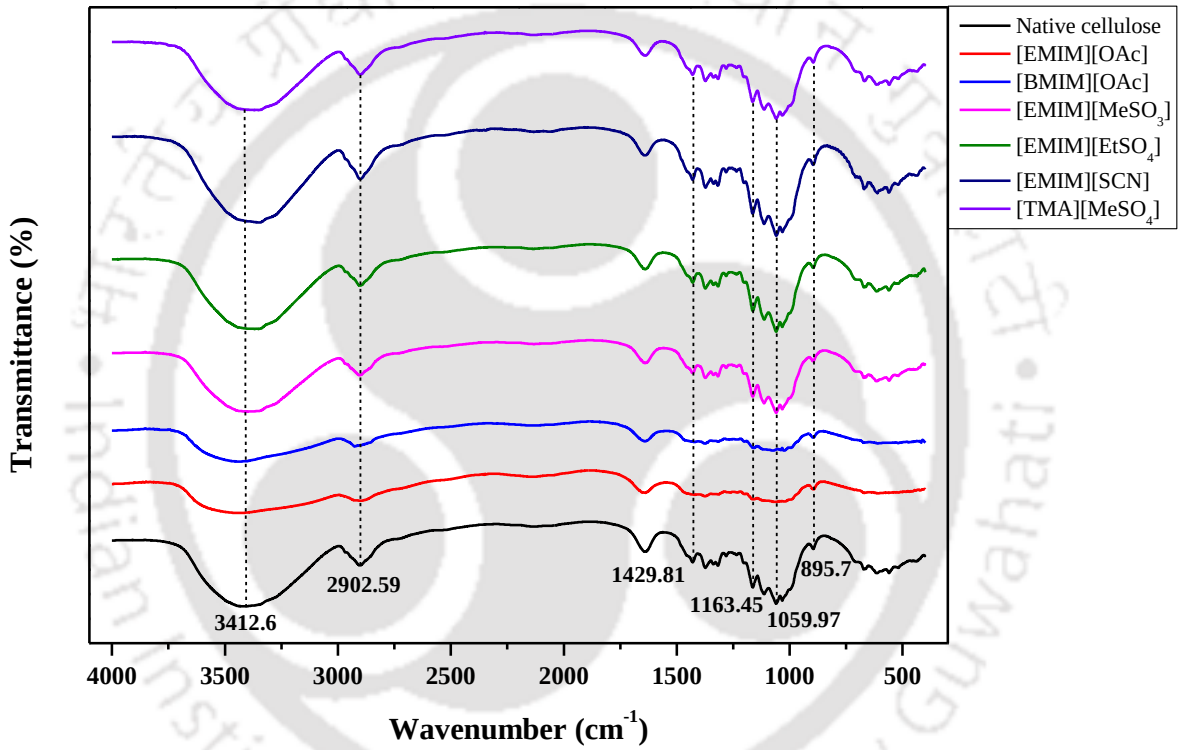

Figure 4.15: FTIR spectra of native and regenerated cellulose from ILs at 110 °C for 1 h of reaction time

The FTIR spectra of native cellulose and regenerated cellulose are depicted in Figure 4.15. From Figure 4.15, it can be observed that the spectra's are quite similar and there is no additional peak observed after regeneration. This indicates that no chemical reaction has occurred during the dissolution and regeneration of cellulose. The band at 3412 cm^{-1} was assigned to the O–H vibration. This band was shifted to a higher wavenumber (3436 cm^{-1}) in the case of [EMIM][OAc] and [BMIM][OAc]. This is attributed to the partial breakage of

hydrogen bonds [75]. The band at 2902 cm^{-1} was assigned for the $–CH_2–$ group. The adsorption band at 1429 cm^{-1} indicates the crystalline region of cellulose [76]. The wavenumber at 1429 cm^{-1} has again shifted to a higher value in [EMIM][OAc] and [BMIM][OAc] ILs. This shift suggests the breakage of intra-molecular hydrogen bonds involved at O6 (Figure 4.6a) [75,77,78]. The band at 895 cm^{-1} represents the C–O–C asymmetric stretching in the amorphous region [79]. Finally, the peak between 1172-1080 cm^{-1} and 1060-1050 cm^{-1} were assigned to C–O–C bending and C–H stretching vibrations, respectively [76]. The presence of such bands in the regenerated cellulose suggests a macromolecular structure of cellulose which is not completely destructed in IL.

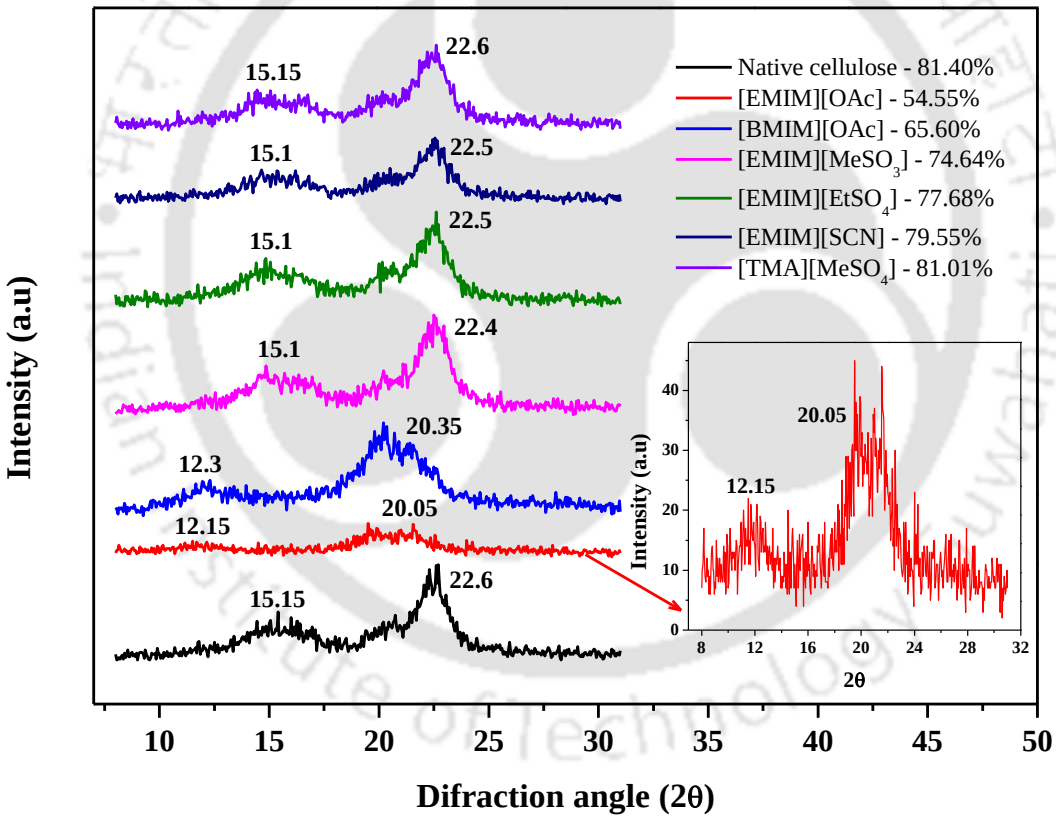

Figure 4.16: X-ray diffraction (XRD) patterns of native cellulose and regenerated cellulose from ILs at 110 °C and 1 h of reaction time. This figure offers the crystallinity of cellulose

The XRD patterns of native and regenerated cellulose are given in Figure 4.16. The original cellulose was labeled as 'cellulose I'. This is indicated by the diffraction angle at 2θ = 15.1° and 22.6° [80]. The regenerated cellulose exhibits similar diffraction patterns except cellulose with [EMIM][OAc] and [BMIM][OAc]. The diffraction angle for cellulose in [EMIM][OAc] and [BMIM][OAc] IL's were found at 2θ = 12.1° and 20.35°, respectively. This transformation indicates a change from cellulose I to cellulose II, which occurrs during the course of dissolution. Similar results were observed by Xu *et al.* (2015) [75], Liu *et al.* (2015) [76], Zhao *et al.* (2012) [81] and Sun *et al.* (2009) [82] during their studies on the dissolution of MCC (DP = 270) and southern yellow pine biomass in [BMIM][OAc]/DMAc, [EMIM][Et_2PO_4] and [EMIM][OAc] solvents, respectively. Additionally, in our samples, the crystallinity of cellulose was determined and was found to decrease at 110 °C (Figure 4.16). [EMIM][OAc] and [BMIM][OAc] gave lower crystallinity when compared to other ILs.

Figure 4.17 shows the thermal decomposition profiles of regenerated cellulose from [EMIM][$EtSO_4$] at 110 °C and original cellulose. There was no extra peak observed in the regenerated cellulose, which implies that cellulose was successfully regenerated. As can be seen from Figure 4.17, the original and regenerated cellulose starts to decompose 295 °C and 270 °C respectively. On the other hand, at 50% weight loss, the corresponding values were 344.7 °C and 339.4 °C. Thus, the thermal stability of regenerated cellulose was a bit lower than original cellulose. This decrement may be due to the partial destruction of the crystalline part.

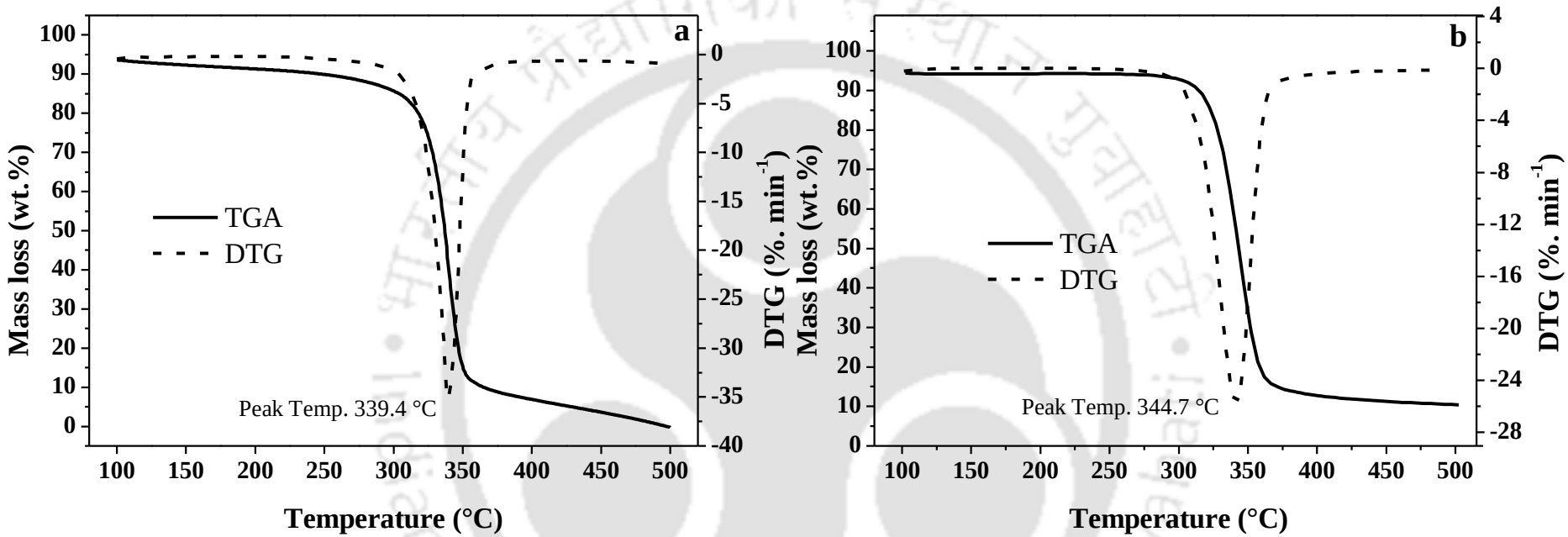

Figure 4.17: Thermal decomposition profiles of (a) regenerated cellulose from [EMIM][$EtSO_4$] at 110 °C, and (b) original cellulose (before dissolution in IL)

4.5 Summary

The current chapter reports the basic understanding of the dissolution behavior of lignocellulosic biomass starting from *ab-initio* theory to classical molecular dynamics. Further to confirm the computational trend, an extensive experiments were carried out to validate the dissolution behavior. Initially, 1428 ILs was screened using COSMO-RS model which is time efficient and computationally inexpensive, thereby allowing us to screen a large number of solvents. After the successful screening of ILs, the potential cation and anion combinations were further screened by QC calculations. $[OAc]^-$ and $[EMIM]^+$ were found to be good candidates for the dissolution of cellulose and hemicellulose. From MD simulations, it was found that the cellulose was bounded with six to seven anions and two to four cations in the first solvation shell. It was also observed that the O-H…O (anion) bond is far stronger than the C-H…O (cation) bonds within cellulose and hemicellulose. From QC and MD simulations, it was noted that acetate anion formed multiple hydrogen bonds with cellulose thereby weaken the crystalline structure of cellulose. Moreover, the effect of anions and cations were studied on the different conformational structures of cellulose and hemicellulose. For theoretical calculations, the consideration of any conformers of cellulose and hemicellulose molecules gives the similar result. The theoretical results were further confirmed by the experimental solubility of cellulose/hemicellulose in ILs which depicted excellent agreement with simulated results. Furthermore, the crystallinity of regenerated cellulose (54.55%) was found to decrease as compared to original cellulose. It was inferred that the anion of the IL is the sole factor in deciding the dissolution mechanism. Incidentally, the cation significantly affects the solubility of cellulose with their acidic protons. This competes on the other side by forming hydrogen bonds with anion. To overcome this issue, adding a suitable co-solvent to the IL can make the dissolution process economically feasible. This very fact is explored in the next chapter.

References

[1] Agbor VB, Cicek N, Sparling R, Berlin A, Levin DB. Biomass pretreatment: fundamentals toward application. Biotechnol Adv 2011;29:675-85.

[2] Lu B, Xu A, Wang J. Cation does matter: how cationic structure affects the dissolution of cellulose in ionic liquids. Green Chem 2014;16:1326-35.

[3] Oliveira HFND, Rinaldi R. Understanding Cellulose Dissolution: Energetics of Interactions of Ionic Liquids and Cellobiose Revealed by Solution Microcalorimetry. ChemSusChem 2015;8:1577-84.

[4] Pinkert A, Marsh KN, Pang A, Staiger MP. Ionic Liquids and Their Interaction with Cellulose. Chem Rev 2009;109:6712–28.

[5] Swatloski RP, Spear SK, Holbrey JD, Rogers RD. Dissolution of Cellose with Ionic Liquids. J Am Chem Soc 2002;124:4974-5.

[6] Conceiçao LJA, Bogel-Łukasik E, Bogel-Łukasik R. A new outlook on solubility of carbohydrates and sugar alcohols in ionic liquids. RSC Adv 2012;2:1846-55.

[7] Balensiefer T, Brodersen J, D'andola G, Massonne K, Freyer S, Stegmann V. Method for producing glucose by enzymatic hydrolysis of cellulose that can be pretreated with an ionic liquid containing a polyatomic anion United States 2008.

[8] Isik M, Sardon H, Mecerreyes D. Ionic liquids and cellulose: dissolution, chemical modification and preparation of new cellulosic materials. Int J Mol Sci 2014;15:11922-40.

[9] Seoud OAE, Koschella A, Fidale LC, Dorn S, Heinze T. Applications of Ionic Liquids in Carbohydrate Chemistry: A Window of Opportunities. Biomacromolecules 2007;8:2629–47.

[10] Mohan M, Goud VV, Banerjee T. Solubility of glucose, xylose, fructose and galactose in ionic liquids: Experimental and theoretical studies using a continuum solvation model. Fluid Phase Equilib 2015;395:33-43.

[11] Carneiro AP, Rodríguez O, Macedo EA. Fructose and Glucose Dissolution in Ionic Liquids: Solubility and Thermodynamic Modeling. Ind Eng Chem Res 2013;52:3424-35.

[12] Carneiro AP, Held C, Rodriguez O, Sadowski G, Macedo EA. Solubility of Sugars and Sugar Alcohols in Ionic Liquids: Measurement and PC-SAFT Modeling. J Phy Chem B 2013;117:9980-95.

[13] Li Y, Liu X, Zhang S, Yao Y, Yao X, Xu J, et al. Dissolving process of a cellulose bunch in ionic liquids: a molecular dynamics study. Phys Chem Chem Phys 2015;17:17894-905.

[14] Kilpeläinen I, Xie H, King A, Granstrom M, Heikkinen S, Argyropoulos DS. Dissolution of wood in ionic liquids. J Agric Food Chem 2007;55:9142-8.

[15] Kahlen J, Masuch K, Leonhard K. Modelling cellulose solubilities in ionic liquids using COSMO-RS. Green Chem 2010;12:2172-81.

[16] Casas A, Palomar J, Alonso MV, Oliet M, Omar S, Rodriguez F. Comparison of lignin and cellulose solubilities in ionic liquids by COSMO-RS analysis and experimental validation. Ind crop prod 2012;37:155–63.

[17] Balaji C, Banerjee T, Goud VV. COSMO-RS Based Predictions for the Extraction of Lignin from Lignocellulosic Biomass Using Ionic Liquids: Effect of Cation and Anion Combination. J Solution Chem 2012;41:1610-30.

[18] Cheng G, Varanasi P, Arora R, Stavila V, Simmons BA, Kent MS, et al. Impact of ionic liquid pretreatment conditions on cellulose crystalline structure using 1-ethyl-3-methylimidazolium acetate. J Phys Chem B 2012;116:10049-54.

[19] Minnick DL, Flores RA, DeStefano MR, Scurto AM. Cellulose solubility in ionic liquid mixtures: temperature, cosolvent, and antisolvent effects. J Phys Chem B 2016;120:7906-19.
[20] Rabideau BD, Agarwal A, Ismail AE. Observed mechanism for the breakup of small bundles of cellulose Iα and Iβ in ionic liquids from molecular dynamics simulations. J Phys Chem B 2013;117:3469-79.
[21] Rabideau BD, Agarwal A, Ismail AE. The Role of the Cation in the Solvation of Cellulose by Imidazolium-Based Ionic Liquids. J Phys Chem B 2014;118:1621-9.
[22] Lovell CS, Walker A, Damion RA, Radhi A, Tanner SF, Budtova T, et al. Influence of Cellulose on Ion Diffusivity in 1-Ethyl-3-Methyl-Imidazolium Acetate Cellulose Solutions. Biomacromolecules 2010;11:2927–35.
[23] Uto T, Yamamoto K, Kadokawa J-i. Cellulose Crystal Dissolution in Imidazolium-Based Ionic Liquids: A Theoretical Study. J Phys Chem B 2017;122:258-66.
[24] Zhao Y, Liu X, Wang J, Zhang S. Effects of anionic structure on the dissolution of cellulose in ionic liquids revealed by molecular simulation. Carbohydr Polym 2013;94:723-30.
[25] Guo J, Zhang D, Duan C, Liu C. Probing anion-cellulose interactions in imidazolium-based room temperature ionic liquids: a density functional study. Carbohydr Res 2010;345:2201-5.
[26] Ding ZD, Chi Z, Gu WX, Gu SM, Liu JH, Wang HJ. Theoretical and experimental investigation on dissolution and regeneration of cellulose in ionic liquid. Carbohydr Polym 2012;89:7-16.
[27] Payal RS, Balasubramanian S. Dissolution of cellulose in ionic liquids: an ab initio molecular dynamics simulation study. Phys Chem Chem Phys 2014;16:17458-65.
[28] Froschauer C, Hummel M, Laus G, Schottenberger H, Sixta H, Weber HK, et al. Dialkyl phosphate-related ionic liquids as selective solvents for xylan. Biomacromolecules 2012;13:1973-80.
[29] Anantharaj R, Banerjee T. COSMO-RS based predictions for the desulphurization of diesel oil using ionic liquids: Effect of cation and anion combination. Fuel Processing Technology 2011;92:39-52.
[30] Mohan M, Balaji C, Goud VV, Banerjee T. Thermodynamic Insights in the Separation of Cellulose/Hemicellulose Components from Lignocellulosic Biomass Using Ionic Liquids. J Solution Chem 2015;44:538-57.
[31] Frisch MJ, Trucks GW, Schlegel HB, Scuseria GE, Robb MA, Cheeseman JR, et al. Gaussian 03. revision C. 02 ed. Wallingford, CT: Gaussian, Inc.; 2004.
[32] Verma NR, Gopal G, Anantharaj R, Banerjee T. (Solid+liquid) equilibria predictions of ionic liquid containing systems using COSMO-RS. The Journal of Chemical Thermodynamics 2012;48:246-53.
[33] Ding Z-D, Chi Z, Gu W-X, Gu S-M, Wang H-J. Theoretical and experimental investigation of the interactions between [emim]Ac and water molecules. J Mol Struct 2012;1015:147-55.
[34] Balachandran V, Nataraj A, Karthick T. Molecular structure, spectroscopic (FT-IR, FT-Raman) studies and first-order molecular hyperpolarizabilities, HOMO-LUMO, NBO analysis of 2-hydroxy-p-toluic acid. Spectrochim Acta A Mol Biomol Spectrosc 2013;104:114-29.
[35] Phillips JC, Braun R, Wang W, Gumbart J, Tajkhorshid E, Villa E, et al. Scalable molecular dynamics with NAMD. J Comput Chem 2005;26:1781-802.
[36] Chen M, Bomble YJ, Himmel ME, Brady JW. Molecular dynamics simulations of the interaction of glucose with imidazole in aqueous solution. Carbohydr Res 2012;349:73-7.

[37] Andanson J-M, Bordes E, Devémy J, Leroux F, Pádua AAH, Gomes MFC. Understanding the role of co-solvents in the dissolution of cellulose in ionic liquids. Green Chem 2014;16:2528-38.
[38] Payal RS, Bejagam KK, Mondal A, Balasubramanian S. Dissolution of cellulose in room temperature ionic liquids: anion dependence. J Phys Chem B 2015;119:1654-9.
[39] Guvench O, Hatcher ER, Venable RM, Pastor RW, Mackerell AD. CHARMM Additive All-Atom Force Field for Glycosidic Linkages between Hexopyranoses. J Chem Theory Comput 2009;5:2353-70.
[40] Guvench O, Greene SN, Kamath G, Brady JW, Venable RM, Pastor RW, et al. Additive empirical force field for hexopyranose monosaccharides. J Comput Chem 2008;29:2543-64.
[41] Gross AS, Bell AT, Chu JW. Thermodynamics of cellulose solvation in water and the ionic liquid 1-butyl-3-methylimidazolim chloride. J Phys Chem B 2011;115:13433-40.
[42] Vanommeslaeghe K, Hatcher E, Acharya C, Kundu S, Zhong S, Shim J, et al. CHARMM general force field: A force field for drug-like molecules compatible with the CHARMM all-atom additive biological force fields. J Comput Chem 2010;31:671-90.
[43] Martyna GJ, Tobias DJ, Klein ML. Constant pressure molecular dynamics algorithms. J Chem Phys 1994;101:4177–89.
[44] Stirnemann G, Giganti D, Fernandez JM, Berne BJ. Elasticity, structure, and relaxation of extended proteins under force. Proc Natl Acad Sci USA 2013;110:3847-52.
[45] R. Bernardi, M. Bhandarkar, A. Bhatele, E. Bohm, R. Brunner, F. Buelens, et al. NAMD User's Guide Version 2.12 Urbana, USA: Theoretical and Computational Biophysics Group, Beckman Institute, University of Illinois.; 2016. p. 260.
[46] Allen MP, Tildesley DJ. Computer simulation of liquids. New York: Oxford University Press; 1987.
[47] Deleeuw SW, Perram JW, Smith ER. Simulation of Electrostatic Systems in Periodic Boundary-Conditions. 3. Furture Theory and Applications. Proc R Soc London, Ser A 1983;388:177-93.
[48] Martinez L, Andrade R, Birgin EG, Martinez JM. PACKMOL: a package for building initial configurations for molecular dynamics simulations. J Comput Chem 2009;30:2157-64.
[49] Zhao Y, Liu X, Wang J, Zhang S. Insight into the cosolvent effect of cellulose dissolution in imidazolium-based ionic liquid systems. J Phys Chem B 2013;117:9042-9.
[50] Parthasarathi R, Balamurugan K, Shi J, Subramanian V, Simmons BA, Singh S. Theoretical insights into the role of water in the dissolution of cellulose using IL/water mixed solvent systems. J Phys Chem B 2015;119:14339-49.
[51] Liu H, Sale KL, Holmes BM, Simmons BA, Singh S. Understanding the interactions of cellulose with ionic liquids: a molecular dynamics study. J Phys Chem B 2010;114:4293-301.
[52] Mohan M, Naik PK, Banerjee T, Goud VV, Paul S. Solubility of glucose in tetrabutylammonium bromide based deep eutectic solvents: Experimental and molecular dynamic simulations. Fluid Phase Equilib 2017;448:168-77.
[53] Humphrey W, Dalke A, Schulten K. VMD: Visual molecular dynamics. J Mol Graphics 1996;14:33-8.

[54] Ozturk I, Irmak S, Hesenov A, Erbatur O. Hydrolysis of kenaf (Hibiscus cannabinus L.) stems by catalytical thermal treatment in subcritical water. Biomass Bioenergy 2010;34:1578-85.
[55] Kumar S, Gupta R, Lee YY, Gupta RB. Cellulose pretreatment in subcritical water: effect of temperature on molecular structure and enzymatic reactivity. Bioresour Technol 2010;101:1337-47.
[56] Ninomiya K, Soda H, Ogino C, Takahashi K, Shimizu N. Effect of ionic liquid weight ratio on pretreatment of bamboo powder prior to enzymatic saccharification. Bioresour Technol 2013;128:188-92.
[57] Kumar S, Gupta RB. Biocrude Production from Switchgrass Using Subcritical Water. Energ Fuel 2009;23:5151-9.
[58] Krossing I, Slattery J, M., Daguenet C, Dyson PJ, Oleinikova A, Weingartner H. Why Are Ionic Liquids Liquid? A Simple Explanation Based on Lattice and Solvation Energies. J Am Chem Soc 2006;128:13427–34.
[59] Prausnitz JM, Lichtenthaler RN, Azevedo EG. Molecular thermodynamics of fluid phase equilibria. 3rd ed. prentice Hall, New Jersey1999.
[60] Andanson JM, Padua AAH, Gomes MFC. Thermodynamics of cellulose dissolution in an imidazolium acetate ionic liquid. Chem Commun 2015;51:4485-7.
[61] Bochek A. Effect of hydrogen bonding on cellulose solubility in aqueous and nonaqueous solvents. Russ J Appl Chem 2003;76:1711-9.
[62] Liu Y-R, Thomsen K, Nie Y, Zhang S-J, Meyer AS. Predictive screening of ionic liquids for dissolving cellulose and experimental verification. Green Chem 2016;18:6246-54.
[63] Vitz J, Erdmenger T, Haensch C, Schubert US. Extended dissolution studies of cellulose in imidazolium based ionic liquids. Green Chem 2009;11:417-24.
[64] Maki-Arvela P, Anugwom I, Virtanen P, Sjöholm R, Mikkola JP. Dissolution of lignocellulosic materials and its constituents using ionic liquids—A review. Ind crop prod 2010;32:175-201.
[65] Wu Y, Sasaki T, Kazushi K, Seo T, Sakurai K. Interactions between Spiropyrans and Room-Temperature Ionic Liquids: Photochromism and Solvatochromism. J Phy Chem B 2008;112:7530-6.
[66] Froschauer C, Hummel M, Iakovlev M, Roselli A, Schottenberger H, Sixta H. Separation of hemicellulose and cellulose from wood pulp by means of ionic liquid/cosolvent systems. Biomacromolecules 2013;14:1741-50.
[67] Zhao H, Baker GA, Song Z, Olubajo O, Crittle T, Peters D. Designing enzyme-compatible ionic liquids that can dissolve carbohydrates. Green Chem 2008;10:696-705.
[68] Kosan B, Michels C, Meister F. Dissolution and forming of cellulose with ionic liquids. Cellulose 2007;15:59-66.
[69] Zavrel M, Bross D, Funke M, Buchs J, Spiess AC. High-throughput screening for ionic liquids dissolving (ligno-)cellulose. Bioresour Technol 2009;100:2580-7.
[70] Barthel S, Heinze T. Acylation and carbanilation of cellulose in ionic liquids. Green Chem 2006;8:301-6.
[71] Wang H, Gurau G, Rogers RD. Ionic liquid processing of cellulose. Chem Soc Rev 2012;41:1519-37.
[72] Zhang J, Zhang H, Wu J, Zhang J, He J, Xiang J. NMR spectroscopic studies of cellobiose solvation in EmimAc aimed to understand the dissolution mechanism of cellulose in ionic liquids. Phys Chem Chem Phys 2010;12:1941-7.
[73] Uto T, Yamamoto K, Kadokawa J-i. Cellulose Crystal Dissolution in Imidazolium-Based Ionic Liquids: A Theoretical Study. J Phys Chem B 2017.

[74] Kan Z, Zhu Q, Yang L, Huang Z, Jin B, Ma J. Polarization Effects on the Cellulose Dissolution in Ionic Liquids: Molecular Dynamics Simulations with Polarization Model and Integrated Tempering Enhanced Sampling Method. J Phys Chem B 2017;121:4319-32.

[75] Xu A, Guo X, Xu R. Understanding the dissolution of cellulose in 1-butyl-3-methylimidazolium acetate+DMAc solvent. Int J Biol Macromol 2015;81:1000-4.

[76] Liu Z, Sun X, Hao M, Huang C, Xue Z, Mu T. Preparation and characterization of regenerated cellulose from ionic liquid using different methods. Carbohydr Polym 2015;117:99-105.

[77] Zhang L, Ruan D, Zhou J. Structure and Properties of Regenerated Cellulose Films Prepared from Cotton Linters in NaOH/Urea Aqueous Solution. Ind Eng Chem Res 2001;40:5923–8.

[78] Nelson ML, O'Connor RT. Relation of certain infrared bands to cellulose crystallinity and crystal latticed type. Part I. Spectra of lattice types I, II, III and of amorphous cellulose. J Appl Polym Sci 1964;8:1311–24.

[79] Mohan M, Banerjee T, Goud VV. Hydrolysis of bamboo biomass by subcritical water treatment. Bioresour Technol 2015;191:244-52.

[80] Oh SY, Yoo DI, Shin Y, Kim HC, Kim HY, Chung YS, et al. Crystalline structure analysis of cellulose treated with sodium hydroxide and carbon dioxide by means of X-ray diffraction and FTIR spectroscopy. Carbohydr Res 2005;340:2376-91.

[81] Zhao D, Li H, Zhang J, Fu L, Liu M, Fu J, et al. Dissolution of cellulose in phosphate-based ionic liquids. Carbohydr Polym 2012;87:1490-4.

[82] Sun N, Rahman M, Qin Y, Maxim ML, Rodríguez H, Rogers RD. Complete dissolution and partial delignification of wood in the ionic liquid 1-ethyl-3-methylimidazolium acetate. Green Chem 2009;11:646-55.

Chapter – 5

Experimental Dissolution Mechanism of Cellulose in Ionic Liquid: Role of Protic and Aprotic Solvents by Molecular Dynamics Simulations

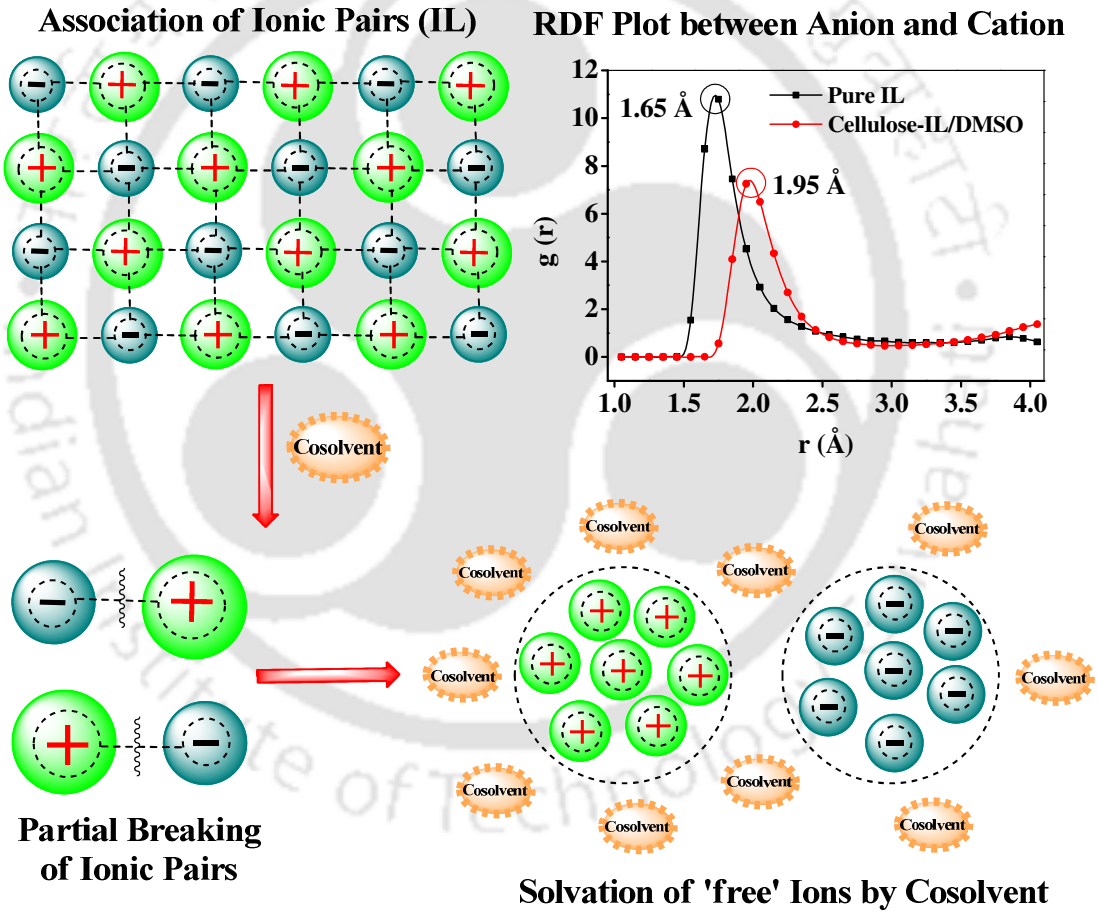

Published Article:

Mohan M, Banerjee, T., Goud V. V. Effect of Protic and Aprotic Solvents on the Mechanism of Cellulose Dissolution in Ionic Liquids: A Combined Molecular Dynamics and Experimental Insight. *Chemistry Select* (2016); 1(15): 4823–4832

5 The Functionality of Protic and Aprotic Solvents on the Dissolution of Cellulose in Ionic Liquid by Molecular Dynamics Simulations

This chapter reports the dissolution mechanism of cellulose in 1-ethyl-3-methylimidazolium acetate ([Emim][OAc]) and [Emim][OAc]/cosolvent mixtures with the aim to increase cellulose solubility in ILs. The protic (formamide (FRM), acetamide (AcM), Ethanol, and Water) and aprotic (dimethylsulfoxide (DMSO), N,N-dimethylformamide (DMF), N,N-dimethylacetamide (DMAc), and acetone) solvents have been chosen to study the role of cosolvents. Initially, quantum chemical calculations are employed to screen the cosolvents by revealing the anion and cation interactions with cosolvents. The dissolution of cellulose in IL and IL/cosolvent mixtures are then determined by following two approaches. The first approach was to apply MD simulations for optimizing the better cosolvent and their molar ratio's with IL. Hence, our aim was to observe the microscopic structure and molecular interactions by radial distribution functions (RDF) and non-bonded interaction energies of the solution. The second approach is to confirm the MD simulations results by solid-liquid equilibria (SLE) experiments within a temperature range of 27-90 °C for the reaction period of 1 h.

5.1 Introduction

ILs has gained more attention towards biorefining operations due to its attractive properties [1,2]. One of the most disadvantages of ILs is its high viscosities which brings the processing and handling of dissolution difficult [3,4]. Adding a polymer into a solvent, it was known that the viscosity of liquid would be increased. As a consequence of this, higher dissolution of a polymer in IL can be restricted by mass transport not only unfavorable solute-solvent interactions [5]. And also in the previous chapter 4, it was noted that the cation significantly affects the solubility of cellulose by forming additional hydrogen bonds with anion. To

overcome this phenomenon, protic or aprotic solvents can be used as a cosolvent which helps to reduce the viscosity of ILs without precipitation of cellulose [6-8]. The decrease in the viscosity of ILs results in a faster mass transfer rate and dissolution of solute. The addition of highly polar cosolvent to ILs has been shown to significantly increase the cellulose dissolution at lower conditions [9]. Therefore, the present chapter focuses on the dissolution of cellulose in IL/cosolvent mixtures.

5.2 Computational Details

5.2.1 Quantum Chemical Calculations

The structures of cellulose, isolated ions, cosolvents, and the pairs of $[OAc]^-$/cosolvents and $[Emim]^+$/cosolvents are drawn in the MOLDEN freeware software [2]. The molecular geometry of all ion-cosolvent pairs and isolated molecules are optimized by the B3LYP/6-31G* level of theory using *Gaussian*03 software [2,10]. The initial configurations of the ion-cosolvent pairs are primarily based on the charge appropriation and electrostatic potential on the detached cation and anion. Thus, the preferred position of the cosolvents has been distributed around C1, C2, and C3 sites of the $[Emim]^+$ cation and O1 and O2 sites of the $[OAc]^-$ anion. The interaction energies of ion-cosolvent pairs are also obtained at the same level of the theory [11,12]. The complex system (ion-cosolvent) energy is then corrected by basis set superposition error (BSSE) using a counterpoise method [13].

5.2.2 Molecular Dynamics Simulations

The microscopic interactions between cellulose and [Emim][OAc] or [Emim][OAc]/cosolvents were examined by MD simulations. For all molecules, the CHARMM force field parameters were employed. The CHARMM force field parameters for cellulose (degree of polymerization, DP = 15) was taken from Guvench *et al*. (2008, 2009) as described in chapter 4 [14,15]. The force field parameters for ionic liquid ($[Emim]^+$, $[OAc]^-$)

and cosolvents (DMSO, DMF, DMAc, FRM and all AcM) were developed by using the existing CHARMM parameters and presented in Appendix C (Table C.1 and C.4) and Appendix D (Table D.1-D.5), respectively along with their structures. Figure 5.1 shows the chemical structures of cellulose, IL, and cosolvents with their atom notations. The developed force field parameters were validated by measuring the density of IL and cosolvents at 27 °C (*i.e.*, 300 K). The MD simulated densities gave an excellent agreement with the experimental densities and represented in Table 5.1. The geometries of cellulose (DP = 15), [Emim][OAc] and isolated cosolvents were then optimized by using *Gaussian*03 package at B3LYP/6-31G* level of the theory [16].

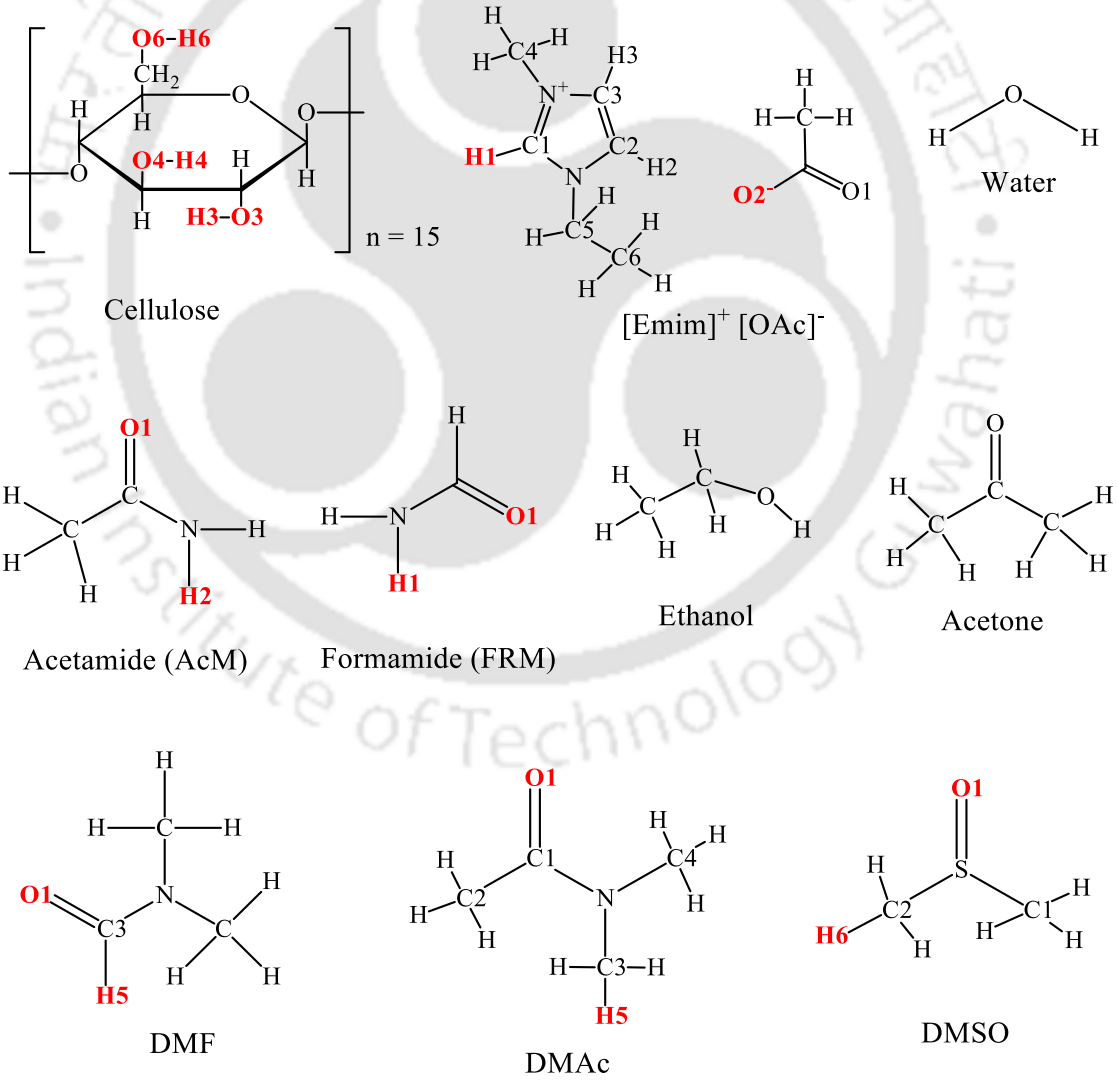

Figure 5.1: Chemical structures and atom notations of the repeat units of glucose in cellulose (DP = 15), ionic liquid, and different cosolvents simulated in this work

Table 5.1: Densities of different [Emim][OAc] and cosolvents obtained from MD simulations and compared with experimental density at 27 °C

Ionic Liquid	ρ_{exp} (g cm^{-3})	ρ_{MD} (g cm^{-3})	Error (%)
[Emim][OAc]	1.0957	1.0946	0.103
DMSO	1.0940	1.1267	-2.99
DMF	0.9427	0.9200	2.412
DMAc	0.9355	0.9185	1.821
Formamide (FRM)	1.1279	1.1182	0.860
Acetamide (AcM)	1.1590	1.1388	1.743

All the MD simulations were performed with the NAMD version 2.10 [17] software at constant temperature and pressure. The details of MD simulations are described in chapter 4 (section 4.2.2). The cut-off distance of 15 Å was kept to treat the long-range electrostatic interactions at a time step of 1 fs [18]. The initial configuration of cellulose-IL and cellulose-IL/cosolvent pairs were prepared by PACKMOL in a cubic box [19]. Each simulated system consisted of one cellulose molecule with DP = 15, [Emim][OAc] and different cosolvents. The IL to cosolvent molar ratio for each IL/cosolvent system is given in Table 5.2. The simulated system energy was minimized for 1 ns. After energy minimization, the system was gradually heated to its desired temperature 27 °C (300 K) for 0.5 ns. At target temperature, the system was equilibrated under NPT ensemble to get the system converge to its experimental condition for 5 ns. Subsequently, the production phase lasted for 5 ns under constant NPT ensemble. This was monitored by measuring the density or the volume of the system. At every 2 ps, the production data was saved for structural analysis. This was viewed with the RDF plots and interaction energy as accessed from the simulated trajectories with VMD software [20]. In the mixture of cellulose, [Emim][OAc], and cosolvent, the interaction energies between two molecular types are given per mole of the substance. Therefore, the interaction energy of IL or cosolvent with cellulose is per mole of cellulose, while the interaction energy of IL with

cosolvent is per mole of IL. The interaction energy between the $[Emim]^+$ and $[OAc]^-$ is per mol of IL.

Table 5.2: Interaction energies between the cellulose-[Emim][OAc]/cosolvents obtained from MD simulations for different systems

Simulated System	Ionic Liquids	Cosolvent	R^a	$E_{elec}{}^b$	$E_{vdW}{}^c$	$E_{inter}{}^d$
Cellulose-IL/DMSO	500	500	1.0	-75290.27	-9822.70	-85112.97
	400	800	2.0	-79872.20	-11491.03	-91363.24
	360	900	2.5	-79543.04	-11033.49	-90576.48
	320	960	3.0	-78183.59	-11857.20	-90040.80
	250	1000	4.0	-76060.164	-12588.60	-88620.65
	225	1125	5.0	-76021.94	-11809.33	-87831.27
Cellulose-IL	300	-	-	-30389.76	-3306.01	-33695.78
Cellulose-IL/DMAc	400	800	2.0	-52532.31	-6905.59	-59437.908
Cellulose-IL/DMF	400	800	2.0	-67249.80	-9465.82	-76715.62
Cellulose-IL/FRM	400	800	2.0	-48929.43	-2395.11	-51324.546
Cellulose-IL/AcM	400	800	2.0	-33347.82	-4693.91	-38041.737

[a] Molar ratio of cosolvent to ionic liquid; [b] electrostatic interaction energy of the system in kcal mol^{-1}; [c] van der Waals interaction energy of the system in kcal mol^{-1}; [d] sum of E_{elec} and E_{vdW} in kcal mol^{-1}

5.3 Materials and Methods

5.3.1 Materials

Microcrystalline cellulose (MCC, DP ≤ 400) powder was used as a feed material and purchased from Merck, India Pvt. Ltd. The solvents, 1-ethyl-3-methylimidazolium acetate [Emim][OAc] (≥ 95%), dimethylsulfoxide anhydrous (DMSO, ≥ 99.9%), N, N-dimethylformamide (anhydrous DMF, ≥ 99.8%), N, N-dimethylacetamide (DMAc, ≥ 99%) and Formamide (FRM, ≥ 99.5%) were purchased from Sigma-Aldrich, Germany. All the purchased chemicals are used without any further purification.

5.3.2 Experimental Procedure

The dissolution of cellulose in ILs/cosolvent mixture was carried out by following the experimental procedure described in chapter 4 (section 4.3.2). In a typical dissolution experiment, [Emim][OAc]/cosolvents mixture was prepared by adding a cosolvent to the [Emim][OAc] at selected molar ratio's (IL to cosolvent 1:1, 1:2, 1:2.5, 1:3, 1:4, and 1:5) in a 25 mL conical flask and stirred for 10-15 min. The temperature of the system was maintained from 27 °C to 90 °C with a precision of ± 0.1 °C (TARSONS SPINOT-magnetic stirrer and hot plate-DIGITAL, MC 02, India). 0.5 g of cellulose was added to a 25 mL of the conical flask containing 6 g of [Emim][OAc] or [Emim][OAc]/cosolvent mixture. The heated solution mixture was magnetically stirred for 1 h at each temperature. After the reaction period, the solution was cooled to room temperature. For the regenerated of undissolved cellulose, distilled water was added to the solution with vigorous stirring for 20-30 min. The resulting cellulose flocs were collected by a vacuum filtration and dried at 50 °C for 48 h. Further, the regenerated cellulose samples were characterized by FTIR, XRD, and TGA and the detailed description of characterization techniques were discussed in chapter 4 (section 4.3.3). The percent cellulose solubility was calculated according to the equation 4.2.

5.4 Results and Discussion

5.4.1 Quantum Chemical Calculations for the Solvation of Ions by Different Cosolvents

Optimized structures of the lowest energy conformers for $[OAc]^-$ and $[Emim]^+$ with different cosolvents are presented in Figure 5.2 to Figure 5.5. Figure 5.2 shows the lowest energy conformer for $[OAc]^-$ with different cosolvents. It is clearly evident that the oxygen (O) atom of $[OAc]^-$ forms weak hydrogen bonds with aprotic solvents (C-H…O) while the contrary is seen with protic solvents. It should be noted that a weak hydrogen bond is denoted by a bond distance greater than 2 Å [21]. Hence in these systems, the length of the C-H…O hydrogen bond was found to be ~2.15-2.83 Å. On the other hand, the hydrogen bond length of the N-H…O (FRM and AcM) and O-H…O (water and ethanol) is ~1.84 Å and ~1.79-2.08 Å, which indeed indicates strong hydrogen bonding between $[OAc]^-$-protic solvents.

In addition, the optimized geometries of $[Emim]^+$-cosolvent pairs are presented in Figures 5.3-5.5. It should be noted that the protons at C1, C2, and C3 sites of $[Emim]^+$ cation could potentially form hydrogen bonds with O atom of cosolvents. These hydrogen bonds (C-H…O) will be inherently weaker than O-H…O and N-H…O. The formation of a hydrogen bond is due to the transfer of charge between the molecules. This can be affirmed by the computation of NPA (natural population analysis) charges for the isolated cosolvent molecules and ion-cosolvent pairs. The aggregate NPA charge for the cosolvents and ion-cosolvent pairs are given in Table 5.3. It can be seen that there is a diminutive charge transfer for ion-cosolvent pairs. A comparison was made to protic and aprotic solvents with $[OAc]^-$ where the protic solvents were found to exhibit a higher charge transfer. The charge transfer was found to decrease as follows: AcM > ethanol > FRM > water > DMSO > DMF > DMAc > acetone. These results suggest that the C-H…O hydrogen bond has a lower charge transfer than N-H…O and O-H…O.

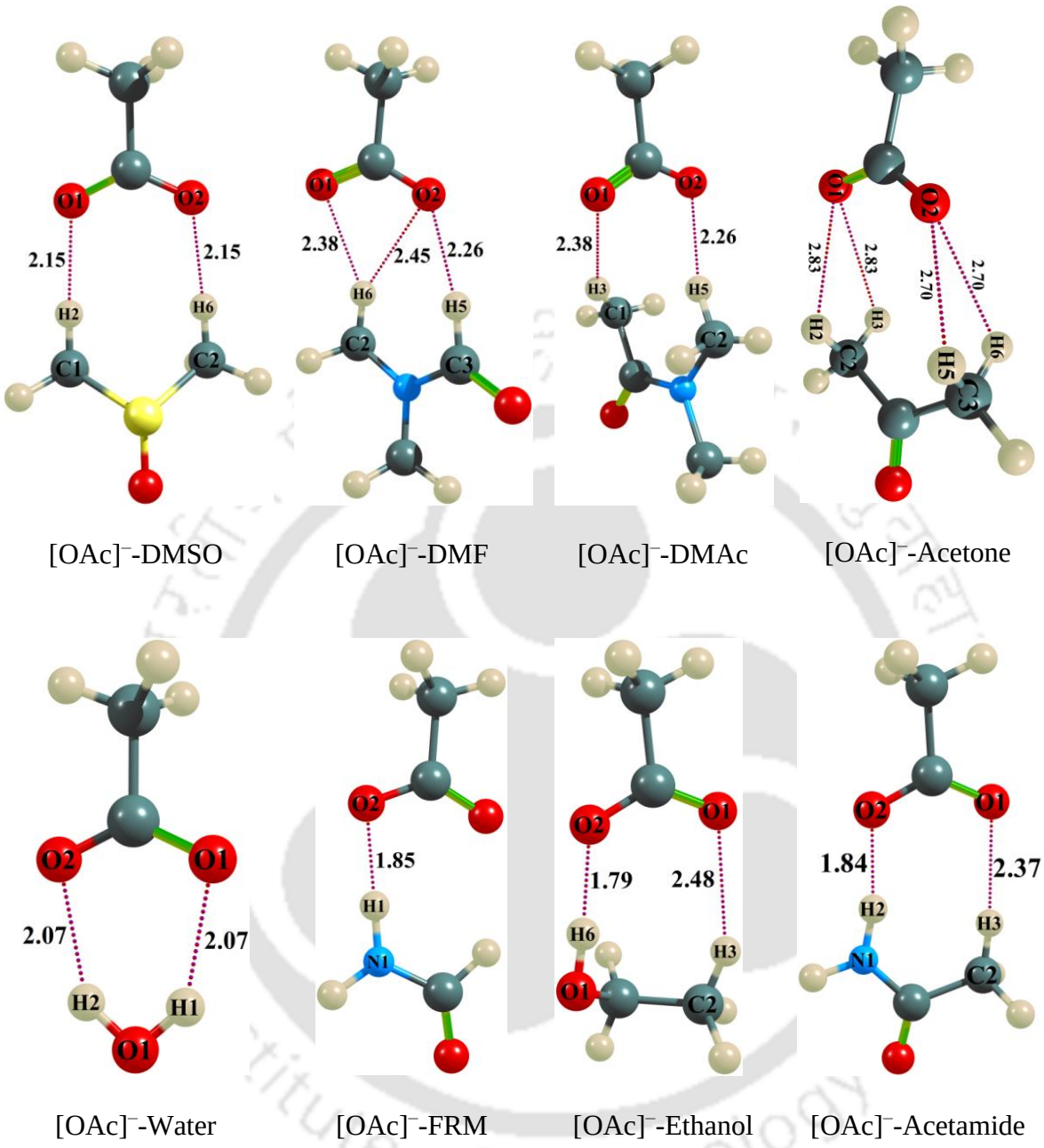

Figure 5.2: Optimized geometries of ion-molecule pairs of anion $[OAc]^-$ with different cosolvent molecules. The dashed lines indicate hydrogen bonds in these pairs. C (cyan), H (white), O (red), S (yellow), and N (blue) are color representation for different atoms.

Table 5.3: NPA charges of isolated cosolvents and $[Emim]^+$ / $[OAc]^-$ with different cosolvent pairs

Entry	Cosolvent	Isolated molecule	$[Emim]^+/[OAc]^-$ - Cosolvent pair	
			$[OAc]^-$	$[Emim]^+$
1.	Ethanol	0.00	-0.0526	0.0156
2.	Water	0.00	-0.0422	0.0134
3.	Formamide (FRM)	0.00	-0.0516	0.0147
4.	Acetamide (AcM)	0.00	-0.0556	0.0179
5.	DMSO	0.00	-0.0407	0.0211
6.	DMF	0.00	-0.0307	0.0183
7.	DMAc	0.00	-0.0305	0.0191
8.	Acetone	0.00	-0.0105	0.0154

Further confirmation can be visualized from Table 5.4, where the interaction energies of $[OAc]^-$-cosolvents and $[Emim]^+$-cosolvents are represented for different cosolvents. From the Table 5.4, it can be seen that the interaction energies of $[OAc]^-$ anion with protic solvents are higher than that of $[OAc]^-$-aprotic solvent pairs. On the other hand, $[Emim]^+$ and $[OAc]^-$ exhibits approximately similar interaction energies with aprotic solvents. This is due to the fact that anion is more preferentially solvated by protic solvents, while for aprotic solvents the solvation is of a similar order for both ions ($[OAc]^-$ and $[Emim]^+$). It should be noted that lower interaction energy is preferable as it allows a free movement of the anions. This allows the anions to interact with the incoming cellulose molecules. Furthermore, in order to understand the solvation of ions by cosolvents, MD simulations have been carried out for [Emim][OAc]/cosolvents and cellulose-[Emim][OAc]/cosolvent frameworks.

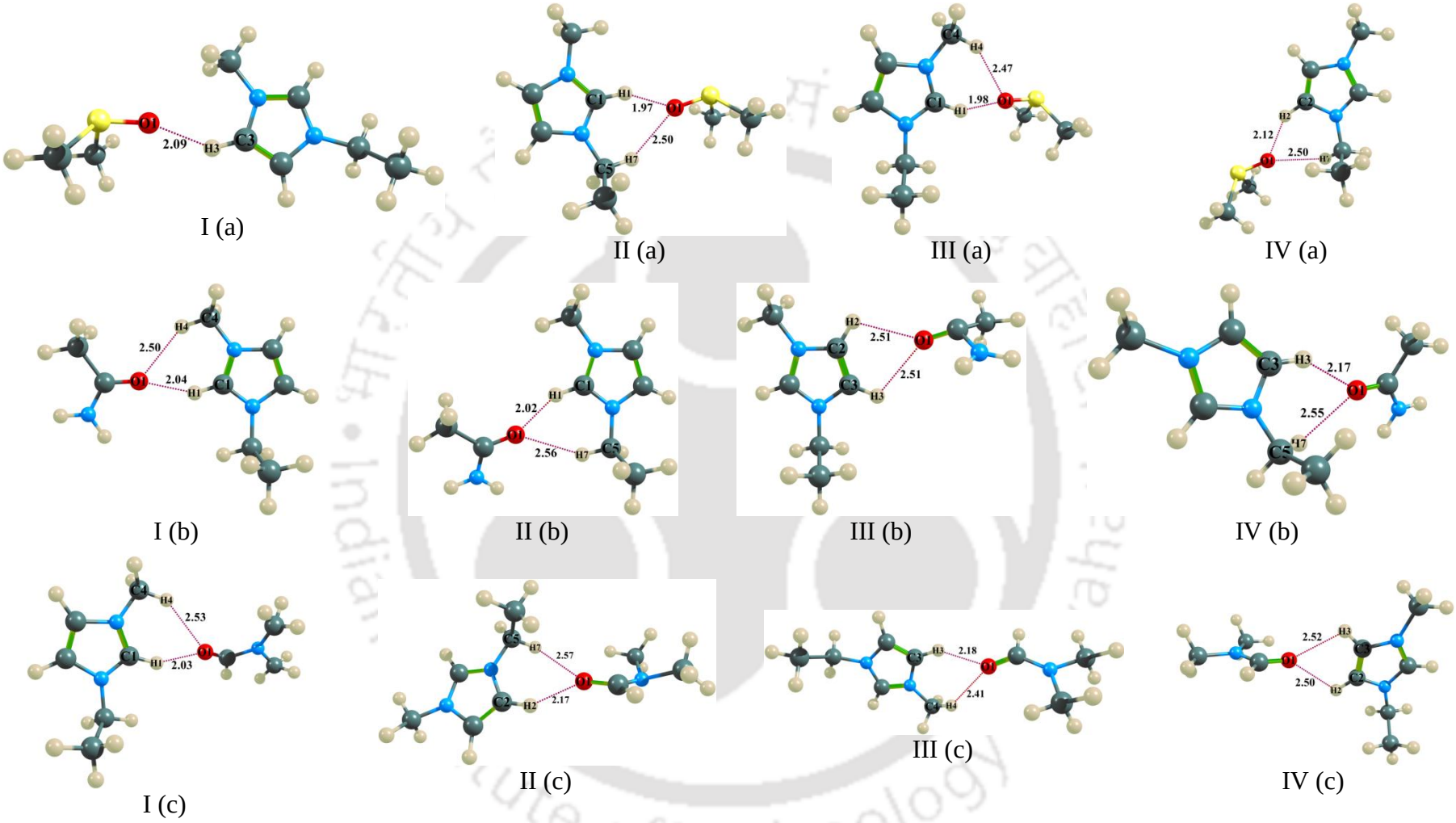

Figure 5.3: Optimized geometries of ion-molecule pairs of cation $[Emim]^+$ with different cosolvent molecules, (a) DMSO, (b) Acetamide, and (c) DMF. C (cyan), H (white), O (red), S (yellow), and N (sky blue) are color representation for different atoms.

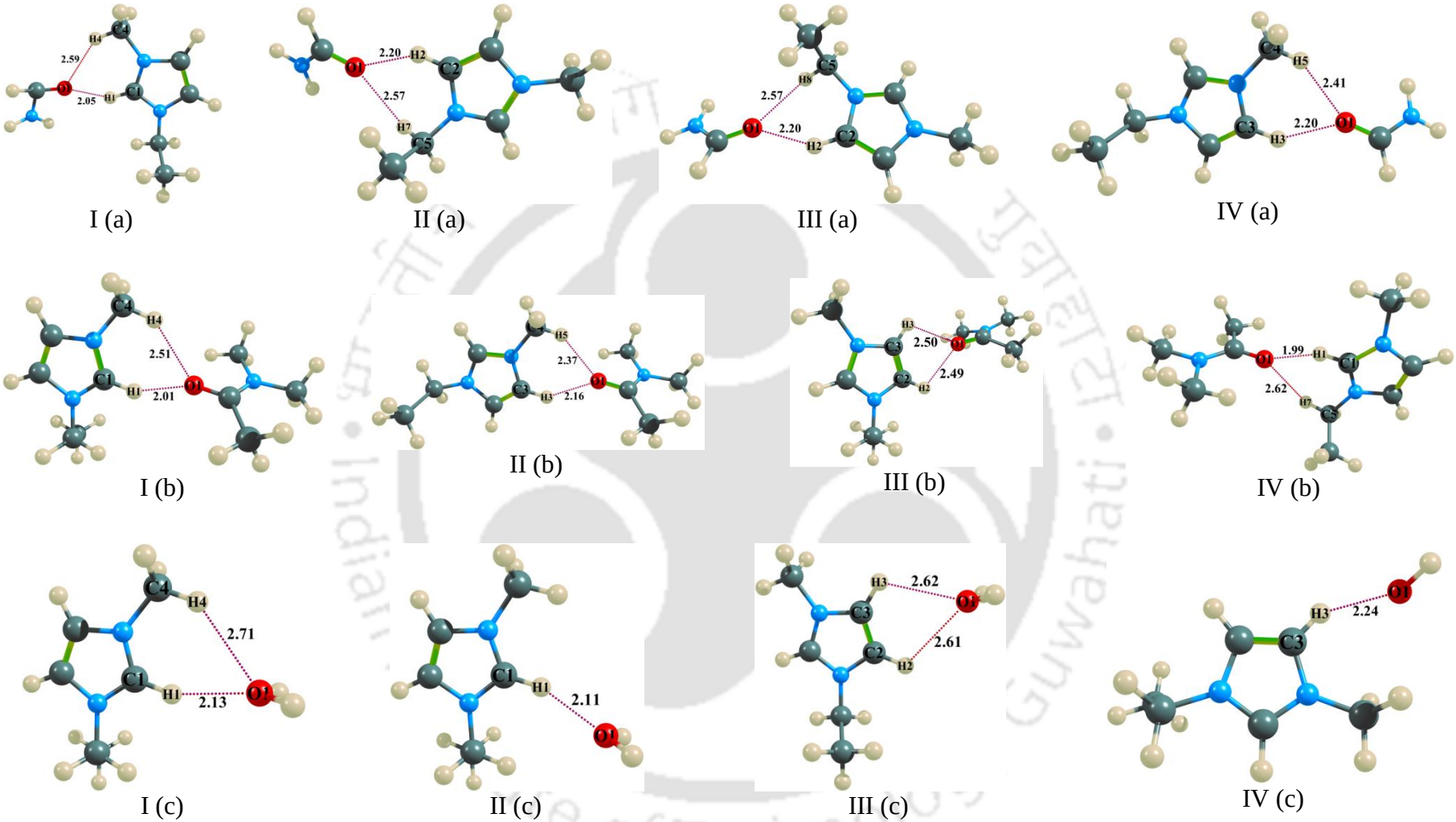

Figure 5.4: Optimized geometries of ion-molecule pairs of cation $[Emim]^+$ with different cosolvent molecules, (a) Formamide, (b) DMAc, and (c) Water. C (cyan), H (white), O (red), and N (sky blue) are color representation for different atoms.

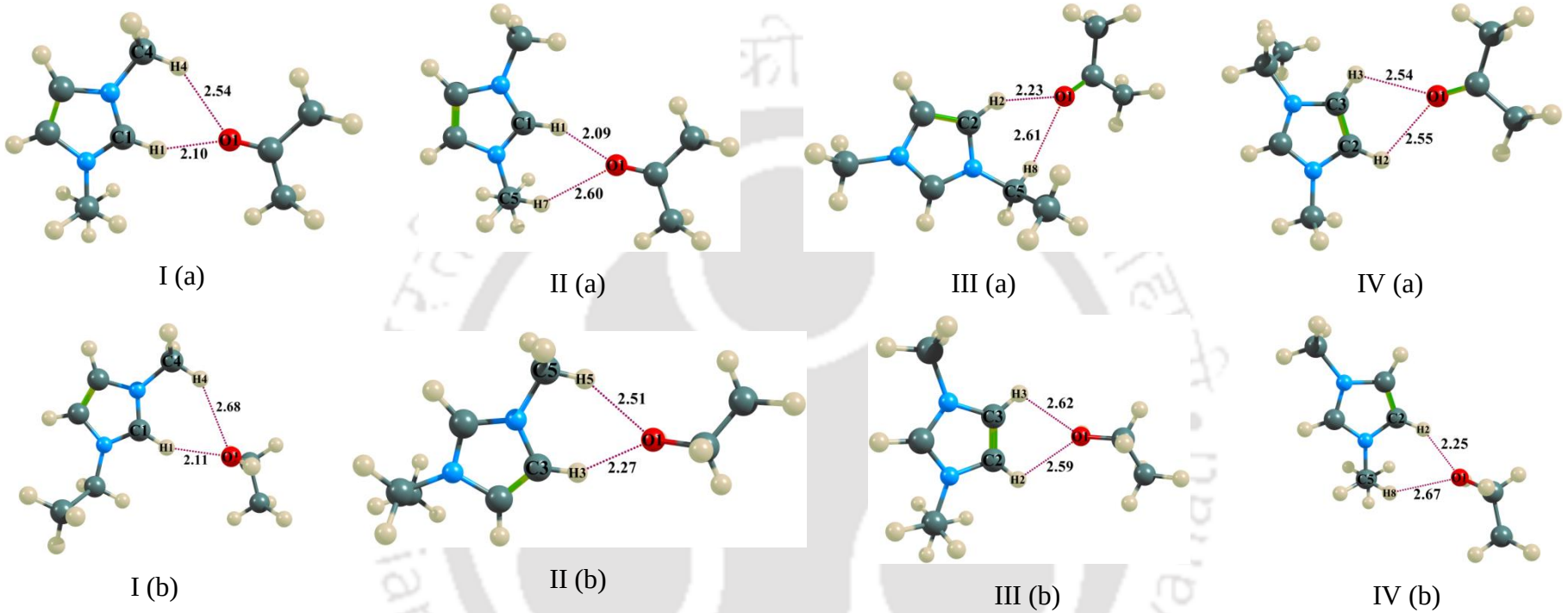

Figure 5.5: Optimized geometries of ion-molecule pairs of cation $[Emim]^+$ with different cosolvent molecules, (a) Acetone, and (b) Ethanol. C (cyan), H (white), O (red), and N (sky blue) are color representation for different atoms.

Table 5.4: Interaction energies (kJ mol^{-1}) of $[OAc]^-$ anion and $[Emim]^+$ cation with different cosolvents obtained from quantum chemical calculations

Entry	Cosolvent	$[OAc]^-$	$[Emim]^+$			
		I.E.	I.E. (I)	I.E. (II)	I.E. (III)	I.E. (IV)
1.	Ethanol	-74.26	-47.15	-36.95	-38.91	-33.14
2.	Water	-80.30	-46.48	-37.15	-36.65	-45.85
3.	Formamide (FRM)	-101.67	-67.32	-55.40	-56.61	-66.99
4.	Acetamide (AcM)	-99.66	-71.13	-58.58	-60.21	-70.92
5.	DMSO	-77.50	-83.40	-69.17	-70.30	-80.96
6.	DMF	-59.62	-73.01	-58.99	-60.21	-52.18
7.	DMAc	-58.45	-78.90	-61.92	-60.1	-73.47
8.	Acetone	-43.10	-59.67	-58.80	-44.73	-58.85

5.4.2 Optimization and Influence of IL to Cosolvent Molar Ratio

5.4.2.1 Optimization of Molar Ratio

To understand the action of cosolvent on cellulose dissolution, a series of MD simulations have been performed for mixtures of cellulose and [Emim][OAc]/co-solvent as a function of their molar ratios. In the MD simulations, the cosolvents such as DMSO, DMAc, DMF, FRM, and AcM have been considered based on their on their physiochemical properties and relative or lower interaction with ions. So in the process, we have eliminated three co-solvents namely acetone, water and ethanol. For a benchmark case, DMSO was chosen to optimize the molar ratio (R_{DMSO}). In such a study, the molar ratio of [Emim][OAc] to DMSO was varied from 1-5. To recommend the optimum cosolvent molar ratio, we have computed the non-bonded interaction energy between anion, cation, and DMSO with cellulose. The MD simulated interaction energies (sum of electrostatic and van der Waals energies) are given in Table 5.2. From Table 5.2, it can be seen that the highest interaction energy for [Emim][OAc]/DMSO mixture with cellulose is obtained at R_{DMSO} = 2. The energy of electrostatic interactions is

much more grounded than the van der Waal energy, which represents the electrostatic portion overwhelming the interaction energy of the complex system. It should be noted that, when DMSO is added to the complex system, the change in the electrostatic energy is higher than the van der Waals energy which implies it is indeed the charge along with the solvation effect which decides the dissolution. This suggests that the addition of DMSO has shown the greater influence on electrostatic energy between the cellulose and [Emim][OAc]/DMSO mixtures. From the study, it was also observed that increase in [Emim][OAc] to DMSO molar ratio (*i.e.*, from 2.5 to 5) results in a decrease of interaction energy. This affirms the MD derived optimized molar ratio namely 2 (R_{DMSO}). In the preceding sections, we further proceed to establish the mechanism for the interaction of the ions (of Ionic Liquids) with cellulose and DMSO.

5.4.2.2 Interactions of Ions with Cellulose

The dissolution process is seen to follow two opposite pathways. While on one side, the cation decreases the cellulose solubility due to its strong binding with an anion, on the other hand, anion helps in providing hydrogen bonds with incoming hydroxyl groups of cellulose [22]. In the current scenario, our goal is to enhance the cellulose-anion interactions by decreasing the anion-cation interactions using cosolvents. Figure 5.6 shows the interaction energy of anion, cation, and DMSO with cellulose at different IL to DMSO molar ratios. From Figure 5.6, it is clear that at R_{DMSO} = 2, the interaction energy between cellulose and $[OAc]^-$ (-2791.55 kJ mol^{-1}) was higher than other molar ratios in cellulose-[Emim][OAc]/DMSO systems. The interaction energy of cellulose-$[Emim]^+$ was found to decrease with increasing cellulose-[Emim][OAc]/DMSO molar ratio. On the contrary, the cellulose-DMSO interaction energy was found to increase with mole ratio. It was also found that the interaction energy of cellulose with $[OAc]^-$ increases from R_{DMSO} = 1 to R_{DMSO} = 2, then decrease from R_{DMSO} = 2.5 to R_{DMSO} = 5 (Figure 5.6) due to the higher interaction energy between anion and cation at their specific

molar ratios. This is due to the fact that cellulose is extensively solvated by anion, which helps to enhance the cellulose solubility.

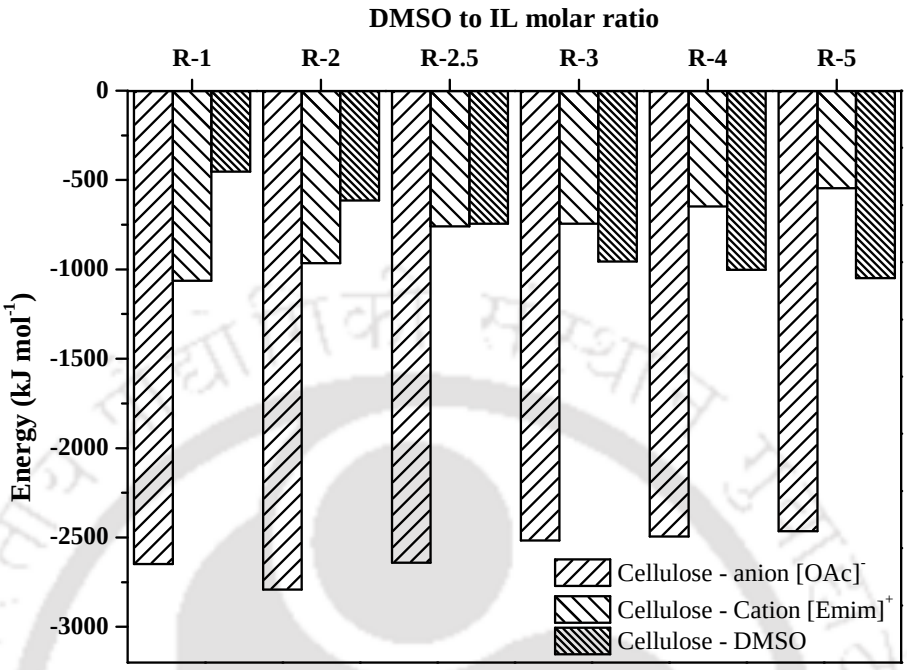

Figure 5.6: Interaction energies of cellulose with anion and cation obtained from MD simulations at different molar ratios of IL to DMSO in the cellulose-[Emim][OAc]/DMSO system

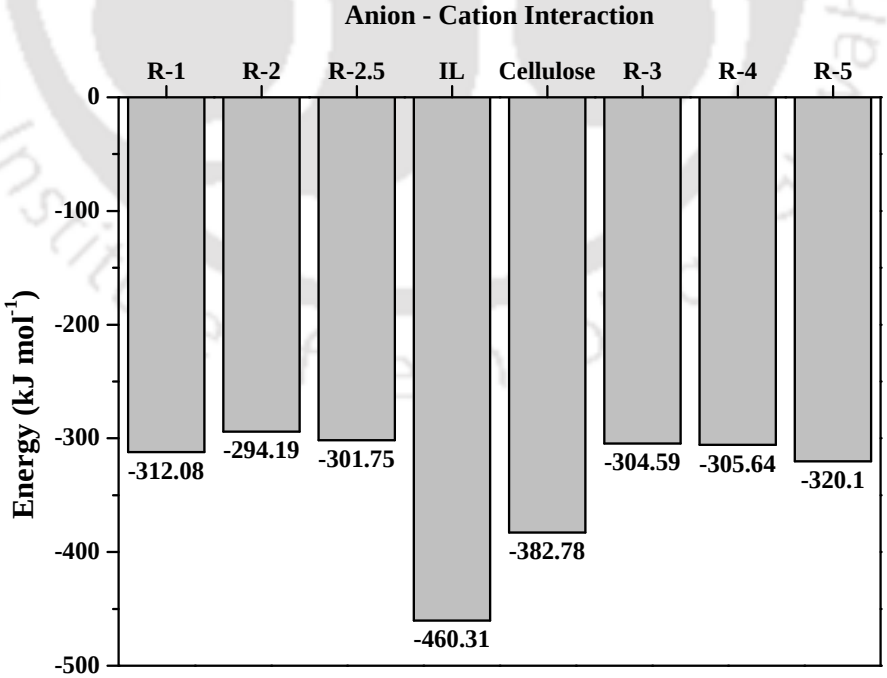

Figure 5.7: Interaction energies between anion and cation in the [Emim][OAc], cellulose-[Emim][OAc] and cellulose-[Emim][OAc]/DMSO systems obtained from MD simulations

5.4.2.3 Interactions of DMSO and Ions

The non-bonded interaction energies between $[OAc]^-$ and $[Emim]^+$ in [Emim][OAc], cellulose-[Emim][OAc], and cellulose-[Emim][OAc]/DMSO systems are presented in Figure 5.7. The interaction energy of $[OAc]^-$ with $[Emim]^+$ was found to be lower in cellulose-[Emim][OAc]/DMSO (-294.19 kJ mol^{-1}) mixture than neat [Emim][OAc] (-460.31 kJ mol^{-1}) and cellulose-[Emim][OAc] pair (-382.78 kJ mol^{-1}) (Figure 5.7). This follows the fact that, strong ionic association is usually present in neat IL due to its inherent electrostatic and hydrogen bonding energies [23]. To dissociate this strong ionic interaction, the cosolvent is added to the [Emim][OAc]. The reduction of interaction energy between anion and cation in the presence of DMSO aid in the production of more free ions. As a result, the produced free ions helps in the formation of strong hydrogen bonds with cellulose. However, the interaction energies of $[OAc]^-$ with DMSO was less than that of $[Emim]^+$-DMSO energies at lower molar ratios (*i.e.*, R_{DMSO} = 1, 2, 2.5, and 3) (Figure 5.8).

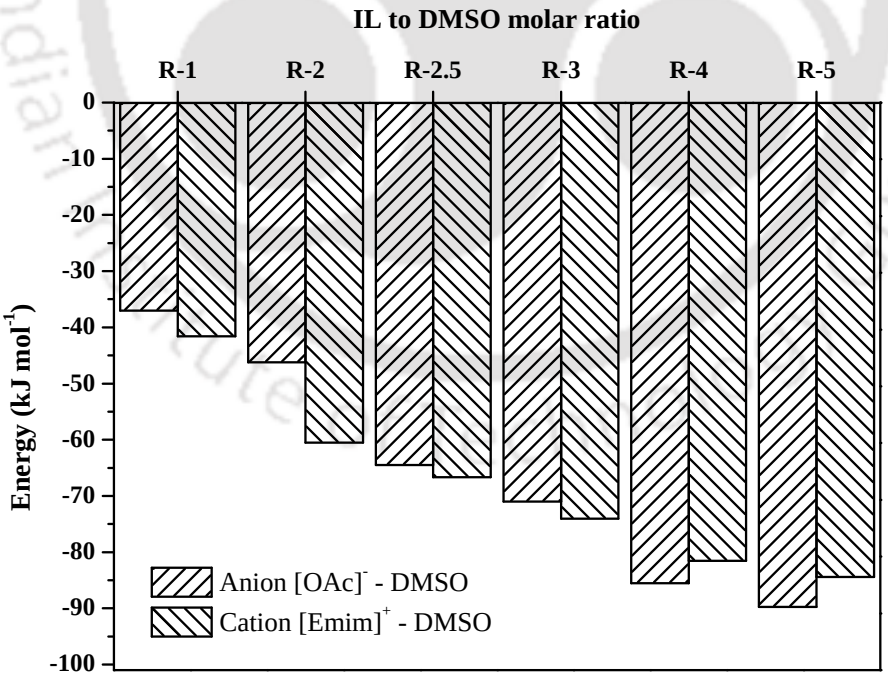

Figure 5.8: Interaction energies of anion and cation with DMSO obtained from MD simulations at different molar ratios of IL to DMSO in the cellulose-[Emim][OAc]/DMSO system.

Further, an increase in the IL to DMSO molar ratio (*i.e.* R_{DMSO} = 4 and 5), resulted in higher interaction energies of $[OAc]^-$-DMSO (Figure 5.8). This outcome proposes the fact that the degree of solvation of anion is higher than that of cation at higher molar proportions which lead to decrease in cellulose solubility. From this study, it is clearly obvious that the recommended molar ratio for IL to co-solvent is 2. Hence, MD simulations were performed for mixtures of cellulose with [Emim][OAc]/different cosolvents (protic and aprotic) at *R*=2.

5.4.3 Effect of Protic and Aprotic Cosolvents

5.4.3.1 Cellulose-IL Interactions in Cellulose-[Emim][OAc]/Cosolvent

After the successful optimization of [Emim][OAc] to DMSO molar ratio, a series of MD simulations were carried for the mixture of cellulose-[Emim][OAc] with different cosolvent systems. The non-bonded interaction energies of $[OAc]^-$, $[Emim]^+$ and different cosolvents with and cellulose were computed and compared with the cellulose-[Emim][OAc] system. To predict the protic and aprotic solvents effect on cellulose solubility, the interaction energies of cellulose with $[OAc]^-$ are investigated and given in Table 5.5. From Table 5.5, the electrostatic interactions are found to be higher than the van der Waals interactions, signifying that the electrostatic interaction is the controlling parameter for cellulose-$[OAc]^-$ interactions. When a cosolvent is added to the cellulose-[Emim][OAc] system, there is a significant change in the electrostatic interactions than van der Waals interactions. This suggests that the addition of a cosolvent has a considerable influence on the electrostatic interactions between cellulose and $[OAc]^-$. It was also observed that the interaction between cellulose-$[OAc]^-$ increases with aprotic solvents such as DMSO, DMF, DMAc. This depicts an opposite trend with the addition of protic solvents (FRM, AcM). Interestingly, the aprotic cosolvents shows a moderate effect on the cellulose interactions in cellulose-[Emim][OAc]/cosolvent system (Figure 5.9). For either solvents, the interaction energy between cellulose and $[Emim]^+$ was found to decrease with the addition of cosolvent in cellulose-[Emim][OAc] (Figure 5.9).

Table 5.5: Interaction energies (kJ mol^{-1}) between cellulose and $[OAc]^-$ obtained from MD simulations in different cosolvent systems

Simulated System	*Select*	E_{vdW}[b]	E_{total}[c]
Cellulose-[Emim][OAc]/DMSO	-3029.13	237.59	-2791.54
Cellulose-[Emim][OAc]/DMAc	-2820.04	323.65	-2496.40
Cellulose-[Emim][OAc]/DMF	-2805.06	297.64	-2507.42
Cellulose-[Emim][OAc]	-2628.06	142.45	-2485.61
Cellulose-[Emim][OAc]/FRM	-2436.83	187.20	-2249.63
Cellulose-[Emim][OAc]/AcM	-2337.91	194.34	-2143.58

[a] electrostatic interaction energy, E_{elec}; [b] van der Waals interaction energy, E_{vdW}; [c] sum of E_{elec} and E_{vdw}

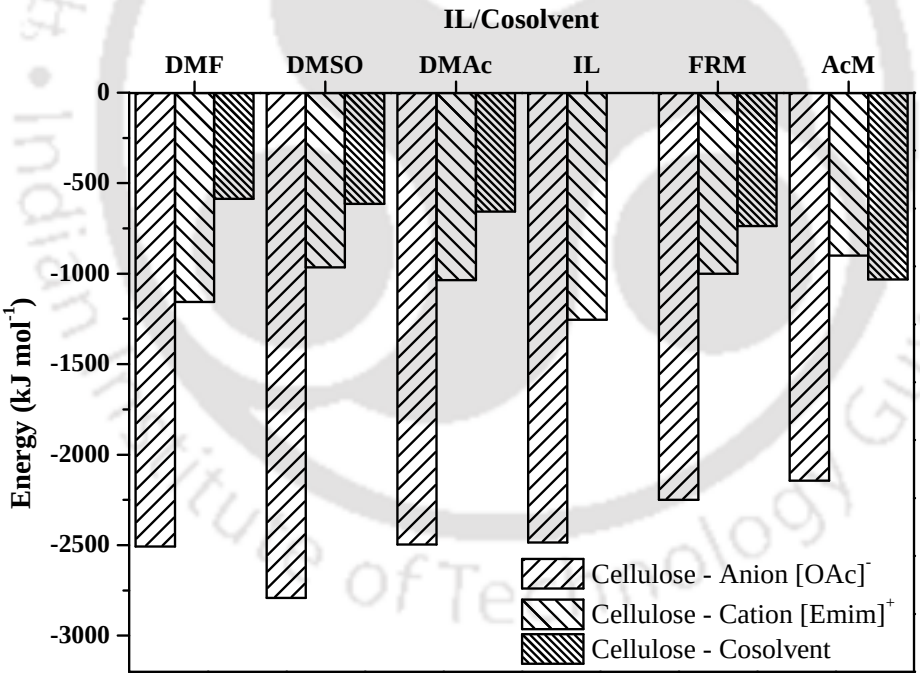

Figure 5.9: Interaction energies of cellulose with an anion, cation and different cosolvents in the cellulose-[Emim][OAc]/cosolvents systems obtained from MD simulations

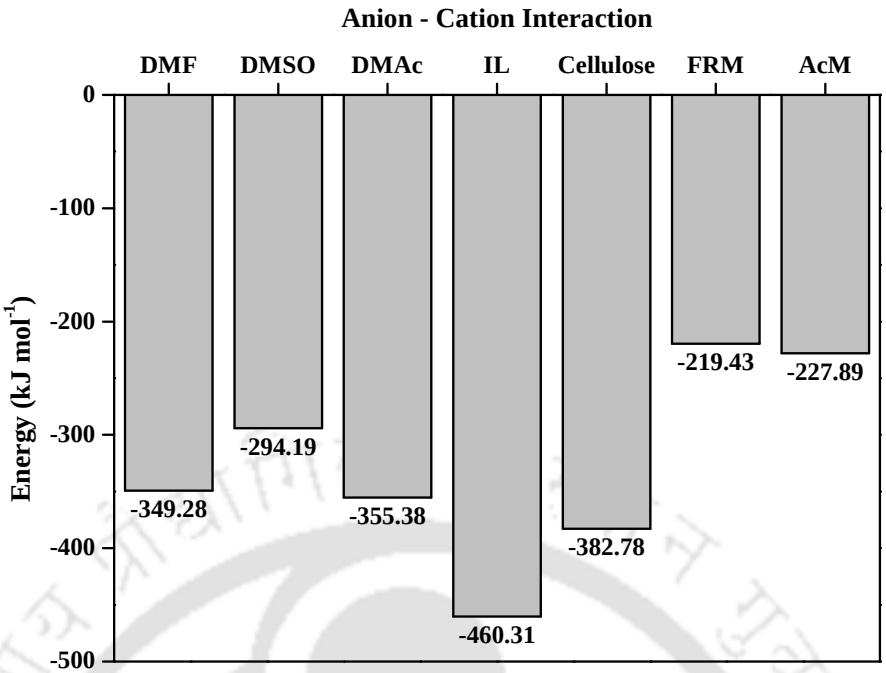

Figure 5.10: Interaction energies between anion and cation in the pure [Emim][OAc], cellulose-[Emim][OAc] and cellulose-[Emim][OAc]/cosolvents obtained from MD simulations

5.4.3.2 Anion-Cation Interactions in Cellulose-[Emim][OAc]/Cosolvent

The dissociation of IL would be an essential step for the cellulose dissolution. To explore the cosolvent effect on ionic dissociation of IL (*i.e.*, cation and anion), the interaction energies between $[OAc]^-$ and $[Emim]^+$ in cellulose-[Emim][OAc] and cellulose-[Emim][OAc]/cosolvent system was calculated and presented in Figure 5.10. In the cellulose-[Emim][OAc] mixture, the interaction energy between $[OAc]^-$ and $[Emim]^+$ was relatively higher than in the cellulose-[Emim][OAc]/cosolvent systems (see Figure 5.10). Hence, when a cosolvent is added to the cellulose-[Emim][OAc] mixtures, the association or binding energy between the anion and cation is partially broken and thereby releases more free ions. The protic solvents (FRM and AcM) was also found to dissociate $[OAc]^-$ and $[Emim]^+$ interactions to a larger extent than the aprotic solvents, nevertheless, they exhibited lower interaction energy between cellulose and $[OAc]^-$. This is mainly due to the higher solvation of $[OAc]^-$ anion by protic solvents (Table 5.6). Due to this reason, protic solvents are known to decrease the

cellulose solubility, whereas, in the case of aprotic solvents, the cation of the IL is found to be more solvated (Table 5.6). Thus, these aprotic solvents produce more number of free anions which eventually forms strong hydrogen bonds with the cellulose molecule. This would finally lead to an increase in the cellulose solubility in IL/aprotic solvent mixtures.

Table 5.6: Interaction energies of $[OAc]^-$ anion and $[Emim]^+$ cation with different cosolvent ratios obtained from MD simulations

Simulated System	$E_{An\text{-}Cos}$ (kJ mol^{-1}) [a]	$E_{Cat\text{-}Cos}$ (kJ mol^{-1}) [b]	$E_{Ani\text{-}Cat}$ (kJ mol^{-1}) [c]
[Emim][OAc]-FRM (*R*=1)	-98.25	-32.91	-279.66
[Emim][OAc]-FRM (*R*=2)	-164.87	-60.39	-230.77
[Emim][OAc]-AcM (*R*=1)	-92.62	-37.49	-274.43
[Emim][OAc]-AcM (*R*=2)	-148.32	-66.00	-227.48
[Emim][OAc]-DMSO (*R*=1)	-39.00	-38.70	-318.08
[Emim][OAc]-DMSO (*R*=2)	-57.08	-61.46	-304.11
[Emim][OAc]-DMSO (*R*=2.5)	-67.38	-64.31	-315.02
[Emim][OAc]-DMSO (*R*=3)	-74.91	-69.76	-315.14
[Emim][OAc]-DMSO (*R*=4)	-80.66	-75.17	-338.33
[Emim][OAc]-DMSO (*R*=5)	-93.38	-86.98	-351.32
[Emim][OAc]-DMF (*R*=1)	-32.19	-37.79	-312.76
[Emim][OAc]-DMF (*R*=2)	-45.48	-55.59	-360.31
[Emim][OAc]-DMAc (*R*=1)	-28.60	-38.79	-325.34
[Emim][OAc]-DMAc (*R*=2)	-36.51	-19.10	-379.40

[a] $E_{An\text{-}Cos}$ is the interaction energy between anion and cosolvent; [b] $E_{Cat\text{-}Cos}$ is the interaction energy between cation and cosolvent, and [c] $E_{Ani\text{-}Cat}$ is the interaction energy between anion and cation.

The degree of cosolvent effect on ionic energy dissociation decreases in the following order: FRM > AcM > DMSO > DMF > DMAc (Figure 5.10). This decrease in the anion-cation interactions can be attributed to the molar volume of the cosolvents (FRM (39.88), AcM (55.7), DMSO (74.84), DMF (76.42), and DMAc (93.06)) [24-26]. Thus, a lower molar volume of the cosolvent causes a higher decrease in the anion-cation interactions as they can solvate cellulose molecules more efficiently within the given volume by executing more hydrogen bonds. This implies that the addition of a smaller cosolvent is encouraging to the dissociation of ionic pairs in the IL. We now move ahead and depict the pair-wise relation between different moieties using RDF and coordination number.

5.4.4 Structural Properties of Cellulose in [Emim][OAc] and [Emim][OAc]/Cosolvent Mixtures

5.4.4.1 Radial Distribution Functions

The spatial correlation between specific interaction sites of cellulose-[Emim][OAc] and cellulose-[Emim][OAc]/cosolvent systems was studied through the radial distribution functions (RDF). The RDF plots between the hydroxyl protons of cellulose molecule (H3, H4, and H6 atoms) with O2 of anion and O1 of cosolvent (DMSO) are depicted in Figure 5.11. Figure 5.11 also depicts RDF of hydroxyl oxygen of cellulose with H1 atom of the cation. For DMF, DMAc, FRM, and AcM cosolvents, the RDF plots are given in Figures D.1-D.5 (Appendix D). The sharp peak of RDF plot is exhibited at 1.65 Å in all *g(r)*'s indicating the formation of strong hydrogen bond between the protons of cellulose and O2 atom of the anion in both cellulose-[Emim][OAc] and cellulose-[Emim][OAc]/cosolvent systems. However, in the case of cellulose-cosolvent RDF plot, the peak was observed at 1.95-2.15 Å. This signifies a formation of a weaker hydrogen bond as compared to cellulose-anion (1.65 Å). For cellulose-cation RDF, the peak was found to lie at 2-2.15 Å representing a weak hydrogen bond. It is

fascinating to note that the proton (H1) of the cation approaches cellulose moiety under 2 Å thereby representing a weak hydrogen bond.

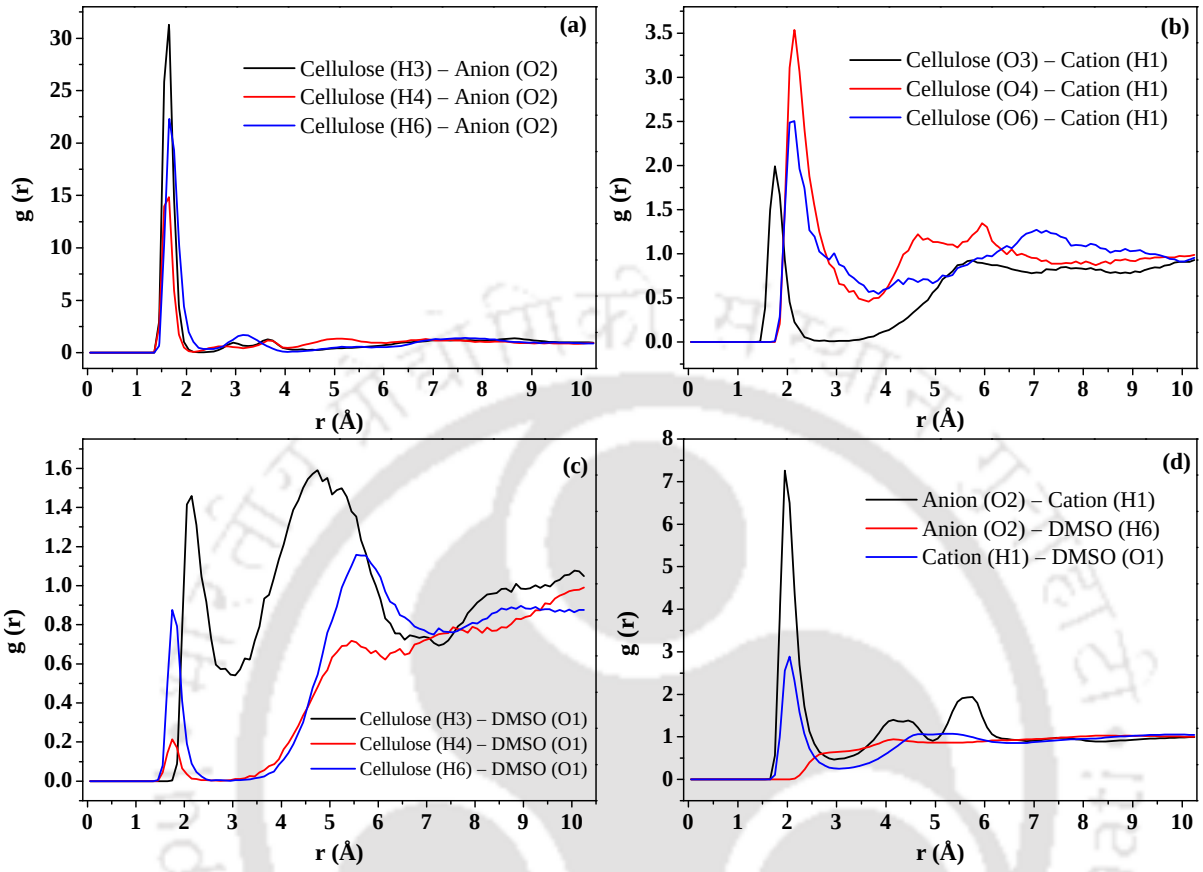

Figure 5.11: RDF between the cellulose molecule with (a) anion (O2), (b) cation (H1), and (c) DMSO (O1) around the selected hydroxyl groups (O3, O4, and O6; see Figure 5.1) of cellulose and (d) RDF between [Emim][OAc]/DMSO in the cellulose-[Emim][OAc]/DMSO system

From the RDF plot of the anion (O2) with a cation (H1), the g(r) peak was obtained at 1.65 Å in pure IL, whereas in the cellulose-IL system, the peak was observed at 1.75 Å (Figure 5.12). This suggests that the interaction between anion and cation was preferably decreased as compared to pure IL interactions. When a cosolvent was added to the cellulose-IL system, the *g(r)* peak has now extended to till 1.95 Å for aprotic solvents and 2.05 Å for protic solvents, respectively (Figure 5.12 and Figures D.1-D.5). This extended peak indicates a weak hydrogen bond between $[OAc]^-$ and $[Emim]^+$. The height of the RDF peak was also found to be higher in [Emim][OAc] as compared to cellulose-[Emim][OAc] and cellulose-

[Emim][OAc]/cosolvent system (Figure 5.12). This obtained result can be supported by their interaction energies (Figure 5.10) and coordination number (Table 5.7) as calculated from MD simulations.

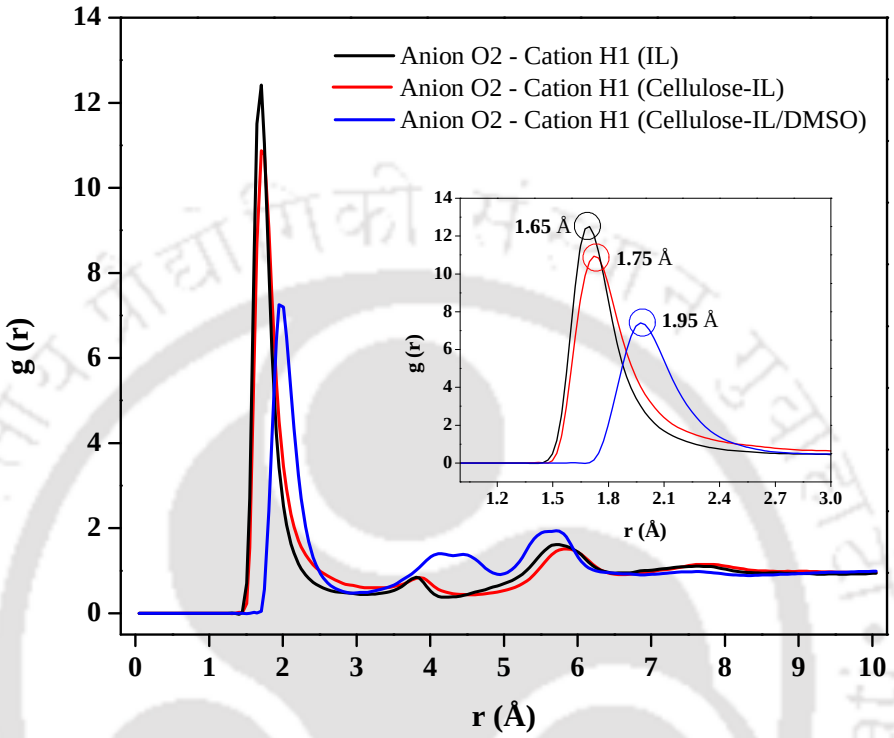

Figure 5.12: RDF between the anion (O2) and cation (H1) of the [Emim][OAc] in the [Emim][OAc], cellulose-[Emim][OAc] and cellulose-[Emim][OAc]/DMSO systems. See Figure 5.1 for atom notations.

5.4.4.2 Coordination Number

The $[OAc]^-$ anion here is found to be surrounded by five to six cations in the first solvation shell of pure IL, and it reduces to four cations in the cellulose-[Emim][OAc] system. Further, the coordination number was found to decrease from 2.04 to 0.91 with the addition of cosolvents. From Table 5.7, it can be seen that each glucose molecule of cellulose is surrounded by three to four anions in the first coordination shell of cellulose-[Emim][OAc]/DMSO system. In a similar manner, three anions are surrounded in the cellulose-[Emim][OAc]. A comparison with cellulose-[Emim][OAc]/DMF, DMAc, FRM and AcM cosolvent systems shows that cellulose was bounded by 3.15, 2.91, 2.73 and 2.36 anions,

respectively in their first coordination shell. For the cellulose-cation system, the glucose molecule of cellulose was surrounded by ~1.46 molecule of cation in cellulose-[Emim][OAc], while, on account of cellulose-[Emim][OAc]/cosolvent system, the coordination number was found to decrease (Table 5.7). This attribution points out to the fact that the interaction between cellulose and cation is less compared to cosolvent system (Figure 5.9).

Table 5.7: Coordination numbers of first solvation shell for the different systems obtained from MD simulations

Simulated System	Cellulose-Anion [a]	Cellulose-Cation [a]	Anion-Cation	Anion-Cosolvent	Cation-Cosolvent
Cellulose-[Emim][OAc]/DMSO	3.84	0.95	1.61	0.52	0.87
Cellulose-[Emim][OAc]/DMF	3.15	1.04	1.94	0.32	0.65
Cellulose-[Emim][OAc]/DMAc	2.91	0.99	2.04	0.28	0.56
Cellulose-[Emim][OAc]	2.87	1.46	4.48	-	-
Cellulose-[Emim][OAc]/FRM	2.73	0.98	0.82	2.40	1.02
Cellulose-[Emim][OAc]/AcM	2.36	0.76	0.91	2.06	1.34
[Emim][OAc]	-	-	5.54	-	-

[a] coordination number is calculated for a single glucose molecule of cellulose (DP = 15)

Furthermore, when a cosolvent was added to the cellulose-[Emim][OAc] system, the interaction between $[OAc]^-$ and aprotic solvents decreases, while it increases for protic solvent systems. The RDF peak *g(r)* of $[OAc]^-$ and cosolvents were found to be at 1.75 Å and 2.75 Å for protic and aprotic solvents, respectively (Figures D.1-D.5 (d)). This ascription suggested that the protic solvents were disturbing the cellulose-$[OAc]^-$ interactions by forming strong hydrogen bonding with anion thereby decreasing the cellulose solubility. Whereas, the RDF peak *g(r)* of $[Emim]^+$ and cosolvents were attained at 2.15 Å and 2.05 Å for aprotic and protic solvents, respectively. Thus, it is clear that the $[Emim]^+$ cation is equally solvated by protic

and aprotic solvents. The coordination number for $[OAc]^-$-aprotic solvents were also found to be lower than $[Emim]^+$-aprotic solvents (Table 5.7). It is thus revealed that the $[Emim]^+$ is more solvated by aprotic solvents than $[OAc]^-$.

In addition to above discussions, recently Andanson *et al.* (2014) reported the effect of cosolvents namely DMSO and water on the interactions between [Bmim][OAc] and cellulose by MD simulations. In their study, they obtained the H-bond formation statistics between hydroxyl groups of glucose units and the different sites of [Bmim][OAc]/cosolvent mixtures [5]. The probability of H-bonds formation between the hydroxyl groups (H2, H3, and H6 as per Figure 5.1) of glucose and acetate anion were found to be 86.6, 89.2, and 84.2%, respectively in cellulose-[Bmim][OAc]/DMSO mixtures. Similar values for hydrogen bonds involved between glucose and DMSO molecules were between 0.1 to 0.6%. It was reported that the oxygen atom of water molecule tends to accept H-bonds from glucose were around 10 times higher than the oxygen atoms in DMSO. These results also imply that the addition of protic solvents decreases the probability of the H-bonds between cellulose and anion of the IL which is the opposite for aprotic solvents. According to the results of Zhao *et al.* (2013) [21] with spatial distribution functions, the aprotic solvents are disseminated in a circle along the C1-C2 axis of $[OAc]^-$, while protic solvents are distributed around the O1 and O2 atoms of $[OAc]^-$ anion. It is well known that O1 and O2 atoms of $[OAc]^-$ anion form strong hydrogen bonds with hydroxyl protons of cellulose molecules. The distribution of protic solvents around O1 and O2 atom of $[OAc]^-$ anion hinders the interaction between cellulose and anion. Thus, in summary, the obtained results of the present study are in good agreement with the reported results of Andanson *et al.* (2014) and Zhao *et al.* (2013).

5.4.5 Experimental Dissolution of Cellulose in [Emim][OAc] and [Emim][OAc]/Cosolvent Mixtures

Apart from the evidence of MD simulations, the experiments were also performed to validate dissolution of cellulose in IL and IL/cosolvents. The temperature during the study was varied in a range of 27 °C to 90 °C for 1 h as shown in Table 5.8. The dissolution of cellulose was found to increase with temperature. From Table 5.8, it can be seen that the aprotic solvents tend to dissolve higher amounts of cellulose at ambient temperature. This is higher than neat IL and IL/protic solvent (FRM) systems where $R_{\text{cosolvent}}$ = 2. The [Emim][OAc]/DMSO mixture system has exposed the highest interaction energy with cellulose than other IL/cosolvent systems (Figure 5.9). This can be explained by the fact that cation of the IL could be preferentially solvated by aprotic solvents through the ion-dipole interaction [27]. This difference in cellulose solubility is partially attributed to the difference in the dipole moments of the cosolvents. The dipole moments of cosolvents are found to decrease in the following order: DMSO (3.96) > DMF (3.86) > DMAc (3.81) > FRM (3.73) [28]. As a result, the solvated strength of $[Emim]^+$ cations by cosolvents and the corresponding concentration of free $[OAc]^-$ anions in the cosolvent systems followed the similar order. On addition of protic solvent (FRM) to the [Emim][OAc], the solubility of cellulose decreases as the anion of IL is preferentially solvated by FRM (Table 5.6). According to the observations of Xu *et al.* (2013) [9], the addition of water or methanol (protic solvents) lowers the solubilities of cellulose in these solvents. Hence, it is suggested that protic solvents like water or methanol may be recommended for the regeneration of cellulose in ILs.

Table 5.8: Experimental solubility of cellulose in [Emim][OAc] and [Emim][OAc]/ different cosolvent system at a selected molar ratio as a function of temperature and time[a]

Entry	Ionic Liquid/Cosolvent	Condition	Solubility (wt. %)
1.	[Emim][OAc]	27 °C, 1 h	2.10
		50 °C, 1 h	6.90
		70 °C, 1 h	9.46
		90 °C, 1 h	14.63
2.	DMSO	27 °C, 1 h	1.22
3.	DMF	27 °C, 1 h	1.15
4.	DMAc	27 °C, 1 h	1.05
5.	FRM	27 °C, 1 h	<1
6.	[Emim][OAc]-DMSO (*R* = 1)	27 °C, 1 h	8.21
7.	[Emim][OAc]-DMSO (*R* = 2)	27 °C, 1 h	9.66
		50 °C, 1 h	14.80
		70 °C, 1 h	17.31
		90 °C, 1 h	22.38
8.	[Emim][OAc]-DMSO (*R* = 2.5)	27 °C, 1 h	7.83
9.	[Emim][OAc]-DMSO (*R* = 3)	27 °C, 1 h	6.35
10.	[Emim][OAc]-DMSO (*R* = 4)	27 °C, 1 h	5.92
11.	[Emim][OAc]-DMSO (*R* = 5)	27 °C, 1 h	4.89
12.	[Emim][OAc]-DMF (*R* = 2)	27 °C, 1 h	7.15
13.	[Emim][OAc]-DMAc (*R* = 2)	27 °C, 1 h	6.30
14.	[Emim][OAc]-FRM (*R* = 2)	27 °C, 1 h	1.41

[a] The standard uncertainty: *u* (*T*) = 0.1 °C and *u* (*sol*) = 1.05 wt % at 95% confidence level

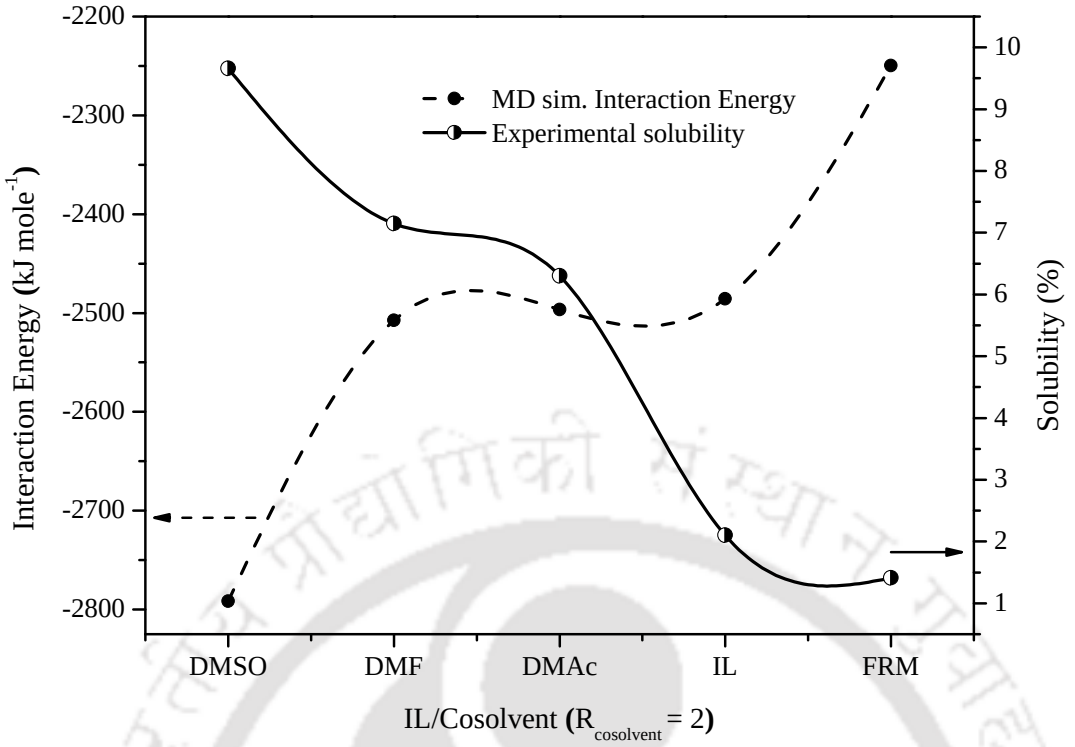

Figure 5.13: Correlation of experimental solubility and simulated interaction energies between $[OAc]^-$ and cellulose in the cellulose-IL/Cosolvent (R = 2) system at room temperature

The experimental solubility of cellulose in [Emim][OAc] and [Emim][OAc]/cosolvent ($R_{cosolvent}$ = 2) are then compared with MD simulated interaction energies of cellulose with $[OAc]^-$ (Figure 5.13). The experimental solubility is bound to be affected by many factors such as purity of IL, the source of chemicals, cellulose degree of polymerization, moisture content, and temperature of the system. Despite these factors, the simulated energies are in good agreement with the experimental solubility (Figure 5.13). From Figure 5.13, it is worthy to note that an inverse relation is obtained between non-bonded interaction energies and the experimental solubility. This suggests that the adopted MD simulated model has correctly described the intermolecular interactions in the mixtures of cellulose, IL, and cosolvents. Consequently, the simulated interaction energies are also helpful in deciding a cosolvent to enhance the dissolving capability of ILs for cellulose. The cellulose dissolution order for cosolvents is thus now found to follow: DMSO > DMF > DMAc > FRM.

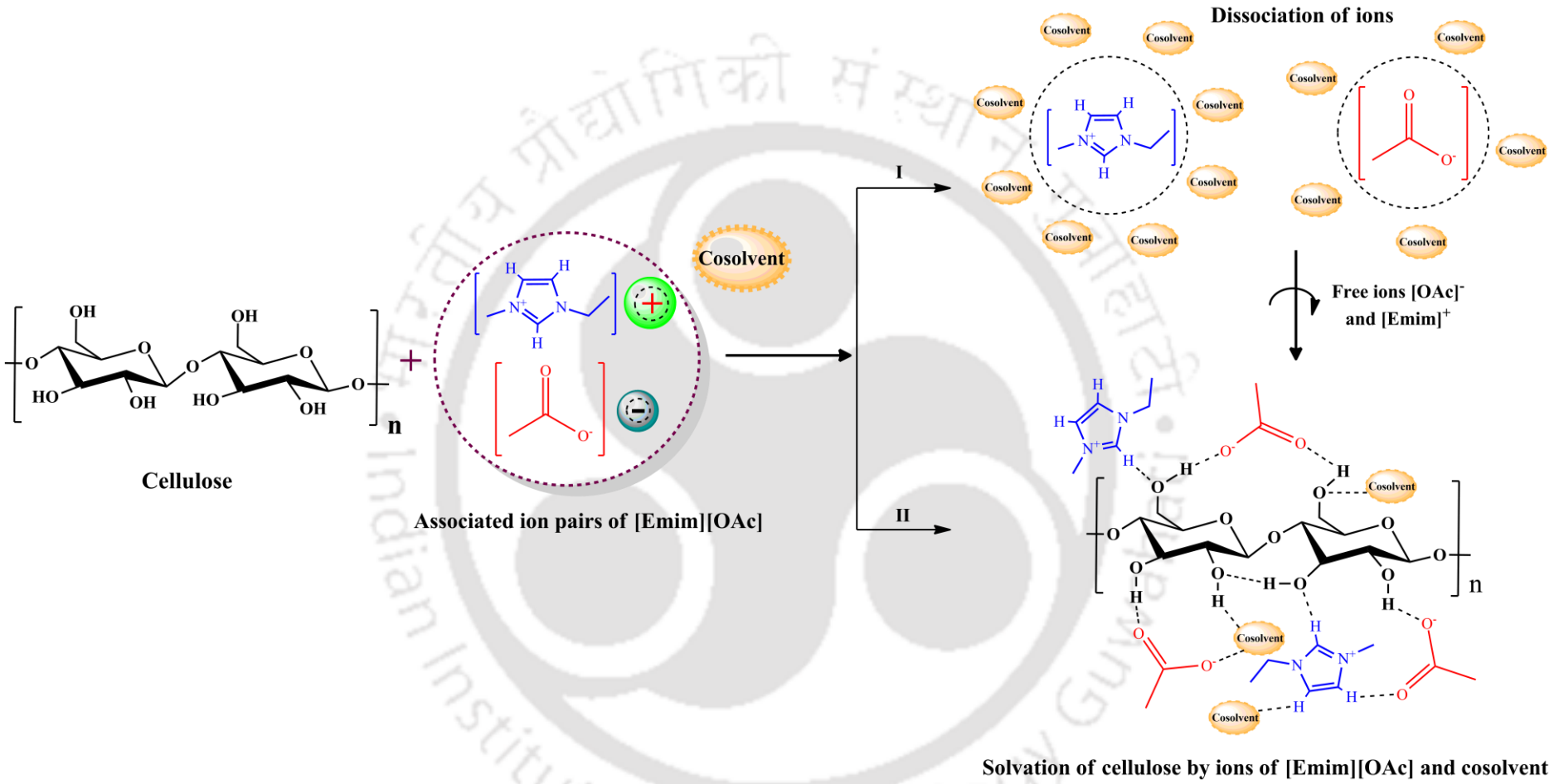

Figure 5.14: Proposed reaction mechanism for cellulose solvation in IL/cosolvent system, (I) Solvation of ions by cosolvent, (II) Mechanism between cellulose and IL/cosolvent

Based on QC, MD, and experimental results, we have further proposed a dissolution mechanism for the cellulose in [Emim][OAc]/cosolvents systems (Figure 5.14). The reaction mechanism is described by two steps. In the first step, we assume a strong association pair of ions in pure ILs. Thus when cosolvents are added to the IL, the strong association is partially destroyed by releasing the more free cations and anions in the solution. In the next and final step, the dissociated free anions interact with cellulose and thereby enhance the cellulose solubility. Hence, from QC, MD, and experiments, it is recommended to use aprotic solvents as it decreases the solvation of anions with its corresponding cation.

5.4.6 Influence of Density and Viscosity on IL/Cosolvent Mixtures

The density and viscosity of the pure [Emim][OAc], cosolvents and [Emim][OAc]/cosolvents mixtures also plays a vital role in the dissolution process. Generally, it is considered that ILs with low viscosity should be recommended for cellulose dissolution. Hence, the density and viscosity of neat [Emim][OAc], cosolvents and [Emim][OAc]/cosolvents systems are measured by a digital densitometer (Anton Paar, DMA-4500 M model) and interfacial rheometer **(**Anton Paar, Physica MCR301 model**)** at a temperature range from 27-90 °C. Table 5.9 depicts the density and viscosity of [Emim][OAc], DMSO, and [Emim][OAc]/DMSO (R_{DMSO} = 2) as a function of temperature. The viscosity of [Emim][OAc]/cosolvents was found to be lower than pure [Emim][OAc]. As the molar ratio of IL/DMSO is increased, the viscosity of mixture systems is found to decrease (Table 5.10). The lower viscosity of IL leads to a higher mass transfer rate and results in higher dissolution of solute. The temperature dependent viscosities of [Emim][OAc], cosolvents and [Emim][OAc]/cosolvent mixtures are then used to fit an Arrhenius equation. It is used to derive the activation energy for viscous flow and the viscosity at an infinite temperature (Eqn 2.14) which has been already discussed in chapter 2 (Section 2.4.3).

Table 5.9: Density and viscosity of isolated IL, DMSO and IL/DMSO (R_{DMSO} = 2) mixtures at different temperatures[a]

T (°C)	Density, ρ (g cm^{-3}) [b]			Viscosity, η (mPa.s) [b]		
	[Emim][OAc]	DMSO	[Emim][OAc]/ DMSO	[Emim][OAc]	DMSO	[Emim][OAc]/ DMSO
27	1.0957	1.0940	1.1002	63.50	1.9820	5.2970
30	1.0939	1.0907	1.0975	54.30	1.8980	4.9080
40	1.0877	1.0807	1.0891	34.70	1.5840	3.8690
50	1.0815	1.0706	1.0807	23.90	1.3390	3.1400
60	1.0755	1.0606	1.0723	16.90	1.1310	2.5960
70	1.0697	1.0506	1.0640	13.00	1.0053	2.2360
80	1.0634	1.0404	1.0555	9.29	0.8893	1.9050
90	1.0572	1.0304	1.0471	7.60	0.7828	1.6160

[a] Standard uncertainty u are u (T) = 0.1 °C, u (p) = 1 kPa; [b] The relative expanded uncertainty U are $U_r(\rho)$ = 0.0001 and $U_r(\eta)$ = 0.03 (0.95 level of confidence)

Figure C.6 shows the variation between of viscosity against temperature. From Figure C.6, the activation energy for viscous flow is obtained from the slope of the straight line and infinite temperature viscosities from the intercept of the fitted curve. The higher value of E_η makes it difficult for the ions to move at a faster rate. The kinetic parameters for all the selected solvent mixtures are given in Table 5.11. The inconsistent data in Table 5.10 suggest that the viscosity is not a key factor for the dissolution of cellulose in a given IL and IL/cosolvent mixture systems [31]. Even though ILs with lower viscosity are easier to handle, however properties such as basicity and polarity of the anions is a prerequisite for cellulose dissolution. This also follows a similar trend as reported in the literature [32].

Table 5.10: Viscosities for isolated cosolvents and IL/cosolvent systems at different IL to cosolvent molar ratios[a,b]

T (°C)	Cosolvents			[Emim][OAc]/DMSO						[Emim][OAc]/Cosolvent ($R_{cosolvent}$ = 2)		
	DMAc	DMF	FRM	R = 1	R = 2	R = 2.5	R = 3	R = 4	R = 5	DMAc	DMF	FRM
27	1.0104	0.8037	3.1430	6.3450	5.2970	3.2650	2.9740	2.5010	2.1860	2.5760	1.9420	5.1450
30	0.9847	0.7835	2.7960	5.7960	4.9080	3.0520	2.7740	2.3290	2.0360	2.4460	1.8330	4.5940
40	0.8593	0.7118	2.2240	4.3300	3.8690	2.3140	2.1350	1.8880	1.6180	1.9980	1.5310	3.3660
50	0.7772	0.6422	1.8140	3.3650	3.1400	1.8560	1.7120	1.5180	1.3650	1.6720	1.3520	2.5410
60	0.6783	0.5707	1.5370	2.6960	2.5960	1.5400	1.4810	1.2430	1.1790	1.3850	1.1169	2.0920
70	0.6094	0.5138	1.3050	2.2840	2.2360	1.3840	1.2067	1.1140	1.0318	1.2140	1.0820	1.7350
80	0.5341	0.4606	1.1709	1.9120	1.9050	1.1363	1.1270	0.9964	0.9189	1.0852	0.9289	1.4570
90	0.4822	0.4121	1.0310	1.7010	1.6160	1.0880	0.9676	0.8907	0.8480	1.1840	0.8288	1.2530

[a] Standard uncertainty u are u (T) = 0.1 °C, u (p) = 1 kPa; [b] The relative expanded uncertainty U is $U_r(\eta)$ = 0.03 (0.95 level of confidence)

Table 5.11: Activation energy and pre-exponential factors for IL/cosolvent systems obtained from viscosity calculations

IL/Cosolvent	Activation energy, E_η (kJ mol^{-1})	Infinite temperature, η_∞ (mPa.s)
[Emim][OAc]	30.67	2.8×10^{-4}
DMSO	13.46	8.9×10^{-3}
DMAc	10.69	1.4×10^{-2}
DMF	9.58	1.7×10^{-2}
Formamide (FRM)	15.80	5.2×10^{-3}
[Emim][OAc]/DMSO (R = 1)	19.23	2.7×10^{-3}
[Emim][OAc]/DMSO (R = 2)	16.91	5.9×10^{-3}
[Emim][OAc]/DMSO (R = 2.5)	16.35	4.5×10^{-3}
[Emim][OAc]/DMSO (R = 3)	16.18	4.4×10^{-3}
[Emim][OAc]/DMSO (R = 4)	15.09	5.7×10^{-3}
[Emim][OAc]/DMSO (R = 5)	13.76	8.4×10^{-3}
[Emim][OAc]/DMAc (R = 2)	12.78	1.4×10^{-2}
[Emim][OAc]/DMF (R = 2)	12.03	1.5×10^{-2}
[Emim][OAc]/FRM (R = 2)	20.24	1.4×10^{-3}

5.4.7 Structure of Regenerated Cellulose

The regenerated cellulose was characterized by XRD, FTIR, and TGA analysis to analyze the chemical structure and thermal decomposition behavior of the regenerated material. FTIR analysis was used to understand the structural changes in the native and regenerated cellulose as depicted in Figure 5.15 and 5.16. The adsorption bands of FTIR spectra were confirmed by the reported literature [33-36]. From Figure 5.15, it can be seen that all the spectra are

relatively similar and no additional peaks are observed after regeneration, which implies that there is no chemical reaction occurred during the dissolution. The adsorption bands of regenerated cellulose from IL and IL/DMSO systems are shifted to higher wavenumbers, which hints for the disturbance of hydrogen bonds within the cellulose to some extent. The peak at 1429 cm^{-1} corresponds to the crystalline region of cellulose. This does not appear at 70 °C and 90 °C for IL/DMSO mixture. This attribution indicates that the crystallinity of regenerated cellulose is found to decrease after dissolution in IL/DMSO solvent mixture.

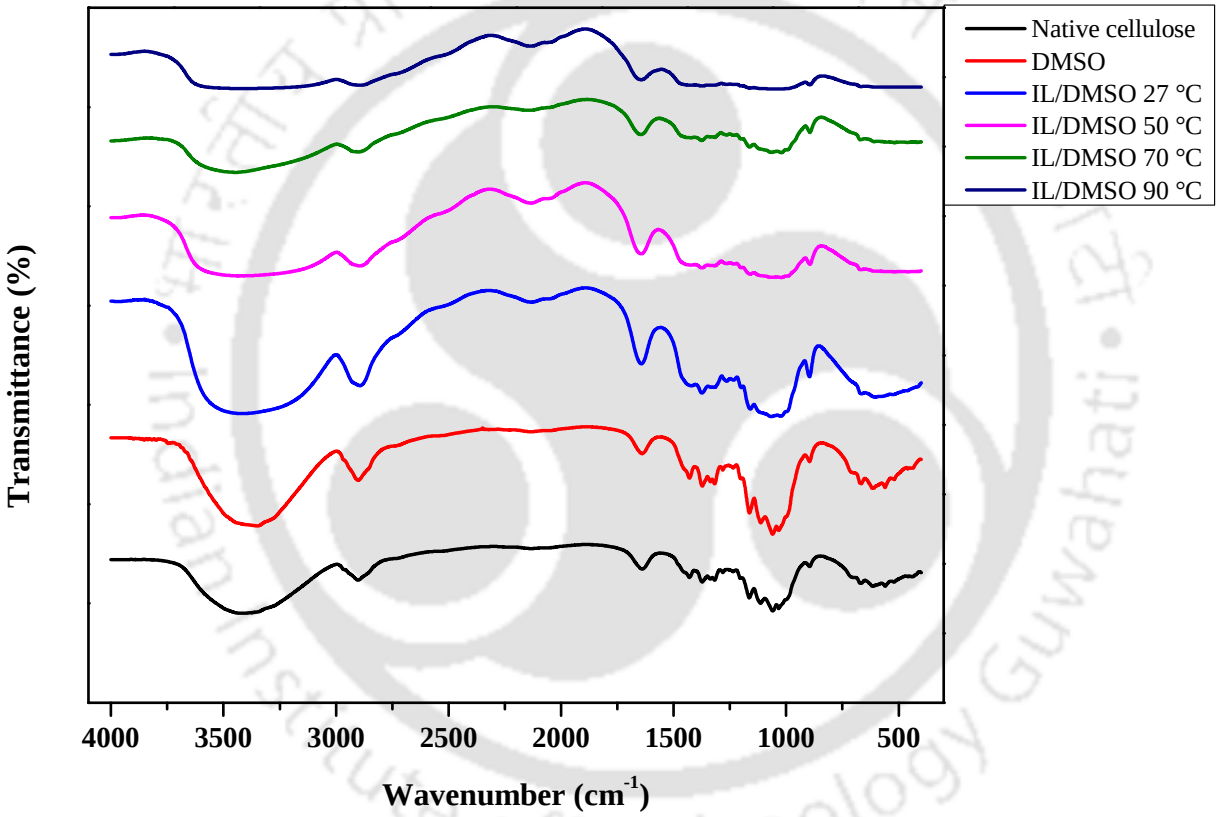

Figure 5.15: FTIR spectra of native cellulose and regenerated cellulose from DMSO and IL/DMSO at different temperatures

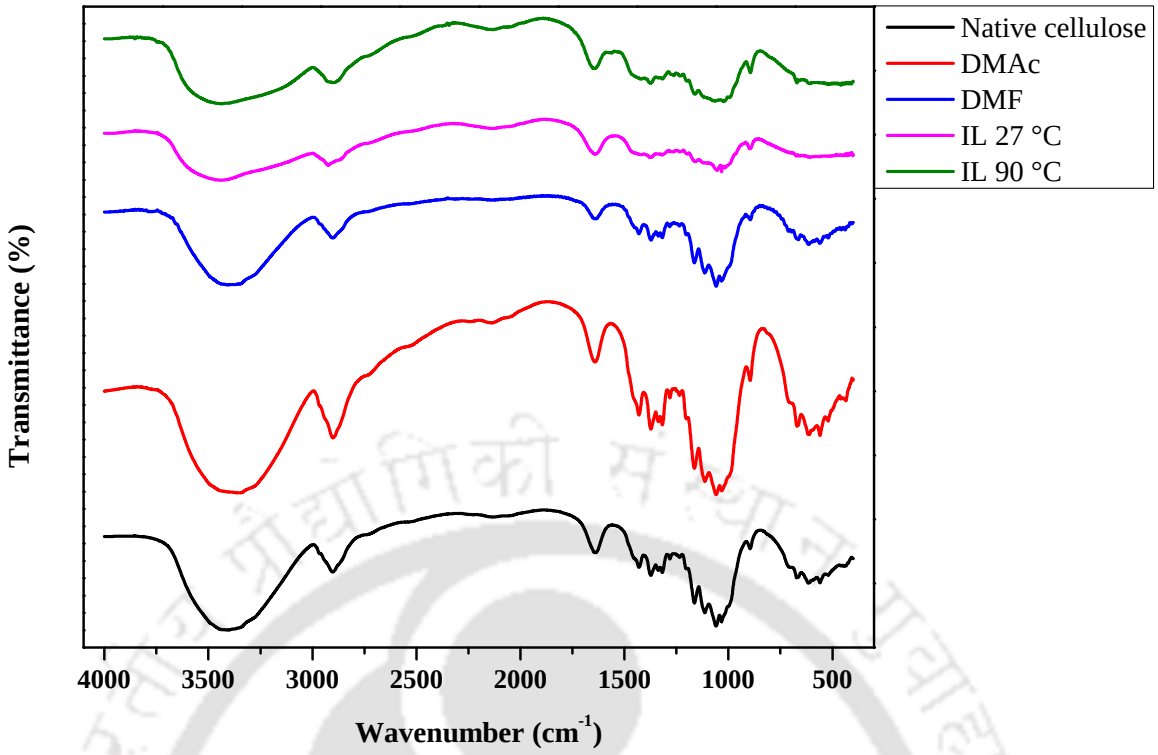

Figure 5.16: FTIR spectra of native cellulose and regenerated cellulose from aprotic cosolvents and IL

The XRD analysis of native and regenerated cellulose is given in Figures 5.17-5.19. The original cellulose is indicated as cellulose I at a diffraction angle (2θ) 15.1° and 22.6° [37,38]. The regenerated cellulose exhibits similar diffraction patterns as obtained in pure cellulose except for the cellulose from IL and IL/aprotic cosolvent mixture systems (Figures 5.18 and 5.19). The diffraction angle for cellulose in [Emim][OAc]/aprotic cosolvents is observed at 12.3° and 20.35°. This indicates that the transformations of cellulose I to cellulose II occurs after the dissolution of cellulose [33,36]. Whereas, in the case of IL/protic solvent system, the peaks at 22.65° and 15.15° are similar to that of original cellulose (Figure 5.19). The result of XRD patterns suggests that the crystallinity of cellulose found to decrease after dissolutions with IL and IL/aprotic solvents. On the other hand, IL/protic solvents do not show a similar effect.

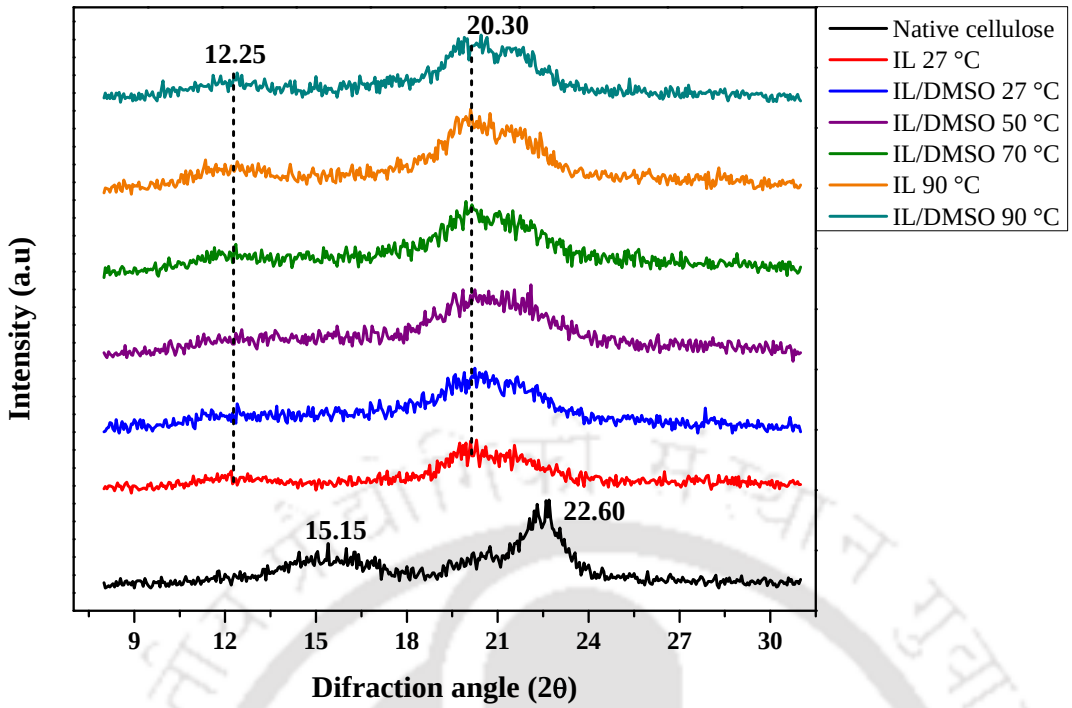

Figure 5.17: XRD patterns of native cellulose and regenerated cellulose form IL ([Emim][OAc]) and IL/DMSO (R_{DMSO} = 2) at different temperatures

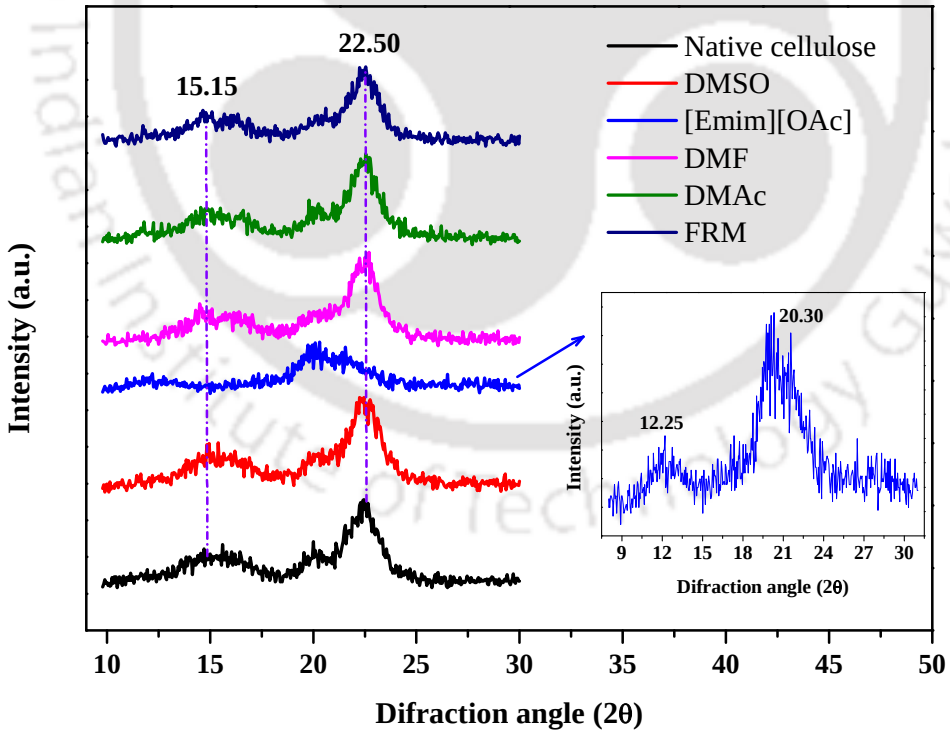

Figure 5.18: XRD patterns of native and regenerated cellulose from IL and cosolvents at room temperature (27 °C). A cosolvent doesn't have a significant effect on cellulose dissolution process

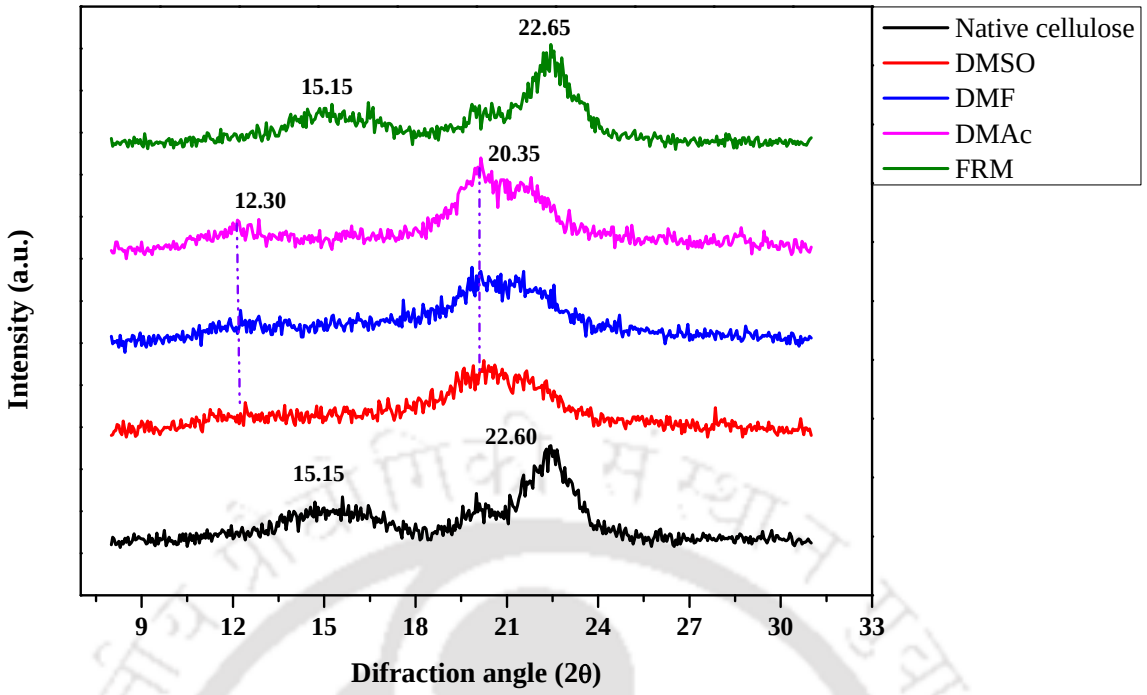

Figure 5.19: XRD patterns of native and regenerated cellulose from [Emim][OAc]/ different cosolvents ($R_{cosolvent}$ = 2) at room temperature (27 °C)

TGA analysis was also performed to check the thermal decomposition behavior of regenerated cellulose. Figure 5.20 shows the thermal decomposition profiles of original and regenerated cellulose from [Emim][OAc]/DMSO (R_{DMSO} = 2) at 27 °C. No extra peak was observed in the regenerated cellulose which implies that the cellulose was successfully regenerated. The thermal stability of regenerated cellulose (342.6 °C) was lower than original cellulose (348.7 °C). This decrement may be due to the partial destruction of the crystalline part in the cellulose. Furthermore, TGA analysis was performed for the pure IL, DMSO, and IL/DMSO (R_{DMSO} = 2) to understand the thermal stability of solvents (Figure 5.21). In the isolated molecules, the [Emim][OAc] has a higher thermal stability (244.3 °C) than DMSO (143.3 °C). The stability of IL and DMSO are also not influenced by the mixture of [Emim][OAc] and DMSO, which demonstrated that no chemical reaction occurred between DMSO and IL.

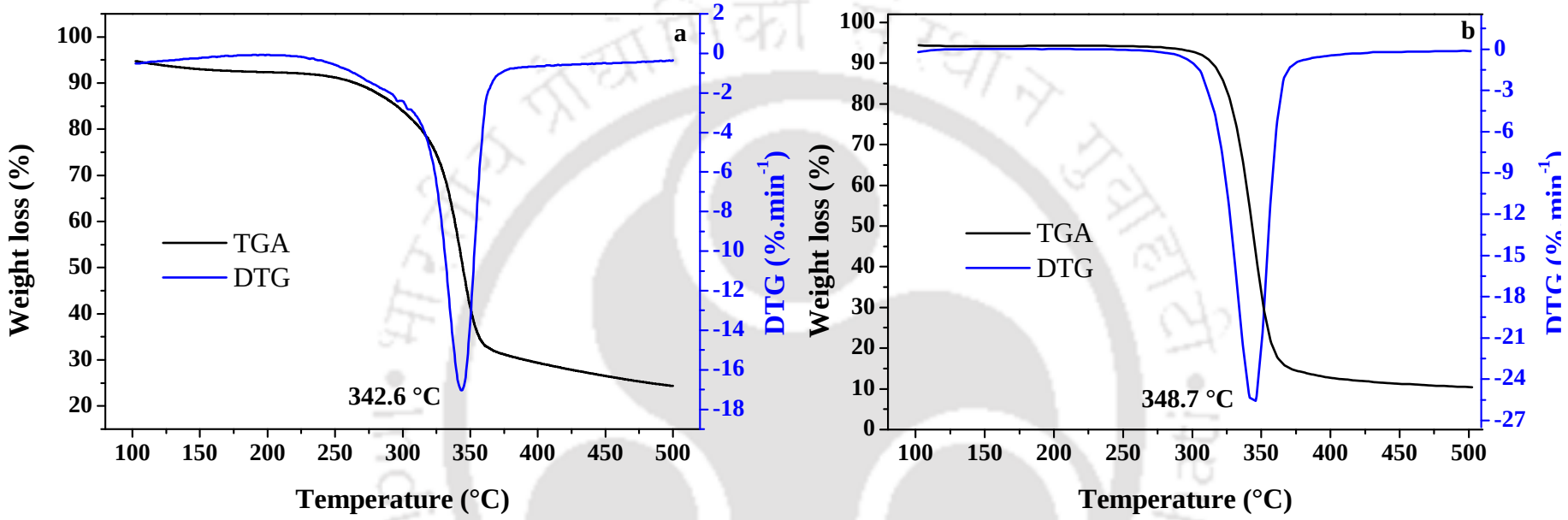

Figure 5.20: Thermal decomposition profiles of (a) regenerated cellulose from [Emim][OAc]/DMSO (*R* = 2) at room temperature and (b) original cellulose

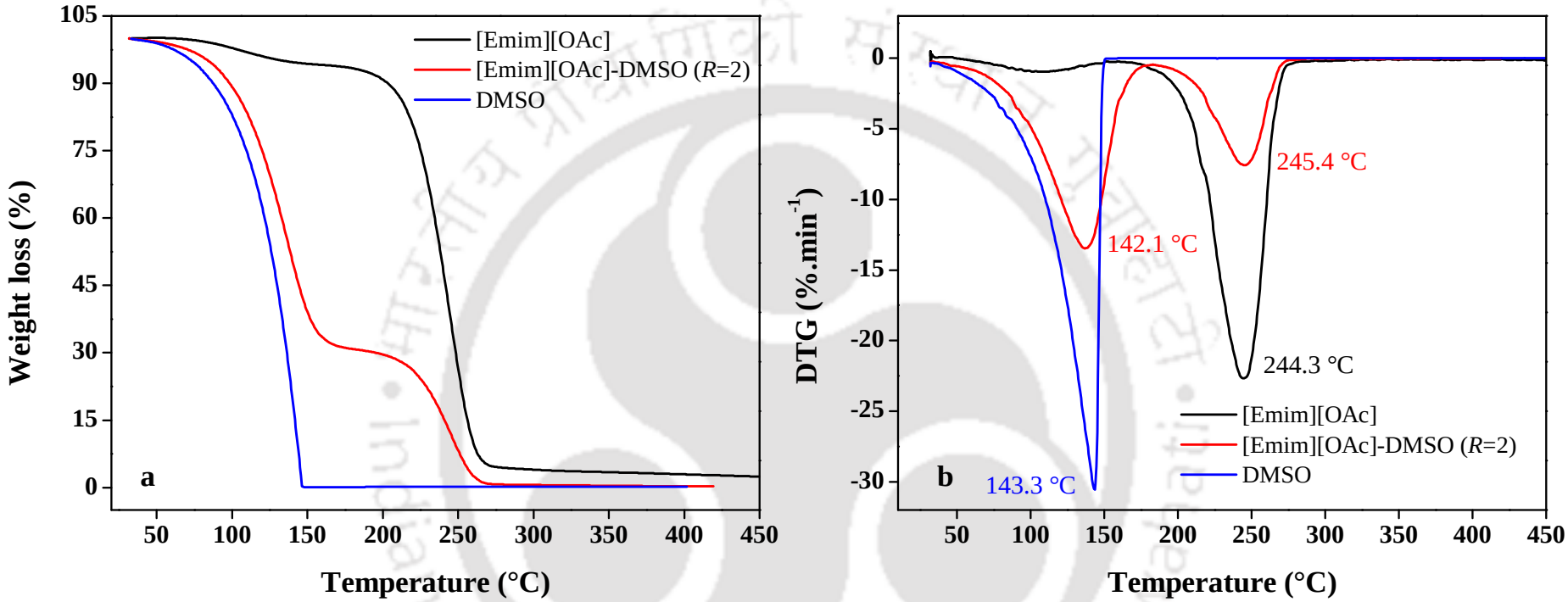

Figure 5.21: Thermal decomposition profiles of different solvent systems (a) TGA, (b) DTG

5.5 Summary

In summary, the present chapter reports the effects of IL and IL/cosolvent mixtures for the cellulose dissolution at 27 °C to 90 °C by MD simulations. This is further complemented by experimental studies. Aprotic solvents (DMSO) are found to be good candidates for the dissolution of cellulose in ILs at a molar ratio of two (R_{DMSO} = 2). With the addition of cosolvent to IL, the strong association pairs of ions would be partially destroyed thereby releasing more number of free cations and anions from IL. The dissociated free anions would then interact with cellulose and increase the solubility of cellulose. The protic solvents could reduce the interactions between cation and anions very efficiently. However, the $[OAc]^-$ anion found to be preferentially solvated by protic solvents through strong (N-H…O) hydrogen bond. On the other hand, the aprotic solvents form weak hydrogen bond (C-H…O) with $[OAc]^-$ and $[Emim]^+$ cations thereby releases more number of free ions. The free ions found to readily interact with cellulose leading to an increase in cellulose solubility. The interaction energies, RDF plots, and coordination numbers of cellulose-[Emim][OAc]/cosolvent systems also revealed the same mechanism. Further, the XRD patterns of regenerated cellulose suggested that the IL/aprotic solvents mixtures could disturb the cellulose crystalline structure. In summary, it is suggested that the solubility of cellulose is mainly determined by the free concentration of anions in the IL. Eventually, aprotic solvents are the recommended choice for the dissolution of cellulose in IL/cosolvent mixtures. On the other hand, the protic solvents can be utilized for the recovery of cellulose in ILs.

References

[1] Barthel S, Heinze T. Acylation and carbanilation of cellulose in ionic liquids. Green Chem 2006;8:301-6.

[2] Mohan M, Goud VV, Banerjee T. Solubility of glucose, xylose, fructose and galactose in ionic liquids: Experimental and theoretical studies using a continuum solvation model. Fluid Phase Equilib 2015;395:33-43.

[3] Froschauer C, Hummel M, Iakovlev M, Roselli A, Schottenberger H, Sixta H. Separation of hemicellulose and cellulose from wood pulp by means of ionic liquid/cosolvent systems. Biomacromolecules 2013;14:1741-50.

[4] Brandt A, Hallett JP, Leak DJ, Murphy RJ, Welton T. The effect of the ionic liquid anion in the pretreatment of pine wood chips. Green Chem 2010;12:672-9.

[5] Andanson J-M, Bordes E, Devémy J, Leroux F, Pádua AAH, Gomes MFC. Understanding the role of co-solvents in the dissolution of cellulose in ionic liquids. Green Chem 2014;16:2528-38.

[6] Xu A, Cao L, Wang B, Ma J. Dissolution Behavior of Cellulose in IL + DMSO Solvent: Effect of Alkyl Length in Imidazolium Cation on Cellulose Dissolution. Adv Mater Sci Eng 2015;2015:1-4.

[7] Huo F, Liu Z, Wang W. Cosolvent or antisolvent? A molecular view of the interface between ionic liquids and cellulose upon addition of another molecular solvent. J Phys Chem B 2013;117:11780-92.

[8] Parthasarathi R, Balamurugan K, Shi J, Subramanian V, Simmons BA, Singh S. Theoretical Insights into the Role of Water in the Dissolution of Cellulose Using IL/Water Mixed Solvent Systems. J Phys Chem B 2015;119:14339-49.

[9] Xu A, Zhang Y, Zhao Y, Wang J. Cellulose dissolution at ambient temperature: role of preferential solvation of cations of ionic liquids by a cosolvent. Carbohydr Polym 2013;92:540-4.

[10] Frisch MJ, Trucks GW, Schlegel HB, Scuseria GE, Robb MA, Cheeseman JR, et al. Gaussian 03. revision C. 02 ed. Wallingford, CT: Gaussian, Inc.; 2004.

[11] Ding ZD, Chi Z, Gu WX, Gu SM, Liu JH, Wang HJ. Theoretical and experimental investigation on dissolution and regeneration of cellulose in ionic liquid. Carbohydr Polym 2012;89:7-16.

[12] Mohan M, Balaji C, Goud VV, Banerjee T. Thermodynamic Insights in the Separation of Cellulose/Hemicellulose Components from Lignocellulosic Biomass Using Ionic Liquids. J Solution Chem 2015;44:538-57.

[13] Boys SF, Bernardi F. The calculation of small molecular interactions by the differences of separate total energies. Some procedures with reduced errors. Mol Phys 1970;19:553-66.

[14] Guvench O, Greene SN, Kamath G, Brady JW, Venable RM, Pastor RW, et al. Additive empirical force field for hexopyranose monosaccharides. J Comput Chem 2008;29:2543-64.

[15] Guvench O, Hatcher ER, Venable RM, Pastor RW, Mackerell AD. CHARMM Additive All-Atom Force Field for Glycosidic Linkages between Hexopyranoses. J Chem Theory Comput 2009;5:2353-70.

[16] Gross AS, Bell AT, Chu JW. Thermodynamics of cellulose solvation in water and the ionic liquid 1-butyl-3-methylimidazolim chloride. J Phys Chem B 2011;115:13433-40.

[17] Phillips JC, Braun R, Wang W, Gumbart J, Tajkhorshid E, Villa E, et al. Scalable molecular dynamics with NAMD. J Comput Chem 2005;26:1781-802.

[18] Deleeuw SW, Perram JW, Smith ER. Simulation of Electrostatic Systems in Periodic Boundary-Conditions. 3. Furture Theory and Applications. Proc R Soc London, Ser A 1983;388:177-93.
[19] Martinez L, Andrade R, Birgin EG, Martinez JM. PACKMOL: a package for building initial configurations for molecular dynamics simulations. J Comput Chem 2009;30:2157-64.
[20] Humphrey W, Dalke A, Schulten K. VMD: Visual molecular dynamics. J Mol Graphics 1996;14:33-8.
[21] Zhao Y, Liu X, Wang J, Zhang S. Insight into the cosolvent effect of cellulose dissolution in imidazolium-based ionic liquid systems. J Phys Chem B 2013;117:9042-9.
[22] Lu B, Xu A, Wang J. Cation does matter: how cationic structure affects the dissolution of cellulose in ionic liquids. Green Chem 2014;16:1326-35.
[23] Tokuda H, Hayamizu K, Ishii K, Susan MABH, Watanabe M. Physicochemical Properties and Structures of Room Temperature Ionic Liquids. 1. Variation of Anionic Species. J Phy Chem B 2004;108:16593–600.
[24] Davis M, I., Hernandez ME. Excess Molar Volumes for N,N-Dimethylacetamide + Water at 25 .degree.C. J Chem Eng Data 1995;40:674-8.
[25] Banerjee T, Singh MK, Sahoo RK, Khanna A. Volume, surface and UNIQUAC interaction parameters for imidazolium based ionic liquids via Polarizable Continuum Model. Fluid Phase Equilib 2005;234:64-76.
[26] Hoiland H. Partial Molar Volumes of Biochemical Model Compounds in Aqueous Solution. In: Hinz HJ, editor. Thermodynamic Data for Biochemistry and Biotechnology. Germany: Springer-Verlag: Berlin; 1986. p. 17-44.
[27] Hanke CG, Atamas NA, Lynden-Bell RM. Solvation of small molecules in imidazolium ionic liquids: a simulation study. Green Chem 2002;4:107-11.
[28] Covington AK, Dickinson T. Physical Chemistry of Organic Solvent Systems. New York: Plenum Press; 1973.
[29] Okoturo OO, VanderNoot TJ. Temperature dependence of viscosity for room temperature ionic liquids. J Electroanal Chem 2004;568:167-81.
[30] Ghatee MH, Bahrami M, Khanjari N. Measurement and study of density, surface tension, and viscosity of quaternary ammonium-based ionic liquids ([N222(n)]Tf2N). J Chem Thermodyn 2013;65:42-52.
[31] Wang H, Gurau G, Rogers RD. Ionic liquid processing of cellulose. Chem Soc Rev 2012;41:1519-37.
[32] Maki-Arvela P, Anugwom I, Virtanen P, Sjöholm R, Mikkola JP. Dissolution of lignocellulosic materials and its constituents using ionic liquids—A review. Ind crop prod 2010;32:175-201.
[33] Xu A, Guo X, Xu R. Understanding the dissolution of cellulose in 1-butyl-3-methylimidazolium acetate+DMAc solvent. Int J Biol Macromol 2015;81:1000-4.
[34] Mohan M, Timung R, Deshavath NN, Banerjee T, Goud VV, Dasu VV. Optimization and hydrolysis of cellulose under subcritical water treatment for the production of total reducing sugars. RSC Adv 2015;5:103265-75.
[35] Mohan M, Banerjee T, Goud VV. Hydrolysis of bamboo biomass by subcritical water treatment. Bioresour Technol 2015;191:244-52.
[36] Liu Z, Sun X, Hao M, Huang C, Xue Z, Mu T. Preparation and characterization of regenerated cellulose from ionic liquid using different methods. Carbohydr Polym 2015;117:99-105.

[37] Oh SY, Yoo DI, Shin Y, Kim HC, Kim HY, Chung YS, et al. Crystalline structure analysis of cellulose treated with sodium hydroxide and carbon dioxide by means of X-ray diffraction and FTIR spectroscopy. Carbohydr Res 2005;340:2376-91.

[38] Park S, Baker JO, Himmel ME, Parilla PA, Johnson DK. Cellulose crystallinity index: measurement techniques and their mpact on interpreting cellulase performance. Biotechnol Biofuels 2010;3:1-10.

Chapter – 6

COSMO-RS Based Screening of Antisolvents for the Separations of Sugars from Ionic Liquids: Experimental and Molecular Dynamics Simulations

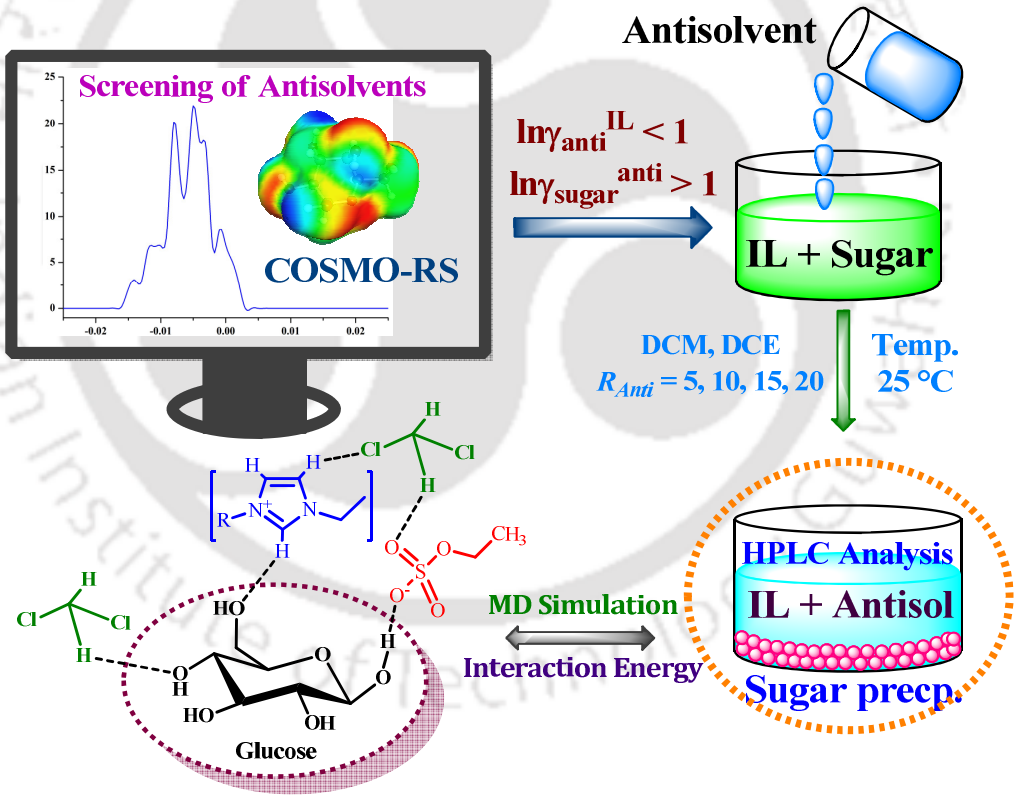

Published Article:

Mohan M, Banerjee, T., Goud V. V. COSMO-RS Based Screening of Antisolvents for the Separation of Sugars from Ionic Liquids: Experimental and Molecular Dynamic Simulations. *ACS Omega* (2018); 3: 7358−7370

6 Separations of Sugars from Ionic Liquids Using Antisolvents

In the earlier chapters, we have discussed the dissolution of monosaccharides, disaccharides, and polysaccharides in ionic liquids. However, the recovery or separation of sugars from IL is not discussed. Therefore, the current chapter reports the computational and experimental facets of separation of carbohydrates from ILs using an antisolvent method. Initially, COSMO-RS model was employed to screen the suitable antisolvent for the separation of sugars from ILs. Thereafter, the selected antisolvents were used for precipitation experiments for the mixtures containing different sugars (i.e., glucose, xylose, fructose, and galactose) and ILs at different experimental conditions. The experimental conditions such as antisolvents, antisolvent to IL molar ratio, and temperature have also been investigated. Furthermore, MD simulations have been performed to understand the basic mechanism of sugar/IL separations using antisolvents.

6.1 Introduction

In recent years, the solubility of simple carbohydrates and sugar alcohols in ILs has been reported with frequency in the literature [1-6]. However, the recovery data of sugars and ILs from their mixtures is scarce. Separation of carbohydrates from ILs as well as its further recycling is extremely important for process economics in biorefineries using ILs. The recovery of IL is essential so to retain the economic feasibility due to the high prices associated with ILs. For the separation of ILs and polysaccharides, it is comparatively easy to precipitate polysaccharides from the IL solutions. However, separation of simple carbohydrates such as monosaccharides and sugar alcohols (xylitol or sorbitol) from ILs remains a stimulating task. There are few techniques which have been attempted for separation such as chromatographic method, aqueous biphasic systems (ABS), solid phase extraction and crystallization/precipitation using antisolvents [7-10].

Feng *et al.* (2011) have studied the separation of glucose from dimethyl phosphate anion based ILs by applying liquid chromatography. They achieved more than 90% of IL and glucose recovery [11]. Further, Mai *et al.* (2012) have separated glucose and xylose from [Emim][OAc] using simulated moving bed chromatography coupled with an ion-exclusion column. 71.38% of glucose, 99.37% of xylose and 98.92% of [Emim][OAc] were recovered from the aqueous mixtures. Despite being very effective, these chromatographic methods requires very expensive columns and this adds costs of operation [12]. Recently, Tonova (2012) have reported the use of ABS to separate xanthan and maltose from water/1-hexyl-3-methylimidazolium tetrafluoroborate and 3-methyl-1-octylimi-dazolium chloride/K_2HPO_4. To separate maltose from IL, the solution mixture was cooled down to 0 °C. It resulted in the formation of two liquid phases namely, an upper layer containing maltose, and IL-rich lower phase for IL recycling and utilization. ABS requires another additional non-volatile solvent to completely recover the sugars from the salt/sugar mixtures [7]. This can be achieved by using the antisolvent method or "solvent out". The antisolvent method has gained a lot of interest in the areas such as drug recovery, separation of nanoparticles, separation of taurine, and fractionation of biomass, and other applications [10,13-15].

Liu *et al.* (2011) and Hassan *et al.* (2013) have reported the potential of the antisolvent method to separate glucose from different ILs. The effect of various experimental variables such as temperature, antisolvent, ILs, antisolvent to IL molar ratio and water content have been investigated [16,17]. In addition, Carneiro *et al.* (2014) have studied the experimental separation of sugar and sugar alcohols from different IL/antisolvent mixtures at room temperatures by varying antisolvent to IL molar ratio (R) from 5 to 35. At optimal conditions, more than 80% of IL recovery and 83% of sugar removal was observed (R = 20) [10]. However, literature in the area of screening of antisolvents and their interactions with sugars and ILs is rather limited. Moreover, the exact physical mechanism of the separation of

carbohydrates from ILs by antisolvents is not established yet. Therefore in this chapter, we have attempted to deduce the application of antisolvents in the separation of sugars from ILs by applying both theoretical and experimental aspects.

6.2 Computational Details

6.2.1 COSMO-RS Model

COSMO-RS is a quantum chemical based solvation model was used for screening of a large number of solvents. The structures of sugars, antisolvents (organic solvents), anions and cations were drawn with the help of Avogadro freeware software [18]. The molecular geometries of all molecules were fully optimized by B3LYP/6-31G* *via Gaussian* 09 package. After molecular geometry optimization, the next step is to generate the COSMO file using the SCRF=COSMORS keyword with the final optimized structure. The detailed methodology of COSMO-RS calculations is described in chapter 2 and hence not reproduced here.

6.2.2 Molecular Dynamics Simulations

The microscopic interactions between the sugars (glucose, xylose, and fructose) and IL/antisolvent mixtures were studied by employing the MD simulations. The partial charges of all the studied molecules were attained by restrained electrostatic potential (RESP) charge derivation method [19]. For all the molecules, the generalized AMBER force field (GAFF) parameters were employed [20]. The generalized AMBER force field parameters were developed by Antechamber [21].

The MD simulations were performed with NAMD ver2.10 at constant temperature (25 °C) and atmospheric pressure using Langevin thermostat and Nose-Hoover Langevin barostat. The details of MD simulations are described in chapter 4 (section 4.2.2). The cut-off distance of 12 Å was kept to treat the long-range electrostatic interactions at a time step of 1 fs. The initial configuration of sugar-IL/antisolvents was prepared by PACKMOL in a cubic box with

a random distribution of molecules [22]. As described in chapter 4 (section 4.2.2), the MD simulation system was minimized for 1 ns and then gradually heated to its desired temperature (25 °C) for 0.5 ns. At the desired temperature, the system was then equilibrated for 10 ns under NPT and allowed the system converge to its experimental condition. Consequently, the production run lasted for 40 ns with NVT ensemble. At every 5 ps, the production run data was saved for structural analysis from the simulated trajectories using VMD software [23]. In the mixture of sugar-IL/antisolvent, the interaction energy and hydrogen bonds between IL-sugar and IL-antisolvent are calculated per mole of IL and for the sugar-antisolvent system, the interaction energy and hydrogen bonds are calculated per mole of sugar.

Table 6.1: List of compounds (monosaccharides, ionic liquids, and antisolvents) used in the experimental study with their chemical purity and application

Chemical Name	Chemical Formula	Mol. Wt. (g mol^{-1})	CAS No.	Purity (mass fraction)	Application
Glucose	$C_6H_{12}O_6$	180.2	50-99-7	≥0.995	Solute
Fructose	$C_6H_{12}O_6$	180.2	57-48-7	≥0.990	Solute
Xylose	$C_5H_{10}O_5$	150.1	58-86-6	≥0.990	Solute
Galactose	$C_6H_{12}O_6$	180.2	59-23-4	≥0.990	Solute
[Emim][SCN]	$C_7H_{11}N_3S$	169.25	331717-63-6	≥0.950	Solvent
[Emim][$EtSO_4$]	$C_8H_{16}N_2O_4S$	236.29	342573-75-5	≥0.950	Solvent
[Emim][$MeSO_3$]	$C_7H_{14}N_2O_3S$	206.26	145022-45-3	≥0.950	Solvent
DCM	CH_2Cl_2	84.927	75-09-2	≥0.995	Antisolvent
DCE	$C_2H_4Cl_2$	98.954	107-06-2	≥0.995	Antisolvent

6.3 Materials and Methods

6.3.1 Materials

Carbohydrates such as glucose, fructose, xylose, and galactose were purchased from Sigma-Aldrich, Germany. The ILs [Emim][SCN], [Emim][$EtSO_4$], and [Emim][$MeSO_3$] were

supplied by Sigma-Aldrich, Germany and were used without further purification. The antisolvents such as dichloromethane (DCM) and 1,2-dichloroethane (DCE) were purchased from Merck, India Pvt. Ltd. These three ILs and two antisolvents are selected based on the COSMO-RS screening results which will be discussed in the later section 6.4.1. The details of the chemicals used are given in Table 6.1.

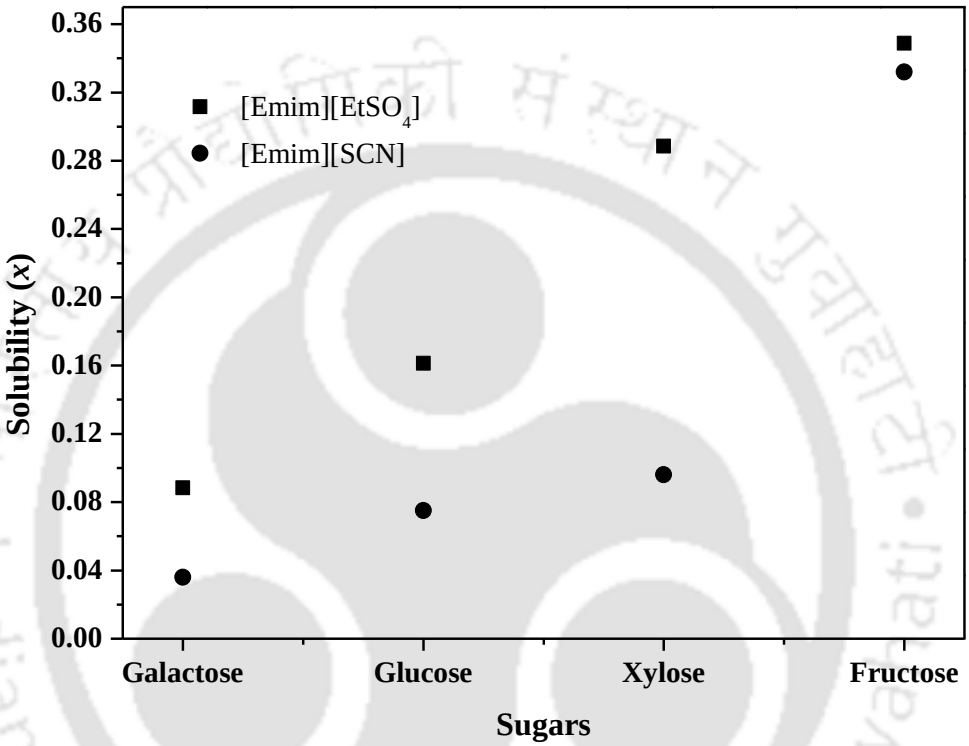

Figure 6.1: Saturated solubilities of monosaccharides in two different ILs at ambient temperature (25 °C). The solubility data of monosaccharides in [Emim][$EtSO_4$] was taken from Carneiro *et al.* (2012) [3]. For [Emim][SCN], the data was taken from chapter 2 (Table 2.8).

6.3.2 Experimental Procedure

The sugar solubility experiments were conducted at various temperatures in different ILs and the results are presented in Figures E.1 and E.2 (Appendix E) [3]. The saturated solubility data of sugars in ILs at 25 °C are reported in Figure 6.1 and used for the separation process. The mixture containing sugar+IL was used without any further pretreatment or drying. For the separation process, the specified amount of sugar+IL (2 g) mixture with a known composition

was mixed with the desired amount of antisolvent in 30 mL flask. The flask was sealed and the mixture was magnetically stirred for 8-10 h to make sure that all the carbohydrate are precipitated. The precipitation experiments were conducted at different sugar-IL/antisolvents, different antisolvent to IL molar ratios (R = 5, 10, 15, 20) and temperatures. All the experiments were performed in duplicate in order to assess the reproducibility of the results.

After precipitation, the carbohydrates were collected by a vacuum filtration and dried at 45 °C for 48 h. Subsequently, the vacuum filtrated liquid portion was collected and the solution was evaporated using rotary evaporator by heating above the boiling point of antisolvent and continued till constant weight was obtained. The recovered IL fraction was weighed and the final concentration of carbohydrates in IL were measured by HPLC. The final liquid solution was filtered with 0.2 µm nylon membrane filter paper (Diameter: 25 mm purchased from AXIVA, India) through a 0.22 µm syringe before HPLC analysis. The quantitative estimation of carbohydrates was carried out by HPLC (Perkin Elmer Series 200, USA) with Hi-Plex H column (7.7×300 mm) connected to guard column (Agilent, USA). The column oven temperature was kept at 65 °C with 0.5 ml min^{-1} flow rate. The samples were analyzed with a refractive index (RI) detector using 0.01 M H_2SO_4 as the mobile phase. The sampling and quantification of the liquid phase were performed in triplicate and average values are reported here. The percentage carbohydrate removal (%CR) was calculated according to the following equation:

$$\%CR = \left(1 - \frac{m_f C^f}{m_0 C^0}\right) \times 100 \qquad (6.1)$$

Where m_0 and m_f are the mass of the initial sample (IL + sugar) and mass of recovered IL, respectively. C_0 and C_f are the concentrations of sugar in the initial and recovered IL, respectively. The percentage of IL recovered (%ILR) is defined as:

$$\%ILR = \frac{m_f \left(100 - C^f\right)}{m_0 \left(100 - C^0\right)} \times 100 \qquad (6.2)$$

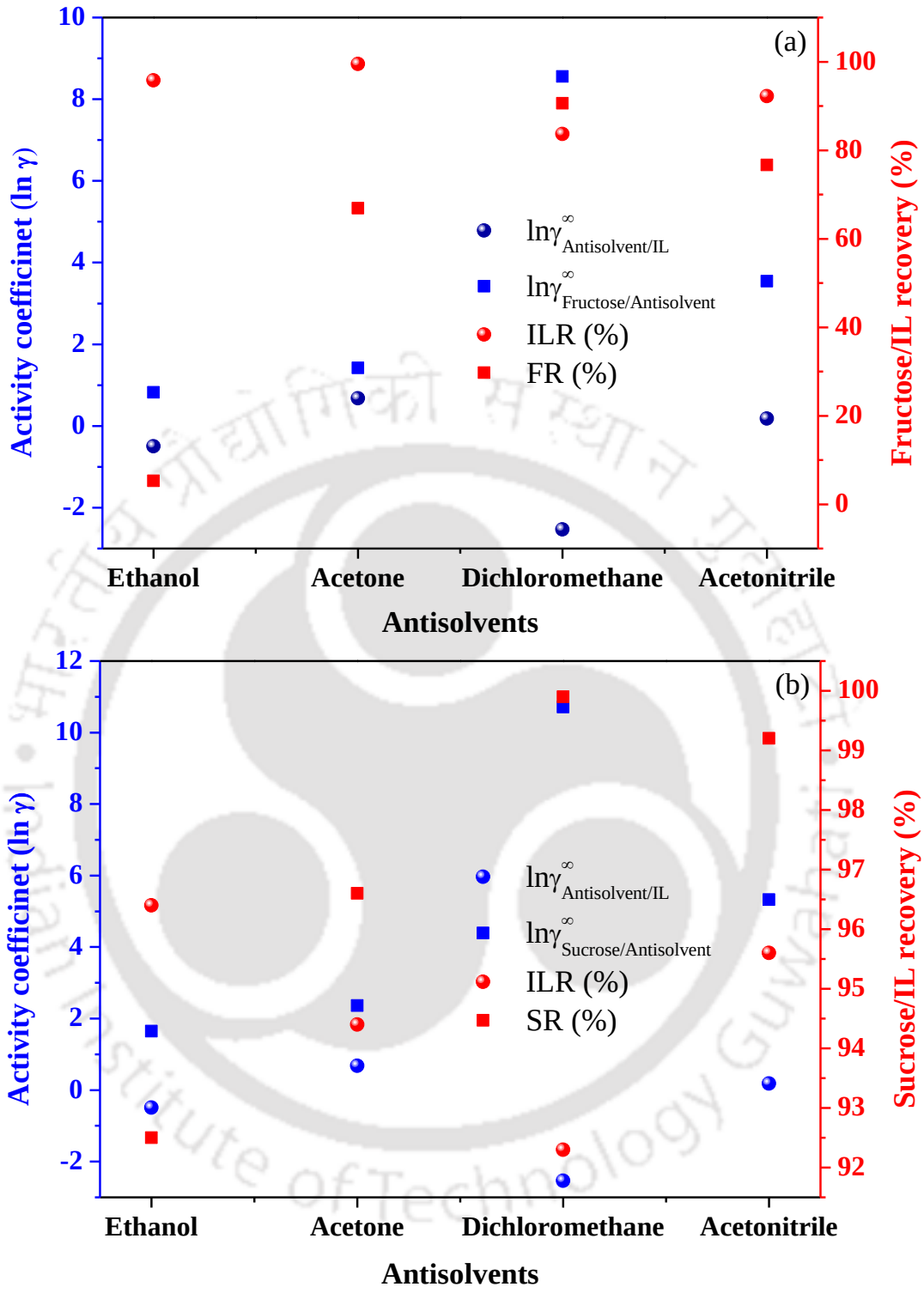

Figure 6.2: Correlation between predicted activity coefficient (COSMO-RS) and experimental recovery of (a) Fructose from [Emim][$EtSO_4$], and (b) Sucrose from [Emim][$EtSO_4$] using four different antisolvents. The antisolvent experimental data was taken from Carneiro *et al.* (2014) [10].

6.4 Results and Discussion

In the present chapter, the carbohydrate + IL mixture was separated by using an antisolvent method. The solubility data of carbohydrates in different ILs were taken from Carneiro *et al.* (2012) [3] (*i.e.*, for [Emim][$EtSO_4$]) and from chapter 2 for [Emim][SCN]), and the antisolvents were screened by COSMO-RS model. In the earlier chapters (2 and 3), we have successfully validated the COSMO-RS model with available experimental infinite dilution activity coefficients (IDAC) of different solutes in ILs. Furthermore, the COSMO-RS model was revalidated with experimental data of sugars (fructose and sucrose) separation from [Emim][$EtSO_4$] using different antisolvents reported in the literature [10]. The summary of the benchmarked predicted results are presented in Figure 6.2a (Fructose-[Emim][$EtSO_4$]/antisolvents) and Figure 6.2b (Sucrose-[Emim][$EtSO_4$]/antisolvents) as a function of logarithmic IDAC (ln γ).

From Figure 6.2, it is observed that lower the IDAC value (*i.e.*, ln $\gamma < 1$) of an antisolvent in IL, higher the recovery of IL. On the other hand, higher IDAC value of sugar in antisolvent results in the higher removal of sugar from IL. The results of the above validation study are in good agreement with experimental data. After the successful benchmarking study, screening exercise has been performed in two steps namely (a) screening of antisolvents in IL, and (b) screening of sugars in antisolvents. The results of both the study will then be used to choose the suitable antisolvent.

6.4.1 Screening of Antisolvents by COSMO-RS Model

The screening study was carried out using, 34 antisolvents, 11 different carbohydrates and 27 ILs (comprised of 1-ethyl-3-methylimidazolium $[Emim]^+$ cation and 27 different anions) by COSMO-RS model. The main aim of COSMO-RS screening study is to provide a suitable antisolvent(s) for the separation of sugar and sugar alcohols from ILs by computing IDAC values.

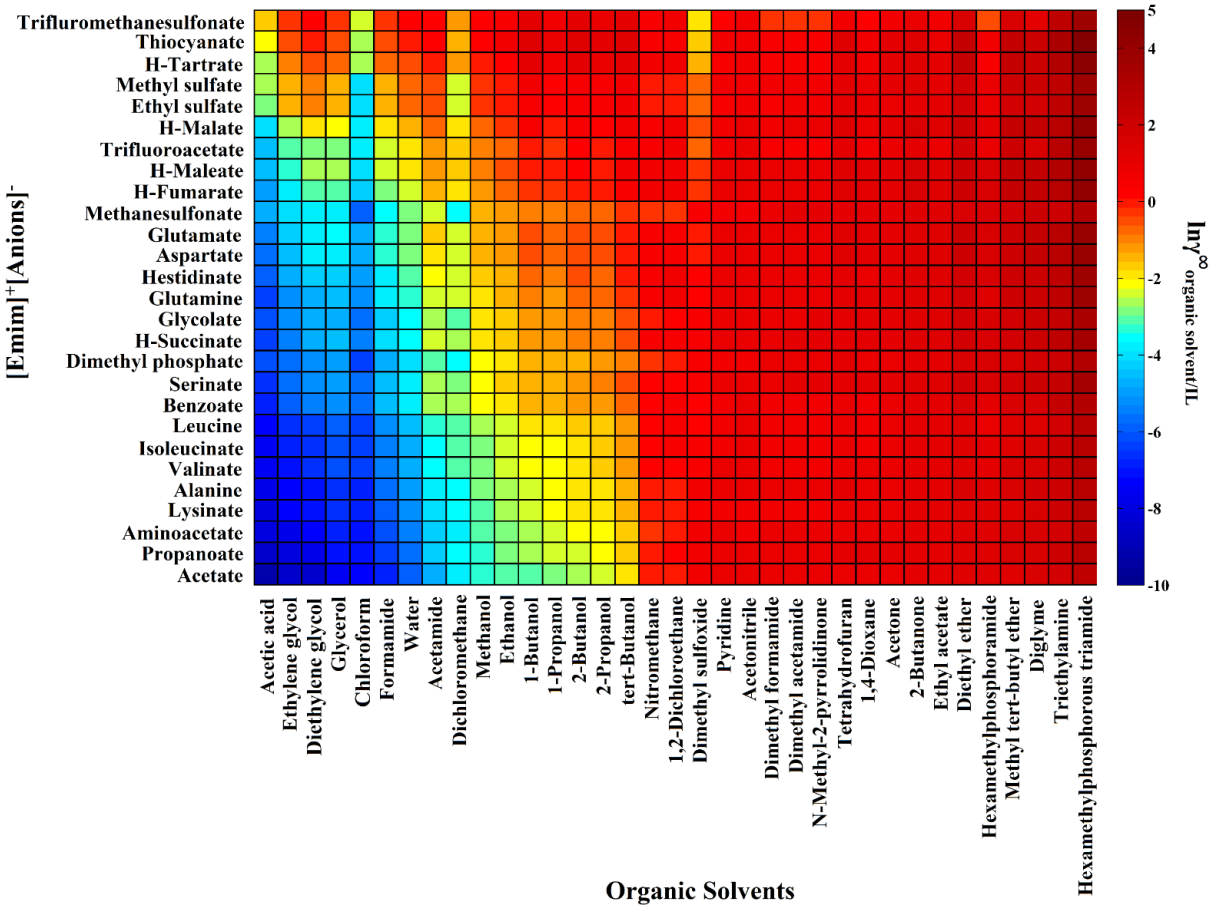

Figure 6.3: Graphical representation of the infinite dilution activity coefficients of 34 antisolvents (organic solvents) in 27 different ILs at 25 °C by COSMO-RS

Figure 6.3 and 6.4 represents the predicted logarithmic IDAC of 34 antisolvents. The logarithmic activity coefficient of antisolvents in ILs (Figure 6.3) and carbohydrates in antisolvents (Figure 6.4), at infinite dilution is considered together as a quantitative measurement for the solvation power of antisolvent. The antisolvents were sorted according to their miscibility capacity and arranged in such way that antisolvents with higher dissolving power (logarithmic negative values of γ *i.e.*, $\ln\gamma \leq 1$) are situated in the left portion of Figures 6.3 and 6.4, and the lower ones (positive values of $\ln\gamma$ *i.e.*, $\ln\gamma >> 1$) are situated at the right portion of Figures 6.3 and 6.4. Lower the activity coefficient values, greater is the tendency for the antisolvent to solvate the IL and carbohydrate. For separation process using an antisolvent method, the antisolvent should be miscible with IL ($\ln\gamma \leq 1$), but not solubilize the

carbohydrate ($\ln\gamma >> 1$). As can be seen from Figure 6.3, the antisolvents such as acetic acid, ethylene glycol, diethylene glycol, glycerol, chloroform, formamide, dichloromethane, and 1,2-dichloroethane are predicted to be miscible with ILs more efficiently. Whereas in the case of carbohydrate-antisolvent system (Figure 6.4), the antisolvents namely acetonitrile, nitromethane, dichloromethane, and 1,2-dichloroethane are predicted to be immiscible with carbohydrates. Therefore, according to the precipitation concept, the chosen antisolvent should be miscible with IL and should not solubilize the carbohydrate. Thus, the following antisolvents namely dichloromethane (DCM) and 1,2-dichloroethane (DCE) have been selected for both experiments and MD simulations.

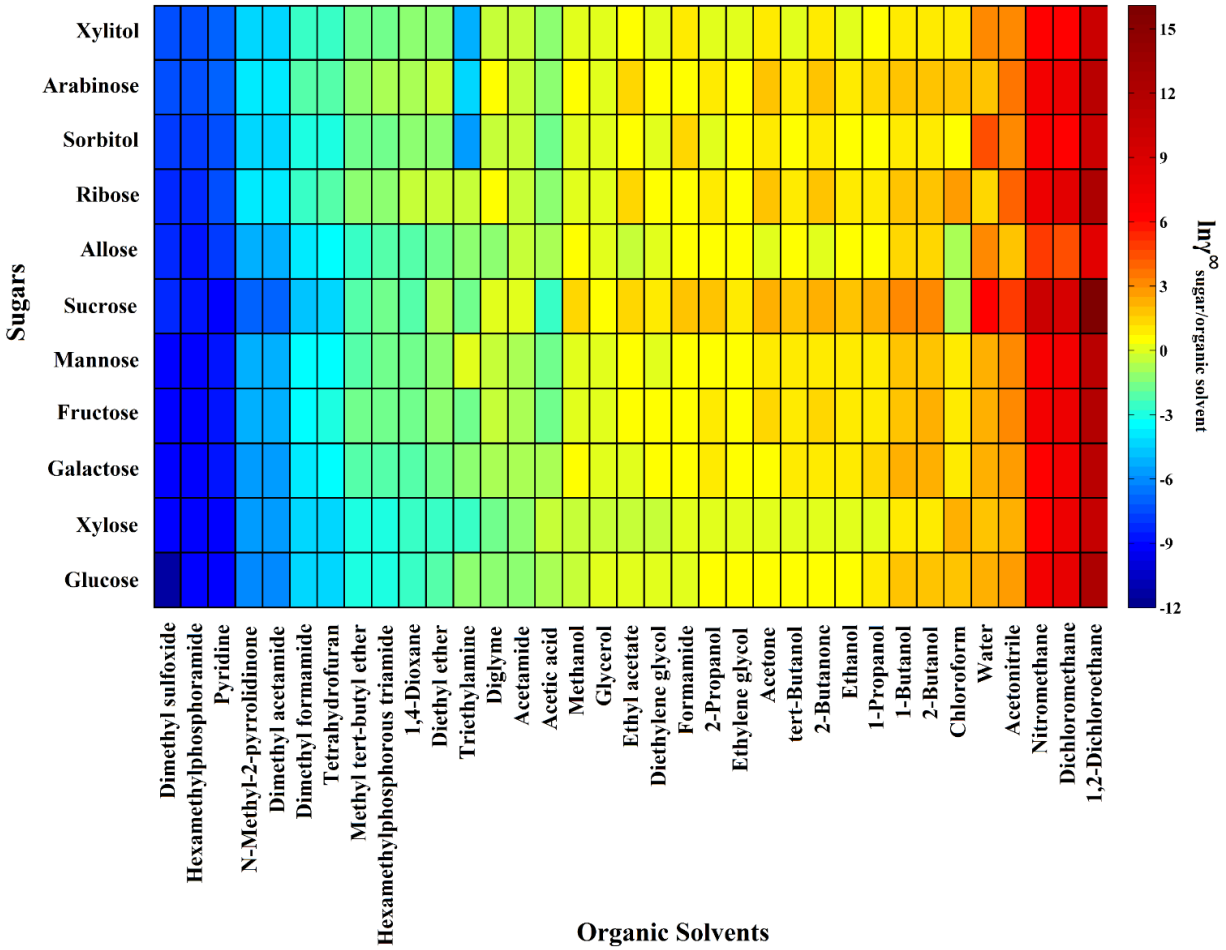

Figure 6.4: Graphical representation of the infinite dilution activity coefficients of 11 carbohydrates in 34 different antisolvents (organic solvents) at 25 °C by COSMO-RS

Moreover, a close look from Figures 6.3 and 6.4, nitromethane is also seemed to be a potential antisolvent similar to DCE, however, DCE was preferred owing to its lower boiling point and economic aspects. On the other hand, nitromethane gave less IDAC values of carbohydrates compared to DCE (for *e.g.*, ln γ of glucose in DCE is 12.37 whereas in the case nitromethane, it is 6.98). Hence, antisolvent nitromethane has been excluded from the separation experiments, although nitromethane could be used as a potential antisolvent in the carbohydrate separation process.

6.4.2 Separation of Sugars from ILs (Experimental Study)

After the successful screening of antisolvents using COSMO-RS model, the precipitation experiments were performed for sugars such as glucose, fructose, xylose, and galactose with ILs ([Emim][$EtSO_4$], [Emim][SCN], and [Emim][$MeSO_3$]) using DCM and DCE as antisolvents. As can be seen from Figure 6.3, the lower IDAC values from 1 *i.e.*, the blue shaded region, the better is the IL. Thus, [Emim][OAc] is the best IL. It should be noted that other than the solubility of IL and antisolvent, the recovery of sugar is also a critical issue. This is primarily done by heating the solution mixture to the boiling point of antisolvent under atmospheric conditions. So for a selection of IL and antisolvent pair, one should have negative values of ln γ (Figure 6.3) and highly positive values of ln γ (Figure 6.4) for sugar in antisolvent. The IL [Emim][OAc] is known to be a powerful solvent in the dissolution of biomass and its derived components namely cellulose, hemicellulose, disaccharides and monosaccharides [16,24,25]. In a preliminary experiment, the separation of glucose from [Emim][OAc] using DCM as an antisolvent, showed lower glucose removal (55%) and IL recovery (40%) percentages which could be due to the strong interactions between [Emim][OAc]-glucose. Hence, for that reason here results of [Emim][OAc] are not reported. The other ILs in the same series namely amino acid-based ILs were not easy to synthesize and

hence not considered for the separation study. Thus, the next set of ILs ([Emim][$EtSO_4$], [Emim][SCN], and [Emim][$MeSO_3$]) were used for the separation process.

It is also a fact that the selected ILs have already proven to be the best in the dissolution of sugars [3,5,6,16]. In the carbohydrate separation process, the monomeric sugars are difficult to recover as compared to disaccharides and oligosaccharides owing to its strong interactions and higher solubility in ILs. For example, the study of Carneiro *et al.* (2014), reported ≥ 93-99% removal of disaccharide *i.e.*, sucrose, whereas the glucose and fructose removal was only 8-75.3% and 5.3-90%, respectively [10]. Therefore, it is very much essential to explore the possibility of monomeric sugars recovery from ILs. The equilibrium solubility data of sugars in respective ILs are taken from chapter 2 and previous literature (Figure 6.1) except for glucose-[Emim][$MeSO_3$] system. The solubility of glucose in [Emim][$MeSO_3$] was measured at 25 °C (Table 6.2). Table 6.2 reports the IL recovery (%ILR) and sugar removal (%CR) with different sugar-IL-antisolvents mixtures at 25 °C and different $a_{ntisolvent}$ (Antisolvent to IL molar ratio). From Table 6.2, it can be observed that the fructose exhibits higher solubility than other sugars. The solubility difference mainly attributed due to the difference in their phase transition properties (such as melting temperature and heat of fusion values). Lower the melting temperature and heat of fusion value, higher the solubility of the solute in the respective solvents [3,5]. For the information, melting properties of investigated sugars are reported in chapter 2 (Table 2.1).

6.4.2.1 Effect of Antisolvent/IL Molar Ratio in Sugar Separation

The effect of antisolvent to IL molar ratio in sugar separation was studied by varying the ratio from R = 5 to R = 20 as shown in Table 6.2. From the Table 6.2 (for glucose-[Emim][$EtSO_4$]/DCM and glucose-[Emim][SCN]/DCM), it was seen that the recovery and removal percentage of ILs and carbohydrates were found to increase with an increase in the IL to antisolvent molar ratio. In the recovery of IL, a significant difference was observed with

increase in the antisolvent molar ratio. At higher antisolvent molar ratio (R = 20), the recovery of [Emim][$EtSO_4$] was about 93% for glucose-[Emim][$EtSO_4$]/DCM system. In the case of carbohydrate removal, the difference in %CR was minimal *i.e.*, 1% from R = 10 to 20. As expected, higher the molar ratio of antisolvent to IL, lower the solubility of carbohydrate in the mixtures.

Table 6.2: IL recovery (%ILR) and carbohydrate removal (%CR) with different sugar-IL-antisolvents at 25 °C and different antisolvent to IL molar ratios (R)[a]

IL/Antisolvent	Sugar	R	x_{sugar}[b]	IL		Carbohydrate	
				Recovery (%)	σ[c]	Removal (%)	σ[c]
[Emim][$EtSO_4$]/DCM	Glucose	5	0.161	76.45	2.01	96.86	1.14
		10	0.161	80.75	1.26	98.15	0.95
		15	0.161	88.46	1.47	98.46	0.74
		20	0.161	92.98	1.70	98.60	0.66
	Fructose	20	0.348	86.02	1.42	90.94	1.90
	Xylose	20	0.288	89.64	1.31	89.49	1.83
	Galactose	20	0.088	98.12	0.87	90.44	1.19
[Emim][$EtSO_4$]/DCE	Glucose	20	0.161	81.79	1.18	99.55	0.40
	Fructose	20	0.348	79.50	2.17	98.55	1.21
	Xylose	20	0.288	77.78	2.74	98.35	0.91
	Galactose	20	0.088	79.74	1.52	99.77	0.14
[Emim][SCN]/DCM	Glucose	10	0.075	81.92	1.80	97.30	0.83
		20	0.075	94.30	1.62	99.23	0.28
	Fructose	20	0.332	85.95	1.60	95.42	1.34
	Xylose	20	0.096	87.07	1.72	92.25	2.05
	Galactose	20	0.036	95.49	1.12	97.78	1.52
[Emim][$MeSO_3$]/DCM	Glucose	20	0.183	87.47	1.80	96.27	1.41

[a] Standard uncertainty for temperature and pressure are u (T) = 0.1 °C and u (p) = 1 kPa; The standard uncertainty for %ILR and %CR are U(ILR) = 1.58 % and U(CR) = 0.82 % at 95% confidence level; [b] Mole fraction of sugar in ionic liquid at 25 °C; [c] Standard deviation

As per the findings of Carneiro *at al.* (2014), an antisolvent molar ratio greater than *R*=20 did not show a significant effect on the recovery and removal percentage of both IL and carbohydrate [10]. It was also reported that in case of ethanol as an antisolvent, the lower molar ratio was preferred since the solubility of carbohydrate in pure ethanol is higher as compared with DCM, acetonitrile, and DCE. Therefore, in the solubility aspects, *R* should not be too high value as it may lead to a lower carbohydrate removal. For this purpose, ethanol can only be used as an antisolvent at lower molar ratios *i.e.*, $R < 3$ for efficient carbohydrate removal [10]. Therefore, the optimum value of *R* should be a balance between separation performance and antisolvent loading. Thus, $R = 20$ was considered as the optimal molar ratio for the separation of carbohydrates from ILs.

For further investigation, three important steps are involved in the experimental design for the separation of sugars from ILs. In the first stage, the separation experiments are performed with ILs [Emim][$EtSO_4$] and [Emim][SCN] in the presence of DCM antisolvent with four different sugars. This step provides the effect of different sugars in the separation process. In the second stage, the IL [Emim][$MeSO_3$] has been tested with glucose in DCM antisolvent to understand the effect of different ILs. Finally to understand the effect of antisolvents, two different antisolvents namely DCM and DCE have been tested for four different sugars using [Emim][$EtSO_4$] at $R = 20$. The selection of all the combination is comprehensive. In Table 6.2, the experimental data are reported for 13 systems out of 24 (3 ILs × 2 antisolvents × 4 sugars). So as to avoid all the combinations, representative combinations were chosen.

6.4.2.2 Effect of Different Sugars

The effect of different sugars such as glucose, xylose, fructose, and galactose on the separation was studied with [Emim][$EtSO_4$] and [Emim][SCN] using DCM as an antisolvent. As can be seen from Table 6.2, the recovery percentage of ILs in galactose-based system was higher than

other sugars. This is mainly due to the weaker interactions and lower solubility of galactose in ILs. Galactose exhibits higher melting properties than other sugars which leads to lower solubility. It should be noted that lower solubility of a solute in the solvent causes weaker interactions. On contrary to galactose, the recovery percentage of ILs in fructose based systems was lower than other sugars. This was due to the lower melting properties of fructose. Therefore, higher solubility of sugar in IL yielded lower recovery of IL (see Table 6.2).

Further, the recovery percentage of [Emim][$EtSO_4$] and [Emim][SCN] ILs with the mixture of different sugars was also assessed. Except for glucose based system, the recovery percentage of [Emim][$EtSO_4$] IL was found to be higher than [Emim][SCN] at R = 20 (Table 6.2). The solubility of carbohydrates in [Emim][SCN] was lower than [Emim][$EtSO_4$] due to the weaker interactions between carbohydrates and [Emim][SCN]. Despite this fact, the recovery percentage of [Emim][$EtSO_4$] in DCM was higher compared to [Emim][SCN] which could be due to the disturbance in the hydrogen bonding network between carbohydrates and [Emim][$EtSO_4$] (see Table E.1 in Appendix E). As can be seen from Table E.1, with the addition of antisolvent to the sugar-IL system, H-bonding and interaction energy values were found to be significantly decreased. Furthermore, the activity coefficient of [Emim][$EtSO_4$] in DCM was also lower than [Emim][SCN] (Table 6.3). This leads to higher miscibility of [Emim][$EtSO_4$] in DCM, resulting in percentage higher recovery.

On the other hand, the removal percentage of glucose was higher than other sugars even though glucose exhibits lower melting properties than galactose. Here, COSMO-RS results also suggested that the $\ln\gamma$ values of glucose in DCM and DCE antisolvents are higher than other sugars (*i.e.*, as per Table 6.3, higher the IDAC value lower the interactions). Further, from Table 6.2, it can be observed that the removal of xylose was lower than fructose although fructose had higher solubility in ILs. This is due to the fact that two parameters are actually affecting the removal of carbohydrates from ILs *i.e.*, the sugar/IL interaction and

sugar/antisolvent interactions. If the sugar/IL interactions are weaker and sugar/antisolvent interactions are stronger, it leads to lower removal of carbohydrate. Thus, lower the interaction energy value, lesser the removal of sugar. Xylose has weaker interactions with ILs and stronger interactions with antisolvents (Table 6.3) as compared to fructose. Therefore, xylose achieved a lower removal percentage.

Table 6.3: COSMO-RS predicted logarithmic infinite dilution activity coefficient (ln γ) of sugar and IL molecules in different antisolvents

Sl. No.	IL/Sugar	DCM	DCE
1.	[Emim][$MeSO_3$]	-3.58	-0.32
2.	[Emim][$EtSO_4$]	-2.42	0.05
3.	[Emim][SCN]	-1.42	0.46
4.	Glucose	8.06	12.37
5.	Fructose	7.50	11.46
6.	Xylose	7.32	10.76
7.	Galactose	7.16	11.94

6.4.2.3 Effect of Different ILs in Sugar Separation

ILs such as [Emim][$EtSO_4$], [Emim][SCN], and [Emim][$MeSO_3$] have also been used to separate glucose from the mixture in presence of DCM as an antisolvent. The ILs [Emim][$MeSO_3$] and [Emim][$EtSO_4$] gave higher solubility (x_{sugar}) of glucose at 25 °C in the studied systems, indicating that these ILs have a strong dissolving capacity for glucose. However, [Emim][SCN] has higher percentage recovery compared to that of other two ILs when they are mixed with glucose in the presence of DCM. On the other hand, the COSMO-RS results suggest that [Emim][$MeSO_3$] and [Emim][$EtSO_4$] have lower activity coefficient value in DCM as compared to [Emim][SCN] (Table 6.3) resulting in lower recovery of IL.

This is due to the fact that [Emim][$MeSO_3$] and [Emim][$EtSO_4$] have strong interactions with glucose than DCM. Therefore, the recovery percentage of [Emim][$MeSO_3$] and [Emim][$EtSO_4$] was lower than [Emim][SCN]. Whereas, in the case of glucose removal, it does not have a general trend. The lower removal percentage of glucose was obtained in [Emim][$MeSO_3$] due to the higher solubility of glucose. However, the percentage of glucose removal in all the three different ILs gave a similar value (~97-99%).

6.4.2.4 Effect of Different Antisolvents

Two different antisolvents namely DCM and DCE were tested for experimental separation of four different sugars from [Emim][$EtSO_4$] at R = 20. From Table 6.2, it can be observed that there is a remarkable difference in the ability of antisolvents to recover [Emim][$EtSO_4$] from these mixtures. As compared with recovery percentage of [Emim][$EtSO_4$] in both antisolvents, a significant difference was not observed in the removal of carbohydrates. The results from Table 6.2 indicates that the recovery percentage of [Emim][$EtSO_4$] was higher in DCM compared to DCE antisolvent. This may be due to the higher interaction between [Emim][$EtSO_4$] and DCM. On the other hand, the removal percentage of carbohydrate was higher in DCE compared to DCM. This ascription was attained due to weaker interactions between the carbohydrates and DCE, which causes lower solubility of carbohydrates in DCE antisolvent.

It should be noted that the investigated antisolvents DCM and DCE are not environmentally benign as compared to ethanol. But, the separation of these antisolvents from the IL phase can be easily performed by using distillation at lower pressure. However, when ethanol is used as an antisolvent in the separation of carbohydrates from ILs, the removal percentage of carbohydrates was lower due to higher interactions between ethanol and carbohydrates [10]. Recently, Hassan *et al.* (2013) performed the glucose dissolution in different ILs and further extracted glucose from ILs using the antisolvent method [17]. 80%

of glucose was extracted from [Emim][SCN] in the presence of ethanol as an antisolvent, whereas in case of acetonitrile, 90% of glucose was extracted from [Emim][SCN] at R = 20. In the present work, 97.3% and 99.23% of glucose were recovered from [Emim][SCN] with DCM antisolvent at R = 10 and 20, respectively. While for ethanol, glucose recovery was 37.15% at R = 10.

In another study, Carneiro *et al.* (2014) investigated the separation of carbohydrates from ILs using an antisolvent method [10]. They have reported fructose recovery of 5.3% from [Emim][$EtSO_4$], and glucose recovery of 8.1% from [Emim][TFA] using ethanol as an antisolvent (at R = 20). Moreover, for acetone and acetonitrile as antisolvent, fructose recovery was 67% and 76.7% from [Emim][$EtSO_4$]. On the other hand, DCM and DCE showed fructose and glucose recovery of 90% and 99% from [Emim][$EtSO_4$], respectively. Further, the COSMO-RS predictions (Figure 6.3 and 6.4) also proves the fact that lower ln γ value of sugars in ethanol results in higher solubility of sugar in ethanol. Therefore, in the present study, DCM and DCE solvents have been chosen to separate carbohydrates from ILs.

6.4.2.5 Effect of Temperature on Sugar Separation

Furthermore, the effect of temperature in the separation of glucose from [Emim][SCN]/DCM (at R = 20) mixture was studied at different temperatures (25 °C, 30 °C, and 40 °C). As can be seen from Figure 6.5, the recovery percentage of [Emim][SCN] and removal percentage of glucose was found to decrease with increasing temperature. The increase of temperature will promote the thermal motion of molecules in the entire system and the volatility of non-volatile solute [26] resulting in an increased solubility of glucose in [Emim][SCN]/DCM mixtures. Hence, low temperature is favorable for the separation of carbohydrates from ILs. Liu *et al.* (2013) also reported similar behavior during their study on the extraction of glucose from different ILs using ethanol as antisolvent [16].

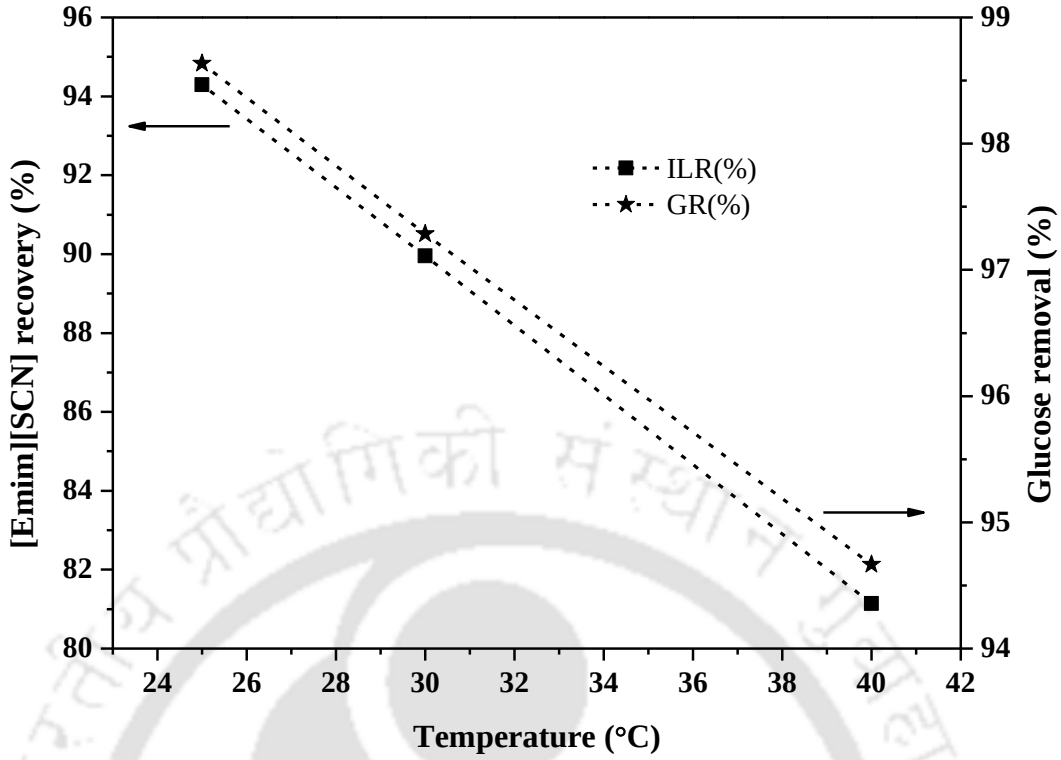

Figure 6.5: Effect of temperature on the separation between glucose and [Emim][SCN] in the presence of DCM at R = 20

6.4.3 Results of Molecular Dynamics Simulations

Apart from experimental evidence, the MD simulations were also carried out to understand the structural properties of carbohydrates with ILs and antisolvents *via* interaction energies (I.E.), average hydrogen bonding (H-bonds) and coordination numbers (CN). For the MD simulation system, carbohydrates namely glucose, xylose and fructose are considered.

6.4.3.1 Non-Bonded Interaction Energy

The MD simulated non-bonded interaction energy is the sum of electrostatic and van der Waals energies. Table 6.4 reports the interaction energies of glucose with three different IL/antisolvent mixtures at 25 °C and R = 20. The interaction energy results of glucose are compared with other two carbohydrate systems *i.e.*, xylose-[Emim][$EtSO_4$]/DCM and fructose-[Emim][$EtSO_4$]/DCM.

6.4.3.2 Interactions of Different IL/Antisolvents with Glucose

Table 6.4 shows the non-bonded interaction energies of anions, $[Emim]^+$, and antisolvents with glucose. As can be seen from Table 6.4, the anions possessed higher interaction energy with glucose and DCM compared to $[Emim]^+$ cation. The higher interaction energy attributed to the formation of stronger intermolecular hydrogen bonding between glucose-anion (1.75 Å) and anion-DCM (≤ 2.15 Å) pairs (Figure E.3). For glucose-$[Emim]^+$, glucose-DCM, and $[Emim]^+$-DCM systems, the intermolecular distances were found within the range of 2.20-3.05 Å (Figure E.3) indicating a weak hydrogen bonding. Which reveals that the anionic part of IL plays a predominating role as compared to the cation. The interaction energy between glucose-[Emim][$MeSO_3$] was found to be higher than [Emim][$EtSO_4$] and [Emim][SCN]. From the experimental data, the solubility of glucose (x) was reported to be higher in [Emim][$MeSO_3$] than other two ILs (Table 6.2). A similar result is reflected in their interaction energies *i.e.*, higher the interaction energy, more the solubility. However, the removal percentage of glucose was less in [Emim][$MeSO_3$] (96%) due to the stronger interaction energy between glucose and [Emim][$MeSO_3$]. Further, the interaction energy between glucose and DCM was higher in glucose-[Emim][$MeSO_3$]/DCM system, as a result, the recovery of glucose was less. Therefore, the interaction energy between glucose-IL and glucose-DCM is crucial in the removal of glucose from IL. On the other hand, the removal percentage of glucose was higher in [Emim][SCN] (99.23%) because of lower solubility and weaker interactions between glucose-[Emim][SCN] and glucose-DCM (Figure 6.6).

Table 6.4: Non-bonded interaction energies (kJ mol^{-1}) for different IL-sugar-antisolvent systems obtained from MD simulations at T = 25 °C and R = 20[a]

Energy Type	$[Emim]^+$-Sugar	$[Anion]^-$-Sugar	$[Emim]^+$-Antisolvent	$[Anion]^-$-Antisolvent	Sugar-Antisolvent
			Glucose-[Emim][$EtSO_4$]-DCM		
Electrostatic (E_{elec})[b]	-8.4	-41.07	36.23	-94.18	-3.98
vander Waals (E_{vdW})[c]	-10.39	-2.02	-33.13	-32.52	-27.03
Total energy (E_{total})[d]	-18.79	-43.08	3.09	-126.69	-31.02
			Glucose-[Emim][$MeSO_3$]-DCM		
Electrostatic (E_{elec})	0.35	-59.06	44.17	-100.1	-4.73
vander Waals (E_{vdW})	-10.88	0.02	-33.92	-21.32	-27.94
Total energy (E_{total})	-10.53	-59.04	10.25	-121.42	-32.67
			Glucose-[Emim][SCN]-DCM		
Electrostatic (E_{elec})	-2.4	-21.8	44.59	-96.62	1.61
vander Waals (E_{vdW})	-6.11	-0.08	-33.55	-12.36	-20.97
Total energy (E_{total})	-8.51	-21.88	11.04	-108.98	-19.36
			Glucose-[Emim][$EtSO_4$]-DCE		
Electrostatic (E_{elec})	-6.83	-43.86	7.57	-51.93	-2.34
vander Waals (E_{vdW})	-11.1	-2.75	-29.12	-31.7	-25.45
Total energy (E_{total})	-17.93	-46.61	-21.54	-83.63	-27.8
			Fructose-[Emim][$EtSO_4$]-DCM		
Electrostatic (E_{elec})	-17.99	-76.33	36.63	-91.1	-3.16
vander Waals (E_{vdW})	-20.58	-5.44	-31.18	-31.65	-25.9
Total energy (E_{total})	-38.58	-81.77	5.44	-122.75	-29.06
			Xylose-[Emim][$EtSO_4$]-DCM		
Electrostatic (E_{elec})	-8.10	-54.77	31.75	-94.09	-5.22
vander Waals (E_{vdW})	-12.31	-3.87	-34.79	-33.55	-23.70
Total energy (E_{total})	-20.41	-58.64	-3.04	-127.64	-28.92

[an] Antisolvent to IL molar ratio; [b] electrostatic interaction energy (E_{elec}) of the system in kJ mol^{-1}; [c] van der Waals interaction energy (E_{vdw}) of the system in kJ mol^{-1}; [some] of E_{elec} and E_{vdw} in kJ mol^{-1}

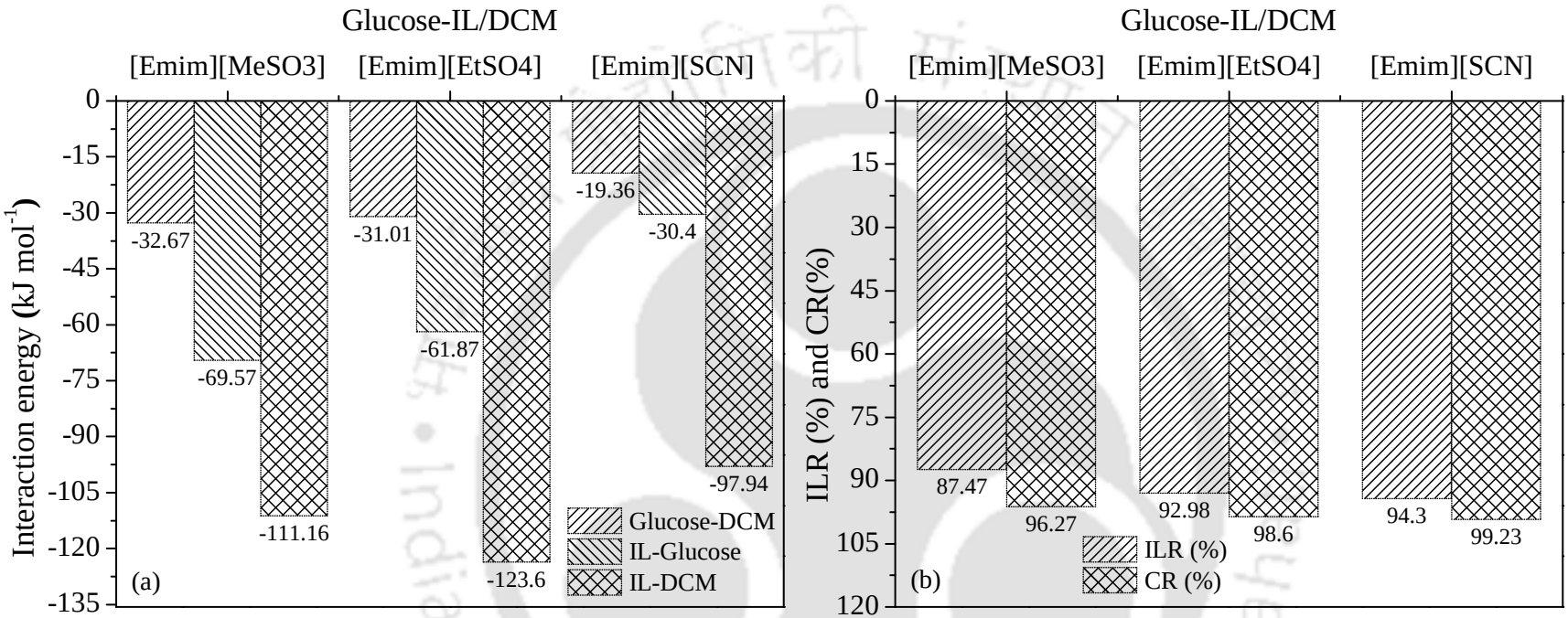

Figure 6.6: Effect of different ionic liquids on the recovery of glucose from ILs in sugar/IL separations by using the DCM antisolvent at 25 °C and *R* = 20 (a) molecular dynamics simulated interaction energies; (b) Experimental %ILR and %CR

Furthermore, among the selected ILs, the recovery percentage of [Emim][SCN] was higher than other two ILs. It was also noted that the recovery percentage of [Emim][SCN] was found to be higher than [Emim][$EtSO_4$] at R = 10 and 20. According to the definition, antisolvent should be miscible or marginally miscible with IL. However, the interaction energy between [Emim][SCN]-DCM was less compared to [Emim][$EtSO_4$]-DCM and [Emim][$MeSO_3$]-DCM systems (Figure 6.6). The recovery of [Emim][$EtSO_4$] and [Emim][$MeSO_3$] was lower due to the stronger interaction energy between glucose-[Emim][$MeSO_3$] and glucose-[Emim][$EtSO_4$] (see Figure 6.6). Hence, the interaction energy between glucose-IL and IL-antisolvent have dominating effect on the recovery of IL. It is worthwhile to note that higher the difference in interaction energy between IL-sugar and IL-antisolvent, higher is the recovery percentage of IL. The magnitude of difference in interaction energy between glucose-[Emim][SCN] and [Emim][SCN]-DCM (-67.55 kJ mol^{-1}) is higher than [Emim][$EtSO_4$] and [Emim][$MeSO_3$] (-61.73 kJ mol^{-1} and -41.60 kJ mol^{-1}). Therefore, the recovery of [Emim][SCN] is higher than [Emim][$EtSO_4$].

In addition, the effect of antisolvent (DCM and DCE) interactions on glucose-[Emim][$EtSO_4$] were also investigated and shown in Table 4 and Figure 6.6. As can be seen from Figure 6.6, the recovery of [Emim][$EtSO_4$] in DCM is higher compared to DCE could be due to the strong interactions between [Emim][$EtSO_4$] and DCM antisolvent. Whereas, the removal percentage of glucose was found higher in DCE antisolvent. It should be noted that DCE possessed lower interaction energy (-27.80 kJ mol^{-1}) with glucose compared to DCM (-31.02 kJ mol^{-1}). Even though the difference between interaction energy is -3.22 kJ mol^{-1}, but it alters the glucose removal percentage from [Emim][$EtSO_4$]. From Table 6.4, it is also noted that higher the difference in interaction energy between IL-sugar and IL-antisolvent, higher is the recovery percentage of IL. However, a contradictory trend is also observed for sugar removal percentage. For example as the energy difference between IL-sugar and sugar-

antisolvent decreases, the removal percentage of sugar found to increase for [Emim][SCN], [Emim][$EtSO_4$], and [Emim][$MeSO_3$] with DCM antisolvent. For the systems with [Emim][$EtSO_4$]-DCM and [Emim][$EtSO_4$]-DCE, the energy difference between IL-glucose and glucose-antisolvent increases with increasing removal percentage of glucose. This attribution may be due to the difference in physiochemical properties of antisolvents.

6.4.3.3 Interaction Energies of Different Sugars with [Emim][$EtSO_4$]/DCM

The interaction energies of glucose, xylose, and fructose with [Emim][$EtSO_4$]/DCM are also reported in Table 6.4 and shown in Figure 6.7. The IL recovery and sugar removal percentage were higher in glucose-[Emim][$EtSO_4$]/DCM compared to xylose and fructose based systems (Figure 6.7). The interaction energy between fructose and IL (-120.35 kJ mol^{-1}) was much stronger than xylose-IL (-79.05 kJ mol^{-1}) and glucose-IL (-61.87 kJ mol^{-1}) which leads to higher removal percentage of glucose (98.60%). Further, it should be noted that higher the interaction energy between the molecules, stronger the formation of hydrogen bonding between them. This makes it difficult to disturb the formed hydrogen bonding between them. In addition, it has been observed that the interaction energy difference between glucose-[Emim][$EtSO_4$] and glucose-DCM was lower than fructose and xylose. Whereas, in case of IL recovery percentage, the interaction energy difference between sugar-[Emim][$EtSO_4$] and [Emim][$EtSO_4$]-DCM was lower in fructose based system (3.04 kJ mol^{-1}) than xylose (-51.63 kJ mol^{-1}) and glucose (-61.73 kJ mol^{-1}) based systems (see Figure 6.7). Consequently, the recovery percentage of IL was less in the fructose based system due to their lower interaction between IL and DCM and stronger interaction between fructose and IL.

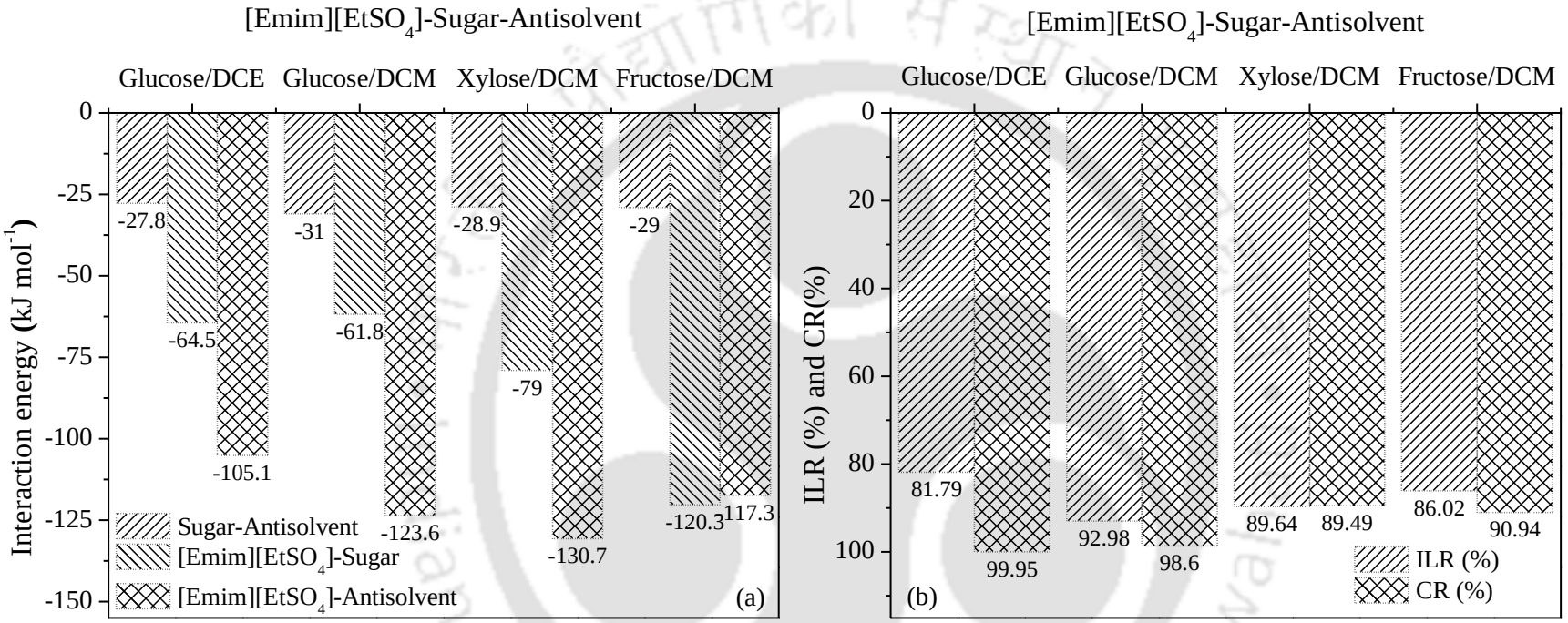

Figure 6.7: Effect of different ionic liquids on the recovery of glucose from ILs in IL-sugar separations by using the antisolvent method at 25 °C and R = 20 (a) molecular dynamics simulated interaction energies, and (b) experimental %ILR and %CR

6.4.3.4 Hydrogen Bonding and Coordination Number

Table 6.5 reports the average number of H-bonds per glucose and IL molecule established between sugar-IL/antisolvent. The criterion for the calculation of H-bonds are as follows: the distance between acceptor-donor molecules is kept at 3.2 Å and the cut off angle for acceptor-H-donor is 120 °. For consistency, we have used the same cut-off distance and angle for all simulated systems. Table 6.5 also reports the CN and total non-bonded interaction energy between the simulated molecules. As can be seen from Table 6.5, the average number of H-bonds formation was higher with increasing CN. However, this trend excludes $[Emim]^+$-sugar and $[Emim]^+$-antisolvent systems. It should be noted that H-bond and CN are two different descriptors. Hydrogen bonds are the type of dipole-dipole interaction formed between the proton of donor group *X*–H (*X*: electronegative atom), with one or more other electronegative atoms (*Y*) having a pair of non-bonded electrons [27,28]. Coordination number is computed from the integration of RDF (radial distribution functions) peak and provides an estimate of how many molecules are in the surrounding environment of the reference molecule. In these calculations, along with the height and width of the RDF peaks, density of the system is also accounted [29,30]. Therefore, HB and CN in Table 6.5 do not provide a direct correlation.

The anion of IL forms a higher number of H-bonds with sugar molecule than either cation of IL or antisolvent as presented in Table 6.5. In contrary to H-bonds, the CN between anion and antisolvent was higher than anion-sugar molecules. This is due to the fact that the cutoff distance between acceptor-donor molecules are only 3.2 Å. On the other hand, the first solvation peak for anion-sugar was obtained at around 2.35-2.65 Å, whereas in the case of anion-antisolvent, the solvation peak was attained at 3.45-3.75 Å (see Table 6.5).

Table 6.5: Average hydrogen bonds (HB), coordination number (CN), and non-bonded interaction energies (E_{total}, kJ mol^{-1}) for different ionic liquid-sugar-antisolvent systems obtained from MD simulations at T = 25 °C and R = 20[a]

Type of measurement	[Emim]$^+$-Sugar	[Anion]$^-$-Sugar	[Emim]$^+$-Antisolvent	[Anion]$^-$-Antisolvent	Sugar-Antisolvent
			Glucose-[Emim][$EtSO_4$]-DCM		
HB[b]	0.67	0.91	0.13	1.13	0.61
CN[c]	1.86 (3.65)	1.22 (2.35)	4.62 (4.25)	5.20 (3.65)	3.24 (3.55)
E_{total}[d]	-18.79	-43.08	3.09	-126.69	-31.02
			Glucose-[Emim][$MeSO_3$]-DCM		
HB	0.66	1.06	0.13	1.04	0.71
CN	1.81 (3.65)	1.38 (2.35)	4.23 (4.15)	4.33 (3.45)	3.59 (3.55)
E_{total}	-10.53	-59.04	10.25	-121.42	-32.67
			Glucose-[Emim][SCN]-DCM		
HB	0.27	0.29	0.12	0.21	0.35
CN	1.07 (3.95)	0.94 (2.65)	4.65 (4.25)	2.05 (3.75)	2.16 (3.55)
E_{total}	-8.51	-21.88	11.04	-108.98	-19.36
			Glucose-[Emim][$EtSO_4$]-DCE		
HB	0.65	0.92	0.10	0.77	0.48
CN	1.82 (3.65)	1.21 (2.35)	2.86 (4.15)	2.88 (3.75)	2.26 (3.65)
E_{total}	-17.93	-46.61	-21.54	-83.63	-27.80
			Fructose-[Emim][$EtSO_4$]-DCM		
HB	1.06	1.51	0.11	0.93	0.51
CN	3.66 (3.65)	2.26 (2.35)	4.33 (4.25)	4.70 (3.65)	3.14 (3.55)
E_{total}	-38.58	-81.77	5.44	-122.75	-29.06
			Xylose-[Emim][$EtSO_4$]-DCM		
HB	0.78	1.00	0.13	1.13	0.50
CN	2.46 (3.65)	1.73 (2.35)	4.98 (4.25)	5.37 (3.65)	2.53 (3.55)
E_{total}	-20.41	-58.64	-3.04	-127.64	-28.92

[an] Antisolvent to IL molar ratio; [b] H-bond cut-off distance 3.2 Å and Angle cut-off 120 °; [c] The values in parentheses denotes the maximum distance of RDF first peak (r, Å) for first solvation shell; [d] sum of E_{elec} and E_{vdw}

Furthermore, anions possess higher interaction energy with sugar molecules, as a result of stronger H-bond formed between anion and sugar molecules. It was interesting to note that in DCE based system, the interaction energy between cation and antisolvent was higher than DCM based system. Nevertheless, DCE based systems had lower H-bonding and CN values than DCM (Table 6.5). The trend is due to the lower electrostatic interactions for $[Emim]^+$-DCE. The interaction energy, average H-bonds, and CNs for glucose-[Emim][$EtSO_4$]/DCM was lower than xylose-[Emim][$EtSO_4$]/DCM and fructose-[Emim][$EtSO_4$]/DCM which revealed a higher recovery of IL and glucose. Furthermore, a close look at Table E.1 reveals that the interaction energy between IL and sugar is much stronger in the pure IL-sugar system. However, upon addition of antisolvent to the sugar-IL system, H-bonding and interaction energy values are reduced. In summary, the antisolvent is indeed efficient in disturbing the hydrogen bonding network between carbohydrates and IL.

6.4.4 Correlation between Theoretical and Experimental Separation Data

Figure 6.8 depicts the relationship between predicted activity coefficient (COSMO-RS), MD simulated interaction energies and experimental fructose removal from [Emim][$EtSO_4$] in the presence of different antisolvents. The experimental separation data for [Emim][$EtSO_4$]/ethanol and [Emim][$EtSO_4$]/acetonitrile have been taken from literature [10]. Figure 6.8, indicates that increase in the interaction energy between fructose and antisolvent lowers the removal percentage of fructose. Higher interaction energy between the molecules leads to the higher solubility of the solute in the solvent. The COSMO-RS calculations suggest that, lower the $\ln\gamma$ value, lower is the removal of fructose (Figure 6.8). It was reported that the solubility of monomeric sugars in ethanol was higher compared to DCM and acetonitrile [16]. Therefore, the removal percentage of fructose was less in ethanol than with other two antisolvents. Overall this observation agrees well with the sugar removal, but not for IL recovery. As can be seen from Table E.2, DCM has lower $\ln\gamma$ value with [Emim][$EtSO_4$]

than ethanol and acetonitrile thus gave less recovery of IL. This is mainly attributed to the fact that COSMO-RS predictions are performed with IL-antisolvent mixture only and does not consider sugar in the mixture. Hence, the activity coefficient prediction follows a separate trend. On the other hand, the MD simulations are conducted with the entire mixture namely: Sugar-IL/antisolvent and the interaction energies showed good correlation with experimental recovery (Table E.2). Further, in order to elucidate the strength of the H-bonds formed between fructose and antisolvents, a separate quantum chemical calculations have been performed and are presented in Appendix E (Section E.1).

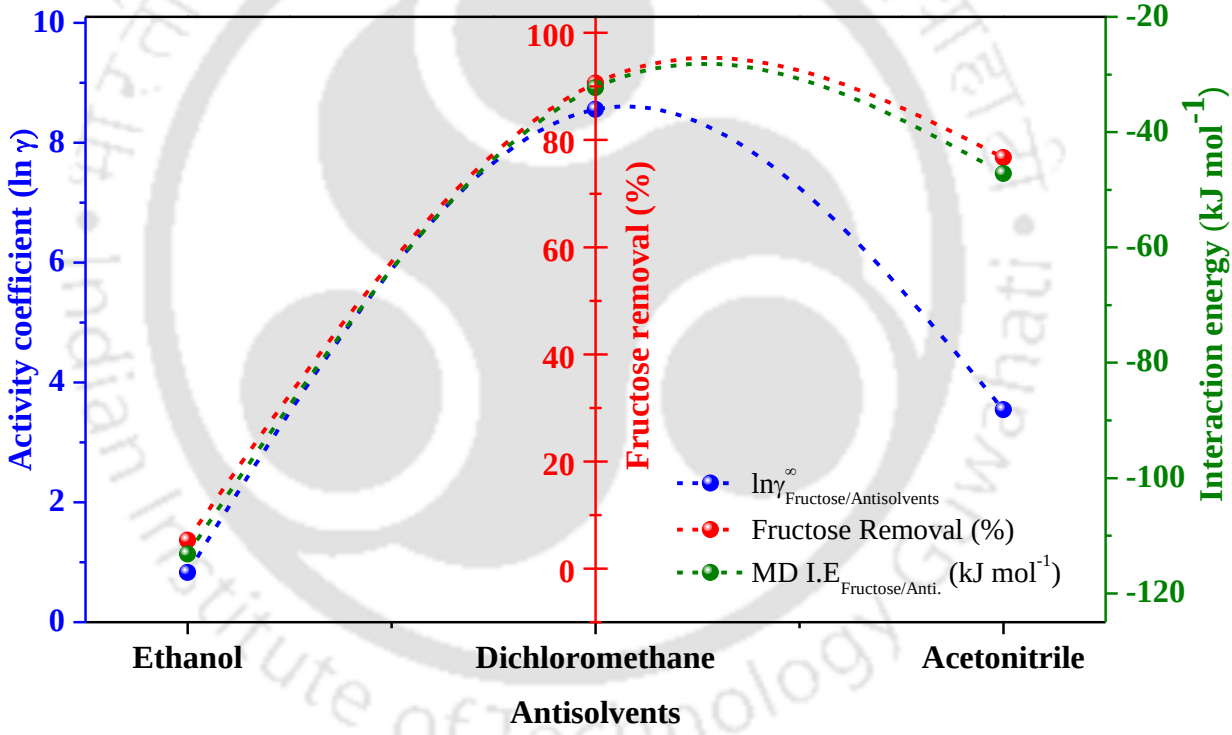

Figure 6.8: Correlation between predicted activity coefficient (COSMO-RS), MD simulated interaction energy and experimental fructose recovery from [Emim][EtSO4] using the different antisolvents. The antisolvent experimental data for ethanol and acetonitrile was taken from Carneiro *et al.* (2014) [10].

6.5 Summary

The chapter summarizes that 34 antisolvents have been screened by COSMO-RS model for the separation of sugars and ILs by means of precipitation process. From the COSMO-RS screening study, DCM and DCE are found to be the efficient antisolvents for the separation process. Thereafter, the precipitation experiments have been conducted with selected antisolvents for the separation of four different sugars from ILs at different process variables. Results of the study revealed 90-99% of carbohydrate removal and 80-98% of IL recovery with DCM antisolvent at an optimal antisolvent molar ratio (R = 20). At higher temperatures, the recovery percentage of [Emim][SCN] and removal of glucose is found to decrease. Furthermore, MD simulations are performed to elucidate the structural properties of carbohydrates with IL/antisolvent mixtures. The interaction energy between glucose and IL is found to be lower than xylose-IL and fructose-IL. This led to higher removal percentage of glucose than xylose and fructose. Higher the difference in interaction energy between IL-sugar and IL-antisolvent, higher is the recovery percentage of IL. A higher removal percentage of glucose is also found in DCE antisolvent. DCE possessed a lower interaction energy (-27.80 kJ mol^{-1}) with glucose compared to DCM (-31.02 kJ mol^{-1}). The interaction energy between carbohydrate-IL and carbohydrate-antisolvent thus having a dominating effect on the removal of carbohydrate from IL. Overall, higher interaction energy (MD) and lower activity coefficient (COSMO-RS) yield lower removal of carbohydrates (experimental).

References

[1] Carneiro AP, Rodríguez O, Macedo EA. Fructose and Glucose Dissolution in Ionic Liquids: Solubility and Thermodynamic Modeling. Ind Eng Chem Res 2013;52:3424-35.

[2] Conceiçao LJA, Bogel-Łukasik E, Bogel-Łukasik R. A new outlook on solubility of carbohydrates and sugar alcohols in ionic liquids. RSC Adv 2012;2:1846-55.

[3] Carneiro AP, Rodríguez O, Macedo EA. Solubility of monosaccharides in ionic liquids – Experimental data and modeling. Fluid Phase Equilib 2012;314:22-8.

[4] Carneiro AP, Rodríguez O, Macedo EA. Solubility of xylitol and sorbitol in ionic liquids – Experimental data and modeling. J Chem Thermodyn 2012;55:184-92.

[5] Mohan M, Goud VV, Banerjee T. Solubility of glucose, xylose, fructose and galactose in ionic liquids: Experimental and theoretical studies using a continuum solvation model. Fluid Phase Equilib 2015;395:33-43.

[6] Mohan M, Banerjee T, Goud VV. Solid Liquid Equilibrium of Cellobiose, Sucrose, and Maltose Monohydrate in Ionic Liquids: Experimental and Quantum Chemical Insights. J Chem Eng Data 2016;61:2923–32.

[7] Tonova K. Separation of poly- and disaccharides by biphasic systems based on ionic liquids. Sep Purif Technol 2012;89:57-65.

[8] Qiao L, Lu K, Qi M, Fu R. Separation performance of guanidinium-based ionic liquids as stationary phases for gas chromatography. J Chromatogr A 2013;1276:112-9.

[9] Tang F, Wu K, Ding L, Yuan J, Liu Q, Nie L, et al. Purification of undiluted ionic liquids from trace-colored impurities for spectroscopy by octadecylsilyl solid-phase extraction. Sep Purif Technol 2008;60:245-50.

[10] Carneiro AP, Rodríguez O, Macedo EA. Separation of carbohydrates and sugar alcohols from ionic liquids using antisolvents. Sep Purif Technol 2014;132:496-504.

[11] Feng D, Li L, Yang F, Tan W, Zhao G, Zou H, et al. Separation of ionic liquid [Mmim][DMP] and glucose from enzymatic hydrolysis mixture of cellulose using alumina column chromatography. Appl Microbial Biotechnol 2011;91:399-405.

[12] Mai NL, Nguyen NT, Kim J-I, Park H-M, Lee S-K, Koo Y-M. Recovery of ionic liquid and sugars from hydrolyzed biomass using ion exclusion simulated moving bed chromatography. J Chromatogr A 2012;1227:67-72.

[13] York P, Kompella UB, Shekunov BY. Supercritical Fluid Technology for Drug Product Development. New York, USA: CRC Press; 2004.

[14] Reverchon E. Supercritical antisolvent precipitation of micro- and nano-particles. J Supercrit Fluids 1999;15:1-21.

[15] Gu Y. Leaching separation of taurine and sodium sulfate solid mixture using ionic liquids. Sep Purif Technol 2004;35:153-9.

[16] Liu W, Hou Y, Wu W, Ren S, Jing Y, Zhang B. Solubility of Glucose in Ionic Liquid + Antisolvent Mixtures. Ind Eng Chem Res 2011;50:6952-6.

[17] Hassan el SR, Mutelet F, Pontvianne S, Moise JC. Studies on the dissolution of glucose in ionic liquids and extraction using the antisolvent method. Environ Sci Tech 2013;47:2809-16.

[18] Hanwell MD, Curtis DE, Lonie DC, Vandermeersch T, Zurek E, Hutchison GR. Avogadro: An advanced semantic chemical editor, visualization, and analysis platform. J Cheminform 2012;4:1-17.

[19] Bayly CI, Cieplak P, Cornell W, Kollman PA. A well-behaved electrostatic potential based method using charge restraints for deriving atomic charges: the RESP model. J Phy Chem 1993;97:10269–80.

[20] Wang J, Wolf RM, Caldwell JW, Kollman PA, Case DA. Development and testing of a general amber force field. J Comput Chem 2004;25:1157–74.

[21] Jakalian A, Bush BL, Jack DB, Bayly CI. Fast, efficient generation of high-quality atomic charges. AM1-BCC model: I. Method. J Comput Chem 2000;21:132–46.
[22] Martinez L, Andrade R, Birgin EG, Martinez JM. PACKMOL: a package for building initial configurations for molecular dynamics simulations. J Comput Chem 2009;30:2157-64.
[23] Humphrey W, Dalke A, Schulten K. VMD: Visual molecular dynamics. J Mol Graphics 1996;14:33-8.
[24] Cruz AG, Scullin C, Mu C, Cheng G, Stavila V, Varanasi P, et al. Impact of high biomass loading on ionic liquid pretreatment. Biotechnol Biofuels 2013;6:52.
[25] Mohan M, Viswanath P, Banerjee T, Goud VV. Multiscale Modeling Strategies and Experimental Insights for the Solvation of Cellulose and Hemicellulose in Ionic Liquids. Mol Phys 2018:doi: 10.1080/00268976.2018.1447152.
[26] Hassan E-SR, Mutelet F, Moïse J-C. From the dissolution to the extraction of carbohydrates using ionic liquids. RSC Adv 2013;3:20219-26.
[27] Maréchal Y. The Hydrogen Bond and the Water Molecule: The Physics and Chemistry of Water, Aqueous and Bio Media. Amsterdam, Netherlands: Elsevier; 2007.
[28] Gupta VP. Principles and Applications of Quantum Chemistry. 1st ed. Boston, US: Academic Press; 2016.
[29] Batista MLS, Passos H, Henriques BJM, Maginn EJ, Pinho SP, Freire MG, et al. Why are some cyano-based ionic liquids better glucose solvents than water? Phys Chem Chem Phys 2016;18:18958-70.
[30] Mohan M, Naik PK, Banerjee T, Goud VV, Paul S. Solubility of glucose in tetrabutylammonium bromide based deep eutectic solvents: Experimental and molecular dynamic simulations. Fluid Phase Equilib 2017;448:168-77.

Chapter – 7

Ionic Liquid and Sulphuric Acid Based Pretreatment of Bamboo: Biomass Delignification and Enzymatic Hydrolysis for the Production of Reducing Sugars

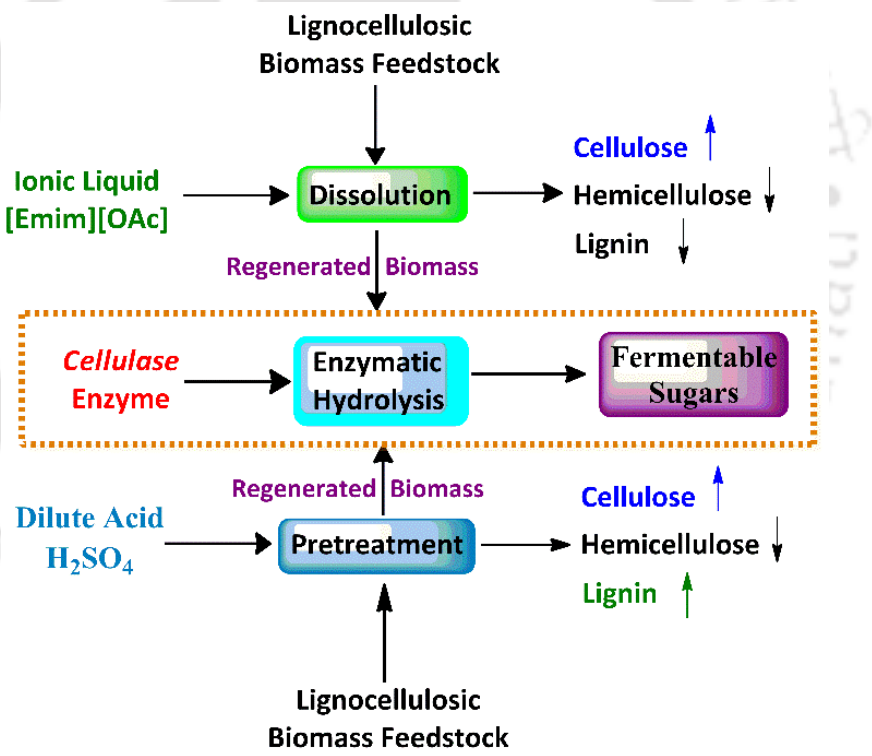

Published Article:

Mohan M, Deshavath N. N, Banerjee T, Goud V. V, Dasu V. V. Ionic liquid and sulphuric acid based pretreatment of bamboo: biomass delignification and enzymatic hydrolysis for the production of reducing sugars. *Ind Eng Chem Res* (2018); 57: 10105–10117

7 Dissolution of Bamboo in Ionic Liquid and its Enzymatic Hydrolysis for the Production of Reducing Sugars

Previous chapters have reported both experimental and computational dissolution phenomena with Ionic Liquids and/or co-solvents. We shall now focus our attention on an actual biomass namely bamboo where very few Ionic Liquid dissolution studies are available in the literature. Hence, the present study attempts to utilize [Emim][OAc] IL for the dissolution of bamboo biomass. The residue biomass shall be used for the production of fermentable sugars by enzymatic hydrolysis. Dilute sulfuric acid pretreatment process will be employed for the bamboo biomass hydrolysis at 121 °C for different acid concentrations (0.2 M, 0.4 M and 0.6 M) for 2 h. Both IL and dilute acid pretreatments are studied for the resultant scarification so as to judge their feasibility for downstream biofuel production. The regenerated biomass will also be further characterized for glucan, xylan and lignin content from both the processes. The physical characterization techniques includes X-ray diffraction (XRD) and thermogravimetric analysis (TGA) which will eventually help us in understanding the crystallinity and thermal decomposition behavior of the regenerated biomass.

7.1 Introduction

With the predictable diminution of petroleum-based resources, there has been an extensive research undertaken in finding the alternative resources, particularly from the renewable resources including lignocellulosic biomass [1,2]. Lignocellulosic biomass has the potential to serve as a low-cost renewable feedstock for the production of biofuels due to their accessibility in huge amounts at a lower price [3,4]. Depending on the source of species, biomass is mainly composed of cellulose (35-50 wt%), hemicellulose (15-30 wt%), lignin (18-30 wt%), and 2-5 wt% of other compounds [5]. The pretreatment of lignocellulosic

biomass is an essential step to enhance the biomass susceptibility for enzymatic hydrolysis and subsequent fermentation of the released sugars [6]. Loss of sugars during pretreatment process and the lack of ability of current pretreatment methods to effectively decrystallise the cellulose results in a high cost of sugars releasing from biomass [6,7]. The difficulty in emerging the effective pretreatment process owing to the presence of lignin, the crystallinity of cellulose and the incidence of extensive covalent cross-linkages between lignin and hemicellulose in the plant cell wall [8]. These factors restrict the effective enzymatic hydrolysis of biomass to produce fermentable sugars in the higher amounts [9,10].

For the above mentioned reasons, an efficient and novel pretreatment process should have the following features: (1) able to disturb the covalent cross-linked matrix of hemicellulose and lignin which embeds the cellulose fibres; (2) also interrupt the strong intra- and intermolecular hydrogen linkages in crystalline cellulose, and (3) increase the porosity and surface area of cellulose for the significant enzymatic hydrolysis [9,11,12]. Several biomass pretreatment methods such as dilute acid, ammonia fiber expansion, hot water, lime and organic solvents are already employed to overcome the recalcitrance of lignocellulosic biomass, resulting in increased efficiency of enzymatic hydrolysis with an improvement in monomeric sugars yield [1,13-15]. Among all the methods, dilute sulphuric acid pretreatment method has emerged as a prominent pretreatment process for biomass conversion which is now in commercial development [15]. Dilute sulphuric acid pretreatment process solubilizes the hemicellulose and thereby disrupting the lignocellulosic biomass structure. However, it can result in the formation of degraded products from polysaccharides and that often provide an inhibitory effect to downstream fermentation organisms which invariably lowers the bio-ethanol yield [5,16,17]. Moreover, the presence of lignin fragments on the surface of the crystalline cellulose after dilute acid pretreatment

can also possibly block the enzyme accessibility to the substrate for the sugar production [7,18].

Among several alternative pretreatment techniques being investigated, an effective process technologies are therefore required for the efficient conversion of lignocellulosic biomass [19,20]. Ionic Liquids (ILs) are the new class of solvents for the dissolution of biomass [11,19,21,22]. Over the past few decades, ILs have already established their potential as a promising solvent for the dissolution of biomacromolecules such as cellulose, silk fibroin, lignin, starch and zein protein, chitin/chitosan etc., with high efficiency [23-27]. Recent reports have also investigated the comprehensive dissolution and partial delignification of hardwood and softwood with various ILs [8,12]. Dissolution of biomass using ILs is also based on the disruption of inter-and intramolecular hydrogen bonding and the formation of new bonds between hydroxyl protons and the anion of IL [3,28]. The IL with carboxylic acid anion has been reported to have low melting points, lesser viscosities, and high hydrogen bond acceptor abilities. All these properties together easily facilitate the dissolution of biomacromolecules [29-31].

Among the various biomass wastes, bamboo is an ancient woody grass and dispersed in tropical, subtropical and mild temperature zones. Generally, bamboo is seen as the "poor man's tree," in recent years it has claimed an innovative, modern crude material and a substitute for wood. According to the State of Forest Report, 2011, which was brought out by the Forest Survey of India (FSI), the total area under bamboo is 13.96 million hectares (8.96 million hectares estimated in 2001). It is found in almost all parts of the country from tropical to the temperature regions. In India, bamboo forests contain 125 indigenous and 11 exotic species of bamboos belonging to 23 genera. The principle bamboo genera occurring in India are *Arundinaria*, *Bambusa*, *Chimonobambusa*, *Dendrocalamus*, *Dinochola*, *Gigantochloa* etc. More than 50% of the bamboo species occur in Eastern India namely

Arunachal Pradesh, Assam, Manipur, Meghalaya, Mizoram, Nagaland, Sikkim, Tripura, and West Bengal. *Bambusa and Dendrocalamus* are found under tropical conditions, whereas *Arundinaria* and its allies occur in the temperature region [32]. In Asia, India is the second richest country in bamboo genetic resources after China. These two nations together have more than half portion of the aggregate bamboo resources universally [33].

Overall, dilute sulphuric acid pretreatment process can be used to produce fermentable sugars from biomass. However, it leads to the formation of higher degradation products from sugars. Therefore in this chapter, we have attempted to produce reducing sugars from biomass using IL pretreatment process with the minimum inhibitory product and also to reduce the time of enzymatic saccharification.

7.2 Materials and Methods

7.2.1 Materials

Bamboo biomass (species name: *Bambusa cacharensis* R. B. Majumdar) used as a feedstock in this study was obtained from nearby IIT Guwahati forest area, Assam, India (26°11′14″N91°41′30″E). The air-dried biomass samples were chopped and sieved (mesh size - BSS 30) to obtain a homogeneous powder having a particle size of 0.5mm. A comprehensive extraction process for bamboo with water, followed by ethanol was performed by means of Laboratory Analytical Procedure (LAP) documented by National Renewable Energy Laboratory (NREL), Golden, Colorado, USA. The extracted bamboo powder was then dried at 45 °C for 48 h until the residual solvent evaporated to avoid the influence of moisture content. The obtained dried samples were stored at room temperature in a sealed plastic bag until further use. Microcrystalline cellulose (MCC, DP≤400) powder and sulphuric acid (≥97%) were purchased from Merck, India Pvt. Ltd. Ionic liquid 1-ethyl-3-methylimidazolium acetate [Emim][OAc] (≥95%) and the enzyme *Cellulase* from Trichoderma reessi ATCC 26921 were purchased from Sigma-Aldrich, Germany. The high-

performance liquid chromatography (HPLC) standards, glucose (≥99.5%), xylose (≥99%), cellobiose (≥98%) and arabinose (≥98%) were procured from Sigma-Aldrich, Germany.

7.2.2 Ionic Liquid and Dilute Sulfuric Acid Pretreatment

In a typical dissolution experiment, 10 g of IL [Emim][OAc] was taken in a 25 ml conical flask. It was then immersed in an oil bath where the temperature of the system can be maintained between 90 °C to 150 °C with an accuracy of ± 1 °C (TARSONSSPINOT-magnetic stirrer and hot plate-DIGITAL, MC 02, India). After the desired temperature was achieved, 0.5 g of bamboo powder was added to the solvent. The temperature inside the flask was measured and maintained at the desired temperature. The mixture was then stirred continuously for 3 h. After completion of the reaction time, the bamboo solution was cooled to room temperature and then regenerated by the addition of distilled water into the solution with 30 min of vigorous stirring. The biomass was collected by using a vacuum filtration unit. Again the biomass residue was washed with an excess of hot water to ensure complete removal of the IL. To confirm the complete removal of IL from the pores of bamboo, we have further characterized the regenerated biomass by TGA. The percentage solubility of bamboo biomass and individual biomass compounds (cellulose, hemicellulose, and lignin) are calculated according to the following equation.

$$\text{Biomass solubility}\ (\%) = \frac{m_b - m_{bf}}{m_b} \times 100 \tag{7.1}$$

$$\text{Solubility of cellulose/hemicellulose/lignin}\ (\%) = \frac{m_o - m_f}{m_o} \times 100 \tag{7.2}$$

Where m_b is the initial mass of bamboo added and m_{bf} the final mass of recovered bamboo, respectively. m_o is the initial mass of cellulose/hemicellulose/lignin in bamboo and m_f the final mass of cellulose/hemicellulose/lignin in bamboo, respectively.

Similarly, pretreatment of bamboo using dilute sulfuric acid was carried out in an autoclave at 1:20 (*w/v*) solid to liquid ratio and 121 °C for 2 h with 0.2 M, 0.4 M and 0.6 M H_2SO_4. The pretreatment of biomass was carried out at different acid molar ratios to know the effect of acid concentration in the biomass pretreatment. After the reaction, samples were withdrawn from hydrolysate for the estimation of reducing sugars *via* HPLC. The solid and liquid portions were separated by 0.2 µm nylon membrane filter. The solid residue was then washed with distilled water until a pH of 7 was obtained. For both the pretreatment processes, the regenerated biomass samples were dried at 50 °C for 48 h before their compositional analysis. Further, the dried biomass samples were characterized by XRD and TGA. The detailed description of XRD and TGA characterizations are already discussed in earlier chapter 4.

The pretreatment of bamboo in IL and dilute sulfuric acid were carried out at different temperatures (*i.e.*, 121 °C for acid pretreatment and 90-150 °C for IL pretreatment) and time (3 h and 2 h). The selection of temperature and time are based on the recovery of reducing sugars and inhibitory product formations. For acid pretreatment we have already optimized the pretreatment process with variety of biomass samples, hence similar condition has been used in the present study to avoid duplication of data [34,35]. Apart from that, the literature data also suggested the similar operating conditions [7]. At 121 °C and 2 h of dilute acid pretreatment, the removal percentage of hemicellulose was higher with minimal concentration of inhibitory products. The results of the study also revealed formation of more inhibitory products under elevated operating condition. Whereas, in the case of IL pretreatment, 3 h of pretreatment time releases maximum sugars and also produces negligible amount of inhibitory products. Moreover, we make an attempt to extending the study for prolonged period but beyond 2.6 h results in the higher viscosity of solution. Therefore, the IL pretreatment was restricted to 3 h.

7.2.3 Enzymatic Hydrolysis

Batch enzymatic hydrolysis of IL (T = 110 °C, 130 °C, and 150 °C) and dilute acid (0.2 M acid, T = 121 °C) pretreated bamboo samples were carried out at 50 °C and 200 rpm for 72 h in a reciprocating shaker. The total duration for IL and dilute acid pretreatment processes was kept for 3 h and 2 h respectively. All samples were diluted in a 50 mM sodium citrate buffer with a pH of 4.8 for enzymatic hydrolysis. The total batch volume for enzymatic hydrolysis was 3 mL with cellulase (ATCC 26921) enzyme concentration of 50 mg protein per g of glucan. The protein concentration present in the *cellulase* (Celluclast 1.5L®) was measured according to the Lowry method by using Folin–Ciocalteu reagent [36]. 0.02% of sodium azide was added to prevent the growth of microorganisms. The reaction was monitored by taking 20 µL supernatant at a specific time intervals to 1.5 mL centrifuge tube containing 180 µL of Millipore water, followed by holding the centrifuge tubes in boiling water for 5 min to denature the cellulase. Thereafter, samples were again centrifuged for 5 min and then the supernatant was analyzed to quantify the reducing sugars using HPLC (Perkin Elmer Series 200, USA) with Hi-Plex H column (7.7×300 mm) connected to guard column. The column oven temperature was kept at 65 °C with 0.5 ml min^{-1} flow rate. The samples were analyzed with a refractive index (RI) detector. 0.01 M H_2SO_4 was used as a mobile phase. Peak identification was confirmed by a standard curve and the correlation coefficient (R^2) was 0.99. The enzymatic hydrolysis yield of glucose and total reducing sugars were determined according to the following equation [12,37].

$$Glucose\ yield\ (\%) = \frac{C_{fg} \times 0.9 \times V}{C_{ig}} \times 100 \tag{7.3}$$

$$TRS\ yield\ (\%) = \frac{C_{fs} \times V}{C_o} \times 100 \tag{7.4}$$

Where C_{fg} is the concentration of glucose after enzymatic hydrolysis (mg.mL^{-1}), C_{ig} is the total concentration of glucose present in bamboo/cellulose after IL or acid pretreatment in mg. C_{fs} is the final concentration of sugars (mg.mL^{-1}), C_o is the initial concentration of bamboo/cellulose after IL or acid pretreatment (mg) and V is the obtained volume of hydrolysate (mL). All the experimental analysis was carried out in duplicate and the average values are reported.

7.2.4 Chemical Composition of Bamboo

The compositional analysis of pretreated and untreated bamboo samples was performed using standard NREL procedures namely LAP-002 and LAP-005 [38,39]. The structural polysaccharides (glucan and xylan) were broken down into monomeric sugars *via* two-step sulfuric acid hydrolysis for HPLC quantification. The amount of acid-soluble lignin (ASL) and acid insoluble lignin (AIL) were measured by NREL/TP-510-42618 [38]. The acid-soluble lignin (ASL) was measured by UV-Vis spectrophotometer at an absorbance of 205 nm with high purity quartz cuvettes with a 1 cm path length.

7.3 Results and Discussion

7.3.1 Pretreatment of Bamboo in [Emim][OAc] IL

In our earlier chapter 4, COSMO-RS (**CO**nductor-like **S**creening **M**Odel for **R**eal **S**olvents) model was employed to screen the 1428 ILs comprised of 42 cations and 34 anions for the dissolution of cellulose and hemicellulose. Based on the logarithmic infinite dilution activity coefficient values ($ln\ \gamma$) and interaction energies of the cellulose and hemicellulose with IL, $[OAc]^-$ anion and $[Emim]^+$ cation proved to be good candidates for the dissolution. Therefore, based on the screening study results and available literature data, [Emim][OAc] IL was selected for the pretreatment of bamboo [3,40,41]. Further, the ILs: [Emim][DEP], [Bmim][OAc], and [Bmim][Cl] are also reported as more effective solvents for the chitin

and biomass dissolution. The IL [Emim][OAc] have shown a higher solvating power for biomass and its constituents in comparison to other ILs [7-9,40]. [Emim][OAc] IL have beneficial properties such as low toxicity (LD_{50} > 2000 mg kg^{-1}), less viscosity (10 mPa.s at 80 °C), lower melting temperature (-20 °C), low corrosiveness, favorable biodegradability and stability up to 300 °C [8]. The chemical and thermal stability of IL ([Emim][OAc]) used in the present study is relatively low as compared to ammonium and phosphonium based ILs [42,43]. However, [Emim][OAc] is the best IL to dissolve biomass and its derived compounds than other cationic-based ILs. Moreover, the [Emim][OAc] can be recovered and reused. There are already several reports available in the literature on the recovery and reuse of [Emim][OAc] [44,45]. Hence, to avoid duplication of data, we have not attempted the recovery and reuse of IL.

The experimental solubility of bamboo biomass was carried out in [Emim][OAc] at the temperature ranging from 90 °C to 150 °C for 3 h of reaction time and results are reported in Table 7.1. From Table 7.1, it can be observed that the solubility of bamboo biomass increases with temperature. This increase in the solubility of bamboo may be due to the higher basicity of acetate anion in [Emim][OAc] (1.107), which efficiently disrupts the inter- and intramolecular hydrogen bonding in biopolymers. At 150 °C, 48.27 wt% of bamboo was solubilized in 3 h of reaction time. The remaining biomass *i.e.*, the residual biomass was precipitated and washed with water and then regenerated with vigorous stirring for 30 min. The regenerated residual bamboo was further used for compositional analysis, physical characterizations and enzymatic hydrolysis.

Table 7.1: Experimental solubility of bamboo biomass in [Emim][OAc] at different temperatures and time and compared with other biomass dissolution in ionic liquids

Ionic Liquid (β)[a]	Biomass Type	Condition (T and t)	Solubility (Wt. %)	References
[Emim][OAc] (1.107)	Bamboo	90 °C, 3 h	20.96	Present study
		110 °C, 3 h	31.65	Present study
		130 °C, 3 h	41.97	Present study
		150 °C, 3 h	48.27	Present study
	Wood flour	90 °C, 1.5 h	17	Lee et al. (2009) [46]
	Southern yellow pine	110 °C, 16 h	98.2	Sun et al. (2009) [8]
	Triticale straw	150 °C, 1.5 h	48.8	Fu et al. (2010) [47]
	Corn Stover	160 °C, 3 h	53.3	Li et al. (2011) [48]
	Switchgrass	160 °C, 3 h	49.3	Li et al. (2010) [7]
	Wheat straw	162 °C, 4.5 h	57.6	Fu and Mazza (2011) [49]
[Choline]Gly	Rice straw	90 °C, 24 h	48.4	Hou et al. (2012) [50]
[Emim][DEP] (1.00)	Cassava pulp	180 °C, 24 h	88	Weerachanchai et al. (2012) [51]
[Bmim]Cl (0.84)	Southern yellow pine	110 °C, 16 h	52.6	Sun et al. (2009) [8]

[a] 'β' is the hydrogen bond basicity

The solubility of different types of biomass in different ILs have also been compared with literature data and presented in Table 7.1 [48-51]. The solubility of bamboo was found to be lower than the triticale straw biomass at 150 °C in [Emim][OAc] [47]. As a test case, between [Emim][OAc] and [Bmim]Cl ILs for the dissolution of southern yellow pine biomass, [Emim][OAc] gave greater dissolving ability than [Bmim]Cl at 110 °C for 16 h [8]. This ascription may be due to the higher hydrogen bond acceptor ability of acetate $[OAc]^-$ anion than the chloride. It is also a well-known fact that the anion of the IL plays a leading role in the dissolution process [3,52,53].

In our previous study, we have proposed few ILs for preferably dissolving cellulose or hemicellulose without impacting the other components of biomass [2]. However, the IL selected in the present study [Emim][OAc] has the capability to dissolve all the three biomass components such as cellulose, hemicellulose, and lignin. The solubility percentage of individual biomass components (cellulose, hemicellulose, and lignin) is measured by using equation 2 and depicted in Figure 7.1. The solubility of cellulose, hemicellulose, and lignin was increasing with increase in the temperature. Hemicellulose exhibits amorphous nature and had higher solubility in [Emim][OAc] then followed by lignin (Figure 7.1). For the dissolution of biomass in ILs, the anion $[OAc]^-$ forms strong hydrogen bonds with both hemicellulose and lignin thereby increasing their solubility. On the other hand, the anion also forms stronger hydrogen bonds with cellulose but results in lower solubility (Figure 7.1). This ascription may be because anion weakens the strong intra- and intermolecular hydrogen bonds of cellulose thereby altering the structure of cellulose which results in lower crystallinity of cellulose.

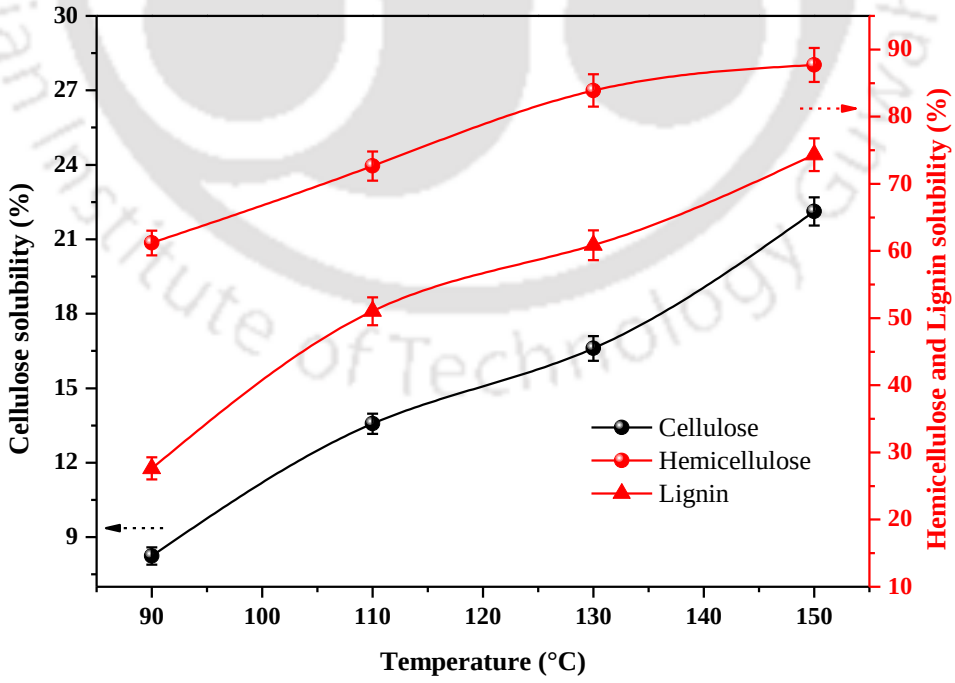

Figure 7.1: Solubility profiles of bamboo components (cellulose, hemicellulose, and lignin) in [Emim][OAc] at different dissolution temperatures.

7.3.2 Compositional Analysis for Ionic Liquid and Dilute Acid Pretreated Bamboo Biomass

Bamboo was pretreated with 0.2 M, 0.4 M, and 0.6 M concentrations of dilute sulfuric acid at 121 °C for 2 h. After dilute acid pretreatment of bamboo, the regenerated residual biomass was used for compositional analysis. The compositional analysis of untreated, IL pretreated and dilute acid pretreated bamboo at various temperatures and acid concentrations are summarized in Table 7.2. Results of the study show that cellulose content in IL pretreated biomass was found to increase, whereas the lignin and hemicellulose content tends to decrease after IL pretreatment. In the residual biomass, cellulose content (cellulose-rich material) found to increase from 45.58% to 68.59% at 150 °C for 3 h reaction time. While the IL pretreatment removes both lignin (26.55% to 13.16%) and hemicellulose (19.95% to 4.90%) in higher amounts at 150 °C. The acid pretreatment removes the hemicellulose very effectively and enhances the cellulose and lignin content in comparison to IL pretreatment process. The hemicellulose content was found to decrease from 19.95% to 1.12% at 0.6 M concentration of dilute sulfuric acid. Overall the acid pretreatment enhances the cellulose and lignin content from 45.48% to 63.78% and 26.55% to 30.48% at 0.2 M concentration of dilute sulfuric acid.

The recovered bamboo samples have shown significant reduction of the lignin content in IL pretreatment as compared to the untreated and acid pretreated bamboo. In comparison, IL pretreatment removed 8.47%, 28.41%, 32.58%, and 50.43% of total lignin with 5.58%, 17.93%, 20.02%, and 24.91% of acid insoluble (Klason) lignin and 2.89%, 10.48%, 12.56% and 25.52% of acid-soluble lignin at 90 °C, 110 °C, 130 °C, and 150 °C, respectively. During the dilute acid pretreatment, lignin content was found to be increased to 14.80%, 9.90% and -0.67% for 0.2 M, 0.4 M, and 0.6 M acid concentrations, respectively. These outcomes showed that IL pretreatment results in a substantial level of delignification.

Table 7.2: Compositional analysis of untreated and pretreated (ionic liquid and dilute acid) bamboo biomass [a,b,c]

Entry	Recovered Biomass (%)	Glucan (%)	Xylan (%)	Arabinose (%)	Total Lignin (%)[d]	AIL (%)	ASL (%)	Ash (%)
Untreated	100 ± 0.0 (300 mg)	45.58 ± 0.8 (136.7)	18.22 ± 0.1 (54.68)	1.72 ± 0.3 (5.17)	26.55 ± 0.9 (79.65)	20.00 ± 0.6 (60.00)	06.55 ± 0.3 (19.65)	4.62 ± 0.3 (13.86)
				Ionic liquid pretreatment				
90 °C	79.03 ± 1.5 (237.1 mg)	52.90 ± 0.6 (125.43)	8.95 ± 1.2 (21.22)	1.155 ± 0.5 (2.74)	24.30 ± 0.8 (57.61)	16.00 ± 0.5 (37.94)	8.30 ± 0.3 (19.67)	4.31 ± 0.2 (10.22)
110 °C	68.33 ± 1.9 (205 mg)	57.62 ± 1.1 (118.15)	7.30 ± 0.3 (14.96)	1.02 ± 0.3 (2.10)	19.01 ± 1.2 (38.99)	12.00 ± 0.9 (24.61)	7.01 ± 0.5 (14.38)	4.13 ± 0.4 (8.46)
130 °C	58.0 ± 2.1 (174 mg)	65.50 ± 0.4 (114.0)	5.06 ± 0.5 (8.81)	0.78 ± 0.3 (1.35)	17.90 ± 1.0 (31.16)	11.00 ± 0.6 (19.15)	6.90 ± 0.4 (12.01)	3.96 ± 0.2 (6.89)
150 °C	51.73 ± 1.3 (155.20 mg)	68.59 ± 0.8 (106.46)	4.33 ± 0.2 (6.72)	0.58 ± 0.2 (0.90)	13.16 ± 0.5 (20.42)	6.50 ± 0.4 (10.09)	6.66 ± 0.1 (10.33)	3.54 ± 0.3 (5.50)
				Dilute acid pretreatment				
0.2 M	62.73 ± 1.7 (188.2 mg)	63.78 ± 0.8 (120.07)	2.31 ± 0.4 (4.35)		30.48 ± 1.1 (57.38)	25.2 ± 0.8 (47.44)	5.28 ± 0.3 (9.94)	3.76 ± 0.3 (7.07)
0.4 M	60.8 ± 2.2 (182.4 mg)	67.50 ± 1.2 (123.10)	1.79 ± 0.7 (3.26)		29.18 ± 0.9 (53.22)	23.40 ± 0.7 (42.68)	5.78 ± 0.2 (10.54)	3.11 ± 0.5 (5.67)
0.6 M	58.57 ± 1.1 (175.7 mg)	71.05 ± 1.7 (124.85)	1.12 ± 0.3 (1.98)		26.37 ± 1.2 (46.35)	20.10 ± 0.8 (35.32)	6.28 ± 0.4 (11.03)	2.43 ± 0.2 (4.27)
Combined Pretreatment	54.7 ± 0.8 (164.17 mg)	81.07 ± 0.9 (133.09)			13.17 ± 0.8 (21.62)	8.50 ± 0.5 (13.95)	4.67 ± 0.3 (7.67)	2.85 ± 0.4 (4.68)

[a] The inability to close the initial mass balance is likely due to the protein and other sugars present in the biomass
[b] Values in parentheses represent the amount of each component recovered from 300 mg total bamboo
[c] Cellulose = Glucan; Hemicellulose = xylan + arabinose
[d] Total Lignin = AIL (Acid Insoluble Lignin (Klason lignin)) + ASL (Acid-Soluble Lignin)

Sun *et al.* (2009) reported the dissolution of southern yellow pine and red oak biomass in [Emim][OAc] at 110 °C for 16 h and results in the delignification of 26.1% for southern yellow pine and 34.9% for red oak, respectively [8]. In a similar manner, Li *et al.* (2010) [7] performed the dissolution of switchgrass in [Emim][OAc] at 160 °C for 3h, and achieved the lignin reduction of 37.6%, which was less than the delignification efficacy of 50.43% at 150 °C for 3 h in this present study. The difference in the delignification effectiveness may be due to the following reasons: (1) the more compelling pretreatments are generally those that utilize higher temperatures and incubation times, showing that there might be an effective lignin glass transition temperature that must be surpassed to proficiently solubilize the lignin, (2) specific ionic liquids have particular interaction with biomass, and those interactions are subject to the cation, anion, temperature, and time utilized as a part of the pretreatment procedure. (3) Lastly, the amount and degree of biomass recalcitrance differs as a component of the biomass itself (*i.e.*, softwood, grass, and hardwood), and is affected by intrinsic variety such as age, harvest methodology, the extent of drying, and storage conditions.

7.3.3 Characterization of Residual Bamboo

7.3.3.1 X-ray Diffraction (XRD) Analysis

The crystallinity index analysis of IL (different temperatures) and dilute acid (0.2 M) pretreated bamboo samples were performed by XRD and compared with the corresponding untreated bamboo sample. The crystallinity is believed to be an important feature affecting the enzymatic saccharification of cellulose. The XRD patterns of IL and acid pretreated bamboo samples are presented in Figure 7.2 and Table 7.3. It was reported that the diffraction peak at 15.6° corresponds to the (1 1 0) plane, whereas the second largest peak at 22.4° corresponds to (0 2 0) plane of cellulose I [54]. After dilute acid pretreatment, the XRD peaks are attained at 15.6° and 22.4° which implies that the recovered biomass shows

cellulose I structure. As can be seen from Table 7.3, the untreated bamboo is highly crystalline (68.90% Crl), and the crystallinity after 0.2 M acid pretreated bamboo sample was higher (75% Crl) than untreated bamboo. The increase in the crystallinity of bamboo after acid pretreated sample suggests that the amorphous cellulose breaks down under acidic condition. Dilute acid pretreatment process is unable to alter inter- and intramolecular hydrogen bonding present in the cellulose. For acid pretreatment, minimal lignin removal and the observed increase in the crystallinity index are consistent with the results reported in the literature [7].

It should be noted that the lower crystallinity index of biomass is essential to enhance the reactivity of cellulosic biomass during enzymatic hydrolysis. In the case of IL pretreated bamboo samples, the XRD peaks at 15.6° and 22.4° (present in the native cellulose) diffraction patterns are significantly weakened and shifted to 12.3° and 20.2° (Figure 7.2a) [3,55]. This transformation indicates a change from cellulose I to cellulose II, which occurs during the dissolution of biomass in ILs [40]. The crystallinity index of IL pretreated bamboo sample is significantly lower than the untreated and acid pretreated bamboo samples. The crystallinity of cellulose was also observed to be decreased with increasing temperature (Table 7.3). This decrease in the cellulose crystallinity reveals that the recovered bamboo samples are amorphous and subsequently has increase cellulose surface accessibility and would be more efficient for enzymatic hydrolysis.

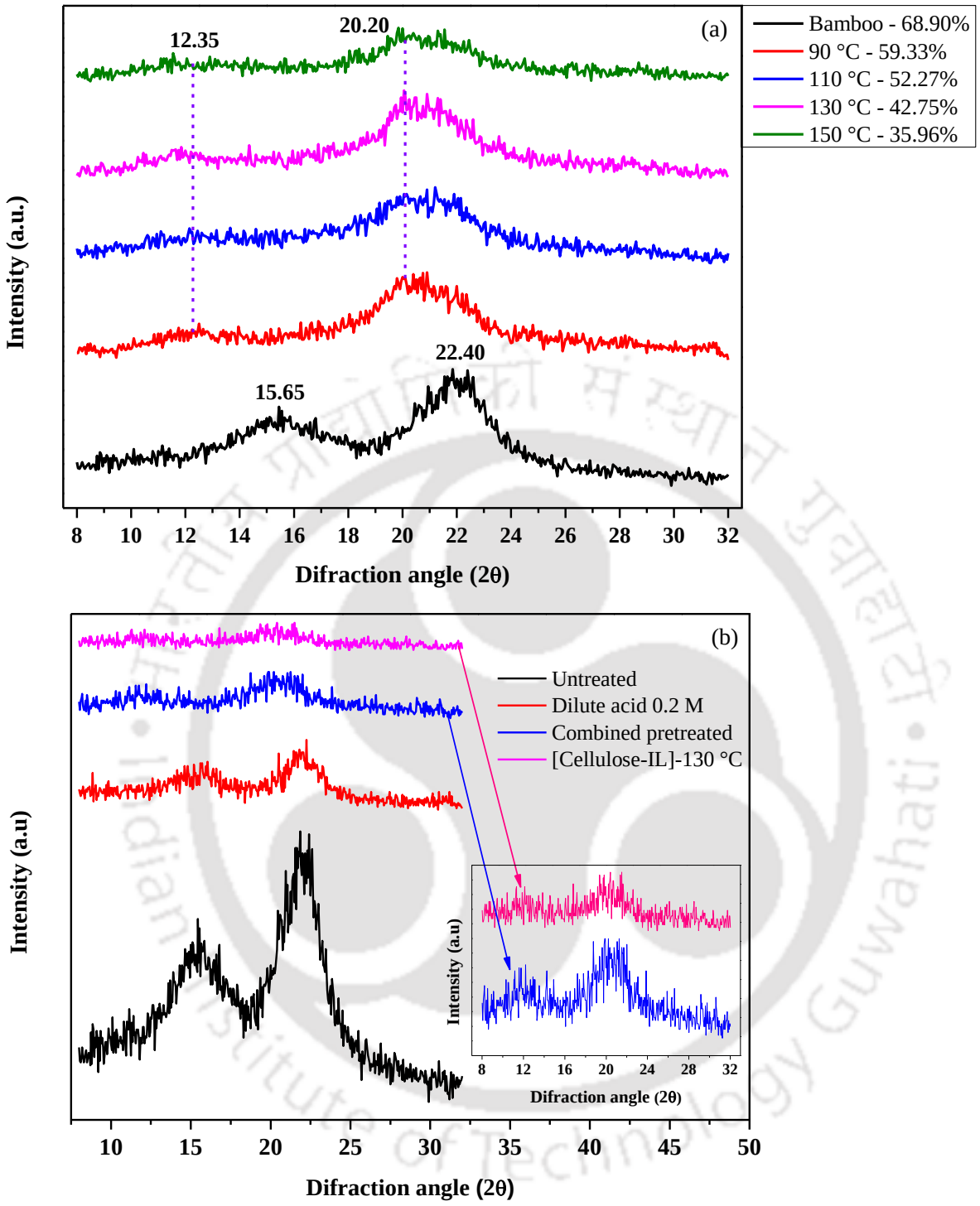

Figure 7.2: XRD patterns of untreated and (a) pretreated (ionic liquid and dilute acid) bamboo biomass, (b) comparison between IL pretreated bamboo/cellulose and combined pretreated bamboo at 130 °C.

Table 7.3: Crystallinity index (*Crl*) and thermal decomposition temperature (T_{dec}) of pretreated and untreated bamboo samples and compared with cellulose and combined pretreatment process

Pretreatment Method	*Crl (%)*	T_{dec} (°C)
Untreated	68.90	363.8
Dilute Acid (0.2 M)	75.00	361.3
Ionic Liquid 90 °C	59.33	354.5
Ionic Liquid 110 °C	52.27	352.1
Ionic Liquid 130 °C	42.75	346.4
Ionic Liquid 150 °C	35.96	344.4
Combined pretreatment	32.38	346.1
Cellulose-IL 130 °C	20.00	342.3

7.3.3.2 Thermogravimetric Analysis (TGA)

Furthermore, TGA analysis was also carried out on a NETZSCH instrument (TG 209 ***F1*** *Libra*®, Germany) under inert atmosphere (N_2). 8-10 mg of sample was loaded into a platinum pan and subjected to a heating rate of 10 °C min^{-1} over the temperature range from 30-600 °C. Appraisal of cellulose, hemicellulose and lignin content of biomass could shed insights on the mechanisms contributing to IL and dilute acid pre-treatment techniques. The thermal decomposition of lignocellulosic biomass took place in four major steps: loss of moisture and volatile matter as the first step (up to 100 °C) [56]. Between 100 to 200 °C, (2) the decomposition of residual hemicellulose was perceived [57]. The peak at 200 to 400 °C, (3) attributed to the decomposition of cellulose, hemicellulose, and lignin [55,57]. The fourth step, above 400 °C and up to 700 °C, corresponds to the final degradation of cellulose, inorganic compounds, and lignin [56-58].

Figure 7.3 shows the thermal decomposition profiles of regenerated and untreated bamboo samples. From DTG curves (Figure 7.3), it can be seen that thermal decomposition of bamboo exhibit two distinct stages for untreated and IL pretreated biomass. In the first stage, decomposition occurred in the temperature range of 200–280 °C which may due to the decomposition of residual hemicellulose. While stage two corresponds to 270–400 °C exhibit the devolatilization of inorganic compounds [59]. The second stage mainly accounted for thermal decomposition of cellulose, hemicellulose and trace amount of lignin. Whereas in the case of an acid pretreated biomass sample, only one peak was obtained in the temperature range of 300-400 °C which mainly corresponds to the decomposition of cellulose and trace amount of hemicellulose and lignin [57]. The absence of hemicellulose decomposition peak in the acid pretreated biomass is due to the complete removal of hemicellulose during the pretreatment step. The acid pretreated biomass showed higher thermal decomposition temperature than IL pretreated biomass which occurred due to the strong crystallinity of biomass (Table 7.3). With an increase in the temperature of IL pretreated biomass, the thermal stability of recovered biomass was found to decrease. From the DTG curves (Figure 7.3a), it can be seen that the peak at 363.8 °C corresponds to the untreated sample. Whereas, in the case of IL pretreated biomass at different temperatures such as 90 °C, 110 °C, 130 °C, and 150 °C, DTG peaks were obtained at 354.5 °C, 352.1 °C, 346.4 °C, and 344.4 °C, respectively. The decrease in thermal stability of biomass related to the lower crystallinity of recovered bamboo samples. The obtained results are in agreement with the reported literature [60,61]. It is also worthwhile to mention that, from the TGA analysis no extra peak was observed in the regenerated biomass which implies that the biomass was successfully regenerated and confirms the removal of IL from the pores of bamboo. After IL and dilute acid pretreatment, the collected residual biomass was further used for enzymatic saccharification.

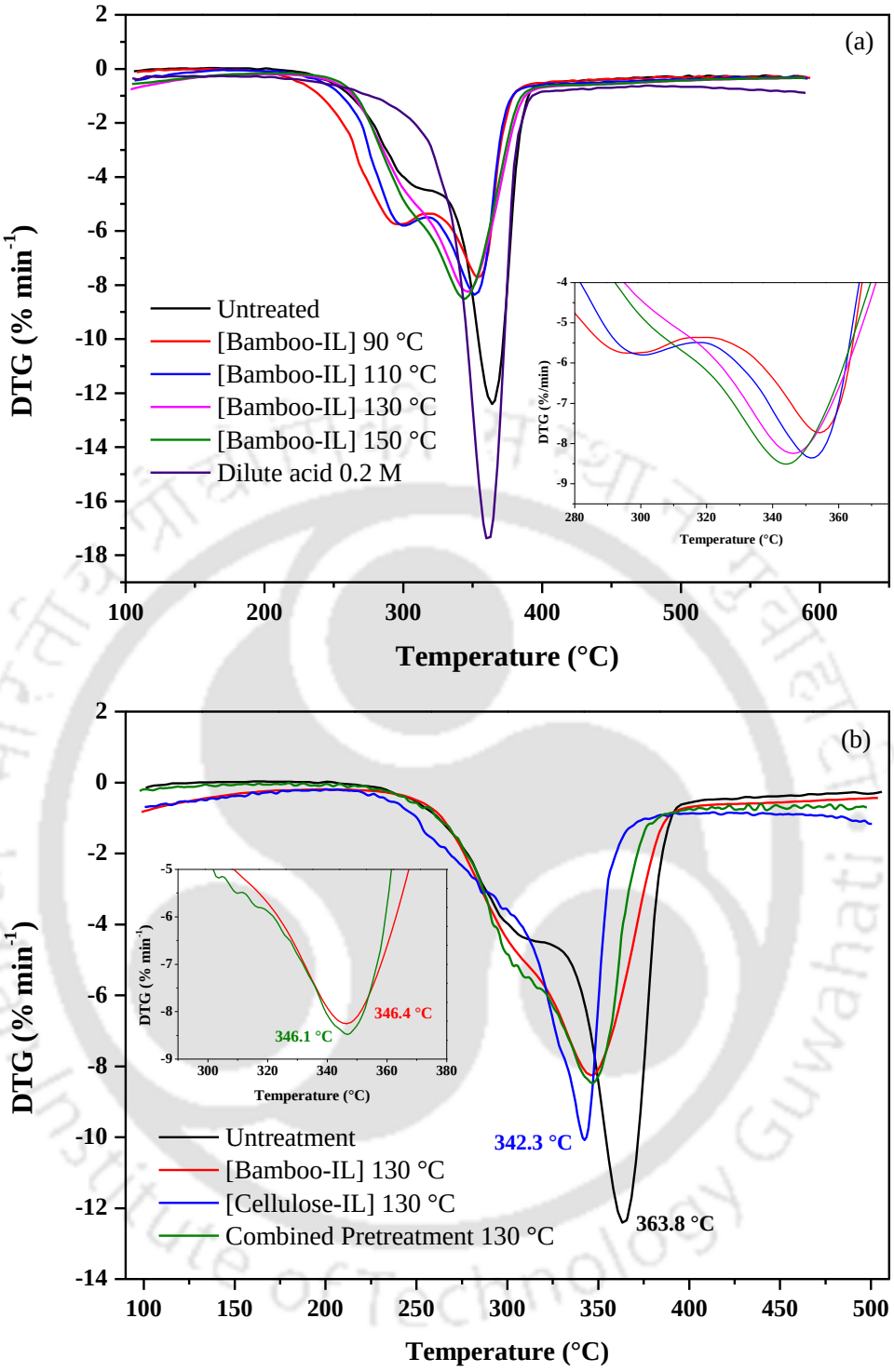

Figure 7.3: DTG plots of untreated and (a) pretreated (ionic liquid and dilute acid) bamboo biomass, (b) comparison between IL pretreated bamboo/cellulose and combined pretreated bamboo at 130 °C.

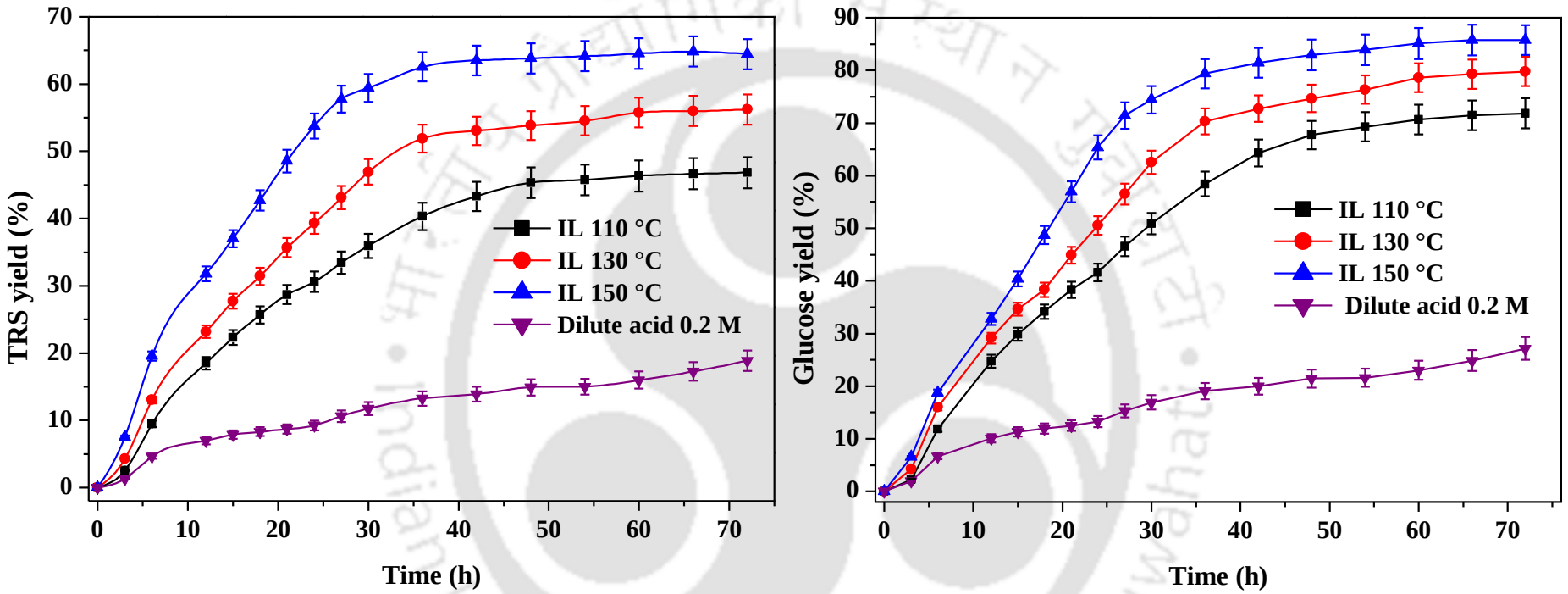

Figure 7.4: Enzymatic hydrolysis of regenerated bamboo after [Emim][OAc] pretreatment at different temperatures and comparison with dilute acid hydrolysed biomass (0.2 M H_2SO_4, 121 °C, 2 h) for the production of (a) total reducing sugars (TRS) and (b) glucose

7.3.4 Enzymatic Saccharification for Ionic Liquid and Dilute Acid Pretreated Biomass

The enzymatic saccharification of both IL and dilute acid pretreated bamboo samples were hydrolyzed to produce reducing sugars and both pretreatment processes were compared. For enzymatic hydrolysis, the IL pretreated bamboo samples at 110 °C, 130 °C, and 150 °C were considered whereas, in case of dilute acid pretreatment, the sample treated at 121 °C with 0.2 M sulphuric acid was chosen due to the lower degradation of sugars (data not shown). Figure 7.4 (a, b) shows the total reducing sugars (cellobiose and glucose) and glucose production profiles of IL and dilute acid pretreated bamboo samples at the same enzyme loading (*i.e.*, 50 mg of protein per g of glucose). As per the stoichiometry of enzymatic hydrolysis, complete hydrolysis of 1 g of cellulose produces 1.1 g of glucose. Figure 7.4a shows that the highest TRS yield of 63% was achieved for the 150 °C IL pretreated biomass at 36 h of enzymatic hydrolysis time as compared to 110 °C (40%) and 130 °C (52%) pretreated biomass. While, in case of dilute acid pretreated biomass, the highest TRS yield (19%) was obtained at 72 h of enzymatic hydrolysis, which took significantly longer time compared to IL pretreated sample (36 h). Over a similar time interval of the enzymatic hydrolysis process by both pretreatment methods, IL pretreated bamboo exhibited significantly higher enzymatic saccharification than acid pretreated biomass.

The enzymatic hydrolysis rate for IL pretreated biomass was found to be 4.7 times higher than the dilute acid pretreated biomass. This may be ascribed due to the difference in the crystallinity and delignification efficiency in IL and acid treated biomass. It was observed that higher the lignin content, lower the enzymatic saccharification. Dilute acid pretreated biomass revealed significantly higher lignin content in residual biomass as compared to IL pretreated biomass. In the present study, the results suggest a strong

correlation between the enzymatic hydrolysis kinetics and biomass delignification efficiency which is consistent with the observations of Li *et al.* (2010) [12] and Lee *et al.* (2009) [46]. On the other hand, it was also observed that higher the crystallinity index of cellulose, lower is the reducing sugar production during the enzymatic hydrolysis. Dilute acid pretreated biomass exhibits higher crystallinity index as compared to IL pretreated biomass (Table 7.3). The loss of intra- and intermolecular hydrogen bonds in cellulose results in amorphous cellulose. This provides an enhanced surface area of cellulose which leads to better enzymatic accessibility and increased binding sites in recovered cellulose fibers.

The strong correlations can be seen between lignin/hemicellulose removal, crystallinity index, and TRS yield for IL pretreatment as shown in Figure 7.5. From Figure 7.5, it is clear that with an increase in the dissolution temperature the lignin and hemicellulose removal percentage was found to increase. Simultaneously, the biomass crystallinity was found to decrease. Higher removal of hemicellulose and lignin components leads to enhance the cellulose content in the residual biomass. The cellulose-rich residual biomass has more possibility to form new hydrogen bonds with ionic liquids thereby decreasing the crystallinity of biomass. On the other hand, lower lignin content and crystallinity of biomass resulted in higher TRS yield during the enzymatic hydrolysis (see Figure 7.4 and Figure 7.5).

Figure 7.4b represents the glucose yield of IL and dilute the acid pretreated sample. From the observation of Figure 7.4b, it can be seen that the enzymatic saccharification yield of glucose was much higher in IL pretreated biomass (80% for 150 °C at 36 h of enzymatic hydrolysis). Only 27% of glucose yield was achieved in dilute acid pretreated biomass after 72 h of enzymatic saccharification. In the case of IL pretreated biomass at 110 °C and 130 °C, glucose yield was 58.5% and 70% for 36 h; and 72% and 80% for 72 h, respectively.

Therefore, it was noticed that the amount of reducing sugars produced was very low and required slightly higher operating conditions. Furthermore, to improve the reducing sugars yield, the dilute acid pretreated biomass (reaction condition: 0.2 M, 121 °C, and 2 h) was again treated with [Emim][OAc] at 130 °C for 3 h. Thereafter, the combined pretreated biomass was enzymatically hydrolyzed at same enzyme loading and the results are compared with IL pretreated sample.

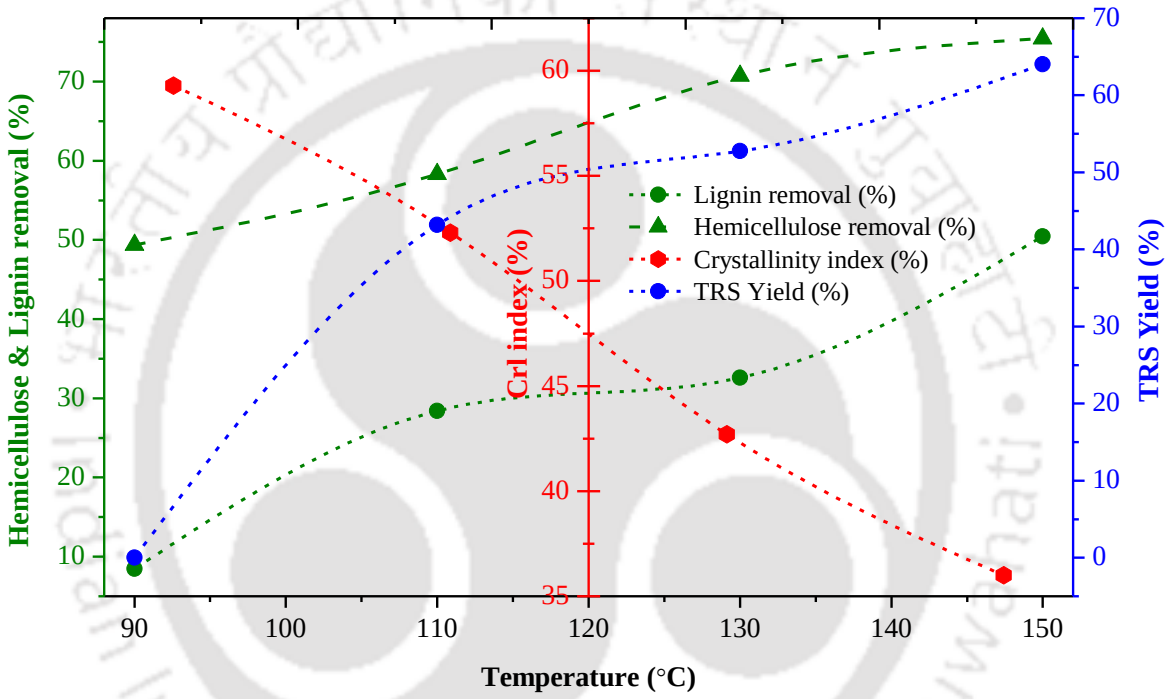

Figure 7.5: Correlation between the removal percentages of hemicellulose/lignin, the impact of biomass crystallinity and the TRS yield (after enzymatic hydrolysis at 42 h) obtained from bamboo biomass during IL pretreatment. The yield of TRS for 90 °C treated biomass is considered as zero due to the enzymatic hydrolysis was not performed.

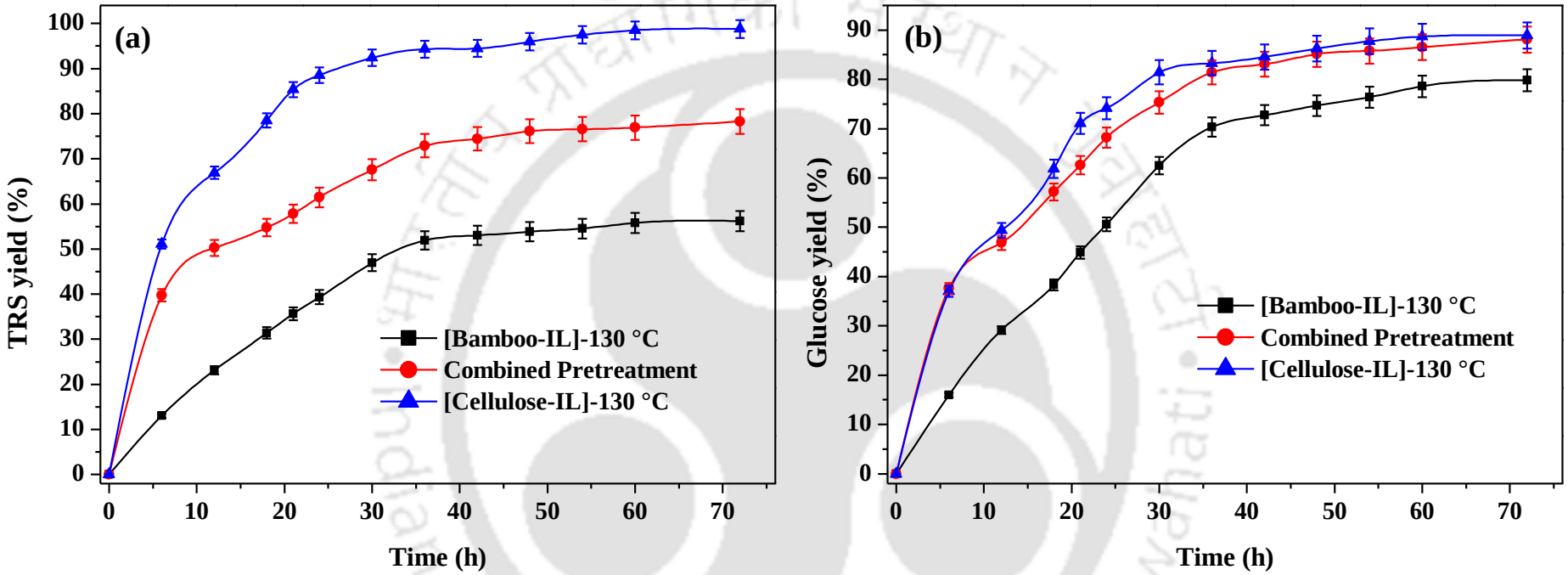

Figure 7.6: Enzymatic hydrolysis of regenerated bamboo/cellulose after [Emim][OAc] pretreatment at 130 °C for 3 h and comparison with combined pretreated bamboo for the production of (a) total reducing sugars (TRS) and (b) glucose

7.3.5 Comparison of Ionic Liquid Pretreated Bamboo/Cellulose and Combined Pretreated Bamboo Biomass

The combined pretreatment process was employed and carried out as a consequence of acid pretreatment followed by IL pretreatment to understand the effect of the combined process on reducing sugars yield. The obtained enzymatic hydrolysis results of IL pretreated bamboo was compared with combined pretreatment process. After dilute acid pretreatment, residual biomass was found to contain 64% of cellulose and ~31% of lignin, respectively. Hence, an attempt has been made to dissolve the dilute acid pretreated biomass in [Emim][OAc] and the study revealed some remarkable results. As can be seen from Table 7.2, the recovered bamboo contains lower lignin content in combined pretreated biomass as compared to IL (130 °C) and acid (0.2 M) pretreated biomass. This could be due to the presence of fewer components in residual biomass which provides greater tendency to [Emim][OAc] IL for higher solubilization of lignin at 130 °C. Thus, the combined pretreatment process removed 50.4% of total lignin which results in higher delignification of recovered biomass at lower pretreatment conditions. The residual biomass recovered at the end of combined pretreatment process found to contain 81.07% cellulose which indicates that the recovered biomass is a cellulose-rich material. Apart from that, this study also reported the pretreatment of pure cellulose (microcrystalline cellulose) in [Emim][OAc] at 130 °C for 3 h and the obtained results are compared with IL and combined pretreatment process (Figure 7.6 (a, b)).

From Figure 7.6a, the TRS yield was found to be higher in IL pretreated cellulose (94% at 36 h) followed by combined pretreated (73% at 36 h) and IL pre-treated (52% at 36 h) bamboo. While in case of glucose yield (Figure 7.6b), the concentration of glucose was observed to be practically comparable in both cellulose and combined pretreated bamboo

(81-83% at 36 h). The XRD analysis (Table 7.3 and Figure 7.2) conferred that the crystallinity index of combined treated biomass was lower than the IL pretreated biomass. This indicates that the recovered biomass is highly amorphous. From Figures 7.4 and 7.6, it is also observed that the obtained glucose yield (~80-81%) was found to be similar in both the pretreatment processes *i.e.*, IL (150 °C) and combined pretreated biomass at 36 h of enzymatic hydrolysis. Similar results are reflected in their crystallinity index values (Table 7.3).

The literature on the hydrolysis of bamboo by ionic liquid pretreatment is rather limited. Therefore, the results of the present study have been compared with the available literature on bamboo and with the other biomass which has the comparable composition to that of bamboo. Wang *et al.* (2017) studied the pretreatment of bamboo in three different ILs (1-H-3-methylimidazolium chloride [Hmim]Cl, N-methyl-2-pyrrolidinium chloride [Hnmp]Cl and Pyridinium chloride [Hpy]Cl) at 90 °C for 0.5 h. The glucose yield reported was 63.5%, 60.8% and 65.5% after 72 h enzymatic saccharification for [Hpy]Cl, [Hnmp]Cl and [Hmim]Cl treated biomass samples, respectively [62]. Whereas, in the present study, 72.2% of glucose yield was obtained after 72 h of enzymatic hydrolysis for 110 °C treated sample. Cheng *et al.* (2017) also reported the hydrolysis of bamboo in [Bmim]Cl IL with chitosan-based solid acid catalysts. The study revealed TRS yield of 54.31%, 49.43% and 58.89% for catalysts Cu^{2+}-SCCR, Zn^{2+}-SCCR, and Fe^{3+}-SCCR, respectively in [Bmim]Cl at 120 °C and 24 h of dissolution time [63].

Further, Li *et al.* (2010) [7] have reported the pretreatment of switchgrass in [Emim][OAc] IL (160 °C for 3 h) followed by its enzymatic saccharification. Almost 85% of glucose yield was observed in 15 h of enzymatic saccharification. As compared to the present study, the crystallinity index of untreated switchgrass (26.2%) was much lower than bamboo (68.9%). During the IL-pretreatment, the crystallinity of switchgrass was reduced to

2.6%, resulting in highly amorphous cellulose. Therefore, there was an increase in the enzymatic hydrolysis efficiency in lesser hydrolysis time. Another study by Lie *et al.* (2011) [48] investigated on the pretreatment of corn stover using [Emim][OAc] IL at 160 °C for 3h resulting in 80% cellulose conversion in 24 h by using *cellulase* enzyme. Perez-Pimienta *et al.* (2013) [40] have reported the pretreatment of agave bagasse in [Emim][OAc] at 160 °C for 3 h. 80% of total reducing sugars were obtained from agave bagasse in 24 h of enzymatic saccharification. However, in the current study, only 65% of TRS was achieved at 36 h (bamboo pretreated at 150 °C in [Emim][OAc]). Qiu *et al.* (2012) [64] and Qiu and Aita, (2013) [65] also studied the pretreatment (120 °C for 30 min) of sugarcane bagasse by an acid catalyzed process in [Emim][OAc]. 80% of glucose yield was obtained after 48 h of enzymatic hydrolysis. In the present study (bamboo pretreated at 130 °C for 3 h), 80% of glucose conversion was achieved within 72 h. In recent year, Sun *et al.* (2016) [66] has studied the effect of combined pretreatment (a method combining solid base catalyst (Na_2SiO_3) and [Bmim]Cl IL) on the spruce, willow, and soybean straw biomass. It was reported that at 55-63% of enzymatic hydrolysis yield was obtained after 72 h, which is lower than the present proposed combined pretreatment method.

From the aforementioned discussions, it can be inferred that lignin content and crystallinity index of cellulose plays a vital role in the enzymatic saccharification of any biomass. Hence, present study results in lower levels of TRS and glucose as compared to those reported in the literature [40,48,64,65]. The diminution in sugars release may depend on the type of biomass, lignin content, and crystallinity of cellulose, pretreatment conditions, enzyme type and enzyme loading. However, it should be noted that IL pretreated bamboo had lower lignin content and crystallinity index value (Table 7.4).

Table 7.4: Comparison of lignin content and crystallinity index (*CrI*) of various biomass at different pretreatment conditions in [Emim][OAc] ionic liquid

Type of biomass	Pretreatment condition (T, t)	Lignin (%)		*CrI* (%)		Reference
		Untreated	After IL-pretreated	Untreated	After IL-pretreated	
Bamboo	90 °C, 3 h	26.55	24.30	68.90	59.33	Present study
	110 °C, 3 h	26.55	19.01	68.90	52.27	Present study
	130 °C, 3 h	26.55	17.90	68.90	42.75	Present study
	150 °C, 3 h	26.55	13.16	68.90	35.96	Present study
Switch grass	160 °C, 3 h	21.80	13.60	26.20	2.60	Li et al. (2010)[7]
Corn stover	160 °C, 3 h	20.50	3.50	36.00	N.R[a]	Li et al. (2011)[48]
Sugar cane bagasse	120 °C, 0.5 h	24.81	19.85	56.28	24.52	Qiu et al. (2012)[64], Qin and Aita (2013)[65]
Agave bagasse	160 °C, 3 h	19.30	10.90	28.60	N.R[a,]	Perez-Pimienta et al. (2013)[40]
	120 °C, 3 h	19.30	16.10	28.60	N.R[a]	Perez-Pimienta et al. (2013)[40]
Spruce[b,c]	120 °C, 1 h	30.70	28.80	46.70	29.70	Sun et al. (2016) [66]
Willow[b,c]	120 °C, 1 h	26.80	24.00	40.10	24.90	Sun et al. (2016) [66]
Soybean straw[b,c]	120 °C, 1 h	17.50	15.40	41.60	23.30	Sun et al. (2016) [66]

[a] N.R. = Not Reported; [b] combined pretreatment ([Bmim]Cl+Na_2SiO_3 at 1:1 ratio); [c] [Bmim]Cl IL was used

The enzymatic hydrolysis results clearly show that soluble sugars released at a faster rate in the combined and IL pretreated process than in the dilute acid pretreatment. Moreover, reduction in enzyme loading, ionic liquid cost, and recovery of ionic liquid are the basis to promote the economy of biorefineries and build up the optimal IL pretreatment. Table 7.5 shows the total processing time to achieve 80% glucose recovery from cellulose or biomass with various pretreatments. Although, the effective dilute acid pretreatment time was 2 h, the total enzymatic saccharification time to attain 80% glucose yield was more than 72 h. In contrast, for IL (150 °C) and combined pretreatments, the total saccharification time to reach 80% of glucose yield was 36 h.

Table 7.5: Total processing time (pretreatment + enzymatic hydrolysis) to recover 80% of the glucan from cellulose using various pretreatment methods

Pretreatment Method	Pretreatment Time (h)	Enzymatic saccharification Time (h)	Total Process Time (h)
Untreated	-	-	-
Dilute acid (0.2 M)	2	>>72	>>74
Ionic liquid 130 °C	3	72	~ 75
Ionic liquid 150 °C	3	37.4	~ 40.4
Combined pretreatment	2 h acid + 3 h IL	34.4	~ 39.4
Cellulose-IL 130 °C	3	28.6	~ 31.6

The application of this novel IL pretreatment for biofuel production appears to offer several advantages as compared to the dilute acid pretreatment. As IL pretreatment process is more convenient and environmentally friendly, requires less processing time for enzymatic hydrolysis, lowers the energy consumption and leads to higher sugar yield. It also offers lesser degradation of monosaccharides and consequently minimum inhibitory product

formation for the downstream saccharification step. These advantages need to be counter balanced by the higher cost associated with IL, but offer further motivation to explore and develop this pretreatment technology. Furthermore, the significant delignification efficiency demonstrated by IL pretreatment likely suggests a promising aspect for recovering and converting lignin as a valuable commercial co-product.

7.4 Summary

Pretreatment of lignocellulosic biomass is an essential step in a commercial biorefinery. A comparison of IL and dilute acid pretreatment of bamboo was carried at different pretreatment conditions. Among the pretreatment techniques used in this study, IL pretreatment reduces the total enzymatic processing time and provide higher reducing sugars yield. Hence, it is a promising alternative to the dilute acid pretreatment. The results also revealed around 80% of glucose yield in the combined pretreatment process while in the case of IL pretreatment (130 °C), 70% of glucose was attained after 36 h of enzymatic hydrolysis. The XRD and TGA analysis of the recovered bamboo showed lower crystallinity index value and lower thermal stability than untreated and dilute acid pretreated biomass. The lower crystallinity of IL pretreated bamboo results in an increase in the cellulose surface accessibility and makes it more easily accessible to enzymatic hydrolysis. IL pretreatment is a comparatively new technique and there is much to be explored before a commercially reasonable process is comprehended. Moreover, it appears to be environmentally benign and offers several advantages over acid pretreatment in terms of total processing time and production of reducing sugars with minimal inhibitory content.

References

[1] Mohan M, Banerjee T, Goud VV. Hydrolysis of bamboo biomass by subcritical water treatment. Bioresour Technol 2015;191:244-52.

[2] Mohan M, Balaji C, Goud VV, Banerjee T. Thermodynamic Insights in the Separation of Cellulose/Hemicellulose Components from Lignocellulosic Biomass Using Ionic Liquids. J Solution Chem 2015;44:538-57.

[3] Mohan M, Banerjee T, Goud VV. Effect of Protic and Aprotic Solvents on the Mechanism of Cellulose Dissolution in Ionic Liquids: A Combined Molecular Dynamics and Experimental Insight. ChemistrySelect 2016;1:4823–32.

[4] Timung R, Mohan M, Chilukoti B, Sasmal S, Banerjee T, Goud VV. Optimization of dilute acid and hot water pretreatment of different lignocellulosic biomass: A comparative study. Biomass Bioenergy 2015;81:9-18.

[5] Sjostrom E. Wood Chemistry: Fundamentals and Applications. 2nd ed. New York: Academic Press (an imprint of Elsevier); 1993.

[6] Cruz AG, Scullin C, Mu C, Cheng G, Stavila V, Varanasi P, et al. Impact of high biomass loading on ionic liquid pretreatment. Biotechnol Biofuels 2013;6:52.

[7] Li C, Knierim B, Manisseri C, Arora R, Scheller HV, Auer M, et al. Comparison of dilute acid and ionic liquid pretreatment of switchgrass: Biomass recalcitrance, delignification and enzymatic saccharification. Bioresour Technol 2010;101:4900–6.

[8] Sun N, Rahman M, Qin Y, Maxim ML, Rodríguez H, Rogers RD. Complete dissolution and partial delignification of wood in the ionic liquid 1-ethyl-3-methylimidazolium acetate. Green Chem 2009;11:646-55.

[9] Kuo C-H, Lee C-K. Enhancement of enzymatic saccharification of cellulose by cellulose dissolution pretreatments. Carbohydr Polym 2009;77:41–6.

[10] Tian X, Rehmann L, Xu CC, Fang Z. Pretreatment of Eastern White Pine (Pinus strobesL.) for Enzymatic Hydrolysis and Ethanol Production by Organic Electrolyte Solutions. ACS Sustainable Chemistry & Engineering 2016;4:2822-9.

[11] Zhao H, Baker GA, Song Z, Olubajo O, Crittle T, Peters D. Designing enzyme-compatible ionic liquids that can dissolve carbohydrates. Green Chem 2008;10:696-705.

[12] Li Q, He YC, Xian M, Jun G, Xu X, Yang JM, et al. Improving enzymatic hydrolysis of wheat straw using ionic liquid 1-ethyl-3-methylimidazolium diethyl phosphate pretreatment. Bioresour Technol 2009;100:3570–5.

[13] Kumara R, Mago G, Balan V, Wyman CE. Physical and chemical characterizations of corn stover and poplar solids resulting from leading pretreatment technologies. Bioresour Technol 2009;100:3948–62.

[14] Mohan M, Timung R, Deshavath NN, Banerjee T, Goud VV, Dasu VV. Optimization and hydrolysis of cellulose under subcritical water treatment for the production of total reducing sugars. RSC Adv 2015;5:103265-75.

[15] Lloyd TA, Wyman CE. Combined sugar yields for dilute sulfuric acid pretreatment of corn stover followed by enzymatic hydrolysis of the remaining solids. Bioresour Technol 2005;96:1967–77.

[16] Schell DJ, Farmer J, Newman M, McMillan JD. Dilute-sulfuric acid pretreatment of corn stover in pilot-scale reactor. Appl Biochem Biotechnol 2003;105:69–85.

[17] Ramos LP. The chemistry involved in the steam treatment of lignocellulosic materials. Quim Nova 2003;26:863–71.

[18] Zhu Z, Sathitsuksanoh N, Vinzant T, Schell DJ, McMillan JD, Zhang YHP. Comparative study of corn stover pretreated by dilute acid and cellulose solvent-

based lignocellulose fractionation: Enzymatic hydrolysis, supramolecular structure, and substrate accessibility. Biotechnol Bioeng 2009;103:715–24.

[19] Cevasco G, Chiappe C. Are ionic liquids a proper solution to current environmental challenges? Green Chem 2014;16:2375-85.

[20] Morais ARC, Pinto JV, Nunes D, Roseiro LB, Oliveira MC, Fortunato E, et al. Imidazole: Prospect Solvent for Lignocellulosic Biomass Fractionation and Delignification. ACS Sustainable Chemistry & Engineering 2016;4:1643-52.

[21] Zhang H, Wu J, Zhang J, He J. 1-Allyl-3-methylimidazolium Chloride Room Temperature Ionic Liquid: A New and Powerful Nonderivatizing Solvent for Cellulose. Macromolecules 2005;38:8272-7.

[22] Mohan M, Goud VV, Banerjee T. Solubility of glucose, xylose, fructose and galactose in ionic liquids: Experimental and theoretical studies using a continuum solvation model. Fluid Phase Equilib 2015;395:33-43.

[23] Swatloski RP, Spear SK, Holbrey JD, Rogers RD. Dissolution of Cellose with Ionic Liquids. J Am Chem Soc 2002;124:4974-5.

[24] Balaji C, Banerjee T, Goud VV. COSMO-RS Based Predictions for the Extraction of Lignin from Lignocellulosic Biomass Using Ionic Liquids: Effect of Cation and Anion Combination. J Solution Chem 2012;41:1610-30.

[25] Xu A, Zhang Y, Zhao Y, Wang J. Cellulose dissolution at ambient temperature: role of preferential solvation of cations of ionic liquids by a cosolvent. Carbohydr Polym 2013;92:540-4.

[26] Biswasa A, Shogrena RL, Stevensonb DG, Willetta JL, Bhowmik PK. Ionic liquids as solvents for biopolymers: Acylation of starch and zein protein. Carbohydr Polym 2006;66:546–50.

[27] Xie H, Zhang S, Li S. Chitin and chitosan dissolved in ionic liquids as reversible sorbents of CO2. Green Chem 2006;8:630-3

[28] Mohan M, Banerjee T, Goud VV. Solid Liquid Equilibrium of Cellobiose, Sucrose, and Maltose Monohydrate in Ionic Liquids: Experimental and Quantum Chemical Insights. J Chem Eng Data 2016;61:2923–32.

[29] Fukumoto K, Yoshizawa M, Ohno H. Room Temperature Ionic Liquids from 20 Natural Amino Acids. J Am Chem Soc 2005;127:2398–9.

[30] Fukaya Y, Sugimoto A, Ohno H. Superior Solubility of Polysaccharides in Low Viscosity, Polar, and Halogen-Free 1,3-Dialkylimidazolium Formates. Biomacromolecules 2006;7:3295–7.

[31] Fukaya Y, Hayashi K, Wada M, Ohno H. Cellulose dissolution with polar ionic liquids under mild conditions: required factors for anions. Green Chem 2008;10:44-6

[32] India State of Forest Report, 2011. Government of India.: Published by the Ministry of Environment and Forests; Forest Survey of India, 2011.

[33] Katwal RPS, Srivastva RK, Kumar S, Jeeva V. State of forest genetic resources convservation and management in India. Forestry Department; 2003.

[34] Timung R, Naik Deshavath N, Goud VV, Dasu VV. Effect of subsequent dilute acid and enzymatic hydrolysis on reducing sugar production from sugarcane bagasse and spent citronella biomass. J Energy 2016;2016.

[35] Deshavath NN, Mohan M, Veeranki VD, Goud VV, Pinnamaneni SR, Benarjee T. Dilute acid pretreatment of sorghum biomass to maximize the hemicellulose hydrolysis with minimized levels of fermentative inhibitors for bioethanol production. 3 Biotech 2017;7:139.

[36] Lowry OH, Rosebrough NJ, Farr AL, Randall RJ. Protein measurement with the folin phenol reagent. J Biol Chem 1951;193:265-75.

[37] An Y-X, Zong M-H, Wu H, Li N. Pretreatment of lignocellulosic biomass with renewable cholinium ionic liquids: Biomass fractionation, enzymatic digestion and ionic liquid reuse. Bioresour Technol 2015;192:165–71.
[38] Sluiter A, Hames B, Ruiz R, Scarlata C, Sluiter J, Templeton D, et al. Determination of Structural Carbohydrates and Lignin in Biomass. In: NREL/TP-510-42618, editor. Golden, Colorado: National Renewable Energy Laboratory; 2004.
[39] Sluiter A, Hames B, Ruiz R, Scarlata C, Sluiter J, Templeton D. Determination of Ash in Biomass. In: NREL/TP-510-42622, editor. Golden, Colorado: National Renewable Energy Laboratory; 2008.
[40] Perez-Pimienta JA, Lopez-Ortega MG, Varanasi P, Stavila V, Cheng G, Singh S, et al. Comparison of the impact of ionic liquid pretreatment on recalcitrance of agave bagasse and switchgrass. Bioresour Technol 2013;127:18–24.
[41] Mohan M, Viswanath P, Banerjee T, Goud VV. Multiscale Modeling Strategies and Experimental Insights for the Solvation of Cellulose and Hemicellulose in Ionic Liquids. Mol Phys 2018:doi: 10.1080/00268976.2018.1447152.
[42] Wang B, Qin L, Mu T, Xue Z, Gao G. Are Ionic Liquids Chemically Stable? Chem Rev 2017;117:7113-31.
[43] Sowmiah S, Srinivasadesikan V, Tseng M-C, Chu Y-H. On the Chemical Stabilities of Ionic Liquids. Molecules 2009;14:3780-813.
[44] Baskar C, Baskar S, Dhillon RS. Biomass Conversion: The Interface of Biotechnology, Chemistry and Materials Science: Springer Berlin Heidelberg; 2012.
[45] Sun J, Shi J, Murthy Konda NVSN, Campos D, Liu D, Nemser S, et al. Efficient dehydration and recovery of ionic liquid after lignocellulosic processing using pervaporation. Biotechnol Biofuels 2017;10.
[46] Lee SH, Doherty TV, Linhardt RJ, Dordick JS. Ionic liquid-mediated selective extraction of lignin from wood leading to enhanced enzymatic cellulose hydrolysis. Biotechnol Bioeng 2009;102:1368–76.
[47] Fu D, Mazza G, Tamaki Y. Lignin Extraction from Straw by Ionic Liquids and Enzymatic Hydrolysis of the Cellulosic Residues. J Agric Food Chem 2010;58:2915–22.
[48] Li C, Cheng G, Balan V, Kent MS, Ong M, Chundawat SPS, et al. Influence of physico-chemical changes on enzymatic digestibility of ionic liquid and AFEX pretreated corn stover. Bioresour Technol 2011;102:6928-36.
[49] Fu D, Mazza G. Optimization of processing conditions for the pretreatment of wheat straw using aqueous ionic liquid. Bioresour Technol 2011;102:8003-10.
[50] Hou X-D, Smith TJ, Li N, Zong M-H. Novel renewable ionic liquids as highly effective solvents for pretreatment of rice straw biomass by selective removal of lignin. Biotechnol Bioeng 2012;109:2484–93.
[51] Weerachanchai P, Leong SSJ, Chang MW, Ching CB, Lee J-M. Improvement of biomass properties by pretreatment with ionic liquids for bioconversion process. Bioresour Technol 2012;111:453-9.
[52] Ding ZD, Chi Z, Gu WX, Gu SM, Liu JH, Wang HJ. Theoretical and experimental investigation on dissolution and regeneration of cellulose in ionic liquid. Carbohydr Polym 2012;89:7-16.
[53] Guo J, Zhang D, Duan C, Liu C. Probing anion-cellulose interactions in imidazolium-based room temperature ionic liquids: a density functional study. Carbohydr Res 2010;345:2201-5.
[54] Wei L, Li K, Ma Y, Hou X. Dissolving lignocellulosic biomass in a 1-butyl-3-methylimidazolium chloride–water mixture. Ind crop prod 2012;37:227-34.

[55] Liu Z, Sun X, Hao M, Huang C, Xue Z, Mu T. Preparation and characterization of regenerated cellulose from ionic liquid using different methods. Carbohydr Polym 2015;117:99-105.

[56] Casas A, Oliet M, Alonso MV, Rodríguez F. Dissolution of Pinus radiata and Eucalyptus globulus woods in ionic liquids under microwave radiation: Lignin regeneration and characterization. Sep Purif Technol 2012;97:115–22.

[57] Liu CF, Xu F, Sun JX, Ren JL, Curling S, Sun RC, et al. Physicochemical characterization of cellulose from perennial ryegrass leaves (Lolium perenne). Carbohydr Res 2006;341:2677-87.

[58] Casas A, Alonso MV, Oliet M, Santos TM, Rodriguez F. Characterization of cellulose regenerated from solutions of pine and eucalyptus woods in 1-allyl-3-methilimidazolium chloride. Carbohydr Polym 2013;92:1946-52.

[59] Kassaye S, Pant KK, Jain S. Hydrolysis of cellulosic bamboo biomass into reducing sugars via a combined alkaline solution and ionic liquid pretreament steps. Renew Energ 2017;104:177-84.

[60] Moniruzzaman M, Ono T. Separation and characterization of cellulose fibers from cypress wood treated with ionic liquid prior to laccase treatment. Bioresour Technol 2013;127:132–7.

[61] Zhang J, Feng L, Wang D, Zhang R, Liu G, Cheng G. Thermogravimetric analysis of lignocellulosic biomass with ionic liquid pretreatment. Bioresour Technol 2014;153:379–82.

[62] Wang F-L, Li S, Sun Y-X, Han H-Y, Zhang B-X, Hu B-Z, et al. Ionic liquids as efficient pretreatment solvents for lignocellulosic biomass. RSC Adv 2017;7:47990-8.

[63] Cheng J, Wang N, Zhao D, Qin D, Si W, Tan Y, et al. The enhancement of the hydrolysis of bamboo biomass in ionic liquid with chitosan-based solid acid catalysts immobilized with metal ions. Bioresour Technol 2016;220:457-63.

[64] Qiu Z, Aita GM, Walker MS. Effect of ionic liquid pretreatment on the chemical composition, structure and enzymatic hydrolysis of energy cane bagasse. Bioresour Technol 2012;117:251-6.

[65] Qiu Z, Aita GM. Pretreatment of energy cane bagasse with recycled ionic liquid for enzymatic hydrolysis. Bioresour Technol 2013;129:532-7.

[66] Sun X, Sun X, Zhang F. Combined pretreatment of lignocellulosic biomass by solid base (calcined Na2SiO3) and ionic liquid for enhanced enzymatic saccharification. RSC Adv 2016;6:99455-66

Chapter – 8

Research Conclusions and Future Work

8 Research Conclusions and Future Work

8.1 Research Conclusions

The major conclusion of this thesis are discussed below:

In the initial part of thesis *i.e.*, chapters 2 and 3, the solubility of monosaccharides and disaccharides in ionic liquids were carried out over the temperature ranging from 303.15 – 373.5 K by employing both experimental and theoretical approaches. The solubility of monosaccharides and disaccharides in ILs were found to increase with increasing temperature. The results showed that dissolving capacity for [EMIM][SCN] was higher than [TMA][$MeSO_4$]. Further, the quantum chemical calculations also confirmed the same trend where higher interaction energy was obtained with both ILs. The COSMO-RS predictions reproduced the experimental trend with a maximum deviation of ~8% in both the ILs. In addition, the NRTL and UNIQUAC models were also successfully correlated with experimental data with a maximum deviation of 5%. From the experimental solubility, the derived interaction parameters of NRTL and UNIQUAC models was very useful because of the scarcity of data involving in ILs especially with respect to UNIFAC model. These binary interaction parameters are usually not available in commercial simulation packages such as ASPEN, HYSIS or CHEMCAD. One way to overcome this issue is to use these parameters directly in the simulation package when NRTL or UNIQUAC is invoked.

The separation of dissolved carbohydrates from ILs were performed using antisolvent method. From the COSMO-RS screening, DCM and DCE were found to be efficient antisolvents for the separation processes. From the experimental results, 90-99% of carbohydrate removal and 80-98% of IL recovery was achieved with DCM antisolvent at a molar ratio of R = 20 moles of antisolvent/mole of Ionic Liquid. Overall, higher interaction energy (MD) and lower activity coefficient (COSMO-RS) value yielded lower removal of carbohydrates.

The thesis further focused on the dissolution behavior of polysaccharides in ILs by observing their structural changes. To design a better combination of cation and anion for the dissolution of cellulose, hemicellulose, and biomass, 1428 ILs was screened using COSMO-RS model. After the successful screening of ILs, the potential cation and anion combinations were further screened by interaction energy and NBO analysis by QC calculations. From MD simulations, it was found that the cellulose was bounded with six to seven anions, and two to four cations in the first coordination shell. For theoretical calculations, the consideration of any conformers of cellulose and hemicellulose molecules gives a similar result. It was also observed that the O-H…O (anion) bond is far stronger than the C-H…O (cation) bond. The experimental solubility of cellulose/hemicellulose in ILs which depicted an excellent agreement with simulated results.

Incidentally, the cation significantly affects the solubility of cellulose with their acidic protons. This competes on the other side by forming hydrogen bonds with anion. To overcome this issue, adding of suitable cosolvent to the IL can make the dissolution process feasible and useful. Therefore, the effect of protic and aprotic solvents have been studied. Aprotic solvents were found to be good candidates for the dissolution of cellulose in ILs at a molar ratio of two. With addition of cosolvent to IL, the strong association pairs of ions would be partially destroyed thereby releasing more number of free cations and anions from IL. The dissociated free anions would then interact with cellulose and increase the solubility of cellulose. On the other hand, the protic solvents could reduce the interactions between cation and anions very efficiently, where the $[OAc]^-$ anion was shown to be preferentially solvated by protic solvents. Eventually, aprotic solvents are the recommended choice for the dissolution of cellulose in IL/cosolvent mixtures. The protic solvents can also be utilized for the recovery of cellulose in ILs.

Pretreatment of lignocellulosic biomass is an essential step in a commercial biorefinery. A comparison of IL and dilute acid pretreatment of actual biomass namely bamboo was carried at different pretreatment conditions. Among the pretreatments, IL pretreatment produces higher reducing sugars yield and lower degradation products. Hence it is a promising alternative to the dilute acid pretreatment process. IL pretreatment process is more convenient and environmentally friendly, requires less processing time for enzymatic hydrolysis and also lowers the energy consumption leading to higher sugar yield.

8.2 Scope of the Future Work

1. It is inferred that lignin content and crystallinity index of cellulose plays a vital role in the enzymatic saccharification of any biomass. In order to enhance the enzymatic saccharification of biomass, alkali pretreatment is employed to remove the lignin content. Thereafter the lignin free biomass gets dissolved in ionic liquids, where the residual biomass can be used for further enzymatic saccharification.
2. In the present work, we have used *Cellulase* enzyme for hydrolysis of biomass for the production of reducing sugars. *Cellulase* enzyme is composed of several amino acids. Therefore, MD simulations can be further explored to understand the highly active sites of *Cellulase* enzyme on biomass or cellulose.
3. Currently Deep Eutectic Solvents (DES) are having more attention towards the application in extraction and dissolution technologies. Lignocellulosic biomass and its derived components such as monosaccharides, disaccharides and cellulose/hemicellulose can be dissolved in DES by applying both experimental and theoretical knowledge. Comparison can therefore be made between IL and DES based solvent for biomass dissolution.

APPENDIX

A Appendix (Chapter-2)

Table A.1: Structures and details of ionic liquids which are studied in this work for screening

Entry	Name of the Ionic Liquid & Acronym	Chem. formula & M. Wt.	Ionic Liquid Structure
1.	1-allyl-3-methylimidazolium dicyanamide [AMIM][DCA]	$C_9H_{15}N_3$ / 165.24	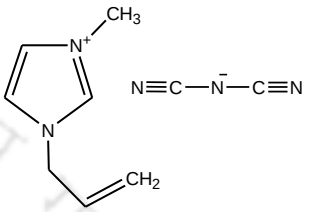
2.	1-allyl-3-methylimidazolium bromide [AMIM][Br]	$C_7H_{11}BrN_2$ / 203.08	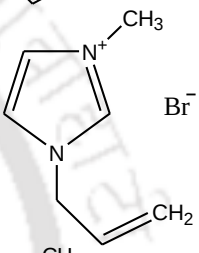
3.	1-allyl-3-methylimidazolium bis(trifluoromethanesulphonyl) imide [AMIM][Tfms]	$C_9H_{11}F_6N_3O_4S_2$ / 403.32	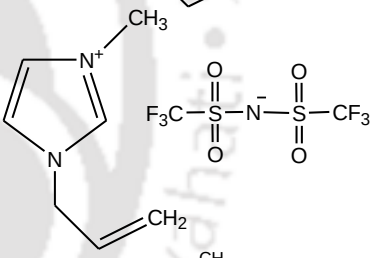
4.	1-benzyl-3-methylimidazolium chloride [BeMIM][Cl]	$C_{11}H_{13}N_2Cl$ / 208.69	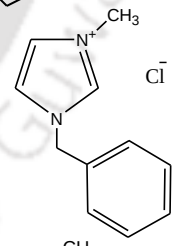
5.	1-benzyl-3-methylimidazolium Tetrafluoroborate [BeMIM][BF_4]	$C_{11}H_{13}N_2BF_4$ / 260.04	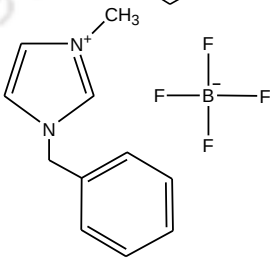
6.	1-butyl-3-methylimidazolium acetate [BMIM][OAc]	$C_{10}H_{18}N_2O_2$ / 198.26	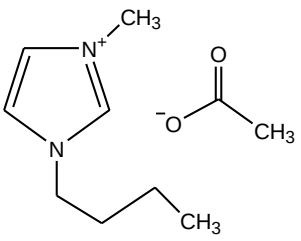

7. 1-butyl-3-methylimidazolium dicyanamide [BMIM][DCN] — $C_{10}H_{15}N_5$ / 205.26

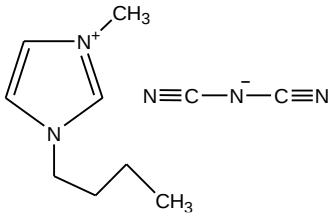

8. 1-butyl-3-methylimidazolium methyl sulphate [BMIM][$MeSO_4$] — $C_9H_{18}N_2O_4S$ / 250.32

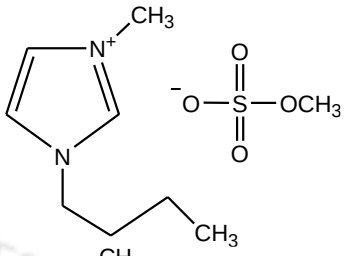

9. 1-butyl-3-methylimidazolium hexafluorophosphate [BMIM][PF_6] — $C_8H_{15}F_6N_2P$ / 284.18

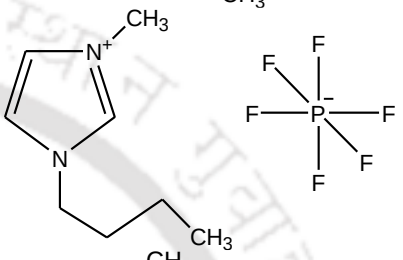

10. 1-butyl-3-methylimidazolium tetrachloroaluminate [BMIM][$AlCl_4$] — $C_8H_{15}AlClN_2$ /308.01

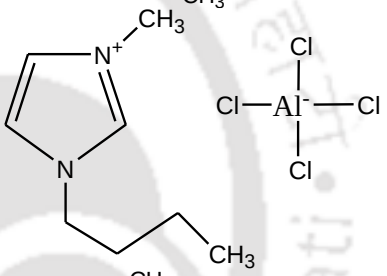

11. 1-butyl-3-methylimidazolium bis(trifluoromethylsulfonyl) imide [BMIM][Tfms] — $C_{10}H_{15}F_6N_3O_4S_2$ / 419.36

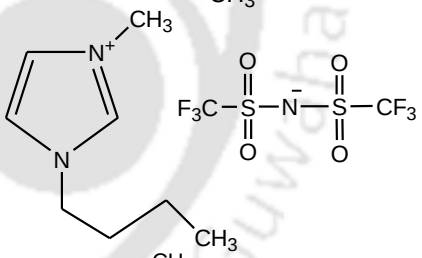

12. 1-butyl-3-methylimidazolium tetrafluoroborate [BMIM][BF_4] — $C_8H_{15}N_2BF_4$ / 226.02

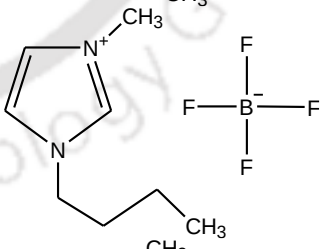

13. 1-butyl-3-methylimidazolium thiocyanate [BMIM][SCN] — $C_9H_{15}N_3S$ / 197.3

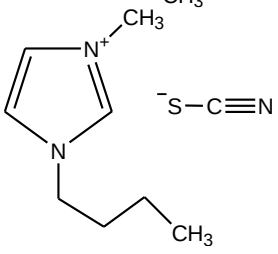

14. 1-butyl-3-methylimidazolium trifluoroacetate [BMIM][AcF$_3$] — $C_{10}H_{15}F_3N_2O_2$ / 252.23

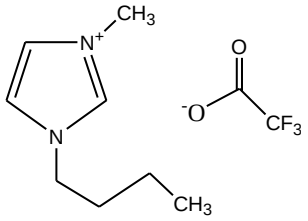

15. 1-butyl-3-methylimidazolium trifluoromethanesulfonate [BMIM][MSF$_3$] — $C_9H_{18}F_3N_2O_3S$ / 288.29

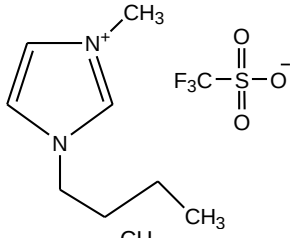

16. 1-ethyl-3-methylimidazolium acetate [EMIM][OAc] — $C_8H_{14}N_2O_2$ / 170.21

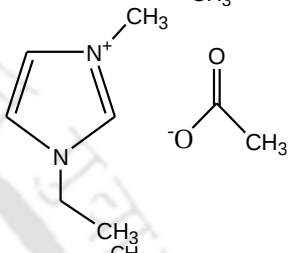

17. 1-ethyl-3-methylimidazolium aminoacetate [EMIM][AMAc] — $C_8H_{15}N_3O_2$ / 185.22

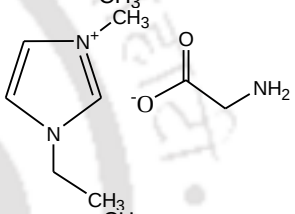

18. 1-ethyl-3-methylimidazolium bis(trifluoromethylsulfonyl) imide [EMIM][Tfms] — $C_8H_{11}F_6N_3O_4S_2$ / 391.31

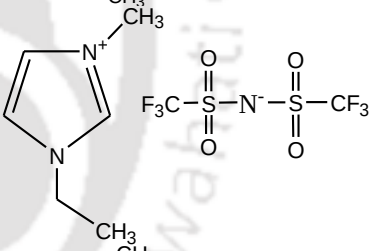

19. 1-ethyl-3-methylimidazolium dicyanamide [EMIM][DCN] — $C_8H_{11}N_5$ / 177.21

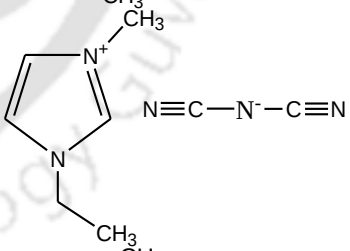

20. 1-ethyl-3-methylimidazolium diethylphosphate [EMIM][Et$_2$PO$_4$] — $C_{10}H_{21}N_2O_4P$ / 264.26

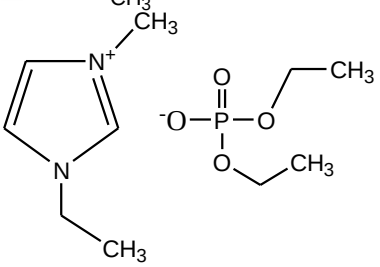

21. 1-ethyl-3-methylimidazolium dimethyl phosphate [EMIM][Me_2PO_4] — $C_8H_{17}N_2O_4P$ / 236.21

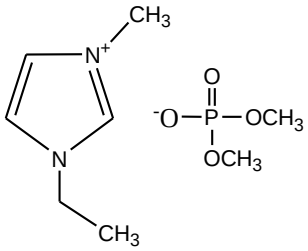

22. 1-ethyl-3-methylimidazolium ethyl sulphate [EMIM][$EtSO_4$] — $C_8H_{16}N_2O_4S$ / 236.29

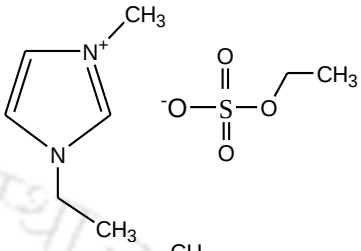

23. 1-ethyl-3-methylimidazolium hydrogensulfate [EMIM][HSO_4] — $C_6H_{12}N_2O_4S$ / 208.24

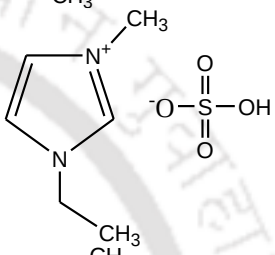

24. 1-ethyl-3-methylimidazolium tetrachloroaluminate [EMIM][$AlCl_4$] — $C_6H_{11}AlClN_2$ / 279.96

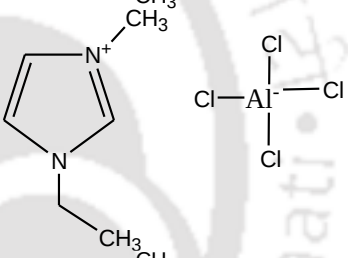

25. 1-ethyl-3-methylimidazolium tetrafluoroborate [EMIM][BF_4] — $C_6H_{11}BF_4N_2$ / 197.97

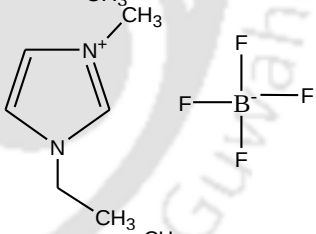

26. 1-ethyl-3-methylimidazolium thiocyanate [EMIM][SCN] — $C_7H_{11}N_3S$ / 169.25

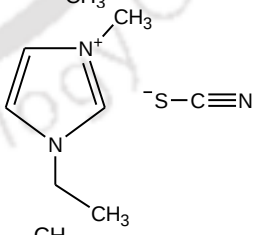

27. 1-ethyl-3-methylimidazolium tosylate [EMIM][Tos] — $C_{13}H_{18}N_2O_3S$ / 282.36

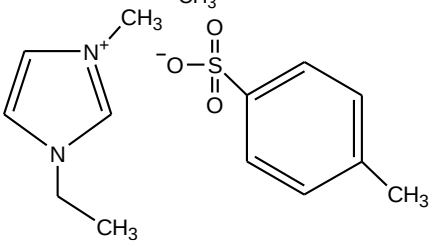

28. 1-ethyl-3-methylimidazolium trifluoromethanesulfonate [EMIM][MSF_3] — $C_7H_{11}F_3N_2O_3S$ / 260.234

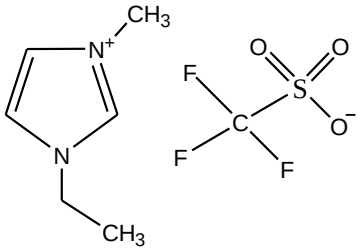

29. 1-ethyl-3-methylimidazolium trifluoroacetate [EMIM][AcF_3] — $C_8H_{11}F_3N_2O_2$ / 224.18

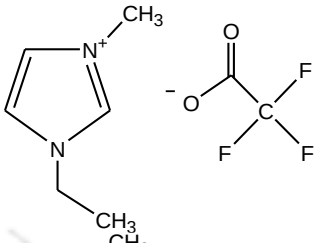

30. 1-hexyl-3-methylimidazolium bis(trifluoromethylsulfonyl) imide [HMIM][Tfms] — $C_{12}H_{19}F_6N_3O_4S_2$ / 447.42

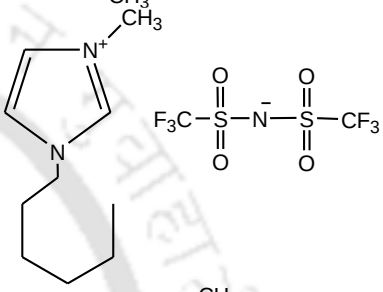

31. 1-hexyl-3-methylimidazolium chloride [HMIM][Cl] — $C_{10}H_{19}ClN_2$ / 202.723

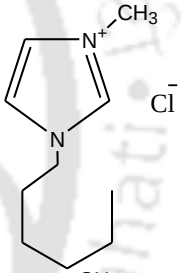

32. 1-hexyl-3-methylimidazolium trifluoromethanesulfonate [HMIM][MSF_3] — $C_{11}H_{19}F_3N_2O_3S$ / 316.34

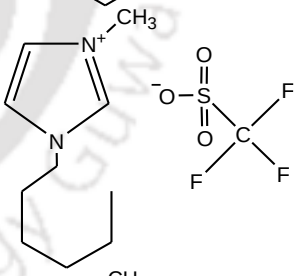

33. 1-hexyl-3-methylimidazolium tetrafluoroborate [HMIM][BF_4] — $C_{10}H_{19}BF_4N_2$ / 254.08

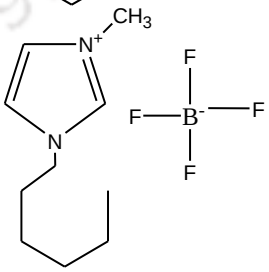

34. 1-methyl-3-octylimidazolium chloride [MOIM][Cl] — $C_{12}H_{23}ClN_2$ / 230.78

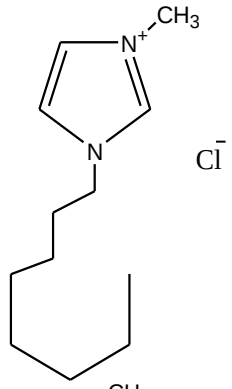

35. 1-methyl-3-octylimidazolium hexafluorophosphate [MOIM][PF_6] — $C_{12}H_{23}F_6N_2P$ / 340.29

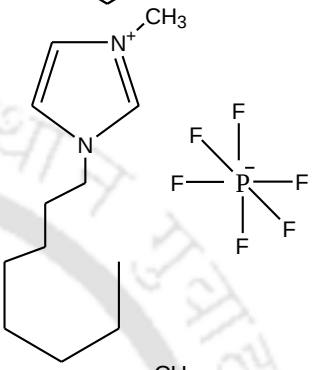

36. 1-methyl-3-octylimidazolium trifluoromethanesulfate [MOIM][MSF_3] — $C_{13}H_{23}F_3N_2O_3S$ / 344.39

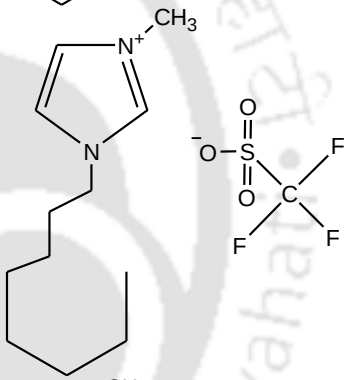

37. 1-propyl-3-methylimidazolium bis(trifluoromethylsulfonyl) imide [PMIM][Tfms] — $C_9H_{13}F_6N_3O_4S_2$ / 405.34

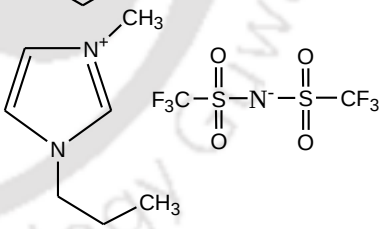

38. 1-butyl-2,3-dimethylimidazolium hexafluorophosphate [BDMIM][PF_6] — $C_9H_{17}F_6N_2P$ / 298.21

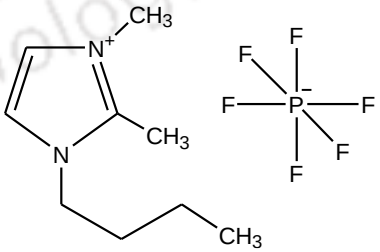

39. 1-(2-hydroxyethyl)-3-methylimidazolium dicyanamide [13MIM][DCN] — $C_8H_{11}N_5O$ / 193.21

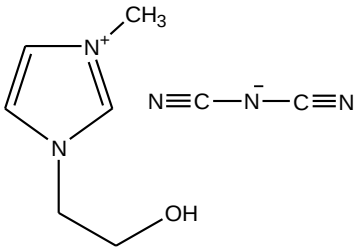

40. 1,3-dimethylimidazolium dimethyl phosphate [13DMIM][Me_2PO_4] — $C_7H_{15}N_2O_4P$ / 222.18

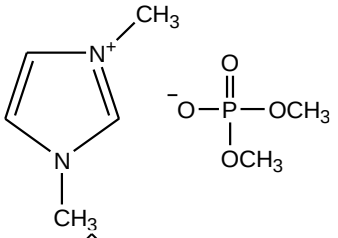

41. 1,2-dimethyl-3-propylimidazolium bis(trifluoromethylsulfonyl) imide [DMPIM][Tfms] — $C_{10}H_{15}F_6O_4S_2$ / 419.36

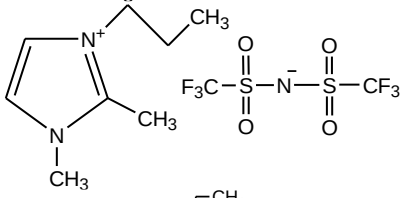

42. Methyltrioctylammonium thiosalicylate [MTOA][ThSal] — $C_{32}H_{59}NO_2S$ / 521.88

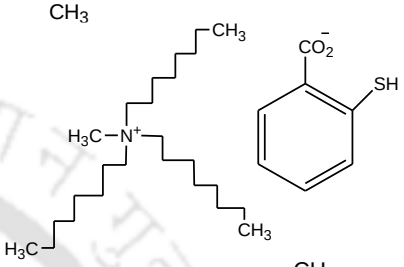

43. Methyl trioctyl ammonium Chloride [Aliquat®336] — $C_{25}H_{54}ClN$ / 404.16

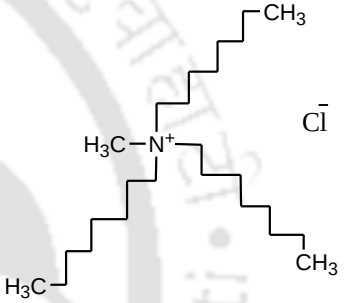

44. Butyltrimethylammonium bis(trifluoromethylsulfonyl) imide [BTMA][Tfms] — $C_9H_{18}F_6N_2O_4S_2$ / 396.37

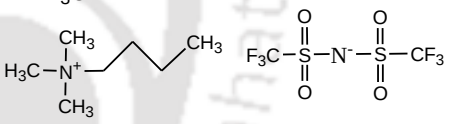

45. Ethylammonium nitrite [EtA][NO_3] — $C_2H_9N_2O_3$ / 108.11

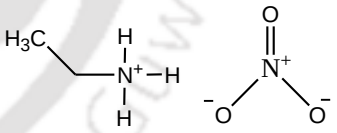

46. Ethyldimethylpropylammonium bis(trifluoromethylsulfonyl) imide [EDMPA][Tfms] — $C_9H_{18}F_6N_2O_4S_2$ / 396.37

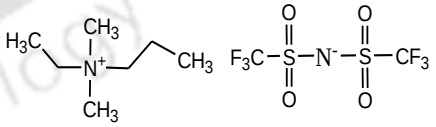

47. Propylammonium nitrite [PrA][NO_3] — $C_3H_{10}N_2O_3$ / 122.12

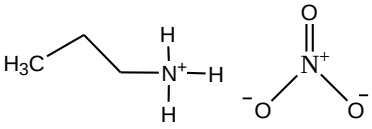

48. Tetramethylammonium hydroxide [TMAM][OH] — $C_4H_{13}NO$ / 91.18

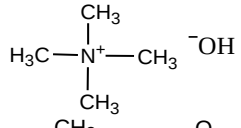

49. Triethylmethylammonium methylcarbonate [TEMA][MC] — $C_9H_{21}NO_3$ / 191.27

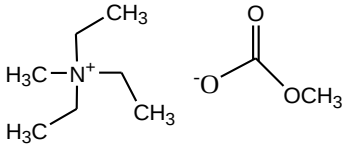

50.	Tris(2-hydroxyethyl) methyl ammonium methylsulphate [TMA][$MeSO_4$]	$C_8H_{21}O_7NS$ / 275.32	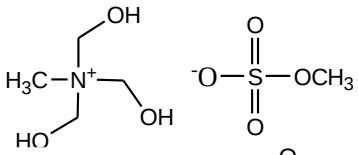
51.	2-hydroxyethyl-trimethylammonium L-lactate[HTMA][Lc]	$C_8H_{19}NO_4$ / 193.24	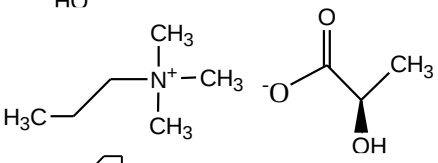
52.	Trihexyltetradecylphosphonium chloride [TTDP][Cl]	$C_{32}H_{68}ClP$ / 519.31	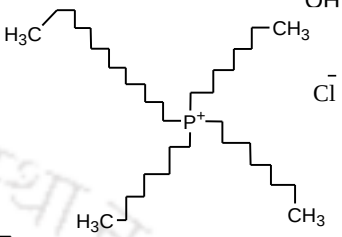
53.	Trihexyltetradecylphosphonium dicyanamide [TTDP][DCN]	$C_{34}H_{68}N_3P$ / 549.9	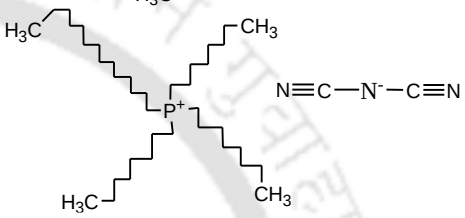
54.	Methyltributylphosphonium methyl sulphate [MTBP][$MeSO_4$]	$C_{14}H_{21}O_7NS$ / 328.45	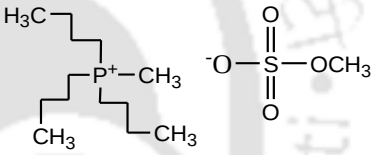
55.	3-methyl-1-propylpyridinium bis(trifluoromethylsulfonyl) imide [MPPy][Tfms]	$C_{11}H_{14}F_6N_2O_4S_2$ / 416.36	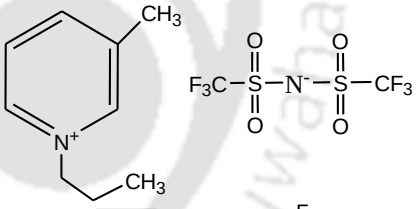
56.	1-butyl-3-methylpyridinium tetrafluoroborate [BMPy][BF_4]	$C_{10}H_{16}BF_4N$ / 237.05	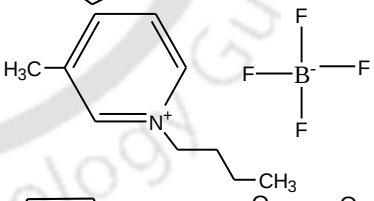
57.	1-butyl-1-methylpyrrolidinium bis(trifluoromethylsulfonyl) imide [BMPyr][Tfms]	$C_{11}H_{20}O_4S_2N_2F_6$ / 422.21	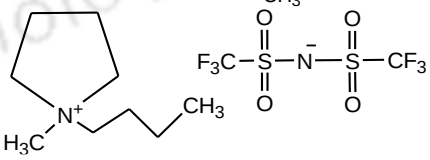
58.	1-butyl-1-methylpyrrolidinium dicyanamide [BMPyr][DCN]	$C_{11}H_{20}N_4$ / 208.3	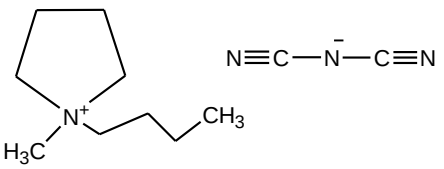

59.	1-butyl-1-methylpyrrolidinium trifluoromethanesulfonate [BMPyr][MSF_3]	$C_{10}H_{20}O_3NSF_3$ / 291.33	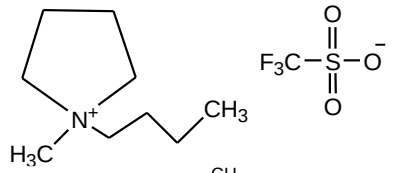
60.	1,2,3tris(diethylamino)cyclopropenylium bis(trifluoromethylsulfonyl) imide [123TCP][Tfms]	$C_{17}H_{30}F_6N_4O_4$ / 532.56	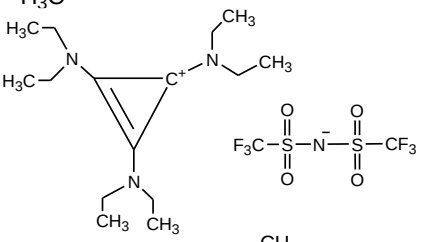
61.	1,2,3-Tris(diethylamino)cyclopropenylium dicyanamide [123TCP][DCN]	$C_{17}H_{30}N_6$ / 318.46	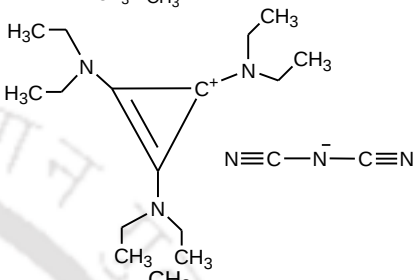
62.	4-ethyl-4-methylmorphalinium methylcarbonate [4EMMP][MC]	$C_9H_{19}NO_4$ / 205.25	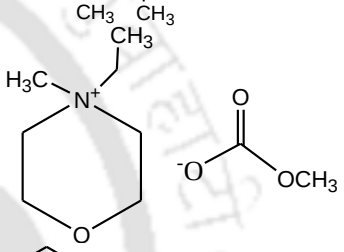
63.	1-butyl-3-methylpipedinium bis(trifluoromethylsulfonyl) imide [BMP][Tfms]	$C_{12}H_{22}O_4S_2N_2F_6$ / 436.43	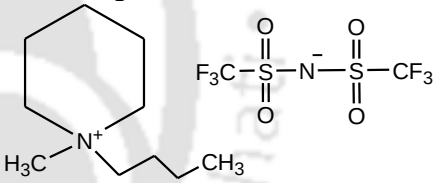
64.	Triethylsulfonium bis(trifluoromethylsulfonyl) imide [TES][Tfms]	$C_8H_{15}O_4S_3NF_6$ / 399.39	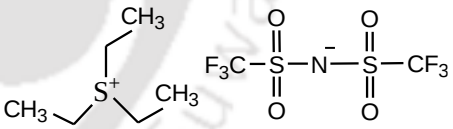

Table A.2: Equations used in the COSMO-RS calculations [1]

Misfit energy	$E_{misfit}(\sigma,\sigma') = a_{eff} e_{misfit}(\sigma,\sigma')$ (a) $E_{misfit}(\sigma,\sigma') = a_{eff}\frac{\alpha}{2}(\sigma,\sigma')^2$ (b) Where $\alpha' = (0.64\times 0.3\times a_{eff}^{3/2})/\varepsilon_o$ (c) $\varepsilon_o = 2.325\times 10^{-4}(e^2 mol/kcal)$ is the permittivity in free space
Hydrogen bond interaction energy	$E_{hb}(\sigma,\sigma') = a_{eff} e_{hb}(\sigma,\sigma')$ $= a_{eff} c_{hb} \min\{0, \min\min(0, \sigma_{don}+\sigma_{hb}) \max\max(0, \sigma_{acc}-\sigma_{hb})\}$ (a) $\sigma_{don} = \min\min(\sigma,\sigma') < \sigma_{hb}$ (b) $\sigma_{acc} = \max\max(\sigma,\sigma') > \sigma_{hb}$ (c)
vander Waals (vdW) energy	$E_{vdW}^X = \sum_{a\in X} x_i P^{x_i}(\sigma)$
Total energy	$E(\sigma,\sigma') = \frac{\alpha'}{2}(\sigma+\sigma')^2 + c_{hb}\min\{0, \min(0,\sigma_{don}+\sigma_{hb})\max(0,\sigma_{acc}-\sigma_{hb})\}$
Sigma profile of component and mixture	$P_s(\sigma) = \sum_{i\in S} x_i p^{x_i}(\sigma)$ Where $p^{x_i}(\sigma)$ is the sigma profile of pure component
Sigma profile averaging	$\sigma_m = \frac{\sum_n \sigma_n^* \frac{r_n^2 r_{eff}^2}{r_n^2+r_{eff}^2}\exp\left(-\frac{d_{mn}^2}{r_n^2+r_{eff}^2}\right)}{\sum_n \frac{r_n^2 r_{eff}^2}{r_n^2+r_{eff}^2}\exp\left(-\frac{d_{mn}^2}{r_n^2+r_{eff}^2}\right)}$, $r_{eff} = \sqrt{a_{eff}/\pi}$, $r_n = \sqrt{a_n/\pi}$
Sigma potential (Chemical potential of segment)	$\mu_s(\sigma) = -kT\ln\left\{\sum_{\sigma'}\exp\left[\frac{-E_{pair}(\sigma,\sigma')+\mu_s(\sigma')}{kT}\right]\right\} + kT\ln p_s(\sigma)$ (a) $p_s(\sigma)\Gamma_s(\sigma) = \exp\left(\frac{\mu_s(\sigma)}{kT}\right)$ (b)
Activity coefficient of segment	$\ln\Gamma_s(\sigma) = -\ln\left\{\sum_{\sigma'} p_s(\sigma)\Gamma_s(\sigma)\exp\left[\frac{-E(\sigma,\sigma')}{kT}\right]\right\}$
Activity coefficient in mixture, $\ln\gamma_{i/s}$	$\ln\gamma_{i/s} = n_i\sum_\sigma P_i(\sigma)\left[\ln\Gamma_s(\sigma) - \Gamma_i(\sigma)\right] + \ln\gamma_{i/s}^{SG}$ (a) $\ln\gamma_{i/s}^{SG} = \ln\frac{\phi_i}{x_i} + \frac{z}{2}q_i\ln\frac{\theta_i}{\phi_i} + li - \frac{\phi_i}{x_i}\sum_j x_j l_j$ (b)
Staverman-Guggenhein term, $\ln\gamma_{i/S}^{SG}$	Where $\theta_i = \frac{x_i q_i}{\sum_j x_j q_j}$, $\phi_i = \frac{x_i r_i}{\sum_j x_j r_j}$, $l_i = \frac{z}{2}\left((r_i-q_i)-(r_i-1)\right)$ (c)

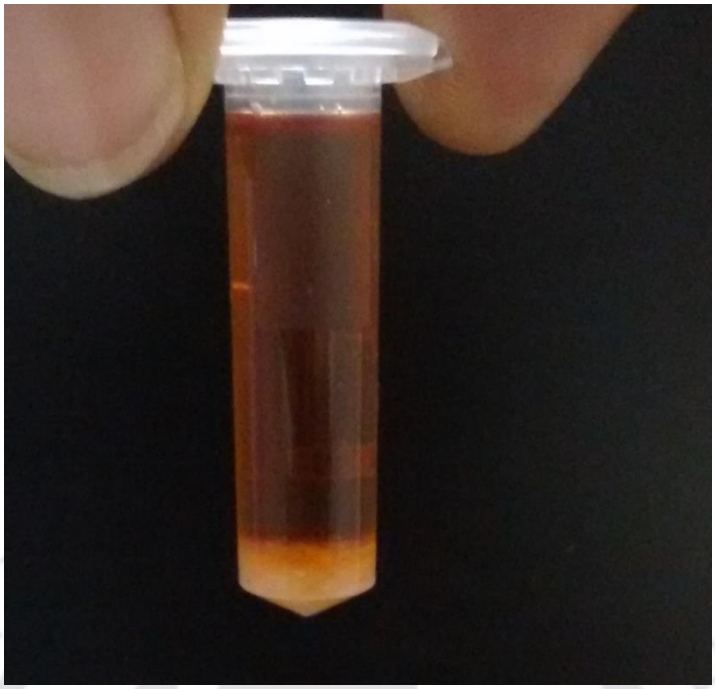

Figure A.1: Experimental solid-liquid equilibrium phase separation of D-(+)-Glucose in [EMIM][SCN] (upper portion *i.e.*, liquid phase contains both solute and solvent, and lower portion is only solid phase)

Reference

[1] Anantharaj R, Banerjee T. COSMO-RS based predictions for the desulphurization of diesel oil using ionic liquids: Effect of cation and anion combination. Fuel Process Technol 2011;92:39-52.

B Appendix (Chapter-3)

Sample Calculation. The example calculation of disaccharides solubility in [EMIM][SCN] was calculated with their corresponding peak area and is given in Table B.1.

Table B.1: Example calculation of disaccharide solubility in [EMIM][SCN]

Complex System	Corresponding Integral value	Mole fraction (x)
[EMIM][SCN]	12.45	0.9226
D-(+)-cellobiose	2.10	0.0774

Here, [EMIM][SCN] and D-(+)-cellobiose possess 11 and 22 hydrogen atoms, respectively. This when divided by their respective integral areas (12.45 and 2.10) gives us an individual H atom value of 1.132 and 0.095 respectively. From here the mole fraction is computed as

$$x_{IL} = \frac{1.132}{1.132 + 0.095} \Rightarrow 0.9226$$

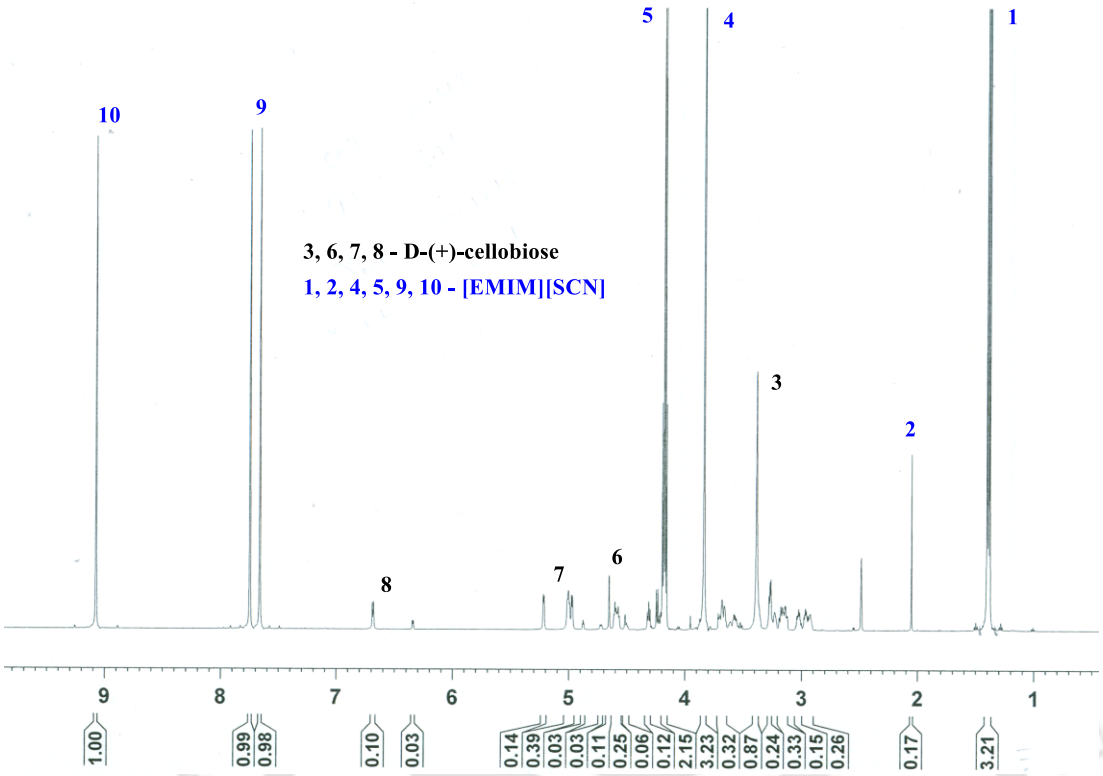

Figure B.1: ^{1}H NMR spectra of D-(+)-cellobiose in [EMIM][SCN]

C Appendix (Chapter-4)

Equation for CHARMM force field

$$U(R) = \sum_{bonds} K_b(r - r_o)^2 + \sum_{angles} K_\theta(\theta - \theta_o)^2 + \sum_{dihedrals} K_\chi\left[1+\cos(n\chi - \delta)\right]$$

$$+ \sum_{UB} K_{UB}(S - S_o)^2 + \sum_{impropers} K_{imp}(\varphi - \varphi_o)^2 + \sum_{nonbonded}\left(\varepsilon_{ij}\left[\left(\frac{R_{\min_{ij}}}{r_{ij}}\right)^{12} - \left(\frac{R_{\min_{ij}}}{r_{ij}}\right)^{6}\right] + \frac{q_i q_j}{\varepsilon_l r_{ij}}\right)$$

Where, Bond parameters K_b is the bond force constant (kcal mol^{-1} Å^{-2}) and r_o is the equilibrium bond length in Å; Angle parameters K_θ is the angle force constant (kcal mol^{-1} radian^{-2}) and θ_o is the equilibrium angle (degree); Dihedral parameters K_χ is the dihedral force constant in kcal mol^{-1} and δ in degree; The Urey-Bradley component (cross-term accounting for angle bending using 1,3 non bonded interactions) comprises the fifth term, where K_{UB} is the respective force constant and S_o is the distance between the 1,3 atoms in the harmonic potential. Improper parameters K_{imp} in kcal mol^{-1} radian^{-2} and φ_o in degree; Non bonded parameters ε in kcal mol^{-1} and R_{min} in Å (Non-bonded interactions between pairs of atoms *(i, j)* are represented by the last two terms. By definition, the non-bonded forces are only applied to atom pairs separated by at least three bonds. The van der Waals (vdW) energy is calculated with a standard 12-6 Lennard-Jones potential and the electrostatic energy with a Coulombic potential. In the Lennard-Jones potential above, the $R_{min,ij}$ term is not the minimum of the potential, but rather where the Lennard-Jones potential crosses the x-axis (*i.e.*, where the Lennard-Jones potential is zero)).

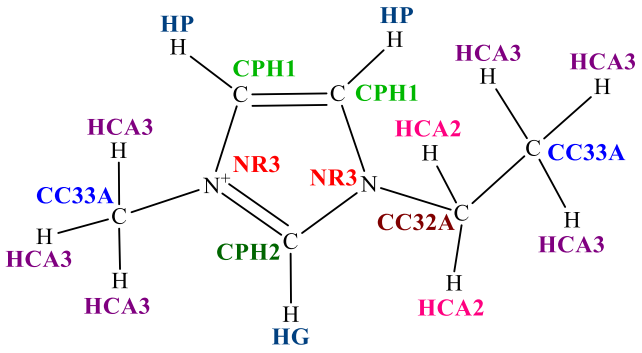

Table C.1: CHARMM force filed parameters file for $[EMIM]^+$ cation with atom types

Bond		K_b	r_o	**Bond**		K_b	r_o
CC32A	HCA2	309.000	1.100	CC33A	HCA3	322.000	1.090
CC32A	CC32A	222.500	1.530	CC32A	CC33A	222.500	1.520
NR3	CPH2	380.000	1.337	CPH1	CPH1	410.000	1.370
NR3	CPH1	380.000	1.370	HP	CPH1	375.000	1.080
HG	CPH2	333.000	1.080	NR3	CC32A	250.000	1.483
NR3	CC33A	250.000	1.470				

Angle			K_θ	θ_o	K_{UB}	S_o
CC33A	CC32A	HCA2	34.500	110.100	22.530	2.179
CC33A	CC32A	HCA3	33.430	110.100	22.530	2.179
HCA2	CC32A	CC32A	32.500	110.100		
HCA2	CC32A	CC33A	34.600	110.100		
HCA2	CC32A	HCA2	35.500	107.000		
HCA3	CC33A	HCA3	35.500	108.400		
HCA3	CC33A	CC32A	34.600	110.100		
CC32A	CC32A	CC32A	58.350	111.600		
CC32A	CC32A	CC33A	58.000	112.000		
CPH2	NR3	CPH1	145.000	108.000		
NR3	CPH1	CPH1	145.000	108.000		
NR3	CPH1	HP	22.000	122.300		
NR3	CPH2	HG	32.000	125.700		
HP	CPH1	CPH1	22.000	130.000		
CC33A	NR3	CPH1	45.000	125.000		
CC33A	NR3	CPH2	45.000	127.000		
CC32A	NR3	CPH1	45.000	125.000		
CC32A	NR3	CPH2	45.000	127.000		
HCA3	CC33A	NR3	50.000	109.500		
HCA2	CC32A	NR3	50.000	105.500		
NR3	CC32A	CC32A	140.000	112.600		
NR3	CPH2	NR3	145.000	109.100		
NR3	CC32A	CC33A	70.000	113.500		

Dihedrals				K_χ	n	δ
HCA2	CC32A	CC32A	HCA2	0.190	3.000	0.000
CC32A	CC32A	CC32A	HCA2	0.190	3.000	0.000
CC33A	CC32A	CC32A	HCA2	0.190	3.000	0.000
HCA2	CC32A	CC33A	HCA3	0.170	3.000	0.000
CC32A	CC32A	CC33A	HCA3	0.170	3.000	0.000
CC33A	CC32A	CC32A	CC32A	0.150	1.000	0.000
CPH2	NR3	CC32A	CC32A	0.000	4.000	0.000
CC32A	CC32A	NR3	CPH1	0.450	2.000	0.000
CC32A	CC32A	NR3	CPH1	0.120	1.000	180.000
HCA2	CC32A	NR3	CPH2	0.000	3.000	0.000
CPH1	NR3	CC32A	HCA2	0.065	3.000	0.000

CC32A	NR3	CPH1	CPH1	5.000	2.000	180.000
HP	CPH1	NR3	CC32A	1.000	2.000	180.000
HG	CPH2	NR3	CC32A	1.000	2.000	180.000
NR3	CPH2	NR3	CC32A	1.000	2.000	180.000
HCA3	CC33A	NR3	CPH2	0.000	3.000	0.000
CPH1	NR3	CC33A	HCA3	0.065	3.000	0.000
CC33A	NR3	CPH1	CPH1	3.500	2.000	180.000
HP	CPH1	NR3	CC33A	1.000	2.000	180.000
HG	CPH2	NR3	CC33A	1.000	2.000	180.000
NR3	CPH2	NR3	CC33A	1.000	2.000	180.000
CPH2	NR3	CPH1	CPH1	12.000	2.000	180.000
HP	CPH1	NR3	CPH2	2.500	2.000	180.000
HG	CPH2	NR3	CPH1	3.000	2.000	180.000
NR3	CPH1	CPH1		12.000	2.000	180.000
NR3	CPH2	NR3	CPH1	12.000	2.000	180.000
NR3	CPH1	CPH1	HP	2.500	2.000	180.000
HP	CPH1	CPH1	HP	1.000	2.000	180.000
CC32A	CC32A	CC32A	NR3	0.300	3.000	0.000
CC32A	CC32A	CC32A	NR3	0.700	1.000	180.000
HCA2	CC32A	CC32A	NR3	0.190	3.000	0.000
HCA3	CC33A	CC32A	NR3	0.200	3.000	0.000
HCA3	CC33A	CC32A	HCA2	0.195	3.000	0.000
CC33A	CC32A	NR3	CPH1	0.450	2.000	0.000
CC33A	CC32A	NR3	CPH2	0.000	4.000	0.000

Improper				K_{imp}	φ_o
HG	NR3	NR3	CPH2	1.000	0.000
NR3	CPH1	CPH2	CC33A	2.000	0.000
NR3	CPH1	CPH2	CC32A	2.000	0.000
CPH1	CPH1	NR3	HP	1.000	0.000
CPH1	NR3	CPH1	HP	1.000	0.000

Non bonded	ε	R_{min}
HCA2	-0.022	1.320
HCA3	-0.022	1.320
HP	-0.046	0.900
HG	-0.046	0.700
CPH1	-0.050	1.800
CPH2	-0.050	1.800
NR3	-0.200	1.850
CC32A	-0.055	2.175
CC33A	-0.080	2.060

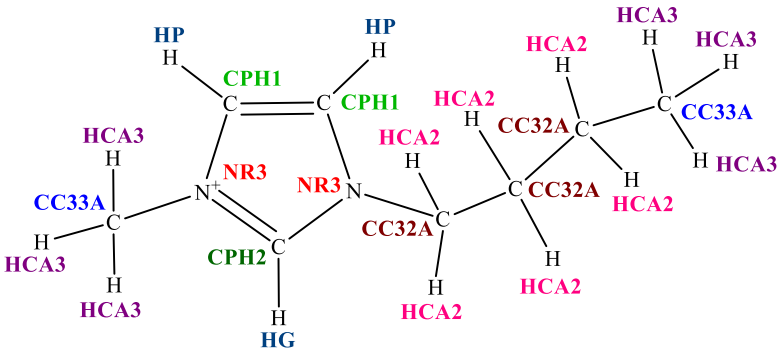

Table C.2: CHARMM force filed parameters file for $[BMIM]^+$ cation with atom types

Bond		K_b	r_o	**Bond**		K_b	r_o
CC32A	HCA2	309.000	1.100	CC33A	HCA3	322.000	1.090
CC32A	CC32A	222.500	1.530	CC32A	CC33A	222.500	1.520
NR3	CPH2	380.000	1.337	CPH1	CPH1	410.000	1.370
NR3	CPH1	380.000	1.370	HP	CPH1	375.000	1.080
HG	CPH2	333.000	1.080	NR3	CC32A	250.000	1.483
NR3	CC33A	250.000	1.470				

Angle			K_θ	θ_o
HAC2	CC32A	CC32A	32.500	110.100
HAC2	CC32A	CC33A	34.600	110.100
HAC2	CC32A	HAC2	35.500	107.000
HAC3	CC33A	HAC3	35.500	108.400
HAC3	CC33A	CC32A	34.600	110.100
CC32A	CC32A	CC32A	58.350	111.600
CC32A	CC32A	CC33A	58.000	112.000
CPH2	NR3	CPH1	145.000	108.000
NR3	CPH1	CPH1	145.000	108.000
NR3	CPH1	HP	22.000	122.300
NR3	CPH2	HG	32.000	125.700
HP	CPH1	CPH1	22.000	130.000
CC33A	NR3	CPH1	45.000	125.000
CC33A	NR3	CPH2	45.000	127.000
CC32A	NR3	CPH1	45.000	125.000
CC32A	NR3	CPH2	45.000	127.000
HAC3	CC33A	NR3	50.000	109.500
HAC2	CC32A	NR3	50.000	105.500
NR3	CC32A	CC32A	140.000	112.600
NR3	CPH2	NR3	145.000	109.100

Dihedrals				K_χ	n	δ
HAC2	CC32A	CC32A	HAC2	0.190	3.000	0.000
CC32A	CC32A	CC32A	HAC2	0.190	3.000	0.000
CC33A	CC32A	CC32A	HAC2	0.190	3.000	0.000
HAC2	CC32A	CC33A	HAC3	0.170	3.000	0.000
CC32A	CC32A	CC33A	HAC3	0.170	3.000	0.000
CC33A	CC32A	CC32A	CC32A	0.150	1.000	0.000
CPH2	NR3	CC32A	CC32A	0.000	4.000	0.000
CC32A	CC32A	NR3	CPH1	0.450	2.000	0.000
CC32A	CC32A	NR3	CPH1	0.120	1.000	180.000
HAC2	CC32A	NR3	CPH2	0.000	3.000	0.000

CPH1	NR3	CC32A	HAC2	0.065	3.000	0.000
CC32A	NR3	CPH1	CPH1	5.000	2.000	180.000
HP	CPH1	NR3	CC32A	1.000	2.000	180.000
HG	CPH2	NR3	CC32A	1.000	2.000	180.000
NR3	CPH2	NR3	CC32A	1.000	2.000	180.000
HAC3	CC33A	NR3	CPH2	0.000	3.000	0.000
CPH1	NR3	CC33A	HAC3	0.065	3.000	0.000
CC33A	NR3	CPH1	CPH1	3.500	2.000	180.000
HP	CPH1	NR3	CC33A	1.000	2.000	180.000
HG	CPH2	NR3	CC33A	1.000	2.000	180.000
NR3	CPH2	NR3	CC33A	1.000	2.000	180.000
CPH2	NR3	CPH1	CPH1	12.000	2.000	180.000
HP	CPH1	NR3	CPH2	2.500	2.000	180.000
HG	CPH2	NR3	CPH1	3.000	2.000	180.000
NR3	CPH1	CPH1	NR3	12.000	2.000	180.000
NR3	CPH2	NR3	CPH1	12.000	2.000	180.000
NR3	CPH1	CPH1	HP	2.500	2.000	180.000
HP	CPH1	CPH1	HP	1.000	2.000	180.000
CC32A	CC32A	CC32A	NR3	0.300	3.000	0.000
CC32A	CC32A	CC32A	NR3	0.700	1.000	180.000
HAC2	CC32A	CC32A	NR3	0.190	3.000	0.000
Improper				K_{imp}	φ_o	
HG	NR3	NR3	CPH2	1.000	0.000	
NR3	CPH1	CPH2	CC33A	2.000	0.000	
NR3	CPH1	CPH2	CC32A	2.000	0.000	
CPH1	CPH1	NR3	HP	1.000	0.000	
CPH1	NR3	CPH1	HP	1.000	0.000	
Non bonded				ε	R_{min}	
HAC2				-0.022	1.320	
HAC3				-0.022	1.320	
HP				-0.046	0.900	
HG				-0.046	0.700	
CPH1				-0.050	1.800	
CPH2				-0.050	1.800	
NR3				-0.200	1.850	
CC32A				-0.055	2.175	
CC33A				-0.080	2.060	

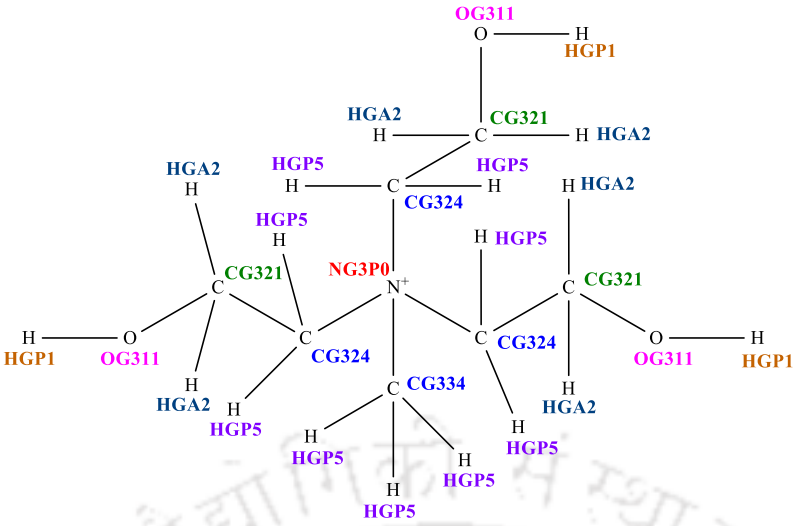

Table C.3: CHARMM force filed parameters file for $[TMA]^+$ cation with atom types

Bond				K_b	r_o	**Bond**				K_b	r_o
CG324	NG3P0			215.000	1.510	CG334	NG3P0			215.000	1.510
CG321	OG311			428.000	1.420	OG311	HGP1			545.000	0.960
CG321	CG324			222.500	1.530	CG321	HGA2			309.000	1.111
CG324	HGP5			300.000	1.080	CG334	HGP5			300.000	1.080
Angle				K_θ	θ_o	K_{UB}		S_o			
CG321	CG324	NG3P0		67.700	115.000						
NG3P0	CG324	HGP5		40.000	109.500	27.000		2.130			
NG3P0	CG334	HGP5		40.000	109.500	27.000		2.130			
CG324	NG3P0	CG324		60.000	109.500	26.000		2.466			
CG324	NG3P0	CG334		60.000	109.500	26.000		2.466			
CG324	CG321	OG311		75.700	112.100						
OG311	CG321	HGA2		45.900	108.890						
CG321	OG311	HGP1		50.000	106.000						
CG324	CG321	HGA2		26.500	110.100	22.530		2.179			
CG321	CG324	HGP5		33.430	110.100	22.530		2.179			
HGA2	CG321	HGA2		35.500	109.000	5.400		1.802			
HGP5	CG324	HGP5		24.000	109.500	28.000		1.767			
HGP5	CG334	HGP5		24.000	109.500	28.000		1.767			
Dihedrals				K_χ	n	δ					
HGA2	CG321	OG311	HGP1	0.000	3.000	0.000					
CG324	CG321	OG311	HGP1	1.130	1.000	0.000					
CG324	CG321	OG311	HGP1	0.140	2.000	0.000					
CG324	CG321	OG311	HGP1	0.240	3.000	0.000					
OG311	CG321	CG324	HGP5	0.195	3.000	0.000					
OG311	CG321	CG324	NG3P0	4.300	1.000	180.000					
OG311	CG321	CG324	NG3P0	-0.400	3.000	180.000					
HGA2	CG321	CG324	HGP5	0.195	3.000	0.000					
HGA2	CG321	CG324	NG3P0	0.195	3.000	0.000					
CG321	CG324	NG3P0	CG334	0.260	3.000	0.000					
HGP5	CG324	NG3P0	CG324	0.260	3.000	0.000					
HGP5	CG324	NG3P0	CG334	0.260	3.000	0.000					
HGP5	CG334	NG3P0	CG324	0.260	3.000	0.000					

CG321	CG324	NG3P0	CG324	0.260	3.000	0.000	
HGP5	CG334	NG3P0	CG324	0.260	3.000	0.000	
Non bonded				ε	R_{min}	$\varepsilon_{1,4}$	$R_{min,1,4/2}$
HGA2				-0.035	1.340		
HGP1				-0.046	0.225		
HGP5				-0.046	0.700		
CG321				-0.056	2.010	-0.010	1.900
CG324				-0.055	2.175	-0.010	1.900
CG334				-0.077	2.215	-0.010	1.900
NG3P0				-0.200	1.850		
OG311				-0.192	1.765		

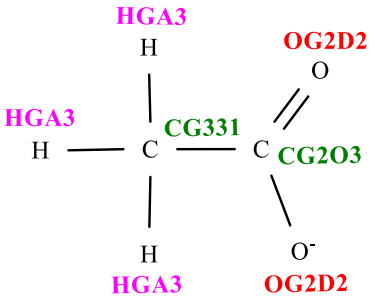

Table C.4: CHARMM force field parameters file for $[OAc]^-$ anion with atom types

Bond	K_b	r_o	**Bond**	K_b	r_o
CG2O3 CG331	200.00	1.522	CG331 HGA3	322.00	1.111
CG2O3 OG2D2	525.00	1.260			
Angle	K_θ	θ_o	K_{UB}	S_o	
CG331 CG2O3 OG2D2	40.00	116.00	50.00	2.353	
OG2D2 CG2O3 OG2D2	100.00	128.00	70.00	2.259	
CG2O3 CG331 HGA3	33.00	109.50	30.00	2.163	
HGA3 CG331 HGA3	35.50	108.40	5.40	1.802	
Dihedrals	K_χ	n	δ		
OG2D2 CG2O3 CG331 HGA3	0.05	6.00	180.00		
Improper	K_{imp}	φ_o			
CG2O3 OG2D2 OG2D2 CG311	96.00	0.00			
CG2O3 CG331 OG2D2 OG2D2	96.00	0.00			
CG331 OG2D2 OG2D2 CG2O3	96.00	0.00			
OG2D2 CG331 OG2D2 CG2O3	96.00	0.00			
CG331 CG2O3 OG2D2 OG2D2	96.00	0.00			
Non bonded	ε	R_{min}	$\varepsilon_{1,4}$	$R_{min,1,4/2}$	
OG2D2	-0.120	1.70			
CG331	-0.078	2.05	-0.010	1.90	
CG2O3	-0.070	2.00			
HGA3	-0.024	1.34			

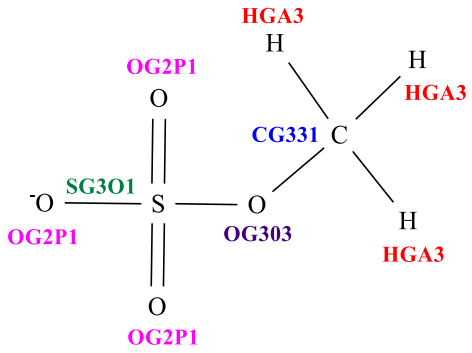

Table C.5: CHARMM force field parameters file for $[MeSO_4]^-$ anion with atom types

Bond				K_b	r_o	**Bond**		K_b	r_o
CG331	OG303			340.000	1.430	CG331	HGA3	322.000	1.111
OG2P1	SG3O1			540.000	1.448	OG303	SG3O1	250.000	1.575
Angle				K_θ	θ_o	K_{UB}		S_o	
OG2P1	SG3O1	OG303		85.000	98.000				
CG331	OG303	SG3O1		15.000	109.000	27.000		1.900	
OG2P1	SG3O1	OG2P1		130.000	109.470	35.000		2.450	
OG303	CG331	HGA3		60.000	109.500				
HGA3	CG331	HGA3		35.500	108.400	5.400		1.802	
Dihedrals				K_χ	n	δ			
HGA3	CG331	OG303	SG3O1	0.000	3.000	0.000			
CG331	OG303	SG3O1	OG2P1	0.000	3.000	0.000			
Non bonded				ε	R_{min}	$\varepsilon_{1,4}$		$R_{min,1,4/2}$	
SG3O1				-0.470	2.100				
CG331				-0.078	2.050	-0.010		1.900	
OG303				-0.100	1.650				
OG2P1				-0.120	1.700				
HGA3				-0.024	1.340				

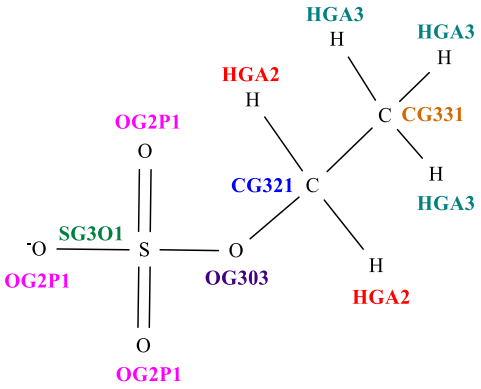

Table C.6: CHARMM force field parameters file for $[EtSO_4]^-$ anion with atom types

Bond			K_b	r_o	**Bond**		K_b	r_o
CG321	CG331		222.500	1.528	CG321	OG303	320.000	1.440
CG321	HGA2		309.000	1.111	CG331	HGA3	322.000	1.111
OG2P1	SG3O1		540.000	1.448	OG303	SG3O1	250.000	1.575
Angle			K_θ	θ_o	K_{UB}		S_o	
OG2P1	SG3O1	OG303	85.000	98.000				
CG331	OG303	SG3O1	15.000	109.000	27.000		1.900	
OG2P1	SG3O1	OG2P1	130.000	109.470	35.000		2.450	
OG303	CG321	HGA2	60.000	109.500				
HGA3	CG331	HGA3	35.500	108.400	5.400		1.802	
CG331	CG321	HGA2	34.600	110.100	22.530		2.179	
CG331	CG321	OG303	70.000	108.400				
CG321	CG331	HGA3	34.600	110.100	22.530		2.179	
CG321	OG303	SG3O1	15.000	109.000	27.000		1.900	
HGA2	CG321	HGA2	35.500	109.000	5.400		1.802	
Dihedrals				K_χ	n	δ		
OG303	CG321	CG331	HGA3	0.160	3.000	0.000		
HGA2	CG321	CG331	HGA3	0.160	3.000	0.000		
CG331	CG321	OG303	SG3O1	0.000	3.000	0.000		
HGA2	CG321	OG303	SG3O1	0.000	3.000	0.000		
CG321	OG303	SG3O1	OG2P1	0.000	3.000	0.000		
HGA3	CG331	OG303	SG3O1	0.000	3.000	0.000		
CG331	OG303	SG3O1	OG2P1	0.000	3.000	0.000		
Non bonded				ε	R_{min}	$\varepsilon_{1,4}$	$R_{min,1,4/2}$	
SG3O1				-0.470	2.100			
CG331				-0.078	2.050	-0.010	1.900	
CG321				-0.056	2.010	-0.010	1.900	
OG303				-0.100	1.650			
OG2P1				-0.120	1.700			
HGA3				-0.024	1.340			
HGA2				-0.035	1.340			

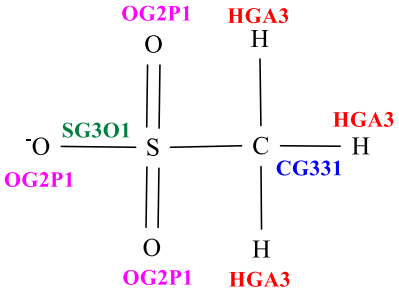

Table C.7: CHARMM force field parameters file for $[MeSO_3]^-$ anion with atom types

Bond			K_b	r_o	**Bond**		K_b	r_o
CG331	OG303		340.000	1.430	CG331	HGA3	322.000	1.111
OG2P1	SG3O1		540.000	1.448	OG303	SG3O1	250.000	1.575
CG331	SG3O1		240.000	1.800				
Angle			K_θ	θ_o	K_{UB}		S_o	
OG2P1	SG3O1	OG303	85.000	98.000				
CG331	OG303	SG3O1	15.000	109.000	27.000		1.900	
OG2P1	SG3O1	OG2P1	130.000	109.470	35.000		2.450	
OG303	CG331	HGA3	60.000	109.500				
HGA3	CG331	HGA3	35.500	108.400	5.400		1.802	
SG3O1	CG331	HGA3	46.100	111.300				
CG331	SG3O1	OG2P1	79.000	106.750				
Dihedrals			K_χ	n	δ			
HGA3	CG331	OG303	SG3O1	0.000	3.000	0.000		
CG331	OG303	SG3O1	OG2P1	0.000	3.000	0.000		
HGA3	CG331	SG3O1	OG2P1	0.200	3.000	0.000		
HGA3	CG331	SG3O1	CG331	0.200	3.000	0.000		
Non bonded				ε	R_{min}	$\varepsilon_{1,4}$	$R_{min,1,4/2}$	
SG3O1				-0.470	2.100			
CG331				-0.078	2.050	-0.010	1.900	
OG303				-0.100	1.650			
OG2P1				-0.120	1.700			
HGA3				-0.024	1.340			

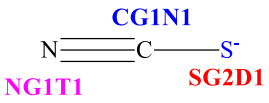

Table C.8: CHARMM force field parameters file for $[SCN]^-$ anion with atom types

Bond	K_b	r_o	**Bond**	K_b	r_o
CG1N1 NG1T1	1053.00	1.1800	CG1N1 SG2D1	300.00	1.6300
Angle	K_θ	θ_o	K_{UB}	S_o	
SG2D1 CG1N1 NG1T1	21.20	180.00			
Non bonded	ε	$R_{min/2}$			
CG1N1	-0.180	1.870			
NG1T1	-0.180	1.790			
SG2D1	-0.565	2.050			

Table C.9: List of cations used in this work

Sl.No.	Name of the cation and Acronym	Chem. Formula / mol. wt.	Chemical structure
1.	1,2,3-trimethylimidazolium $[123TMIM]^+$	$C_6H_{11}N_2^+$ / 111.09	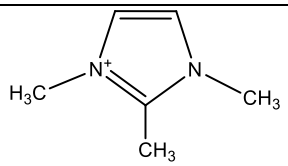
2.	1-allyl-3-methylimidazolium $[AMIM]^+$	$C_7H_{11}N_2^+$ / 123.09	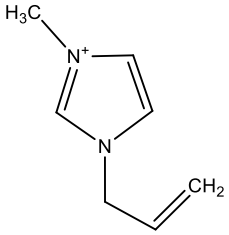
3.	1-butyl-3-methylimidazolium $[BMIM]^+$	$C_8H_{15}N_2^+$ / 139.12	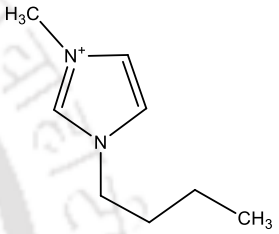
4.	1-(3-Cyanopropyl)-3-methylimidazolium $[13CyMIM]^+$	$C_8H_{12}N_3^+$ / 150.10	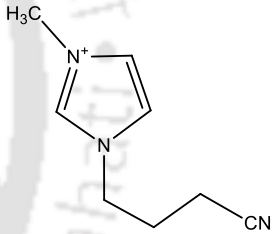
5.	1-ethyl-2,3-dimethylimidazolium $[EDMIM]^+$	$C_7H_{13}N_2^+$ / 125.11	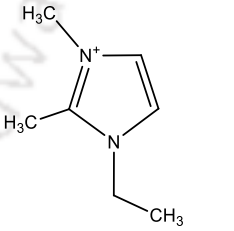
6.	1-ethyl-3-methylimidazolium $[EMIM]^+$	$C_6H_{11}N_2^+$ / 111.09	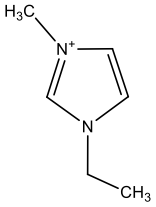
7.	1-hexyl-3-methylimidazolium $[HMIM]^+$	$C_{10}H_{19}N_2^+$ / 167.15	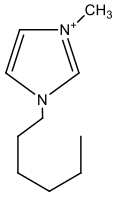
8.	1, 3-dimethylimidazolium $[DMIM]^+$	$C_5H_9N_2^+$ / 97.08	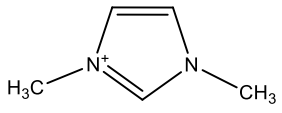

9.	1-octyl-3-methylimidazolium $[OMIM]^+$	$C_{12}H_{23}N_2^+$ / 195.19	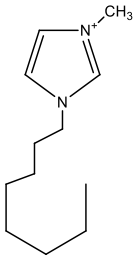
10.	1-benzyl-3-methylimidazolium $[BeMIM]^+$	$C_{11}H_{13}N_2^+$ / 173.11	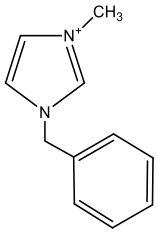
11.	Benzyltrimethylammonium $[BeTMA]^+$	$C_{10}H_{16}N^+$ / 150.13	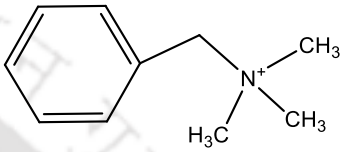
12.	Ethyldimethylpropylammonium $[EdMPA]^+$	$C_7H_{18}N^+$ / 116.14	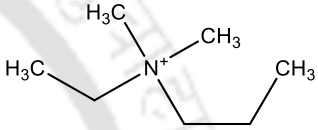
13.	Diethyl methyl(2-methoxyethyl)ammonium $[DEMA]^+$	$C_8H_{20}NO^+$ / 146.15	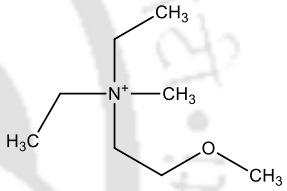
14.	Tetrabutylammonium $[TBA]^+$	$C_{16}H_{36}N^+$ / 242.28	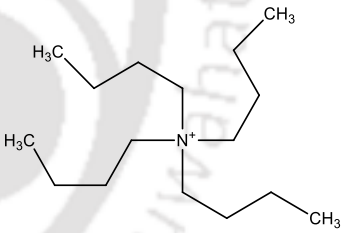
15.	Tetraethylammonium $[TEA]^+$	$C_8H_{20}N^+$ / 130.16	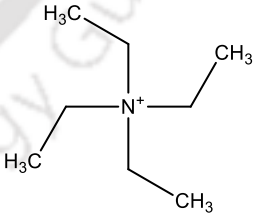
16.	Tetramethylammonium $[TMeA]^+$	$C_4H_{12}N^+$ / 74.10	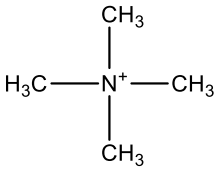
17.	Triethylmethylammonium $[TEMA]^+$	$C_7H_{18}N^+$ / 116.14	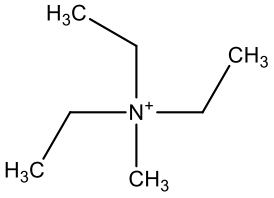

18.	Tris(2-hydroxyethyl) methylammonium $[TMA]^+$	$C_7H_{18}NO_3^+$ / 164.13	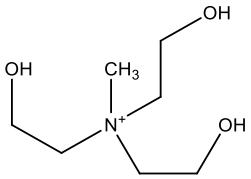
19.	Methyltrioctylammonium $[MTOA]^+$	$C_{25}H_{54}N^+$ / 368.43	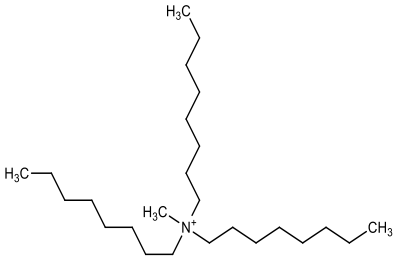
20.	Cholin $[Chln]^+$	$C_5H_{14}NO^+$ / 104.11	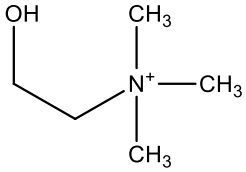
21.	1-butylpyridinium $[BPy]^+$	$C_9H_{14}N^+$ / 136.11	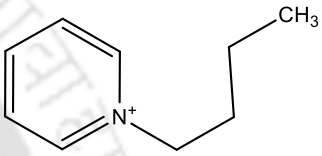
22.	1-ethylpyridinium $[EPy]^+$	$C_7H_{10}N^+$ / 108.08	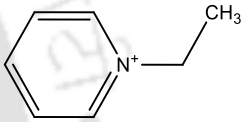
23.	1-hexylpyridinium $[HPy]^+$	$C_{11}H_{18}N^+$ / 164.14	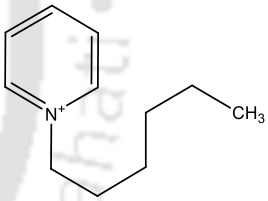
24.	1-octylpyridinium $[OPy]^+$	$C_{13}H_{22}N^+$ / 192.17	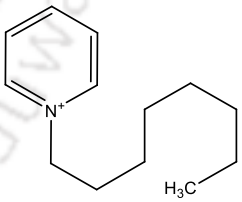
25.	1-butyl-3-methylpyridinium $[B3MPy]^+$	$C_{10}H_{16}N^+$ / 150.13	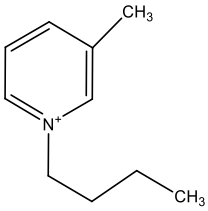
26.	1-butyl-4-methylpyridinium $[B4MPy]^+$	$C_{10}H_{16}N^+$ / 150.13	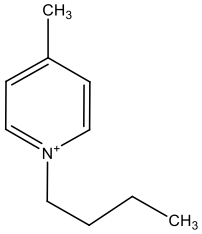

27.	1-butyl-1-methylpyrrolidinium $[BMPyr]^+$	$C_9H_{20}N^+$ / 142.16	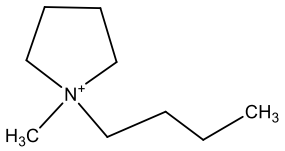
28.	1-ethyl-1-methylpyrrolidinium $[EMPyr]^+$	$C_7H_{16}N^+$ / 114.13	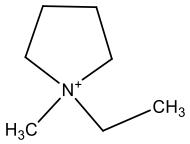
29.	1-hexyl-1-methylpyrrolidinium $[HMPyr]^+$	$C_{11}H_{24}N^+$ / 170.19	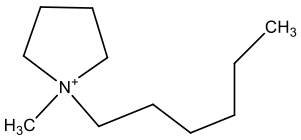
30.	1, 1-dimethylpyrrolidinium $[DMPyr]^+$	$C_6H_{14}N^+$ / 100.11	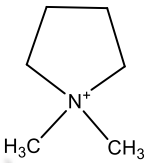
31.	1-butyl-1-ethylpyrrolidinium $[BEPyr]^+$	$C_{10}H_{22}N^+$ / 156.17	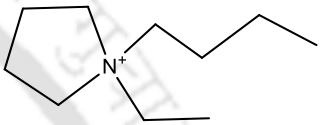
32.	1, 1-dipropylpyrrolidinium $[DPPyr]^+$	$C_{10}H_{22}N^+$ / 156.17	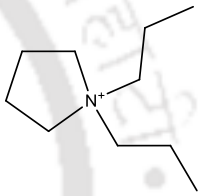
33.	Benzyltriphenylphosphonium $[BeTPP]^+$	$C_{25}H_{22}P^+$ / 353.15	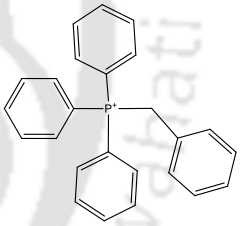
34.	Tributylmethylphosphonium $[TBMP]^+$	$C_{13}H_{30}P^+$ / 217.21	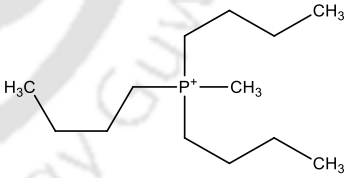
35.	Triethylmethylphosphonium $[TEMP]^+$	$C_7H_{18}P^+$ / 133.11	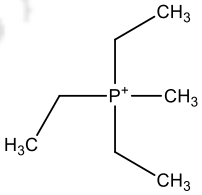
36.	Trihexyltetradecylphosphonium $[TTDP]^+$	$C_{38}H_{80}P^+$ / 567.60	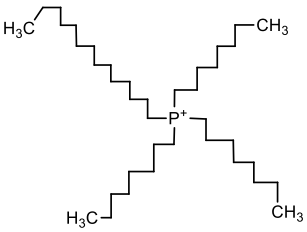
37.	1-butyl-1-methylpiperidinium $[BMPd]^+$	$C_{10}H_{22}N^+$ / 156.17	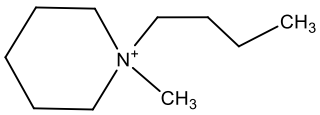

38.	1-ethyl-1-methylpiperidinium $[EMPd]^+$	$C_8H_{18}N^+$ / 128.14	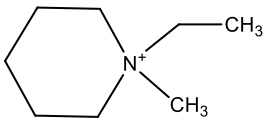
39.	1,2,4-Trimethylpyrazolium $[124TMPz]^+$	$C_6H_{11}N_2^+$ / 111.09	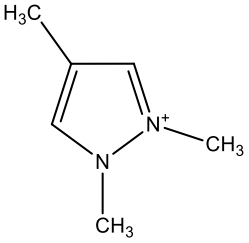
40.	4-ethyl-4-methylmorpholinium $[4E4MMp]^+$	$C_7H_{16}NO^+$ / 130.12	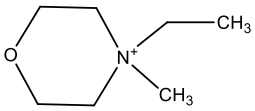
41.	1-octylquinolinium $[1OQn]^+$	$C_{17}H_{24}N^+$ / 242.19	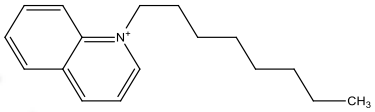
42.	Triethylsulfonium $[TES]^+$	$C_6H_{15}S^+$ / 119.09	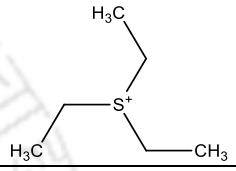

Table C.10: List of anions used in this work

Sl.No.	Name of the anion and Acronym	Chem. Formula / mol. wt.	Chemical structure
1.	Acetate $[OAc]^-$	$C_2H_3O_2^-$ / 59.01	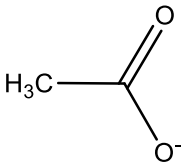
2.	Bromide $[Br]^-$	Br^- / 79.90	
3.	Chloride $[Cl]^-$	Cl^- / 35.45	
4.	Dibutyl phosphate $[DBPO_4]^-$	$C_8H_{18}O_4P^-$ / 209.09	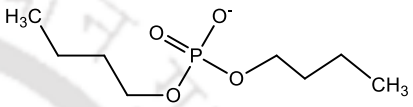
5.	Decanoate $[Dec]^-$	$C_{10}H_{19}O_2^-$ / 171.14	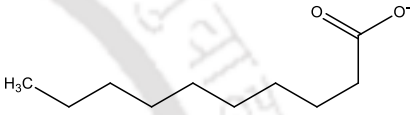
6.	Diethyl phosphate $[Et_2PO_4]^-$	$C_4H_{10}O_4P^-$ / 153.03	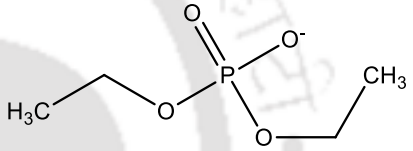
7.	Methylsulfonylacetamide $[MSAc]^-$	$C_3H_6NO_3S^-$ / 136.01	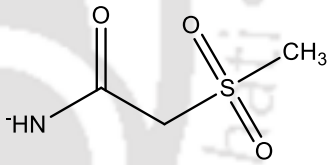
8.	Methylsulfonate $[MSO_3]^-$	$CH_3O_3S^-$ / 94.98	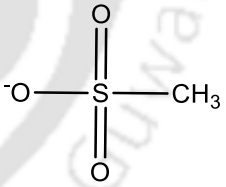
9.	Nitrate $[NO_3]^-$	NO_3^- / 61.99	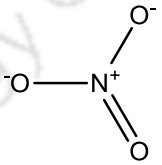
10.	Hydrogen carbonate $[HC]^-$	CHO_3^- / 60.99	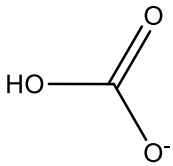
11.	Methyl carbonate $[MC]^-$	$C_2H_3O_3^-$ / 75.01	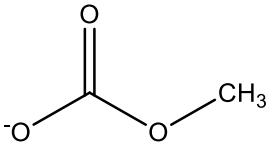

12.	Succinimide $[Succ]^-$	$C_4H_4NO_2^-$ / 98.02	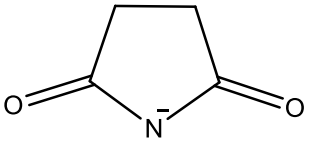
13.	Thiophenolate $[Thph]^-$	$C_6H_5S^-$ / 109.01	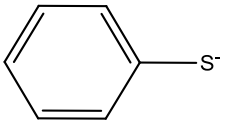
14.	Thiosalicylate $[ThSal]^-$	$C_7H_5O_2S^-$ / 153	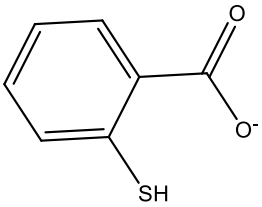
15.	Propionate $[Prop]^-$	$C_3H_5O_2^-$ / 73.03	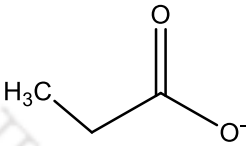
16.	Dimethyl phosphate $[Me_2PO_4]^-$	$C_2H_6O_4P^-$ / 125	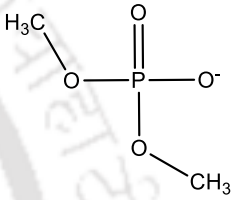
17.	Benzoate $[BEN]^-$	$C_7H_5O_2^-$ / 121.03	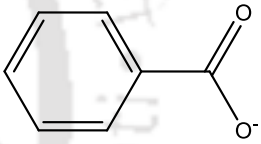
18.	Salicylate $[Sal]^-$	$C_7H_5O_3^-$ / 137.02	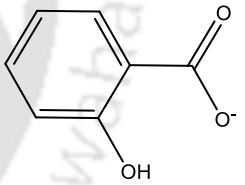
19.	Tosylate $[Tos]^-$	$C_7H_7O_3S^-$ / 171.01	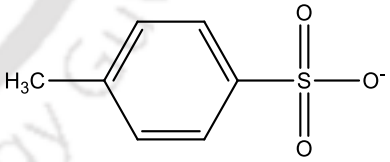
20.	Trifluoroacetate $[AcF_3]^-$	$C_2F_3O_2^-$ / 112.99	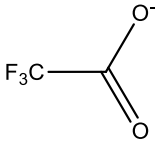
21.	Thiocyanate $[SCN]^-$	CNS^- / 57.98	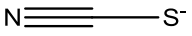
22.	2-(2-methoxyethoxy)ethyl sulfate $[22MESO_4]^-$	$C_5H_{11}O_6S^-$ / 199.03	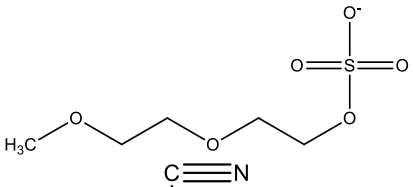
23.	Dicyanamide $[DCN]^-$	$C_2N_3^-$ / 66.01	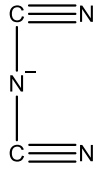

24.	Ethyl sulfate $[EtSO_4]^-$	$C_2H_5O_4S^-$ / 124.99	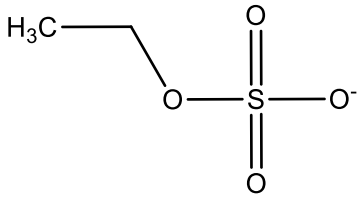
25.	Hydrogen sulfate $[HSO_4]^-$	HO_4S^- / 96.96	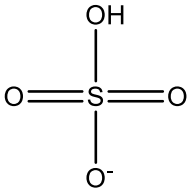
26.	Methylsulfate $[MeSO_4]^-$	$CH_3O_4S^-$ / 110.98	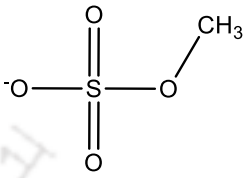
27.	Octyl sulfate $[OtSO_4]^-$	$C_8H_{17}O_4S^-$ / 209.09	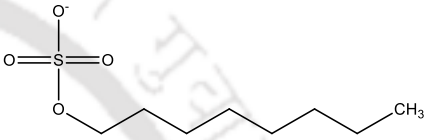
28.	Trifluoromethanesulfonate $[MSF_3]^-$	$CF_3O_3S^-$ / 148.95	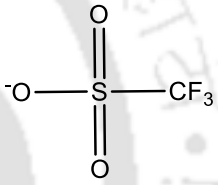
29.	Bis(methylsulfonyl)amide [BMA]$^-$	$C_2H_6NO_4S_2^-$ / 171.97	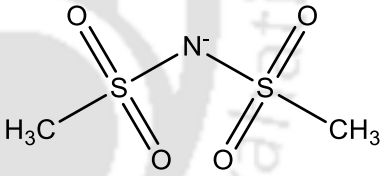
30.	Tetrafluoroborate $[BF_4]^-$	F_4B^- / 87.0	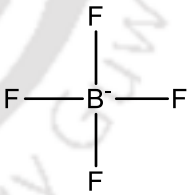
31.	Tetracyanoborate $[B(CN)_4]^-$	$C_4N_4B^-$ / 115.02	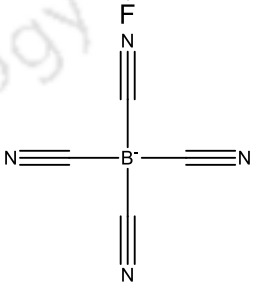
32.	Bis oxalato(2-) borate [BOB]$^-$	$C_4BrO_8^-$ / 254.88	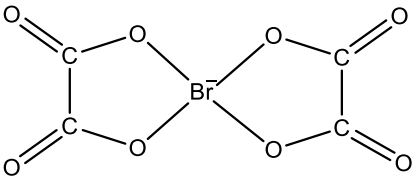

33.	Bis (trifluoromethylsulfonyl) imide $[Tfms]^-$	$C_2F_6NO_4S_2^-$ / 279.92	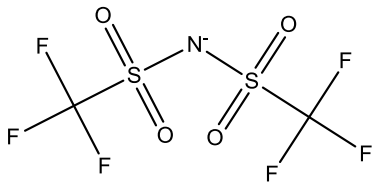
34.	hexafluorophosphate $[PF_6]^-$	F_6P^- / 144.96	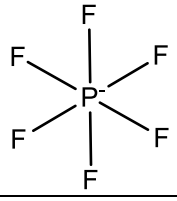

Table C.11: Bond lengths (Å) and partial charges of cellulose-anions[a]

Atom name	Anion									
	$[OAc]^-$	$[MC]^-$	$[HC]^-$	$[AcF_3]^-$	$[Cl]^-$	$[NO_3]^-$	$[Me_2PO_4]^-$	$[MSF_3]^-$	$[MeSO_4]^-$	$[SCN]^-$
O3	-0.852	-0.857	-0.845	-0.844	-0.828	-0.840	-0.779	-0.823	-0.835	-0.857
H3	0.587	0.593	0.556	0.597	0.502	0.584	0.493	0.563	0.591	0.490
O4	-0.839	-0.772	-0.724	-0.841	-0.852	-0.826	-0.770	-0.860	-0.847	-0.590
H4	0.543	0.479	0.436	0.567	0.507	0.545	0.447	0.532	0.546	0.389
O"1	-0.859	-0.820	—	-0.824	—	-0.718	—	—	-0.741	—
O"2	-0.867	-0.875	-0.826	-0.810	—	-0.716	-0.766	-0.765	-0.745	—
S	—	—	—	—	—	—	—	—	—	-0.694
Cl	—	—	—	—	-0.862	—	—	—	—	—
O3-H-O″1	1.72	1.72	1.75	1.78	2.20	1.80	1.75	1.87	1.82	
O4-H-O″2	1.67	1.71	1.69	1.74	2.19	1.78	1.73	1.84	1.79	
O3-H-S										2.44
O4-H-S										2.40
O3-H-Cl					2.20					
O4-H-Cl					2.19					

[a] Cellobiose-anti-syn is the cellulose model

Table C.12: Bond lengths (Å) and partial charges of hemicellulose-anions[a]

Atom Name	Anion								
	$[OAc]^-$	$[MC]^-$	$[HC]^-$	$[AcF_3]^-$	$[Cl]^-$	$[NO_3]^-$	$[Me_2PO_4]^-$	$[MeSO_4]^-$	$[SCN]^-$
O3	-0.723	-0.687	-0.721	-0.753	-0.764	-0.753	-0.762	-0.736	-0.775
H3	0.505	0.455	0.504	0.456	0.476	0.473	0.526	0.459	0.479
O4	-0.875	-0.863	-0.882	-0.773	-0.771	-0.742	-0.867	-0.692	-0.778
H4	0.533	0.528	0.536	0.475	0.473	0.464	0.560	0.422	0.475
O8	-0.828	-0.862	-0.791	-0.797	-0.785	-0.766	-0.789	-0.820	-0.765
H8	0.526	0.553	0.476	0.486	0.467	0.461	0.496	0.500	0.465
O"1	-0.895	-0.850	-0.911	-0.777		-0.627	-0.924	-0.506	
O"2	-0.848	-0.902	-0.771	-0.855		-0.715	-0.818	-0.762	
S									-0.661
Cl					-0.849				
O3-H-O″2	1.76	1.79	1.79	1.80	2.31	1.91	1.81	1.85	
O4-H-O″2	1.87	1.89	1.89	1.95	2.47	1.83	1.86	1.95	
O8-H-O″1	1.77	1.78	1.79	1.84	2.34	1.98	1.76	1.89	
O3-H-N									2.19
O4-H-N									2.03
O8-H-S									2.49
O3-H-Cl					2.31				
O4-H-Cl					2.47				
O8-H-Cl					2.34				

[a] Xylose+Glucose is the hemicellulose model

Table C.13: The electron donor and acceptor orbitals of cellulose conformers with anions and their corresponding second order interaction energies $E^{(2)*}$ (NBO analysis)

Donor	Acceptor	Cellobiose-anti-syn			Cellobiose-anti-anti		
		$[OAc]^-$	$[AcF_3]^-$	$[MC]^-$	$[OAc]^-$	$[AcF_3]^-$	$[MC]^-$
LP (1) O″1	BD*(1) O3 — H	31.76	32.51	40.96	29.19	28.86	37.47
LP (2) O″1	BD*(1) O3 — H	113.80	80.04	101.09	79.17	53.74	71.34
LP (1) O″2	BD*(1) O4 — H	35.19	37.61	38.83	42.32	34.08	34.04
LP (2) O″2	BD*(1) O4 — H	140.46	95.27	108.49	86.69	68.54	78.29
LP (3) O″2	BD*(1) O4 — H	11.67	7.53	–	15.77	7.23	9.28
LP (1) O″2	BD*(1) O′6 — H	–	–	–	70.55	49.14	56.75
LP (2) O″2	BD*(1) O′6 — H	–	–	–	13.42	6.90	4.85
LP (3) O″2	BD*(1) O′6 — H	–	–	–	7.28	12.17	9.74

Table C.14: The electron donor and acceptor orbitals of cellulose conformers with cations and their corresponding second order interaction energies $E^{(2)*}$ (NBO analysis)

Donor	Acceptor	Cellobiose-anti-syn		Cellobiose-anti-anti	
		$[EMIM]^+$	$[BMIM]^+$	$[EMIM]^+$	$[BMIM]^+$
LP (1) O2	BD*(1) C″1 — H	3.81	3.60	3.60	3.18
LP (2) O2	BD*(1) C″1 — H	13.18	12.55	12.80	11.71

Table C.15: The electron donor and acceptor orbitals of hemicellulose conformers and anions with their corresponding second order interaction energies $E^{(2)*}$ (NBO analysis)

Donor	Acceptor	Xylose+Glucose			Xylobiose		
		$[OAc]^-$	$[AcF_3]^-$	$[MC]^-$	$[OAc]^-$	$[AcF_3]^-$	$[MC]^-$
LP (1) O″2	BD*(1) O3 — H	20.63	25.61	24.18	35.17	33.54	40.52
LP (2) O″2	BD*(1) O3 — H	103.55	77.40	81.84	122.32	75.82	93.97
LP (3) O″2	BD*(1) O3 — H	—	0.38	0.38	12.63	8.32	–
LP (1) O″2	BD*(1) O4 — H	39.33	31.46	35.27	–	–	–
LP (2) O″2	BD*(1) O4 — H	4.81	2.05	4.27	–	–	–
LP (3) O″2	BD*(1) O4 — H	37.66	26.11	36.11	–	–	–
LP (1) O″1	BD*(1) O8 — H	43.60	41.88	52.55	–	–	–
LP (2) O″1	BD*(1) O8 — H	78.78	50.75	61.63	–	–	–
LP (1) O″1	BD*(1) O4 — H	–	–	–	30.65	34.04	37.26
LP (2) O″1	BD*(1) O4 — H	–	–	–	109.57	83.81	97.61

Table C.16: The electron donor and acceptor orbitals of hemicellulose conformers and cations with their corresponding second order interaction energies $E^{(2)*}$ (NBO analysis)

Donor	Acceptor	Xylose+Glucose		Xylobiose	
		$[EMIM]^+$	$[BMIM]^+$	$[EMIM]^+$	$[BMIM]^+$
LP (1) O4	BD*(1) C″1 — H	–	–	9.07	14.30
LP (2) O5	BD*(1) C″1 — H	–	–	13.09	8.74
LP (1) O10	BD*(1) C″1 — H	34.14	32.10		

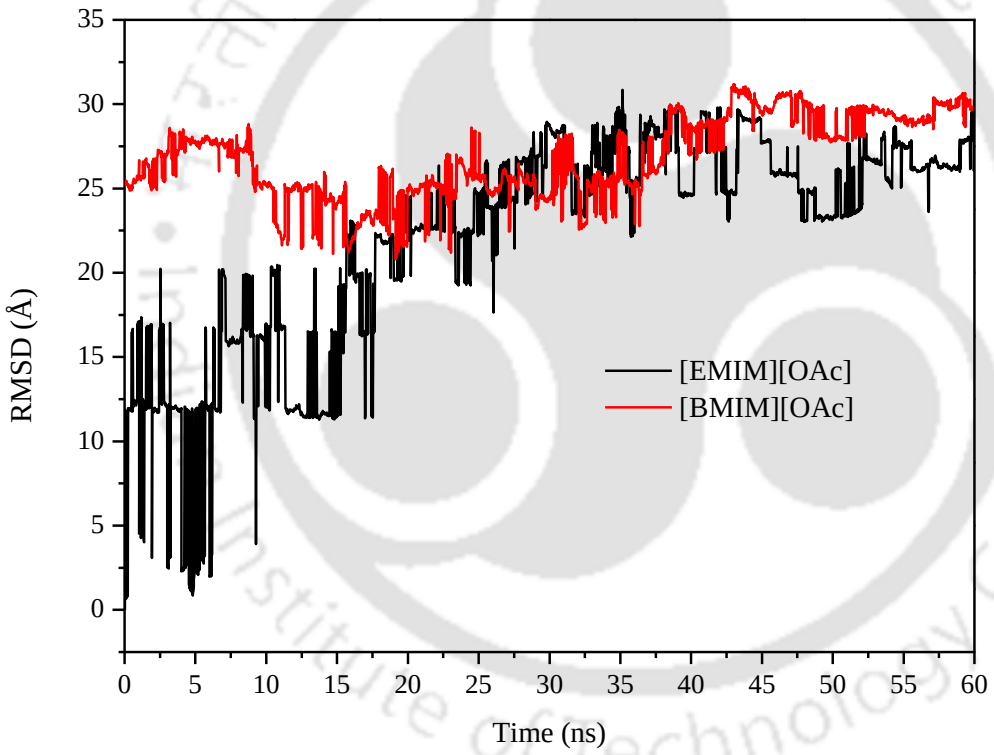

Figure C.1: RMSD of cellulose (*i.e.*, cellobiose) molecules in [EMIM][OAc] and [BMIM][OAc]

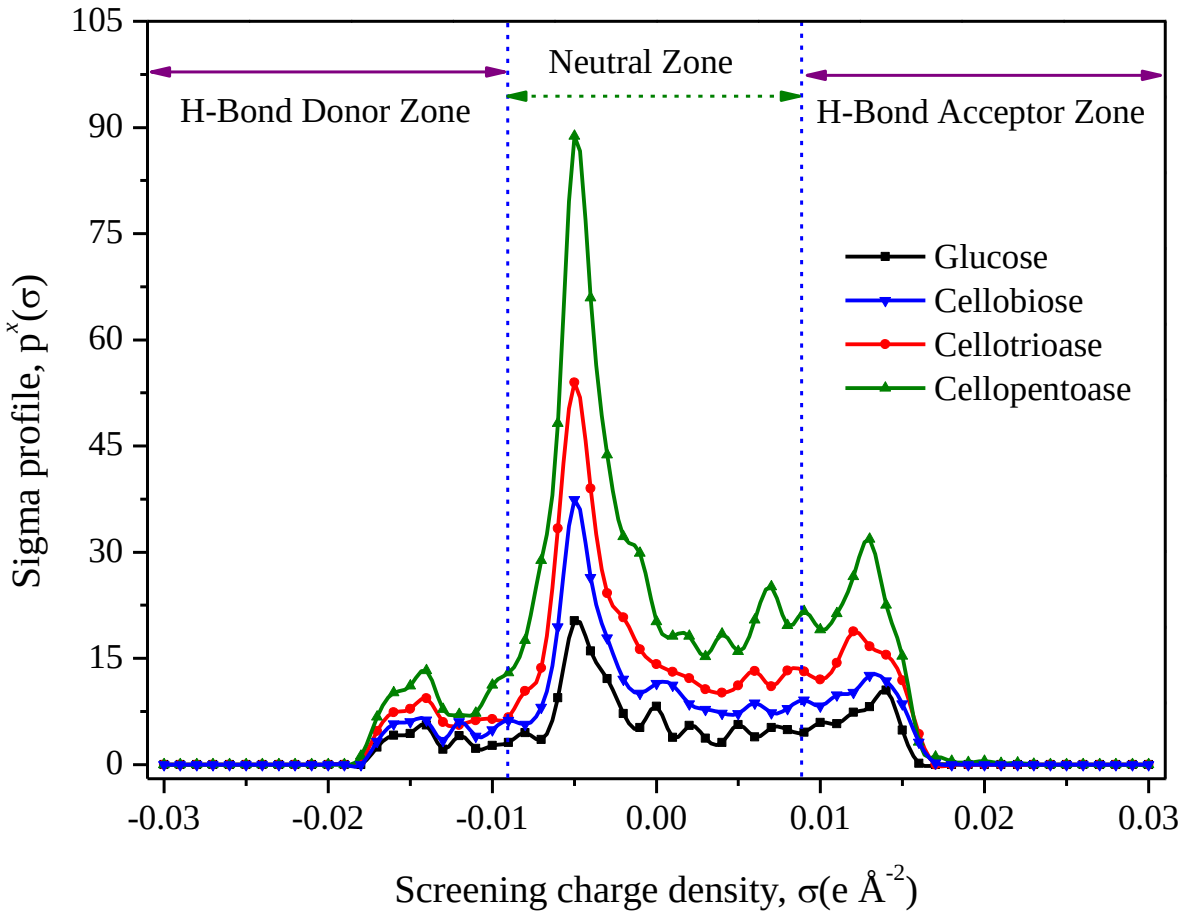

Figure C.2: Sigma profiles for different chemical structures of cellulose

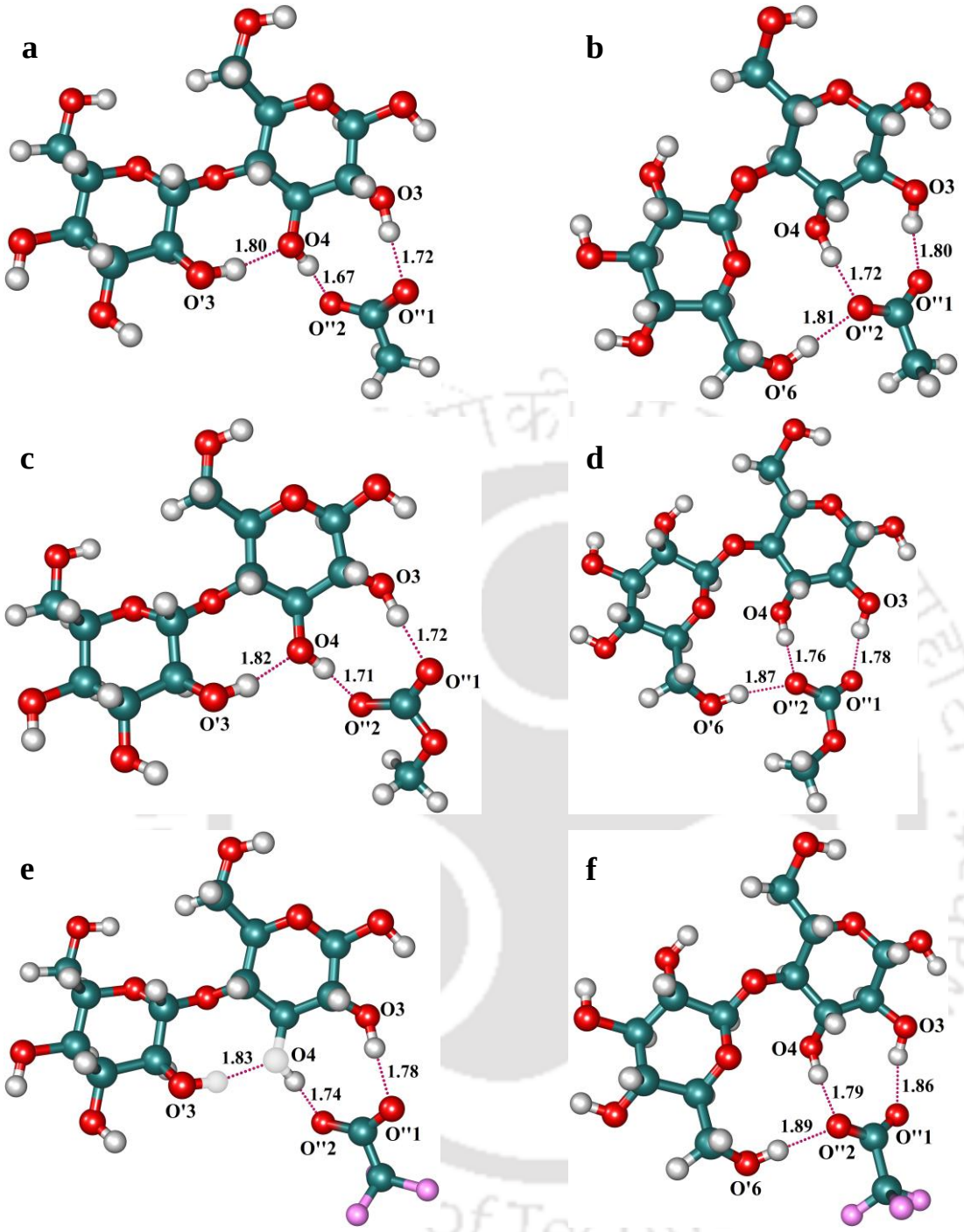

Figure C.3: Optimized geometries for cellulose conformers with different anions (a) cellobiose-(anti-syn)-$[OAc]^-$, (b) cellobiose-(anti-anti)-$[OAc]^-$, (c) cellobiose-(anti-syn)-$[MC]^-$, (d) cellobiose-(anti-anti)-$[MC]^-$, (e) cellobiose-(anti-syn)-$[AcF_3]^-$ and (d) cellobiose-(anti-anti)-$[AcF_3]^-$. The H-bonds are indicated by dotted lines, the bond lengths are in Angstrom (Å) and given with corresponding cellulose atom numbers (Figure 4.6)

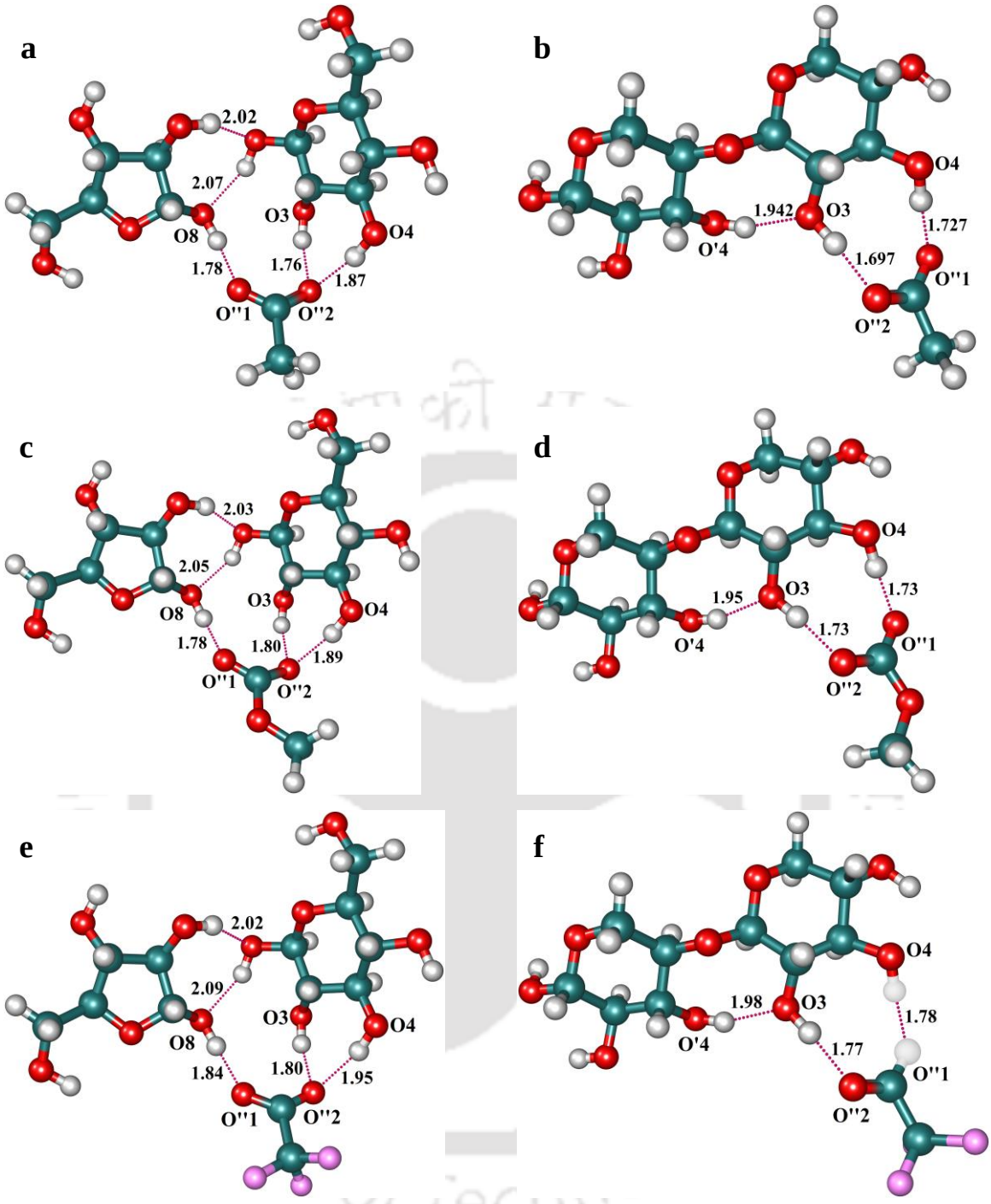

Figure C.4: Optimized geometries for hemicellulose conformers with different anions (a) [xylose+glucose]-$[OAc]^-$, (b) xylobiose-$[OAc]^-$, (c) [xylose+glucose]-$[MC]^-$, (d) xylobiose-$[MC]^-$, (e) [xylose+glucose]-$[AcF_3]^-$ and (d) xylobiose-$[AcF_3]^-$. The H-bonds are indicated by dotted lines, the bond lengths are in Angstrom (Å) and given with corresponding hemicellulose atom numbers (Figure 4.6)

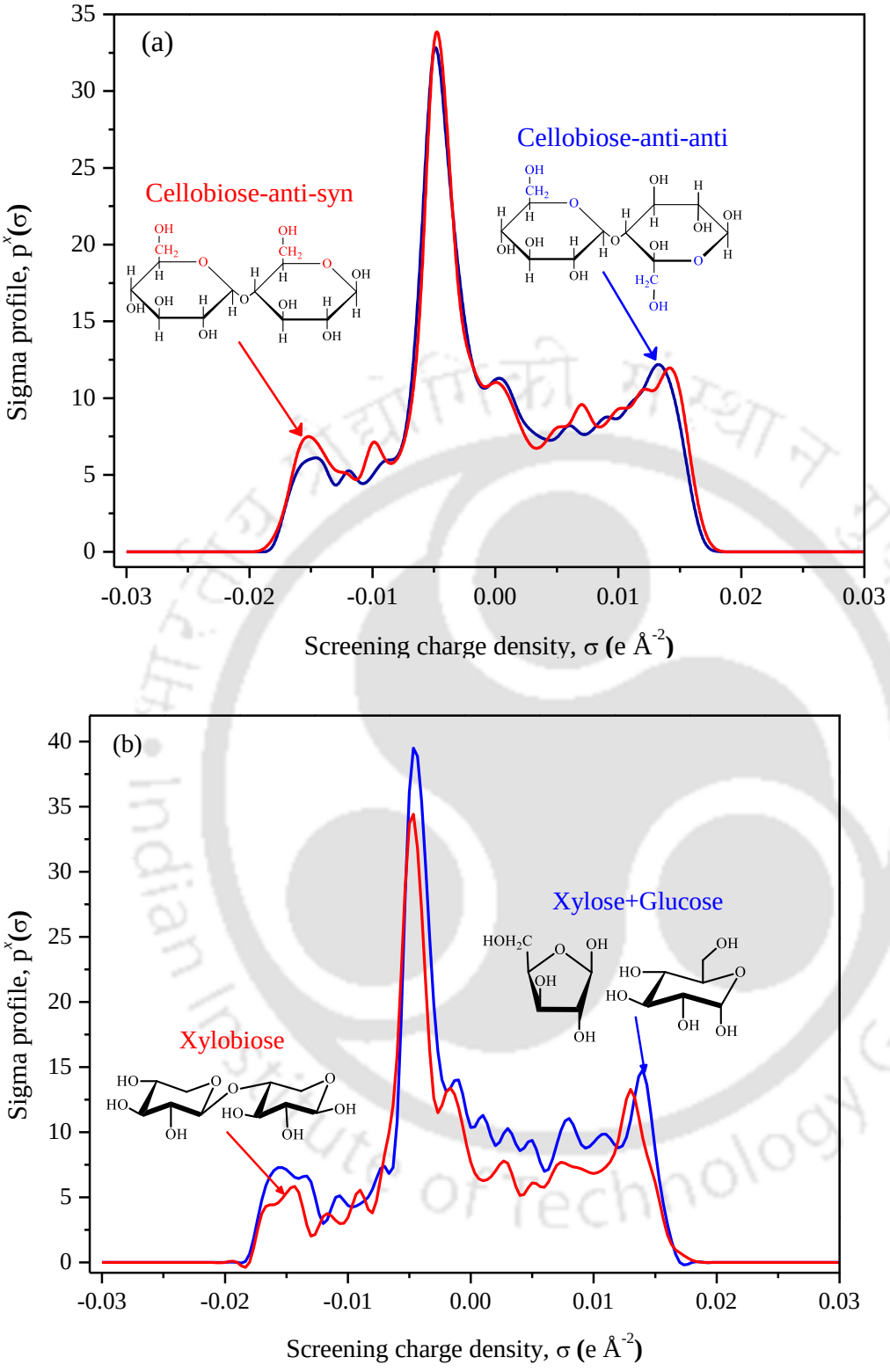

Figure C.5: Sigma profiles of (a) cellulose and (b) hemicellulose conformers

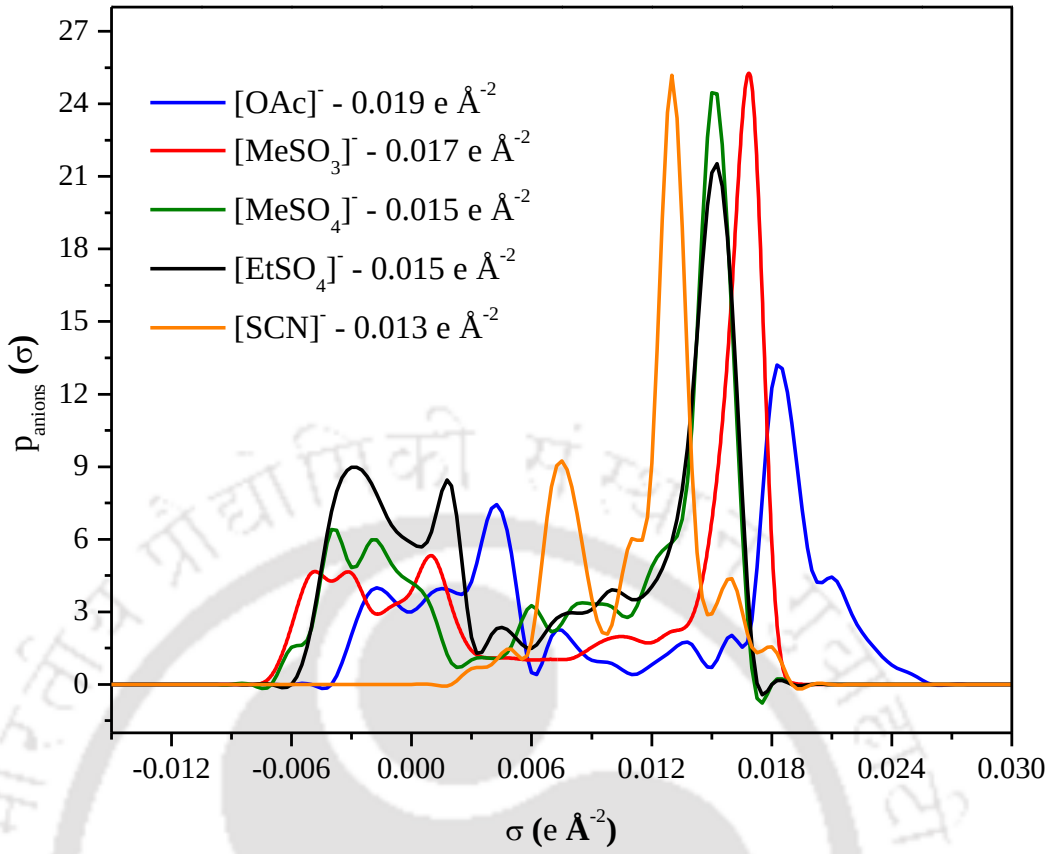

Figure C.6: Sigma profiles of different anions. The peak is lying in the positive region because of negative charge of atom/molecule. Higher the polarity, larger the value of screening charge density.

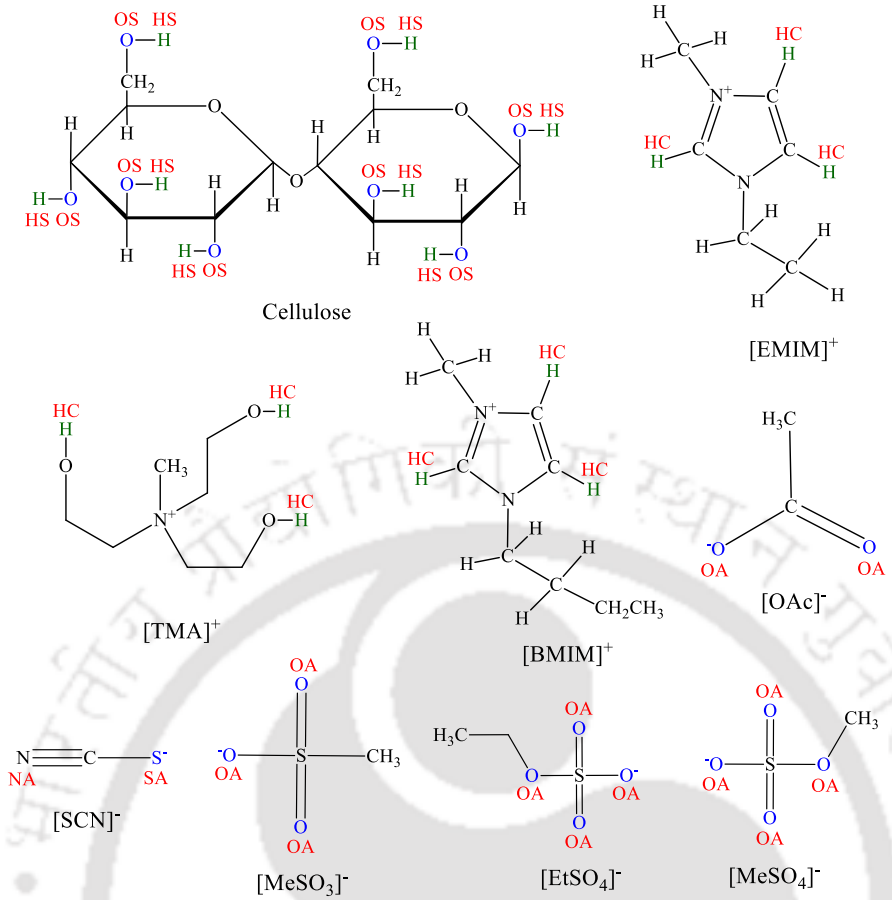

Figure C.7: Chemical structures and atom notations of the cellulose, anions and cation of ionic liquids simulated in this work

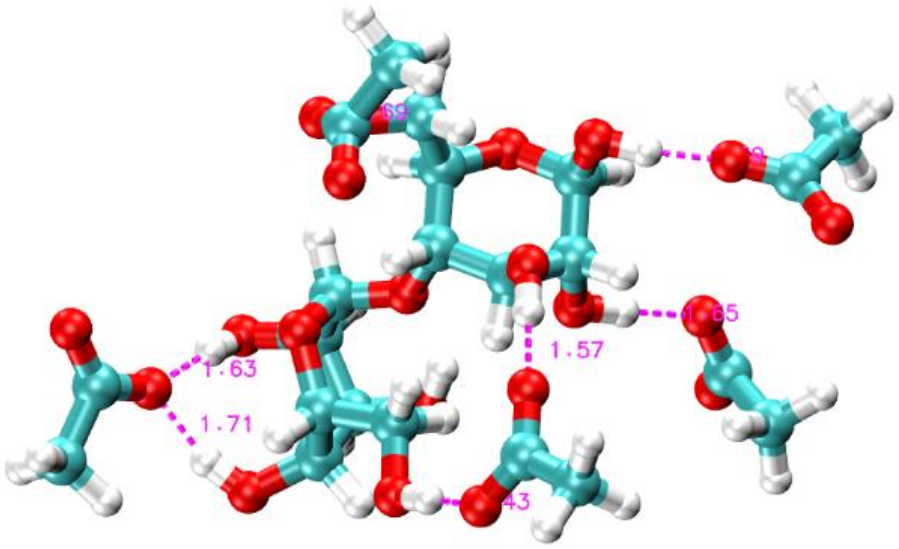

Figure C.8: Snapshot from simulation exhibiting the neighborhood of cellulose in an ionic liquid. Only one of the OA atoms of the acetate anion is hydrogen bonded to HS of cellulose. Five anions present around cellulose are shown for the sake of clarity within a distance of 1.8 Å.

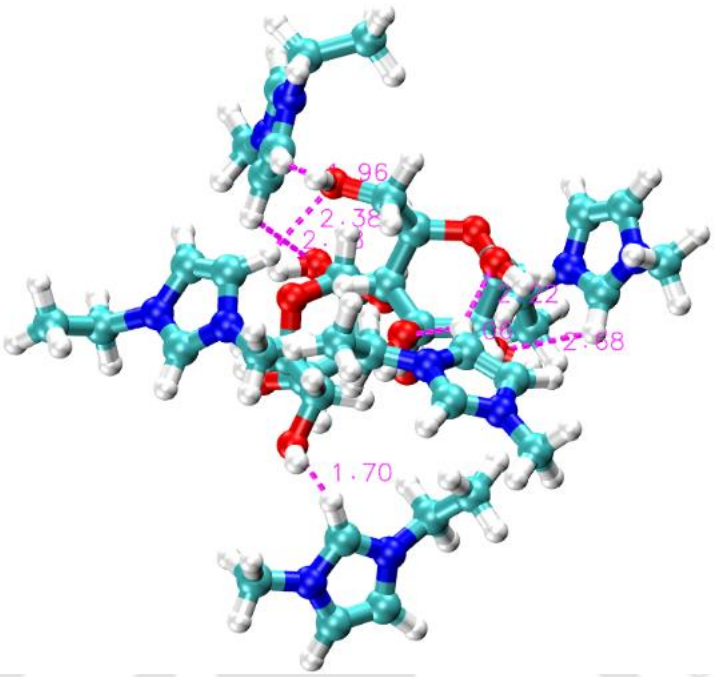

Figure C.9: Snapshot from simulation exhibiting the neighborhood of cellulose in an ionic liquid. HC atoms of the $[EMIM]^+$ cation is hydrogen bonded to OS atom of cellulose. Five cations present around cellulose are shown for the sake of clarity within a distance of 3.15 Å (first solvation shell).

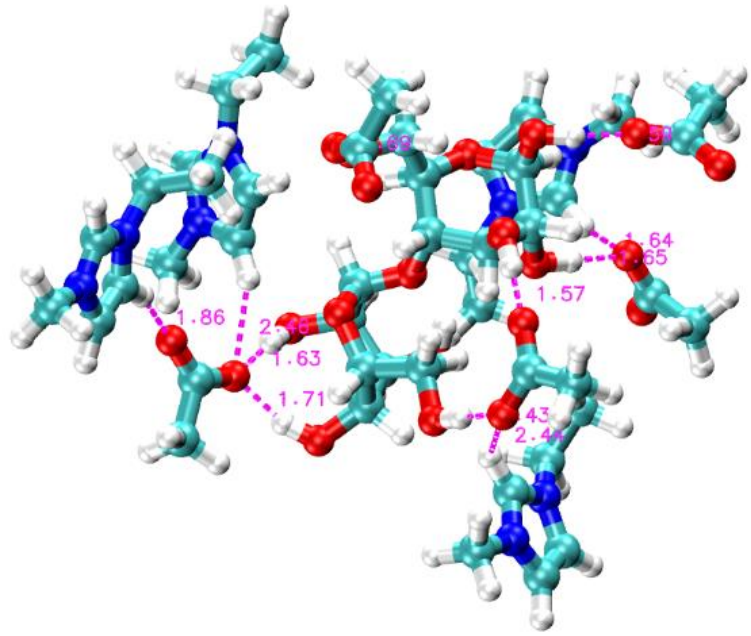

Figure C.10: Snapshot from simulation exhibiting the neighborhood of cellulose in an ionic liquid. Acetate of the IL was forming multiple hydrogen bonds with cellulose as well as with cation also (shown for the sake of clarity).

D Appendix (Chapter-5)

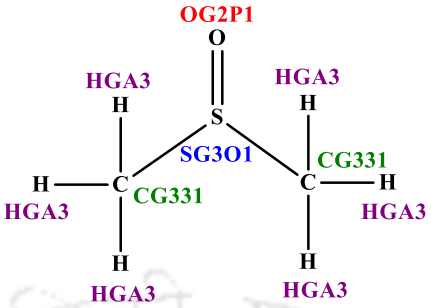

Table D.1: CHARMM force field parameters file for dimethylsulfoxide (DMSO) with atom types

Bond	K_b	r_o	**Bond**	K_b	r_o
CG331 HGA3	322.00	1.1110	CG331 SG3O1	240.00	1.8000
OG2P1 SG3O1	540.00	1.4480			
Angle	K_θ	θ_o	K_{UB}	S_o	
SG3O1 CG331 HGA3	46.10	111.30			
HGA3 CG331 HGA3	35.50	108.40	5.40	1.802	
SG3O1 CG331 HGA3	46.10	111.30			
CG331 SG3O1 CG331	34.00	95.00			
CG331 SG3O1 OG2P1	79.00	106.75			
Dihedrals	K_χ	n	δ		
HGA3 CG331 SG3O1 CG331	0.2000	3	0.00		
HGA3 CG331 SG3O1 OG2P1	0.2000	3	0.00		
Non bonded	ε	R_{min}	$\varepsilon_{1,4}$	$R_{min,1,4/2}$	
SG3O1	-0.4700	2.1000			
OG2P1	-0.1200	1.7000			
CG331	-0.0780	2.0500	-0.01	1.9	
HGA3	-0.0240	1.3400			

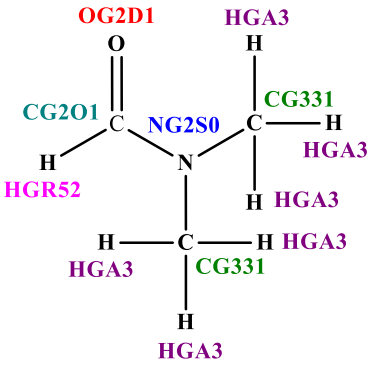

Table D.2: CHARMM force field parameters file for dimethylformamide (DMF) anion with atom types

Bond	K_b	r_o	**Bond**	K_b	r_o
CG331 HGA3	322.00	1.111	CG2O1 HGR52	317.13	1.100
CG2O1 OG2D1	620.00	1.230	CG2O1 NG2S0	430.00	1.350
CG331 NG2S0	315.00	1.434			
Angle	K_θ	θ_o	K_{UB}	S_o	
HGA3 CG331 HGA3	35.50	108.40	5.40	1.802	
NG2S0 CG331 HGA3	50.00	105.00			
NG2S0 CG2O1 HGR52	43.00	115.00			
OG2D1 CG2O1 HGR52	44.00	122.00			
NG2S0 CG2O1 OG2D1	80.00	124.00			
CG2O1 NG2S0 CG331	42.00	119.50			
CG331 NG2S0 CG331	45.00	121.00			
Dihedrals	K_χ	n	δ		
HGA3 CG331 NG2S0 CG2O1	0.000	3	0.00		
HGA3 CG331 NG2S0 CG331	0.420	3	0.00		
HGR52 CG2O1 NG2S0 CG331	2.600	2	180.0		
OG2D1 CG2O1 NG2S0 CG331	2.600	2	180.0		
Non bonded	ε	R_{min}	$\varepsilon_{1,4}$	$R_{min,1,4/2}$	
HGA3	-0.024	1.340			
HGR52	-0.046	0.900			
OG2D1	-0.120	1.700	-0.1200	1.40	
CG2O1	-0.110	2.000			
NG2S0	-0.200	1.850	-0.0001	1.85	
CG331	-0.078	2.050	-0.0100	1.90	

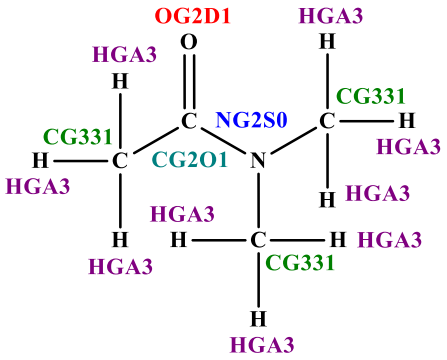

Table D.3: CHARMM force field parameters file for dimethylacetamide (DMAc) with atom types

Bond	K_b	r_o	**Bond**	K_b	r_o
CG2O1 NG2S0	430.00	1.350	CG331 NG2S0	315.00	1.434
CG2O1 OG2D1	620.00	1.230	CG331 HGA3	322.00	1.111
CG2O1 CG331	250.00	1.490			
Angle	K_θ	θ_o	K_{UB}	S_o	
CG331 CG2O1 NG2S0	40.00	115.00			
NG2S0 CG331 HGA3	50.00	105.00			
CG2O1 NG2S0 CG331	42.00	119.50			
CG331 NG2S0 CG331	45.00	121.00			
CG331 CG2O1 OG2D1	80.00	121.00			
NG2S0 CG2O1 OG2D1	80.00	124.00			
CG2O1 CG331 HGA3	33.00	109.50	30.00	2.163	
HGA3 CG331 HGA3	35.50	108.40	5.40	1.802	
Dihedrals	K_χ	n	δ		
NG2S0 CG2O1 CG331 HGA3	0.000	3	0.00		
CG331 CG2O1 NG2S0 CG331	2.600	2	180.00		
OG2D1 CG2O1 NG2S0 CG331	2.600	2	180.00		
HGA3 CG331 NG2S0 CG2O1	0.000	3	0.00		
HGA3 CG331 NG2S0 CG331	0.420	3	0.00		
OG2D1 CG2O1 CG331 HGA3	0.000	3	180.00		
Improper	K_{imp}	φ_o			
CG2O1 CG331 NG2S0 OG2D1	71	0			
CG2O1 NG2S0 OG2D1 HGR52	50	0			
OG2D1 NG2S0 CG331 CG2O1	71	0			
CG2O1 NG2S0 OG2D1 CG331	71	0			
CG2O1 OG2D1 CG331 NG2S0	71	0			
NG2S0 CG2O1 CG331 CG331	71	0			
NG2S0 CG331 CG331 CG2O1	71	0			

CG331	CG2O1	CG331	NG2S0	71	0
CG331	NG2S0	OG2D1	CG2O1	71	0
CG2O1	NG2S0	CG331	OG2D1	71	0
NG2S0	OG2D1	CG331	CG2O1	71	0

Non bonded	ε	R_{min}	$\varepsilon_{1,4}$	$R_{min,1,4/2}$
NG2S0	-0.200	1.850	-0.0001	1.85
OG2D1	-0.120	1.700	-0.120	1.40
CG2O1	-0.110	2.000		
CG331	-0.0780	2.050	-0.010	1.90
HGA3	-0.024	1.340		

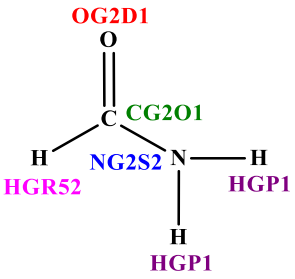

Table D.4: CHARMM force field parameters file for formamide (FRM) with atom types

Bond	K_b	r_o	**Bond**	K_b	r_o
CG2O1 NG2S2	430.00	1.360	NG2S2 HGP1	480.00	1.000
CG2O1 OG2D1	620.00	1.230	CG2O1 HGR52	317.13	1.100
Angle	K_θ	θ_o	K_{UB}	S_o	
NG2S2 CG2O1 OG2D1	75.00	122.50	50.00	2.370	
NG2S2 CG2O1 HGR52	44.00	111.00	50.00	1.980	
CG2O1 NG2S2 HGP1	50.00	120.00			
HGP1 NG2S2 HGP1	23.00	120.00			
OG2D1 CG2O1 HGR52	44.00	122.00			
OG2D1 CG2O1 HGP1	50.00	121.70			
Dihedrals	K_χ	n	δ		
OG2D1 CG2O1 NG2S2 HGP1	1.40	2	180.00		
HGR52 CG2O1 NG2S2 HGP1	1.40	2	180.00		
Non bonded	ε	R_{min}	$\varepsilon_{1,4}$	$R_{min,1,4/2}$	
NG2S2	-0.200	1.850			
OG2D1	-0.120	1.700	-0.12	1.40	
HGR52	-0.046	0.900			
HGP1	-0.046	0.2245			
CG2O1	-0.110	2.000			

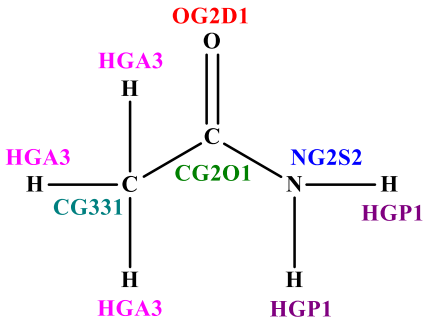

Table D.5: CHARMM force field parameters file for acetamide (AcM) with atom types

Bond	K_b	r_o	**Bond**	K_b	r_o
CG331 HGA3	322.00	1.111	NG2S2 HGP1	480.00	1.000
CG2O1 NG2S2	430.00	1.360	CG2O1 OG2D1	620.00	1.230
CG2O1 CG331	250.00	1.490			
Angle	K_θ	θ_o	K_{UB}	S_o	
HGA3 CG331 HGA3	35.50	108.40	5.40	1.802	
CG2O1 CG331 HGA3	33.00	109.50	30.00	2.163	
HGP1 NG2S2 HGP1	23.00	120.00			
CG2O1 NG2S2 HGP1	50.00	120.00			
CG331 CG2O1 NG2S2	50.00	116.50	50.00	2.450	
CG331 CG2O1 OG2D1	80.00	121.00			
NG2S2 CG2O1 OG2D1	75.00	122.50	50.00	2.370	
Dihedrals	K_χ	n	δ		
NG2S2 CG2O1 CG331 HGA3	0.00	3	0.00		
OG2D1 CG2O1 CG331 HGA3	0.00	3	180.00		
CG331 CG2O1 NG2S2 HGP1	1.40	2	180.00		
OG2D1 CG2O1 NG2S2 HGP1	1.40	2	180.00		
Non bonded	ε	R_{min}	$\varepsilon_{1,4}$	$R_{min,1,4/2}$	
HGA3	-0.0240	1.340			
HGP1	-0.0460	0.2245			
OG2D1	-0.1200	1.7000	-0.1200	1.40	
CG331	-0.0780	2.0500	-0.0100	1.90	
CG2O1	-0.1100	2.0000			
NG2S2	-0.2000	1.8500			

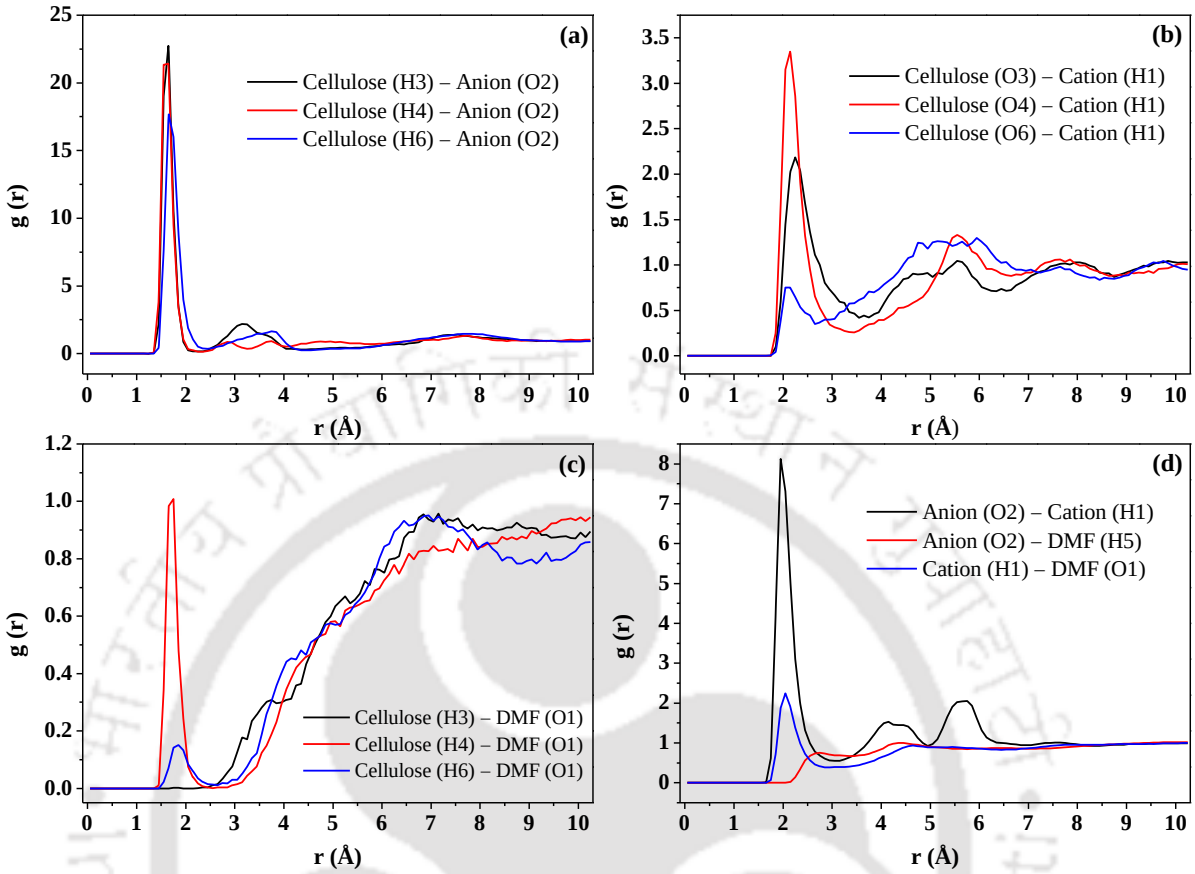

Figure D.1: RDF between the cellulose molecule with (a) anion (O2), (b) cation (H1), and (c) DMF (O1) around the selected hydroxyl groups (O3, O4, and O6; see Figure 5.1) of cellulose and (d) RDF between [Emim][OAc]/DMF in the cellulose-[Emim][OAc]/DMF system

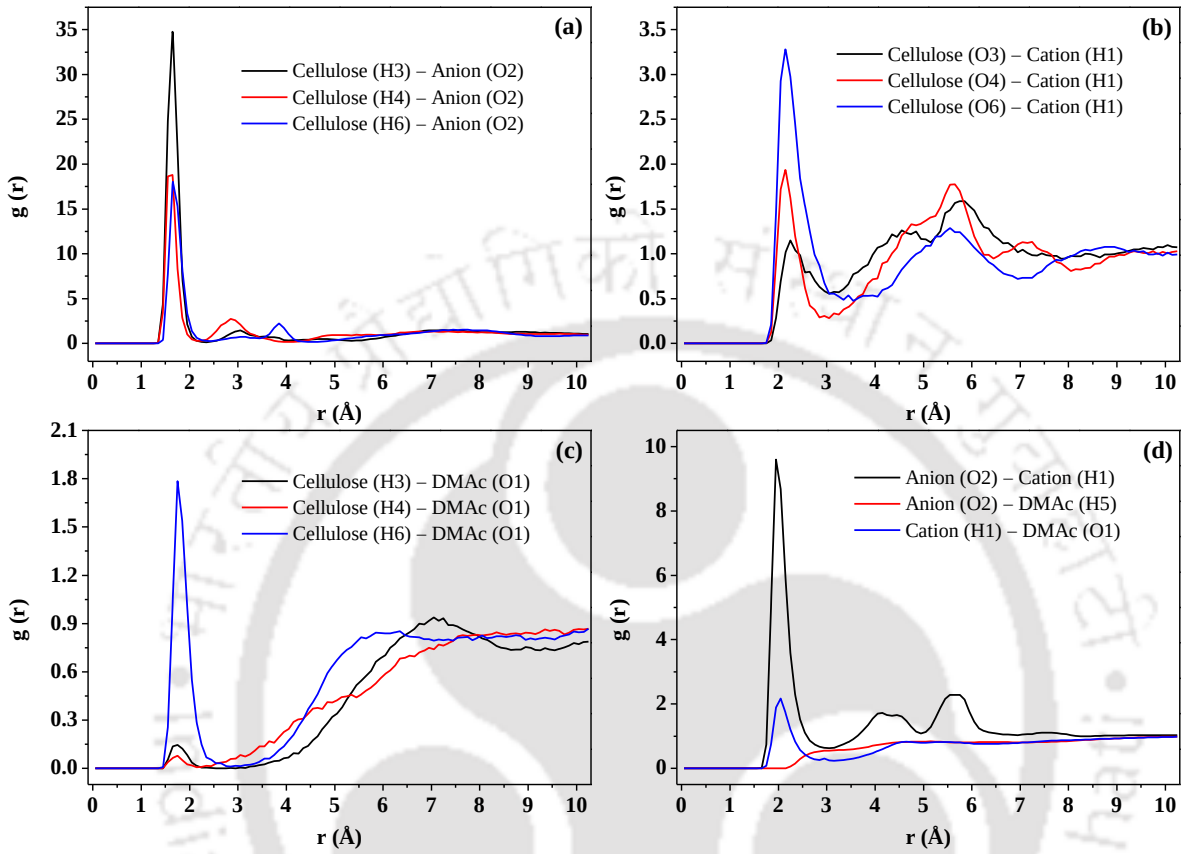

Figure D.2: RDF between the cellulose molecule with (a) anion (O2), (b) cation (H1), and (c) DMAc (O1) around the selected hydroxyl groups (O3, O4, and O6; see Figure 5.1) of cellulose and (d) RDF between [Emim][OAc]/DMAc in the cellulose-[Emim][OAc]/DMAc system

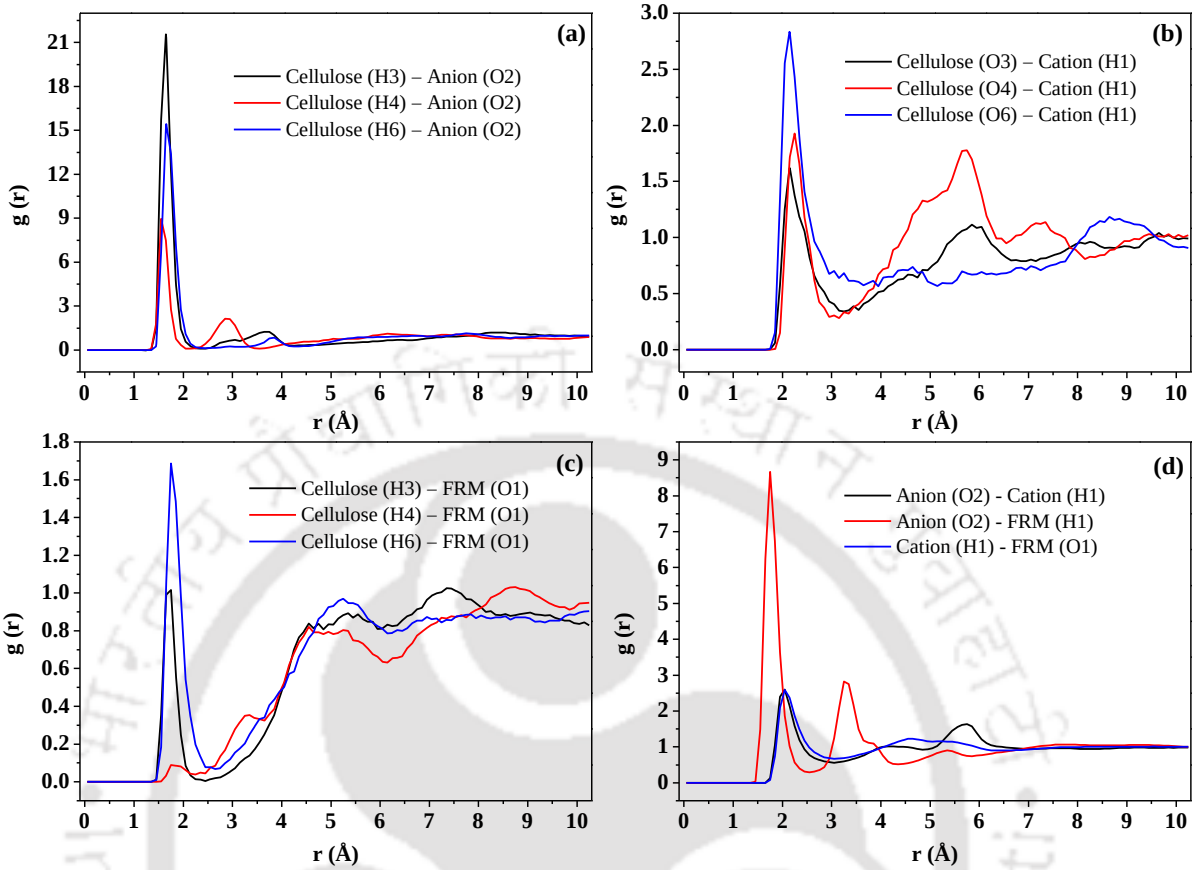

Figure D.3: RDF between the cellulose molecule with (a) anion (O2), (b) cation (H1), and (c) FRM (O1) around the selected hydroxyl groups (O3, O4, and O6; see Figure 5.1) of cellulose and (d) RDF between [Emim][OAc]/FRM in the cellulose-[Emim][OAc]/FRM system

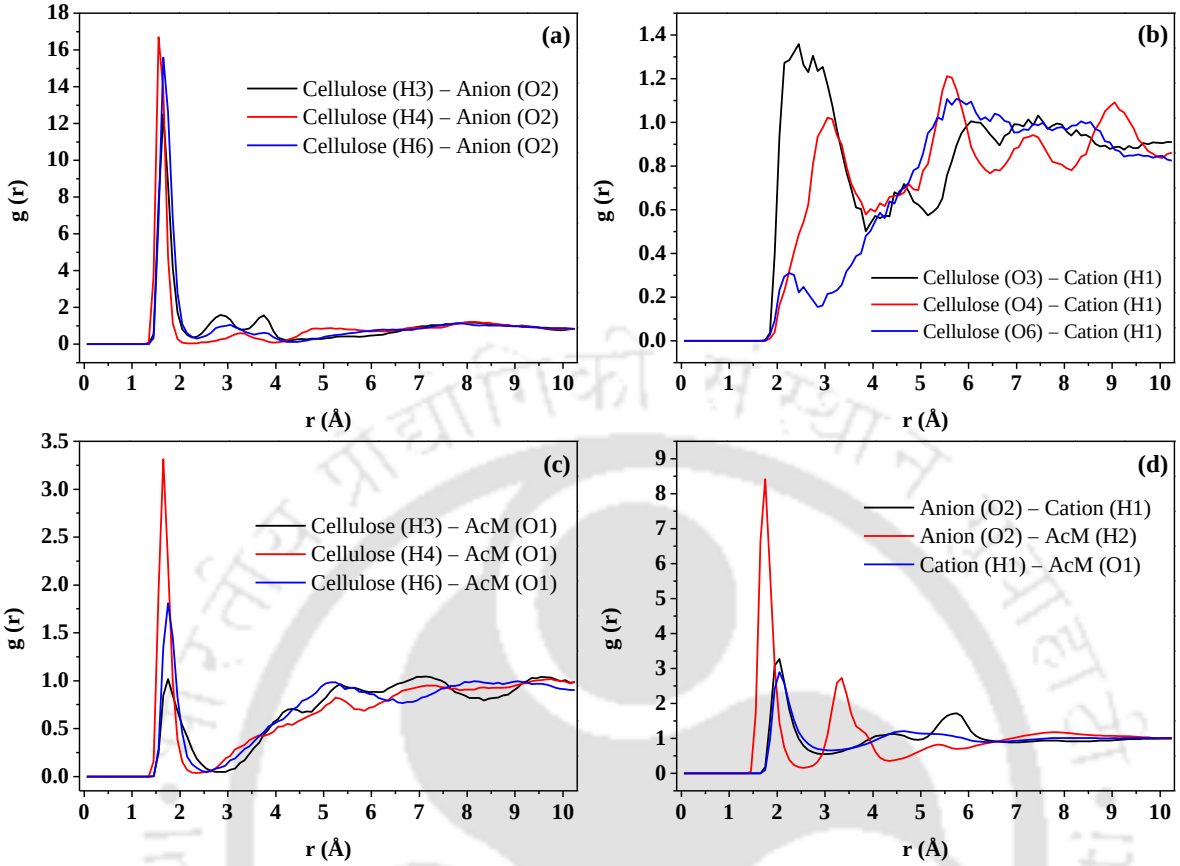

Figure D.4: RDF between the cellulose molecule with (a) anion (O2), (b) cation (H1), and (c) AcM (O1) around the selected hydroxyl groups (O3, O4, and O6; see Figure 5.1) of cellulose and (d) RDF between [Emim][OAc]/AcM in the cellulose-[Emim][OAc]/AcM system

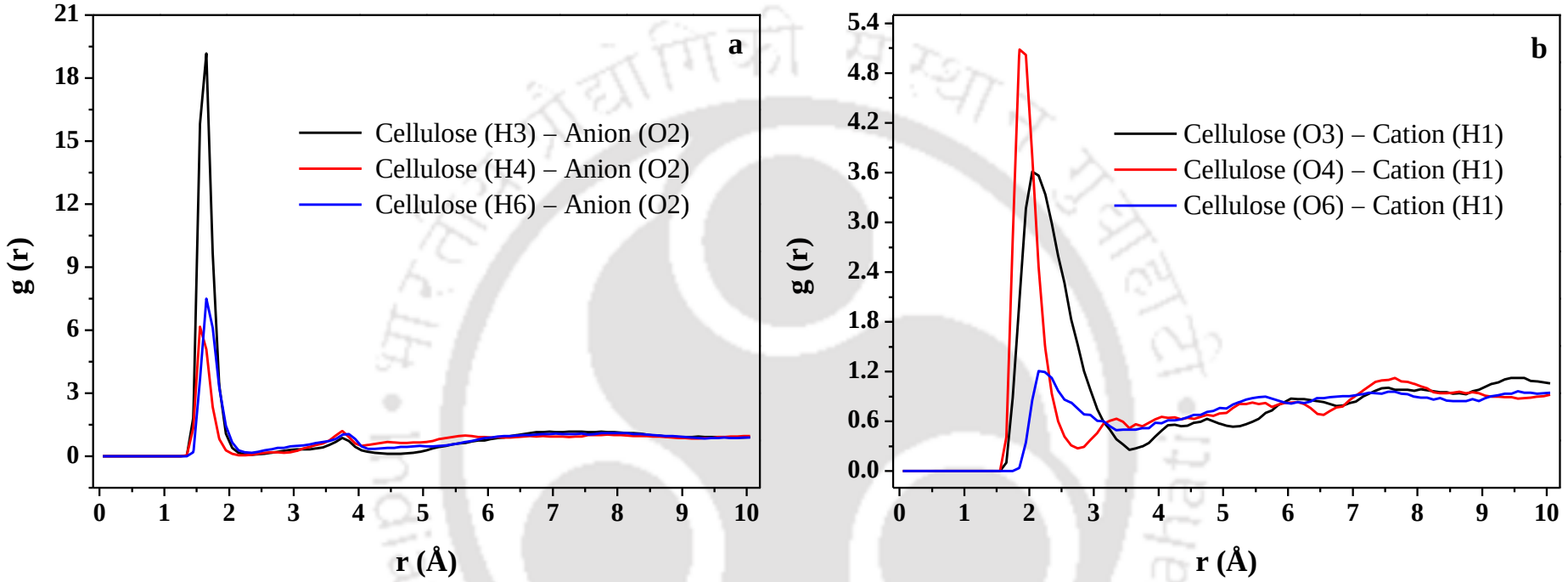

Figure D.5: RDF between the cellulose molecule with (a) anion (O2), and (b) cation (H1) around the selected hydroxyl groups (O3, O4, and O6; see Figure 5.1) of cellulose in the cellulose-[Emim][OAc] system

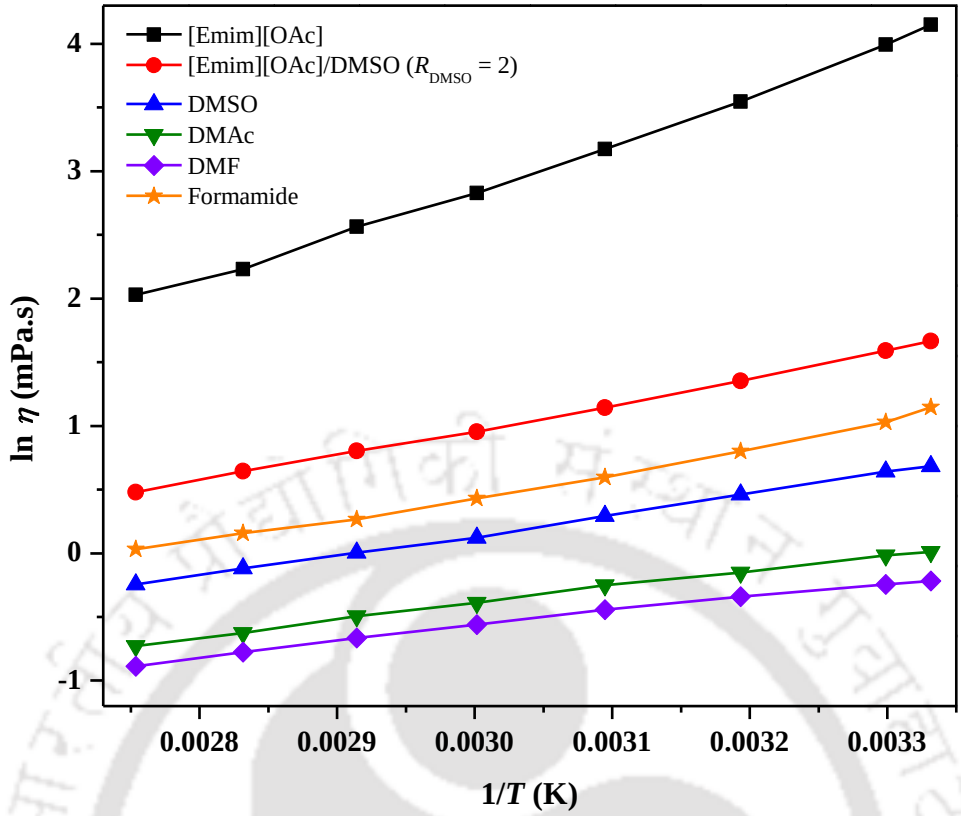

Figure D.6: Arrhenius plot for ionic liquid and cosolvents as a function of temperature

E Appendix (Chapter-6)

E.1. Natural Bonding Orbital Analysis

In order to elucidate the strength of the H-bonds formed between fructose and antisolvents, a separate quantum chemical calculations *i.e.*, natural bonding orbital (NBO) analysis was performed at B3LYP/6-31G* level of theory using *Gaussian*09 software. The results of NBO analysis are reported in Table E.3. The lone pair (LP) electron of ethanol (oxygen atom) molecule forms strong H-bond with antibonding orbital (BD*) of fructose (hydroxyl proton). These electron donor-acceptor orbitals are responsible for the formation of strongest H-bonding between them. The bond energy $E^{(2)*}$ (54.70 kJ mol^{-1}) of ethanol posses stronger interaction energies with fructose (Table E.3) and reveals lower removal of fructose.

Table E.1: Average hydrogen bonds (HB) and non-bonded interaction energies (E_{total}) for different ionic liquid-sugar-antisolvent and ionic liquid-sugar systems obtained from MD simulations at T = 25 °C

Type of measurement	$[Emim]^+$-Sugar	$[Anion]^-$-Sugar	$[Emim]^+$-Sugar	$[Anion]^-$-Sugar
	Glucose-[Emim][$EtSO_4$]-DCM[a]		Glucose-[Emim][$EtSO_4$]	
HB[b]	0.67	0.91	0.87	1.39
E_{total}[c]	-18.79	-43.08	-21.76	-56.48
	Glucose-[Emim][$MeSO_3$]-DCM		Glucose-[Emim][$MeSO_3$]	
HB	0.66	1.06	0.78	1.75
E_{total}	-10.53	-59.04	-16.42	-73.51
	Glucose-[Emim][SCN]-DCM		Glucose-[Emim][SCN]	
HB	0.27	0.29	0.35	0.43
E_{total}	-8.51	-21.88	-13.59	-35.48
	Glucose-[Emim][$EtSO_4$]-DCE		Glucose-[Emim][$EtSO_4$]	
HB	0.65	0.92	0.87	1.39
E_{total}	-17.93	-46.61	-21.76	-56.48
	Fructose-[Emim][$EtSO_4$]-DCM		Fructose-[Emim][$EtSO_4$]	
HB	1.06	1.51	1.43	2.21
E_{total}	-38.58	-81.77	-43.75	-97.04
	Xylose-[Emim][$EtSO_4$]-DCM		Xylose-[Emim][$EtSO_4$]	
HB	0.78	1.00	1.12	1.67
E_{total}	-20.41	-58.64	-28.45	-72.51

[a] Antisolvent to IL molar ratio is R = 20; [b] H-bond cut-off distance 3.2 Å and Angle cut-off 120 °; [c] sum of E_{elec} and E_{vdw} in kJ mol^{-1}

Table E.2: Correlation between predicted activity coefficients (COSMO-RS), MD simulated interaction energy and experimental [Emim][$EtSO_4$] recovery from fructose using the different antisolvents

Sl. No.	Fructose-[Emim][$EtSO_4$]/Antisolvent	ln γ	$I.E._{Anti/IL}$	%ILR
1.	Ethanol	-0.07	-327.01	95.80
2.	Dichloromethane	-2.41	-111.17	83.70
3.	Acetonitrile	0.57	-177.88	92.20

Table E.3: The electron donor and acceptor orbitals with their corresponding second order interaction energies $E^{(2)*}$ (NBO analysis).

Donor	Acceptor	$E(2)^*$ (kJ mol^{-1})
	Ethanol-Fructose	
LP (2) O1	BD*(1) O2 – H2	33.12
LP (2) O1	BD*(1) O3 – H3	54.70
	DCM-Fructose	
LP (1) Cl1	BD*(1) O3 – H3	5.27
	Acetonitrile-Fructose	
LP (1) N1	BD*(1) O3 – H3	21.33

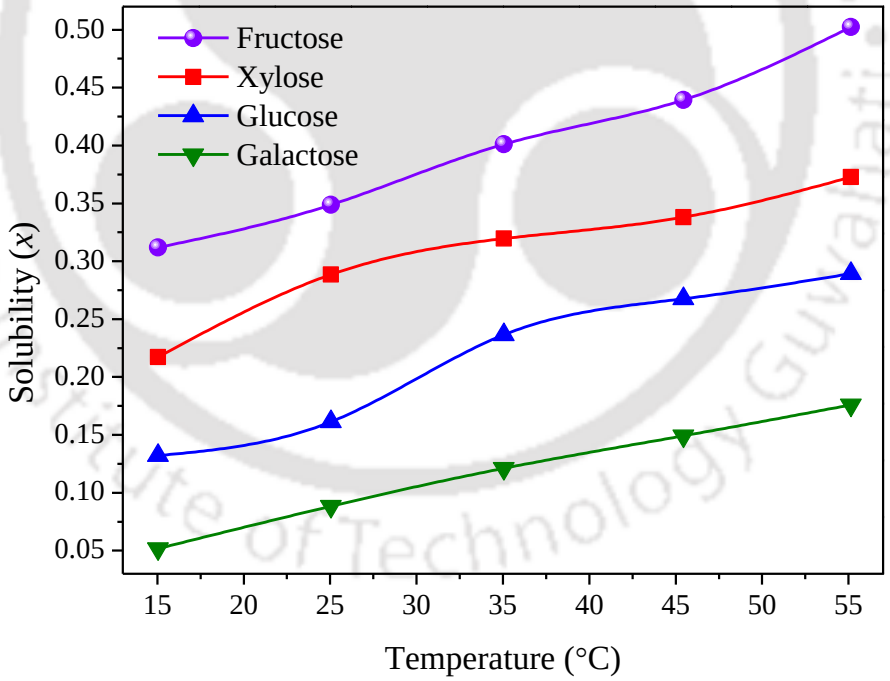

Figure E.1: Experimental solubility of monosaccharides in the [Emim][$EtSO_4$] at different temperatures. The monosaccharides solubility data was taken from Carneiro *et al.* (2012); Fluid Phase Equilib 2012;314:22-28.

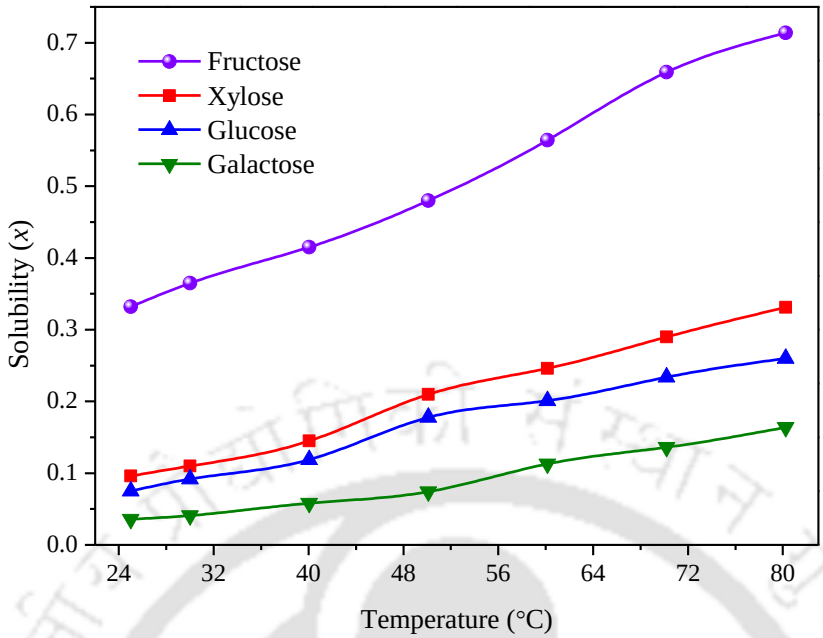

Figure E.2: Experimental solubility of monosaccharides in the [Emim][SCN] at different temperatures. The monosaccharides solubility data was taken from Chapter 2 (Table 2.8).

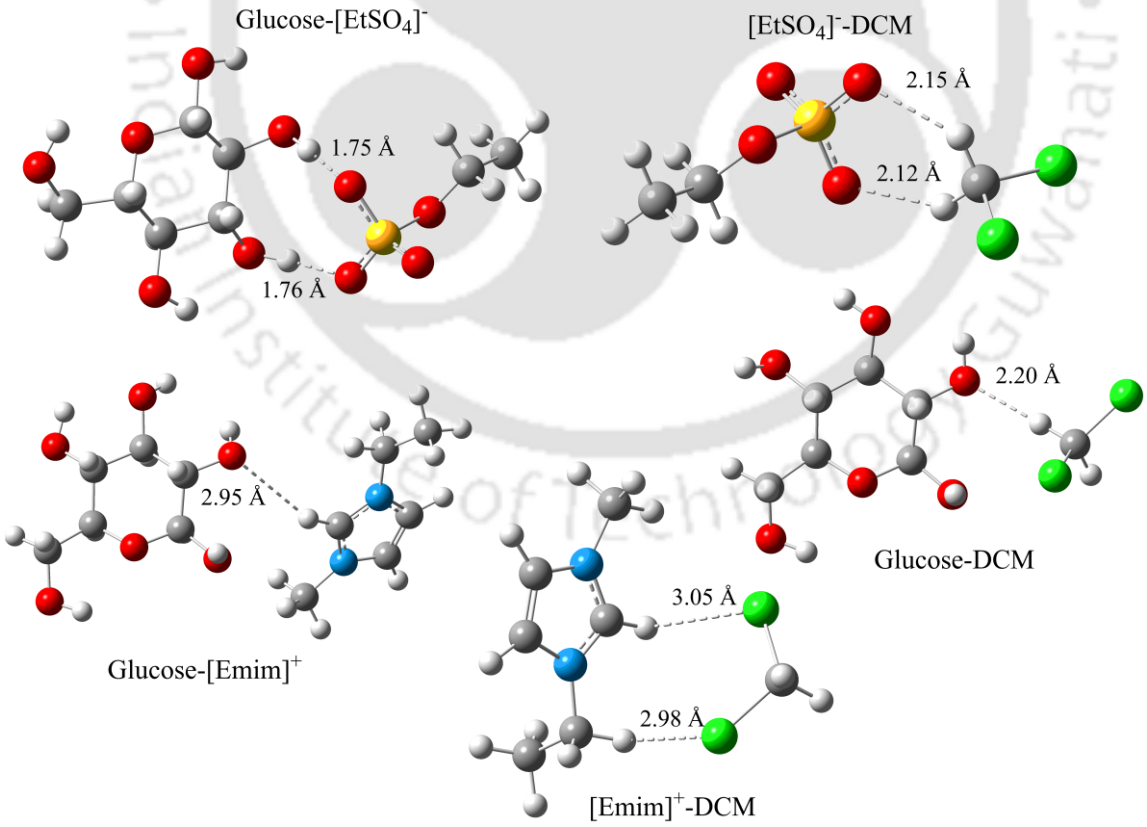

Figure E.3: Optimized molecular geometries of glucose-anion ($[EtSO_4]^-$), anion ($[EtSO_4]^-$)-DCM, glucose-$[Emim]^+$, glucose-DCM, and $[Emim]^+$-DCM pairs.

List of Publications

Published Articles

1. **Mohan M**, Balaji C, Goud VV, Banerjee T. Thermodynamic Insights in the Separation of Cellulose/Hemicellulose Components from Lignocellulosic Biomass Using Ionic Liquids. *J Solution Chem* 2015;44:538-57
2. **Mohan M**, Goud VV, Banerjee T. Solubility of glucose, xylose, fructose and galactose in ionic liquids: Experimental and theoretical studies using a continuum solvation model. *Fluid Phase Equilib* 2015;395:33-43
3. **Mohan M**, Banerjee T, Goud VV. Hydrolysis of bamboo biomass by subcritical water treatment. *Bioresour Technol* 2015;191:244-52
4. **Mohan M**, Timung R, Deshavath NN, Banerjee T, Goud VV, Dasu VV. Optimization and hydrolysis of cellulose under subcritical water treatment for the production of total reducing sugars. *RSC Adv* 2015;5:103265-75
5. **Mohan M**, Banerjee T, Goud VV. Solid-Liquid Equilibrium of Cellobiose, Sucrose and Maltose Monohydrate in Ionic Liquids: Experimental and Quantum Chemical Insights. *J Chem Eng Data* (2016); 61(9): 2923–2932
6. **Mohan M**, Banerjee T, Goud VV. Effect of Protic and Aprotic Solvents on the Mechanism of Cellulose Dissolution in Ionic Liquids: A Combined Molecular Dynamics and Experimental Insight. *Chemistry Select* (2016); 1(15): 4823–4832
7. **Mohan M**, Naik PK, Banerjee T, Goud VV, Paul S. Solubility of Glucose in Tetrabutylammonium Bromide based Deep Eutectic Solvents: Experimental and Molecular Dynamic Simulations. *Fluid Phase Equilib* (2017); 448: 168-177
8. **Mohan M**, Viswanath P, Banerjee T, Goud VV. Multiscale modeling strategies and experimental insights for the solvation of cellulose and hemicellulose in ionic liquids. *Mol Phys* (2018); 116: 2108-2128
9. **Mohan M**, Banerjee T, Goud VV. COSMO-RS Based Screening of Antisolvents for the Separation of Sugars from Ionic Liquids: Experimental and Molecular Dynamic Simulations. *ACS Omega* (2018); 3: 7358−7370
10. **Mohan M**, Deshavath N. N, Banerjee T, Goud V. V, Dasu V. V. Ionic liquid and sulphuric acid based pretreatment of bamboo: biomass delignification and

enzymatic hydrolysis for the production of reducing sugars. *Ind Eng Chem Res* (2018); 57: 10105–10117

11. **Mohan M**, Banerjee T, Goud VV. Phase Transition Properties, Chemical Purity and Solubility of Coniferyl Alcohol and D-Mannose: Experimental and COSMO-RS Predictions. *Can J Chem Eng* (2018); *Accepted*
12. Timung R, **Mohan M**, Chilukoti B, Sasmal S, Banerjee T, Goud VV. Optimization of dilute acid and hot water pretreatment of different lignocellulosic biomass: A comparative study. *Biomass Bioenergy* 2015; 81: 9-18
13. Deshavath NN, **Mohan M**, Veeranki VD, Goud VV, Pinnamaneni SR, Benarjee T. Dilute acid pretreatment of sorghum biomass to maximize the hemicellulose hydrolysis with minimized levels of fermentative inhibitors for bioethanol production. *3 Biotech* (2017); 7: 139

Other Publications

1. Naik PK*, **Mohan M***, Banerjee T, Paul S, Goud VV. Molecular Dynamic Simulations for the Extraction of Quinoline from Heptane in the Presence of Low-Cost Phosphonium Based Deep Eutectic Solvent. *J Phy Chem B* 2018; 122 (14), 4006–4015 * *equal authorship*

Manuscript under Revision

1. Verma R*, **Mohan M***, Goud VV, Banerjee T. Operational Strategies and Comprehensive Evaluation of Menthol Based Deep Eutectic Solvent for the Extraction of Lower Alcohols from Aqueous Media. *ACS Sustainable Chem Eng* (2018, Under revision). **equal authorship*

International Conferences and Workshops

1. **Mohan M**, Goud VV, Banerjee T. Solubility of monosaccharides and disaccharides in ionic liquids by COSMO-RS. *International Conference on Membrane and Applications-13*, 22-23 Nov 2013, CGCRI-CSIR, Kolkata, India.
2. **Mohan M**, Goud VV, Banerjee T. COSMO-RS based Predictions for the screening of ionic liquids for the solubility of monosaccharides. First Symposium on Advances in Sustainable Polymers (ASP), 10-11 Jan 2014, Dept. of Chemical Engineering, IIT Guwahati, India.
3. Timung R, **Mohan M**, Chilakoti B, Sasmal S, Banerjee T, Goud VV. Dilute acid

pretreatment of bamboo (*Bambusa cacharensis*) for the production of reducing sugar. *National Seminar on Science, Technology and Innovation: It's Impact on Communities of N. E. India,* 10-11 Sept 2015, Gauhati University, India.

4. Timung R, **Mohan M**, Banerjee T, Goud VV, (2016). Production of reducing sugars from sugarcane bagasse by subcritical water hydrolysis. 1st International Conference on Bioscience and Biotechnology "*Molecular Life Sciences for the Development in the 21st Century", BioTech-2016*, 12-13 January 2016, the International Institute of Knowledge Management (TIIKM), Colombo, Srilanka.
5. **Mohan M**, Naik PK, Goud VV, Banerjee T. Experimental and Quantum Chemical Calculations for the Dissolution of Cellulose/Hemicellulose in Ionic Liquids, *Gaussian16: Theory and Practice Workshop*, 16-20 Jan 2017, SCUBE Scientific Software Solutions (P) Ltd, New Delhi.
6. **Mohan M,** Goud VV, Banerjee T. Phase Transition Properties, Chemical Purity and Solubility of Coniferyl Alcohol and D-Mannose by Differential Scanning Calorimetry. International Conference on Sophisticated Instruments in Modern Research (ICSIMR-2017), 30th Jun to 1st July 2017, IIT Guwahati, India.
7. Banerjee T, Paul S, Naik PK, Goud VV, **Mohan M**. Solid-Liquid Equilibria and Molecular Modeling Predictions of Glucose in Tetra Butyl Ammonium Bromide based Deep Eutectic Solvents. *Liquids 2017 (10th Liquid Matter Conference)*, 17-21 July 2017, Ljubljana, Slovenia.
8. **Mohan M,** Banerjee T, Goud VV. Dissolution Mechanism of Cellulose in Ionic Liquids: Understanding the Role of Protic and Aprotic Solvents by Molecular Dynamic Simulations. *Thermodynamics 2017*, 5th - 8th Sept 2017, Edinburgh, UK.
9. Attended the *Gaussian16: Theory and Practice Workshop* to be organized by SCUBE Scientific Software Solutions (P) Ltd, held at Radisson Blu, 16th-20th Jan 2017, Delhi (Workshop).
10. Attended the Molecular Simulations Workshop to be organized by Indian Institute of Chemical Engineers - Guwahati Regional Centre (IIChE-GRC), held at Department of Chemical Engineering, IIT Guwahati on 27th Sept, 2017.